Investigating the role of FMRP, CYFIP1 and DDX3X in the processes of mRNA localisation and translation within mesenchymal cells.

Thesis submitted for the degree of
Doctor of Philosophy
at the University of Sussex

By Simon J. Cooper B.Eng (Hons), BSc.
School of Life Sciences
University of Sussex

September 30th 2016

Intentionally left blank.

Acknowledgements

My thanks to Professor Simon Morley, not only for his initial generosity in adopting me within his research group but for his continued support and encouragement to pursue the routes of enquiry which I have taken during my time here.

I have been extremely lucky to have worked with a great postdoctoral researcher - Dr Alice Copsey who has brought a raft of ideas into the laboratory. I am very grateful for her encouragement, constructive criticism and friendship throughout my time in the department.

Other people who I wish to thank for their support in my research include: Dr Mark Willett, for giving me the initial training in tissue culture and microscopy which has enabled me to take images of cells of which I can be proud; Dr Roger Phillips, for his excellent technical support and his wonderful suggestion to investigate use of the *in situ* Proximity Ligation Assay method – which now forms the backbone of this thesis; Dr Mark Osborne, who spent a great deal of time introducing me to laser spectroscopy and super resolution imaging, using his own ingenious design of total internal reflection microscope.

At my time in Sussex I have made many friends, not least my office chums – those clever people who sit and work around me every day and make me happy to be here. To Marta, Alice, Heather, Heena, Ella, Mark, Cat, Karen, Laurie, Deema and Victoria: “VHF! It’s been a lot of fun, thank you.”

Dedications

I dedicate this work to my loving mother, father and sister. Also to Vicki, who picked me up when life tripped me up. And to Bubs, whose harsh but fair words made her by far the wisest cat I ever knew.

University of Sussex

Submitted for the degree of Doctor of Philosophy

Investigating the role of FMRP, CYFIP1 and DDX3X in the processes of mRNA localisation and translation within mesenchymal cells.

Summary

This thesis undertakes to elucidate the roles of the proteins Fragile-X Mental Retardation Protein (FMRP), Cytoplasmic FMRP Interacting Protein (CYFIP1) and the helicase DDX3X, within mesenchymal cells.

Total Internal Reflection Microscopy (TIRFM) was used to look for spatiotemporal colocalisation of FMRP and CYFIP1, as prior work suggests that they function in concert, acting as translational repressors within neuronal cells.

Biochemical methods provided evidence of a Ribonucleoprotein complex consisting of four participants – mRNA, eIF4E, CYFIP1 and FMRP. Using super-resolution microscopy techniques, the interaction of FMRP and CYFIP were established at the leading edge of spreading fibroblasts with a resolution of 50nm.

DXX3X has a known structural helicase domain and evidence suggests that it may be involved in the up-regulation of mRNA translation. Within this thesis, biochemical methods are complemented with standard immunocytochemistry (ICC) to elucidate the role and subcellular location of DDX3X. Using ICC and post-acquisition imaging techniques such as deconvolution, colocalisation of DDX3X with actin stress fibres suggests that DDX3X may be transported intracellularly via actin filaments. Using *in situ* Proximity Ligation Assay (PLA), a bespoke analysis program ‘PLAY’ provides evidence to suggest that DDX3X interacts with the eukaryotic initiation factor eIF4E, whilst travelling along filamentous actin structures to the cell periphery. The interaction between DDX3X and eIF4E at the leading edge of cells appears to correlate with an upregulation in local metabolism and morphology change, suggesting that DDX3X may be involved in the transport and localised translation of proteins needed for cell spreading and motility.

Contents

List of Abbreviations

3B	Bayesian analysis of blinking and bleaching
4E-BP	eIF4E binding protein
Å	Ångström
ADP	Adenosine diphosphate
AJC	Apical junction complex
AMPK	AMP activated protein kinase
APS	Ammonium persulfate
ATP	Adenosine triphosphate
AU	Airy Units
BiFC	Bimolecular fluorescence complementation
BRET	Bioluminescence resonance energy transfer
CASPASE	Cysteine aspartate protease
CDK	cyclin-dependent kinase
CLSM	Confocal Laser Scanning Microscope
CRM1	Chromosome region maintenance-1
CYFIP1	Cytoplasmic FMRP Interacting Protein 1
DAPI	4′,6-diamidino-2-phenylindole
DIC	Differential interference contrast
DISC	Death-inducing signalling complex
DMEM	Dulbecco’s modified eagle medium
DMSO	Dimethylsulfoxide
DOC	Deoxycholate
dsDNA	Double-stranded DNA
ECL	Enhanced chemiluminescence
ECM	Extracellular matrix
EDTA	Ethylenediamine tetra-acetic acid
eEF	Eukaryotic elongation factor
EGF	Epidermal growth factor
EGFR	Epidermal growth factor receptor
eIF	Eukaryotic initiation factor
EMCCD	Electron multiplying charge coupled device
EMT	Epithelial-mesenchymal transition
ERK	Extracellular signal-regulated kinase
FAK	Focal adhesion kinase
FCS	Foetal calf serum
FGFR	Fibroblast growth factor receptor
FISH	Fluorescence in situ hybridisation
FMRP	Fragile-X mental retardation protein
FRET	Förster resonance energy transfer
FWHM	Full-width half max
GAP	GTPase activating protein
GDP	Guanosine diphosphate
GLOX	Glucose oxidase antifade buffer

Grb2	Growth factor receptor-bound protein 2
gRNA	Genomic RNA
GTP	Guanosine triphosphate
HBV	Hepatitis B virus
HCV	Hepatitis C virus
HIV	Human immunodeficiency virus
HR	Homologous recombination
hTERT	Human telomerase reverse transcriptase
ICC	Immunocytochemistry
IF	Immunofluorescence
IgG	Immunoglobulin G
IRES	Internal ribosomal entry site
LMB	Leptomycin-B
M^7GTP	7-methyl guanosine triphosphate
MAPK	Mitogen activated protein kinase
MEK	Mitogen activated protein kinase kinase
MEM	Minimal essential medium
MGMT	0-6-methylguanine-DNA methyltransferase
mLST8	mammalian lethal with sec13 protein 8
Mnk1/2	MAPK-interacting protein kinase 1/2
mRNA	Messenger RNA
MTOC	Microtubule organisation centre
mTOR	Mechanistic target of rapamycin
mTORC1/2	Mechanistic TOR complex 1/2
NA	Numerical aperture
NHEJ	Non-homologous end joining
NLS	nuclear localisation signal
ORF	Open reading frame
p70S6K	70 kDa ribosomal protein S6 kinase
PABP	Poly(A) binding protein
PAGE	Polyacrylamide gel electrophoresis
PALM	Photo-activated localization microscopy
PBS	Phosphate buffered saline
PI3k	Phosphatidylinositide-3-kinase
PIP2	Phosphatidylinositol (4,5)-bisphosphate
PIP3	Phosphatidylinositol (3,4,5)-trisphosphate
PLA	Proximity ligation assay
PLC	Phospholipase C
PMY	Puromycin
PSF	Point spread function
PTEN	Phosphatase and tensin homologue
PVDF	Polyvinylidine difluoride
QD	Quantum Dot
Raptor	Regulatory-associated protein of mTOR
RBP	RNA binding proteins
RCA	rolling circle amplification

RCP	Rolling circle amplicon product
Rictor	Rapamycin-insensitive companion of mTOR
RNA	Ribonucleic acid
RNP	Ribonucleoprotein
RPM	Ribopuromycylation
RRE	Rev response element
RTK	receptor tyrosine kinase
s/n	Signal-to-noise ratio
SDS	Sodium dodecyl sulphate
SG	stress granule
SOFI	Superresolution optical fluctuation imaging
ssDNA	Single stranded DNA
STORM	Stochastic optical reconstruction microscopy
TBS	Tris buffered saline
TCA	Trichloroacetic acid
TEMED	Tetramethylethylenediamine
TIR	Total internal reflection
TIRF	Total internal reflection fluorescence
TIRFM	Total internal reflection fluorescence microscopy
TOS motif	TOR signalling motif
TRAIL	TNF-related apoptosis-inducing ligand
tRNA	Transfer RNA
UTR	Untranslated region
VCA	Verprolin, central, acidic domain
WASP	Wiskott-Aldrich syndrome protein
WAVE	WASP verprolin homologous

1 Introduction

1.0 Overview

Since the conception of biology's central dogma (Crick 1970) and the gradual unravelling of the enigma which is the process of eukaryotic gene expression, it has become clear that there are many hundreds of human RNA binding proteins (RBPs), each of which play a pivotal role in the regulation of intricate metabolic processes - from the transcription of genetic code into precursor mRNA, through to the processes of RNA splicing, its polyadenylation, transport, translation and its ultimate degradation and recycling. Should any of these RNPs malfunction, entire signalling pathways may falter, potentially leading to the onset of human disease and disorders spanning the realms of physical development, intellectual retardation and tumourigenesis (Lukong et al. 2008). Of the 424 known human RBPs (Cook et al. 2011), the work described in this thesis examines the role of a handful of translation-specific mediators. These include eukaryotic translation initiation factors (eIFs) and associated helicases, as well as Fragile X Mental Retardation Protein (FMRP) and its companion protein, Cytoplasmic FMRP Interacting Protein 1 (CYFIP1). These selected proteins interact to control mRNA translation, allowing for responsive, flexible and sometimes subtle second-order modulation of protein synthesis in a spatiotemporal manner.

1.1 Eukaryotic cap-dependent translation

Eukaryotic cap-dependent translation initiation is an exquisitely regulated process. Its role is to properly assemble a translationally competent 80S ribosome at the start codon of the open reading frame of mRNA, in anticipation of translation commencement (Figure 1.1). Translation initiation is generally considered to be the predominant rate-limiting step of the entire process of translation, and the stage which offers the ability for a multitude of regulatory pathways to influence spatiotemporal control of protein expression (Sonenberg & Hinnebusch 2009; Jackson et al. 2010).

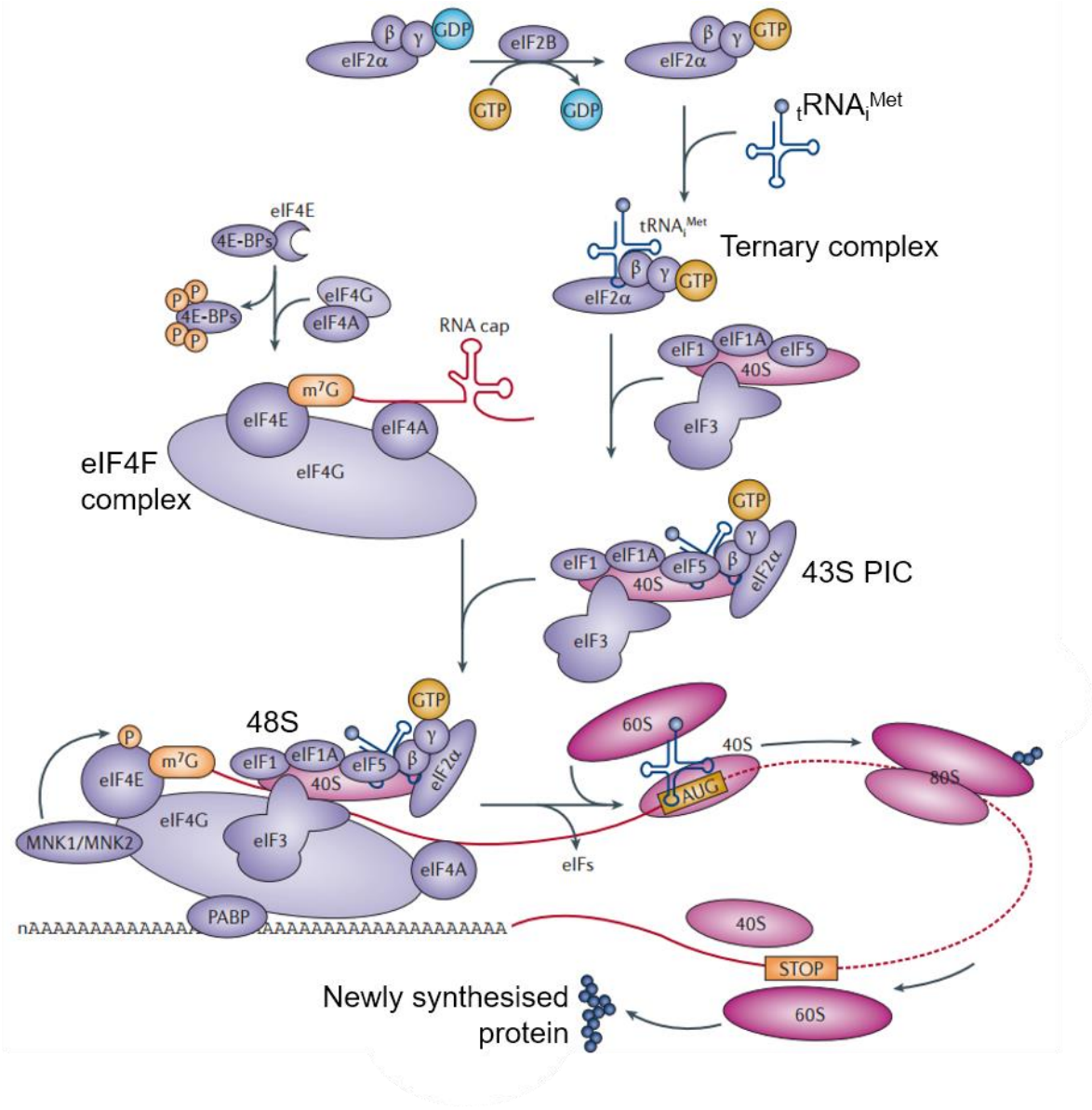

Figure 1.1 An overview of cap-dependent translation initiation

Cap-dependent translation progresses in four phases: initiation, elongation, termination and ribosome recycling.
The assembly of the 43S pre-initiation complex (PIC) is a rate-limiting step, involving the association of the 40S ribosomal subunit with several eukaryotic translation initiation factors (eIF1, eIF1A, eIF3, eIF5) with the ternary complex (TC). eIF4F (a multifactorial complex made up of the cap-binding protein - eIF4E, the scaffold protein - eIF4G, and the RNA helicase -eIF4A), aided by eIF3, recruits the 43S PIC to the mRNA template for the assembly of a 48S initiation complex. Poly(A)-binding protein (PABP) interaction with eIF4G circularises and stabilises the mRNA to increase translation efficiency. The 43S PIC scans the mRNA until it recognises the initiation codon, whereupon eIFs are released and the 60S ribosomal subunit joins to create a translation-competent 80S ribosome, marking the end of the initiation process.

Adapted from Bhat et al. 2015.

To properly understand the initiation process, we must first consider the native structure of mRNA. Newly transcribed mRNAs contain 5' and 3' untranslated regions (UTRs) often programmed to carry specific instructions for their subcellular localisation. To these UTRs, specific RNA binding proteins (RBPs) may attach (Shahbabian & Chartrand 2012). One set of RBPs acts specifically as cytoplasmic chaperones, creating structurally stable ribonucleoprotein particles (RNPs) with the ability to transport mRNA in a translationally repressed state until it arrives at its subcellular destination. Having arrived at their destination, RBPs receive signals to allow for the de-repression of the mRNA cargo, allowing for the activation of eukaryotic initiation factors (Jung et al. 2011; Willett et al. 2013; Keene & Tenenbaum 2002). Initiation can be divided into 8 key stages, all of which are followed by stages consisting of translational elongation, termination and ultimately the recycling of factors (Figures 1.1 and 1.2):

- Met-tRNA$_i$ ●eIF2●GTP ternary complex formation
- Formation of a 43S pre-initiation complex (PIC)
- mRNA activation
- mRNA recruitment of the 43S PIC
- 43S scanning of the mRNA
- Start codon recognition and formation of the 48S complex
- Recruitment of 60S ribosomal subunit to the 48S complex
- Formation of the 80S ribosomal complex

<u>Met-tRNA$_i$ ●eIF2●GTP ternary complex formation</u>

In order that the initiator methionyl-tRNAi (Met-tRNA$_i$) can successfully be delivered to the 40S ribosomal subunit, it is first necessary that a stable ternary complex (TC) is formed consisting of Met-tRNA$_i$ ●eIF2●GTP (Kimball 1999).

Eukaryotic translation initiation factor 2 (eIF2) is a heterotrimeric protein consisting of subunits α, β and γ. It binds initiator methionyl-tRNA in a GTP-dependent manner, yet it exhibits a higher affinity for GDP than for GTP (Erickson & Hannig 1996). Formation of the ternary complex,

Met-tRNA$_i$ ●eIF2●GTP is therefore made possible with the help of a guanine exchange factor (GEF), eukaryotic translation initiation factor 2B (eIF2B). eIF2B is a mediator of general and gene-specific control which is regulated by several diverse signalling pathways (Pavitt 2005). It exhibits multiple regulatory subunits α-, β-, and δ-, all of which are regulated *via* phosphorylation of the γ- subunit. Together, the ε- and γ- subunits performs the catalytic guanine nucleotide-exchange function (Figure 1.2). During nutritional stresses, the α-subunit of eIF2 becomes phosphorylated on Serine 51, and causes eIF2 to change from being a substrate of eIF2B to a competitive inhibitor of eIF2B, thus stopping the guanine exchange from taking place and bringing translation to a halt. In times of stress, lack of availability of a functional eIF2B GEFs causes the formation of a TC to become the rate-limiting step in translation initiation.

Formation of a 43S pre-initiation complex (PIC)

Initiation factors eIF1, 1A, 3 and 5 together induce the 40S 'open' conformation necessary for the accommodation of the ternary complex to form the 43S preinitiation complex (PIC), ready for recruitment to activated mRNA (Trachsel & Staehelin 1978).

eIF1 helps mediate the creation of the 43S PIC, but is also thought to play a part both in start codon recognition (alongside eIF1A) as well as by preventing eIF5 from initiating downstream elongation events until the start codon is reached (Sonenberg & Hinnebusch 2009; Jackson et al. 2010).

mRNA activation

Activation of mRNA, making it ready to receive the 43S PIC, is made possible by the unwinding of the mRNA cap-proximal region, in an ATP-dependent manner by eIF4F in conjunction with eIF4B.

mRNA recruitment of the 43S PIC

Activated mRNA recruits the 43S PIC near the 5' end of the mRNA (Trachsel & Staehelin 1978).

43S scanning of the mRNA

Once recruited to the mRNA, in an open state the 43S ribosomal complex scans the 5' untranslated region (UTR) of the mRNA base by base, in

a 5’ to 3’ direction until a start codon is located. This process requires a number of initiation factors including eIF4A, eIF4B, eIF4F, eIF1 and eIF1A (Sonenberg & Hinnebusch 2009; Jackson et al. 2010). eIF4A, eIF4B and eIF4F are thought to be involved in the remodelling the mRNA secondary structure in the 5’ UTR to allow the 43S pre-initiation complex to scan past secondary structure that would have otherwise inhibit its progression.

Start codon recognition and formation of the 48S initiation complex

Scanning of the mRNA by the 43S PIC is halted upon location of the start codon - with the highest probability being ‘AUG’ codons in the context of the GCCGCC(A/G)CCAUGG consensus sequence (Kozak,1989). Recognition of the AUG start codon lowers the affinity between the ribosome and eIF1, causing its release and bringing a halt to RNA scanning by the concomitant hydrolysis of eIF2●GTP to eIF2●GDP, greatly reducing eIF2’s affinity to initiator methionyl-tRNA, prompting the release of eIF2 - an irreversible step in the initiation stage (Maag et al. 2005). The 43S PIC changes from open to closed and the 48S initiation complex is thus formed.

Recruitment of 60S, and formation of the 80S ribosomal complex

With eIF1 and eIF2 no longer present at the initiation complex, eIF1A and eIF5B/GTP recruit the 60S large ribosomal subunit, joining it to the 40S subunit to create a much larger 80S ribosomal complex, whilst ensuring that the Met-tRNAi is left stably bound at the ribosome peptidyl site. The GTPase activity of eIF5B ensures its dissociation from the complex (Pestova et al. 2001).

At the open reading frame (ORF) and with the presence of the methionine tRNA already set deep into its P site, the 80S ribosome is primed for further anticodon-codon recognition and binding. With the effect of placing the empty ribosomal A site (acceptor site) precisely over the second codon of the ORF in readiness for the arrival of a cognate amino-acyl-tRNA, delivered by eEF1, the process of polypeptide elongation can begin.

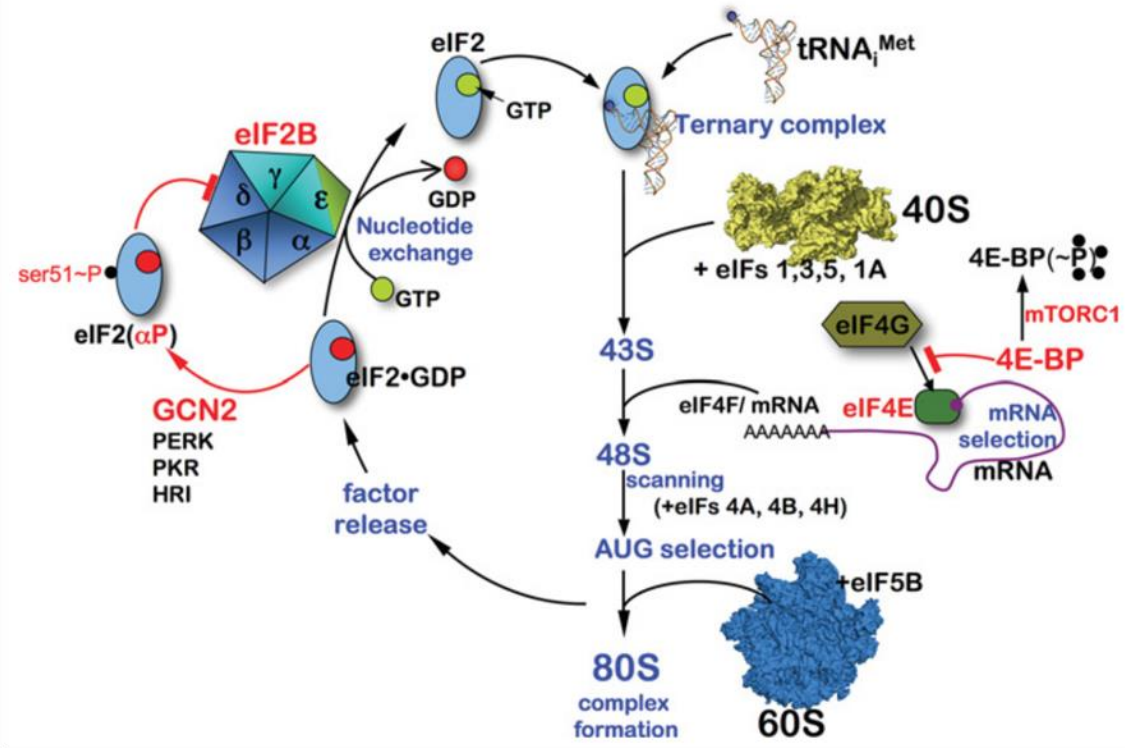

Figure 1.2 Regulatory steps in translation initiation

There are two main regulatory steps controlling translation initiation.
i. Phosphorylation of eIF2 at serine 51 forms a dead-end complex with limiting amounts of eIF2B.
ii. The mRNA cap binding activity of eIF4E is downregulated in the presence of unphosphorylated 4E-BP which has affinity to eIF4E's dorsal surface. mTORC1 phosphorylation of 4E-BPs hinders their ability to bind eIF4E and therefore facilitates cap binding and translation initiation (see text for details).

Figure from Pavitt & Proud 2009.

1.1.1 Helicases and mRNA binding to the 43S PIC

The 43S ribosomal complex is assembled near the 5' end of the mRNA and has to scan along a sometimes structurally complex UTR to reach a start codon. eIF4A, eIF4B and eIF4F are thought to be involved in the remodelling of such secondary structures to allow 43S PIC progression. The helicase eIF4A is thought to unwind structures formed in the UTR via a non-processive mechanism, however, it has been shown to have an ATP-dependent processive helicase activity when complexed with eIF4G and eIF4B (Garcia-Garcia et al. 2015), facilitating the unwinding of such structures. eIF1 and eIF1A are thought to be required to facilitate structural change in the 40S subunit – modulating the shape of the mRNA binding cleft or to reposition the tRNA in the 43S complex (Pestova et al., 2001). Several helicases, including eIF4A (a member of the DEAD-box helicase family, also known as DDX2) bind RNA in the presence of ATP and are utilised in the unwinding of the mRNA 5' UTR secondary structures to help promote ribosomal binding. The exact mode of unwinding remains a contentious issue, with some evidence supporting eIF4A helicase functionality working in parallel with 40S subunit remodelling by DEAH-box helicase DHX29 to help it overcome 5'UTR structures.

There is evidence that many other helicases belonging to the DEA(D/H)-box family may also be recruited to aid in the unwinding of RNA (Parsyan et al. 2011), depending on the secondary structure of the UTR and the docking location of eIF4F with respect to the start codon. The weak helicase activity of eIF4A, additionally stimulated by eIF4G and eIF4B, is known to potentiate ribosome recruitment to eIF4F by proximal duplex unwinding (Garcia-Garcia et al. 2015). Accessory proteins eIF4H and eIF4B share a common binding site on eIF4A, and act on eIF4A in a mutually exclusive manner, providing it with enhanced ability to unwind stable duplexes by modulating eIF4A's affinity to ATP (Rozovsky et al. 2008; Rogers et al. 2001). Other helicases are also important in the unwinding of particularly stable secondary RNA structures. In particular, DEAH-box protein DHX29 has been shown to be required for cap-dependent translation of RNAs with highly structured 5'UTRs (Parsyan et al. 2011), associating with the 40S ribosomal subunit and strongly stimulating 48S complex formation (Pisareva et al. 2008; Parsyan et al. 2009).

Another helicase, DDX3X, has been of particular interest to researchers in recent years. DDX3X is an ATPase-dependent RNA helicase, found in many eukaryotes including humans and yeast (Jankowsky 2011), and has been found to participate in both nuclear functions and cytoplasmic functions, working as a chaperone taking RNA between these two cellular compartments. It is implicated in various and varied roles with respect to RNA metabolism (Rosner & Rinkevich 2007), including RNA splicing, mRNA transport (Mahboobi et al. 2015), and cell cycle regulation and apoptosis (Li et al. 2014). Most interestingly for this research, DDX3X has also been suggested to have important roles in translational control with evidence for interactions with eukaryotic initiation factors eIF4A, eIF4E, eIF4G and PABP1 (Lai et al. 2008; Lai et al. 2010; Soto-Rifo et al. 2012).

1.1.2 Cap-binding protein eIF4E

eIF4E stimulates cap-dependent translation, with mRNAs expressing different dependencies on this cap-binding protein. mRNAs with large amounts of structure in their 5' UTR rely more on eIF4E for translation initiation than those with less structure (Robert et al., 2009). In 1977 the three-dimensional structure of slightly truncated mouse and yeast eIF4E bound to the cap analogue m^7GDP was solved by X-ray crystallography and NMR, respectively (Marcotrigiano et al. 1997; Matsuo et al. 1997). In addition, high-resolution crystal structures of human eIF4E bound to the cap analogues m^7GTP and m^7GpppA have been determined (Tomoo et al. 2005) (Figure 1.3). Collectively, these high-resolution structures revealed that the cap-binding protein has an overall shape of a cupped hand. Cap-binding occurs in the narrow hydrophobic slot on the concave surface of eIF4E by specific interactions with the m^7GTP moiety and with the 'downstream' phosphate groups. eIF4E associates with the mRNA *via* the mRNA cap and with eIF4G *via* a common site it shares with 4E-BP1 (YXXXXLφ, where φ is either Leu, Met or Phe) (Asano & Sachs, 2007. Robert & Pelletier, 2009). eIF4E is a phosphoprotein and its major phosphorylation site is found at Ser209 in humans; phosphorylation is implicated in protein synthesis regulation and mediated by Mnk1 and Mnk2 (see later). eIF4E phosphorylation at Ser209 has been shown to be required for the oncogenic properties of eIF4E (Furic et al. 2010; Ueda et al. 2010).

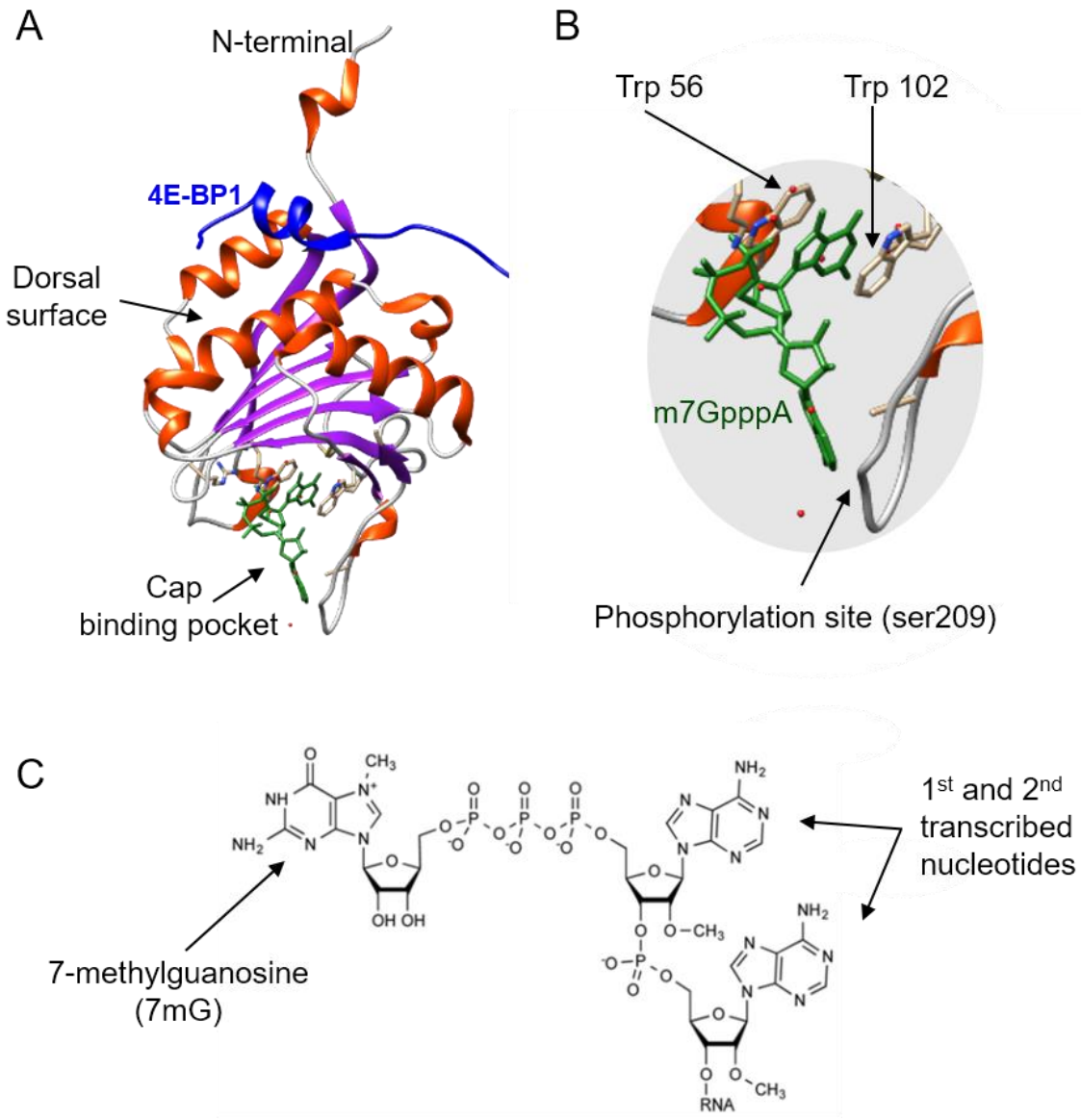

Figure 1.3 The structure of the eukaryotic cap-binding protein, eIF4E

Figures visualised using UCSF Chimera (Pettersen et al. 2004) and based on data from PDB ID: 1WKW (Touw et al. 2016; Tomoo et al. 2005).
Panel A. eIF4E is an 8-stranded antiparallel β sheet core (shown magenta) with a dorsal surface of three long α helices. A ventral concave surface in eIF4E provides a binding site for the 7-methylguanosine (7mG) mRNA cap structure (green stick visualisation of the ligand). Binding protein 4E-BP1 shown in blue. **Panel B.** 7mG recognition by eIF4E is mediated by two conserved tryptophans, Trp 56 and Trp 102, as well as by the formation of three hydrogen bonds and a van der Waals contact between its methyl group and a third conserved tryptophan (Marcotrigiano et al. 1997). The most studied post-translational modification of eIF4E is phosphorylation at Serine 209 (Flynn & Proud 1995). **Panel C.** The 7mG cap structure, including a depiction of the first and second nucleotides.

1.1.3 eIF4G

Mammalian eIF4G is a large protein that serves as an assembly platform for other components of the translational apparatus (reviewed in Sonenberg & Hinnebusch 2009; Jackson et al. 2010). Two forms of mammalian eIF4G have been characterised, eIF4GI and eIF4GII. The predominant form, eIF4GI, consists of a family of five isoforms, which differ by the length and sequence of their amino-termini (Imataka et al. 1998). The individual isoforms of eIF4G share similar biochemical activities and have distinct, but ill-defined roles in the initiation process. The binding regions for several binding partners of eIF4G have been mapped by deletion and mutation analysis.

The amino-terminal fragment of eIF4G interacts directly with eIF4E (Mader et al. 1995; Imataka et al. 1998) and PABP (Imataka et al. 1998). The interaction between eIF4E and eIF4G occurs by an induced-fit mechanism, whereby the unstructured eIF4E-binding region of eIF4G assumes the structure of an α-helix with two turns upon binding to eIF4E (Marcotrigiano et al. 1999; Mathews et al. 2007). The phylogenetically conserved central fragment of eIF4G contains binding sites for eIF4A (Imataka & Sonenberg 1997; Lamphear & Panniers 1989) and eIF3 (Lamphear & Panniers 1989; Villa et al. 2013) and possesses RNA-binding activity (Goyer et al. 1993). This central segment constitutes the primary ribosome recruitment module via interaction with eIF3 subunits c ,d, and e (Villa et al. 2013). The carboxy-terminal fragment of eIF4G contains a second, independent binding site for eIF4A (Lamphear et al. 1995). A conserved region at the extreme c-terminus of eIF4G, the W2 domain, which shows homology to eIF5 and eIF2Bε (Aravind & Koonin 2000), serves as a binding site for the eIF4E kinase, Mnk1 (Khaleghpour et al. 1999). Besides serving as a scaffold for the assembly of the translational machinery, eIF4G also influences the activity of other initiation factors. Binding of eIF4G to eIF4E markedly increases eIF4E binding affinity for the mRNA cap (Matsuo et al. 1997; Haghighat & Sonenberg 1997), and the interaction of eIF4G with PABP increases the helicase activity of eIF4F (Sonenberg & Hinnebusch 2009). The eIF4F cap-binding complex (eIF4E, 4A, 4G) conducts the 43S preinitiation complex to the 5' end of the mRNA via interactions between the m^7G cap of the mRNA and eIF4E, and between the central region of eIF4G and eIF3 (see

Figure 1.1). In addition, eIF4G also serves to create a physical link between the 3'UTR and the translational apparatus via its interaction with poly(A) binding protein (PABP). Thus, circularisation of the mRNA is performed using PABP and eIF4F as a bridge between 5' and 3' ends of the mRNA (Tarun & Sachs 1996), stabilising the RNA in a 'closed loop'. This reduces the susceptibility of the mRNA to degradation by exonucleases, as well as activating the mRNA as a potential translational substrate, and enhancing ribosome reinitiation during translation. Regulation of this interaction is through the targeting of the interface between eIF4E and eIF4G by inhibitory eIF4E binding proteins (eIF4E-BPs).

1.1.4 4E-BP1 and translational control

In a hypophosphorylated state, 4E-BP1 strongly competes with eIF4G for eIF4E, by way of common binding motifs (Mader et al. 1995). When 4E-BP1 is hyperphosphorylated by a hormone/growth factor-stimulated, Mammalian Target of Rapamycin Complex 1 (mTORC1) (Gingras et al. 1999), there is an abrogation of eIF4E-binding, allowing eIF4G to bind to eIF4E and the eIF4F complex to form (Gingras et al. 2001). The signalling pathway is summarised in Figures 1.4 and 1.5. The PI3K-mTORC1 pathway collects signals coming in from growth factors and hormones and converts it into an effect on eIF4E availability. Growth factor signals are received at the plasma membrane by receptor tyrosine kinase receptors, which then phosphorylate and activate PI3K. PI3K activation leads to the activation of Akt/PKB. Akt inhibits the Rheb-GAP TSC2. The Rheb-GTP binds to and activates mTORC1 on the lysosome. Growth factors also regulate mTORC2 by an ill-defined mechanism (Laplante & Sabatini 2013b). One role of mTORC2 is to phosphorylate AGC kinases, such as AKT, which regulate cell survival and cell cycle progression (Hsieh et al. 2012; Zoncu et al. 2011). The role of mTORC2 as a central regulator of the cytoskeleton is also well established (Zoncu et al. 2011). In contrast, mTORC1 is well studied and phosphorylates several other proteins including 4E-BP1. 4E-BP1 has the same eIF4E-binding region as eIF4G: YXXXXLϕ (Joshi et al. 2004; Joshi 2014). Therefore, when hypo-phosphorylated, 4E-BP1 competes with eIF4G for eIF4E binding. Following the binding of a growth factor to a receptor tyrosine kinase on the cell membrane,

the PI3K-Akt-mTOR signalling cascade is activated resulting in mTORC1 kinase-dependent phosphorylation of 4E-BP1. Initially, this occurs on Thr37 and Thr46 (Figure 1.5A), requiring the recruitment of 4E-BP1 *via* its RAIP motif to Raptor, a component of the mTORC1 complex (Laplante & Sabatini 2013b). Hyperphosphorylation of 4E-BP1 on Ser65 and Thr70 is mediated by an unknown mTORC1-associated kinase recruited to 4E-BP1. This five amino acid sequence found in the N-terminus of all known S6 kinases and in the C-terminus of the 4E-BPs, has been named the TOR signaling (TOS) motif, and is considered absolutely necessary for phosphorylation and regulation of S6K1 and 4E-BP1 by mTOR (Schalm & Blenis 2002). Under these hyper-phosphorylated conditions, 4E-BP1 is unable to bind to eIF4E. In short, this means that the output of a growth factor receptor or hormone binding to a receptor on the plasma membrane is an increase in available eIF4E. Recent evidence suggests mTORC1 may not be the only kinase responsible for phosphorylating 4E-BP1. Having confirmed the effect of mTOR kinase inhibitors, one study showed that in a colorectal cancer cell line, absence of mTORC1 kinase activity did not preclude the phosphorylation of 4E-BP1 (Jiang et al. 2015). Another study has showed that the Mnk1/2 can phosphorylate 4E-BP1, which means it could be the activity of the Mnk1/2 which is responsible for this phosphorylation of 4E-BP1 in the absence of mTORC1 kinase activity (Grzmil et al. 2011). One of the other targets of mTORC1 is S6K1. This kinase can inactivate IRS1, upstream of mTOR, as part of an established feedback loop (Laplante & Sabatini 2012; Hou et al. 2012). S6K1 also has quite a broad input in terms of cell physiology, impacting on transcription, metabolism and (Laplante and Sabatini, 2012, Hou, 2012). Nutrient availability, cellular energy and oxygen availability - crucial factors in a cell's decision to divide - all feed into the PI3K-Akt-mTOR pathway at different levels (Laplante & Sabatini 2013a). Nutrient and amino acid availability is sensed by the Rag proteins on the lysosomal surface. When amino acids are plentiful, Rag proteins activate mTORC1 present on the lysosome surface (Laplante and Sabatini, 2012, Hou, 2012) to promote protein synthesis and cell growth.

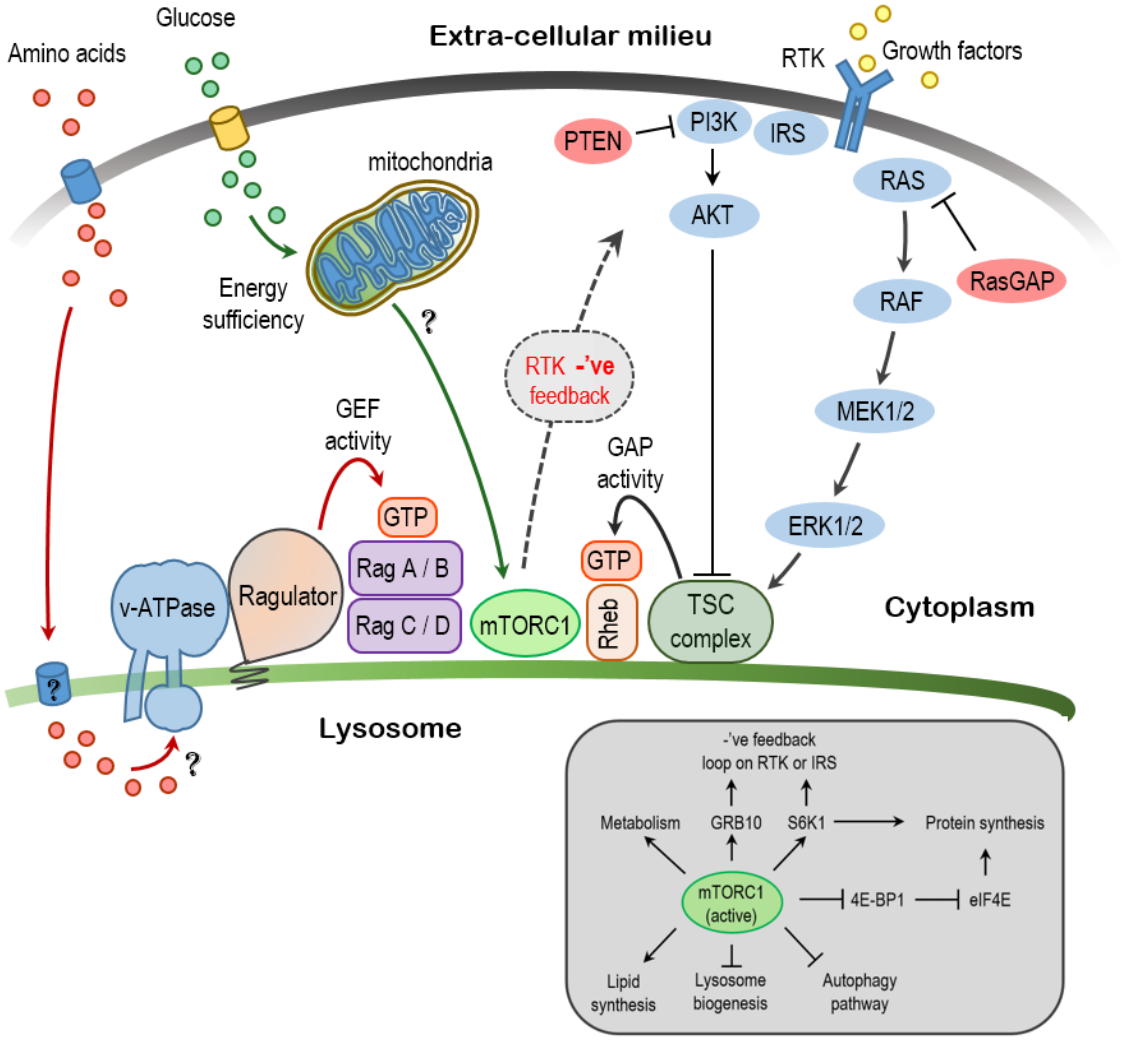

Figure 1.4 mTOR signalling regulates 4E-BP1 phosphorylation.

Activation of receptor tyrosine kinases (RTKs) by growth factors promotes PtdIns(3,4,5)P_3 production through phosphoinositide 3-kinase (PI3K), an event that is required for the activation of AKT. This promotes mTORC1 action by phosphorylating and inactivating the tuberous sclerosis complex (TSC), a protein complex composed of TSC1 and TSC2 (see Laplante and Sabatini 2013). TSC1 and TSC2 are key upstream regulators of mTORC1 and function as a GTPase-activating protein (GAP) for the Rheb GTPase. The GTP-bound form of Rheb directly interacts with mTORC1 on the lysosome and strongly stimulates its kinase activity. TSC1 and 2 impair mTORC1 by converting Rheb into its inactive GDP-bound state. The extracellular-signal-regulated kinase 1/2 (ERK1/2) and ribosomal S6 kinase (RSK1), which are both activated by the Ras pathway downstream of RTKs, also promote mTORC1 activity by phosphorylating and inhibiting TSC1 and TSC2. Sustained activation of mTORC1 leads to the retro-inhibition of RTK signalling *via* GRB10, S6K1and mTORC1 itself. mTORC1 also phosphorylates and inhibits 4E-BP1; along with S6K, this promotes translation.

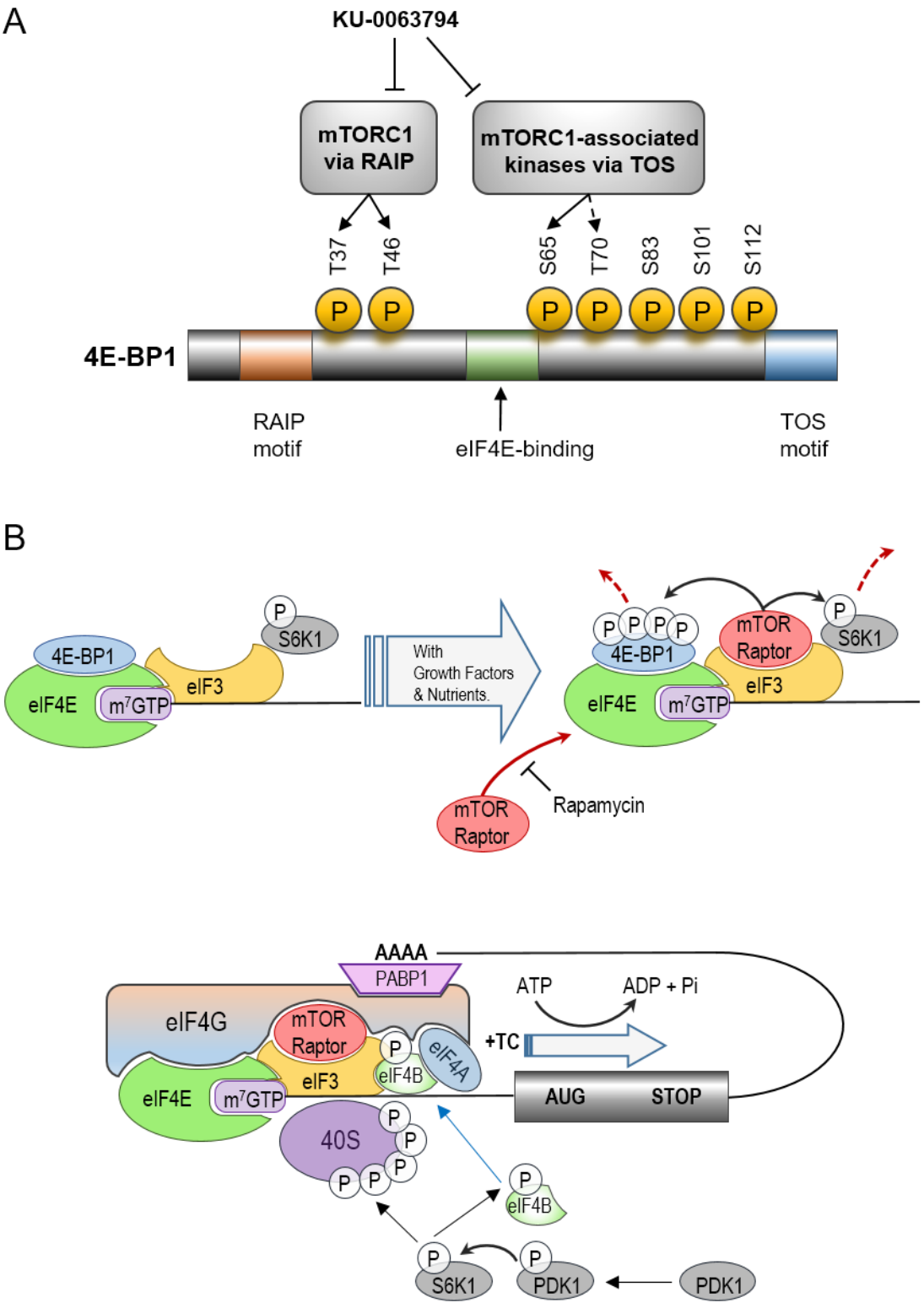

Figure 1.5 mTORC1 influences translation initiation
Panel A. mTORC1-dependent phosphorylation sites on 4E-BP1 regulate binding to eIF4E. **Panel B.** Model of Dynamic Interaction between the eIF3 Complex and mTOR/Raptor, S6K1, and eIF4B. Adapted from Holz *et al.*, 2005.

1.1.5 eIF4E phosphorylation

The role of eIF4E in translational control has been intensively studied since it was determined that phosphorylation correlates with an increase in protein synthesis and cell growth (Scheper et al. 2002; McKendrick et al. 2001). Treatment of cells with various growth-promoting agents results in an increase in eIF4E phosphorylation and a concomitant increase in protein synthesis rates. In contrast, conditions that promote a decrease in protein synthesis are associated with the dephosphorylation of eIF4E. In mammalian cells, eIF4E is phosphorylated at Ser209 in response to serum, growth factors, hormones, phorbol esters, cytokines and various stresses (Xie et al., 2016). The kinases responsible, the MAP-kinase signal-integrating kinases 1 and 2 (Mnk1/2) act at the convergence point for the mitogen-activated protein kinase (MAPK/Erk) and p38 MAP kinase signalling pathways (Waskiewicz et al. 1997). Mnk1/2 phosphorylates eIF4E on serine 209 both *in vitro* and *in vivo* (Pyronnet et al. 1999; Waskiewicz et al. 1999), with the latter being dependent upon its interaction with eIF4G (Pyronnet et al. 1999). Two Mnk human genes have been identified, expressing Mnk1 and Mnk2 proteins that are ~72% identical in their amino acid sequence (Slentz-Kesler et al. 2000). Alternative splicing in the two Mnk genes further revealed the existence of four isoforms: Mnk1a, Mnk1b, Mnk2a, and Mnk2b (Waskiewicz et al. 1997). Bearing a nuclear localisation signal and a polybasic sequence in the common basic N-terminal stretch which interacts with eIF4G, all four isoforms preferentially phosphorylate eIF4E. This pathway is essentially distinct from mTORC1 signalling which regulates the availability of eIF4E to participate in translation initiation. Whilst phosphorylation has only a small effect on the binding efficiency of eIF4E to the mRNA cap, it is a major driver of oncogenesis in a number of tumours (Bramham et al. 2016).

1.1.6 Signalling pathways investigated in this work

Translational control, like most signalling pathways, is highly complex and adaptable, which makes it difficult to find suitable drug targets to efficiently target this process. The negative feedback loops and interconnectivity of signalling pathways combined with the ability of other pathways to adapt and compensate for others mean that cancer cells can acquire resistance to drugs targeting signalling proteins. Examples of this include the acquired resistance to AZD6244, the MEK inhibitor, and trastuzumab, which targets the HER2 receptor. Another problem is that particular domains - catalytic domains and, especially, ATP-binding sites - are well conserved amongst kinase proteins meaning drugs designed to target a particular signalling protein often affect other signalling proteins.

The Mnk1/2 inhibitor CGP57380 had been shown to be effective at inhibiting the growth of cancer cells, in particular, the breast cancer cell line AU565. AU565 cells over-express HER2, which is frequently mutated in aggressive breast cancers (Chrestensen et al. 2007). These cells also exhibit increased Mnk1 and Mnk2 activity (Chrestensen et al. 2007). However, when CGP57380 was tested against an extensive panel of kinases it was found to be a relatively weak inhibitor of the Mnk1/2 and more worryingly that it inhibits other kinases such as MKK1, CK1 and BRSK2 with similar potency (Bain et al. 2007). In addition, CGP57380 was also found to inhibit RSK, which is involved in a negative feedback control loop. RSK and Mnk1/2 are activated by ERK, and RSK then acts upstream to inhibit MEK – the kinase responsible for activating ERK, which subsequently inhibits the activity of Mnk1/2 (Figure 1.6). By inhibiting RSK and thereby blocking the negative feedback loop, CGP57380 was shown to slightly induce Mnk1/2 activity (Zhang et al. 2008). Despite the explicit concern of Bain et al – “CGP 57380 is not a specific inhibitor of MNK isoforms and results obtained from its use in cell-based assays are difficult to interpret” – CGP57380 is still commonly used in published studies (Bain et al. 2007). This means that any findings based on experiments using CGP57380 have to be taken with a degree of caution or be backed up with genetic knockout studies or more selective Mnk inhibitors.

Rapamycin, an allosteric mTORC1 inhibitor which binds to cellular FKBP-12, has provided the basis for many functional studies of TOR proteins. Although rapamycin is effective at inhibiting mTORC1, mTORC2 is insensitive to rapamycin and 4E-BP1 is often insensitive to rapamycin (Choo et al. 2008). 4E-BP1 can still be phosphorylated in the presence of rapamycin and cap-dependent translation can still occur (Choo et al. 2008). Consequently, cells continue to proliferate in the presence of rapamycin (Dowling et al., 2010). To find out more about how mTOR regulates cell proliferation, ATP-competitive mTOR inhibitors such as PP242, have been developed to inhibit mTORC1. Although ATP-competitive inhibitors are more effective than rapamycin at inhibiting cell proliferation the effect is not due to the additive inhibition of mTORC2 (Feldman et al. 2009). Instead, the stronger anti-proliferative effect of TORKinibs is due to the improved inhibition of mTORC1 kinase (Feldman et al. 2009). One such inhibitor, KU0063794 has been used in the work described here; it functions to inhibit both mTORC1 and mTORC2 in mammalian cells (Figure 1.6). The adaptability and interconnectivity of signalling pathways and the problem this poses for specifically inhibiting pathways is illustrated by AZD8055, a dual mTORC1 and mTORC2 inhibitor. A study by Cope at al. (2014) showed that cells grown in the presence of AZD8055 could acquire resistance to AZD8055 by overexpressing eIF4E (Cope et al. 2014).

The interconnectivity of the RAS/MEK/Mnk1/2 and PI3K/Akt/mTOR pathways means that inhibiting one pathway on its own, PI3K/Akt/mTOR, is not sufficiently potent. Some of the crossovers between the two pathways are only just being uncovered. Over the last few years, there have been several papers linking Mnk2 and mTOR. Mnk2 was seen to inhibit mTOR-dependent phosphorylation of p70S6K, but also rapamycin, an inhibitor of mTORC1, appeared to increase phosphorylation of eIF4E by phosphorylating a site (Ser437) on Mnk2a (Stead & Proud 2013; Zhang et al. 2015). A more recent study has suggested that this rapamycin-dependent increase in eIF4E phosphorylation might not be solely dependent on Mnk2 (Teo, Yang, et al. 2015). One way of overcoming the problem of acquired resistance in cancer cells is to use drugs in combination. Combination therapies involving the combined inhibition of the RAS-MEK-Mnk1/2 and PI3K-Akt-mTOR pathways have yielded some promising results. The combined use of AZD6244 and

rapamycin in two prostate cancer models (BxPC-3 and MIA PaCa-2) increased the levels of cell cycle arrest and apoptosis. This caused a marked improvement in growth inhibition compared to that caused by each inhibitor on its own. A common caveat to combination therapies is increased toxicity. Crucially, the combined use of AZD6244 and rapamycin did not appear to have any toxicity (Cope et al. 2014). This lack of apparent toxicity is somewhat surprising; an explanation could be that both drugs act on proteins relatively far down their respective signalling pathways, which limits the number of additional pathways they might affect. Another reason is that these pathways have a common output: eIF4E availability.

An increasing body of evidence has demonstrated the potential antileukaemic properties of Mnk1/2 inhibitors (Altman et al. 2013; Diab et al. 2014). Cercosporamide, a nonselective Mnk1/2 inhibitor (Konicek et al. 2011), reduced proliferation in MM6, K562, and U937 cell lines in a dose-dependent manner (Altman et al. 2013). The cell-specific effects of Mnk1/2 inhibition have been recently confirmed (Diab et al. 2014). A new generation of Mnk1/2 inhibitors is under investigation. A potent dual-specific Mnk1/2 inhibitor (MnkI-19, 4-((4-fluoro-2-isopropoxyphenyl)amino)-5-methylthieno[2,3-d]pyrimidine-6-carboxylic acid) has been used to provide mechanistic insights into the effects of Mnk isoforms on leukaemia cells. MnkI-19 reduced the level of phosphorylated eIF4E and subsequently caused G1 phase cell cycle arrest and apoptosis in AML cells (Teo, Lam, et al. 2015). The combination MnkI-19 and rapamycin resulted in a more pronounced reduction in levels of p-4E-BP1^{T70} than when either a Mnk inhibitor or rapamycin was used alone. Coincident with this reduction in p-4E-BP1^{T70}, was a reduction in eIF4E-eIF4G binding and cell proliferation (Teo, Lam, et al. 2015). MnkI-19 has been used in this work to investigate the role of Mnks in cell migration and localisation of eIF4E in spreading cells (Figure 1.6).

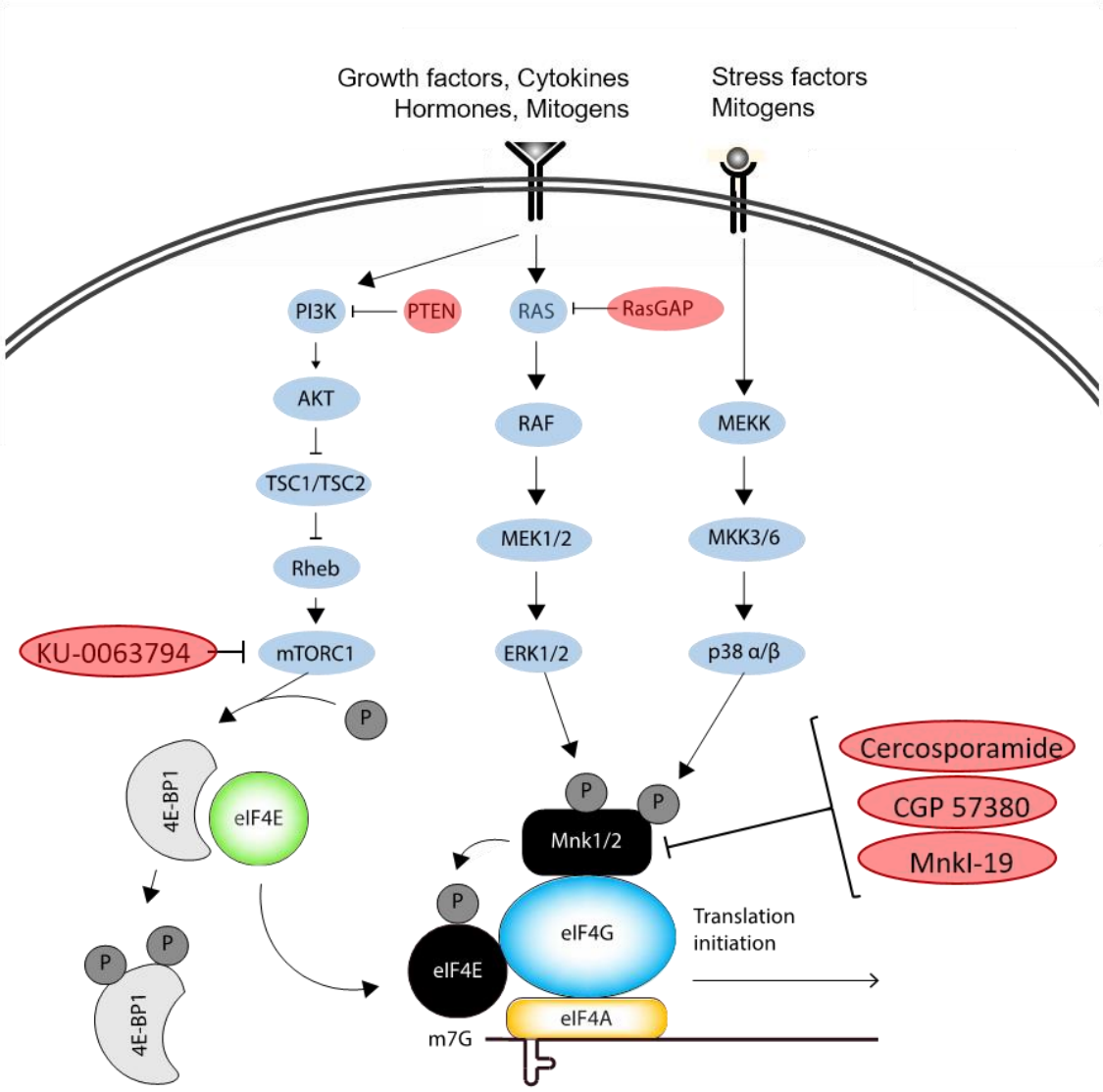

Figure 1.6
An outline of the key signalling pathways responsible for regulating Mnk kinase activity and phosphorylation of eIF4E.

The Mnk-eIF4E axis serves as a convergence point for signals initiated at the surface of the cell – the plasma membrane – by growth factors and other ligands binding to receptors, such as the receptor tyrosine kinases (RTKs). The RAS-RAF-MEK-ERK pathway and the MEKK-p38MAPK pathway activate Mnk1/2 activity directly by phosphorylating distinct sites on the Mnks. PI3K-AKT-mTORC1 activity, indirectly, influences Mnk-dependent phosphorylation of eIF4E: phosphorylation of 4E-BP1, by mTORC1, releases eIF4E, which can then bind to eIF4G where it can then be phosphorylated by the Mnks.

Action sites of inhibitors used in this work (Cercosporamide , CGP 57380, MnkI-19 and KU-0063794) are shown.

1.2 Cell migration

Cell migration plays a critical role throughout human development and physiology, including the spatial orientation of cells within an embryo through to the ability to heal a wound (Yamaguchi & Condeelis 2007). Not all cell migration is beneficial. Cell migration allows cancer cells to spread to other parts of the body. This process, metastasis, is responsible for 90% of all cancer deaths (Chaffer & Weinberg 2011). Therefore, an understanding of the cellular processes involved in cell migration, will improve our understanding of some key physiological processes, but also help to guide the development of anti-cancer drugs (Chaffer & Weinberg 2011; Yamaguchi & Condeelis 2007). Cell migration relies on the driving force of a particular type of cell membrane protrusion called a lamellipodium (Yamaguchi & Condeelis 2007). Lamellipodia are sheet-like protrusions, which attach to a substrate and pull the cell forward (Yamaguchi & Condeelis 2007). Another membrane protrusion, called filopodia, are also believed to be important in directing cell movement in response to external cues. However, the precise role of filopodia in migration is not known (Yamaguchi & Condeelis 2007).

1.3 Cytoskeletal rearrangement

The formation of cellular protrusions is an active process driven by rearrangements of the cytoskeleton. These cytoskeletal rearrangements are initiated by signalling pathways activated in response to the sensing of external chemo-attractants. Lamellipodia, the protrusions that produce the driving force for cell migration, are formed as a result of localised actin polymerisation (Figure 1.7). Actin polymerisation requires free barbed ends. Free barbed ends can either be produced by forming new actin filaments, a process initiated by the Arp2/3 complex, causing breaks in existing actin filaments by cofilin, or uncapping barbed ends on existing actin filaments (Zigmond 2004; Yamaguchi & Condeelis 2007).

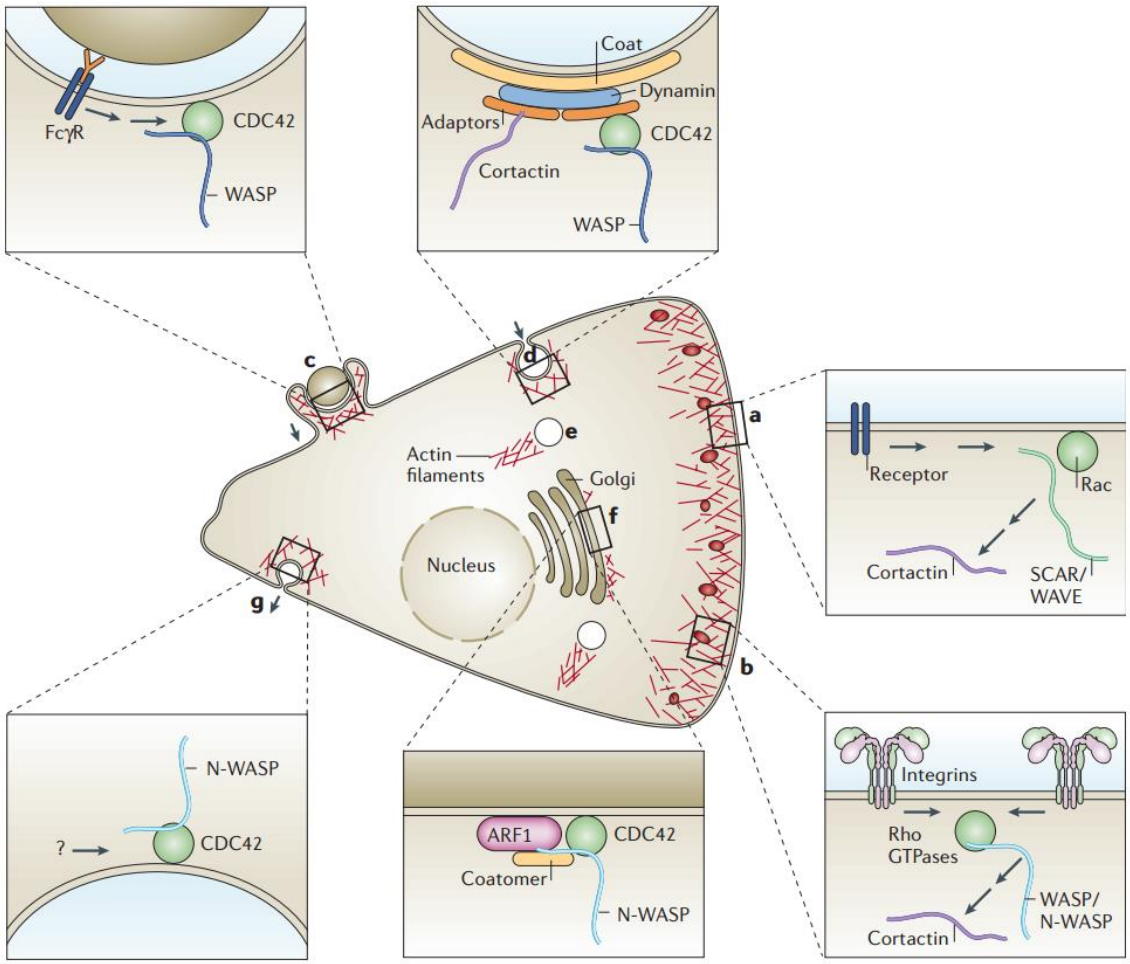

Figure 1.7 WASP and WAVE1 proteins during cell migration

The actin-related protein-2/3 (ARP2/3) complex organises actin filaments (red lines) into branched networks that are capable of generating protrusive force and resisting mechanical deformation. Its nucleation and branching activities are implicated in (a) lamellipodial protrusion, (b) adhesion and podosome formation, (c) phagocytosis, (d) endocytosis, (e) vesicle and organelle motility, (f) trafficking within and from the Golgi apparatus, and (g) exocytosis. Insets illustrate the nucleation-promoting factors (NPFs) that have been demonstrated to be involved. During lamellipodia protrusion (a) and adhesion (b), engagement of transmembrane proteins (integrins and receptors) causes activation of Rho-family GTPases (CDC42 and Rac) and NPFs, leading to ARP2/3-mediated actin polymerisation.

Adapted from Goley & Welch 2006

1.4 WASP and WAVE

The activity of the Arp2/3 complex is regulated by the WASP protein family, and are characterised by their tripartite VCA (verprolin, central, acidic) domain which is capable of binding actin monomers and the Arp2/3 complex to stimulate actin polymerization (Cory et al. 2003). In mammalian cells, the WASP protein family consists of five proteins: WASP, N-WASP, WAVE1, WAVE2 and WAVE3 (Yamaguchi & Condeelis 2007). Several upstream signalling pathways converge on, and activate, the WASP proteins, which by activating Arp2/3 complex drives the actin nucleation necessary for cell migration (Millard et al. 2004). There are several signalling pathways believed to link receptors responding to chemoattractants at the cell surface to the WASP proteins, which initiate the formation of cellular protrusions (Figure 1.8). In a resting state, the WASP and N-WASP proteins are auto-inhibited and its own amino-terminal domain binds the VCA, which is responsible for binding to and activating the ARP2/3 complex. It is only when a Rho GTPase, such as Cdc42 or Rac binds to WASP or N-WASP that its auto-inhibition is removed and ARP2/3 can be activated (Eden et al. 2002). WASP is only expressed in hematopoietic cells, such as macrophages and dendritic cells. N-WASP is expressed ubiquitously but is particularly abundant in the brain. Several reports link WASP and N-WASP to a role in membrane protrusions called invadopodia, which are involved in cell invasion. It is thought that WASP and N-WASP are involved in the endocytosis of matrix components that have been degraded as a result of cell invasion. Cell invasion is an important part of metastasis, as it allows cancer cells to break out of their tissues. N-WASP has been shown to play an important role in invadopodia formation in carcinoma cells – cancer of the epithelial cells. The role of WASP in driving invadopodia formation in macrophages and dendritic cells is a vital part of the immune system. In patients with Wiskott–Aldrich syndrome, characterised by immune deficiency, their macrophages are unable to form invadopodia due to a mutation in WASP (Yamaguchi & Condeelis 2007).

WAVE1 is regulated differently. WAVE1 exists in a complex which inhibits its activity (Eden et al. 2002). This complex contains PIR121 (also known as CYFIP) NCKAP1, Abi, NAP125 and HSPC300 (Eden et al. 2002).

What is clear is that Rac1 invadopodia and Nck activate WAVE1 by causing WAVE1 to dissociate from the inhibitory complex (Figure 1.9) (Eden et al. 2002; Kurisu & Takenawa 2010). PIP3, a phosphoinositide, a product of PI3K activity has also been shown to be important for recruiting WAVE2 to polarised membranes in order to induce lamellipodia formation (Oikawa et al. 2004). As well as regulating the WAVE proteins, phosphoinositides have also been reported to regulate WASP (Yamaguchi & Condeelis 2007). CYFIP1 and CYFIP2 (also known as PIR121) are members of a gene family highly conserved during evolution (Schenck et al., 2001). They are components of the canonical WAVE regulatory complex (Figure 1.9B). The WAVE complex transduces Rac signalling via CYFIP1 to trigger Arp2/3-dependent actin nucleation (Cory and Ridley, 2002; Derivery et al., 2009; Abekhoukh and Bardoni, 2014). CYFIP1/2 interact with the small Rho GTPase Rac1. Upon this binding the sub-complex CYFIP1/2, Nckap1/ABI1 leaves the inactive WAVE holo-complex. While WAVE can now interact with Arp2/3, the CYFIP1-containing sub-complex is available to interact with other proteins (Figure 1.9) and then also with FMRP. Previous work has shown that the FMRP/CYFIP interaction is GTP-dependent (Bardoni et al. 2001; Schenck et al. 2003). Purified Rho GTPase, Rac1, can bind and activate recombinant WAVE complex in vitro (Lebensohn & Kirschner 2009) and the crystal structure of the WAVE complex identified a potential binding site for Rac1 in CYFIP1 (Chen et al. 2010).

WAVE 2, like N-WASP, is ubiquitously expressed. Particularly high levels of WAVE2 are found in hematopoietic cells. WAVE 1 and WAVE 3 are expressed at low levels in a range of tissues but are expressed at high levels in the brain. WAVE 2 is believed to be an important driver of metastasis in cancer. Analysis of patient samples, by immunohistochemistry, showed that WAVE 2 was expressed in metastatic human lung cancer cells (Semba et al., 2006). An association was also drawn between WAVE 2 expression and patient prognosis (Semba et al., 2006). An experiment in a mouse melanoma cell line showed that WAVE 1 and WAVE 2 expression correlates with the progression towards metastasis: WAVE1 was later found to have little influence on this progression, suggesting that it was primarily down to the role of WAVE2 (Kurisu & Takenawa 2009). Suppressing WAVE2 expression has also been shown to inhibit

lamellipodia and, consequently, metastasis in a human sarcoma cell line (Huang et al. 2006). Interestingly, WAVE2 does not appear to be important for invadopodia formation in cancer. The role of WAVE2 seems to be restricted to lamellipodia formation and cell migration (Yamaguchi & Condeelis 2007). WAVE3 has been linked with cancer cell migration, but its exact role is unclear (Sossey-Alaoui, Li, et al. 2005). Evidence from knockdown studies in adenocarcinoma cell lines suggests that WAVE3 could be important for regulating the expression of matrix metalloproteinases, which are important for cell invasion (Sossey-Alaoui, Ranalli, et al. 2005).

1.5 Cofilin

The direction a cell moves in is dictated by the activity of cofilin (Ghosh et al. 2004). Cofilin activity has been shown to be important for directional cell migration of carcinoma cells in response to epidermal growth factor (EGF) stimulation (Mouneimne et al. 2004). Cofilin is a protein capable of binding to both actin monomers and filaments, in which it can induce a break. At rest, cofilin exists in a trans-inhibitory complex with Phosphatidylinositol (4,5)-bisphosphate (PIP2). Activation of phospholipase C (PLC), for example in response to EGF binding to an EGF receptor, hydrolyses PIP2 releasing cofilin (Mouneimne et al., 2004). As well as initiating the release of cofilin, EGF simultaneously activates LIM kinase. LIM kinase then activates the free cofilin in localised bursts (Song et al. 2006). The localised bursts of cofilin activity cause localised actin polymerisation, which results in the formation of lamellipodia to pull the cell forward in a particular direction (Song et al. 2006; Yamaguchi & Condeelis 2007). The balance between LIM kinase activity and cofilin activity is also important for cell motility: too much activity of either LIM or cofilin inhibits migration (Wang et al. 2006; Yamaguchi & Condeelis 2007).

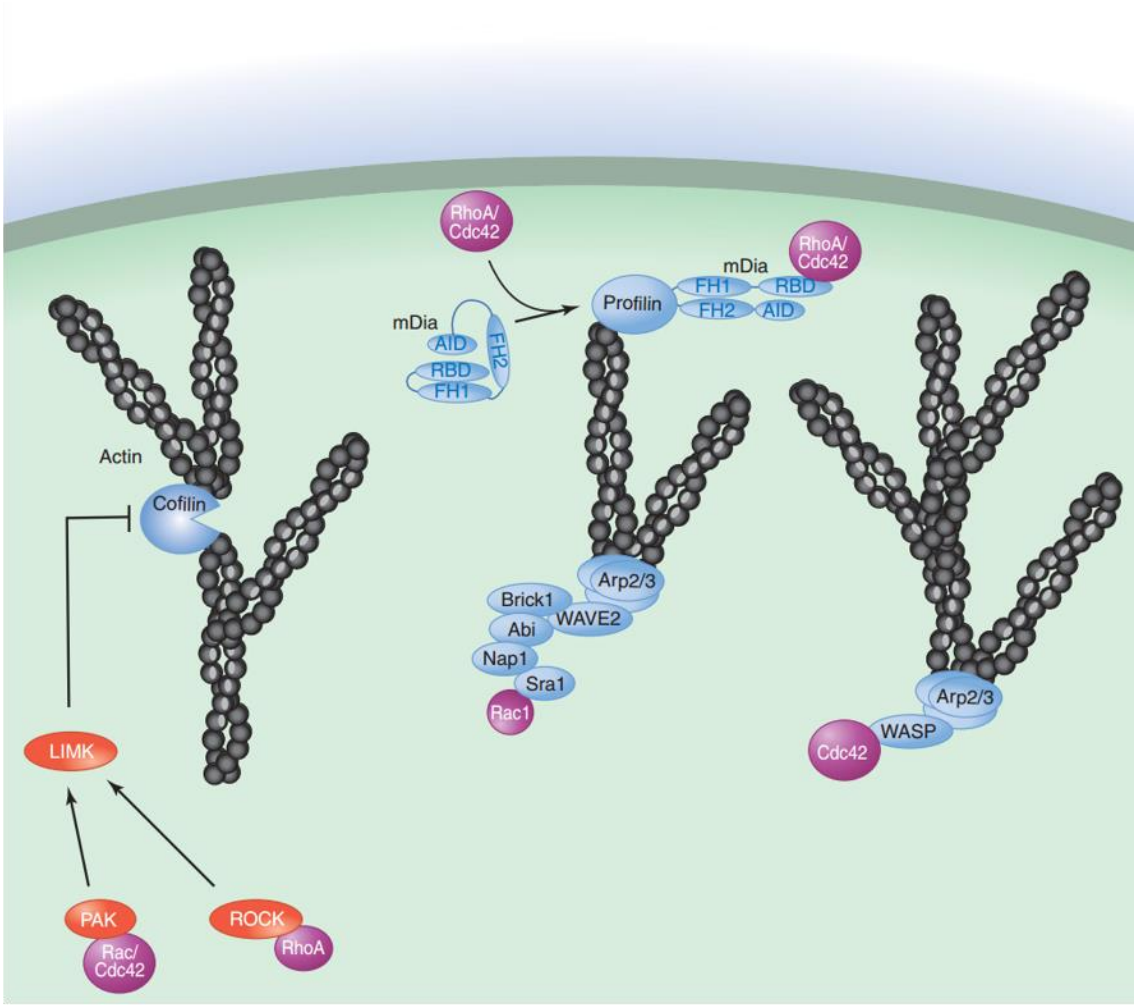

Figure 1.8 Regulation of actin dynamics by formins and Arp2/3 in cellular protrusions

The Rho GTPases Rac, RhoA, and Cdc42 regulate actin dynamics at the leading edge *via* their effects on the activities of formins (mDia), Arp2/3 complex, and LIM kinase (LIMK). Arp2/3 nucleates actin branches that are seen in broad protrusions. Its activity is regulated by Cdc42 and Rac1, which act on WASP/WAVE-containing protein complexes. RhoA acts on mDia1 and Cdc42 acts on mDia2 to promote actin polymerisation using a processive capping mechanism. RhoA also activates profilin, which binds to actin monomers and increases the rate of polymerization (Machacek et al. 2009). AID, autoinhibitory domain; FH, formin homology domains; RBD, Rho-GTPase-binding domain. Adapted from Devreotes and Horwitz, 2015

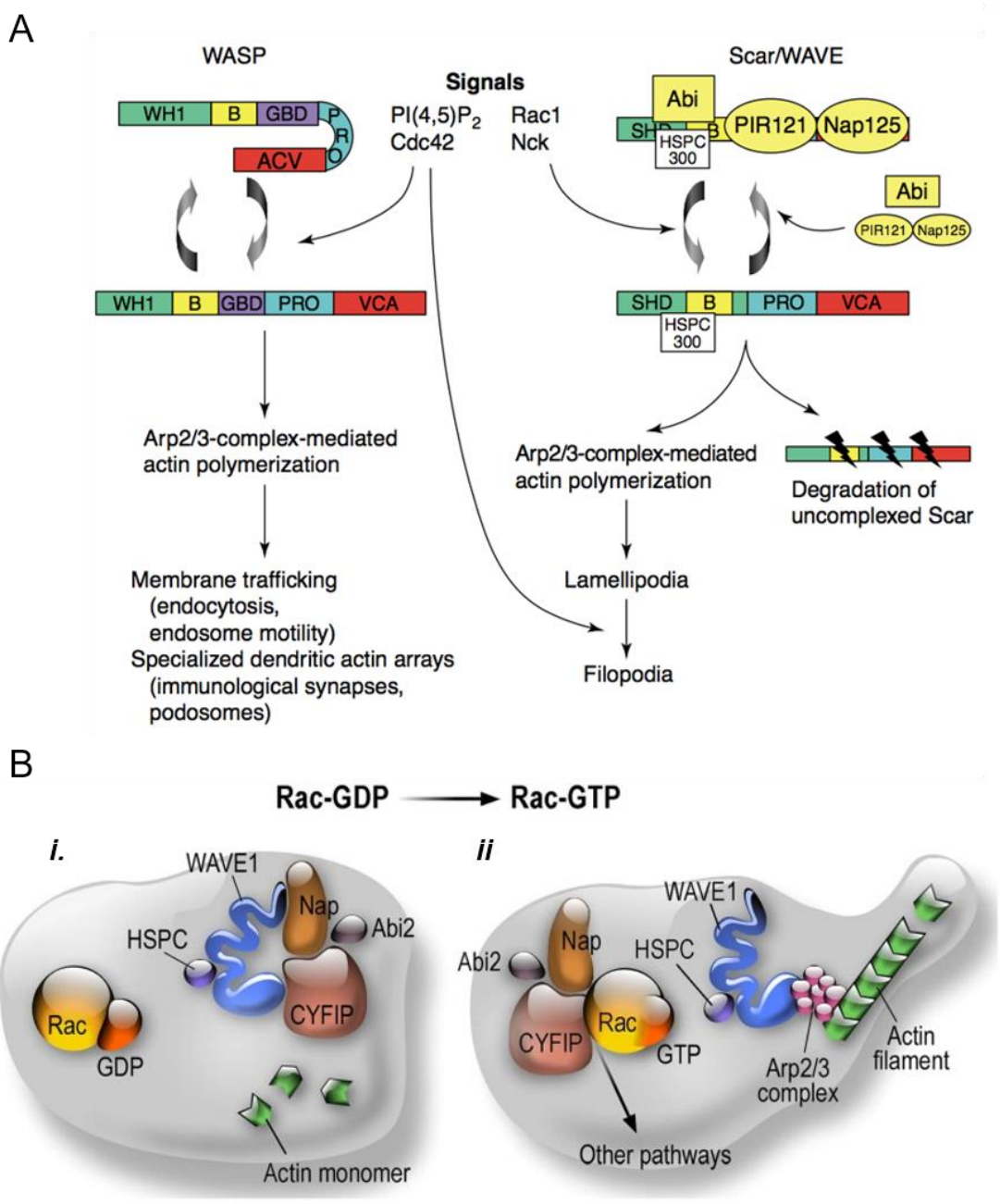

Figure 1.9 Regulation of actin dynamics in cellular protrusions

Panel A. The Arp 2/3 is activated through two main groups of nucleation promoting factors, WASP and Scar/WAVE, which act by inducing conformational changes in the complex and delivering the initial actin monomer to the filament. Activation through the Scar/WAVE pathway plays a role in cell front protrusion during cell migration. Adapted from Takenawa 2010. **Panel B.** Dynamics of CYFIP Proteins in the context of the WAVE complex and actin polymerization. ***i.*** Structural organisation of the WRC in the Rac-GDP condition; ***ii.*** Structural organisation of the WRC in the Rac-GTP condition. Adapted from Abekhoukh and Bardoni (2014).

1.6 Cortactin

Cortactin, like cofilin, is an actin-binding protein that is important for cell migration. For instance, knocking out cortactin has been shown to impair the ability of cancer cells to migrate and invade (Bryce et al. 2005). The role cortactin plays in cell migration is, however, very different to that of cofilin. Cortactin knockout cells could still produce lamellipodia, but they did not persist as long as in wild type cells (Bryce et al. 2005). This observation suggests that cortactin plays an important role in the formation of cell adhesions, which are what allow lamellipodia to persist. As with lamellipodia formation, ARP2/3 dependent actin polymerisation is an important part of cell adhesion (DeMali et al. 2003). It is perhaps surprising that cortactin plays such an important role in actin reorganisation when cortactin activity alone has a relatively small effect on Arp2/3-dependent actin nucleation (Uruno et al. 2001). Instead of acting directly on actin nucleation, cortactin supplements the activities of the Arp2/3 complex. For instance, it is believed that cortactin stabilises actin filaments produced by the Arp2/3 complex (Weaver et al. 2001). There is also evidence that cortactin activates N-WASP, which then activates Arp2/3 (Martinez-Quiles et al. 2004). Cortactin is believed to be phosphorylated in response to cell adhesion and growth factor stimulation (Lua & Low 2005). How cortactin activity is regulated during lamellipodia and invadopodia formation is not clear. Src has been shown to phosphorylate cortactin of tyrosine during invadopodia formation, but another study showed that knocking out cortactin had no effect on invadopodia formation (Lua & Low 2005). These findings do not rule out a role for cortactin in stabilising the invadopodia, as it does in lamellipodia. There is also some evidence to suggest ERK could regulate cortactin activity (Lua & Low 2005).

1.7 Localised translation

The targeting of mRNAs to sub-cellular compartments prior to translation, is currently viewed as a prevalent mode of protein expression within eukaryotic cells. Such spatial restriction of protein synthesis has been best-studied in *Saccharomyces cerevisiae* where ASH1 mRNA is restricted to expression within the daughter cell during mating-type switching (Takizawa et al. 1997), and has also been eluded to in mammalian cells (Shestakova et al.

2001; Mili et al. 2008). Localised translation of mRNAs encoding WAVE1, ArpC2, β-actin and Rac1 at the leading edge of migrating cells have been shown to be important in lamellipodia formation (Willett et al. 2013). Our laboratory also published an earlier paper showing how proteins involved in translation initiation colocalise with the leading edge of migrating fibroblasts (Willett et al. 2011). One of these proteins was eIF4E which is central to cap-dependent translation and metastasis. Willett et al (2011) also showed that phosphorylated eIF4E, which is indicative of Mnk1/2 kinase activity, could be localised to the leading edge of the cell. Several papers since – including data presented in the results section of this thesis - have shown that Mnk plays an important role in cell migration (Ramalingam et al. 2014; Beggs et al. 2015).

1.8 Cell polarity

The regulation of cell adhesion is important for converting the individual transient cellular protrusions into a concerted movement. For a cell protrusion to last, it must form new cell adhesions with the extracellular matrix and other cells (Ridley et al. 2003). Once several protrusions have formed and adhered at the leading edge of a cell, signals are transmitted to the rear of the cell causing the removal of cell adhesions. The cell is now polarised (Figure 1.7)

In a polarised cell the molecular processes going on at the front of the cell are distinct from those at the rear of the cell. The distinct molecular processes between the front and rear of the cell arise within a relatively narrow extracellular concentration gradient of chemoattractant. The signals responsible for converting a small extracellular concentration gradient into cell polarity are the phosphoinositides, PIP3 and PIP2 (Ridley et al. 2003). PI3K, which generates the phosphoinositides' third phosphate groups, accumulates at the leading edge of the cell; whilst PTEN, which removes the phosphoinositides' third phosphate groups, becomes localised to the rear and sides of the cell (Ridley et al. 2003). It has been shown that cells that have defective PI3K or PTEN can still migrate but do not respond to a chemoattractant gradient (Ridley et al., 2003). The high levels of PIP3 at the leading edge of migrating cells appears to be important for activating Cdc42, which can initiate actin nucleation (Ridley et al., 2003). Cdc42 is important for guiding the directionality of cell

migration: if Cdc42 is activated all over the cell, the cells are unable to migrate, which highlights the importance of localised activation of Cdc42 at the leading edge of cells (Ridley et al., 2003). This also helps restrict lamellipodia formation to the leading edge of cells. As well as initiating actin nucleation, Cdc42 is also important in directing changes in the microtubule structure of a polarized cell (Ridley et al., 2003). Cdc42 is believed to be responsible for moving the microtubule organising centre (MTOC) and Golgi apparatus towards the leading edge of the cell; or, in front of the nucleus so as to re-orientate the organelles inside a polarised cell (Ridley et al., 2003). Cdc42 then initiates the growth of microtubules from the MTOC into the leading edge of the cell (Ridley et al., 2003). The microtubules then facilitate the transport of vesicles from the Golgi, containing proteins required for lamellipodia formation to the leading edge (Ridley et al., 2003). The protein complexes involved in maintaining apical-basal cell polarity in epithelial cells are well conserved throughout multicellular organisms and the various tissues types within each organism (Royer and Lu, 2011). The complexes involved in maintaining apical-basal polarity help resist tumour formation by establishing orientation within the cell during asymmetric cell division and by linking cell polarity to the apical junction complex (AJC) (Royer & Lu 2011). There are three main complexes Par, Crumbs and Scribble which together help establish and maintain apical-basal cell polarity (Royer and Lu, 2011). Par and Crumbs establish and maintain the apical membrane phenotype, whereas Scribble is central to the basolateral membrane phenotype (Royer and Lu, 2011).

The AJC consists of tight and adherens junction complexes (Royer and Lu, 2011). The complexes responsible for maintaining apical-basal cell polarity help stabilise the tight and adherens junctions (Royer and Lu, 2011). A central component of the adherens junction is E-cadherin. The loss of apical cell polarity during the late stages of EMT is coincident with a loss of E-cadherin and the AJCs, which allow the cells to become motile (Royer and Lu, 2011). The maintenance of apical-basal cell polarity protects against epithelial cells becoming mesenchymal and migrating away from the tissues of which they are a part (Royer and Lu, 2011).

1.9 Integrins

Integrins are what link the dynamic interactions between the extracellular matrix (ECM) and changes in intracellular actin polymerisation that drive cell migration (Hynes, 2002). Integrins are heterodimeric receptors, made up of α and β chains, with large extracellular domains and short cytoplasmic domains (Takada et al., 2007). In humans, there are twenty-four different integrin heterodimers, made up of different combinations of eighteen α and eight β chains (Takada et al. 2007). The different combinations determine which extracellular ligands the integrins can bind. Integrin ligands include fibronectin, collagen, laminin, and cell surface receptor proteins ICAM-1 and V-CAM1 (Takada et al., 2007). Each integrin heterodimer has different adhesive properties. This means that the strength and persistence with which a cell adheres to a particular matrix, and consequently how it migrates, is determined by the particular assortment of integrin heterodimers that are involved (Takada et al., 2007). Altering the integrin profile of a cell can affect how well a cell migrates, for instance: $\alpha v\beta 3$ expression on melanoma cells has been shown to correlate with tumour invasion, whilst $\alpha 2\beta 1$ integrin is associated with rhabdomyosarcoma migration (Seftor et al., 1992, Chan et al., 1991). If cells only formed strong permanent adhesions, they would not be able to migrate. The turnover of adhesions is as important to cell migration as the formation of cell adhesions. The rate of cell migration is at its optimum when the rate of formation and turnover of cell adhesions is balanced (Zamir & Geiger 2001). Implicit in this is the need for intermediate levels of particular integrins, $\alpha 5\beta 1$ or $\alpha 2\beta 1$, and intermediate concentrations of ligand, such as fibronectin or collagen (Huttenlocher & Horwitz 2011). The rate of cell adhesion formation is coupled to the rate of actin polymerisation (Huttenlocher and Horwitz, 2011). The precise mechanism behind the formation of adhesions is not known, although it is thought to involve clustering of activated integrins in response to binding to integrin ligand (Huttenlocher and Horwitz, 2011).

Integrins coordinate the generation of tractable forces in a cell with intracellular signalling pathways which as well as feeding back into effects on cell migration also govern cell proliferation, gene expression and cell survival (Huttenlocher and Horwitz, 2011). The rate of the protrusion is linked to

downstream signalling pathways by the amount of tension generated across the integrin-actin linkages (Huttenlocher and Horwitz, 2011). Proteins that have been implicated in linking integrins to the actin cytoskeleton at focal adhesions include talin, vinculin, and α-actinin (Zamir and Geiger, 2001). The rate of cellular protrusion formation is determined by the difference between the rate of actin polymerisation and depolymerisation at the leading edge of a cell. When cell adhesions form, they inhibit actin depolymerisation, which means the rate of protrusion increases (Huttenlocher and Horwitz, 2011). This is thought to generate a shunting force on the extracellular matrix component. Some of this force is absolved by the molecular slippages that are believed to occur within the linkages (Huttenlocher and Horwitz, 2011). It is thought that on some more pliable extracellular matrix components the forces generated by this shunting force could translate into movements within the extracellular matrix (Huttenlocher and Horwitz, 2011).

Several signalling pathways activated by integrin clusters are thought to converge on the Rho GTPases, which regulate actin polymerisation and also a feedback onto cell adhesion. Although the size of the focal adhesions varies widely, there is generally an inverse correlation between the size of a focal adhesion and rate of cell migration. The focal adhesions are the most well characterised of the integrin-based adhesion complexes (Huttenlocher and Horwitz, 2011).

1.10 Focal adhesions

Focal adhesions, or focal contacts, are aggregates of transmembrane proteins, mainly composed of integrins, which link the extracellular matrix to the actin cytoskeleton and a large intracellular signalling hub (Zamir and Geiger, 2001). The intracellular signalling hub of focal adhesions is highly complex, with over 50 different proteins known to associate with it (Zamir and Geiger, 2001). Together, the various anchor proteins and signalling proteins coordinate intracellular responses to changes in cell adhesion. Focal adhesion kinase (FAK) is an example of one of the many kinases associated with focal adhesion complexes. As well as interacting with the intracellular domain of integrins, FAK also responds to signals from receptor

tyrosine kinases (Turner, 2000). FAK phosphorylates another protein, paxillin, which has two important roles in coordinating responses to changes in cell adhesion (Turner, 2000). One role of paxillin is to link integrins with the actin cytoskeleton, *via* another protein called vinculin which provides a physical link between paxillin and the actin cytoskeleton (Turner, 2000). Paxillin, following phosphorylation by FAK, also activates the MAPK signalling pathway and can initiate changes in gene expression (Turner, 2000).

1.11 Epithelial-Mesenchymal Transition

Cell migration is an important part of Epithelial-Mesenchymal Transition (EMT). EMT is a transient process by which epithelial cells lose their epithelial phenotype and gain a mesenchymal phenotype. The process is an integral part of development but is also reactivated during wound repair, fibrosis and in cancer cells. EMT was first observed in chick embryos in the early 1980s (Hay, 1995). Originally, the process was called Epithelial-Mesenchymal Transformation, but it was changed to Epithelial-Mesenchymal Transition (EMT) when it was discovered that it was, in fact, a transient process: the reverse is called Mesenchymal-Epithelial Transition (MET) (Lamouville et al. 2014). Epithelial cells can transition between EMT and MET multiple times (Samy et al., 2014).

Epithelial cells usually exist in single layers or in multilayer tissues (Figure 1.10). They form the permeable boundaries between different organs and tissues (Huang et al., 2012). The function of particular epithelial cells is defined by the basement membranes that they adhere to (Samy et al., 2014). The adhesion to the basement membrane helps establish an apical-basal polarity (Samy et al., 2014). Epithelial cells also form tight junctions between adjacent epithelial cells, which allow them to communicate with each other (Samy et al., 2014). The loss of these properties, which define epithelial cells, are the key steps in EMT (Samy et al., 2014). The exact process of EMT can vary between different tissues, but there are a few key processes common to all forms of EMT. These include: the loss of the cell-cell junctions; the loss of apical-basal polarity, to be replaced with a front-rear polarity; reorganisation of the cytoskeleton; the replacement of epithelial gene expression with

mesenchymal gene expression; increased cell motility; and, in many cases, the acquisition of the ability to invade other tissues and degrade the extracellular matrix (Samy et al., 2014). Following EMT, cells also become more resistant to apoptosis and senescence (Sleeman & Thiery 2011).

During EMT, cells transition from co-operative cells working together as tissue, to cells that act independently of the tissue from which they are derived. Once EMT is initiated, the cell-cell contacts - tight junctions, adherens junctions, desmosomes, gap junctions – are degraded (Figure 1.10). It is the degradation of adherens junctions which leads to the degradation of an established marker of epithelial cells: epithelial-cadherin (E-Cadherin)(Yilmaz & Christofori 2009). E-cadherin forms part of the adherens junction in epithelial cells. When the adherens junctions are degraded, E-cadherin is cleaved at the plasma membrane and degraded (Yilmaz and Christofori, 2009). Reduced E-cadherin levels cause a reduction in cell adhesion and increased cell motility (Samy et al., 2014). Epithelial cells have a cortical actin cytoskeleton, which is important for the cell-cell contacts and interactions with the basement membrane (Figure 1.7) (Samy et al., 2014). During EMT, the actin cytoskeleton changes so that it becomes more focused on driving the formation of cellular protrusions, such as lamellipodia or invadopodia, which allow cells to migrate or invade (Yilmaz and Christofori, 2010). Cells that have undergone EMT also redirect their actin towards the formation of actin stress fibres which cause the cells to contract (Figure 1.10).

Rho GTPases are thought to play a central role in the reorganisation of the actin cytoskeleton during EMT (Nelson 2009). RhoA promotes actin stress fibre formation during EMT. Rac1 and Cdc42 promote actin nucleation to initiate the formation of lamellipodia. Rho-associated kinase (ROCK) promotes actin polymerisation and stabilises actin filaments by activating LIM kinase, which inactivates cofilin, creating breaks in actin filaments (Narumiya et al. 2009). ROCK is also responsible for increasing contractility in cells undergoing EMT, by inducing myosin light chain phosphorylation (Narumiya et al., 2009). Rho-GTPases also play an important role in the transition from apical-basal polarity to front-rear polarity (Nelson, 2009). RhoA localises at the rear of the cell where it promotes the removal of adhesion complexes, which causes the cell to retract (Nelson, 2009).

The way cells interact with their ECM also changes during EMT. Epithelial cells express integrins such as $\alpha6\beta4$ which interact with the basement membrane, but during EMT these integrins get replaced with other integrins, such as $\alpha5\beta1$, which binds to fibronectin and $\alpha1\beta1$ and $\alpha2\beta1$, which bind to collagen (type 1) (Samy et al., 2014). In addition, $\alpha1\beta1$ and $\alpha2\beta1$ integrins reinforce the removal of E-cadherin by disrupting the adherens junctions (Samy et al., 2014). The increased expression of integrins $\alpha v\beta6$ and $\alpha v\beta3$ during EMT is thought to contribute to increased invasiveness by increasing the expression of metalloproteases (MMPs) and their association with invadopodia Samy et al., 2014). The release of MMPs from the invadopodia allows invasive cells to break down the extracellular matrix (Nisticò et al., 2012). It is believed that some MMPs also target the extracellular domain of E-cadherin contributing to its removal and the loss of adherens junctions (Nisticò et al., 2012). MMP secretion is also believed to feedback into the EMT progression by unlocking growth factors from the extracellular matrix, such as TGFβ, which activate signalling pathways that promote EMT (Sheppard, 2005). Active TGFβ stimulates the release of collagen and fibronectin helping to remodel the extracellular matrix into one with which integrins expressed by mesenchymal cells can interact (Samy et al., 2014).

The change in cell phenotype during EMT is due to a reprogramming of gene expression. This reprogramming of gene expression is driven by the transcription factors SNAIL, TWIST, ZEB1 and bHLH (basic helix-loop-helix) transcription factors (Samy et al., 2014). The expression of these transcription factors is activated early in EMT to coordinate the repression of genes that define an epithelial phenotype and activate the expression of mesenchymal genes. Some of these transcription factors can both repress epithelial genes and induce the expression of mesenchymal genes. SNAIL1 is activated by TGFβ, Wnt signalling, Notch and RTKs (Samy et al., 2014). By cooperating with ETS1, SNAIL1 activates MMP) expression in response to MAPK activation (Jordà et al., 2005). SNAIL1 also cooperates with SMAD3-SMAD4 to repress E-cadherin and occludin expression in response to TGFβ (Theresa et al., 2009). The basic loop-helix-loop transcription factor TWIST1 plays an important role in the ‘cadherin switch’ during EMT (Samy et al., 2014). TWIST1 binds to both the

promoters in the E-cadherin and N-cadherin genes and recruits the methyltransferase SET8 (Yang et al., 2012). SET8 methylates histone H4K20, which in the E-cadherin promoter leads to repression, but in the N-cadherin promoter, induces expression (Yang et al., 2012). It is this dual response to the histone H4K20 that defines the switch from E-cadherin to N-cadherin expression in mesenchymal cells (Yang et al., 2012). Activity along the MAPK signalling pathway helps prolong TWIST1 activity by protecting it from degradation (Hong et al., 2011).

1.12 Translation at the leading edge of the cell

The expression of proteins involved in EMT can be controlled by events at both the transcriptional and post-transcriptional levels. There is extensive literature showing the compartmentalisation and trafficking of mRNA in eukaryotic and mammalian cells (Besse & Ephrussi 2008), facilitating localised protein synthesis. However, the regulatory interactions between the translational machinery, localised mRNAs, cellular structures and fibroblastic cell spreading/migration are relatively unexplored. Previous work from the Morley lab has shown that eIF4G, 4E-BP1 and ribosomal subunits colocalise with eIF4E in the lamellipodia of migrating fibroblastic cells (Willett et al., 2010, Willett et al., 2011), suggesting the regulation of localised translation in this cells compartment.

Another protein implicated in localised translation at the leading edge of cells is Fragile X Mental Retardation Protein (FMRP) (Bagni et al., 2005), a known regulator of translation which binds to polysomes. FMRP binds its cargo mRNAs in the nucleus and in mammals is able to recognise a large number of mRNAs (Miyashiro et al. 2003; Darnell et al. 2011) and some miRNAs (Barbee et al., 2006). FMRP contains a central region with two RNA-binding KH domains and a C-terminal RGG box (Bagni et al., 2005). The N-terminal region forms a novel RNA-binding domain (Andolfini et al., 2005; Zalfa et al., 2003). An I304Q mutation derived from a fragile X syndrome patient prevents polysome association and translational inhibitory effects of FMRP (Miyashiro et al., 2003). This mutant protein has a decreased ability to inhibit translation but localises mRNA in neurones to a similar extent as the wild type protein. The RGG box is

crucial for the interaction with mRNAs containing a G-quadruplex (G4) motif (Lacoux et al., 2012). FMRP can co-sediment with the monomeric 80S ribosomes and polysomes, CYFIP1, and translation initiation factors (Figure 1.11). In fibroblasts, FMRP-mediated repression of translation requires a sub-population of FMRP to interact with CYFIP1 which is recruited to active Rac1/GTP as part of the WAVE complex. Binding of FMRP to CYFP1 increases the affinity of CYFIP1 for capped mRNAs (Napoli et al., 2008), stabilising CYFIP1 on specific mRNAs to repress translation at the leading edge of spreading cells (Figure 1.9B).

CYFIP1 binds directly to eIF4E (and hence mRNA) using a surface similar to that of 4E-BP1. In the brain, CYFIP1 forms a complex with specific FMRP-target mRNAs; reduced levels of either CYFIP1 or FMRP cause an increase in the synthesis of MAP1B, αCaMKII, and APP (Bagni et al., 2005; Westmark, 2007), and promotes neurite migration. Loss of CYFIP1 in fibroblasts is associated with a tumourigenic phenotype (Napoli et al. 2008). When FMRP is phosphorylated by p70S6K on Ser499, N-terminal to the RGG box (Narayanan et al. 2007), FMRP represses the translation of specific mRNAs, such as MAP1B, αCaMKII, PSD-95, SAPAP3 (Narayanan, Nalavadi, Nakamoto, Thomas, Ceman, Gary J Bassell, et al. 2008). Synaptic activity promotes the PP2A-mediated dephosphorylation of FMRP and the release of CYFIP1 and bound mRNAs from eIF4E, resulting in the alleviation of translation repression (Figure 1.11). The CYFIP1-FMRP complex has also been shown to play an important role in regulating the translation of both E-cadherin and vimentin (Lucá et al. 2013). It has been shown that FMRP-dependent repression of E-cadherin expression is important in driving EMT and metastasis of breast tumours in mice (Lucá et al., 2013). The same publication also suggests that FMRP mRNA levels correlate with, and stimulate, expression of vimentin. However, this study also shows that knocking out FMRP reduces vimentin mRNA levels, so it could be acting *via* transcription rather than via translation (Lucá et al., 2013). The study also showed that knocking down FMRP using siRNA reduced the number of cell protrusions. Recent suggest that CYFIP1-FMRP binding to eIF4E correlates with a reduction in the proportion of vimentin mRNAs associated with polysomes (Beggs et al. 2015). The study shows that inhibiting eIF4E phosphorylation by the Mnk1/2 increases CYFIP1

binding whilst, in the same cell type, reducing vimentin expression (Beggs et al., 2015). These recent studies have suggested that active Mnk1/2 can promote the release of the CYFIP1/FMRP from eIF4E allowing for the translation of specific mRNAs (Figure 1.11). Previous work from the Morley lab shows that lamellipodia of migrating fibroblasts are enriched for foci active in protein synthesis. mRNAs encoding some structural and regulatory components of the WAVE complex (including Arpc2, WAVE1 and β-actin mRNA), were also seen to be localised to the leading edge of the cell and were associated with sites of active translation (Willett et al. 2013; Willett et al. 2011). This suggests that the regulation of localised translation may play a role in cell spreading and migration. As CYFIP1 is also a part of the WAVE complex, these data suggest that a mechanism of CYFIP1/FMRP translational regulation might have a role in localised translation at the leading edge of the cell. Work presented in this thesis adds to evidence that such regulation may be happening during fibroblast cell spreading.

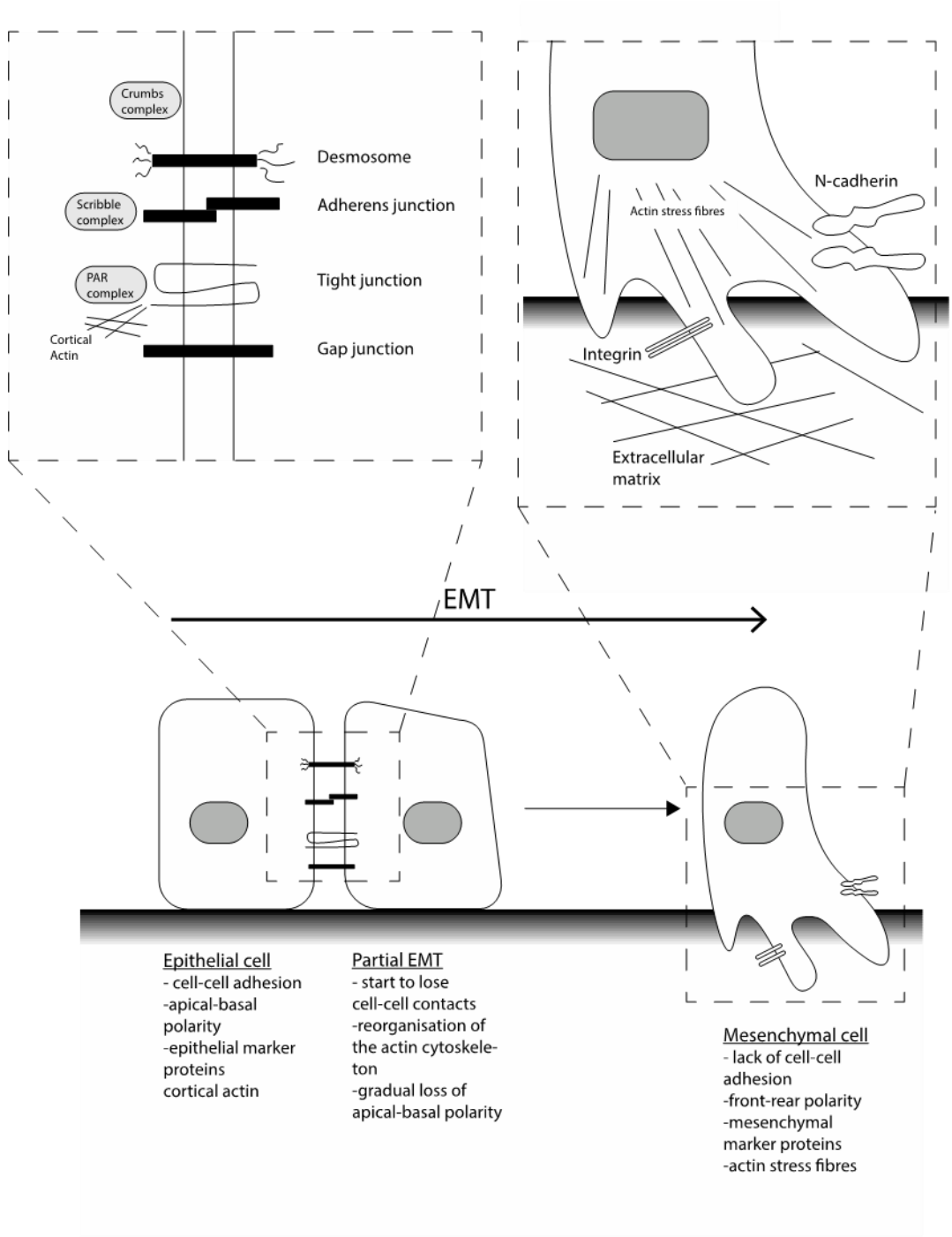

Figure 1.10 Schematic representation of epithelial–mesenchymal transition

Adapted from Samy et al., 2014.

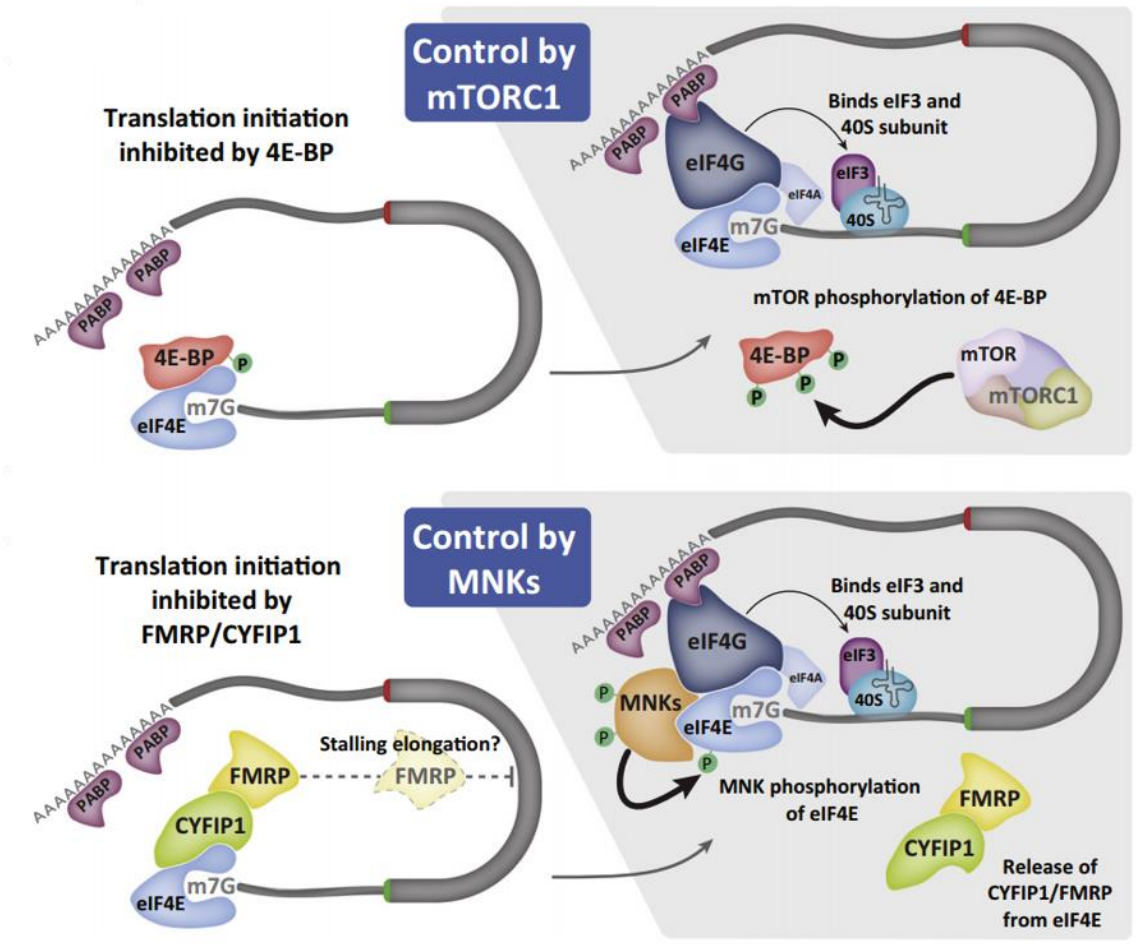

Figure 1.11 Schematic representation of competition for binding between 4E-BP1 and CYFIP1

Active Mnk1/2 stimulates the release of the cytoplasmic FMRP-interacting protein (CYFIP1)/FMRP complex from eIF4E, prompting enhanced translation of several FMRP-target mRNAs involved in process outgrowth and remodelling of the extracellular matrix. Recruitment of CYFIP1 to the WAVE regulatory complex contributes to actin cytoskeletal remodeling. Adapted from Bramham et al, (2016).

1.13 Aims of this Thesis:

To test for the presence of a CYFIP1-FMRP-eIF4E complex in spreading fibroblasts:

i. Using biochemical means, including m7GTP–sepharose chromatography and co-immunoprecipitation.
ii. Using biophysical methods such as immunocytochemistry (ICC) and fluorescence in situ hybridisation (FISH), to localise mRNPs under the translational control of CYFIP1 and FMRP.
iii. Using super-resolution techniques for nanometre accuracy when colocalising constituent parts of a translationally repressed mRNP, techniques such as deconvolution, FRET, SOFI and 3B will be used.
iv. Using my results, to postulate a hypothesis on the role of CYFIP1 and FMRP in fibroblasts.

To develop software specifically for the analysis of *in situ* Proximity Ligation Assay (PLA):

i. To design and implement a PLA analysis program which maximises the quantity of information harvested from the PLA method.
ii. The program must be entirely novel and provide dataset manipulation and analyses routines which are not currently available from any other PLA analysis package.

To investigate the role of DDX3X in human fibroblasts:

i. Using CRISPR/Cas9 gene editing to produce a new cell line with reduced DDX3X expression.
ii. Using immunocytochemistry techniques to visualise the steady-state location of DDX3X, with super-resolution accuracy.
iii. To use PLA and a novel PLA analysis program to test for the quantity and precise intracellular location of DDX3X interactions with the cap-binding protein eIF4E, under different cellular stresses. And to correlate the change in interactions with any gross changes in cellular morphology.
iv. To postulate a hypothesis on the role of DDX3X in fibroblasts.

2 Materials and Methods

2.0 General

MRC5 human foetal lung fibroblasts, SV40 transformed (Huschtscha & Holliday 1983), were sourced from the European Collection of Cell Cultures (ECACC), UK., 1BR3 hTERT human skin fibroblasts from the Genome Damage and Stability Centre (GDSC), University of Sussex, UK.

m^7GTP-sepharose 4B resin and Polyvinylidine Difluoride (PVDF) were from Amersham Biosciences, UK., [Cat# 10600023]. CGP57380 a kind gift from Dr Hermann Gram (NOVARTIS Pharma AG, Basel, Switzerland). Microcystin LR was purchased from Alexis Corporation. Leptomycin B (LMB) and cercosporamide were from Tocris Bioscience, UK. Unless otherwise stated, all other kits and reagents were supplied by Sigma-Aldrich (UK) and were of analytical quality.

2.1 Secondary antibodies

Fluorescently labelled secondary antibodies and their working dilutions are detailed in Table 2.1. and were all sourced from Invitrogen (UK). Horseradish peroxidase-conjugated sheep anti-mouse IgG and donkey anti-rabbit IgG secondary antibodies for enhanced chemiluminescence (ECL) were from Amersham Biosciences (UK).

Table 2.1

Secondary Antisera	**Dilution**	**Supplier**	**Specificity**
Alexa Fluor 488	1:300	Invitrogen	Goat anti-mouse
Alexa Fluor 555	1:300	Invitrogen	Goat anti-rabbit
Alexa Fluor 568	1:300	Invitrogen	Goat anti-rabbit
Alexa Fluor 633	1:300	Invitrogen	Goat anti-mouse

2.2 Primary antibodies

All primary antibodies used in these studies are detailed in Table 2.2. alongside their working dilutions. All antibodies were supplied by Abcam unless otherwise stated.

Table 2.2

Ab#	Antisera name and manufacturer product code	Specificity	ICC dilution 1:n	Immuno-blotting dilution 1:n
1	4E-BP1 (53H11) mAb #9644	Rb mAb	200	1000
7	Phospho-4E-BP1 (Thr37/46) (236B4) #2855	Rb mAb	200	2000
8	eIF4E (ab1126)	Rb Ab	200	1000
9	eIF4E (phospho S209) (ab76256)	Rb mAb	500	1000
11	HuR	Rb Ab	100	1000
12	FMRP (ab27455)	Rb Ab	300	1000
13	FMRP (phospho S499) (ab48127)	Rb Ab	200	1000
14	Paxillin [Y113] (ab32084)	Rb mAb	250	1000
18	CYFIP1 AB6046	Rb Ab	250	1000
19	Phospho-eIF4E (Ser209) #9741	Rb Ab	100	2000
23	S6 Ribosomal Protein (5G10) #2217	Rb mAb	50	1000
24	PABP	Rb Ab	500	1000
28	Phospho-4E-BP1 (Ser65) #9451	Rb Ab	-	1000
29	CYFIP1 [EPR10782] (ab156016)	Rb mAb	200	1000
30	PIR121-1/Sra-1 (07-531)	Rb Ab	200	1000
32	Mouse Anti-alpha-Tubulin	Ms mAb	250	1000
34	FMRP mouse monoclonal (1C3) MAB2160	Ms mAb	300	1000
36	Phospho-S6 Ribosomal Protein (Ser240/244) #2215	Rb	100	1000
41	Phospho-p70 S6 Kinase (Thr389) #9205	Rb	250	1000
44	Phospho-4E-BP1 (Thr70) II #5078	Rb	100	1000
52	DDX3 (ab128206)	Rb Ab	500	1000
53	eIF4E (homemade "XF")	Rb Ab	100	1000
54	DDX3 (sourced from Harvard)	Rb Ab	450	1000
58	Puromycin	Ms mAb	25	2000
59	Tubulin-FITC (sourced from Simon Morley)	Ms mAb	1:200	1000
62	Anti-DDX3 [6G8-F4-E3] (ab196032)	Ms mAb	500	1000
69	phospho-eIF4E(ser209)	Rb Ab		1000
75	phospho-p70 S6 Kinase (T421/S424) #9204	Rb Ab	-	1000
83	Phospho-4E-BP1 (Thr70) #9455	Rb Ab	-	1000
87	Phospho-S6 Ribosomal Protein (Ser240/244) (D68F8) #5364	Rb mAb	800	1000
100	Anti-DDX3 [6G8-F4-E3] (ab196032)	Ms mAb	200	5000
106	Anti-eIF4E [5D11] (ab171091)	Ms mAb	150	1000

2.3 Other fluorescent particles and conjugate systems

Table 2.3

Specific Fluorophores and Fluorophore conjugates	Supplier	Dilution
CytoPainter Phalloidin-iFluor 488 Reagent	Abcam	1:50
Alexa Fluor® 633 Phalloidin (A22284)	Invitrogen	1:50
TetraSpeck™ Microspheres, 0.1 µm	Invitrogen	~1.8×10^{11} /mL
Phalloidin-FITC	Simon Morley	1:50
Qdot® Antibody Conjugation Kit (A10197)	Invitrogen	See text
QD625	Invitrogen	See text

2.4 Cell-permeable inhibitors

Table 2.4

NAME	TARGET	STOCK CONCENTRATION	SUPPLIER
CERCOSPORAMIDE	Mnk1/2	10mM	Tocris Bioscience
MnkI_19	Mnk1/2	10mM	Prof S. Morley
CGP57380	Mnk1/2	10mM	Tocris Bioscience
KU-0063794	mTOR	10mM	Tocris Bioscience
PUROMYCIN	Ribosomes	50 mg/ml (v/v)	Sigma Aldrich (UK)
EMETINE	Ribosomes	100 mg/ml (v/v)	Sigma Aldrich (UK)
LEPTOMYCIN-B	CRM1	10mM	Tocris Bioscience
Cycloheximide	Ribosomes	355µM	Sigma Aldrich

Unless otherwise stated, all inhibitors were dissolved in DMSO to the stock concentrations shown and used at the final concentrations as described in the text.

Puromycin: Puromycin dihydrochloride was diluted in water before being 0.22 µm filtered to make a final stock solution of 50 mg/ml (v/v). Aliquots were stored at -20˚C.
Emetine: Emetine dihydrochloride hydrate was diluted in water before being 0.22 mm filtered to make a final stock solution of 100 mg/ml (v/v). Aliquots were stored at -20˚C.
Cycloheximide Wash: Cycloheximide was diluted in Dulbecco's Phosphate Buffered Saline both with calcium chloride and magnesium chloride, to 355µM.

2.5 Tissue Culture

2.5.1 Tissue culture reagents

FBS: FBS Good Forte, filtered bovine serum was from Pan Biotech [Cat# P40-47100M]; **MEM:** Minimal Essential Medium with Glutamax and Earl's salts was from Gibco [Cat# 41090-028]; **TripLE Select (trypsin alternative):** was from Gibco [Cat# 12563-011]; **PBS:** Dulbecco's Phosphate Buffered Saline without calcium chloride or magnesium chloride was from Sigma Aldrich [Cat# D8537];

2.5.2 Cell lines

MRC-5 SV2: Human male foetal lung fibroblasts, SV40 transformed (Huschtscha & Holliday 1983); 1BR3 hTERT: Human male skin fibroblasts (Taylor et al. 1975).

2.5.3 Cell growth and care

Typically, cells were cultivated in CELLSTAR flasks (Greiner Bio One) utilising MEM supplemented with 15% (v/v) FBS as the culture media. All cells were grown at 37ºC in a humidified atmosphere containing 5% CO_2.

2.5.4 Cell Dissociation Procedure

Typically, cells were cultivated in CELLSTAR T-75 flasks (Greiner Bio-One) utilising MEM supplemented with 15% (v/v) FCS as the culture media, prior to harvesting during log-phase growth at approximately 70% confluence. Using pre-warmed media (37°C), cells were detached from the tissue culture flasks by pouring off their media, rinsing twice in PBS, before an application of 5mL of 0.25% (w/v) trypsin/EDTA (Invitrogen) or TrypLE™ Select Enzyme (Gibco). After 10 seconds, excess dissociation media was aspirated from the flask, and the flask incubated at 37°C for 4 minutes (MRC-5 SV2 cells) or up to 7 minutes for more adherent cell lines. Cells were dissociated from clumps by gentle back and forth aspiration using a hand-held pipette, before re-suspension in tissue culture medium containing 15% (v/v) foetal calf serum, for cell counting prior to subculture or seeding.

2.5.5 Subculture

Using the method described in Section 2.5.4, sub-culturing of cells was typically performed by applying $15x10^3$ cells/cm^2 to a new T-flask, with MEM + 15% (v/v) FCS.

2.5.6 Cell seeding for experimental uses.

Using the method described in Section 2.5.4, and using the original decanted media for cell seeding and culturing (typically +/- drugs), seeding of cells to coverslips was typically performed by applying $1x10^6$ cells onto 15 cm plates for *in vitro* assays. For immunocytochemistry, 1.5 x 10^3 cells/cm^2 were seeded onto coverslips coated with 8µg/cm^2 collagen I, as described in the Materials and Methods. Cells were then harvested or fixed at appropriate times as described in the individual figure legends.

2.5.7 Drug treatment of cells

Cells were typically grown to reach a confluency of 70-80% prior to the addition of the drug under test. Once the drug was added, cells were typically allowed to grow for 2 hours, before re-seeding onto plates or coverslips as described in Section 2.5.5, with re-application of the saved media (+/- drugs).

2.5.8 Sodium arsenite treatment of cells

Cells were typically grown to a confluency of 70-80% prior to re-seeding onto plates or coverslips as described in Section 2.5.5. After leaving 30 minutes for cells to establish ECM adherence, sodium arsenite was added for a further 30 minutes. Cells were then harvested or fixed at appropriate times as described in the individual figure legends.

2.5.9 Serum deprivation and re-feeding of cells

Cells were grown in complete medium (MEM + 15% FCS) at a density of 15000 cells/cm^2. Cells were then washed twice with serum-free MEM and incubated at 37ºC in starvation medium (MEM + 0.1% FCS) for 24 hours. Following starvation, cells were harvested or re-fed with complete medium for the indicated times.

2.6 Biochemistry techniques

2.6.1 Cell harvest protocol

Harvest Buffer: PBS containing 2mM benzamidine, and 40mM β-glycerophosphate (BGP).
Lysis Buffer: 20mM MOPS (KOH) pH7.2, 25mM KCl, 2mM $MgCl_2$, 2mM benzamidine, 2mM EGTA, 0.1mM GTP, 0.5mM DDT, 10% (v/v) glycerol and protease inhibitor cocktail (Roche, UK)

Cytoplasmic lysate fractionation at 10,000 × g, produces an 'S10' cell extract containing soluble cytoplasmic proteins and ribosomes, without contamination by mitochondria. To prepare S10 extracts, tissue culture plates seeded with cells were transferred onto ice and the medium removed. Cells were scraped in 1 mL of ice cold Harvest Buffer and centrifuged at 10,000 × g for 5 minutes at 4ºC. For serum starvation/refeeding experiments, an extra wash with 1 mL of ice-cold harvest buffer was used to ensure complete removal of FCS. Cell pellets were re-suspended in 100 µL of Lysis Buffer containing 0.5% (v/v) igepal and 0.5% (v/v) deoxycholate (DOC) to release free and cytoskeletal-bound ribosomes. Following vortexing, lysates were centrifuged at 10,000 × g for 5 minutes at 4ºC to isolate the cell debris and the resulting supernatants flash-frozen in liquid nitrogen and stored at -80ºC. Bradford assays (Bio-Rad) were used to determine the protein concentration of cell extracts alongside known amounts of bovine serum albumin (BSA), which were used to create a standard curve.

2.6.2 m^7GTP-sepharose-mediated purification of eIF4E

m^7GTP-sepharose buffer: 20mM MOPS (KOH) pH7.3, 25mM KCL, 2mM benzamidine, 1mM magnesium acetate, 7mM β-mercaptoethanol, 0.1mM GTP, 0.25% (v/v) igepal, 10mM sodium fluoride, EDTA-free protease inhibitor cocktail (Roche, UK)
Optional: 1 mg/ml cytochrome *c* to block non-specific binding of proteins to the resin.

eIF4E and its mRNA-associated proteins were isolated *via* a cap analogue, m^7GTP, coupled to sepharose beads (Webb et al. 1984). 50% (v/v) m^7GTP-sepharose 4B resin was washed by centrifugation for 5 minutes at 10,000 × *g* and the storage buffer discarded. The storage buffer was replaced by an equal amount m^7GTP-sepharose buffer containing cytochrome *c*. Aliquots of S10 extracts containing equal amounts of protein were added to the washed resin, and incubated at 4ºC for 15 minutes, with gentle agitation. The resin was isolated by centrifugation at 10,000 × *g* for 5 minutes at 4ºC. The supernatant was aspirated and non-specifically bound proteins removed by washing twice with 300 µL of the m^7GTP-sepharose buffer. Bound proteins were eluted by boiling the sepharose beads in SDS-PAGE sample buffer for 5 minutes and centrifugation at 10,000 × *g* for 5 minutes.

2.6.3 Immunoprecipitation protocol

IP wash buffer: 150nM NaCl, 10mM Tris (HCl) pH7.4, 1mM EDTA, 1mM EGTA, 0.2mM sodium orthovanadate, 0.2mM PMSF, 1% (v/v) Triton X-100, 0.5% igepal.

Protein A/G (25µL of a 50% (v/v) slurry) magnetic beads (New England Biolabs) were added to 100uL of 1mg/mL protein cell extract prepared by S10 cytoplasmic lysis as described above and agitated for 1 hour at 4ºC. The extract was subjected to a magnetic field and the supernatant aspirated into a new microfuge tube. Anti-FMRP / anti-CYFIP1 antibody (5µL) was added and the mixture agitated for 1 hour at 4ºC. Protein A/G magnetic beads (25µL) were added to the pre-cleared extract which was then agitated for a further hour at 4ºC. The magnetic beads were washed three times with 1mL of IP wash buffer and recovered protein was eluted into 30µL of SDS-PAGE sample buffer for SDS-PAGE and immune-blotting procedures.

2.6.4 SDS-PAGE

Sodium dodecyl sulphate polyacrylamide gel electrophoresis (SDS-PAGE) separates proteins according to their molecular mass. Sodium dodecyl sulphate (SDS) binds to proteins, denaturing them and conferring onto them a negative electric charge proportional to the size of the protein. In this study,

samples were analysed using either 10 % or 15% one-dimensional PAGE according to the standard method for the Protean II mini-gel system (Bio-Rad, UK).

10% Separating gel (10mL): To 4.1mL H_2O, was added: 2.5mL 1.5M Tris(HCl) pH8.8, 50µL 20% (w/v) SDS, 3.3mL acrylamide 30% (v/v), 50µL APS 10% (w/v), 10µL TEMED.
(Acrylamide was supplied pre-mixed, 30%(w/v) 29:1 A:Bis-A).
15% Separating gel (10mL): To 2.4mL H_2O, was added: 2.5mL 1.5M Tris(HCl) pH8.8, 50µL 20% (w/v) SDS, 5.0 mL acrylamide 30% (v/v), 50µL APS 10% (w/v), 10µL TEMED.
Stacking Gel: To 4mL Stacking Gel Mix, was added: 40µL SDS 20% (v/v), 40µL APS 10% (w/v), 10µL TEMED.
Sample buffer: Pre-mixed Laemmli 2x. Product number S3401 supplied by Sigma Aldrich (UK).
Running buffer: 25 µM Tris (HCl), 0.1% SDS, 192mM Glycine, adjusted to pH 8.5.

2.6.5 Protein transfers to PVDF membrane

Following SDS-PAGE, proteins were transferred onto PVDF membrane using a semi-dry blotting unit (Bio-Rad Trans-Blot Turbo). A stack consisting of four sheets of filter paper soaked in Anode 1 buffer, followed by two sheets of filter paper soaked in Anode 2 buffer was assembled. The PVDF membrane, soaked in methanol was placed on top of this, followed by the resolved polyacrylamide gel. Four sheets of filter paper soaked in Cathode buffer completed the stack, which was then placed in the blotting apparatus and proteins transferred to the PVDF membrane by applying 30 mA/cm^2 for 25 minutes.

Anode 1: 0.3 M Tris base, pH 10.0, 20% (v/v) methanol.
Anode 2: 25 mM Tris base, 20% (v/v) methanol.
Cathode: 25 mM Tris base, 40 mM 6-NH_2 hexanoic acid, 20% (v/v) methanol.
TBS-Tween: 50 mM Tris (HCl), 150 mM NaCl, 0.5% (v/v) Tween-20, adjusted to pH 8.5.

2.6.6 Enhanced chemiluminescence (ECL) staining of proteins

Prior to immunological detection, non-specific binding sites were blocked by incubating the PVDF membrane in TBS-Tween containing 3% (w/v) BSA for 30 minutes at room temperature. Membranes were then incubated with primary antibody (diluted in TBS-Tween/BSA solution) overnight at 4ºC on a rocker. All antibodies were appropriately diluted to ensure that detection was within the linear range. Blots were then rinsed for three 10 minute periods in TBS-Tween solution at room temperature. Depending on the required detection method, rabbit or mouse IgG conjugated to either horseradish peroxidase (HP) or alkaline phosphatase (AP) was diluted in TBS-Tween/BSA (at a 1/2000 or 1/1000 dilution, respectively) and applied to the membrane for a period of 2 hours at room temperature. The blots were then washed for three 10-minute periods in TBS-Tween.

HP-conjugated antibody/antigen complexes were detected using an enhanced chemiluminescence (ECL):

Luminol solution: 0.1 M Tris-phosphate pH 8.6, 0.5 mg/ml sodium luminol.
Enhancer solution: 1.1 mg/ml parahydroxy-coumaric acid in DMSO.
Final ECL solution: 1 mL luminol solution, 10 µl enhancer solution, 3.1 µl 3 % (v/v) hydrogen peroxide.

The PVDF membrane was incubated with ECL solution (1 mL per mini-gel) for 60 seconds, after which the solution was removed and the blot sandwiched between overhead projector transparency sheets prior to exposure to Fuji RX X-ray film for periods of between 2 seconds and 15 minutes.

2.6.7 Biochemical techniques

2.6.8 Transformation of competent cells

Subcloning efficiency DH5α competent cells:
F^- ϕ80*lac*ZΔM15 Δ(*lac*ZYA-*arg*F)U169 *rec*A1 *end*A1 *hsd*R17(r_K^-, m_K^+) *pho*A *sup*E44 *thi*-1 *gyr*A96 *rel*A1 λ^-

Subcloning efficiency DH5α competent cells (Invitrogen) were thawed on ice. Ligation products or plasmid DNA (10 ng) were added to 50 µL of the cells and incubated on ice for 30 minutes. After heating the mixture at 37ºC for 30 seconds to induce DNA uptake, the cells were placed back on ice to recover for 2 minutes.150 µL of un-supplemented LB medium was added to induce the expression of antibiotic resistance genes and the mixture incubated at 37ºC for 45 minutes. Finally, the sample was spread onto a pre-warmed LB agar plate containing 100µg/ml ampicillin and incubated at 37 ºC for 16-20 hours.

2.6.9 Small-scale preparation of plasmid DNA

DNA was prepared using the QIAprep Spin Miniprep kit (QIAGEN). A single colony of transformed DH5α competent cells was spread and onto 4 mL of LB media containing 100µg/ml ampicillin and incubated overnight at 37ºC in a shaking incubator. 1.5 mL of the culture was decanted into a labelled tube and the bacteria pelleted by centrifugation. The cell pellet was re-suspended in 250 µL of ice-cold Solution P1 (50mM Tris (HCl), pH8.0, 10 mM EDTA, 100 µg/ml RNase A). 250 µL of Solution P2 (200mM NaOH, 1% (v/v) SDS) was added to lyse the bacteria and the solutions were mixed gently by inversion. The sample was then incubated at room temperature for 5 minutes, after which 350 µL of Buffer N3 was added to neutralise the solution and to ensure the lysate was in the correct high salt conditions required for plasmid binding to the QIAprep spin column. After briefly mixing the solutions by inversion, the precipitated matter was isolated by centrifugation at 12,000 × *g* for 5 minutes and the supernatant removed to a QIAprep spin column. The DNA was then bound to the silica matrix in the QIAprep spin column by centrifugation of the DNA solution for 1 minute at 12,000 × *g* and the flow-through was discarded and the DNA washed by addition of 750 µL of a high salt-wash buffer containing ethanol (PE) and centrifugation of the column for 1 minute. After removal of the flow-through, a further 1 minute centrifugation ensured complete removal of the wash buffer from the column. DNA was eluted, under low salt conditions, into a fresh microcentrifuge tube by the addition of 50 µL of sterile deionised water to the column, followed by a 1 minute incubation at room temperature and

centrifugation as before. Diagnostic restriction digests were performed using 3 µL of this solution.

2.6.10 Transfection of plasmid DNA into MRC-5 SV2 cells

In a 6-well plate, $5x10^5$ cells were seeded to achieve 70% confluency at the time of transfection. 3.75 µL Lipofectamine 3000 reagent was diluted in 125 µL Opti-MEM medium and mixed well. A master mix of DNA was prepared by diluting 5 µg DNA in 250 µL Opti-MEM medium, then adding 10 µL P3000 reagent and mixing well. 125 µL diluted DNA was added to 125µL diluted Lipofectamine and incubated for 15 minutes at room temperature. To each well, 250 µL of the mixture was added. Cells were incubated for 3 days at 37ºC in a 5% CO_2 environment. For plasmids expressing Includes Neomycin / Kanamycin resistance, 400µg/mL of selection agent G-418 (Geneticin) was added after day two.

2.7 Creation of a CRISPR/Cas9 DDX3X Knockout cell line

The genomic DNA sequence for DDX3X was aligned with the genomic sequence using the Benchling (www.benchling.com; S.C. Li, Benchling, Inc., personal communication) and the Benchling CRISPR sgRNA design tool was used to identify 20-base pair sequences upstream of the 5' NGG PAM sequence. Benchling ranked the sgRNA sequences in order of their predicted on and off-target DNA affinities. The three highest ranked sgRNA sequences were chosen for use, on the basis that their differing efficiency as guides would render different results for each.

Table 2.5

5'-3' Oligonucleotide	3'-5' Oligonucleotide
CACCGAACAAACACTCGCTTAGCAG	AAACCTGCTAAGCGAGTGTTTGTTC
CACCGGTGGCAGTGGAAAATGCGCT	AAACAGCGCATTTTCCACTGCCACC
CACCGCGAGTTCTCGGTACTCTTCA	AAACTGAAGAGTACCGAGAACTCGC

Primers were designed for the surveyor assay using Primer blast (www.ncbi.nlm.nih.gov/tools/primer-blast/)

Table 2.6

Oligonucleotide	5’-3’
Forward primer (pF)	AAAGGGGAGCGAATGCGTAA
Reverse primer (pR)	TTTCCACTCCGGAAACGCAG

sgRNAs were phosphorylated and annealed by diluting the gRNA to a final concentration of 100 µM. To 1 µl of top and bottom primers, 1 µL T4 DNA ligase buffer (10x), 1 µL T4 PNK, and 6 µL nuclease-free H_2O were added. Phosphorylation and annealing of the oligos were performed in a thermocycler at 37°C for 30 min; 95°C for 5 min; with a ramp down to 25°C at 5°C min^{-1}. The final reaction product was diluted at 1:200. Cloning of the sgRNA oligos into the pspCas9(BB) cassette was performed by taking 2 µL of reaction product, and adding 18 µL of master mix made from: 1 µL PspCas9 (BB), 2 µL 10x FastDigest, 1 µL DTT, 1 µl ATP, 1 µL FastDigest (Bpi1) restriction enzyme, 11.5 µL nuclease-free H2O, and lastly, 0.5 µL T7 DNA ligase. This process was repeated for a pSpCas9(BB)-only negative control. The samples were incubated in a thermocycler at 37°C for 5 minutes, 21°C for 5 minutes, and repeated for a total of 6 cycles. A PlasmidSafe reaction was performed to ensure the digestion of unwanted linearised DNA. To 11 µL of the ligation reaction, 1.5 µL PlasmidSafe buffer (10x), 1.5 µL ATP (10mM), and 1 µL of PlasmidSafe exonuclease was added. The mix was then incubated in a thermocycler at 37°C for 30 minutes, followed by 70°C for 30 minutes. The transformation of plasmids into subcloning efficiency DH5α competent cells was performed by mixing 50 µl of subcloning efficiency DH5α with 5 µl of the Plasmidsafe reaction product, then incubating this on ice for 10 minutes prior to heat shock at 42ºC in a water bath for 30 seconds before being returned immediately to ice for 2 mins. 100 µl of pre-warmed (to 37ºC) LB was added and the entire mixture incubates in a 37ºC water bath for 30 mins. Each putative transformation, including the negative control assay (a linearised product of a pSpCas9(BB) plasmid), was spread on an LA (1 µL/mL ampicillin) dish and left to grow overnight at 37ºC. Colonies were picked and added to 2 mL of LB with 100 µg/ml ampicillin for incubation overnight in a 37ºC shaker. Plasmids were isolated from bacterial cultures using a QIAprep spin mini-prep kit, and the final

product checked for its DNA concentration by nanodrop, prior to being sent off for sequencing. Sequencing results were referenced against the pSpCas9(BB) cloning vector sequence to verify that the 20-nt guide sequence was properly inserted between the U6 promoter and the remainder of the sgRNA scaffold. Transfection of the CRISPR plasmid into MRC5 cells was performed by the seeding of cells onto a 6 well plate, one well for each proposed CRISPR assay, with another well for a GFP-control plasmid. 500 ng of each pSpCas9(sgRNA) plasmid sample was applied to each well using, and transfection reagent Lipofectamine 3000 Reagent utilised with its generic transfection protocol was utilised for each transfection into MRC5-SV2 cells. Cells were Incubated at 37^{o}C in an environment with 5% CO2, for 24 hours, after which transfection efficiency of the YFP control plasmid control was verified using a standard epi-fluorescent microscope. After a further 48 hrs, G418 selection was added at 400µg/mL, with continued incubation of the cells for 5 more days, with media refreshment every other day to dispose of cellular debris. The Cas9 transfected cells were enzymatically dissociated from their substrate, pelleted at 300 x g for 4 minutes and re-suspended in 1 mL MEM with 15% (v/v) FCS. 100 µL was utilised in the surveyor assay, the rest reseeded and allowed to grow in number for a limiting dilution and monoclonal selection after 21 days. Using a Genelute mammalian genomic DNA miniprep kit, DNA was extracted from each cell line and diluted with nuclease-free water to 100 ng/mL. PCR was performed on each cell line (including wild type MRC-5 SV2 cells), by adding 100 ng of the extracted DNA to 4 µL 5x Phusion HF buffer, 0.4 µL of 10 mM dNTPs, 0.5 µL forward primer, 0.5 µL reverse primer, 0.5 µL Phusion DNA polymerase, making up to a total of 20 µL with nuclease-free water. Incubation proceeded in a thermocycler using the following conditions:

Table 2.7

CYCLE STEP	*CYCLE #*	*TEMP*	*TIME*
Initial Denaturation	1	95 ˚C	2 minutes
Denaturation	2-30	95 ˚C	20 seconds
Annealing		60 ˚C	20 seconds
Extension		72 ˚C	30 seconds
Final Extension	32	72 ˚C	3 minutes
Hold	1	4 ˚C	infinity

5 µL of PCR product added to 2 µL of loading dye (Gel loading Dye Purple, Biolabs #B7024) and 3 µL H_2O and resolved on a 1% (w/v) agarose gel before staining the gels in a stain bath for 30 minutes prior to imaging and validation of single-band products. The remaining 15 µL of PCR product was added to 2 µL of NEB buffer#2, 2.5 µL of H_2O and 0.5 µL of T7E1. The mixture was then incubated at 37^{o}C for 30 minutes, prior to the addition of 1 µL 0.5M EDTA to halt the reaction. 15 µL of the product was added to 2 µL of loading dye and 3 µL H_2O and run on a 1% (w/v) agarose gel before staining the gels in a stain bath for 30 minutes prior to imaging and validation of dual-band products indicative of successful cleavage by the CRISPR/Cas9.

2.8 Microscopy

DPBS+: Dulbecco's Phosphate Buffered Saline both with calcium chloride and magnesium chloride from Sigma Aldrich [Cat# D8662];
Collagen stock solution: 1mg/mL collagen from rat tail (Bornstein and Traub type I powder from SIGMA [Cat# C7661]) dissolved by constant stirring with 0.1M Acetic acid for 3hours at RT.
Saponin: Saponin from Sigma [Cat# 47036] is diluted to a 1% (w/v) with PBS+, once 0.22 µm filtered, and stored at +4˚C for up to one week.
Mowiol mounting solution: 10% (w/v) Mowiol 4-88, 25% (v/v) glycerol, 0.1 M Tris (HCl), pH 8.5. Mixed overnight at room temperature, then clarified by centrifugation at 4,000 × *g* for 20 minutes prior to addition of 2.5% (w/v) 1,4-diazabicyclo-[2.2.2]octane (DABCO) antifade reagent.
Puromycin: From Sigma (Cat# P8833), puromycin dihydrochloride is soluble in water to realise a stock solution of 50 mg/ml (v/v), once 0.22 µm filtered, was be stored in aliquots at -20˚C.
Emetine: From Sigma (Cat# E 2375), Emetine dihydrochloride hydrate is soluble in water to realise a stock solution of 100 mg/ml (v/v); once 0.22 µm filtered, it was stored in aliquots at -20˚C and defrosted at room temperature at least 1 hour before use.
Cycloheximide Wash: Cycloheximide from Sigma [C7698] was diluted in DPBS+ to 355µM final concentration.

2.8.1 Coverslip Preparation

2.8.1.1 Cleaning

i. For epifluorescence and confocal microscopy:
High tolerance, round, No.1.5 glass coverslips of diameter 18mm, (Warner Instruments catalogue number 64-0714) were rinsed in an ethanol / hydrochloric acid solution (50% ethanol in 1M HCl) and allowed to dry at room temperature in a class II tissue culture (TC) hood.

ii. For the Proximity Ligation Assay:
35mm petridishes, with 14mm micro-wells of No.1.5 coverglass (MatTek corporation) No.1.5 glass, were rinsed in 0.1M acetic acid for 30 minutes and allowed to dry at room temperature in a class II TC hood.

iii. Coverslip cleaning for TIRF microscopy:
No.1.5 borosilicate coverslips were first flame cleaned, ozonated for 30 minutes to remove any trace of autofluorescence, and incubated in deionised water with 0.05% (v/v) Tween 20 in order to prevent aggregation or surface adhesion. Coverslips were rinsed with deionised water before use.

2.8.1.2 Application of tissue-matrix proteins to coverslips

Collagen stock was made to 1mg/mL by dilution of Collagen from rat tail Bornstein and Traub Type I, powder (SIGMA catalogue number C7661) in 0.1M Acetic acid, stirring for 3 hours at room temperatureuntil dissolved, then stored at -20^{o}C.

Application of surface tissue matrix proteins was performed on coverslips cleaned as described above.

i. **For epifluorescence, confocal and TIRF microscopy:** 350 μL of collagen working solution [330 μL (30% (v/v) ethanol / PBS+)

with 20 μL collagen stock solution] was pipetted onto each coverslip, to give a total coverage of 8 μg/cm^2 of collagen coverage. They were then dried overnight in a TC hood at room temperature. Coverslips were UV sterilised for 30 mins, then rinsed in PBS+ before use.

ii. **For the Proximity Ligation Assay:** 200 μL of collagen working solution [188.7 μL (30% (v/v) ethanol / PBS+) with 12.3 μL collagen stock solution] was pipetted onto each coverslip, to give a total coverage of 8 μg/cm^2 of collagen coverage. They were then dried overnight in a TC hood. Coverslips were UV sterilised for 30 mins, then rinsed in PBS+ before use.

2.8.1.3 Qdot nanocrystal: Antibody conjugation protocol

Using Qdot® Antibody Conjugation Kits (A10197) from Invitrogen), 300 μL of antibody at 1 mg/mL was pipetted into a centrifugation tube, to which was added 6.1 μL of DTT solution (Component C). The mixture was vortexed for 5 seconds and incubated at room temperature before adding 20 μL of dye labelled marker. Desalting columns were prepared as per the manufacturer's instructions. The desalting column was filled with exchange buffer before the immediate addition of the antibody mix to the top of the gel bed. The antibody mix was allowed to fully enter the gel prior to the addition of 1 mL of exchange buffer to the top of the gel bed to elute the antibody. Reduced antibody was collected into a centrifuge tube when the first coloured drops eluted. 500 μL was collected in total.

To 14 μL of SMCC solution, 125 μL of Qdot nanocrystals was added and vortexed to mix prior to a one-hour incubation at room temperature. The desalting column was filled with exchange buffer before the immediate addition of the activated Qdot nanocrystal mix to the top of the gel bed. The Qdot nanocrystal mix was allowed to fully enter the gel prior to the addition of 1 mL of exchange buffer to the top of the gel bed to elute the antibody. Desalted and activated Qdot nanocrystals were collected into a centrifuge tube when the first coloured drops eluted. 500 μL was collected in total. The elute was then mixed briefly. Reduced antibody and activated Qdot nanocrystals solutions were

mixed at a 1:1 ratio and incubated at room temperature for 1 hour. To this mixture was added 10 µL of 10 mM 2-mercaptoethanol and incubated at room temperature for 30 minutes. To the prepared separation column (component F), 0.5 mL of distilled water was gently added to the top of the gel. To the tip of the column, was attached one end of the tubing (Component J). To the other end of the tubing was attached to a syringe (Component H) that had the plunger completely depressed. The syringe plunger was slowly drawn out to withdraw the solvent from the column and PBS added to the top of the settled gel bed to keep it from drying. The column was re-filled with PBS two more times, using the syringe to draw the PBS through. This quenched conjugation reaction elute was split into two ultrafiltration devices (component K) for concentrating to approximately 20 µL by centrifuging at 4000 x g for 10 minutes. The concentrated conjugate reaction from the two ultrafiltration devices were added to a separation column after which 50 µL of PBS was added and allowed to run into the gel bed. The first 10 drops of coloured conjugate to elute the column were collected in centrifugation tube (component L) to which sodium-azide was added at a final concentration of 0.01% (w/v) to serve as a preservative, prior to long-term storage at 4˚C.

2.9 Fixation of cells for immunofluorescence microscopy

2.9.1 Preparation of Paraformaldehyde working solution

Stock solutions of methanol and RNAase free 20% (w/v) paraformaldehyde solution, EM grade (Electron Microscopy Sciences, UK), was diluted at 1:5 with ice cold PBS+ in the confines of a fume cupboard. The solution was kept on ice for 30 minutes before use.

2.9.2 Paraformaldehyde fixation method

Cells were typically seeded onto sterile, PBS+ rinsed, collagen-covered coverslips individually placed into wells of a 6-well plate or pre-adhered into 35 mm diameter dishes. After the appropriate incubation period, typically 40 minutes to 24 hours, tissue culture medium was aspirated and the cells washed on ice, with ice-cold PBS+. Cells were fixed by incubation with a working

solution of 4% (w/v) paraformaldehyde, within a fume hood and on ice, for 17 minutes, and then washed three times in PBS+. Cells were then permeabilised for 2.5 minutes with 0.1% (v/v) Triton X-100 in PBS at room temperature, or *via* a saponin based permeabilisation method where saponin is an integral part of all of the blocking, wash and antibody dilution buffers.

2.9.3 Pre-permeabilisation method

Cells were prepared as above. At the appropriate time, the tissue culture medium was removed and cells were washed on ice, in ice-cold PBS+. Cells were incubated for 30 seconds in cytoskeleton buffer containing 0.0375% (w/v) saponin. Cells were fixed by incubation with a working solution of 4% (w/v) paraformaldehyde, within a fume hood and on ice, for 17 minutes, and then washed three times in PBS+. Cells were then permeabilised for 2.5 minutes with 0.1% (v/v) Triton X-100 in PBS at room temperature, or *via* a saponin based permeabilisation method, as described above.

2.10 Immuno-cytochemistry (ICC) protocol

Prior to fixation, cells were seeded on collagen-coated coverslips in 12-well plates (for 18mm diameter coverslips) or 6 well plated (for 22 mm diameter coverslips), to a density of 15000 cells/cm^2. Cells were incubated for 45 minutes for “cell spreading” assays, or for 2-6 hours for “cell growing” assays. Fully confluent cells were obtained after 24 hrs of incubation, depending on cell type and stage in the cell-cycle. Depending on the experiment, cells were pretreated with different inhibitors, as described in the individual figure legends.

The protocol for direct immunofluorescence analysis using antibodies directly conjugated to fluorescent particles (be they Quantum dots or fluorescent peptides) is the same, but without the secondary antibody incubation step.

Cell Wash: PBS+ supplemented with EDTA-free protease inhibitors.
10% Block: PBS+ supplemented with 10% (w/v) Normal goat serum (NGS) and EDTA-free protease inhibitors (Roche).
Antibody buffer: PBS+ supplemented with 4% (w/v) normal goat serum (NGS) and EDTA-free protease inhibitors.

2.10.1 Nuclear Staining and coverslip mounting:

(i) *Utilising DAPI and Mowiol*

Nuclei were stained with 12.5 ng/ml 4',6'-diamidino-2-phenylindole hydrochloride (DAPI) for 5 minutes. The stained cells were washed once with PBS+, then once with pure water and coverslips mounted directly onto methanol cleaned slides using 20 µL of Mowiol mounting solution and sealed with clear nail varnish.

(ii) *Utilising Vectashield*

Coverslips were mounted directly onto methanol-cleaned slides using 20 µL of vectashield and sealed with clear nail varnish.

(iii) *Utilising Prolong Diamond*

Coverslips were mounted directly onto methanol-cleaned slides using 20 µL of Prolong Diamond (with DAPI). Coverslips gently pressed down onto the slides and the mounting media allowed to solidify overnight in the dark at room temperature, before imaging and long-term storage at 4˚C.

(iv) *For TIRF Microscopy*

No DAPI staining was applied. Coverslips were mounted directly onto methanol-cleaned slides using 20 µL of GLOX antifade buffer (see below) and sealed with clear nail varnish.

GLOX antifade buffer: 10% (w/v) glucose in nuclease-free water; 1 M Tris-HCl, pH 8.0; 20x SSC; Nuclease-free water; Glucose oxidase (diluted to 3.7 mg/mL in 50 mM sodium acetate, pH5), from Sigma [Cat# G0543]; Catalase from Sigma [Cat# C3155]. For a working solution, 0.85 mL of nuclease-free water and add 100 µL of 20x SSC were mixed together, followed by the addition of 40 µL 10% glucose and 10 µL of 1 M Tris-HCl. The mix was vortexed and then100µL of this “GLOX” buffer transferred to another tube. 1 µL of the glucose oxidase stock was added along with 1 µL of mildly vortexed catalase suspension. To adherent cells on a collagen-covered coverslip, GLOX antifade buffer was applied directly to the coverslip prior to immediate imaging.

2.10.2 ICC using Triton-X permeabilisation

Following the desired incubation period, under the conditions described in the text, the coverslips were rinsed with ice-cold wash buffer, before a 17 minute incubation on ice in freshly-made ice-cold PFA fixation solution (4% PFA in PBS+). All subsequent steps were performed at room temperature: After three washes, cells were then incubated in Triton-X permeabilisation solution (0.1% TX100 in PBS+) for 2 minutes 30 seconds, then washed a further three times. Block was added to counter non-specific binding, and all coverslips placed in an opaque humidified chamber for 30 minutes at room temperature. Following incubation in primary antibody solution for 60 minutes, the cells were washed three times, then incubated with the appropriate secondary antibodies and/or phalloidin-conjugates in for 60 minutes at room temperature in a light-proof humidified chamber. Samples were washed for ten minutes, three times, on a rocker at room temperature, and were then ready for nuclear staining and mounting.

2.10.3 ICC using Saponin permeabilisation

Following the protocol described in section 2.10.2 above, the step for permeabilisation by Triton-X was omitted, and 0.0375% (w/v) saponin added to most washes and all blocks, up to and including the ‘Final Wash’. Saponin wash was made from PBS+ supplemented with 0.0375% (w/v) saponin and EDTA-free protease inhibitors; Saponin block was PBS+ supplemented with 10% (v/v) NGS and 0.0375% (w/v) saponin and EDTA-free protease inhibitors. All antibodies are made in saponin buffer of PBS+ supplemented with 4% (v/v) NGS and 0.0375% (w/v) saponin and EDTA-free protease inhibitors.

Following the desired incubation period, under the conditions described in the text, the coverslips were washed twice with ice-cold PBS+ before a 17 minute incubation on ice in freshly-made ice-cold PFA fixation solution. All subsequent steps were performed at room temperature. After three washes with PBS+, blocking and initial permeabilisation was performed by applying saponin block for 30 minutes at room temperature in a light-proof humidified chamber. Following incubation with a saponin buffer based primary antibody solution for 60 minutes, the cells were washed three times with saponin wash, then

incubated with the appropriate saponin buffer based secondary antibodes and/or phalloidin-conjugates in for 60 minutes at room temperature in a light-proof humidified chamber. Using a rocker at room temperature, samples were washed twice in saponin wash for 10 minutes, before a final 10 minute wash in PBS+, before being ready for nuclear staining and mounting.

2.10.4 The Ribopuromycylation Method (RPM)

The ribo-puromycylation method (RPM) closely follows the protocol described in Section 2.11.3 with slight changes. These changes accommodate the need to arrest ribosomal action and inhibit the early release of nascent chain polypeptides from the ribosome with the use of elongation inhibitors, as well as preventing RNAse from destabilising key RNAs.

RPM wash was made from PBS+ supplemented with 0.0375% (w/v) saponin, EDTA-free protease inhibitors and 10 U/ml RNaseOut; RPM block was PBS+ supplemented with 10% (v/v) NGS, 0.0375% (w/v) saponin, EDTA-free protease inhibitors and 10 U/ml RNaseOut. All antibodies were made in RPM buffer of PBS+ supplemented 0.0375% (w/v) saponin, 4% (v/v) NGS, EDTA-free protease inhibitors and 10 U/ml RNaseOut.

Following the desired incubation period, under the conditions described in the text, cells were supplemented for the last 5 minutes of incubation with 91 µM puromycin and 208 µM emetine. Using ice-cold reagents and performing the next steps on ice, media was aspirated and the cells quickly washed with ice-cold permeabilisation buffer (PBS+, 355 µM cycloheximide, EDTA-free protease inhibitors, 10 U/ml RNaseOut and 0. 0375% (w/v) saponin). They were then incubated in permeabilisation buffer for a full 2 minutes, before a 17 minute incubation in freshly-made methanol-free fixation buffer (PBS+ supplemented with 4% (v/v) PFA). After three washes with RPM wash, non-specific binding was blocked by the addition of RPM block for 30 minutes. Cells were incubated with primary antibodies (including anti-puromycin mAb for 60 minutes (to a pre-determined titre), in RPM buffer. The cells were washed three times with RPM wash, then incubated with the appropriate secondary antibodies and/or phalloidin-conjugates in RPM buffer, for a further 60 minutes. Using a rocker at room temperature, samples were washed twice in RPM wash for ten minutes,

before a final 10 minutes wash in PBS+, before being ready for nuclear staining and mounting.

2.10.5 Proximity Ligation Assay (PLA)

The first section of this protocol closely follows the protocol described in Section 2.11.3 using the saponin buffers described above. Following the desired incubation period under the conditions described in the text, the coverslips were washed twice with ice-cold PBS+ before a 17 minute incubation on ice in freshly-made ice-cold PFA fixation solution. All subsequent steps were performed at room temperature. After three washes with PBS+, blocking and initial permeabilisation was performed by applying saponin block for 30 minutes. Following incubation with a saponin buffer based primary antibody solution for 60 minutes, the cells were washed three times with saponin wash. Plus and minus PLA probes were diluted 1:5 in antibody buffer and set aside for 20 minutes at room temperature before use. The PLA probe solution was added to the dishes and incubated in a pre-heated opaque humidity chamber for 30 minutes at 37˚C. The cells were washed with Wash Buffer A twice for 5 minutes each, under gentle agitation. The Ligase and Ligation solution were mixed according to the manufacturer's instructions, vortexed and applied to slides. Slides were incubated in a pre-heated humidity chamber for 30 minutes at 37˚C. Amplification stock was prepared (initially without polymerase). Slides were washed in Wash Buffer twice for 2 minutes each, under gentle agitation. The polymerase was added to the amplification solution were mixed as per manufacturer's instructions before being applied to slides, which were then incubated in a pre-heated humidity chamber for 2 hours at 37˚C. The slides were washed twice in wash Buffer for 10 minutes each and then again in 0.01 x Wash Buffer for 1 minute. The minimal volume of Duolink *In Situ* mounting medium with DAPI was added to just cover the cells, incubated for 15 minutes before analysis using an oil-immersion objective. After imaging, the slides were stored at -20˚C in the dark.

2.10.6 Antigen retrieval and immunocytochemistry.

> **Antigen Retrieval Buffer:** 100 mM Tris (HCl) pH 9.5, 5% (w/v) urea.

Following the desired incubation period, under the conditions described in the text, the coverslips were rinsed with ice-cold wash buffer, before a 17 minute incubation on ice in freshly-made ice-cold PFA fixation solution (4% PFA in PBS+). Coverslips were rinsed in PBS+ for 5 minutes at room temperature then immersed in Antigen Retrieval Buffer for 10 minutes at 95˚C, prior to rinsing in PBS+ for 5minutes on a rocker at room temperature. Slides were then processed as described in Section 2.11.3.

2.10.7 Combined Fluorescence *in situ* Hybridization (FISH) and Immunocytochemistry (ICC)

This process was based on Stellaris protocols for Simultaneous Stellaris FISH and Immunofluorescence using Adherent Cells, but was altered to incorporate the use of block at the IF stage. All reagents were RNAse-free. For this protocol, the initial pre-fixation washes used PBS+ supplemented with EDTA-free protease inhibitors unless a ribopurymycylation assay was being used in conjunction with FISH. In this case, RPM wash was used prior to fixation. All other washes were performed using 2X SSC unless otherwise stated. Blocks consisted of PBS+ supplemented with 10% (w/v) NGS and EDTA-free protease inhibitors and all antibody buffers were made with PBS+ supplemented with 4% (w/v) NGS and EDTA-free protease inhibitors:

Coverslips were cleaned as described above. Following the desired cell incubation period and under conditions described in the text, the coverslips were rinsed with ice-cold wash buffer. The wash was aspirated and slides incubated for 17 minutes on ice in freshly-made ice-cold PFA fixation solution (4% PFA in PBS+). After three washes, cells were incubated in 70% (v/v) ethanol for 1 hour at 4^{o}C, then washed three times. The ethanol was aspirated off and 1 mL of Stellaris wash buffer was added, letting it stand for 5 minutes before removal of the buffer. 100µL Stellaris mRNA probe in hybridization buffer was added and coverslips were incubated in a dark humidified chamber at 37^{o}C

for 4 hours. Block was added to each coverslip which was then incubated for 30 minutes in an opaque humidity chamber at room temperature. Coverslips were washed 3 times, primary antibodies added and incubated for 60 minutes at room temperature in a light-proof humidified chamber. Cells were washed three times, then incubated with the appropriate secondary antibodies for 60 minutes at room temperature in a light-proof humidified chamber. Samples underwent three 10 minute washes, on a rocker at room temperature, and were then ready for nuclear staining and mounting. Nuclei were stained for 5 minutes with 5 ng/ml DAPI in wash buffer and washed three more times prior to coverslip mounting. Coverslips were mounted directly onto methanol-cleaned slides using 20 µL of GLOX antifade buffer, sealed with clear nail varnish and immediately imaged.

2.11 Microscopy

2.11.1 Configuration of the Leica SP8 scanning confocal microscope

Cells were analysed using a Leica SP8 scanning confocal equipped with a 63 × oil immersion objective and fitted with the appropriate filter sets. The cell images were processed using ImageJ and Fiji imaging software. Greyscale images were pseudo-coloured to correspond to the red (TRITC/Alexa Fluor 555), green (FITC/Alexa Fluor 488) or blue (DAPI) fluorescence and the digital images merged. PLA experiments had all images analysed by PLAY software (discussed in Chapter 5).

2.11.2 Configuration of the Total Internal Reflection Microscope (TIRFM)

A TIRF microscope (Axelrod 2008) was custom built, and kindly offered for use by Dr Mark Osborne (Figure 2.1). Built around the body of a Nikon TE2000U inverted microscope, with a Nikon PLAN APO TIRF 60x/1.45 oil immersion objective and TIRF objective lens (Thorlabs, LA1708-N-BK7 Plano-Convex Lens, Ø1", f = 200.0 mm, Uncoated). A Spectra Physics water-cooled Beamlock 2060/65 Krypton-Argon Laser provided the source of 488nm excitation light, with 473 and 561nm excitation lines from separate solid-state diodes. Light from the array of lasers would first be forced into convergence

through a dichroic mirror array to reflect all incoming excitation beams onto a single common path, initially directed through the optical axis of the objective lens. To condition the light, the excitation beam passed through a spatial filter consisting of two lenses separated by a pinhole placed in their focal distance, allowing only for the transit of the central noise-limited maximum of the diffraction pattern. The excitation beam was circularly polarised using a quarter-wave plate (Thorlabs UK, WPMQ05M), and attenuated to the desired power using a variable ND filter wheel. The beam was focused on the back focal plane of the objective prior to the introduction of a TIRF lens. The TIRFM plano-convex lens was then be manoeuvred to take the excitation beam off the optical axis such that the emergent beam at the sample interface was near-collimated with an angle of incidence greater than the critical angle (θ_C) of ~67˚ for the glass/water interface. This generated a 30 µm diameter TIRF footprint with power densities in the typically in the range of 1.2-12.5 kW cm^{-2} at the coverslip, accounting for near-field enhancement by evanescent excitation. Optical coupling of the coverslip to the TIRF objective lens was performed using index-matching immersion oil (n= 1.51, Nikon, UK). Fluorescence emission was collected by the objective and emission light filtered through the relevant dichroic mirrors (Semrock), then magnified by a variable zoom (Edmund Optics). At the point of light ingress to a Photometrics Evolve 512 back-illuminated EMCCD Camera, appropriate band-pass filters were selected to protect it from any high-power stray or reflected excitation laser lines. The control of excitation and emission filter wheels, as well as all camera exposure timings, pixel binning and movie frame rates was performed via the Windows-based open source microscopy software, Micro-manager (versions 1.3.48 to 1.41). All movies were taken as 16-bit images, with 100ms exposures and a frame interval of 20ms.

A

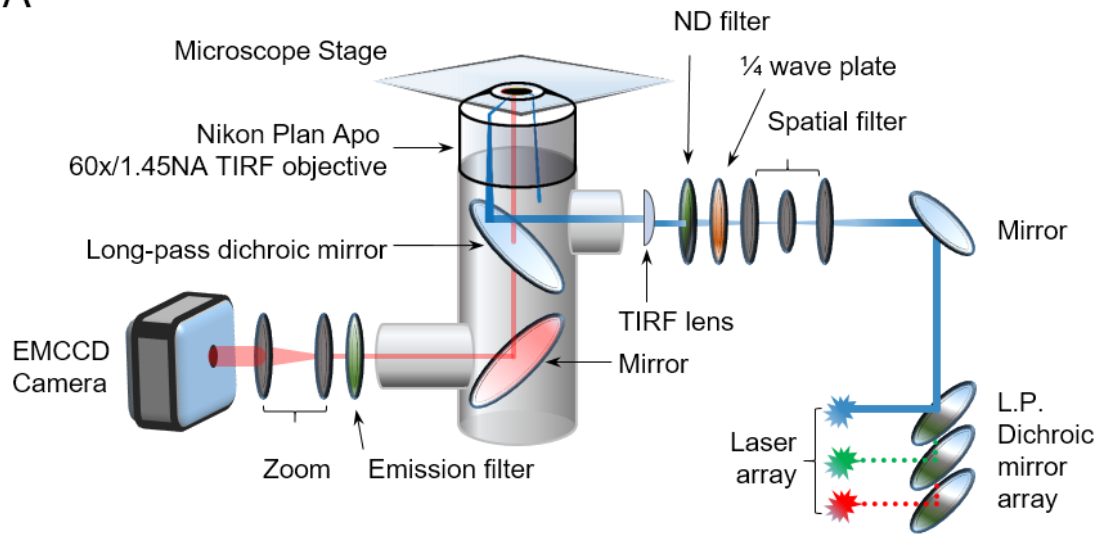
Microscope Stage
ND filter
¼ wave plate
Spatial filter
Nikon Plan Apo
60x/1.45NA TIRF objective
Mirror
Long-pass dichroic mirror
TIRF lens
EMCCD
Camera
Mirror
L.P.
Dichroic
mirror
array
Laser
array
Zoom
Emission filter

B

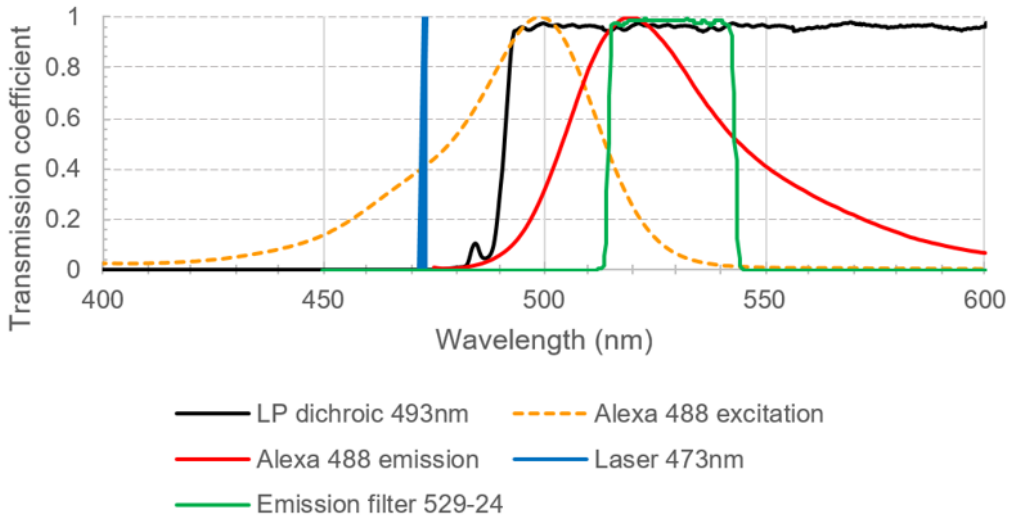
Transmission coefficient
1
0.8
0.6
0.4
0.2
0
400
450
500
550
600
Wavelength (nm)
LP dichroic 493nm
Alexa 488 excitation
Alexa 488 emission
Laser 473nm
Emission filter 529-24

C

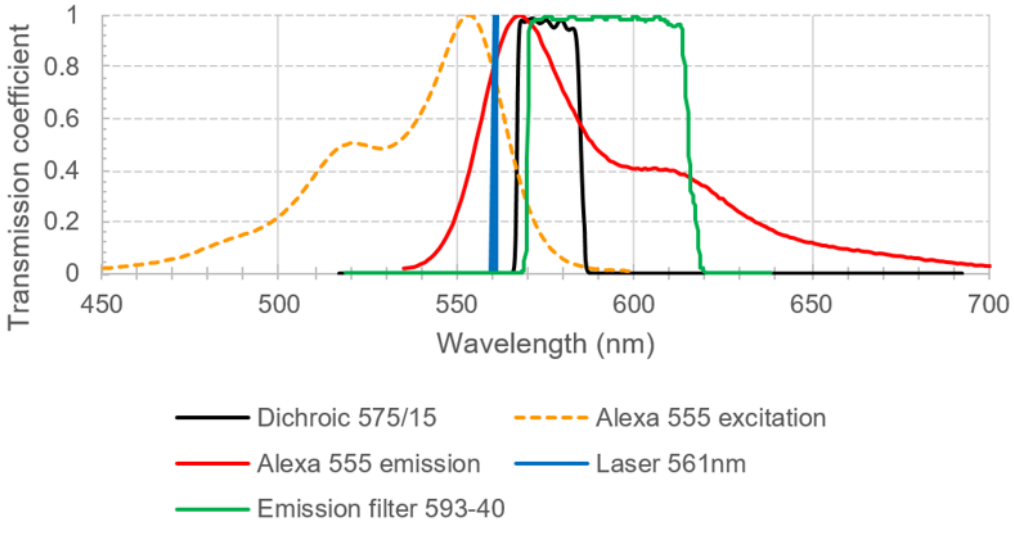
Transmission coefficient
1
0.8
0.6
0.4
0.2
0
450
500
550
600
650
700
Wavelength (nm)
Dichroic 575/15
Alexa 555 excitation
Alexa 555 emission
Laser 561nm
Emission filter 593-40

Figure 2.1 Configuration of the Total Internal Reflection Microscope
Panel A. The Total internal reflection microscope (TIRFM) setup, constructed on a 3 metre anti-vibration bench with an array of laser diodes configured to have near-perfect co-axial light rays entering the microscope by fine adjustment of the dichroic array. A spatial was used to give the beams Gaussian intensity profiles; a quarter-wave plate converted the lasers' linear polarised light to circular polarisation; neutral density (ND) filters were used to manually adjust laser excitation power; the TIRF lens (a simple planoconvex lens) directed the beam to the outer limits objective lens whilst still maintaining a co-axial path. Prior to entering the objective, the excitation light of the laser reflects off an especially-chosen long-pass dichroic lens. Light emerging from the objective becomes collimated, ensuring the full beam impinged on the cover-glass at a common angle. Subtle alteration of the incident angle onto the coverslip was performed by mirror and TIRF lens adjustments. Fluorochromes situated within 100-200nm of the coverslip, are excited by the evanescent field, and a proportion of the fluorescent emission light travels through the objective, which columnates it prior to it passing through the long-pass dichroic mirror (used to reflect the excitation light into the objective). A mirror in the microscope directs the beam out of the microscope apparatus, where the emission filter ensures that only emission light passes through to the zoom apparatus into the Photometrics Evolve camera - a 16bit, 512 by 512 pixel, cooled electron multiplying charged coupled device (EMCCD) unit. Camera operation and shutter control was automated by use of Micro-Manager open source microscopy software
(www.micro-manager.org).
Panel B. Laser and filter choice used to image fluorescence from Alexa Fluor 488 fluorochromes: Laser 473nm; dichroic 493; emission filter 529-24.
Panel C. Laser and filter choice used to image fluorescence from Alexa Fluor 555 fluorochromes: Laser 561nm; dichroic 575; emission filter 593-40.

2.11.3 Imaging *in situ* Proximity Ligation Assays.

Using a Leica SP8 confocal microscope with a 63x 1.40 Oil objective and 2.016 x 2.016 megapixel resolution and confocal scanning of just the two essential channels (DAPI and the red PLA channel), images were gathered using a single slide created using the PLA protocol (as described in Chapter 5) where primary antibodies were applied at the same concentrations used for ICC. In general, achieving a consistent focus between specimen was performed in the following manner: The DAPI channel was configured with a 1 AU diameter pinhole, and UV laser and associated detector gain set appropriately high, prior to the location of the mid-z-section of the lamellipodia. To ensure that as many spots were captured within the image, the confocal pinhole for the red PLA channel was opened to its maximum of 6.28 AU, allowing foci out of the field of focus to contribute more of their emission light to the final image. This also effectively allowed the entire depth of the lamellipodia and a significant proportion of the cytoplasm to contribute to a bigger portion of their PLA emission light. Without such a large pinhole on the red channel, a significant number of foci were not seen in the image. No further image processing was performed.

2.12 PLA Analysis

PLA images in compressed LIF file format were imported into Fiji using Bio-Formats Importer, using a composite colour mode, hyper-stack importation, and no autoscaling. Brightness and contrast were enhanced on all slices to properly view the cell peripheries (usually adequately performed via the DAPI stained channel in combination with the PLA channel). To ease such repetitiveness, a small Fiji macro was employed in batch mode or on an image by image basis, with the saturation value modified appropriately:

```
n = nSlices();
for (i=1; i<=n; i++) {
     setSlice(i);
     run("Enhance Contrast", "saturated=0.4");
     run("5 ramps");
     }
```

The resulting images were contrast enhanced using ‘5 ramps’ pseudo-colouring for improved perception of the cell periphery. Using the Polygon selections default button for on the Fiji toolbar, multiple points were selected around all the cell peripheries visible on each image. Care was taken that the polygon vector hinges were not located too close to neighbouring regions of interest (ROIs)/cell peripheries. Once all ROIs have been added the ROI manager, each image was saved as a TIF, and the associated ROI file containing multiple ROIs saved as a .zip file with a name which clearly associates it with its image. Both file types were saved in the same Experiment folder. With the 4PLAY script (4play.imj) executed, each image file was selected with its associated ROI zip file. At this point 4PLAY created a new folder within which the results from its foci and cellular morphology analysis would be stored. A distance discriminator of 110 pixels (equivalent to 10 µm) was selected for the Adjacencies mapping threshold. To allow 4PLAY to continue analysis, several selection criteria were enabled, including ‘convert to composite image’; ‘spline fit’ (enabled only when images of highly confluent cells were imaged); ‘Number of channels in the image’ was set to 2; ‘DAPI channel’ was set as 1; ‘PLA channel number’ set to 2; Save output hierarchical filing system, close results images, close results tables and count PLA maxima on edges of nuclei and cell boundaries were all enabled. When defining the nuclei boundaries, Gaussian blurring was employed in a consistent manner, with a blur factor of 8 pixels being adequate for all images. Thresholding of nuclei was performed manually. Once 4PLAY had completed its analysis, the PLAYsheet was configured and the location of images directories defined (within which all images and associated ROI files were directly available without traversing further into the operating System’s file system). From a system command prompt, “PLAY.py” was executed, which prompted for the names of any drugs/signalling pathway inhibitors used in each assay. Results were accessed via the PLAYmate PLA analysis and visualisation studio, from where statistics and visual representations of the PLA foci and cellular morphologies were accessed.

2.12.1 Imaging streptavidin-conjugated fluorophores with TIRFM

Coverslips were flame dried and ozonated for 30 minutes to remove any auto-fluorescence before imaging. 100 µL of a solution containing Biotin-conjugated bovine serum albumin (Sigma, A-8549, 1 mg/ml) in deionised water was incubated for 10 minutes on the coverslip and washed with deionised water. A 100 nM solution of streptavidin conjugated with Alexa Fluor 546 was added and left to settle for 30 minutes, prior to rinsing with deionised water. A layer of deionised water was left on the coverslip to facilitate total internal reflection using TIRFM.

2.13 Using the SOFI algorithm

Two-channel images were aligned using the GDSC alignment software “align FFT”. For the FFT version of the SOFI algorithm (kindly provided by Dr Remi Boulineau and the laboratory of Dr. Mark Osborne), the Convolve3D plugin first needed to be installed from: http://www.optinav.com/Convolve_3D.htm. Each movie was cropped to a square in the x-y plane prior to its importation. Fiji allocated memory for Java was increased to is maximum (using EDIT > OPTIONS > Memory and Threads). For stacks of over 100 frames, a "virtual stack" plugin was utilised (File > Import > TIFF Virtual Stack). SOFI processing was implemented using the SOFI FFT macro, with "setBatchMode(true)" was remarked out of the SOFI algorithm prior to execution.

3 Techniques and Methods Optimisation

3.1 Microscopy

3.1.1 Biological Imaging; a brief history

The seminal breakthrough in biological imaging (Figure 3.1A) came from the publication of Micrographia (Hooke 1665) in which Hooke utilised a primitive compound microscope to illuminate the hitherto little-known world of plant architecture and micro-organisms (Figure 3.1B). After diligently shaving a slither of cork with his razor-sharp pen-knife, placed onto a microscope and with light cast upon it by a deep plano-convex glass, Hooke plainly perceived the honeycomb-like partitions which he was to refer to, for the very first time, as ‘cells’ (Figure 3.1C).

In the late seventeen-hundreds, lens-making was still a nascent art. Although compound microscopes were easier to use, because of the difficulty in grinding and blowing lenses without introducing spherical and chromatic aberration (Figure 3.1D., insets i. and ii.), the quality of lenses still couldn’t match the magnification of the much more powerful, albeit awkward single-lens magnifying glass system. The latter was used in the years proceeding Micrographia allowing the Dutch scientist Antoni van Leeuwenhoek to widen significantly the breadth of our understanding of the natural world. This included a huge amount of discoveries ranging from human erythrocytes, animal spermatozoa, parthenogenesis in aphids, and most celebrated of all, single-celled organisms (originally referred to as animalcules) including bacteria.

In the early 1800s, developments in the field of optical glass making were progressing quickly, aided by such people as Joseph von Fraunhofer with the introduction of more autonomous glass polishing machines. Furthermore, Vernon Harcourt’s development of high refractive index glasses, and Joseph Jackson Lister’s development of achromatic lenses (minimising spherical aberration by defined spatial separation of the lens combinations) enabled the manufacture of powerful and practicable compound microscopes (Figure 3.1D., inset iii.). These apparatus, although useful for the study of microorganisms and tissue, were unable to provide great insights into the internal composition of

cells until the invention in 1858 of differential staining techniques by Joseph von Gerlach, utilising solutions of carmine to discriminate nuclei and stress granules within the cytoplasm.

Although fluorescence had been known about for some time (Stokes 1853), it took two major breakthroughs of the 20th century to make fluorescent microscopy a practical tool in the laboratory. Heimstädt introduced the first usable system in 1911. It relied on the auto-fluorescent properties of specimens after they had been exposed to a high-energy ultraviolet light. The system was limited in its use, primarily because of the inherent noise of the system, its reliance on autofluorescence of the specimen, and a need for darkfield condensers. Even to Heimstädt, it seemed that such microscopes would be of limited use (Heimstädt 1911). In 1929, epifluorescent microscopy was invented, which incorporated a primitive filter system to attenuate the intensity of excitation light reflected from the specimen, and so increased the signal to noise ratio dramatically over other contemporary systems (Ellinger & Hirt 1929). With the discovery of soluble fluorochromes and the development of precision dichromatic mirrors or band-pass filters, by 1967 discrimination of internalised fluorescent markers with high resolution and contrast was made possible with epifluorescent microscopy (Borel & Jansen 2009), perfectly complementing the then nascent science of immunofluorescence (Coons 1961). However, the study of mammalian cells was virtually impossible with these modern microscopes. In 1932, transparent biological materials were studied for the first time using Frits Xernike's invention of the phase-contrast microscope. This phase-contrast microscope allowed for the study of colourless and transparent biological materials for which he was awarded the Nobel Prize in Physics in 1953.

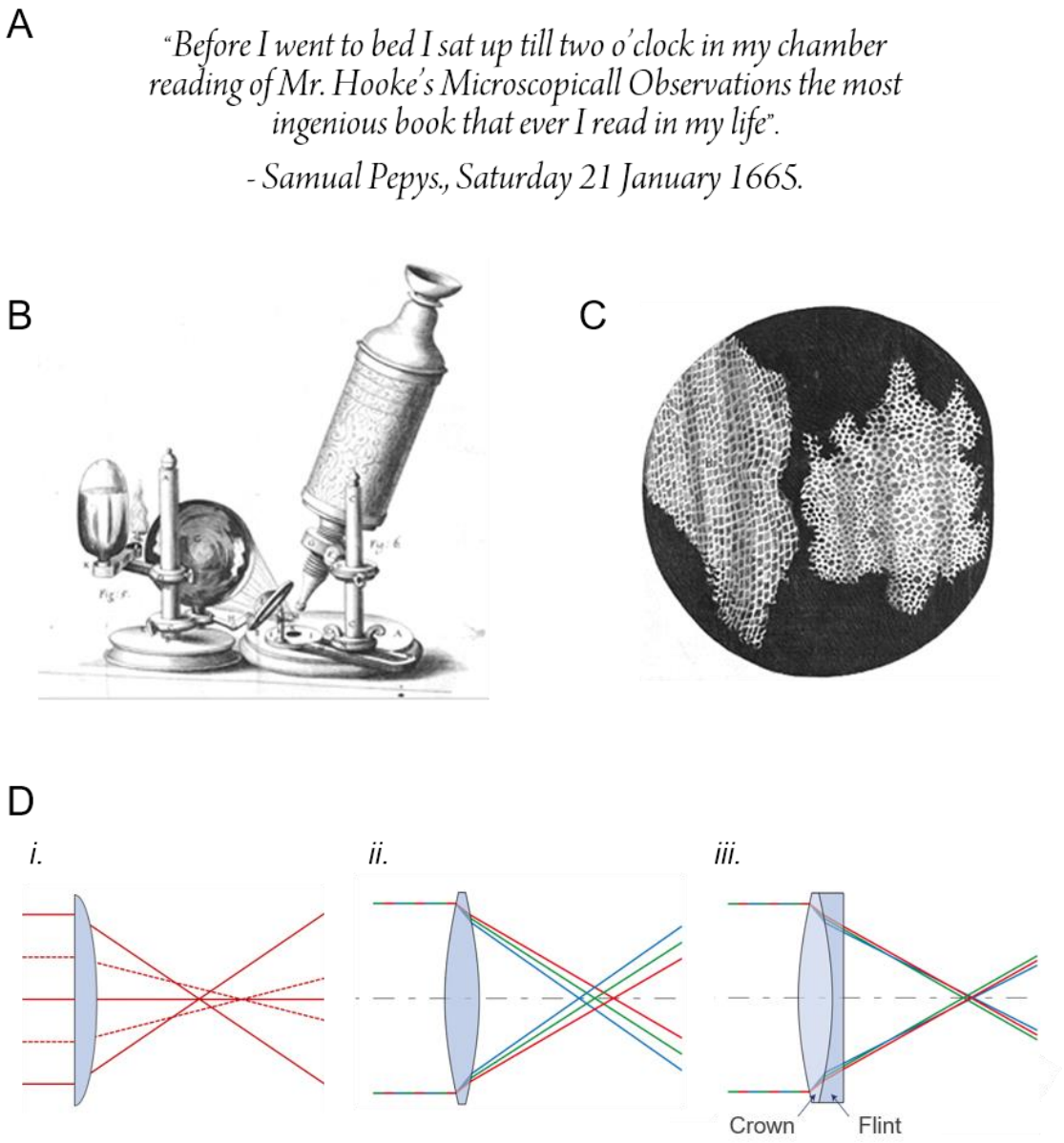

Figure 3.1 Microscopes come of age in the 17th and 18th Century

Panel A. The impact of Hooke's Micrographia was profound and far-reaching: A quote from the diary of Samuel Pepys, Saturday 21 January 1665.

Panel B. Robert Hooke's drawing of his London-manufactured microscope, adapted from Micrographia (Hooke 1665), with kind permission from The Royal Society. Light is directed from an oil lamp to the specimen *via* a water-filled glass spherical condenser.

Panel C. Hooke termed the word 'cells' when describing the tiny compartments found within a razor-thin slither of cork. **Panel D.** ***i.*** Spherical aberration: Light traversing a planoconvex lens focuses more tightly when entering further from the optical axis. ***ii.*** Standard biconvex lenses introduce chromatic aberration to images. ***iii.*** An achromatic doublet with the near-perfect ability to obtain a common focus for all colours.

3.1.2 Obtaining high contrast in transmitted light illumination

Standard bright-field microscopy is not adequate for visualisation of colourless and transparent specimens; such objects tend to absorb very little light, leaving the amplitude of the waveform virtually free from attenuation and leaving image contrast negligible. Staining of the cells with coloured dyes offers a simple and cost-effective way to change the light absorption characteristics of particular compartments of a cell, resulting in increased visual contrast between stained and unstained areas. Staining introduces a plethora of issues that must be borne in mind, not least the toxic effects of staining reagents. Another way to increase the contrast between cellular compartments is to leverage the effect of refraction using either phase contrast microscopy or differential interference contrast (DIC). When passing through an essentially transparent object such as monolayers of adherent cells, light undergoes a number of modes of propagation including refraction, absorption, scattering, and diffraction (the angular deviation around the edges of an object or aperture).

The refractive index (η) of any medium is defined by the speed of light travelling through it (v), compared with its speed through a vacuum (c).

$$\eta = \frac{\mathrm{c}}{\mathrm{v}}$$

When light passes between media of differing refractive indexes, its speed changes and it undergoes refraction (angular deviation from its original course). Although the intensity of the light may remain unaffected, the phase of the light wave will vary in comparison to coherent light which does not undergo the same angular divergence. The reflective scattering of light will also induce a similar phase shift phenomenon, but unfortunately, both cameras and human eyes employ phase agnostic image sensors; thus the change of phase is impossible to visualise directly.

In 1942 Fritz Zernike invented a microscopy technique which would take advantage of the phase shift phenomenon, called Phase Contrast microscopy. An object standing in media of lesser refractive index will cause light passing through it to slow, effectively retarding the phase of the light wave

compared to light not transiting the object, an effect that is more apparent with increased depth of the object. Light passing the edge of the object will also undergo diffraction, also creating a phase change. Phase contrast microscopy employs an optical mechanism to make use of these phase change characteristics, based around the concept of being able to cause amplitudinal wave interference between zeroth order or 'surround wave' (which is neither refracted nor diffracted in its path) and that of wave fronts which interact with the specimen. The latter are deviated in their path by modes of refraction and diffraction and receive a change to their optical path length, consequently undergoing a relative phase shift. In a practical system, a cell culture monolayer will create a path length difference of around 0.125 μm, equivalent to a quarter-wavelength phase lag for green light. Smaller cellular components will, of course, introduce less of an optical path difference and phase shift.

This optical ingenuity of a phase contrast microscope is enabled by a combination of an annular ring to control the azimuth of coherent light prior to it passing through the focal plane on which the specimen resides, and through an objective-mounted annulus. Any surround wave passes through the thinnest section of the annulus (situated co-axially with respect to the annular ring), before arriving at the image plane of the eyepiece. Light refracted by the specimen will undergo a phase shift of approximately - $^1/_4$ λ exiting the specimen, and is forced (by its change in azimuth) to pass through the thickest part of the annulus being phase shifted once more by approximately - $^1/_4$ λ. This total - $^1/_2$ λ phase shift between surround wave and refracted wave fronts allows for phase differences to be expressed as amplitude or image intensity differences due to constructive and destructive wave front interference at the image plane of the eyepiece, and resulting in an overall higher-contrast image.

Images were taken using phase contrast exhibit artefacts at the edges of each object, in the form of a bright or dark shadowing which gives a three-dimensional appearance to the objects. This is an unfortunate by-product of edge diffracted light passing through the phase ring as well as the non-phase areas of the ring, and interfering at the image plane.

Differential Interference Contrast (DIC) microscopy enhances the contrast at interfaces between specimen compartments with differing refractive indexes. This provides an image of very thin optical section which is particularly

useful when used in combination with fluorescent images gathered from a confocal microscope. The DIC microscope is essentially a bright-field microscope with the addition of a polarising lens at the condenser, a DIC beam splitting prism, a beam combining prism located at the objective, and an analyser in the infinity space of the tube. Light is first polarised and the two transverse beams split into different paths that travel close and perpendicular each other. If they pass through exactly the same specimen materials then their wave fronts remain in phase and when combined by the combining prism they produce a grey image at the image plane. If one of the transverse wave fronts were to have its optical path length changed (e.g. by passing through an object of different refractive index) it will undergo a relative phase shift with respect to its transverse counterpart, when combined constructive or destructive interference will render the projected spot either very much darker or brighter.

Confocal Microscopy was invented in 1955 (Minsky 1988) and today's Confocal Laser Scanning Microscope (CLSM) implementations are based around a fluorescent microscope with the addition of a variable diameter aperture (pinhole) in a conjugate plane to the image. Excitation laser light illuminates the sample in a sequential point-scanning raster pattern, with emission light from the specimen tightly focused through the aperture, allowing the operator to variably restrict the quantity of out-of-focus light that passes through it before hitting the camera sensor array. In many ways, the CLSM is a modern-day *camera obscura*. With such strict limitation on the depth of the focal plane, optical sectioning of large specimens is possible, with axial resolution greatly improved in comparison to standard wide-field fluorescent microscopes. The background signal is considerably reduced when compared to widefield microscopes; however, the practical consequence of using a single excitation beam and collecting emitted light through a single aperture means that scanning rates for entire frames are generally substantially greater than with widefield techniques. Furthermore, the consequent reduction in light passing through to the detector means that with the necessary use of high power, photo-destructive excitation lines renders this technique useless for many live-cell imaging applications. The spinning disk confocal microscope allows for faster scanning of samples than the CLSM can afford; by utilising a spinning disk array of apertures holding micro-lenses, a single excitation laser beam is

effectively wider in diameter when focused onto the aperture disk. In a single revolution of the disk, the laser excitation light will have swept by, illuminating every micro-lens, which in turn acts as a confocal aperture allowing excitation light to pass through to the specimen and emission light to return from the focal plane. An entire image is formed almost instantaneously, with crosstalk minimised during the light collection by the placement of micro-lenses such that they are at a significant distance from each other.

3.1.3 TIRF microscopy

Total internal reflection fluorescence (TIRF) microscopy is a near-field evanescent wave illumination technique which was first devised in order to study the characteristics of cell-substrate contact by means of limiting the depth of penetration of an excitation laser into the specimen under observation (Axelrod 1981). The first iteration of TIRFM development utilised a glass prism in close proximity to the specimen, separated only by a thin layer of immersion oil. This prism acted as a simple waveguide helping to create the evanescent wave capable of excitation of a fluorophore within a highly-defined, shallow, continuous lamina at the physical boundary between prism and specimen (Ambrose 1956). In the standard setup, collimated excitation light is directed by way of lenses or mirrors, through a glass prism set directly on a specimen of lower refractive index (generally within aqueous media of refractive index close to 1.3). The excitation light is set to an angle greater than the critical angle of refraction when it meets the specimen-prism interface, causing the light to undergo total internal (internal to the prism) reflection with the production of a standing wave (evanescent field) emanating from the boundary into the media of the specimen. The phenomenon is explained through the use of Snell's law and by Maxwell's equations.

Snell's law determines the direction of reflected and transmitted electromagnetic waves across a boundary of two materials of differing refractive indexes. Use of Maxwell's equations with well-defined boundary conditions (using Fresnel's formulae) further provides amplitude information for both waves. Total internal reflection only happens when light propagates from a high refractive index material to one of a lower index. i.e. $\eta_1 > \eta_2$ (Figure 3.2A).

Snell's law states that the angle of reflection (θ_2) is equal to the angle of incidence (θ_1) regardless of the surface material. At angles less than the critical angle, the incident beam creates a penetrating transmitted beam with an angle (θ_2) dependent upon the refractive index of the two materials (Figure 3.2A).

$$n_1 \sin(\theta_1) = n_2 \sin(\theta_2)$$

At the critical angle of incidence (θ_c), the transmitted wave has an angle of 90°, such that it propagates along the interface between high and low refractive index media.

$$\theta_c = \sin^{-1}\left(\frac{n_2}{n_1}\sin(90)\right) = \sin^{-1}\left(\frac{n_2}{n_1}\right) = \sin^{-1}\left(\frac{1.34}{1.52}\right) = 61.8°$$

TIRF microscopy utilises an incident beam that is at a very slightly more oblique angle than the critical (θ_c). Where there is an oil-water or oil-glass-water interface at incident angles of approximately 62 degrees to the perpendicular, the wave is totally reflected (Panel A). However, as electromagnetic waves simply cannot abruptly stop at any boundary, they penetrate a small distance in the order of one wavelength into the second medium. This penetrating evanescent field is a standing wave, without oscillatory form (Figure 3.2C); it is well characterised by the amplitude (I) with which it decays as it penetrates with perpendicular distance (z) into the aqueous media:

$$I = I_o\, e^{-\left(\frac{d}{z}\right)}$$

In practice, excitation light from sources such as laser diodes have a Gaussian-like profile, so these formulae apply to theoretically infinitely wide excitation beams. Where I is the intensity, and the evanescent wave at any depth z from the media interface; I_o is the intensity of the evanescent wave at the boundary – equivalent to the full intensity of the incident beam; d is the characteristic exponential decay depth as defined:

$$d = \frac{\lambda_0}{4\pi n_2} \left(\frac{\sin^2 \theta}{\sin^2 \theta_c} - 1 \right)^{-\frac{1}{2}}$$

Applicable when the angle of incidence (θ) is greater than the critical angle (θ_c); where λ_0 is the wavelength of incident light in a vacuum. Characteristic depth (d) decreases with an increasing incident angle (θ), except for when θ_c and θ are close.

TIRF microscopy performed using a glass prism to facilitate the application of an evanescent wave presents inherent difficulties. Primarily, access to the sample is substantially physically hindered. Moreover, the microscope's lens is required to be of a water-immersion type which inherently limits image resolution compared to an oil-based objective which in general may have a greater numerical aperture. The TIRF microscopes used in this research are 'objective type' TIRF microscopes, where an especially developed TIRF objective takes on a dual role – the role of prism for excitation light, and as a pure oil-based objective for the specimens' emission light.

Access to the specimen is unhindered by any prism (Figure 3.2C), and the oil objective raises potential image resolution compared to water objectives. The compromises for such a TIRFM design are mainly expense-related; TIRF objectives are highly complex in their make-up, and highly discriminatory band-pass filter sets are needed (see the later schematic in Figure 3.11). In addition, as a dark-field technique, highly sensitive cameras employing photo-multiplier tubes or EMCCD sensors are often necessary to view the specimens.

Evanescent illumination is not without its drawbacks; even proprietary enclosed systems tend to require substantial manual configuration by the operator. This is primarily to ensure the centring of the excitation beam with respect to the optical axis of the objective. Such configuration is required to fine-tune the angle of incidence since the critical angle changes slightly with both the refractive index of the specimen (which in practice is never quite homogenous) and the wavelength of light used.

A

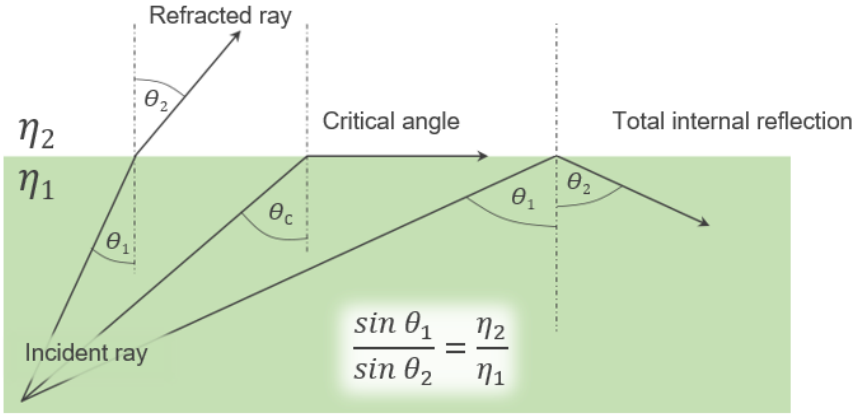

B ***i.***

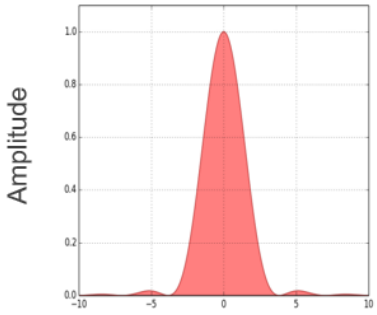

ii.

The Convolution Equation:

$$g = h * f$$

Where the image (g) is product of the convolution of all light sources from the object (f), with the point spread function (PSF) of the microscope (h)

C ***i.***

Evanescent Field Strength Equation:

$$I_Z = I_0^{\frac{-z}{d}}$$

Where

$d = (\lambda_o / 4\pi) . (\eta_2{}^2 . (\sin\theta)^2 - \eta_1{}^2)^{-1/2}$

and I_0 and λ_0 are field strength and excitation wavelength respectively, measured at the boundary of reflection.

ii.

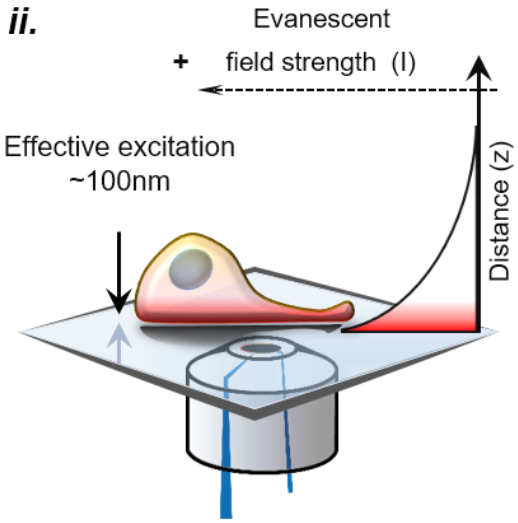

Objective-based TIRFM

Figure 3.2 TIRF and super-resolution microscopy

Panel A. Snell's law describes the relationship between the angles of incidence and refraction as light rays pass between media of different refractive indices (η). **Panel B.** ***i.*** The Airy function ***ii.*** The convolution equation. **Panel C.** ***i.*** The evanescent field strength equation. ***ii.*** In biological applications for objective-based TIRF microscopy imaging, effective excitation of fluorophores is constrained to a depth of ~100nm.

3.1.4 Image Resolution

The word ‘resolution’ is often interpreted as some vague concept of how small an object can be whilst still being rendered perceivable by the imaging device, be it a camera, microscope, or telescope. Yet that definition might well better characterise the brightness of the object under scrutiny rather than the quality of any optical system used. To discriminate properly the quality of any microscope or microscope technique, it is important to understand the meaning of resolution and how specialised light sources, optical components, microscopy techniques, and post-acquisition processing may be employed to maximise it. ‘Spatial resolution’ in microscopy generally refers to the minimum distance between two point sources at which the system is able to distinguish one object from the other. The fundamental variables that help define the maximum spatial resolution of any microscope can be understood when considering a microscope to be a linear system with a finite impulse response.

3.1.5 The microscope as a Linear system

A microscope without an attached camera is an analogue device which fits the criteria of a linear system, which is to say it fulfils the following criteria:

- **Homogeneity of response:**
  Input signal amplitude changes, give corresponding output changes.
  $x(t) \rightarrow y(t)$
  $2.x(t) \rightarrow 2.y(t)$
- **Superposition of input signals:**
  Where two input signals result in the combining of what would have been the two individual output signals, in an additive manner.
  $x_1(t)+x_2(t) \rightarrow y_1(t)+y_2(t)$
- **Shift invariance:**
  The characteristics of the system do not change with time.
  $x(t) \rightarrow y2(t)$
  $x(t-\tau) \rightarrow y(t-\tau)$

Where x is the input signal, y is the output signal, t is time and τ is a specific time shift/delay.

Having established microscopes to be linear systems, it is clear that microscopes will treat all light sources in a predictable manner. Thus, by modelling the simplest of possible light sources that may enter the device, we can establish how the microscope will react to all potential sources of light emanating from any possible object. Not only can this modelling be performed mathematically, but it has great utility in practice too when it comes to achieving super-resolution images through the process of image deconvolution.

3.1.6 Defining the limits of optical resolution

To model mathematically how a simple point of light propagates through a microscope lens system, a basic understanding of light wave interference patterns is necessary. Building on Christiaan Huygens' original work 'Traitė de la Lumiere' or 'Treatise on Light' (Huygens 1690; Thompson 2005), Fresnel (Fresnel 1816; Fresnel 1826) was able to yield the first modern explanation of light propagation, known today as the Huygens-Fresnel principle, which describes many aspects of light wave propagation, including refraction, interference and diffraction phenomena.

Diffraction is the deviation of light due to obstruction of its wavefront, by an obstacle, or sharp edge. If diffraction is observed in the near-field, i.e.: close to the obstacle or slit/edge which causes it, it's described as Fresnel diffraction. If, however, the diffraction pattern is observed far from its source or if the diffracted light passes through a lens before the image projection plane, then it is referred to as 'Fraunhofer diffraction', after Joseph von Fraunhofer (1787-1826). When considering the propagation of light through a microscope objective lens, a simple Fraunhofer diffraction model provides the evidence to show how this linear system responds to a single point light source by the creation of a light interference and diffraction model. This renders a projected image in the image focal plane not at all looking like the original point light source, but as a central bright disk shape (known as an Airy disk), surrounded

by an infinite number of concentric and repeating dark then bright rings of diminishing intensity.

$$D_{Airy} = 2\left(\frac{1.22\ \lambda\ f}{D_{App}}\right)$$

Where D_{Airy} is the diameter of the Airy Disk, f is the focal distance, D_{App} is the diameter of the lens (and therefore of the circular aperture defined by the boundary of the lens). As with all linear systems, which have a defined response to a simple system input or 'δ impulse', the impulse response of an optics systems is known specifically as its PSF (Pulse Spread Function) which will closely resemble the theoretically derived Airy function in its radial amplitude variation (Figure 3.2B). In essence, the Airy function is a mathematical description of the diffraction pattern of light when passing through an aperture or objective lens, as such, it is a useful approximation of the real PSF of a microscope.

The resultant image projection and spatial resolution of any microscope are not limited by camera sensitivity or magnification. Ultimately, the maximum obtainable resolution is limited only by the width of the main lobe of its PSF when measured at its half-power point in the intensity response (-3dB from the PSF maxima). This measurement is often more commonly known as the FWHM (Full-width at half-maximum). Once the PSF of an optical system is established, use of the Rayleigh criterion enables spatial resolution of the system to be defined: The Rayleigh criterion states two identical diffraction limited spots cannot be distinguished if their separation distance is less than r, a value defined as:

$$Rayleigh\ resolution_{\ x,y}\ (r)\ = \frac{0.612\ \ \lambda}{\eta \sin(\theta)} \quad \equiv \quad \frac{0.612\ \ \lambda}{NA}$$

Where d is the resolvable distance between two objects; λ is the wavelength of reflected or emitted light; η index of refraction of medium (usually air, water, glycerin, or oil) between point source and lens, relative to free space; α half the angle of the cone of light from specimen plane accepted by the

objective (half aperture angle in radians); 'η sin (θ)' is often expressed as the numerical aperture (NA) of the objective, defined as 'the sine of the angular semi-aperture in the object space multiplied by the refractive index of the objective space'. Relating this to a system's PSF and Airy disk dimension:

$$Raleigh\ resolution_{\ x,y}\ (r)\ = \frac{0.612\ \lambda}{NA}\ \approx\ r_{Airy}\ \approx\ PSF_{FWHM}$$

In practical terms, for lateral resolution (on the x-y plane) two identical diffraction-limited point sources are only resolvable if the distance between their maxima is, at least, the radius of the Airy disk or of the system PSF, so clearly the narrower the system PSF, the greater the maximum achievable system resolution. To increase lateral resolution, d needs to decrease, by either a decrease in the wavelength of collected/observed light or an increase in the NA of the objective lens.

No discussion of resolution limits would be complete without referring to German physicist Ernst Abbe, who, in 1873 derived a resolution criterion for the finest periodical structures that could be resolved by a diffraction-limited microscope:

$$Abbe\ resolution_{x,y} = \frac{0.5\ \lambda}{\eta \sin(\theta)} \quad \equiv \quad \frac{\lambda}{2.NA}$$

Where λ is the wavelength of reflected or emitted light; η the index of refraction of the medium; θ Is the half aperture angle in radians; NA is the numerical aperture of the objective. As can be seen, there is commonality between the Abbe and Rayleigh criteria, with a small difference only in the value of the coefficient, essentially due to the difference in how they defined what it means for two objects to be resolved and distinct from one another in an image. In practical terms, the difference of their equations is of minimal importance and both definitions are commonly used for defining the limits of microscopes' resolving powers. Typically, lateral resolvable distance is limited to 200 - 250nm. Modern oil objective lenses typically have NAs of 1.45 to 1.49, meaning axial resolution (resolving objects differing in their z-plane location only) is less

than half that achievable on the lateral plane, with resolvable distance defined as such:

$$Abbe\ resolution_z = \frac{2\lambda}{NA^2}$$

Where Abbe resolution $_z$, is the resolvable axial distance; λ is the wavelength of reflected or emitted light; NA is the numerical aperture of the objective; η the index of refraction of the medium between point source and lens, relative to free space.

Both axial and lateral resolution can be improved at shorter wavelengths but in practice, the photo-destructive effects of UV light are often enough to make its use impracticable, particularly for live-cell imaging.

3.1.7 Image noise

The overall resolution of any digital microscope depends not only on its spatial resolution but also on the amount of intensity quantisation detail within each pixel. Often quantisation is performed using 8-bit accuracy, but for some studies where high precision is necessary, 12bit and 16bit images are not uncommon. The disadvantage of greater quantisation is the corresponding exponential rise in computational power necessary to store and manipulate such large data arrays. The sensitivity of detectors is also paramount, particularly when examining small numbers of fluorophores, or when dark-field imaging. Photomultiplier tubes (PMTs) or the newest Electron Multiplying Charge Coupled Device (EMCCD) cameras are best utilised for their ability to detect single photon events without compromising quantum efficiency or without concomitant amplification of readout noise normally associated with CCD technology. Optical magnification of an image may prove useful to view any specimen more easily, but it will partially degrade the system's characteristic point spread function (PSF). Digitisation of a projected image is tuned to meet the Nyquist criterion to prevent the loss of information. Regardless of system resolution, localisation precision is greatly dependent on the number of photons collected, the amount of unwanted photons emanating from the image plane (out-of-focus light or specimen auto-fluorescence), from photo-detectors or the

electrical circuitry of the camera. All light falling on the image plane, when not adding information to the image, can be considered unwanted noise which causes a reduction in the signal/noise ratio of the image as a whole, consequently degrading image resolution.

3.1.8 Super Resolution Techniques

With the NAs of objective lenses close to the maximum achievable (with the cone angle of light collection nearing 90^{o} for modern objectives), substantially further narrowing a high-quality system PSF by achieving greater NA values is an unsatisfactory route to pursue for manufacturers of modern microscopes. However, resolution improvements can be achieved mathematically by means of new imaging techniques combined with post-acquisition signal processing. Over the last decade, many techniques have evolved leading to numerous ways to 'break the diffraction barrier' (Huang et al. 2010; Klar et al. 2001) or to achieve 'super-resolution' with resulting images having a spatial resolution smaller than the 200-250nm limit of conventional diffraction-limited microscopy. A host of super-resolution imaging techniques have evolved, the most cited being Photo-activated Localisation Microscopy (PALM; Henriques et al. 2011; Microscopy et al. 2010; Brown et al. 2011), and stochastic optical reconstruction microscopy (STORM) (Rust et al. 2006; Henriques et al. 2011). This thesis achieves resolutions beyond those achievable from diffraction-limited methods through the use of deconvolution (Sibarita 2005); QuickPALM (Henriques et al. 2010); Förster resonance energy transfer (FRET) (Sekar & Periasamy 2003); superresolution optical fluctuation imaging (SOFI) (Dertinger et al. 2009); 3B (Cox & Jones 2013; Cox et al. 2012; Rosten et al. 2013); and the *in situ* Proximity Ligation Assay (PLA) (Koos & Söderberg 2015; Söderberg et al. 2006). All such post-acquisition processing techniques are theoretically able to eliminate many of the resolution restrictions imposed on imaging system by their finite objective numerical aperture objectives.

3.1.8.1 Super-resolution optical fluctuation imaging

Single-molecule microscopy is significantly enhanced by the use of algorithms which can effectively sharpen the apparent PSF of any fluorescent point-source prior to Gaussian curve fitting. Dertinger et al (2011), show that the apparent PSF can be narrowed by applying n^{th} order SOFI analysis to a movie, such that the PSF's full-width half max (FWHM) is reduced by a factor of $n^{(-½)}$. The SOFI algorithm kindly used in this thesis was kindly provided by Dr Remi Boulineau and the laboratory of Dr. Mark Osborne.

3.1.8.2 Point source extraction

The *de facto* standard of point source extraction algorithms is Högbom's CLEAN (Cornwell 2008), of which there are now many derivatives available (Akhdar et al. 2009; Rich et al. 2008; Cornwell 2008; Henriques et al. 2010). CLEAN's core algorithm performs an iterative procedure: First it finds the pixel on the original image (aka., the 'dirty map') with the greatest intensity ('flux'), and assigns a fraction of that flux to a new 'clean' image map. That same fractional flux component is subtracted from the dirty map at coordinates associated with its PSF centred on that pixel. This process is repeated on the residual dirty map for a specific number of iterations or until the peak absolute flux in the residual map is negative. As a general process, CLEAN is accepted to be fast and reliable but fails to cope well with extended (elongated) spots. When applied to super-resolution microscopy, CLEAN's failings come mainly in its inability to handle extended objects and overlapping spots. QuickPALM (Henriques et al. 2010) is an integrated solution designed for real-time imaging of PALM (Betzig et al. 2006) and STORM (Rust et al. 2006; Bates et al. 2013), based on the concept of sequentially imaging sparse subsets of photo-switchable molecules, in order to achieve resolutions of 40nm or better. QuickPALM uses CLEAN's method for spot finding, followed by a modified centre of mass algorithm to compute the x,y spot position and facilitate the axial co-ordinates. It has a processing time of 30-50ms per image, equating to few minutes of processing time for typical z-stacks, without having much of a dependence on the number of spots present on each image. Indeed,

processing rates are so high that QuickPALM is able to calculate spot positions in real-time when used alongside EMCCD cameras which are generally frame-rate limited to approximately 100fps (Krishnaswami et al. 2014). QuickPALM is also able to interpolate positions for fiduciary landmarks in order to account for sample drift, even if the landmark is blinking.

With the advent of distributed computing and High-Performance Clusters (HPCs) much more computationally expensive post-acquisition image processing techniques have become practicable, although complex to utilise without programming experience. Many of these solutions rely on Bayesian models to determine the relative probability of the image space being best described as empty or as a point source of light. Bayesian techniques of source extraction have again been championed in the area of astrophysics, with algorithms such as SUSSEXtractor (Savage & Oliver 2005; Smith 2012) created to analyse images of deep space and determine flux magnitude, point source localisation to sub-pixel accuracy with associated uncertainty values for each attributed. A huge advantage offered by this technique is that there can be simultaneous background estimation and further subtraction, in theory providing a huge advantage over the more common median filtering which is biased by the presence of sources. Bayesian analysis of bleaching and blinking data (3B analysis) (Hu et al. 2013; Rosten et al. 2013) also utilises a Bayesian technique of modelling. It utilises stochastic blinking as well as bleaching events to provide a spatial resolution in the range of 50nm, even for fluorophores which have overlapping PSFs, or which are in an off state for a fraction of the movie. The 3B predictive model is based on a dataset consisting of a sequence of high frame rate images generated from large numbers of fluorophores undergoing blinking and bleaching processes, and as with any Bayesian modelling, the state of the model is statistically linked to the observation at any one time. 3B builds a probability map of fluorophore positions with any ambiguity in the final model blurred such that false positive point sources become unlikely outcomes.

3.1.9 Deconvolution

The PSF of a microscope is usually best derived experimentally by imaging beads directly. However, this can often be a challenge due to the small

size of the beads used. Theoretically calculated PSFs can often provide a good working estimation. When refractive index mismatches are an issue, working with an estimated PSF is recommended, as mismatch distorts the real PSF. Deconvolution reverses the convolution process (Figure 3.2B), and theoretically retrieves an image of point sources of light undispersed by the effects of diffraction (Cannell et al. 2006). Background noise limits the ability of deconvolution techniques and can introduce artefacts (Sibarita 2005). Although the result of deconvolution is a sharper image with diffuse light re-associated with its source, leaving the background darker and the point sources more intense with higher s/n, the precision of localisation of individual point sources is enhanced to a greater effect with a Gaussian fit model (Schermelleh et al. 2010). When using the Leica SP8 scanning confocal microscope for $FRET_{AcceptorBleaching}$, several assays were used to establish its reliability. By comparing results from a number of experiments with the Leica FRET report it was possible to confirm that the Leica software was using the FRET efficiency calculation: $1-(I^{Pre} / I^{Post})$.

3.1.10 Förster resonance energy transfer

Förster resonance energy transfer (FRET), also known as 'Fluorescence resonance energy transfer' or simply 'Resonance energy transfer' is a physical process by which energy is transferred non-radiatively from one excited fluorophore known as a donor (D) to another, acceptor (A) fluorophore residing up to 100Å apart. In a standard *in situ* dual-immunofluorescence assay (with caveats on the choice of fluorophores, discussed later), upon receiving excitement energy from a laser beam a donor fluorophore will convert all the received energy into heat and fluorescent light. In a second scenario, if an acceptor fluorophore is located in close vicinity (<100Å) to the donor, a fraction of the excitement energy absorbed by the donor will be directly transferred in a non-radiative manner to the acceptor, thereby reducing the energy pool from which the donor can fluoresce. The acceptor essentially quenches the fluorescence response of the donor. By photo-bleaching the acceptor, the acceptor is no-longer able to receive non-radiative energy from the donor, so the donor will fluoresce once again at a higher intensity as in the

first scenario without an acceptor present. $FRET_{AcceptorBleaching}$ microscopy takes advantage of this effect of donor quenching by an acceptor fluorophore. By measuring and comparing fluorescence intensity of the donor prior to acceptor bleaching, and post-acceptor bleaching, an estimate of the percentage of energy transferred from donor to acceptor can be calculated. Because energy transfer between donor and acceptor is proportional to the distance (Figure 3.10A), the distance between both molecules can be robustly estimated.

Energy transfer is performed via a mechanism of long-range dipole-dipole coupling, which due to its energy transfer efficiency profile over small distances - a decay proportional to the sixth power of distance (R) between donor and acceptor (Figure 3.10A), makes it an incredibly accurate spectroscopic ruler, and a useful technique in the observation of protein-protein interactions (Clegg 1995; Stryer 1978). The highest sensitivity obtainable by FRET is when fluorophores are separated by the critical transfer distance, or Förster radius – a distance specific to fluorophore pairs. This distance, specific to each donor-acceptor fluorophore type, indicates the distance at which this non-radiative energy transfer reaches 50% efficiency. Förster radii are typically 60-80Å for fluorophores used in ICC. For FRET to work, three criteria must be met. (i) There must be an overlap between the donor emission and the acceptor excitation spectra. This has very practical implications and limits the fluorophore pairs that can be used in an assay. Functional FRET pairs will invariably have their Förster radius value predetermined by the fluorophore manufacturer. In the case of the FRET pairs used in these assays, Alexa Fluor 488 and 555 dye pairs have a Förster radius (R_0) of 70Å. (ii.) Donor and acceptor fluorophores must be further than 10Å apart but within 100Å of each other. At extremely small distances of less than 10Å, other energetic interactions dominate the usual long-range dipole-dipole coupling of FRET, thus complicating distance evaluations (Pengguang, Wu., Brand 1994). At distances further than 100Å, resonance transfer efficiency is minimal and cellular auto-fluorescence will tend to unduly overwhelm FRET readings. (iii.) Donor and acceptor transition dipole orientations must be approximately parallel. As with any transmitter and receiver, alignment makes a huge difference to reception capability and a fully unaligned receiver will not absorb any energy from a source, no matter how close the source is to it. Fluorophores act as dipole transceivers for non-

radiative energy, and as such energy transfer efficiency will vary upon their alignment. For FRET studies, the effect of these dipole orientations is a great area of debate for physicists. Problems with background auto-fluorescence can be mitigated with use of a FRET derivative, Bioluminescent resonance energy transfer (BRET) where a bioluminescent luciferase becomes the energy donor without the need of having an excitation laser source which can cause cellular auto-fluorescence and/or simultaneously bleach the acceptor when there is excitation spectral overlap (Weibrecht et al. 2010). A recent development called the i*n situ* Proximity Ligation Assay, which comes close to the resolution of FRET is discussed in detail in Chapter 6.

3.2 Optimisation of immunofluorescence staining protocols

Using microscopy to investigate protein localisation at the leading edge of fixed cells requires immunofluorescence (IF) staining protocols which do not significantly compromise the structural integrity of fragile components of the cell, such as lamellipodia and focal adhesions. For this reason, many laboratory procedures were thoroughly reviewed to ensure that cells would be exposed to minimum mechanical stresses during the process of fixation and staining, prior to imaging.

3.2.1 Optimisation of the permeabilisation steps in IF staining

Triton X-100 (TX100), is a non-ionic surfactant widely used as a permeabilising agent for immunocytochemistry. Recommended concentrations for cell lysis vary between 0.1% up to 0.5% (v/v) concentration. Both concentrations are above the critical micelle concentration (CMC) of approximately 0.23 mM. Due to its non-selective solubilisation of lipids from the membrane (Scheffler et al. 2014), it is a general concern that membrane-interacting proteins and transmembrane proteins such as integrins (Rathinam & Alahari 2010) could be solubilised along with the lipid membrane during cell preparation prior to imaging. Previous work in the Morley lab has shown that permeabilisation of adherent MRC-5 SV2 cells is successful when they are incubated in 0.1% (v/v) Triton X-100 in PBS+ for 5 minutes at room temperature prior to *in situ* immunofluorescence staining. It was my intention to discover if

this incubation time could be reduced without degrading final images. To address this issue, cells were seeded onto collagen-covered coverslips and allowed to spread for 40 minutes. Cells were fixed using 4% (v/v) paraformaldehyde (PFA) and permeabilised using 0.1% (v/v) Triton X-100 for varying times at room temperature, prior to dual immunofluorescence staining with anti-paxillin and anti-α-Tubulin. Results from three different permeabilisation durations are shown in Figure 3.3. These data show that incubating cells in Triton X-100 for less than 2 minutes allowed only partial staining of the cells. However, incubations of 2.5 to 5 minutes consistently resulted in similar, well-stained cells. As a result of these assays, the permeabilisation protocols were changed to use 2.5 minute incubation times.

3.2.2 Optimisation of media application using modified pipette tips

Immunofluorescence staining of cells requires several media applications to fixed cells, including fixation solutions, permeabilisation solutions, blocking agents, antisera and mounting solutions, as well as multiple and prolonged wash steps. To find the gentlest procedure for the application of media, two different methods of media application were tested. One IF assay was conducted using the standard method of utilising a 1 mL pipette tip for the application of all media. Cells were seeded onto collagen-covered coverslips and allowed to spread for 40 minutes. Cells were fixed then permeabilised, prior to staining with phalloidin-conjugated Alexa Fluor fluorophore, and DAPI. Cells were then imaged. In a comparative study, 5 mL pipette tips were cut diagonally to produce a pipette tip with an enlarged egress area, such that the exit velocity of media would be substantially lowered to reduce the physical stresses exerted on cells by high-velocity hydrodynamics. The experiment (above) was repeated using the customised tips. Visual inspection of cells showed that the application of media using a modified 5 mL pipette tip was effective in lessening structural damage during the staining process. This new method of media application was formally adopted for all IF work. No comparative figures are shown here.

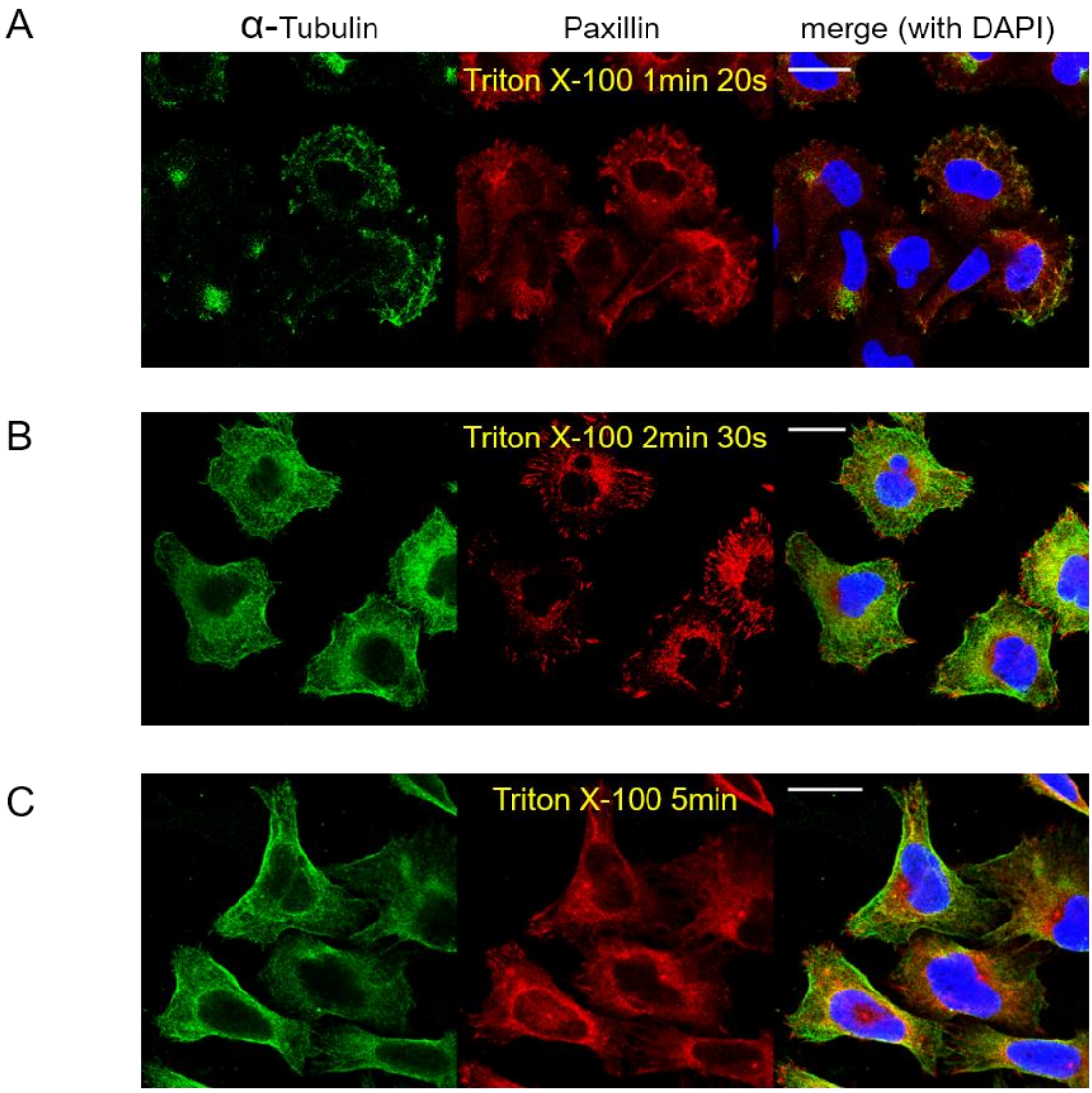

Figure 3.3 Cell permeabilisation using Triton X-100

MRC-5 SV2 cells were seeded onto coverslips coated with 8µg/cm^2 collagen I, at a density of 15,000 cells/cm^2 and incubated in MEM supplemented with 15% (v/v) FCS at 37ºC for 40 mins. Cells were fixed using 4% (v/v) paraformaldehyde (PFA), and permeabilised using 0.1% (v/v) Triton X-100 for varying times at room temperature, prior to dual immuno-fluorescence staining with anti-paxillin (Ab14) diluted at 1:200 (shown in red), anti-α-Tubulin (Ab32) diluted at 1:200 (shown in green), as described in the Materials and Methods. Images were obtained using a Leica SP8 confocal microscope at 63x magnification. Scale bars indicate 20µm.

Panel A. Permeabilisation by Triton X-100 for 1 minutes 20 seconds.
Panel B. Permeabilisation by Triton X-100 for 2 minutes 30 seconds.
Panel C. Permeabilisation by Triton X-100 for 5 minutes.

3.2.3 Optimisation of cell washing methods

Immunofluorescence staining of cells requires a number of prolonged wash steps, usually adopting the use of a rocker to induce more kinetic energy into the washes. It was important to find a wash procedure which would not induce unnecessary structural damage to fragile lamellipodia. To address this potential issue, cells were seeded onto collagen-covered coverslips and allowed to spread for 40 minutes. Cells were fixed and permeabilised prior to staining with phalloidin-conjugated Alexa Fluor fluorophore and DAPI. Different washing processes were employed in each comparative assay, with and without the use of a mechanical rocker. Figure 3.4 shows that extensive use of a rocker for enhanced movement of wash buffer slightly disrupts the most fragile parts of newly-developed lamellipodia. This happens to a greater extent than by simply allowing the Brownian motion to perform the same washing task without additional external stimuli. Confirmation that this type of gentle rocker-less washing technique was still effective in the removal of excess fluorescence stain was sought and confirmation of its validity accrued over many further experiments (eg: Figure 3.9). This new method of washing was formally adopted for all IF work.

3.3 Collagen-embedded fiducial markers

Fiducial markers are highly useful in the procedure of image registration and are particularly useful in the correction of lateral drift in movies (Rees et al. 2012). Fiducial markers necessarily have to be stabilised on a substrate to stop any form of movement. To address this need, TetraSpeck microspheres were embedded in the collagen substrate prior to cell seeding for immunofluorescence staining and imaging. Coverslips were rinsed in an ethanol / hydrochloric acid solution (50% (v/v) ethanol in 1M HCl) and allowed to dry at room temperature in a class II tissue culture (TC) hood. Different titrations of Tetraspeck beads were added to the collagen solution, prior to the application of 8µg/cm^2 collagen I to the coverslips. The coverslips were then allowed to dry in a sterile environment at room temperature before the application of cells. Cells were incubated for 40 minutes, fixed and permeabilised, prior to dual immunofluorescence staining with anti-paxillin or anti-α-tubulin antiserum.

Figure 3.5 shows how high a concentration of microsphere beads led to collagen losing adhesion with the coverslip. When this specimen was imaged, it was seen that the focal plane of lamellipodia did not match the focal plane of the beads, therefore, the proposition of using ECM embedded beads as fiducial markers was unrealistic for future work.

3.4 Colocalisation of phospho-rpS6(Ser240/244) at sites of active translation

Previous work in the Morley laboratory has shown that eukaryotic translation factors, including eIF4E and eIF4G, colocalise to sites of active translation in migrating fibroblasts (Willett et al. 2011). To perform this experiment the ribopuromycylation method (RPM) was utilised (David et al. 2011; David et al. 2013; David et al. 2012). RPM utilises puromycin, a Tyr-tRNA mimetic which enters the ribosome A site and terminates translation (Pestka 1971). Using puromycin antiserum, artificially stalled ribosomes can be viewed *in situ*, by immunofluorescence microscopy. Ribosomal protein S6 (rpS6) is one of 33 proteins in the 40S ribosomal subunit (Thomas et al. 1979), and is localised to the mRNA binding site junction between the small and large ribosomal subunits (Nygård & Nilsson 1990). Evidence suggests that the phosphorylation of rpS6 leads to more efficient binding and translation of mRNA (Burkhard & Traugh 1983). S6K1, a downstream effector of the environmental sensor mTORC1, is known to phosphorylate rpS6 and thereby facilitates mRNA translation in dividing cells (Bandi et al. 1993). There is some evidence to show that the mTOR-independent, Ras/ERK signalling cascade also stimulates rpS6 phosphorylation at Ser235/236 when p90 ribosomal S6 kinases (RSKs) are activated by growth factors (Roux et al. 2007). Our laboratory has already shown that translation factors and phosphorylated rpS6(Ser240/244) colocalise to sites of active translation in migrating fibroblasts (Willett et al. 2011).

To investigate the link between phosphorylated rpS6(Ser240/244) and active ribosomes in more detail, An experiment was performed using the same experimental procedure as described by Willet et al. 2011. The aim here was to analyse the results on a confocal microscope, before conducting further analyses using TIRF microscopy. Therefore, cells were seeded onto collagen-

covered coverslips and incubated for a total of 35 minutes. Using the ribopuromycylation method, as described in the Materials and Methods, cells were supplemented for the last 5 minutes of incubation with puromycin and emetine prior to washing in cycloheximide buffer. Cells were fixed and permeabilised using 0.00375% (w/v) saponin in NGS blocking solutions and diluted antisera. Dual immunofluorescence staining was performed for anti-phospho-rpS6 (Ser240/244) and anti-puromycin antiserum. Phalloidin-conjugated Alexa Fluor was employed to visualise the actin cytoskeleton and DNA monitored with DAPI. In Figure 3.6, these data show extremely high levels of colocalisation between stains for p-rpS6(Ser240/244) and active ribosomes, monitored with anti-puromycin staining. Manders coefficients of colocalisation are in the highest decile ($_{T}$M1=0.9961, $_{T}$M2=0.9681) (Figure 3.6). Crucially, some cells remained unpermeabilised and therefore unstained. It became apparent that partial permeabilisation of membranes was enough to allow the stain to enter some compartments, but washes were not sufficient to clear non-specific binding. It was clear that permeabilisation by saponin treatment had to be optimised before this assay could be repeated.

3.5 Optimisation of a saponin-based permeabilisation protocol

In planning a method to improve the saponin permeabilisation of cells, it became evident that saponin would be the preferred method of permeabilisation for my investigations into proteins on or close to the leading edge of cells. By adopting saponin as the detergent of choice, the amount of transmembrane or membrane-attached proteins lost during the permeabilisation process was likely to be greatly reduced when compared to permeabilisation by Triton X-100. Saponins are amphiphilic glycosides, making them emulsifiers, and allowing them to form micelles. Unlike non-ionic detergents, Quillaja saponins have a much greater affinity to cholesterol than other lipids of the bi-lipid membrane and are able to aggregate with them to form mixed saponin/cholesterol micelles (Lorent et al. 2014). This characteristic also gives saponins the ability to be used for differential permeabilisation of intracellular membranes for processes such as cell lysis for protein harvesting (Wassler et

al. 1987). Saponins also facilitate superior staining of endosomes when compared to detergents such as Triton X-100.

To develop a new protocol for saponin permeabilisation, cells were stained for paxillin and F-actin. The paxillin provides a good indication of any basal membrane disruption during the permeabilisation step, with F-actin facilitating visualisation of the cytoskeletal structure. Cells were grown on coverslips for dual immunofluorescence staining for paxillin and F-actin (using Phalloidin-conjugated fluorophores). After fixation, blocking was performed using titrations of saponin, prior to the addition of primary antisera. The protocol for dual immunofluorescence staining continued as described in the Materials and Methods, with no other use of saponin. In a parallel experiment, cells were treated in the same manner as above, except titrations of saponin were put in all buffers and washes apart from the last wash. Cells were imaged on a confocal microscope. From Figure 3.7, it is clear that permeabilisation using saponin concentrations up to 0.025% (w/v) in the first block only, produced only partial permeabilisation of cells. Hot spots of fluorescence shown reflect where fluorophore conjugates have entered the cells *via* punctured membranes. However, they have no easily accessible route to exit the cytoplasmic compartment after the lipid membrane has reorganised itself for repaired in the absence of saponin. Data shown in Figure 3.8 indicate that saponin at 0.0375% to 0.05% (w/v) in all buffers and washes (except for the very last wash), is enough to adequately permeabilise the cells. In contrast, the study shown in Figure 3.8C demonstrates that concentrations of 0.025% (w/v) are insufficient to adequately permeabilise the cells. Figure 3.9 shows that this new saponin treatment protocol is not simply antisera specific. This study also reconciles all the protocol adjustments which had been made to media applications using an adapter pipette tip, and less aggressive washing methods (Figure 3.4).

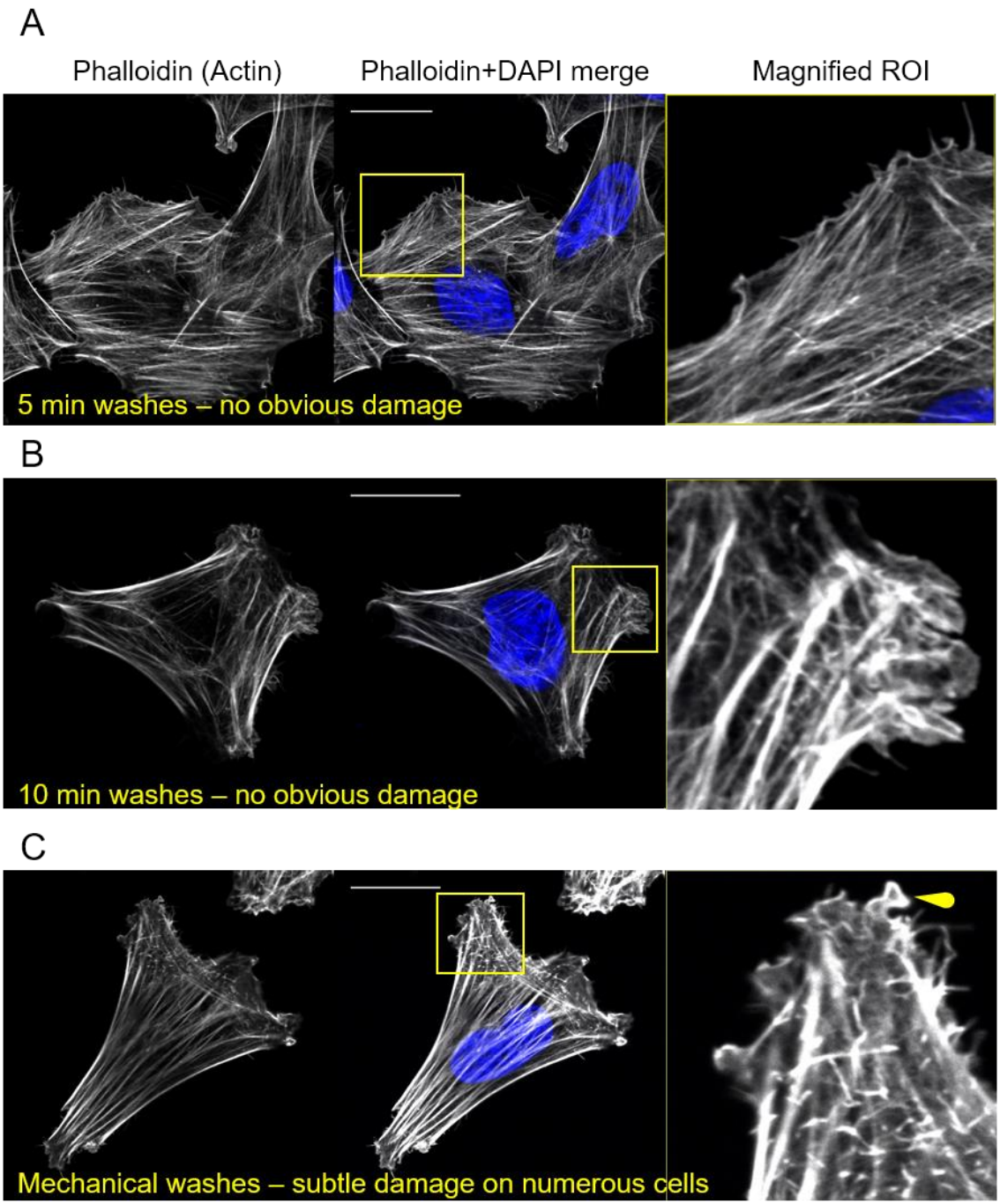

Figure 3.4 The structural robustness of lamellipodia after wash processes

Cells were grown on coverslips for dual-immuno-fluorescence staining as described in Figure 3.3. The addition of a primary antisera was skipped, and instead of the application of secondary antisera, a phalloidin-conjugated Alexa Fluor 488 was used at a dilution of 1:50. Scale bars indicate 20µm.

Panel A. Three 5 minute PBS+ immersions. **Panel B.** Three 10 minute PBS+ immersions; subtle structural damage to membranes. **Panel C.** Three 10 minute PBS+ immersions on a rocker; subtle structural damage to membranes.

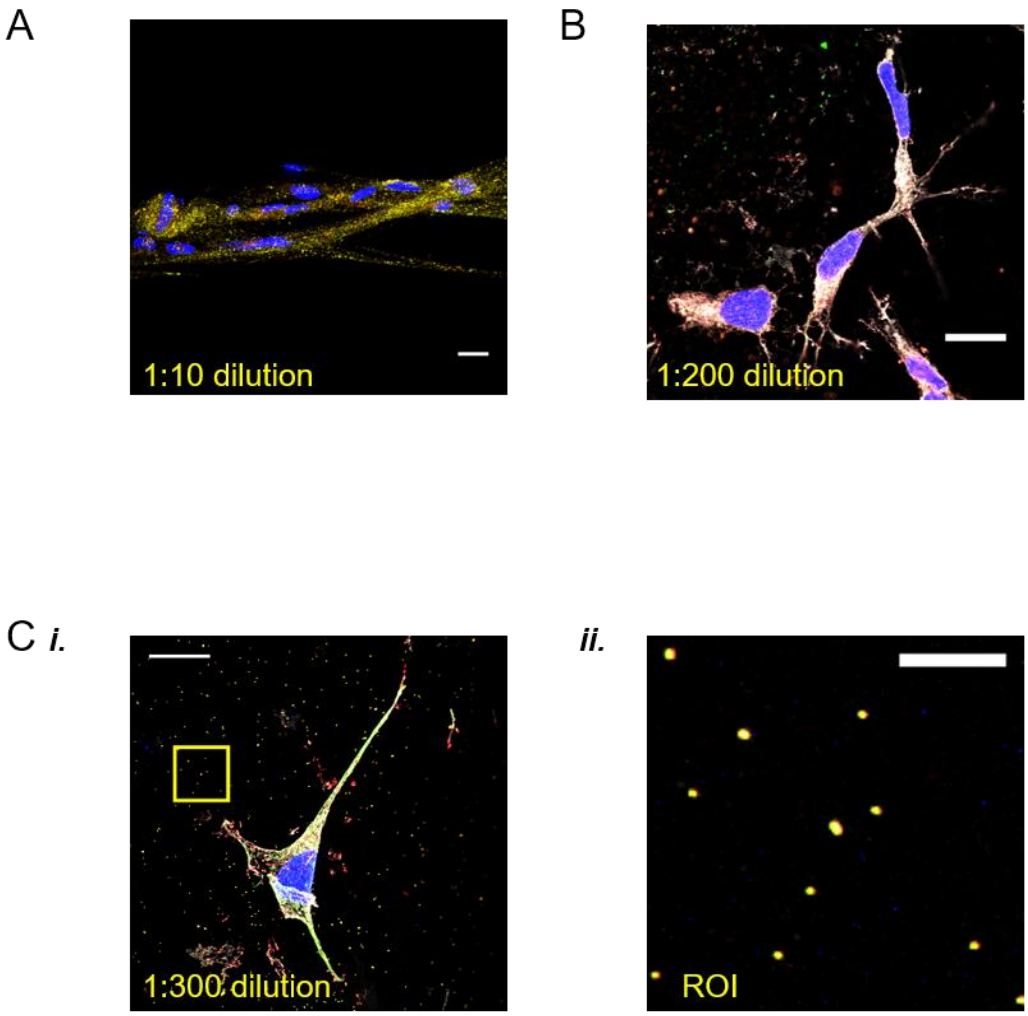

Figure 3.5 Embedding TetraSpeck beads within a collagen ECM

100nm diameter TetraSpeck microspheres were diluted to various concentrations (as described) into 8µg/mL rat-tail collagen I, prior to its application to ethanol-washed and flame-cleaned coverslips. Cells were grown on the coverslips for phalloidin-Alexa Fluor 488 staining as described in Figure 3.4. Unless otherwise stated, scale bars indicate 20µm.

Panel A. TetraSpeck microspheres diluted at 1:10 hindered collagen adhesion to the coverslip and facilitated the formation of a fibroblast 'Swiss Roll'. **Panel B.** TetraSpeck microspheres diluted at 1:200 hindered collagen adhesion to the coverslip and induced stress to adherent cells.
Panel C*.i.* TetraSpeck microspheres diluted at 1:300. ***ii.*** An expanded ROI from inset *i.*, showing diffraction-limited 100nm diameter TetraSpeck microspheres. Scale bar indicates 5µm.

A

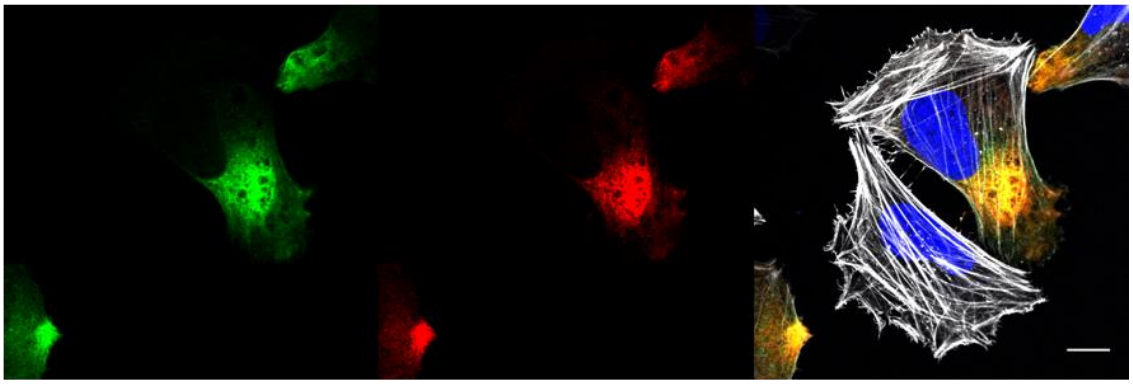

B *i.* *ii.* *iii.*

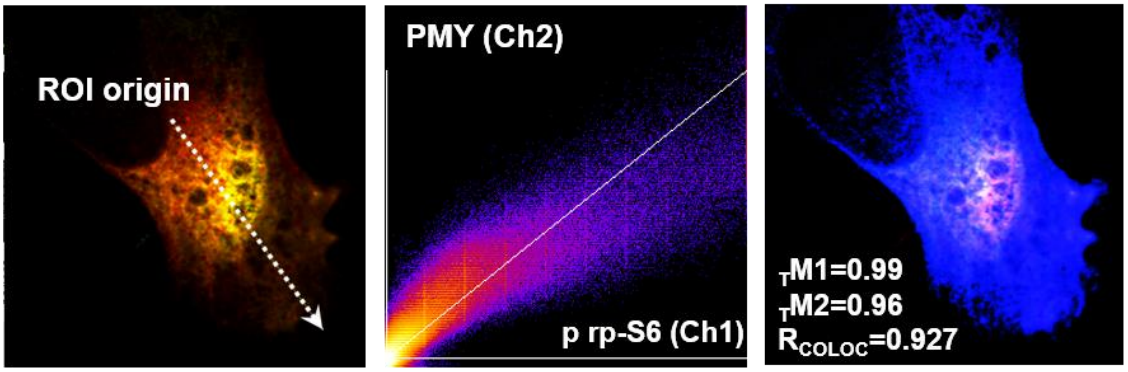

C

R_{COLOC}	0.927	Pearson's correlation coefficient for pixels above both channel thresholds
$_TM1$	0.9961	Manders coefficient for the Ch1 pixels above channel threshold
$_TM2$	0.9681	Manders coefficient for the Ch2 pixels above channel threshold
Itter	100	Itterations used in Coste's thresholding method
$_{CH}1$	1	Channel1 threshold
$_{CH}2$	6	Channel2 threshold
Pixel#	554584	Number of pixels in each channel

D

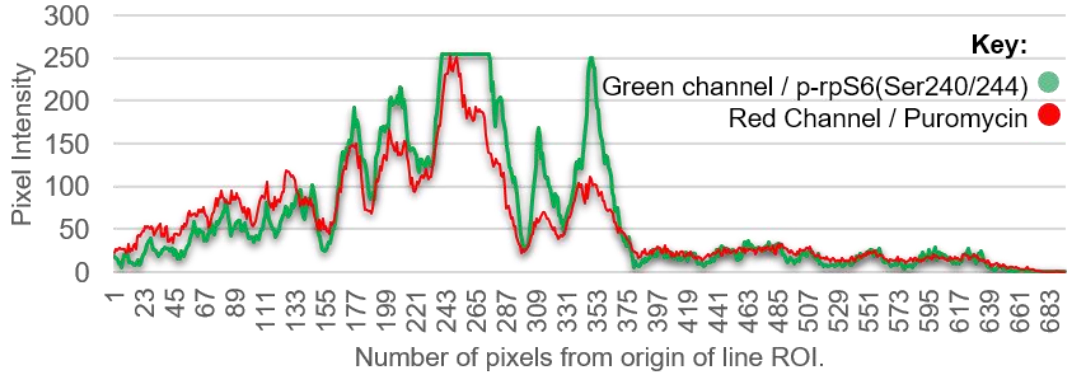

Figure 3.6 Colocalisation of phospho-rpS6(Ser240/244) at sites of active translation

MRC-5 SV2 cells were seeded onto coverslips coated with 8µg/cm^2 rat tail collagen I, at a density of 15,000 cells/cm^2 and incubated in MEM supplemented with 15% (v/v) FCS at 37ºC for a total of 40 mins.
Using the ribopuromycylation method (RPM), as described in the Materials and Methods, cells were supplemented for the last 5 minutes of incubation with 91µM puromycin and 208 µM emetine prior to washing in cycloheximide buffer. Cells were fixed using 4% (v/v) PFA, and permeabilised using 0.00375% (w/v) saponin in NGS blocking solutions and antibody buffers during dual immuno-fluorescence staining using anti-phosphor-rpS6 (Ser240/244) (Ab36) diluted at 1:200, anti-puromycin diluted at 1:25, and a phalloidin-conjugated Alexa Fluor 488 at a concentration of 1:50, as described in the Materials and Methods. Images were obtained using a Leica SP8 confocal microscope at 63x magnification. Scale bar indicates 20µm.
Panel A. Puromycin and phospho-rpS6 (Ser240/244) are seen to be co-localised by simple visual means (yellow in the merged frame). Scale bar indicates 10µm. **Panel B*. i*.** An ROI line is drawn laterally, from which the pixel intensities of both channels are derived (Panel C). ***ii.*** Colocalisation analysis shows a high correlation between both channels. ***iii.*** Colocalised pixels are shown in blue, with a stronger blue as both channel intensities tend to equalise. R_{COLOC}=0.927; $_{T}$M1=0.99; $_{T}$M2=0.96. ; where $_{T}$M*N* is the Manders coefficient for the Ch*N* pixels above the channel threshold. **Panel C.** Colocalisation statistics. **Panel D.** Intensity profile of channels p-rpS6 (green) and PMY (red) as taken from the ROI line drawn in Panel B*i*.

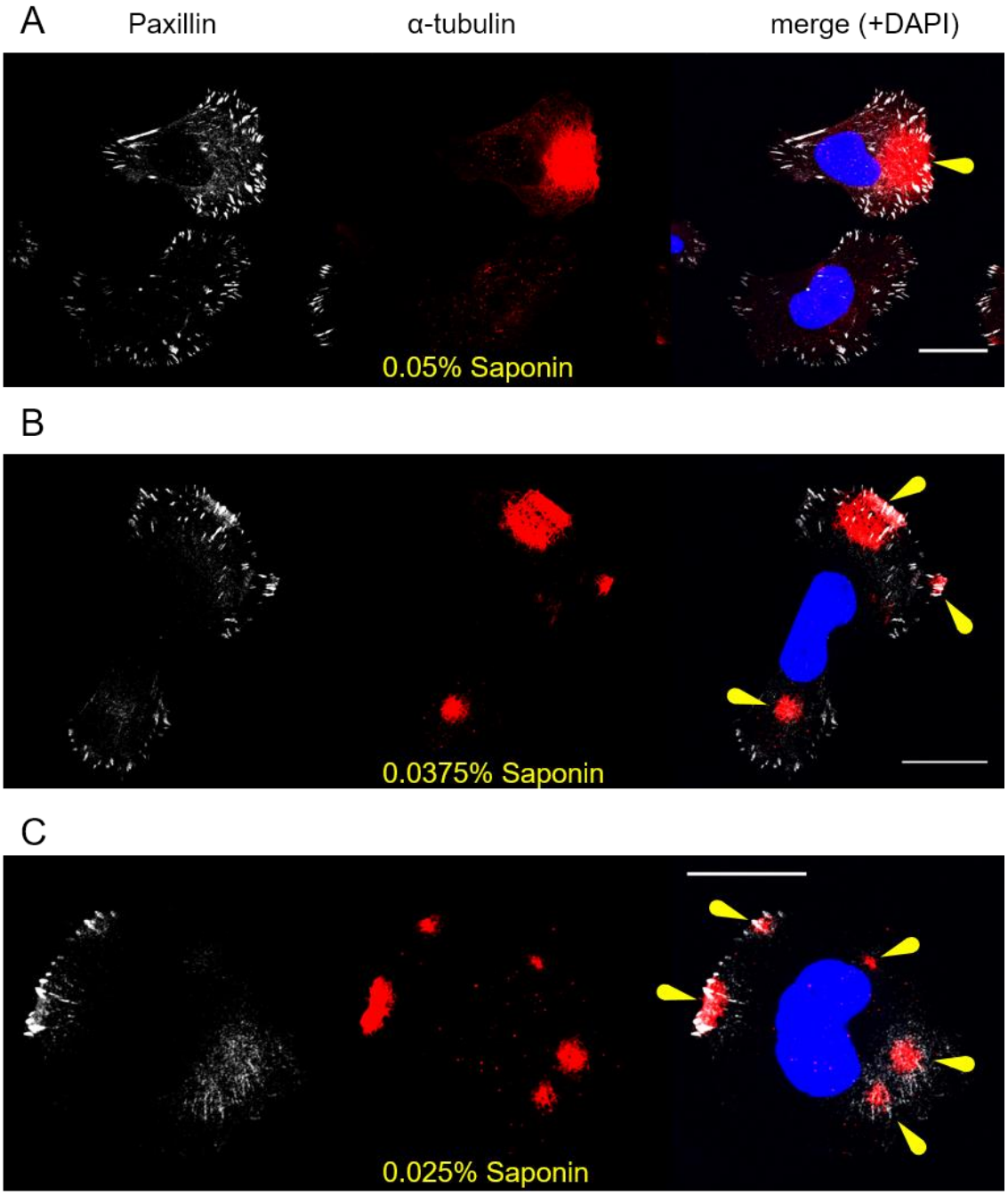

Figure 3.7 The effect adding different concentrations of saponin at the initial ICC blocking stage only

Cells were grown on coverslips for dual-immuno-fluorescence staining as described in Figure 3.6, with saponin only in the first 10% (v/v) normal goat serum (NGS) block at concentrations indicated in each panel. Primary antibody anti-paxillin (Ab14) was diluted at 1:250, and a phalloidin-conjugated Alexa Fluor 488 was used at a dilution of 1:50, as described in the Materials and Methods. Images were obtained using a Leica SP8 confocal microscope at 63x magnification. Scale bars indicate 20µm. Arrows point to areas of partially permeabilised membrane. **Panel A.** 0.05% saponin. **Panel B.** 0.0375% saponin. **Panel C.** 0.025% saponin.

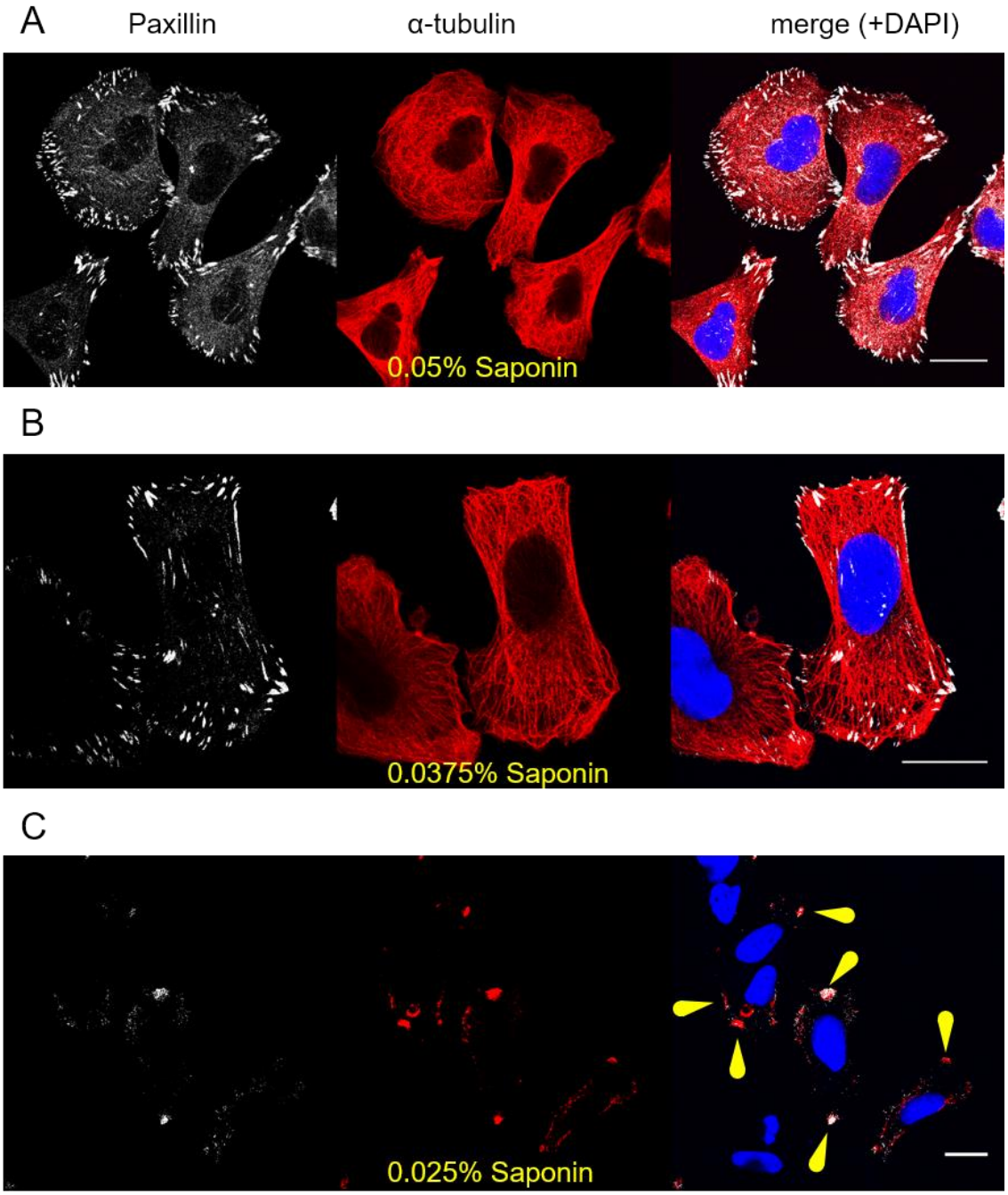

Figure 3.8 The effect adding different concentrations of saponin in all blocking and antibody buffers

Cells were grown on coverslips for dual-immuno-fluorescence staining as described in Figure 3.6, with final concentrations of saponin in all blocking buffers and antibody buffers at concentrations indicated in each panel. Primary antibody anti-paxillin (Ab14) was diluted at 1:250, and a phalloidin-conjugated Alexa Fluor 488 was used at a dilution of 1:50, as described in the Materials and Methods. Images were obtained using a Leica SP8 confocal microscope at 63x magnification. Scale bars indicate 20µm. Arrows point to areas of partially permeabilised membrane. **Panel A.** 0.05% saponin. **Panel B.** 0.0375% saponin. **Panel C.** 0.025% saponin.

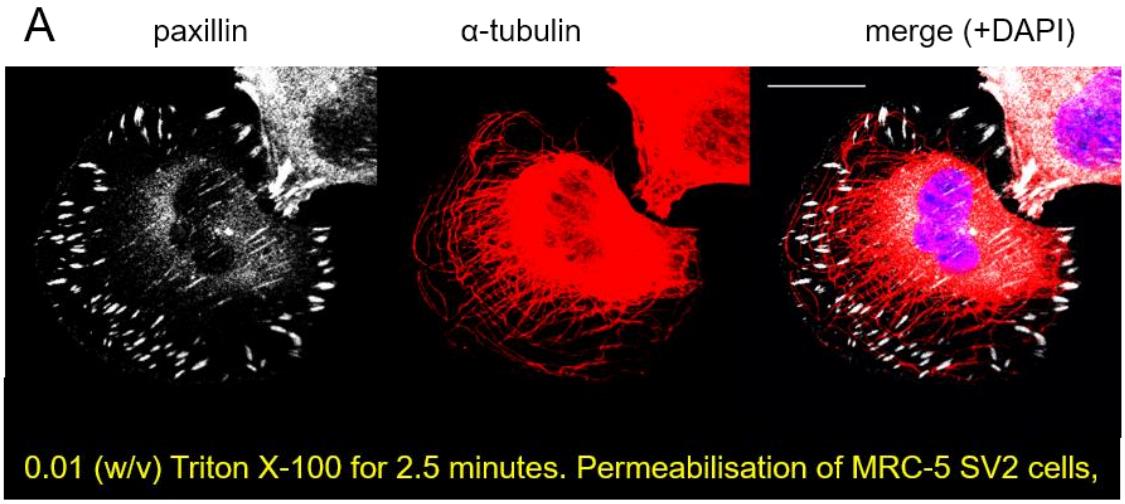
A
paxillin
α-tubulin
merge (+DAPI)
0.01 (w/v) Triton X-100 for 2.5 minutes. Permeabilisation of MRC-5 SV2 cells,

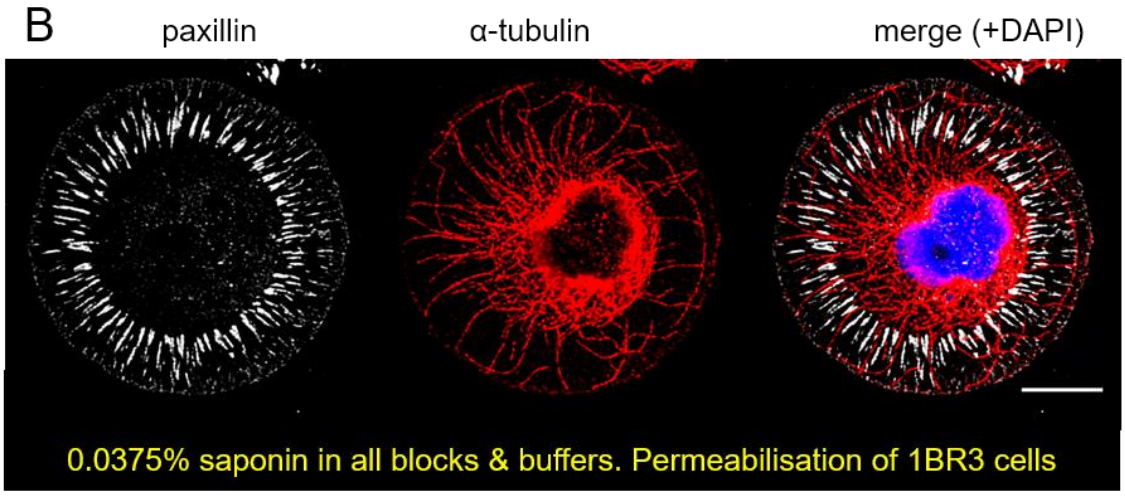
B
paxillin
α-tubulin
merge (+DAPI)
0.0375% saponin in all blocks & buffers. Permeabilisation of 1BR3 cells

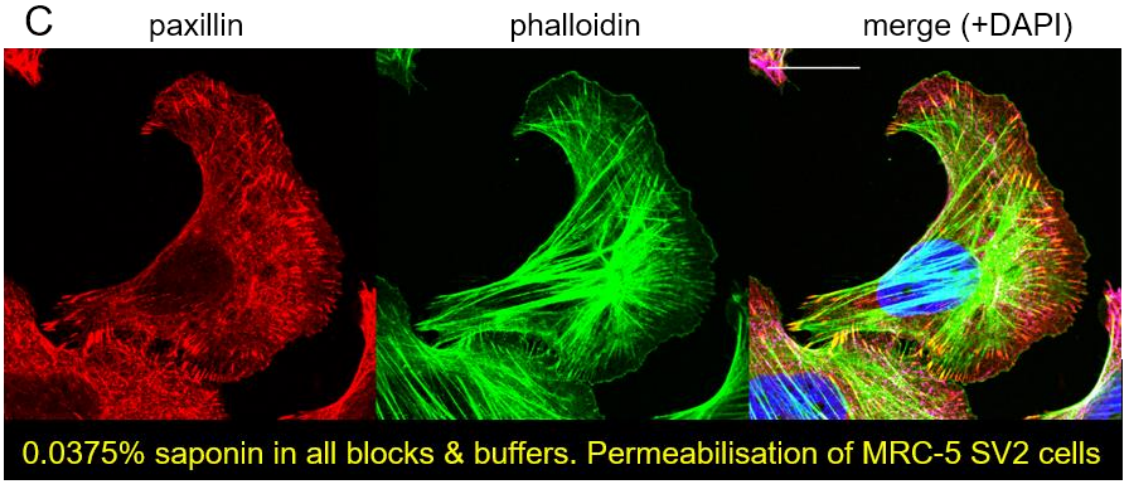
C
paxillin
phalloidin
merge (+DAPI)
0.0375% saponin in all blocks & buffers. Permeabilisation of MRC-5 SV2 cells

Figure 3.9 Validation of saponin as a replacement for Triton X-100 permeabilisation

Cells (MRC-5 SV2, or 1BR3 where appropriate) were seeded onto coverslips coated with 8µg/cm^2 rat tail collagen I, at a density of 15,000 cells/cm^2 and incubated in MEM supplemented with 15% (v/v) FCS at 37ºC for 40 mins. Cells were fixed using 4% (v/v) PFA, and permeabilised using the methods described in each panel. Dual immuno-fluorescence staining was performed as described in the Materials and Methods. Images were obtained using a Leica SP8 confocal microscope at 63x magnification. Scale bars indicate 10µm.
Panel A. Using MRC-5 SV2 cells and Triton X-100 permeabilisation for 2.5mins on ice. Primary antibodies: anti-paxillin (Ab14) was diluted at 1:250, and mouse anti-α-tubulin (Ab32) was diluted at 1:250. **Panel B.** Using 1BR3 cells and 0.0375% (w/v) saponin in all blocks and buffers. Primary antibodies: anti-paxillin (Ab14) was diluted at 1:250, and mouse anti-α-tubulin (Ab32) was diluted at 1:250. Image deconvolution was performed using Huygens Professional, with default settings: s/n = 20dB. **Panel C.** Using MRC-5 SV2 cells and 0.0375% (w/v) saponin in all buffers. Primary antibodies: anti-paxillin (Ab14) was diluted at 1:250, and a phalloidin-conjugated Alexa Fluor 488 was diluted at 1:50. Image deconvolution was performed using Huygens Professional, with default settings: s/n = 20dB.

3.6 Optimisation of Förster resonance energy transfer

Biochemical means to establish molecular interactions are well established for the ensemble of proteins within cellular compartments. However, *in situ* colocalisation necessitates the use of microscopy. In order to test for the colocalisation of proteins of interest here, (including FMRP, CYFIP1, DDX3X and eIF4E (Chapters 4, 6 and 7, respectively)), $FRET_{Acceptor\ Bleaching}$ was utilised. Figure 3.10 shows a repeat of a preliminary experiment conducted in our laboratory (Willett et al. 2010). Cells were seeded onto collagen-coverslips and incubated for 40 minutes. Cells were fixed and permeabilised before being dual immunofluorescence stained for α-tubulin and eIF4E. The FRET fluorophores used were secondary antibody conjugates of Alexa Fluor 488 and 555. The data presented in Figure 3.10 initially looked promising, with an apparent high FRET efficiency at locations which may have included the microtubule organisation centre (MTOC) (Lüders & Stearns 2007). This is an area of concentrated interaction between α-tubulin and eIF4E previously identified in fibroblasts (Willett et al. 2011). No other ROIs on this image produced FRET efficiencies to indicate protein colocalisation within 10nm. However, after multiple assays consistency results was not achieved, and both positive and negative controls failed to provide reliable and realistic FRET efficiency values. With FRET efficiency values reliant on a microscopy system with no lateral or z-plane drift, the Leica SP8 platform appeared to be unsuitable for analyses using $FRET_{Acceptor\ Bleaching}$. However, by performing a manual calculation of FRET bleaching using pre- and post-bleaching images and the equations shown in Figure 3.10, it could be shown that the efficiency calculation algorithm in the Leica SP8 microscope's software was performing correctly.

A *i.* *ii.*

$$E_{FRET} = \frac{No.\ quanta\ transferred, D\ to\ A}{No.\ quanta\ absorbed\ by\ D} \qquad E_{FRET} = \frac{R_0^6}{R_0^6 + R^6}$$

Where E_{FRET} is FRET efficiency; R is the distance between Acceptor and Donor; R_0 is the Förster radius or critical transfer distance.

ii.

$$E_{FRET} = 1 - \frac{I^{pre}}{I^{post}} \cdot \frac{I_D^{pre}}{I_D^{post}} \approx 1 - \left(\frac{I^{pre}}{I^{post}}\right)$$

Where I^{Pre} and I^{Post} are the pre- and post-bleached donor emissions from a sample containing D and A conjugates; I_D^{Pre} and I_D^{Post} are the pre- and post-bleached donor emissions from a negative control sample containing only D conjugates

B

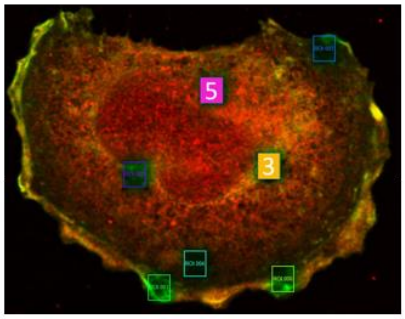

C *i.* *ii.*

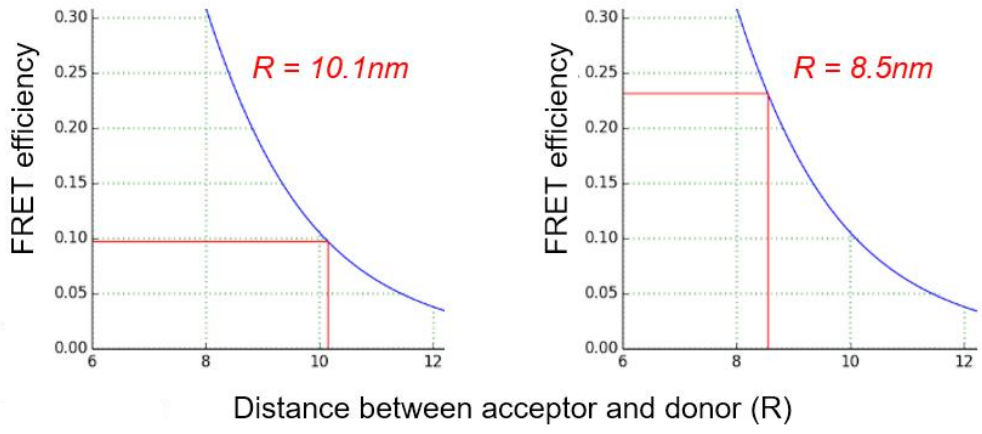

Figure 3.10 FRET$_{\text{Acceptor Bleaching}}$

MRC-5 SV2 cells were seeded onto coverslips coated with 8µg/cm^2 rat tail collagen I, at a density of 15,000 cells/cm^2 and incubated in MEM supplemented with 15% (v/v) FCS at 37ºC for 40 mins. Cells were fixed using 4% (v/v) PFA, and permeabilised before being dual immuno-fluorescence stained using α-tubulin diluted at 1:50, and eIF4E (Ab55) diluted at 1:200, as described in the Materials and Methods. FRET fluorophores were Alexa Fluor 488 (goat anti-mouse) and Alexa Fluor 555 (goat anti rabbit), both at the standard dilution of 1:300. FRET acceptor bleaching was performed using the Leica SP8 confocal microscope at 63x magnification. Green channel signifies eIF4E; red channel signifies α-tubulin.

Panel A. *i.* and *ii*. Theoretical FRET efficiency equations. ***iii*.** A FRET efficiency calculation for practical use. **Panel B.** MRC-5 SV2 cell post-bleaching. ROIs indicate regions of bleaching and FRET measurement. **Panel C.** FRET efficiency and distance calculations: ***i.*** For ROI 3: FRET efficiency (*R*) = 9.73% ≡ 10.1nm ***ii.*** For ROI 5: FRET efficiency (*R*) = 23.2% ≡ 8.5nm

3.7 Titration of antibodies for single-molecule imaging

After having been hindered in the visualisation of sites of active translation due to issues with permeabilisation by saponin, it was still of interest to visualise whether active sites of translation were found at the leading edge of cells. In order to test images obtained by TIRF microscopy, it was first necessary to discover the best antisera titrations. To address this requirement, cells were seeded on ozonated coverslips coated with collagen I, in preparation for TIRF microscopy. Cells were allowed to spread for 35 minutes before a 5 minute incubation in puromycin, emetine and cycloheximide according to the RPM method. Cells were fixed using 4% (v/v) PFA, and permeabilised using 0.1% (v/v) Triton X-100, prior to dual immunofluorescence staining performed using anti-puromycin or anti-rpS6 antiserum. Movies were taken with 100ms frame exposures. The results shown in Figure 3.11 provide varying regions of highly intense fluorescence. For super-resolution or single molecule imaging, dilutions of antisera had to allow for single molecules or singular point sources of fluorescence to be definable. From initial inspection by eye, these data show that the titration of anti-rpS6 antiserum at a dilution of 1:600 either met or came close to meeting such a criterion. Likewise, anti-puromycin antiserum diluted to 1:800 gave appropriate results.

3.8 Imaging streptavidin-conjugated fluorophores with TIRFM

Images rendered from TIRF microscopy examining IF stained rpS6 and puromycin (Figure 3.11) highlight how the low-noise environment of an evanescent field (Figure 3.2C) can yield useful fluorescence signals using antisera dilutions many times lower than would be necessary for confocal imaging. However, a high signal to noise (s/n) ratio still doesn't render super-resolution images without further image processing. To address this issue, 100 µL of a solution containing Biotin-conjugated bovine serum albumin in deionised water was incubated for 10 minutes on a cleaned coverslip. A 100nM solution of streptavidin conjugated with Alexa Fluor 546 was added and left to settle, prior to rinsing with deionised water and imaging by TIRFM. On two putative single fluorescent Alexa Fluor molecules in close vicinity to each other, the blinking

and bleaching characteristics of each of their brightest pixels were tracked (Figure 3.12A).

With the availability of algorithms offering the ability to convert the diffraction-limited movie into a single super-resolution image, it was decided to evaluate a super-resolution technique, based on the statistical evaluation of stochastic fluctuations stemming from single emitters, dubbed Super-resolution optical fluctuation imaging (SOFI) (Dertinger et al. 2009). SOFI was performed using an algorithm kindly provided by Dr Rémi Boulineau (Figure 3.12B). These data show that organic fluorophores can be spatially separated to perform single-molecule or near-single molecule imaging in vitro. The blinking and bleaching characteristics of the organic fluorophores are enough to facilitate super-resolution imaging using second-order SOFI, The specific improvement in resolution was quantified in a separate experiment (Section 3.9).

3.9 Second-order SOFI with *in situ* fluorophores

The resolution improvement rendered by second-order SOFI appeared subjectively to be weak for *in vitro* tests, and it was uncertain how super-resolution might be achieved *in situ*. To address this issue, cells were seeded on ozonated coverslips coated with collagen I, in preparation for TIRF microscopy. Cells were spread for 35 minutes before a 5 minute incubation in puromycin, emetine and cycloheximide according to the RPM method. Cells were fixed and permeabilised prior to dual immunofluorescence staining using anti-puromycin antiserum. Movies were taken with 100ms frame exposures. Using a 100 frame-averaged image, ten putative single molecules had their intensity profiles averaged. This reference profile was compared with the average profile of the same ten spots after SOFI processing (Figure 3.13). These data show that for *in situ* fluorophores, second-order SOFI processing reduced the width of each fluorescent spot by on average 24%, effectively making SOFI a useful tool to break the diffraction barrier.

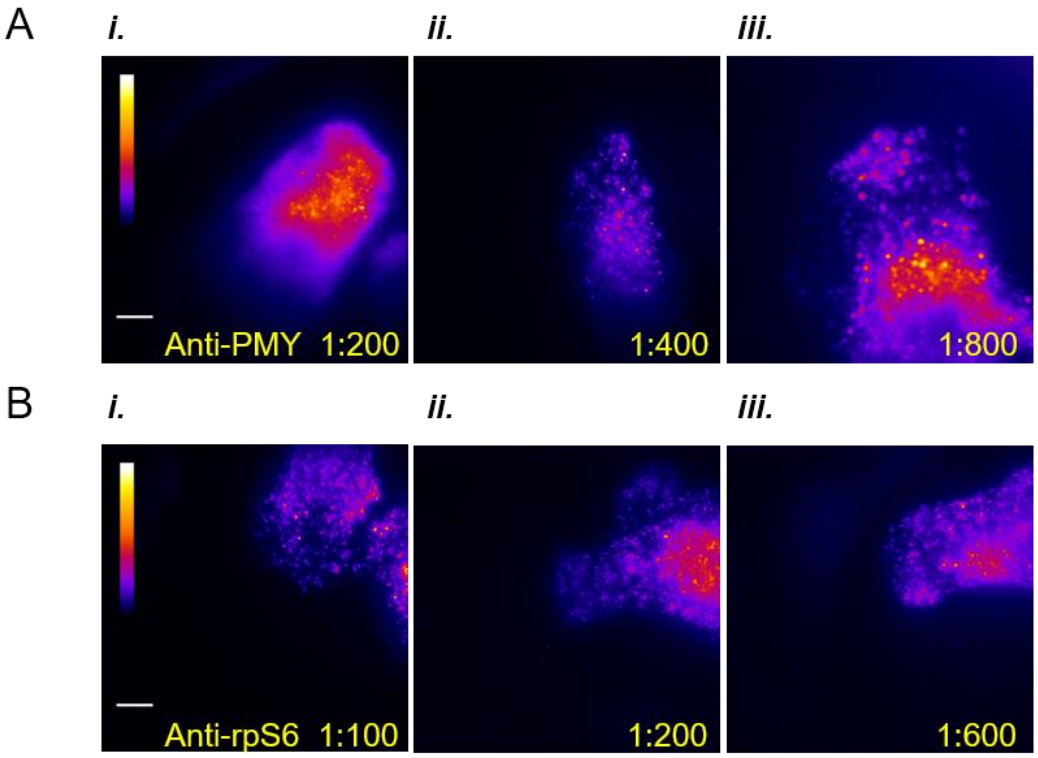

Figure 3.11 Titration of anti-puromycin and anti-rpS6 antibodies to obtain single molecule resolution

MRC-5 SV2 cells were seeded onto methanol-cleaned, and ozonated coverslips coated with 8µg/cm^2 rat tail collagen I, at a density of 15,000 cells/cm^2 and incubated in MEM supplemented with 15% (v/v) FCS at 37ºC for 40 mins. For the ribopuromycin (RPM) assay, puromycin (diluted at 2µg/mL) and emetine (diluted at 100µg/mL) were added to the media for the last 5 mins of spreading. Cells were fixed using 4% (v/v) PFA, and permeabilised using 0.1% (v/v) Triton X-100 prior to dual immuno-fluorescence staining performed using anti-puromycin (anti-PMY) or anti-rpS6, with Alexa Fluor 555 secondary antibodies, as described in the Materials and Methods. The TIRF microscope setup utilised a 561nm laser diode; dichroic 575nm and emission filter 593-40nm (Figure 3.11, Panel C). Movies were taken with 100ms frame exposures and a frame interval of 20ms. Images are derived from an averaging of the first 50 frames of each movie sequence, and were registered and normalised to produce an image of full intensity range, before pseudo-colouring. This work was performed jointly with Dr. Mark Willett. Scale bars indicate 5µm.

Titrations of anti-puromycin and anti-rpS6 primary antibodies were performed with the objective of obtaining near-single molecule resolution. Secondary antibody dilutions were kept constant throughout, at 1:300.
Panel A: Titrations of anti-puromycin: ***i.*** Diluted at 1:200 ***ii.*** Diluted at 1:400 ***iii.*** Diluted at 1:800. **Panel B:** Titrations of anti-rpS6: ***i.*** Diluted at 1:100 ***ii.*** Diluted at 1:200 ***iii.*** Diluted at 1:600

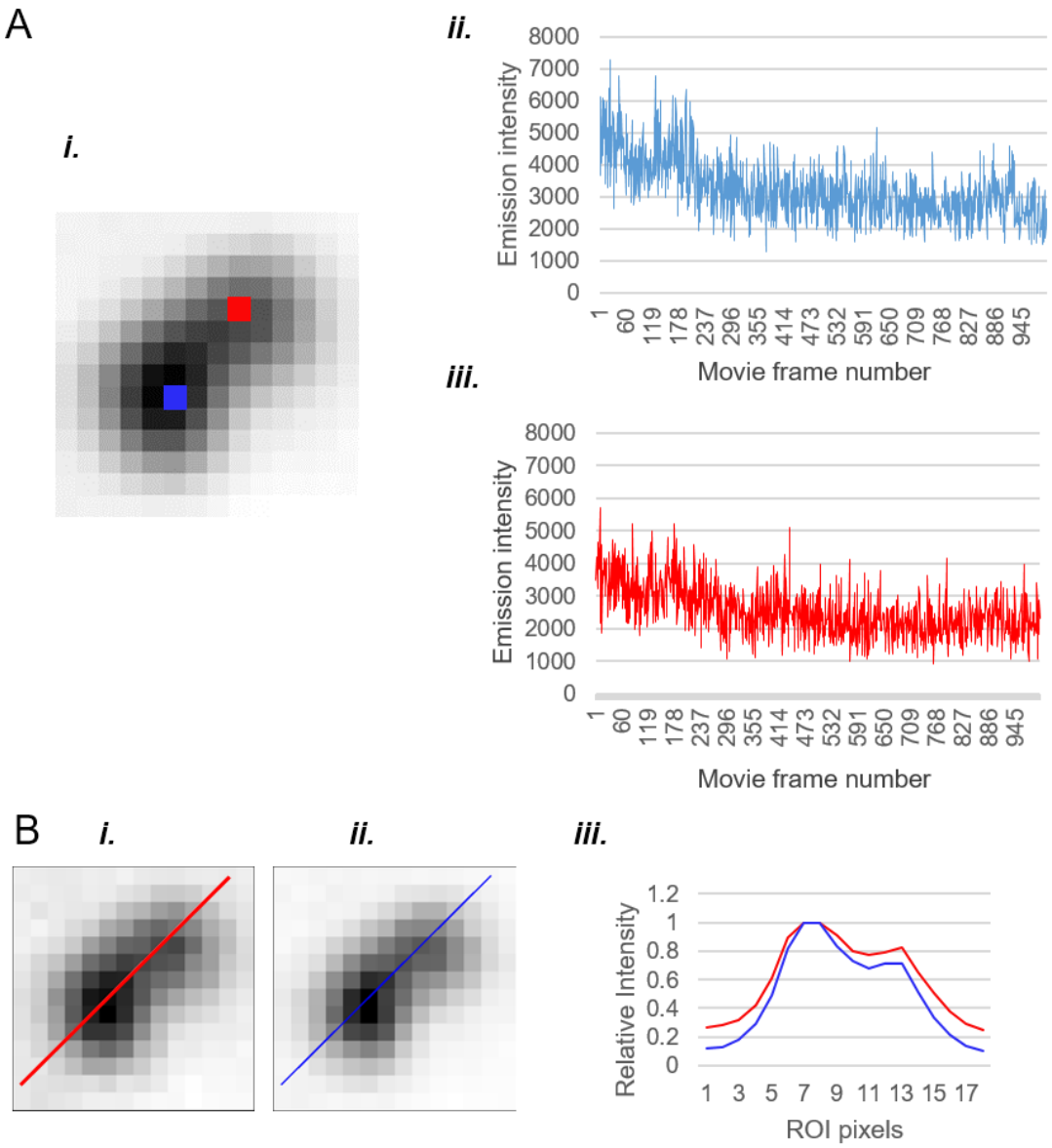

Figure 3.12 Second-order SOFI processing with organic fluorophores

100 µL of a solution containing Biotin-conjugated bovine serum albumin in deionised water was incubated for 10 minutes on the coverslip. A 100 nM solution of streptavidin conjugated with Alexa Fluor 546 was added, and left to settle, prior to rinsing with deionised water, as described in the Materials and Methods.
Panel A. ***i.*** 1000 frame averaged image of two Alexa Fluor molecules in close vicinity, with ROI insets. ***ii. and iii.*** Blue and red ROIs of inset *i.*, intensity plotted over the course of the entire 1000 frame movie. **Panel B.** ***i.*** Original 1000 frame averaged image with line ROI. ***ii.*** SOFI-processed image ***iii.*** Pixel intensity comparison of pre-SOFI (red) and post-SOFI (blue) processed images, taken over the red and blue ROIs shown in insets i., and ii., spanning left to right.

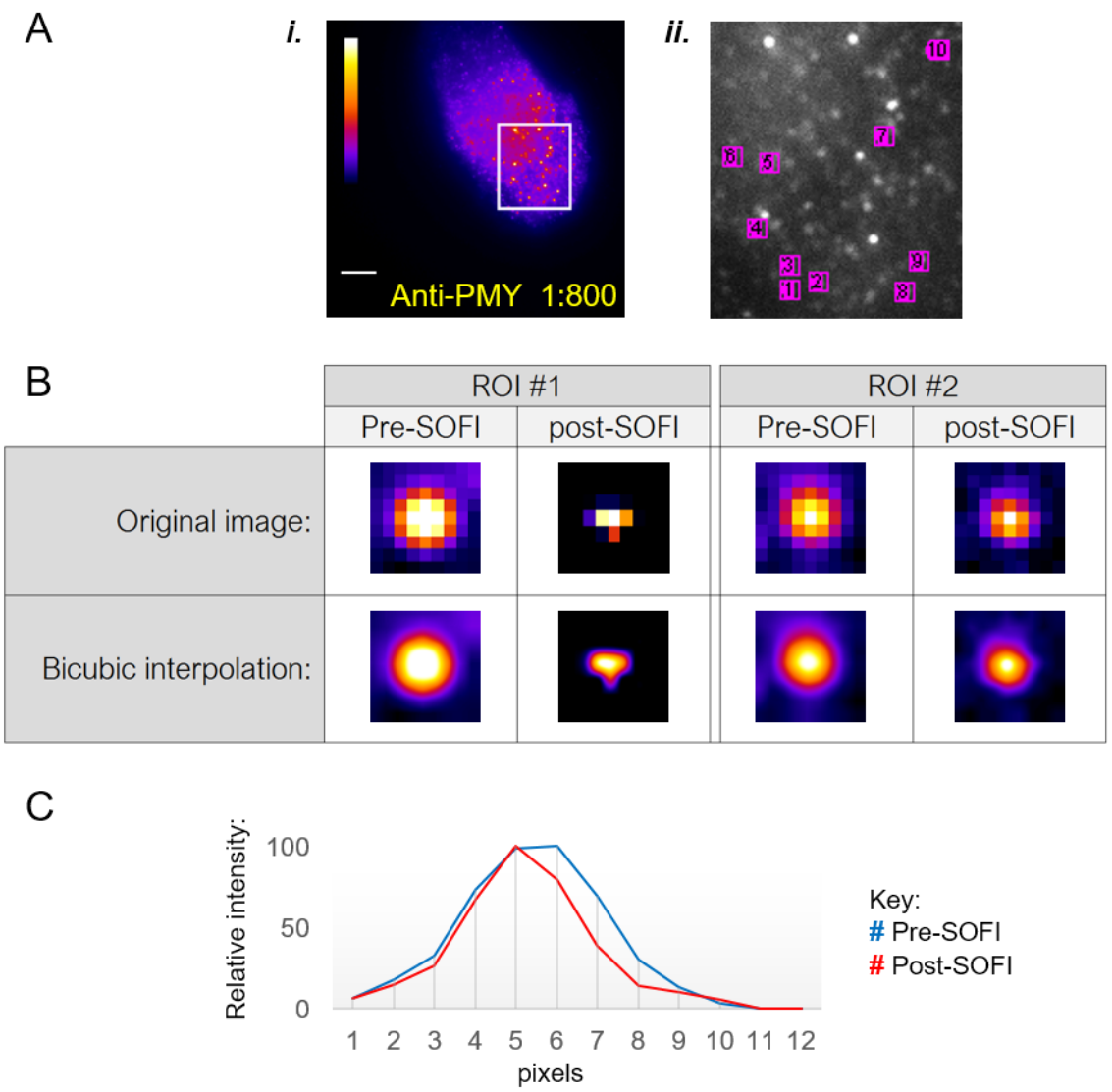

Figure 3.13 Second-order SOFI with *in situ* fluorophores

Cells were prepared for TIRF microscopy imaging using the ribopuromycylation method (RPM) of adding puromycin and emetine to the cell cultures in the last 5 mins of cell spreading, as described in Figure 3.12. Mouse-raised anti-puromycin primary antibodies were used at the dilution of 1:800. Cells were imaged in the manner described in Figure 3.12., and movies taken of 100 frames in length.

Panel A. ***i.*** Discrete foci of anti-puromycin staining *in situ* within a fixed cell. Scale bar indicates 5µm ***ii.*** 100 frame averaged image, with 10 ROI insets. **Panel B.** Two putative single IgG molecules, pre- and post-SOFI processed, shown as original pixelated images and in bicubic interpolated form. **Panel C.** The average intensity profile of each putative single molecule (IgG) as selected from the ROIs in Figure A*ii.*, showing an implied full width half maximum (FWHM) bandwidth narrowing of 24% .

3.10 Polysome imaging using TIRF and TEM

SOFI has been seen to provide super-resolution imaging for *in situ* immunofluorescence microscopy using TIRFM. With the availability of transmission electron microscope images of polysomes, this seemed like a good opportunity to test the *in situ* super-resolution imaging technique of SOFI, against a known imaged target. To address this challenge, cells were seeded on ozonated coverslips coated with collagen I, in preparation for TIRF microscopy, as described above. In parallel, another assay was created for standard dual immunofluorescence using cells which were allowed to spread for 40 minutes in the absence of drugs. Cells were then fixed and permeabilised prior to dual immunofluorescence staining with anti-puromycin antiserum according to the RPM method, and with anti-rpS6 antiserum for the standard IF method. Cells were imaged using TIRFM, and images processed using SOFI. The diameter of putative polysomes was measured in both assays and compared with measurements of polysomes in TEM images. These data shown in Figure 3.14 indicate that the resolution improvement obtained by SOFI was not great enough to allow TIRF images to come close enough to being comparable to TEM-derived images of polysomes.

3.11 Titration of antisera and mRNA probes for IF and FISH imaging with TIRFM

In order to investigate the localisation and/or colocalisation of both proteins and mRNA using TIRF, titrations of FMRP, CYFIP1, β-actin mRNA FISH probes, as well as other probes of interest needed to be titrated. To this end, cells were cultured for dual-immunofluorescence staining and for FISH probe hybridisation, as per the protocols described for each in the Materials and Methods. Probes and antisera were applied in titrated quantities and images were studied by eye to find the best dilutions i.e. where there appeared to be single small foci, rather than large clumps of fluorescent foci. The ability to initially identify single small foci in each image was considered an appropriate starting point for the future identification of putative single or near-single molecule definition. From the results presented in Figures 3.15 and 3.16, it can be seen that optimal dilutions were achieved for protein antisera of CYFIP1

(1:1000) and FMRP (1:2000), and for probes for ArpC2 mRNA (1:800) and β-actin mRNA (1:400).

3.12 Imaging of single quantum dots

In previous assays, colocalisation of two proteins or protein/mRNA complexes has been dependent on image alignment techniques, with and without fiducial markers (see above). Colocalisation of *in situ* fluorophores has been dependent on super-resolution algorithms such as SOFI. However, at near single molecule imaging, cellular auto-fluorescence causes a degradation in the signal to noise (s/n) ratio of the image. Moreover, the finite exposures of each frame in a movie lead to a loss of accuracy in the localisation of the molecule fluorescence emitter (Deschout et al. 2014; Ober et al. 2004). To address this technical issue of improving the s/n ratio *in situ*, and also to improving the accuracy in the localisation of fluorophores, QD625 quantum dots were serially titrated in deionised water and applied to cleaned and ozonated coverslips for imaging using TIRFM. Movies were acquired of single QDs, their intensity profiles analysed, and any stage drifts calculated at subpixel resolution using my own Image Drift Calculator code (see Appendix). This was carried out both before and after image registration by the GDSC AlignFFT ImageJ plug-in (Figure 3.17). These data show that QDs are large and extremely intense emitters of fluorescence light (Panels A and B), and blinking events in single QDs are almost binary on/off in nature (Panels D and E). However, some QDs expressed a ternary blinking mode, which would be characteristic of not one but two colocalised QDs. When both QDs are emitting, the total emitted light is approximately double that of when only one is in the on state (Panel F). Image drift was found to be significantly improved with the use of the GDSC AlignFFT imageJ plugin.

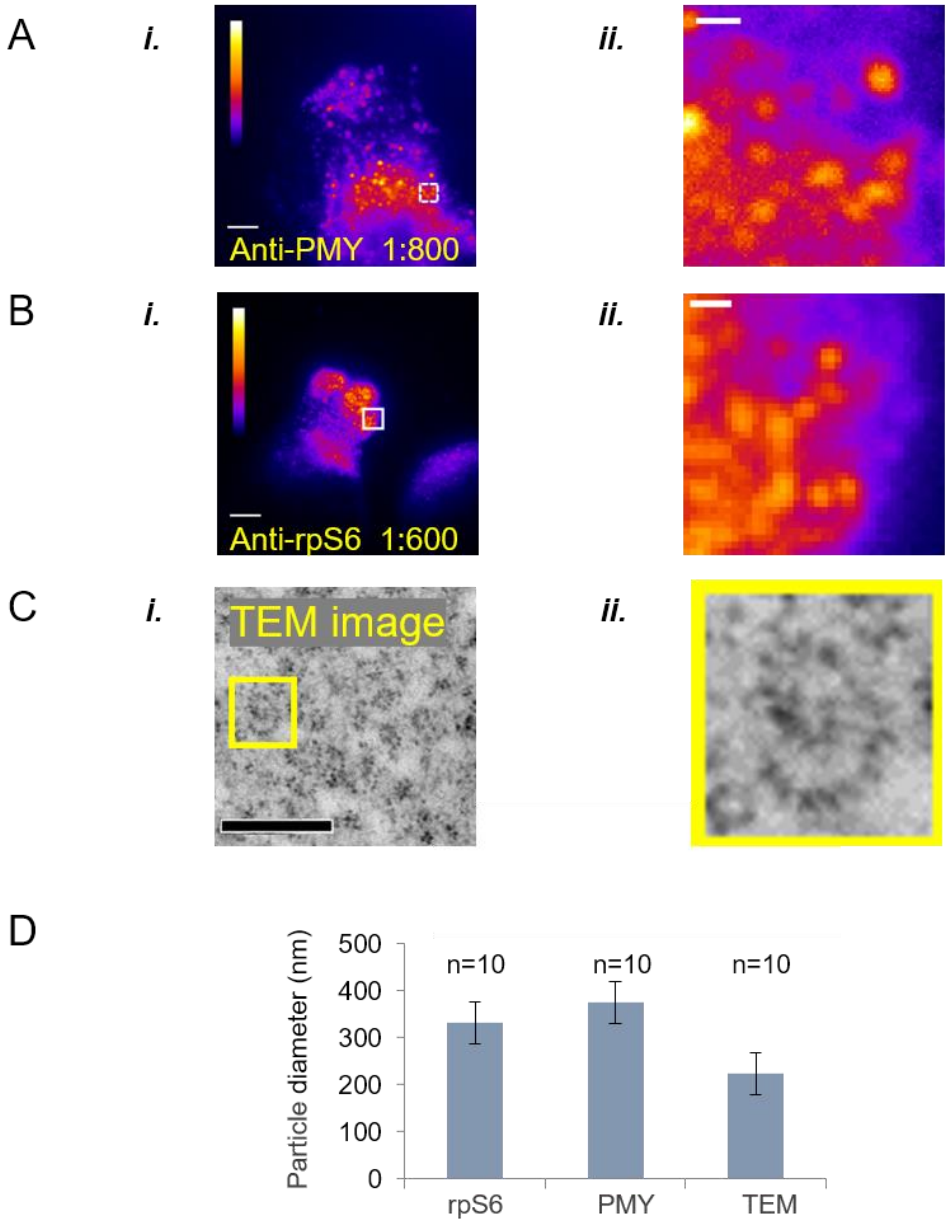

Figure 3.14 Polysome imaging using TIRF and TEM

Cells were prepared for TIRFM imaging using both RPM and standard dual-immuno-labelling for rp-S6, both as described in Figure 3.12. Anti-puromycin antibodies were used at a dilution of 1:800, and anti-rp-S6 used at 1:100. Movies taken were 100 frames in length, SOFI-processed and pseudo-coloured as indicated in the calibration bars Scale bars indicate 5µm. (This work was performed jointly with Dr. Mark Willett). **Panel A.** ***i.*** Anti-PMY 1:800 ***ii.*** Magnified ROI. **Panel B.** ***i.*** anti-rpS6 1:600 ***ii.*** Magnified ROI. **Panel C.** ***i.*** Transmission electron microscope (TEM) image of polysomes in an MRC5 cell, as imaged by Dr. Julian Thorpe. ***ii.*** A single polysome. **Panel D.** Anti-rpS6 and anti-puromycin stained SOFI deconvolved particles were measured in diameter and compared those in TEM images. Standard error bars applied. n=10 in all cases.

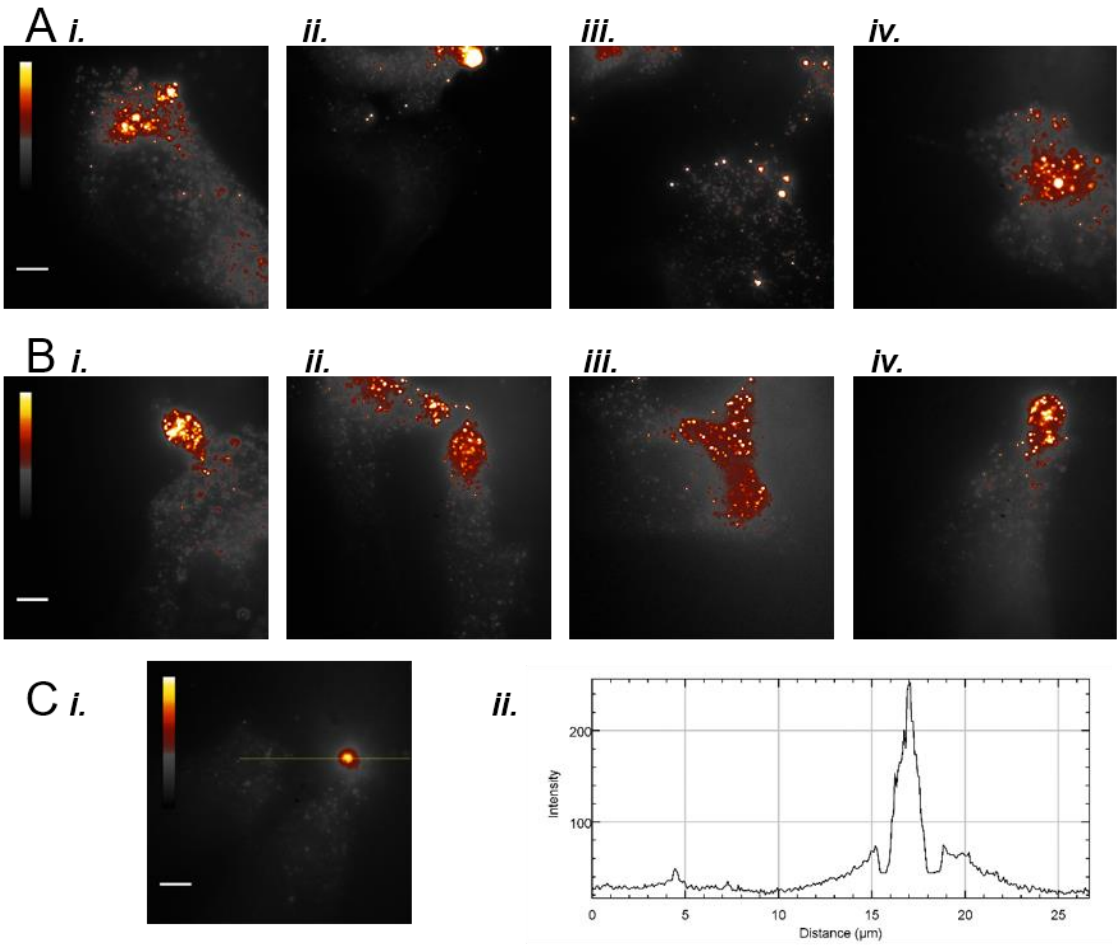

Figure 3.15 Titration of anti-FMRP and anti-CYFIP1 antibodies for single-molecule imaging

MRC-5 SV2 cells were seeded onto methanol-cleaned, and ozonated coverslips coated with 8µg/cm^2 rat tail collagen I, at a density of 15,000 cells/cm^2 and incubated in MEM supplemented with 15% (v/v) FCS at 37ºC for 40 mins. Cells were fixed using 4% (v/v) PFA, and permeabilised using 0.1% (v/v) Triton X-100 prior to dual immuno-fluorescence staining using serial dilutions of antibodies for either FMRP or CYFIP1. Alexa Fluor 555 secondary goat-raised antibodies were applied at the same concentration throughout (1:300), as described in the Materials and Methods. The TIRF microscope setup utilised a 561nm laser diode; dichroic 575nm and emission filter 593-40nm (Figure 3.11C). Movies were taken with 100ms frame exposures and a frame interval of 20ms. Images are derived from an averaging of the first 50 frames of each movie sequence prior to pseudo-colouring. This work was performed jointly with Dr. Mark Willett. Scale bars indicate 5µm. **Panel A.** CYFIP1 primary antibody titrations ***i.*** Diluted at 1:500 **ii.** Diluted at 1:1000 **iii.** Diluted at 1:2000 **iv.** Diluted at 1:4000 **Panel B**. FMRP primary antibody titrations **Insets *i.*** Diluted at 1:500 **ii.** Diluted at 1:1000 **iii.** Diluted at 1:2000 **iv.** Diluted at 1:4000 **Panel C.*i.*** Control. Secondary antibodies only, with maximum laser power. ***ii.*** Intensity distribution over the ROI from inset *i*. (left to right).

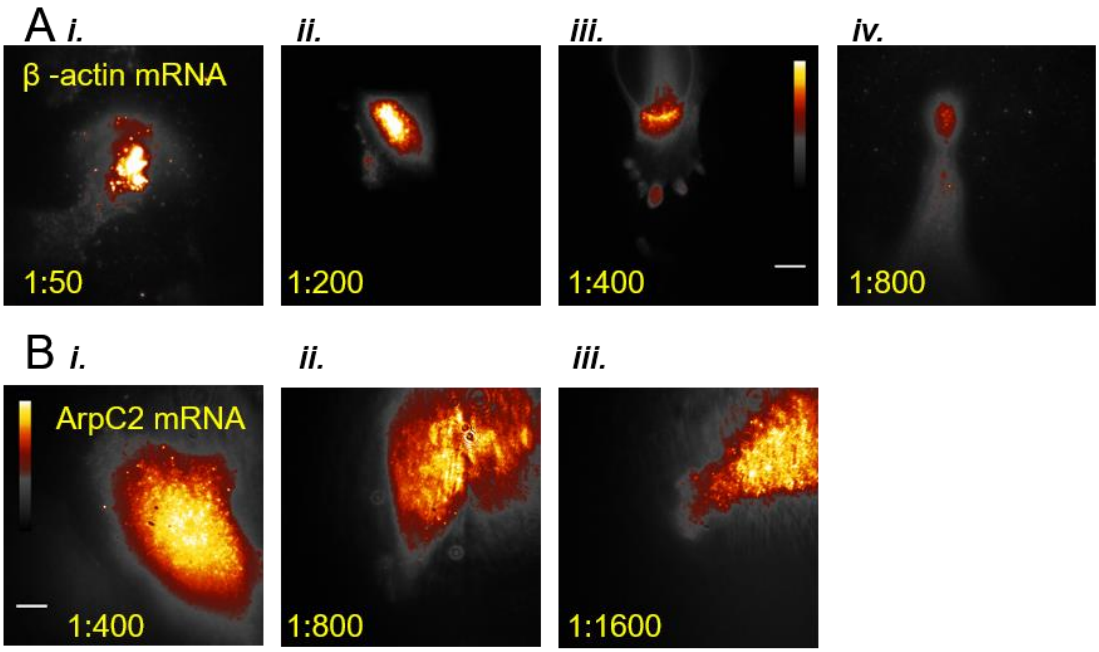

Figure 3.16 Titration of Stellaris mRNA probes for single-molecule imaging.

MRC-5 SV2 cells were seeded onto methanol-cleaned, and ozonated coverslips coated with 8µg/cm^2 rat tail collagen I, at a density of 15,000 cells/cm^2 and incubated in MEM supplemented with 15% (v/v) FCS at 37ºC for 40 mins. Cells were fixed using 4% (v/v) PFA, and permeabilised using ethanol treatment for fluorescence *in situ* hybridisation of either β-actin mRNA or ArpC2 mRNA, as described in the Materials and Methods. Stellaris Cal Fluor Orange mRNA probes with peak excitation at 538nm and emission at 559nm required a 561nm laser, a long-pass 575nm dichroic mirror and an emission filter of 593-40. Movies were taken with 100ms frame exposures and a frame interval of 20ms. Images are derived from an averaging of the first 50 frames of each movie sequence, prior to pseudo-colouring. This work was performed jointly with Dr. Mark Willett. Scale bars indicate 5µm.

Panel A. β-actin mRNA probe titration **Insets i.** Diluted at 1:50 **ii.** Diluted at 1:200 **iii.** Diluted at 1:400 **iii.** Diluted at 1:800
Panel B. ArpC2 mRNA titrations **Insets i.** Diluted at 1:400 **ii.** Diluted at 1:800 **iii.** Diluted at 1:1600

A

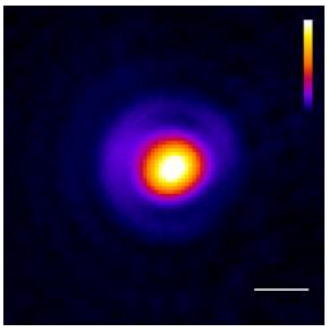

B

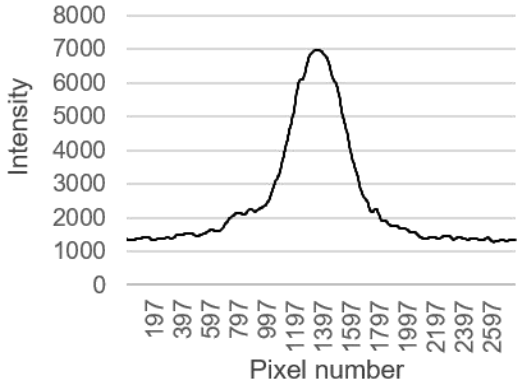
Intensity
8000
7000
6000
5000
4000
3000
2000
1000
0
197
397
597
797
997
1197
1397
1597
1797
1997
2197
2397
2597
Pixel number

C

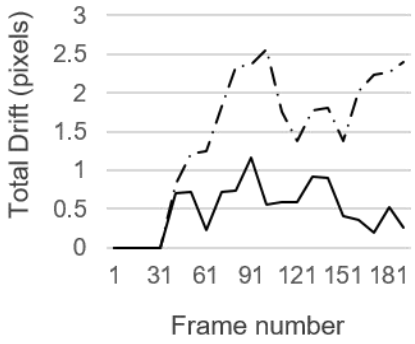
Total Drift (pixels)
3
2.5
2
1.5
1
0.5
0
1
31
61
91
121
151
181
Frame number

D

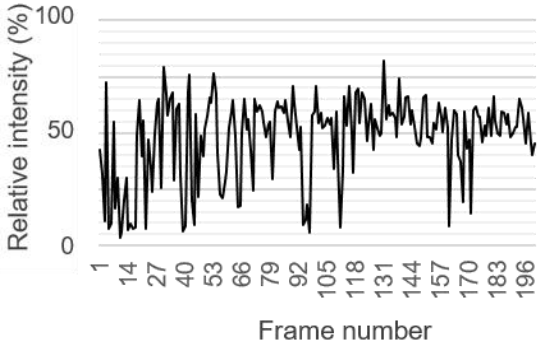
Relative intensity (%)
100
50
0
1
14
27
40
53
66
79
92
105
118
131
144
157
170
183
196
Frame number

E

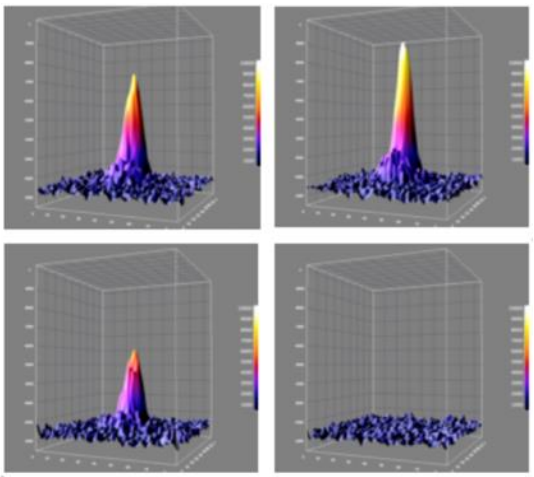

F

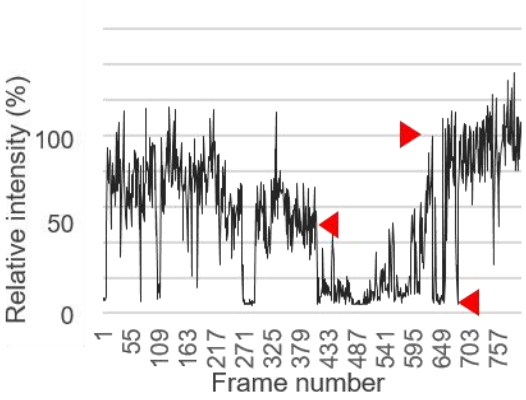
Relative intensity (%)
100
50
0
1
55
109
163
217
271
325
379
433
487
541
595
649
703
757
Frame number

Figure 3.17 Imaging of Single Quantum Dots

QD625 quantum dots were serially titrated in deionised water and 100µL applied to methanol-cleaned and ozonated coverslips, prior to an application of 50µL of PBS. Total internal reflection (TIR) was obtained using a 473nm excitation laser beam, Nikon Plan Apo 60x/1.45NA TIRF objective and a TIRFM setup as described in Figure 3.11, employing a long-pass 547nm dichroic mirror and an emission filter of 593-40nm.

Panel A. A single QD625, 40 frame averaged with bicubic interpolation and pseudo-colouring. Scale bar indicates 500nm.
Panel B. The QD625 intensity profile.
Panel C. Pixel drift in absolute terms, from over 200 movie frames. Drift in x and y axes have their magnitudes combined for a 'Total Drift' value, plotted in the resulting figure. A dashed line signifies the pixel drift of the QD625 in the original movie. The full line shows the total drift calculated after an alignment process using GDSC ImageJ FFT alignment plug-in (supplied by Dr. A. Herbert)
Panel D. Post-alignment plotting of the QD625 maxima intensity over 200 frames.
Panel E. 3D rendering of single frames from the movie.
Panel F. QD fluctuation profiles showing ternary fluctuations at approximately 0%, 50% and 100% of the maximum intensity level indicate the presence of two QDs.

3.13 Cellular immunofluorescence using QD625:IgG conjugates in ethanol permeabilised fixed cells

Having established QDs to be highly fluorescently intense as well as being photostable, it was considered that application of antibody-conjugated QDs would be a tool worthy of investigation for *in situ* localisation studies of translation initiation factors. To this end, eIF4E IgG:QD625 conjugates were prepared using a method described in the Materials and Methods (Section 2.8.1.3). Cells were then seeded on collagen-coated coverslips and allowed to spread for 40 minutes. Cells were subsequently fixed and permeabilised using 70% (v/v) ethanol prior to immunofluorescence staining using serial dilutions of eIF4E IgG:QD625 conjugates. Movies were acquired. The images shown in Figure 3.18 suggest that QDs are certainly bright enough to provide substantial emission fluorescence *in situ*. Ethanol permeabilisation allowed these large conjugate bodies to enter the cell without hindrance (Sapsford et al. 2006). However, each frame of the movie was substantially different to the next, with many fluorescence sources apparently freely moving in the mounting buffer (Panel B), rendering these images unacceptable for protein studies.

3.14 Cellular immunofluorescence using QD625:IgG conjugates in Triton X-100 permeabilised fixed cells

Use of eIF4E IgG:QD conjugates in ethanol permeabilised cells rendered free-floating QDs. To investigate if the permeabilisation solution of ethanol was the cause of this inability for the eIF4E IgGs to bind eIF4E proteins *in situ*, the assay of Section 3.13 was repeated using Triton X-100 as the permeabilisation agent. Figure 3.19 shows that cells were efficiently permeabilised under these conditions, with very little free-floating eIF4E IgG:QD conjugates. eIF4E staining in this manner suggests that during spreading, eIF4E traverses the cytoskeleton with a steady-state flow of proteins towards the leading edge of the cell (Panel B). The large IgG:QD constructs appeared not to prevent the localisation of eIF4E in the mid-body of post-mitotic cells (Figures C and D).

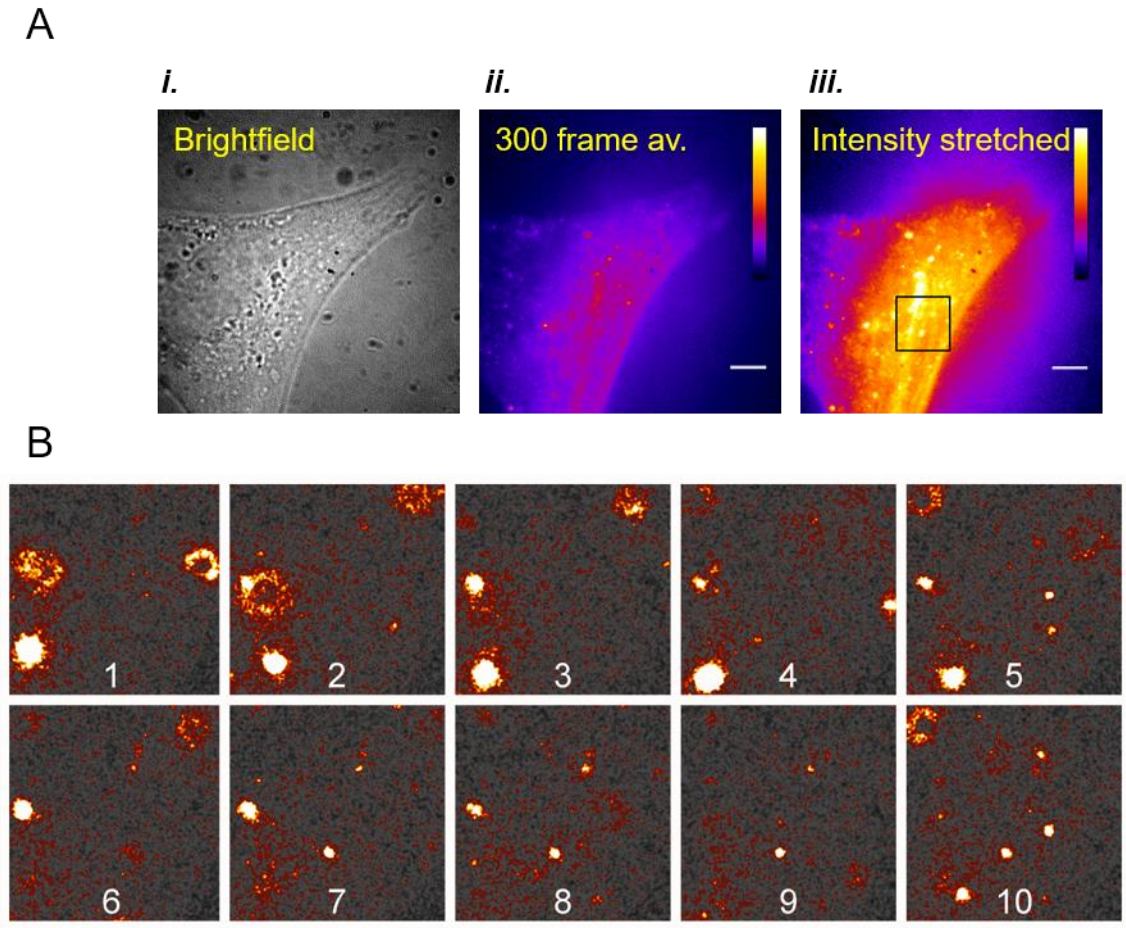

Figure 3.18 Cellular Immuno-fluorescence using QD625:IgG conjugates in ethanol permeabilised fixed cells

eIF4E IgG:QD625 conjugates were made using a method described in the Materials and Methods. MRC-5 SV2 cells were seeded onto methanol-cleaned, and ozonated coverslips coated with 8µg/cm^2 rat tail collagen I, at a density of 15,000 cells/cm^2 and incubated in MEM supplemented with 15% (v/v) FCS at 37ºC for 40 mins. Cells were fixed using 4% (v/v) PFA, and permeabilised using 70% (v/v) ethanol prior to immuno-fluorescence staining using serial dilutions of eIF4E IgG:QD625 conjugates. TIR was obtained using a 473nm excitation laser beam, Nikon Plan Apo 60x/1.45NA TIRF objective and a TIRFM setup as described in Figure 3.11, employing a long-pass 547nm dichroic mirror and an emission filter of 593-40. Scale bars indicate 5µm.

Panel A.*i.* Brightfield image averaged over 300 frames. ***ii.*** TIRF image averaged over 300 frames. **iii.** Image from inset ii., intensity stretched. **Panel B.** From the ROI in Panel A.*iii*, Each of the first 10 frames is shown, with associated frame numbers, in pseudo-colour.

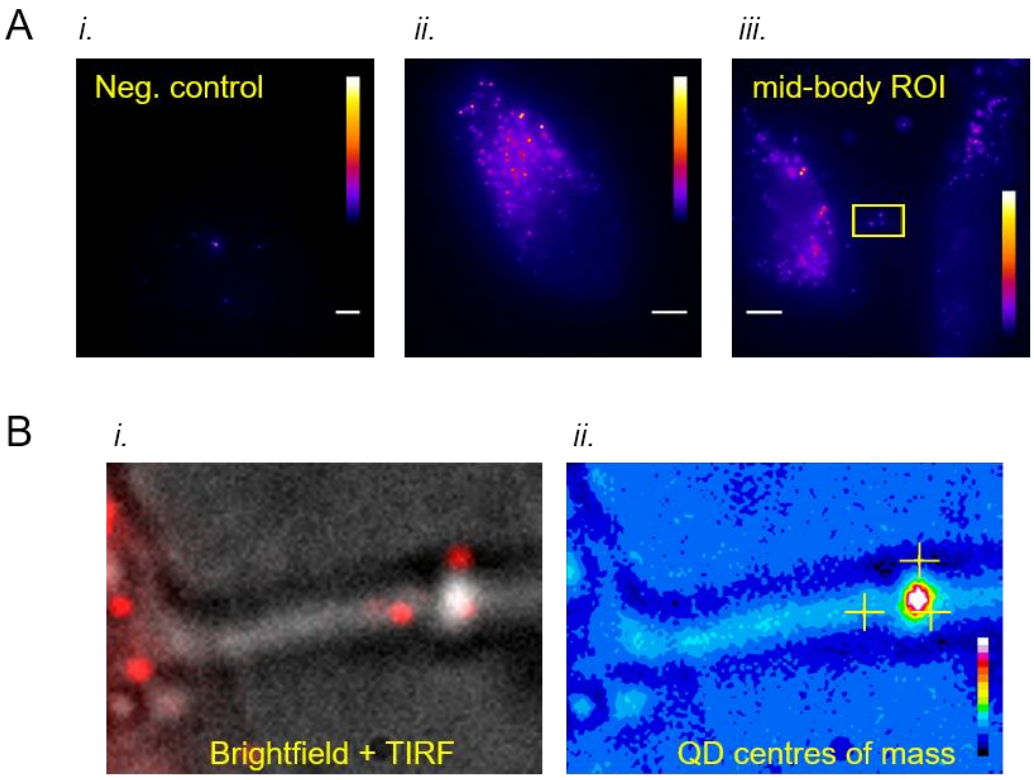

Figure 3.19 Cellular Immuno-fluorescence using QD625:IgG conjugates in Triton X-100 permeabilised fixed cells.

MRC-5 SV2 cells were seeded onto methanol-cleaned, and ozonated coverslips coated with 8µg/cm^2 rat tail collagen I, at a density of 15,000 cells/cm^2 and incubated in MEM supplemented with 15% (v/v) FCS at 37ºC for 40 mins. Cells were fixed using 4% (v/v) PFA, and permeabilised using 0.1% (v/v) Triton X-100 prior to immuno-fluorescence staining using serial dilutions of eIF4E IgG:QD625 conjugates. TIR was obtained using a 473nm excitation laser beam, Nikon Plan Apo 60x/1.45NA TIRF objective and a TIRFM setup as described in Figure 3.11, employing a long-pass 547nm dichroic mirror and an emission filter of 593-40nm. All TIRF images were intensity-averaged over 300 frames.

Panel A.*i.* Negative Control without quantum dots present. ***ii.*** A single cell showing strong fluorescence in its lamellipodium. ***iii.*** Two cells, with an ROI Idrawn around the mid-body.
Panel B.*i.* Magnified view of the ROI shown in Panel A.i., showing a 300-frame averaged brightfield view in greyscale, with a composite red-scaled TIR image. ***ii.*** A pseudo-coloured 300-frame averaged brightfield image, superimposed with cross-hairs marking the points of maximum intensities of the locations of three quantum dots closest to the mid-body.

3.15 Stage Drift measurement, and correction by FFT Alignment

In previous assays, collagen-embedded TetraSpeck beads were not seen to be appropriate for use as fiducial markers (Section 3.3). However, it was thought that the qualities of QD offered inherent fiducial characteristics which could be used to align movie frames using methods such as auto-correlation. Using movie images acquired from Section 3.14, coverslip drift was calculated both pre- and post-alignment by the GDSC AlignFFT ImageJ plug-in, using my own Image Drift Calculator to calculate lateral drift to a sub-pixel resolution (see Appendix). Results are shown in Figure 3.20. These data suggest that using the inherent features of QDs to act as fiducial markers, coverslip drift during the image capture process can be significantly reduced.

3.16 Comparison of SOFI to 3B

In experiments thus far SOFI has been seen to provide resolution enhancement of approximately 24% (Figure 3.13). This is associated with theoretical resolution improvements of between 1.4- and 2-fold (Dertinger & Heilemann 2010). Bayesian analysis of bleaching and blinking (3B) (Hu et al. 2013; Rosten et al. 2013) also utilises stochastic blinking as well as bleaching events to provide a spatial resolution in the range of 50nm. This is true even for fluorophores which have overlapping PSFs, or which are in an off state for a fraction of the movie. The 3B predictive model is based on a dataset consisting of a sequence of high frame rate images generated from large numbers of fluorophores undergoing blinking and bleaching processes. As with any Bayesian modelling, the state of the model is statistically linked to the observation at any one time. 3B builds a probability map of fluorophore positions with any ambiguity in the final model as blurred; this means that false positive point sources become unlikely outcomes.

To better understand which super-resolution algorithms functioned best with IF utilising eIF4E IgG:QD625 conjugates, a comparative study was performed. Using movie images acquired from Section 3.14, registered movie images were processed on a selected ROI (Figure 3.21Ai) using SOFI and 3B.

In Figure 3.21, these images show how 3B reduces background noise considerably when compared to SOFI. 3B significantly enhanced image resolution for *in situ* QD labels compared to SOFI.

3.17 Morphological implications of using ethanol permeabilisation techniques

Section 3.13 shows evidence for ethanol permeabilisation causing some issues with the ability of IgG:QD conjugates to bind to their cognate proteins in situ. Ethanol permeabilisation is a key protocol step in mRNA visualisation using fluorescence in situ hybridisation (FISH). For this reason, differential interference contrast (DIC) microscopy was employed jointly with fluorescence imaging of FISH when investigating the localisation of β-actin mRNA in spreading cells. Cells were seeded onto collagen-covered coverslips and allowed to spread for 40 minutes. Cells were fixed using 4% (v/v) PFA and permeabilised using 70% (v/v) ethanol at 4ºC for 1hour, prior to hybridisation of Stellaris FISH probes for the fluorescence staining of β-actin mRNA, as described in the Materials and Methods. Images were taken on a Leica SP8 confocal microscope using DIC and fluorescence imaging. Results from ethanol permeabilisation over a period of 1 hour facilitated the visualisation of β-actin mRNA in the cytoplasm as well as in lamellipodia. However, mechanical stress was apparent, with instances for complete disintegration of fine structures seen most clearly with DIC (Figure 3.22).

3.18 Ethanol permeabilisation assay

To better understand the effect of ethanol permeabilisation on fixed cells, this issue was addressed by seeding cells and allowing them to spread for 40 minutes. Cells were fixed prior to incubation of the cells in titrations of ethanol at 4ºC for different durations. Images were taken of the cells using a standard brightfield microscope at different time periods. From Figure 3.23, these images confirm that cell membrane disintegration was happening after just 20 minutes immersion in 70% or 100% ethanol. No disintegration of cell structures was visible in the PBS+ control.

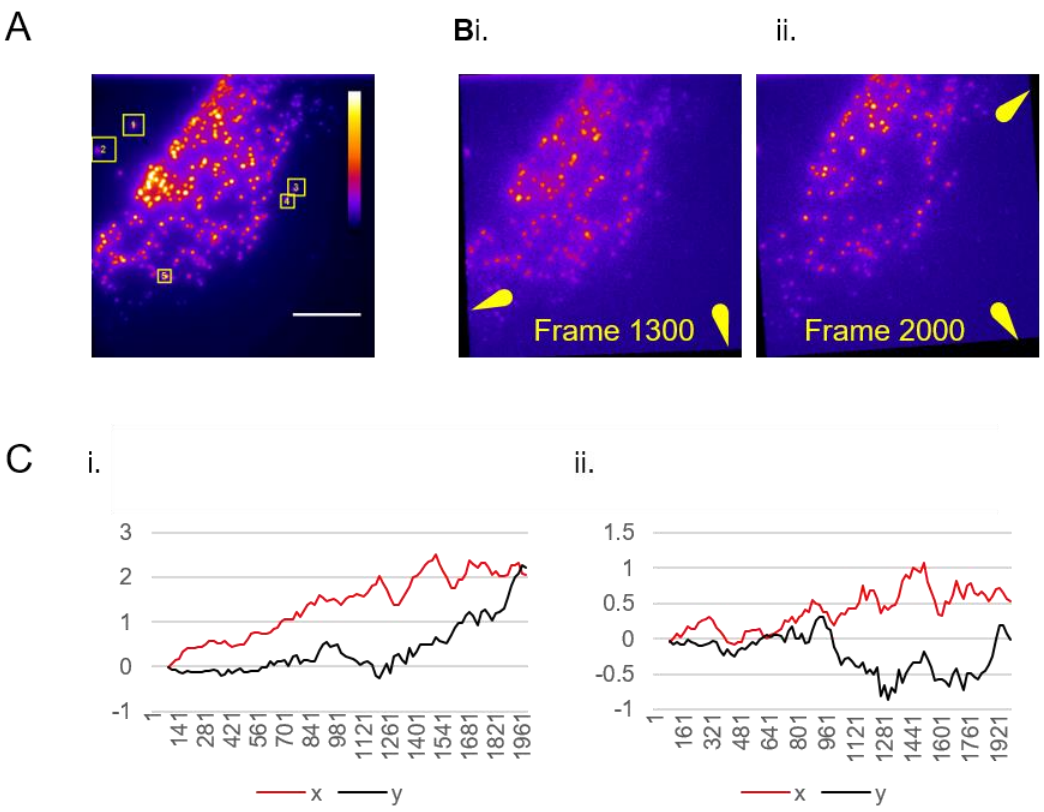

Figure 3.20 Stage Drift measurement, and correction by FFT Alignment

Cell were grown, fixed, Triton X-100 permeabilised, immuno-fluorescence labelled with eIF4G IgG:QD625 conjugates, prior to imaging (as described in Figure 3.21). Drift alignment was performed using two separate methods, including SIFT (Lowe 2000), and GDSC AlignFFT (with settings: Window function: NONE; sub-pixel method Gaussian; Interpolation BICUBIC; Normalised). Drift values were calculated at sub-pixel resolution using “Image Drift Calculator” (Appendix A).

Panel A. Quantum dot conjugate anti-eIF4E antibodies visualised within a Triton X-100 permeabilised MRC-5 SV2 cell. 5 single quantum dots (highlighted in yellow) were chosen to act as fiducial markers by which stage drift was calculated. **Panel B.** Linear Stack Alignment using SIFT (Lowe 2000) causes unwanted high magnitude image transposition, as highlighted by the arrows showing a bright image frame on a null background. ***i.*** Frame 1300 ***ii.*** Frame 2000. **Panel C.*i.*** Averaging over all 5 ROIs in Panel A, image drift in x and y directions was calculated using a my own drift analysis program (Appendix A). Over 1921 frames, the image drifted by 2 pixels in either direction. Drift analysis performed by my own imageJ macro. ***ii.*** After aligning the move using the GDSC AlignFFT image alignment plug-in for ImageJ, drift in the x direction was minimised to 0 pixels, and to 0.5 pixels in the y direction.

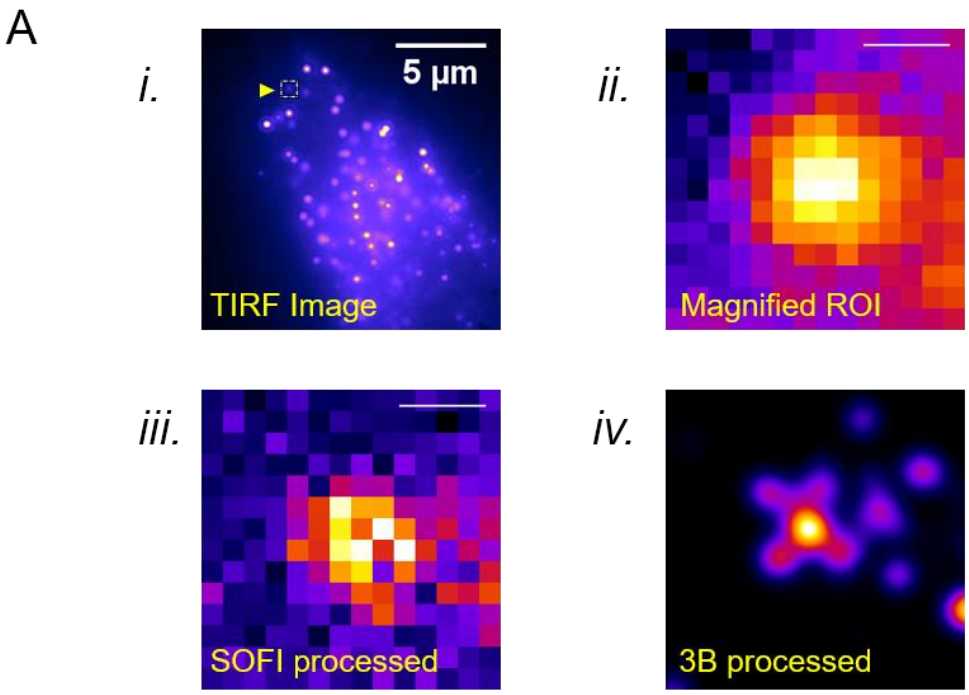

Figure 3.21 Comparison of SOFI to 3B

Cell were grown, fixed, Triton X-100 permeabilised, immuno-fluorescence labelled with eIF4G IgG:QD625 conjugates, prior to imaging (as described in Figure 3.21). Drift alignment was performed using GDSC AlignFFT (with settings: Window function: NONE; sub-pixel method Gaussian; Interpolation BICUBIC; Normalised), prior to further image processing of a small region by superresolution optical fluctuation imaging (SOFI; Dertinger et al. 2009) and Bayesian analysis of blinking and bleaching (3B; Cox & Jones 2013; Rosten et al. 2013). Scale bars indicate 250nm unless otherwise stated.

Panel A i. A 100-frame averaged image showing eIF4E IgG:QD625 conjugates bound within an MRC-5 SV2 fibroblast **ii.** The ROI from panel Ai., shows fluorescence from one or more eIF4E IgG:QD625 conjugates. **iii.** The SOFI processed ROI from inset i. **iv.** The 3B processed ROI from inset i.

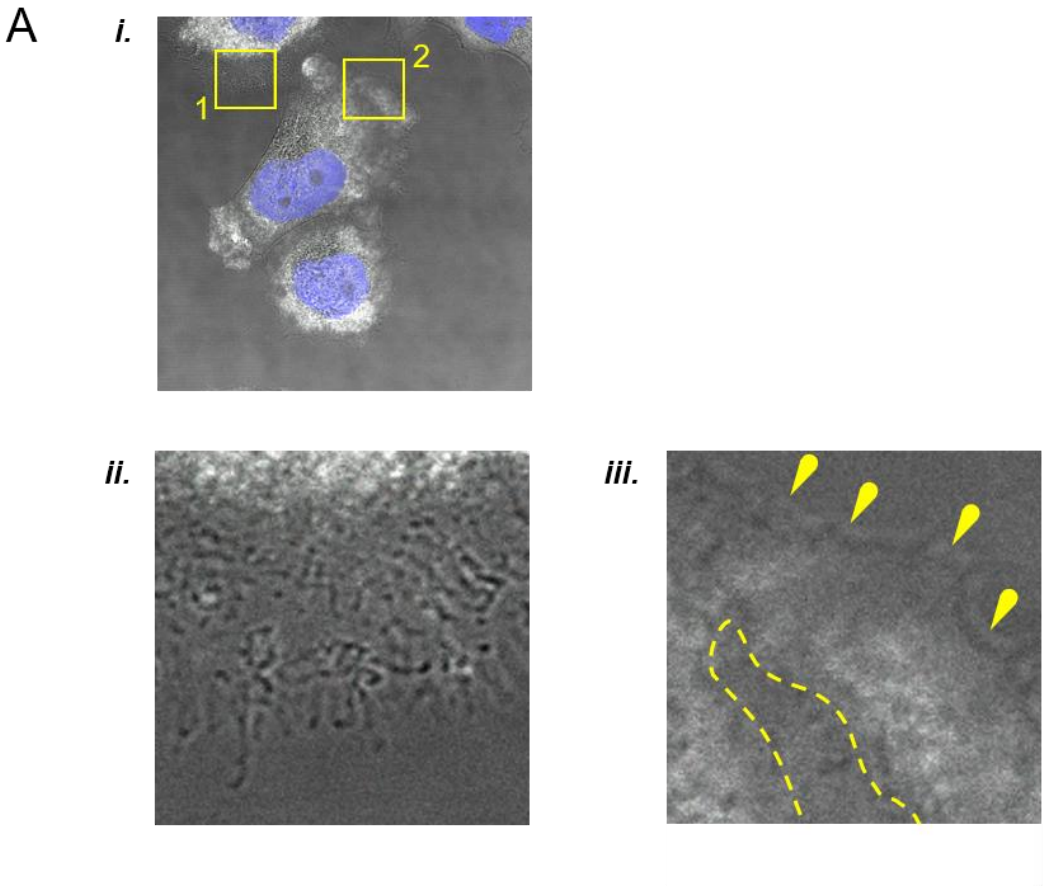

Figure 3.22 Morphological implications of using ethanol permeabilisation techniques

MRC-5 SV2 cells were seeded onto methanol-cleaned, and ozonated coverslips coated with 8µg/cm^2 rat tail collagen I, at a density of 15,000 cells/cm^2 and incubated in MEM supplemented with 15% (v/v) FCS at 37ºC for 40 mins. Cells were fixed using 4% (v/v) PFA, and permeabilised using 70% (v/v) ethanol at 4ºC for 1hour prior to hybridisation of Stellaris FISH probes for the fluorescence staining of β-actin mRNA, as described in the Materials and Methods. Images were taken on a Leica SP8 confocal microscope.

Panel A *i.* A composite image of an MRC-5 SV2 cell, showing grey-scale differential interference contrast (DIC) light, with DAPI in blue, and grey-scale FISH probes indicating the presence of β-actin mRNA in the lamellipodium. ***ii.*** From ROI #1 of the mean image, membrane breakdown at the leading edge of the cell. ***iii.*** From ROI#2 of the main image, a large fracture in the lamellipodium is evident. Yellow dashed line highlights the fracture area, with arros highlighting the front leading edge of the cell.

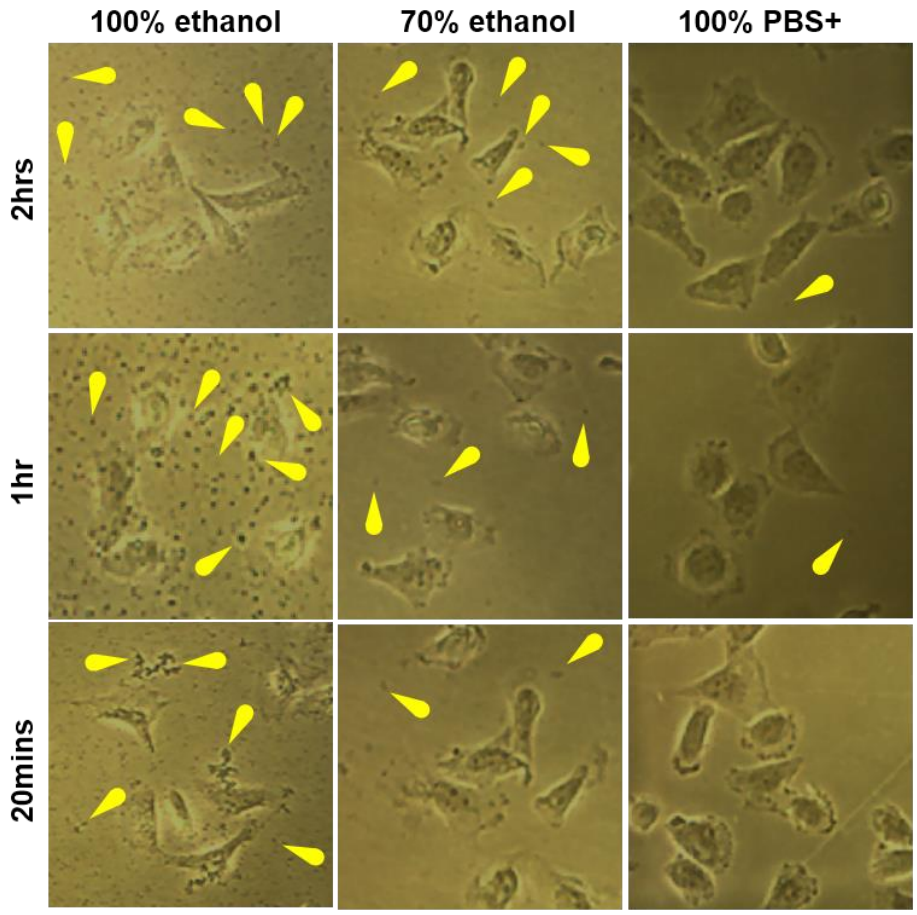

Figure 3.23 Ethanol permeabilisation assay

MRC-5 SV2 cells were seeded onto methanol-cleaned, and ozonated coverslips coated with 8µg/cm^2 rat tail collagen I, at a density of 15,000 cells/cm^2 and incubated in MEM supplemented with 15% (v/v) FCS at 37ºC for 40 mins. Cells were fixed using 4% (v/v) PFA prior to permeabilisation with titrations of ethanol held at 4ºC (with ethanol stock supplemented with magnesium chloride hexahydrate at 100mg/L, and calcium chloride dehydrate at 132.5mg/L). Images were taken using a standard brightfield microscope at different time periods. Typical images are shown here for cells after 20mins, 1hr and 2hrs of treatments. Magnifications differ in each image. Arrows highlight some of the cellular detritus on each image, all of which is due to the breakdown of cellular membranes.

3.19 Morphological implications of ethanol permeabilisation

The manufacturer's instructions for Stellaris FISH probe application advise a 1-hour incubation in ethanol in order to permeabilise cell membranes prior to fluorescence staining. Having performed ethanol titration studies (Section 3.18) it was decided that future permeabilisation steps would have to be performed differently. To address this issue cells were grown and prepared for the staining of β-actin mRNA, using FISH in the manner described in Section 3.17, with one change to the permeabilisation step: Cells were permeabilised with 0.1% Triton X-100 for 5 minutes, followed by a short duration equilibration step involving immersion of cells in 70% ethanol for only 10 minutes at 4ºC. Images were taken on a Leica SP8 confocal microscope. These results (Figure 3.24) show that FISH is possible using Triton X-100 pre-permeabilisation and reducing the duration of exposure of cells to ethanol, without any obvious degradation in the way in which the FISH probes appeared to function. The presence of β-actin mRNA was noted in lamellipodia, as well as in putative stress granules in a minority of cells.

3.20 Transfection of MRC-5 cells with CYFIP1-eYFP

As part of the investigation into the role of CYFIP1 in localised translation during cell spreading, stable cell lines expressing CYFIP1-eYFP would provide an alternative method of CYFIP localisation using live or fixed cell imaging, as well as an additional way to perform the CYFIP1 co-immunoprecipitation assay.

To address this line of enquiry, an eYFP-CYFIP1 vector was kindly donated by Dr Claudi Bagni (DeRubeis et al. 2013; Bagni & Greenough 2005; Lucá et al. 2013). Following standard methods of transfection as described in the Materials and Methods, a CYFIP1-eYFP plasmid was successfully transfected into MRC-5 SV2 cells using G418 as a selector in MRC-5 SV2 cells (successfully expressed eYFP conjugate proteins are shown in green in Figure 3.25). Western blotting of cell lysate showed the presence of eYFP-CYFIP1 when probed with anti-GFP antibodies, however, co-immunoprecipitation using anti-GFP agarose beads failed to pull down additional proteins. No further tests were performed on this cell line (Figure 3.25).

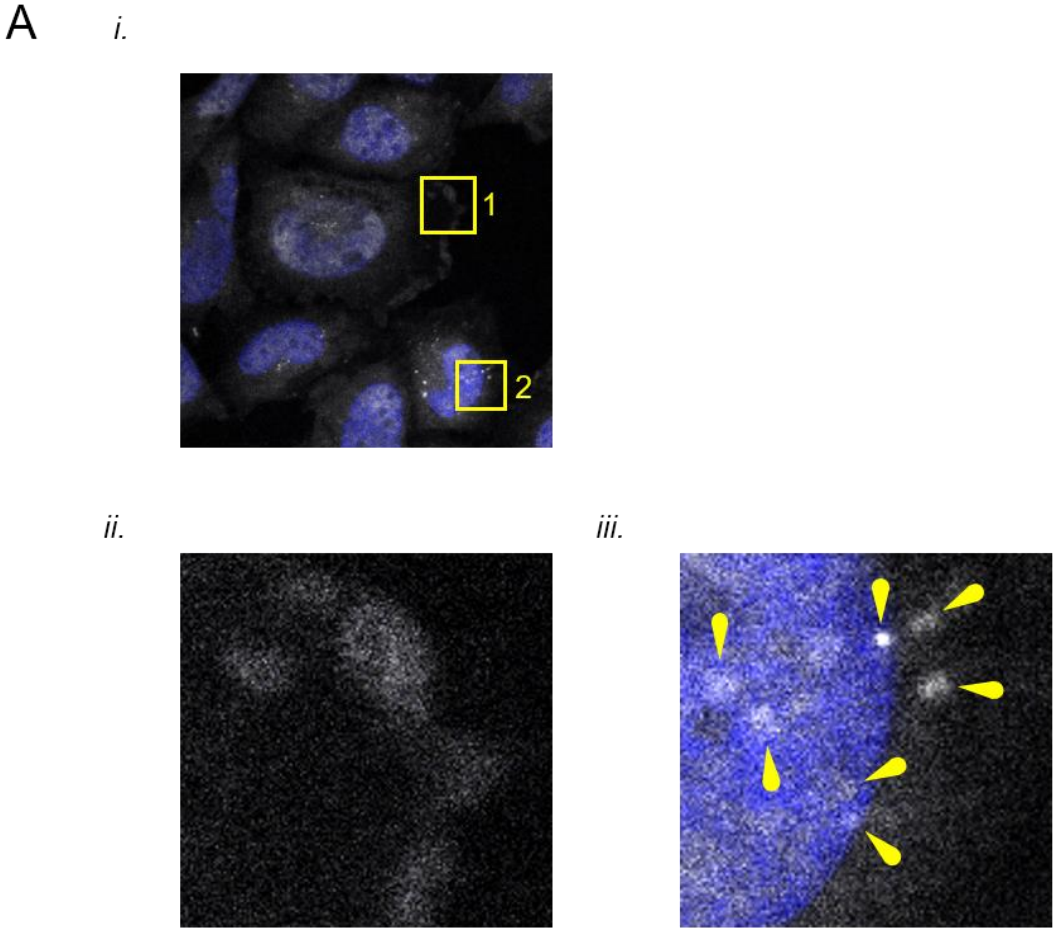

Figure 3.24 Morphological implications of ethanol permeabilisation

MRC-5 SV2 cells were seeded onto methanol-cleaned, and ozonated coverslips coated with 8µg/cm^2 rat tail collagen I, at a density of 15,000 cells/cm^2 and incubated in MEM supplemented with 15% (v/v) FCS at 37ºC for 40 mins. Cells were fixed using 4% (v/v) PFA, and permeabilised using 0.1% Triton X-100 for 2.5mins, then 70% (v/v) ethanol at 4ºC for 10 mins prior to hybridisation of Stellaris FISH probes for the fluorescence staining of β-actin mRNA, as described in the Materials and Methods. Images were taken on a Leica SP8 confocal microscope.

Panel A i. A composite image of an MRC-5 SV2 cell, showing DAPI in blue, and grey-scale FISH probes indicating the presence of β-actin mRNA. **ii.** A magnified view of ROI #1, indicating the presence of β-actin mRNA in the lamellipodium. **ii.** A magnified view of ROI #2 indicating the presence of β-actin mRNA possibly in stress granules or P-bodies (highlighted by arrows).

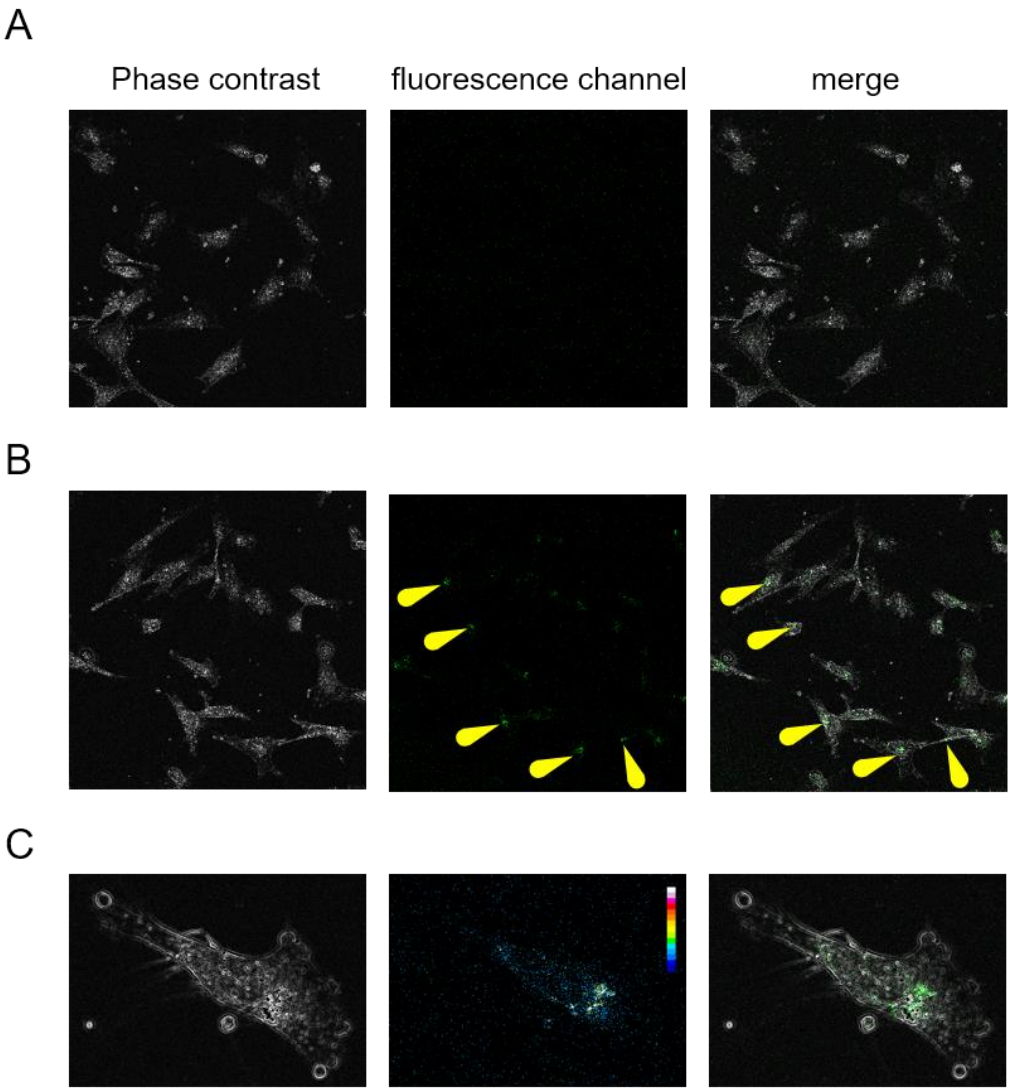

Figure 3.25 Transfection of MRC-5 cells with CYFIP1-eYFP

Amplification of the CYFIP1-eYFP plasmid in subcloning efficiency DH5α competent cells was performed, prior to small-scale preparation of plasmid DNA and further transfection into MRC-5 SV2 cells as described in the Materials and Methods. After day 5 post-transfection the cells were imaged on a Leica SP8 confocal microscope. Images pseudo-coloured with a 'Fire' LUT.

Panel A. Non-transfected MRC5 cells. **Panel B.** Transfected MRC5 cells. Arrows indicate areas of eYFP fluorescence. **Panel C.** Magnified image of a transfected cell.

3.21 Summary

To optimise methods used for the imaging and colocalisation of proteins and mRNAs, the emphasis had been placed on modifying already proven generic protocols, so that the very best results could be obtained when imaging targets close to, or in contact with the very fragile nascent growing plasma membranes of fibroblast cells. Consideration was also made for the types of imaging techniques - both hardware and software employed for image realisation.

After investigating different permeabilisation techniques, rather than relying on the popular Triton X-100 non-iconic detergent, saponin was adopted as the preferred reagent given its ability to selectively sequester cholesterol from the plasma membrane, leaving the phospholipid bi-layer and consequently many of the membrane-interacting proteins intact and *in situ*. After many trial titrations, permeabilisation was found to be optimal at a saponin concentration of 0.0375% (w/v).

Optimisation of media applications as performed using modified 5 mL pipette tips cut at an angle, allowed buffers and reagents to exert less mechanical stress on fixed cells due to the concomitant reduction in media exit velocity when compared to standard, uncut, 1mL pipetters.

Wash processes undertaken as part cell staining protocols (IF and FISH), were seen to provide less structural damage to the cells when the use of a mechanical washer was excluded. Reliance on simple Brownian motion in conjunction with a plentiful supply of wash buffer was enough to expel excess staining reagents from the cell body.

Collagen-embedding of TetraSpeck beads was attempted with the goal of producing a substrate for cell spreading which could be relied-upon to hold none-moving fiducial markers - especially useful for dual-channel imaging. Embedding of 100 nm beads gave fiducial markers which were too far below the usual working focal plane when imaging cells on a confocal microscope. Thus, embedding of such markers was deemed impractical.

$FRET_{Acceptor\ Bleaching}$ using Alexa Fluor 488 donor, and Alexa Fluor 555 acceptor fluorophores were used to test for interactions between a number of target proteins. Interactions between α-tubulin and eIF4E previously identified in

fibroblasts (Willett et al. 2011) were tentatively verified as interacting. However, over multiple assays consistency in results for both positive and negative controls were inconsistent. FRET was seen to be unreliable, probably due to stage drift during the bleaching process.

Using eIF4E IgG conjugated quantum dots and ethanol permeabilisation techniques, eIF4E appeared to be shown traversing the cytoplasm utilising the cytoskeletal features. More importantly, quantum dots were used as fiducial markers, facilitating sub-pixel drift measurements of the TIRFM stage during movie capture. Further experimentation using QDs was hindered by the adverse effect of ethanol on the phospholipid membrane of cells.

Imaging of putative single molecules was performed using TIRFM in conjunction with resolution improvement algorithm implementing second-order SOFI. Results showed putative interactions between Arpc2 mRNA and CYFIP1 at specific locales close to the leading edge of spreading cells. TIRF images were recorded showing actively translating ribosomes using anti-rpS6-based dual-immunofluorescence staining and the RPM. After SOFI processing, comparison of the resulting images failed to show that the putative polysomes gathered using TIRF were comparable in size to those imaged using TEM.

Comparison of SOFI to the Bayesian-based algorithm ‘3B’, showed that 3B has the potential to offer a significantly better resolution of images gathered using TIRF microscopy. 3B would be the algorithm of choice for further superresolution imaging.

Transfection of MRC-5 SV2 cells with a plasmid containing CYFIP1-eYFP was successful, and although the plasmid was seen to express the tagged protein of interest, co-immunoprecipitation using anti-GFP antibodies proved unsuccessful.

4 The role of FMPR and CYFIP1 in fibroblasts

Overview

Previous work from the Morley laboratory has shown that lamellipodia of migrating fibroblasts are enriched for foci active in protein synthesis and mRNAs encoding some structural and regulatory components of the WAVE [WASP (Wiskott-Aldrich syndrome protein) verprolin homologous] complex. These included mRNAs encoding ArpC2, WAVE1 and β-actin mRNA, a population of which was localised to the leading edge of the cell and associated with sites of active translation (Willett et al. 2013; Willett et al. 2011). These pivotal studies indicated that the regulation of localised translation could play a pivotal role in cell spreading and migration. As CYFIP1 is also a part of the WAVE complex (see Chapter 1), these data suggest that a mechanism of CYFIP1/FMRP/mRNA translational regulation might have a role in localised translation at the leading edge of the cell (Bramhan et al., 2016).

4.1 CYFIP1 and FMRP associate with eIF4E in spreading MRC-5 SV2 cells.

Although FMRP, CYFIP1 and selected mRNAs are known to interact in neuronal cells (Bagni & Oostra 2013), it is unclear if they interact in early spreading fibroblastic cells. To address this, MRC-5 SV2 cells were seeded onto culture dishes and allowed to spread for 40 minutes, prior to harvesting and cell lysis as described in the Materials and Methods. m^7GTP–sepharose chromatography was used to isolate eIF4E and associated proteins. Figure 4.1A shows that eIF4E, FMRP and CYFIP1 interact together either directly or indirectly through affinity with mRNA. There is little recovery of these proteins with the sepharose 4B resin alone. In addition, FMRP was recovered by immunoprecipitation and interacting proteins visualised using SDS-PAGE and Western blotting. Panel B shows that both CYFIP1 and eIF4E co-immunoprecipitate specifically with FMRP, providing initial evidence for the presence of an eIF4E-CYFIP1-FMRP interaction in spreading fibroblasts.

With an understanding that all three proteins possibly interact somewhere in the cell, the next step was to assess the location of the FMRP and CYFIP1 using immunocytochemistry (ICC).

4.2 FMRP and CYFIP1 have characteristically different expressions

To understand where FMRP and CYFIP1 might be interacting with eIF4E in spreading cells, ICC was performed to visualise the proteins and look for points of putative interaction (Figure 4.2, Panels A-C). For this, cells were seeded onto collagen-coated coverslips and allowed to spread for 40 minutes. To visualise the proteins, cells were fixed, permeabilised and dual-immunofluorescence stained with anti-CYFIP1 and anti-FMRP antibodies. With a scanning confocal microscope images were obtained firstly at the focal plane of the basal membrane (Panel A). At this focal point, proteins within the entirety of the lamellipodial outgrowths could be visualised. FMRP was seen in a perinuclear locale, and strongly at the leading edge of lamellipodial outgrowths. CYFIP1 was more dispersed in the cytoplasm and not especially concentrated at the leading edges of lamellipodia. By raising the focal plane of the confocal microscope (Panel B), it was seen that CYFIP1 was extremely abundant on what may be part of the endomembrane system (Figure 4.2C). The next step was to confirm within exactly which part of the endomembrane system CYFIP1 may be located.

4.3 Staining with giantin confirms that CYFIP1 localises with the Golgi apparatus

Previous work has shown that CYFIP1 can couple actin dynamics at the leading edge of cells with that of carrier vesicle biogenesis in the trans-Golgi network (TGN) (Anitei et al. 2010). The images shown in Figure 4.2 imply that such a mechanism may be utilised in fibroblasts. To test this, a simple experiment using the positive control of giantin, a known marker for the Golgi apparatus, was employed. Calnexin, a marker for the endoplasmic reticulum (ER) was originally also used in a larger assay, but the antiserum failed to show adequate specificity for the ER (data not shown) and so could not be utilized in this experiment alongside giantin. Due to the anti-CYFIP1 and anti-giantin

antibodies being raised in the same species, this experiment was never going to be 100% conclusive, as there was no possibility of performing 2-channel imaging. However, colocalisation using a single fluorescence channel would be highly informative using visual interpretation alone. For this assay, cells were seeded onto collagen-coated coverslips and allowed to spread for 40 minutes. Cells were then fixed, permeabilised and dual-immunofluorescence stained using DAPI nuclear marker and anti-CYFIP1 antibodies, in the absence or presence of anti-giantin antibodies. The results shown in Figure 4.3 highlight the possibility that both CYFIP1 and giantin colocalised on the Golgi apparatus. The next step was to investigate colocalisation between eIF4E, CYFIP1 and FMRP in the cytoplasmic compartment.

4.4 FMRP shows greater levels of colocalisation with eIF4E than does CYFIP1

Although apparently colocalised in neuronal cells (Bagni & Oostra 2013), the previous ICC assay between FMRP and CYFIP1 shown in Figure 4.2 indicated little obvious colocalisation of these proteins in spreading fibroblasts. Therefore, an experiment was performed to look for colocalisation between eIF4E and FMRP or CYFIP1. For this, cells were seeded onto collagen-coated coverslips and allowed to spread for 40 minutes, fixed, permeabilised and dual-immunofluorescence stained with anti-eIF4E and either anti-CYFIP1 or anti-FMRP antiserum. DAPI was used in all cases as a nuclear marker. By visual inspection, Figure 4.4 shows that FMRP and eIF4E colocalise at the leading edge of the spreading cell (Panels A and C). In contrast, CYFIP1 and eIF4E do not appear to be colocalised to any great extent (Panels B and D). Visual interpretation of colocalisation is a pragmatic approach, but when colocalisation is partial then objective statistics-based measurements are necessary. The next step, therefore, was to take a more analytical approach to the estimation of colocalisation between these proteins of interest.

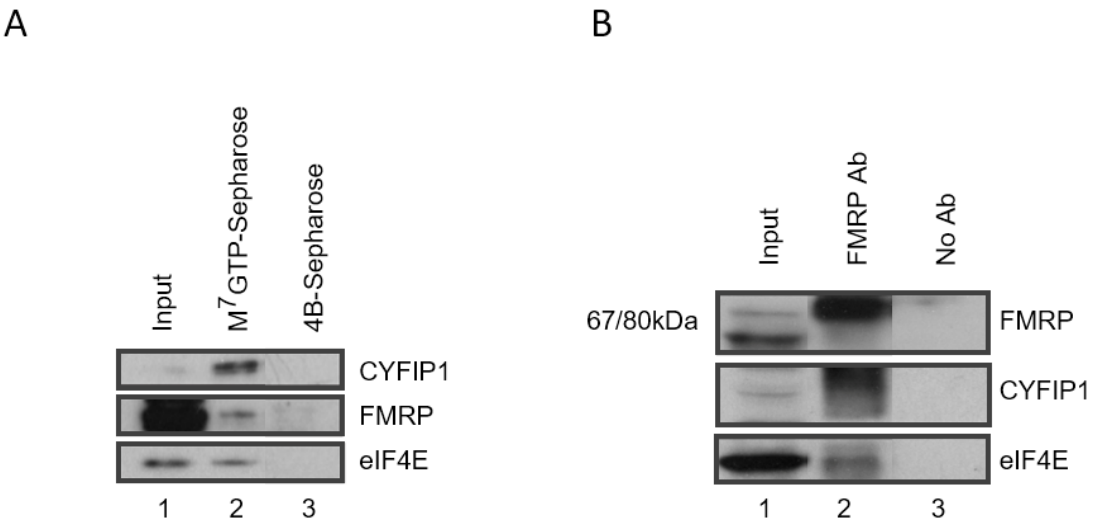

Figure 4.1 CYFIP1 and FMRP associate with eIF4E in spreading MRC-5 SV2 cells

Growing cells were detached from their growth substrate and allowed to spread on tissue culture dishes for 40 mins. Cells were harvested and aliquots of extract containing 20µg of protein subjected to: **Panel A;** M^7GTP–sepharose chromatography to isolate eIF4E and associated proteins as described in the Materials and Methods. **Panel B;** In addition, aliquots containing 200µg protein were subject to immunoprecipitation in the absence or presence of anti-FMRP antiserum as described in the Materials and Methods. The recovery of eIF4E, CYFIP1 and FMRP was then visualised using SDS-PAGE and Western blotting. FMRP isoforms are seen at ~67k and ~80kDa as expected (Verheij et al. 1993; Verheij et al. 1995). Input shown is 10% of the experimental amounts.

Imaged bands were taken from non-consecutive lanes from the same Western blots. Irrelevant lanes are removed from the final image.

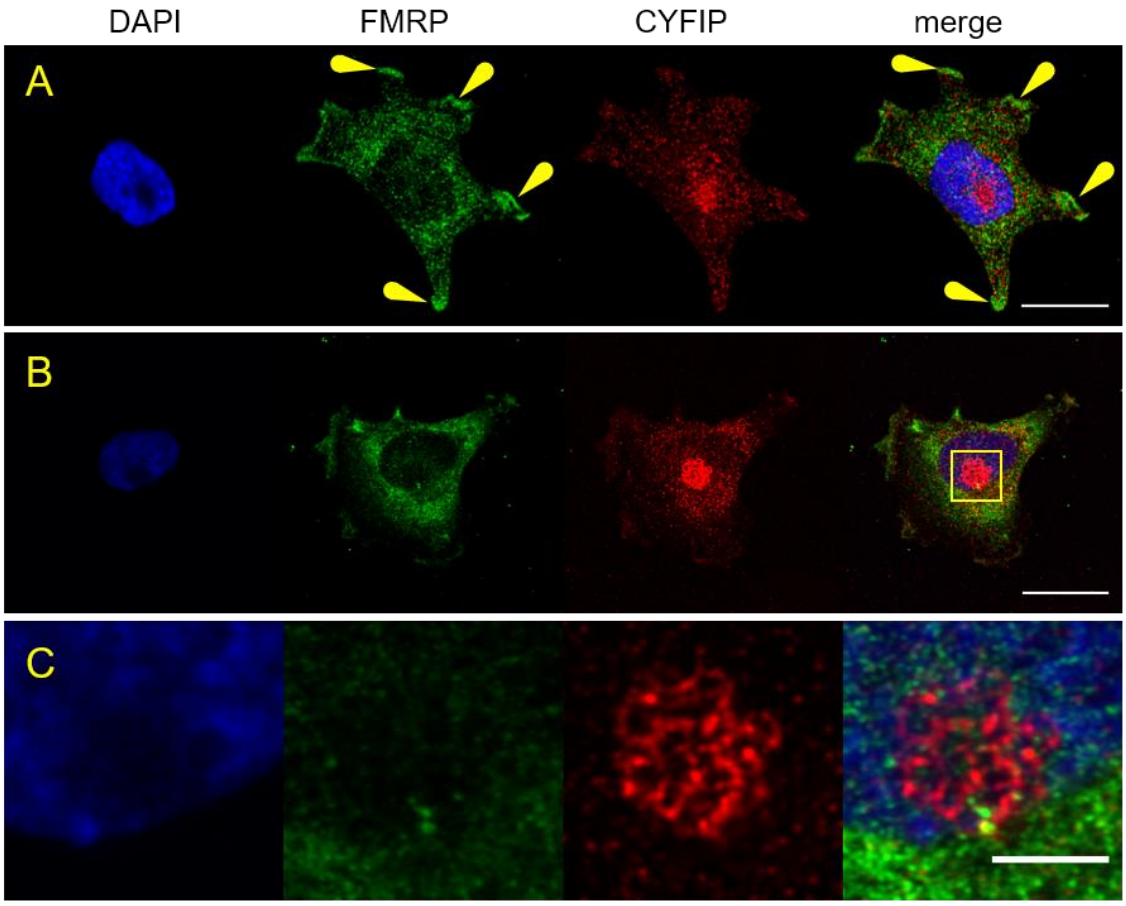

Figure 4.2 FMRP and CYFIP1 have characteristically different localisation

MRC-5 SV2 cells were seeded onto coverslips coated with 8µg/cm^2 collagen I, at a density of 15,000 cells/cm^2 and incubated in MEM supplemented with 15% (v/v) FCS at 37ºC for 40 mins. Cells were fixed using 4% (v/v) paraformaldehyde (PFA), saponin permeabilised and dual immuno-fluorescence stained with anti-CYFIP1 (Ab30) diluted at 1:200 and anti-FMRP (Ab33) diluted at 1:200, as described in the Materials and Methods. Images were obtained using a Leica SP8 confocal microscope with 63x oil objective. These data are representative of those obtained from at least three separate experiments.

Panel A. With a focal plane near the basal membrane. Arrows indicate areas of high-concentration of anti-FMRP and lamellipodial tips. Scale bar indicates 20µm. **Panel B.** With the focal plane raised away from the coverslip, so that is close to the very top of the nucleus. Scale bar indicates 20µm. **Panel C.** A magnified view of the ROI shown in Panel B. The staining of CYFIP1 clearly highlights membrane folding of the reticulum. Scale bar indicates 5µm.

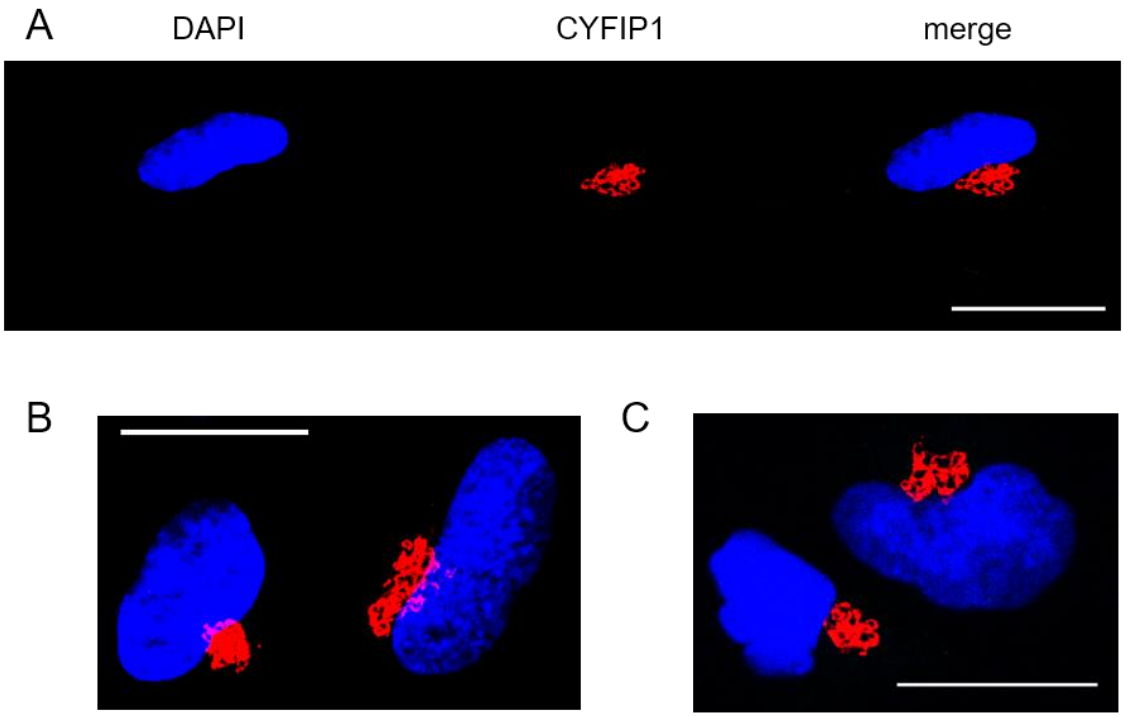

Figure 4.3 Staining with giantin confirms that CYFIP1 localises with the Golgi apparatus

MRC-5 SV2 cells were seeded onto coverslips as in Figure 4.2. Cells were fixed using 4% (v/v) PFA, saponin permeabilised and dual immuno-fluorescence stained with DAPI and anti-CYFIP1 (Ab30) diluted at 1:200, and/or anti-giantin diluted at 1:500, as described in the Materials and Methods. Images were obtained using a Leica SP8 confocal microscope at 100x magnification. Scale bars indicate 20µm. These data are representative of those obtained from at least three separate experiments.

Panel A. Treatment with DAPI and dual immuno-fluorescence stained with anti-CYFIP1 clearly defines 'a body' upon which CYFIP1 is highly abundant. **Panel B.** Treatment with DAPI and dual immuno-fluorescent staining with anti-giantin defines the Golgi apparatus. **Panel C.** Treatment with DAPI and dual immunofluorescence staining with anti-giantin and anti-CYFIP1 define what appear to be single common bodies – the Golgi apparatus - upon which both giantin and CYFIP1 are highly abundant.

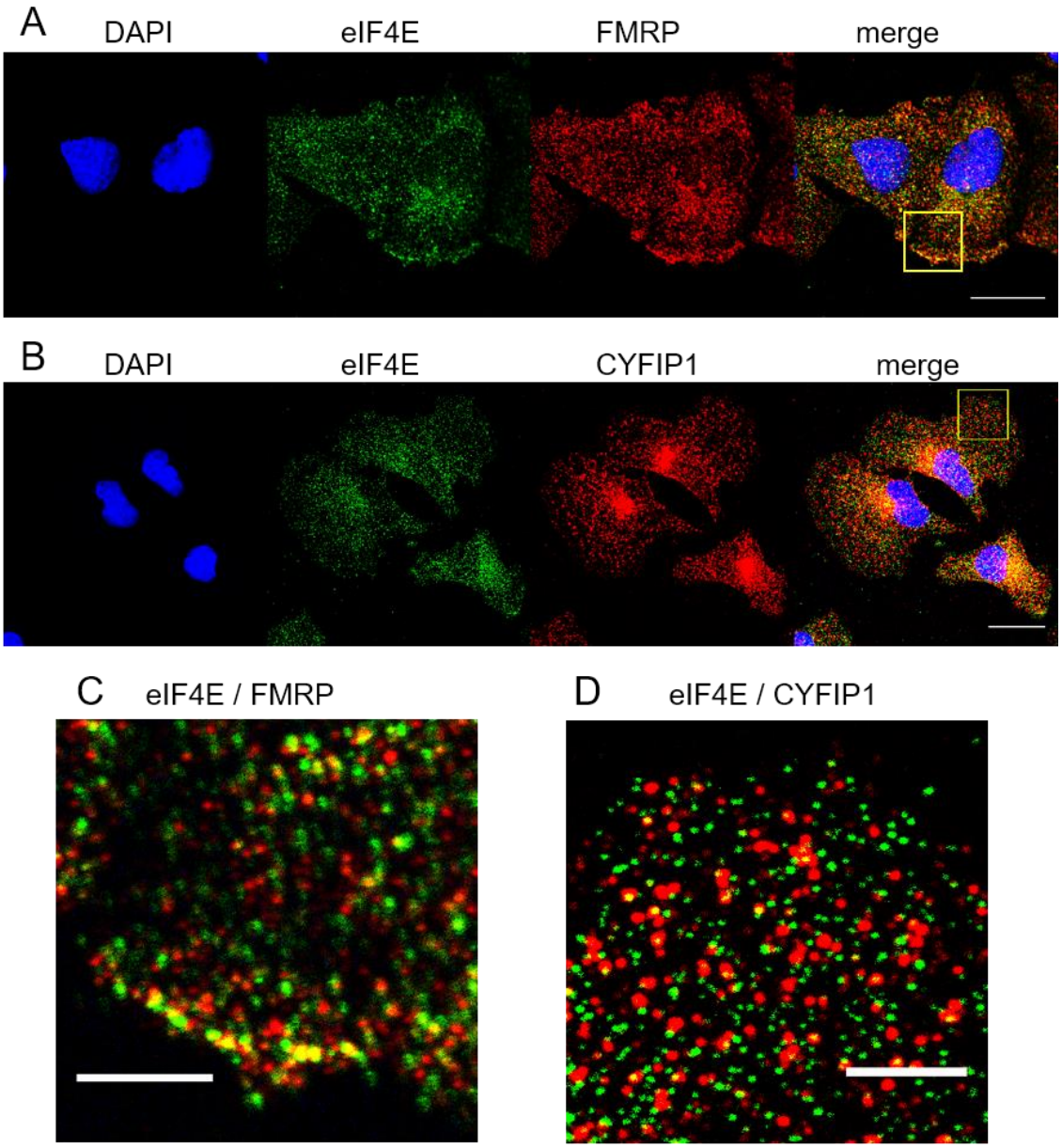

Figure 4.4 FMRP shows greater levels of colocalisation with eIF4E than does CYFIP1 in a serum starvation assay

MRC-5 SV2 cells were seeded onto coverslips as in Figure 4.2. Cells were fixed using 4% (v/v) PFA, saponin permeabilised and dual immuno-fluorescence stained with anti-eIF4E (Ab53) and either anti-CYFIP1 (Ab30) diluted at 1:200 or with anti-FMRP (Ab34) diluted at 1:300, as described in the Materials and Methods. Images were obtained using a Leica SP8 confocal microscope at 63x magnification. These data are representative of those obtained from at least three separate experiments.
Panel A. FMRP and eIF4E colocalise at the leading edge of the cell. Scale bar indicates 20μm. **Panel B.** CYFIP1 and eIF4E do not appear to be colocalised to any great extent. Scale bar indicates 20μm. **Panel C.** A magnified view of the ROI shown in Panel A. Scale bar indicates 5μm. **Panel D.** A magnified view of the ROI shown in Panel B. Scale bar indicates 5μm.

4.5 Colocalisation of FMRP and CYFIP1 after serum starvation.

In serum-deprived HEK293T cells, CYFIP1 & FMRP were rapidly released from 4E upon addition of serum and were then slowly re-associated (DeRubeis et al. 2013). This suggested that serum starvation might facilitate the creation of translationally repressive CYFIP/FMRP/eIF4E complexes. To address this possibility directly, MRC-5 SV2 cells were seeded onto culture dishes and allowed to spread in complete medium for 30 minutes. Cells were then washed in serum-free media and allowed an additional 30 minutes of spreading time in the absence of serum. Cells were subsequently fixed using 4% (v/v) PFA, saponin permeabilised and dual-immunofluorescence stained with anti-CYFIP1 and anti-FMRP antiserum, and processed for imaging using a confocal microscope (Figure 4.5). Dual-channel images of CYFIP1 and FMRP staining were processed using colocalisation software which can highlight colocalised pixels in both channels relative to background levels. Two-dimensional colocalisation results are shown in Figure 4.5, Panel A suggests that CYFIP1 and FMRP may colocalise after serum starvation. Linear patterns in the colocalisation image apparent in Panel B*i*, and highlighted in Panel B*ii*., suggest that putative interactions between FMRP and CYFIP1 may happen on a cytoskeletal component such as microtubules or stress fibres. This hypothesis would corroborate previous findings by our group that eIF4E is transported on the microtubule network (Willett et al. 2013).

4.6 FMRP colocalises with actin at the periphery of cells in the early stages of spreading

In order to test the hypothesis that components of the cytoskeletal network interact with eIF4E/CYFIP1/FMRP in fibroblasts, another cell line was employed as a model system. It has already been shown that the human telomerase reverse transcriptase (hTERT)-immortalised skin fibroblast cell line (1BR3) provides a good model cell line for visualisation of the cytoskeleton (Figure 3.9B); their relatively large size and manner in which they spread aggressively when coming into contact with a collagen ECM bears much functional and morphological resemblance to MRC5-SV2 cells. In order to test for the colocalisation of FMRP and CYFIP1 in this model system 1BR3 cells

were allowed to spread, then were dual-immunofluorescence stained with anti-CYFIP1 and anti-FMRP antibodies, as described in Figure 4.2. In addition, cells were stained with phalloidin-conjugated fluorophores to visualise the actin cytoskeleton. Cells were imaged and post-acquisition processed to provide colocalisation information for FMRP and actin, as well as CYFIP1 and actin.

Figure 4.6A shows that actin stress fibres spread laterally towards the cell periphery in these cells. FMRP takes a striated form in the cytoplasm (Panel B), being more homogenously spread at the cell perimeter; it is, however, highly colocalised with actin stress fibres (Panel Biv and Cii). In contrast, CYFIP1 is much less colocalised with stress fibres (Panel C). These data suggest that a large proportion of the FMRP pool is likely to be transported on stress fibres, whereas little if any CYFIP1 utilises stress fibres for transport.

4.7 Phosphorylated FMRP appears in distinct compartments

With the hypothesis that FMRP is transported to the leading edge of cells using the actin cytoskeleton to facilitate its travel, it was of interest to see whether the phosphorylation state of FMRP affected its localisation to different cellular compartments. Previous work has shown that FMRP is phosphorylated on Ser499 in an mTORC1-independent manner and that this modification is associated with translational repression in neuronal cells (Bartley et al, 2014). To investigate whether phosphorylated FMRP is localised to any compartment of MRC-5 SV2 fibroblasts, cells were seeded onto culture dishes and allowed to spread in complete medium for 40 minutes. Cells were then fixed using 4% (v/v) PFA, saponin permeabilised and dual-immunofluorescence stained with anti-phospho-FMRP (Ser499) antiserum and processed for imaging using confocal microscopy. Figure 4.7A shows that phospho-FMRP was enriched at the leading edge of the cells, suggesting that this pool of FMRP might be involved in translational repression of a pool of mRNA at this location (Ceman et al 2003). To see whether such localisation changed over time, cells were left for 48 hours. Figure 4.7B shows that under these conditions, phospho-FMRP did not appear to be extensively localised but was clearly associated with punctate foci particularly in mitotic cells.

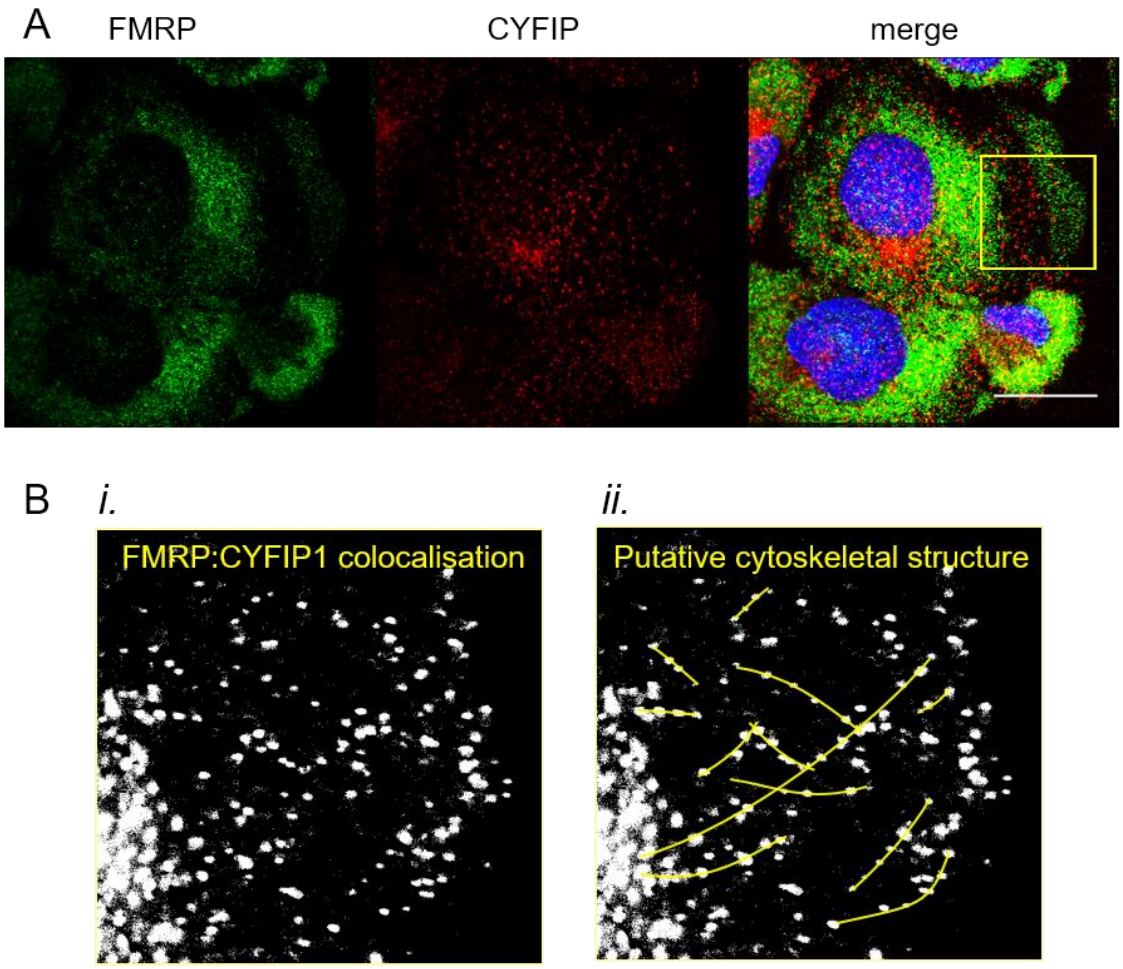

Figure 4.5 Colocalisation of FMRP and CYFIP1 after serum starvation

MRC-5 SV2 cells were seeded onto coverslips coated with 8µg/cm^2 collagen I, at a density of 15,000 cells/cm^2 and incubated in MEM supplemented with 15% (v/v) FCS at 37ºC for 30 mins. Cells were rinsed twice in serum-free media and incubated for an additional 30 mins in the absence of serum. Cells were fixed using 4% (v/v) PFA, saponin permeabilised and dual immuno-fluorescence stained with anti-CYFIP1 (Ab30) diluted at 1:250 and anti-FMRP (Ab33) diluted at 1:300, as described in the Materials and Methods. Images were obtained using a Leica SP8 confocal microscope at 100x magnification. Using ImageJ GDSC colocalisation plugin, colocalised pixels were visualised as described in the Materials and Methods.

Panel A. FMRP is present at the leading edge. Scale bar indicates 20µm. **Panel B.** ***i.*** FMRP and CYFIP1 colocalised pixels potentially show lateral striations emanating towards the leading edge. ***ii.*** A graphical representation of the possible underlying cytoskeletal upon which an FMRP/CYFIP1 repression complex may traverse – highlighted in yellow.

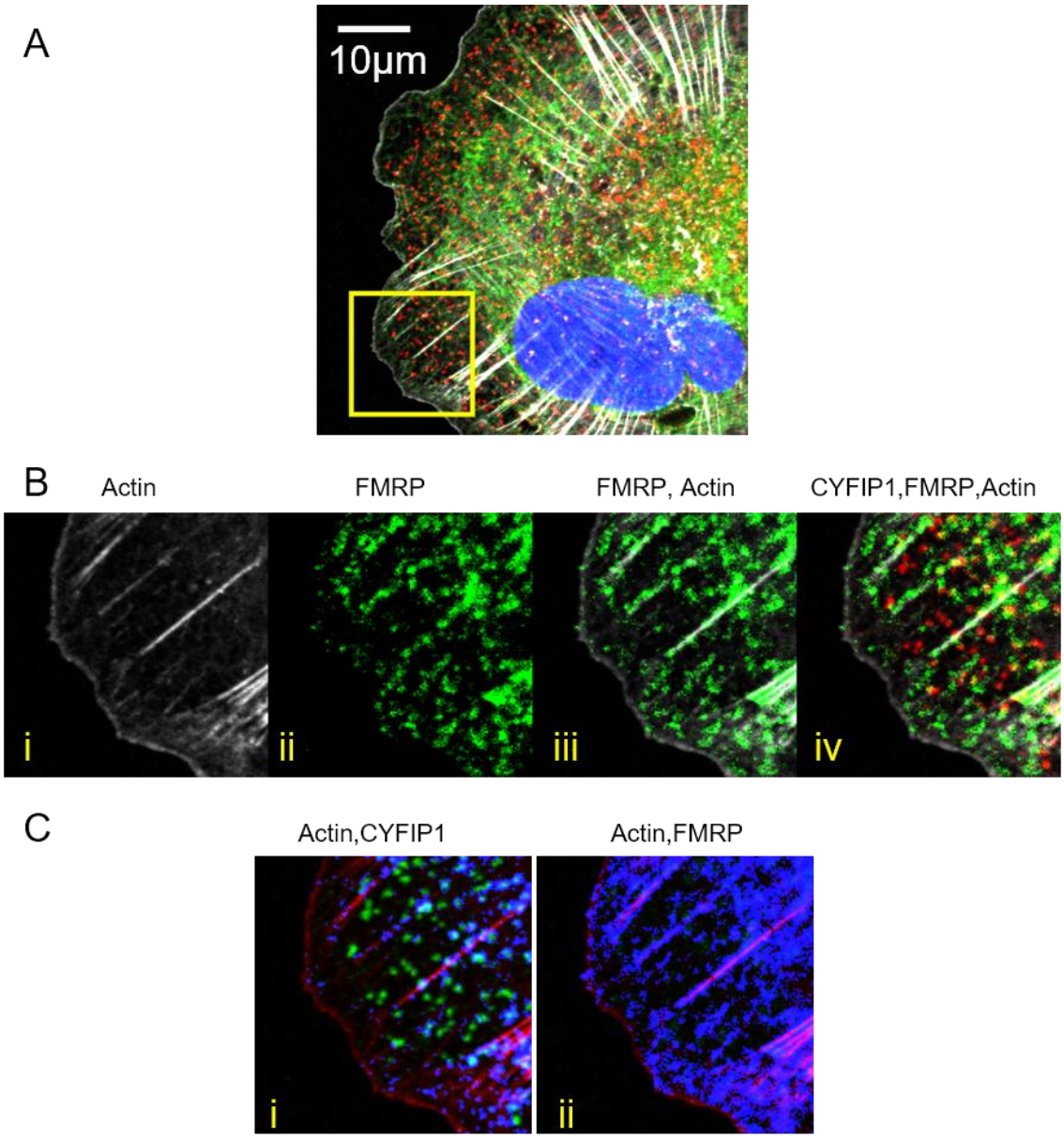

Figure 4.6 FMRP colocalises with actin at the periphery of cells in the early stages of spreading

The *hTERT*-immortalized skin fibroblast cell line (1BR3) was grown, spread and treated for dual-immunofluorescent imaging as described in Figure 4.2, with the additional application of phalloidin-Alexa Fluor 633 diluted at 1:50 during the incubation with secondary antibodies. Colocalisation processing was performed using the imageJ GDSC Colocalisation Threshold plug-in. **Panel A.** A four channel merged image cell. blue:DAPI; red:CYFIP1; green: FMRP; greyscale: actin. **Panel B.** A magnified view of the ROI in Panel A. ***i.*** Actin ***ii.*** FMRP ***iii.*** FMRP and Actin ***iv.*** CYFIP1, FMRP and actin. **Panel C.** Colocalisation assays show shades of blue indicative of the strength of colocalisation of the protein of interest and the actin cytoskeleton. Non-colocalised actin is shown in red. Non-colocalised protein of interest is shown in green. ***i.*** A CYFIP1 colocalisation assay. ***ii.*** An FMRP colocalisation assay.

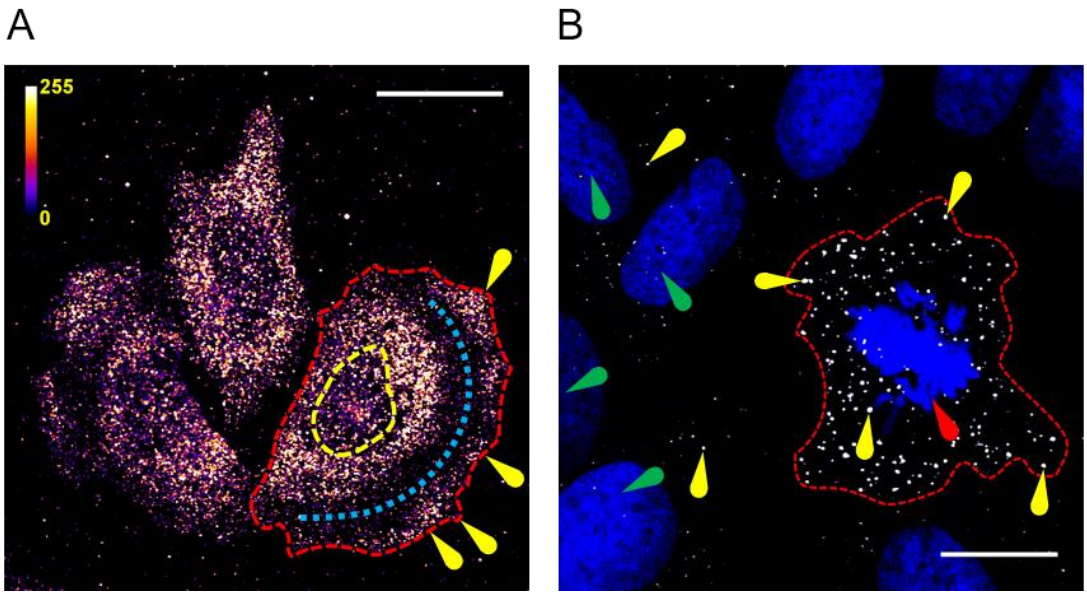

Figure 4.7 Phosphorylated FMRP appears in distinct compartments

MRC-5 SV2 cells were seeded onto coverslips as described in Figure 4.2, and allowed to spread for either 40 mins or 48hrs. Cells were fixed using 4% (v/v) PFA, saponin permeabilised and dual immuno-fluorescence stained with anti-phospho-FMRP(Ser499) (Ab13) diluted at 1:200, as described in the Materials and Methods. Images were obtained using a Leica SP8 confocal microscope at 100x magnification. Scale bars indicate 20µm.

Panel A. In cells seeded for 40 minutes only, phospho-FMRP(Ser499) is found in abundance at the leading edge of cells, as shown with the applied 8-bit intensity heat-map as described in the calibration bar (top left corner). A single cell is outlined with a red dashed line; its nucleus approximated with a yellow dashed line; the centre of the lamellum region is highlighted with a blue dashed line; the lamellipodial leading edges are partially highlighted with yellow arrows.

Panel B. In cells seeded for 48hours and which were approximately 70% confluent, phospho-FMRP(Ser499) was found in much higher abundance (coloured white) in punctate foci in M-phase cells (a selected cell is outlined with a red dashed line), a subset of which are highlighted by yellow arrows. Red arrows highlight areas of chromosome condensation during mitosis. Green arrows highlight nuclei of cells passing through interphase.

4.8 Phosphorylated FMRP is associated with stress granules in spreading cells

The punctate foci observed above could reflect the manifestation of processing bodies (P-bodies), sites of mRNA storage and triage, or stress granules, a known site of mRNA storage. P-bodies are believed to participate in mRNA storage as well as decay, and contain many RNA-binding proteins including the helicase DDX6, decapping enzymes, Argonaute 2 (Ago2) as part of the micro (mi)RNA network, and eIF4E, but with ribosomes and other translation factors being excluded from these granules (reviewed in Eulalio et al 2007). In contrast, stress granules often induced by sodium arsenite, contain many translation factors as part of stalled initiation complexes following the phosphorylation of eIF2α, but lack Ago2 and DDX6 (reviewed in Protter and Parker, 2016).

To investigate whether phosphorylated FMRP was associated with stress granules, cells were incubated with sodium arsenite for 30 minutes after spreading for 30 minutes. Figure 4.8A shows that under conditions of arsenite stress FMRP was seen in stress granules; a similar pattern was seen for eIF4E (Panel B). In contrast, Ago2 (Panel A) and DDX6 (Panel B) were seen only minimally in these granules, which appears to show some consistency with them being stress granules (Protter and Parker, 2016). Following arsenite-treatment of cells, phospho-FMRP was colocalised to stress granules with eIF4E (Figure 4.8C). These data confirm that eIF4E and FMRP can be found in repressive complexes in fibroblasts.

4.9 Using TIRF microscopy to investigate the localisation of CYFIP1

In previous confocal imaging experiments, evidence was starting to accumulate for the translocation of FMRP over the actin cytoskeleton (Figure 4.6) to the leading edge of spreading cells where it has been found colocalised with eIF4E (Figure 4.4). However, colocalisation of CYFIP1 to its putative cognate partner FMRP remains questionable (Figure 4.5B). In order to elucidate how CYFIP1 might be interacting with the cytoskeleton or other proteins of interest such as eIF4E and FMRP, it was decided to employ total internal reflection (TIRF) microscopy.

MRC-5 SV2 cells were seeded onto flame cleaned, ozonated and collagen coated borosilicate coverslips and allowed to adhere and spread for 40mins. Cells were fixed then permeabilised with Triton X-100, then dual-immunofluorescence stained with anti-CYFIP1 antiserum diluted at 1:1000. GLOX, an oxygen-scavenging mounting solution was applied to the sample before optical coupling of the coverslip to the TIRF objective. The specimen was excited by a columnated laser, which was designed to undergo total internal reflection at the coverslip. Movies were made of the specimen spanning 2000 frames, as described in the Materials and Methods. With single protein-stained specimens, it was expected that the low noise environment of TIRF microscopy might offer tangible evidence for the trafficking of CYFIP1 through the cytoplasm by way of visualisation of CYFIP1 in a pattern which might indicate the use of the cytoskeleton. In an image constructed from the averaging of 2000 movie frames, discrete foci representing small numbers of CYFIP1 molecules were visualised (Figure 4.9A). By using QuickPALM, software developed to locate the centres of fluorescent foci, a high-resolution map of the cell lamellipodium was prepared. Figure 4.9B shows that CYFIP1 appeared punctate, dispersed and with no obvious localisation or pattern in its distribution in the cell. Single-channel imaging of CYFIP1 rendered no suggestion of a highly utilised intra-cytoplasmic trafficking mode.

4.10 FMRP and CYFIP1 colocalise in lamellipodia of spreading cells

Dual-channel imaging using TIRF microscopy was utilised for colocalisation studies of CYFIP1 and FMRP in early spreading MRC5 cells. Cells were seeded fixed and permeabilised in readiness for dual-immunofluorescence staining as described in Section 4.9. Cells were stained for CYFIP1 and FMRP using antiserum at the appropriate concentrations for single-molecule imaging (Figure 3.16) and movies were acquired for each channel. Each channel had its frames registered then aligned using the imageJ plugin ‘Align FFT’, prior to being processed using SOFI software. The resulting images show CYFIP1 (Figure 4.10B) and FMRP (Figure 4.10A). SOFI generated super-resolution images of each channel were then superimposed and manually aligned. Using this super-resolution image processing, these data

provide some initial evidence to suggest that CYFIP1 and FMRP may be colocalised at the leading edge of spreading cells (Figure 4.10C).

4.11 Arpc2 mRNPs associate with CYFIP1 at the lamellipodium

It has been shown that during lamellipodia assembly in spreading fibroblasts there is an increase in the association of Arpc2 mRNA with ArpC2 protein and with ribosomes, suggesting the possibility that the *de novo* synthesis of Arp2/3 complex protein components may regulate lamellipodial structures at the leading edge of migrating cells (Willett et al. 2013). In neurones it has been shown that CYFIP1 represses translation of specific mRNAs when part of the CYFIP1-FMRP-eIF4E complex (see Chapter 1). BDNF signalling *via* Rac1 and GTP-Rac1 facilitates a conformational change in CYFIP1 which releases it to allow it to join the WAVE regulatory complex (WRC) as an active subunit. Assembly of this complex has a direct influence over structural changes required at the edge of the cell to promote migration (DeRubeis et al. 2013). The mechanism for how CYFIP1 is localised to the leading edge of the cell as part of this CYFIP1-FMRP-eIF4E complex is not known. It is possible that CYFIP1 facilitates the transport of translationally repressed ArpC2 mRNA from the nucleus to the leading edge of the cell where it can be activated for translation during cell spreading and migration.

To address this hypothesis, cells were seeded on collagen-covered coverslips and allowed to spread for 40 minutes. Cells were fixed and permeabilised using ethanol treatment for fluorescence *in situ* hybridisation of ArpC2 mRNA, as described in the Materials and Methods. FISH probes sources from Stellaris were used, with Stellaris Cal Fluor Orange mRNA probes applied as well as antiserum for immunofluorescence staining of CYFIP1. Two-channel fluorescence imaging was performed using the TIRFM, and movie frames from each channel aligned before being SOFI processed. The two super-resolution channel images were superimposed to render a dual channel image of ArpC2 mRNA and CYFIP1. Although these data suggest the possibility that ArpC2 mRNA and CYFIP1 colocalise at certain places in the lamellipodia, lending support to the hypothesis that Arpc2 mRNA is being translationally repressed by

a CYFIP1:eIF4E complex (with or without FMRP) during its transit to the leading edge of the spreading fibroblast (Figure 4.11).

Limitations of the TIRFM system hardware mean that these data are in no way conclusive. Dual-channel imaging was performed over several minutes leading to some stage movement, and without dual-band fiducial markers manual alignment of the two channels will have introduced a small amount of unquantifiable alignment error.

4.12 3B provides evidence to show that FMRP and CYFIP1 may colocalise in the lamellipodia of spreading cells

There is some evidence that FMRP and CYFIP1 may colocalise at the leading edge of spreading cells (Section 4.10). Evidence has accumulated from diffraction-limited colocalisation techniques (Figure 4.5), as well as a super-resolution techniques (SOFI) which increase the spatial resolution of images by 24% in *in situ* single molecules studies (Figure 3.14). To further test this possible interaction, 3B super-resolution processing was performed on images obtained from TIRF microscopy (Cox & Jones 2013; Rosten et al. 2013). Cells were seeded, fixed and permeabilised in readiness for dual-immunofluorescence stained as described in Figure 4.9. Cells were stained for CYFIP1 and FMRP using antiserum at the appropriate concentrations for single-molecule imaging (Figure 3.16) and movies were acquired for each channel. Each channel had its frames registered prior to processing using Bayesian analysis of blinking and bleaching (3B), a Bayesian super-resolution algorithm (Cox & Jones 2013; Rosten et al. 2013). Pre-processed images (Figures 4.12A and B), once processed using 3B, were used to localise synthetic 50 nm Gaussian spots. Patterns were established visually in both super-resolution images of FMRP and CYFIP1 stained channels. This facilitated manual alignment of the two super-resolution channels to achieve the best fit (Figures 4.12C and D). These aligned super-resolution images of FMRP and CYFIP1 were frozen in their alignment and individually super-imposed on their respective grey-scale diffraction limited images. These super-imposed super-resolution images corresponded visually with the underlying diffraction limited landscape (Figures 4.13A and B). Both super-resolution images were then

superimposed on the original pseudo-coloured diffraction-limited image (Figure 14.13C) to present the entirety of the information available from diffraction limited and super-resolution images. These super-resolution processed images obtained from TIRF microscopy present strong evidence for the interaction of CYFIP1 and FMRP at the leading edge of spreading cells. This suggests that model systems for FMRP/CYFIP1 translational repression in neurones are possibly also representative of the mechanics of mRNA translational repression in spreading fibroblast cell lines.

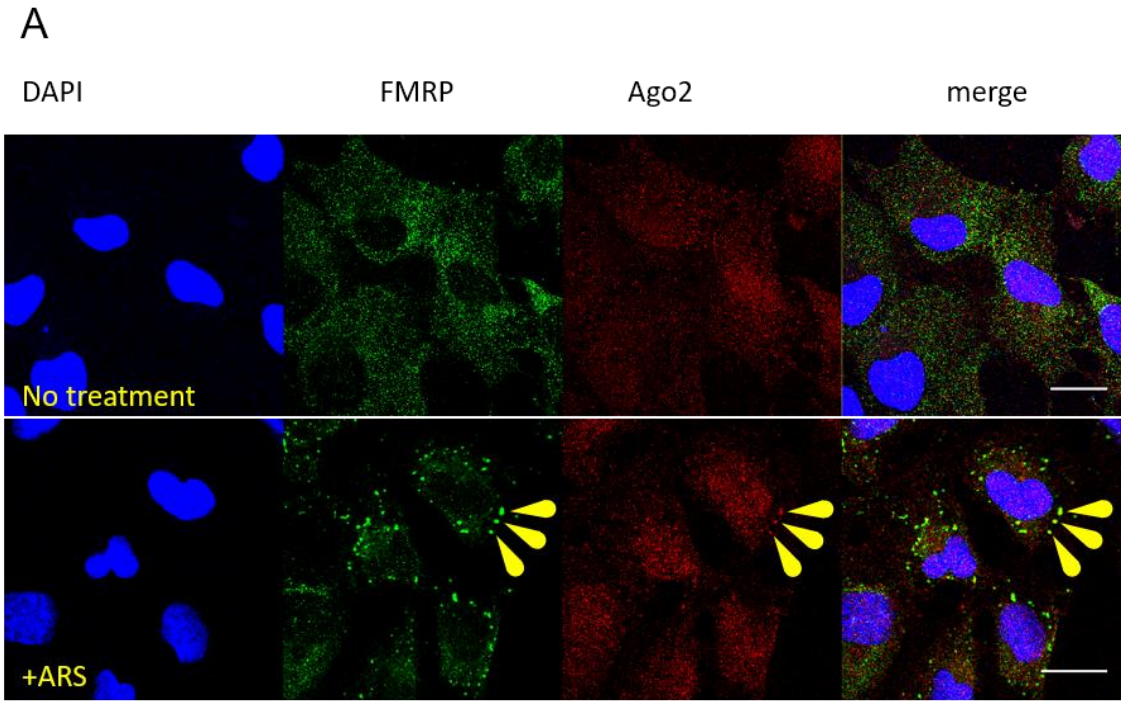
A
DAPI
FMRP
Ago2
merge
No treatment
+ARS

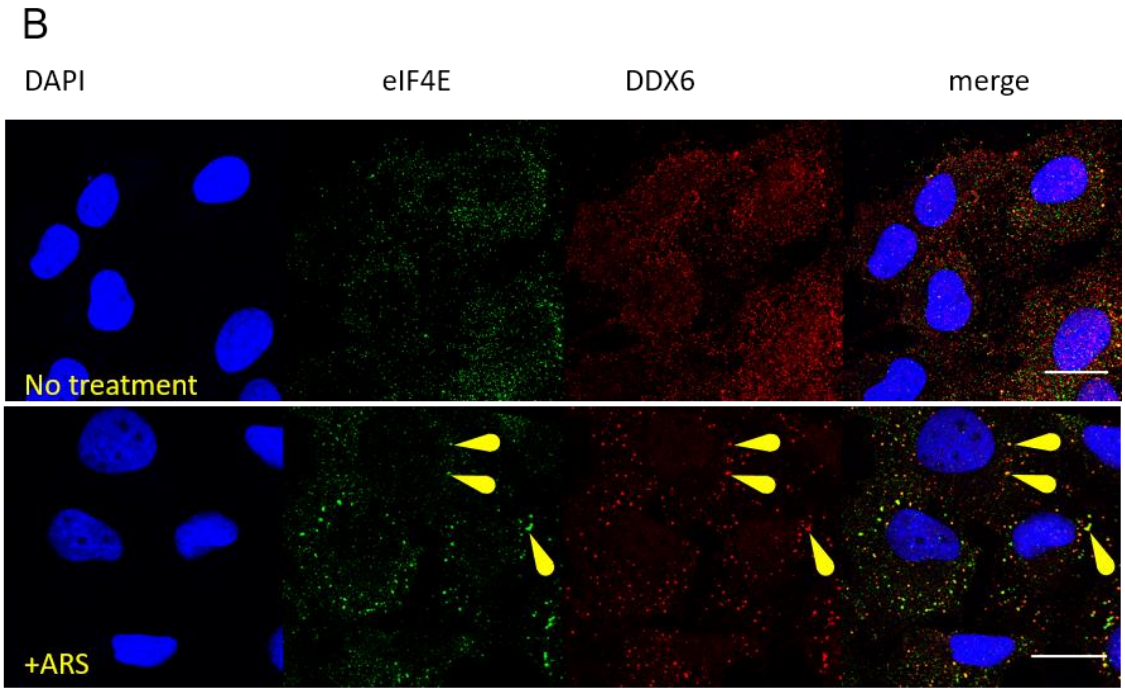
B
DAPI
eIF4E
DDX6
merge
No treatment
+ARS

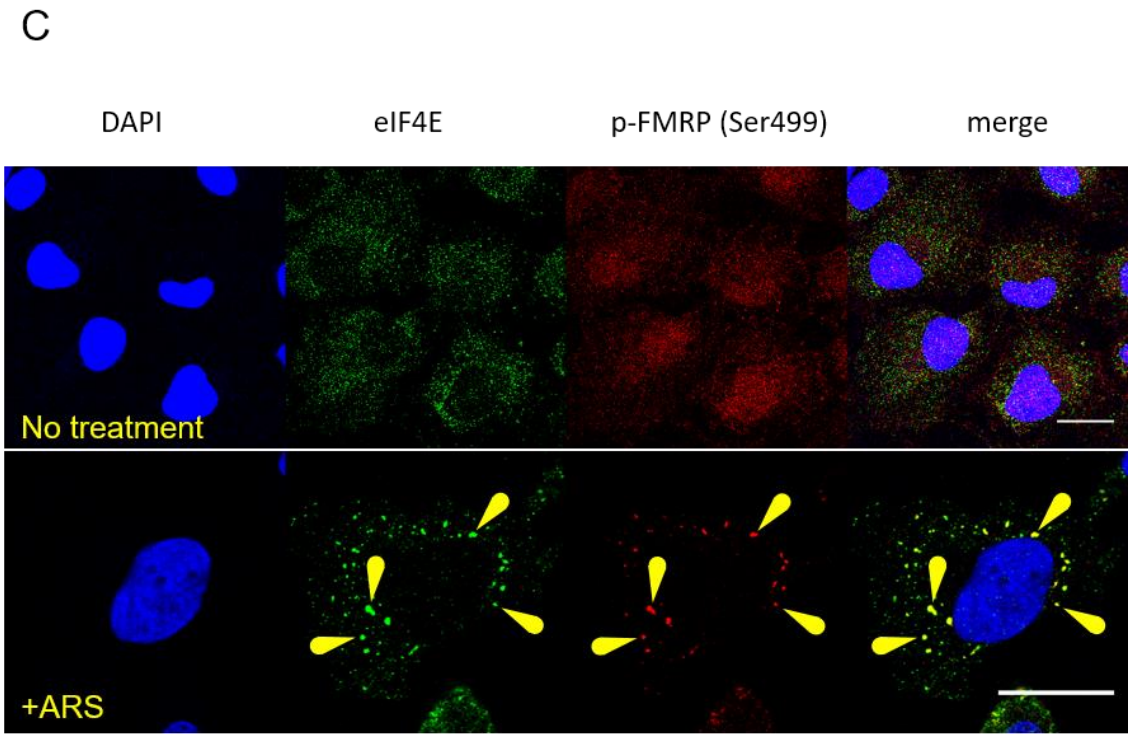

Figure 4.8 eIF4E, FMRP and p-FMRP(Ser499) associate with stress granules after treatment with sodium arsenite

MRC-5 SV2 cells were seeded onto coverslips coated with 8µg/cm^2 collagen I, at a density of 15,000 cells/cm^2 and incubated at 37ºC for 30 mins. Cells were then incubated in the absence or presence of 10mM sodium arsenite for an additional 30 minutes. During stress, cells were fixed using 4% (v/v) PFA, saponin permeabilised and dual immuno-fluorescence stained with anti-Ago2(Ab3), anti-DDX6 (Ab61), anti-p-FMRP(Ser499) (Ab13), anti-FMRP (Ab34), anti-eIF4E (Ab55), according to the dilutions described in Table 2.1 and as described in the Materials and Methods. Images were obtained using a Leica SP8 confocal microscope at 63x magnification. These data are representative of those obtained from at least three separate experiments. Scale bars indicate 20µm. Yellow arrows highlight a subset of colocalised proteins.

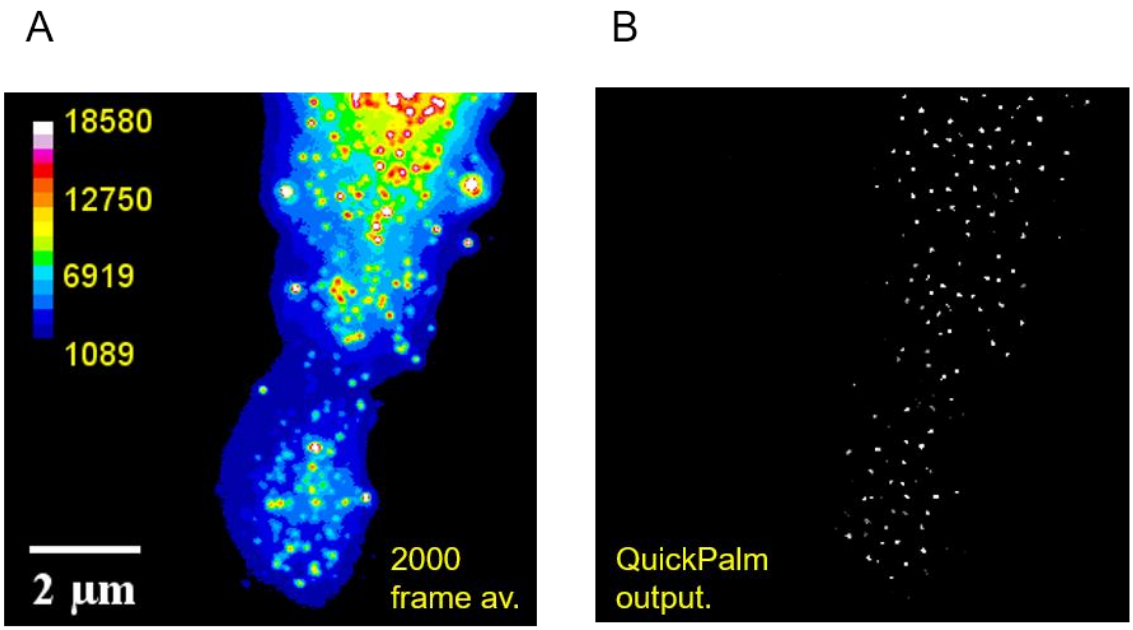

Figure 4.9 QuickPALM applied to *in situ* organic fluorophores

MRC-5 SV2 cells were seeded onto No.1.5 borosilicate coverslips coated with 8µg/cm^2 collagen I, at a density of 15,000 cells/cm^2 and incubated at 37ºC for 40 mins. Cells were fixed using 4% (v/v) PFA, 0.1% (v/v) Triton X-100 permeabilised and dual immuno-fluorescence stained with anti-CYFIP1 (Ab30) diluted at 1:1000, and treated with an application of GLOX mounting fluid for TIRF imaging. A movie was taken spanning 2000 frames, at a frame rate of 8fps and with 100ms exposure times.

Panel A. Average of 2000 frames. 16-colour LUT applied.

Panel B. The QuickPalm result from the processing of 2000 frames, provides the estimated location of emitting fluorophores at super-resolution.

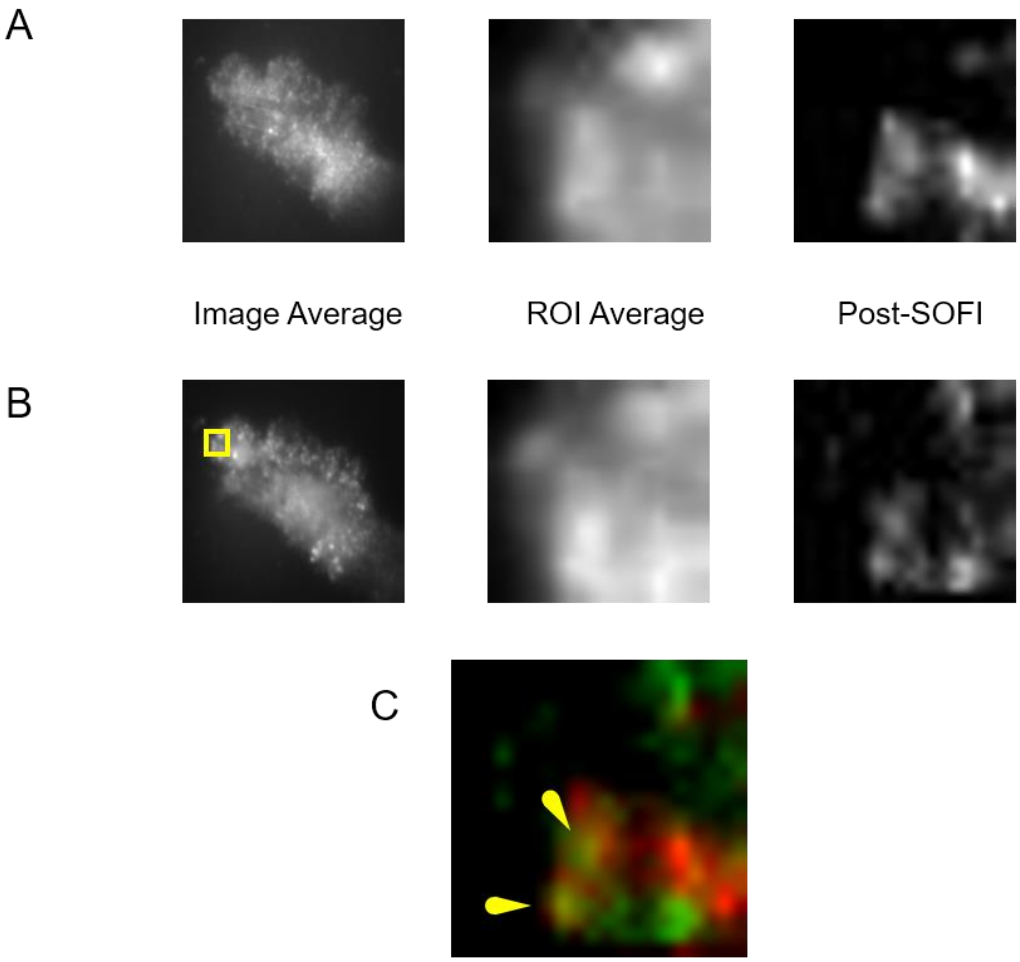

Figure 4.10 FMRP and CYFIP1 colocalise in lamellipodia of spreading cells

MRC-5 SV2 cells were seeded as described in Figure 4.9. After spreading, cells were fixed using 4% (v/v) PFA, 0.1% (v/v) Triton X-100 permeabilised and dual immuno-fluorescence stained with anti-CYFIP1 (Ab30) diluted at 1:1000, and anti-FMRP (Ab33) diluted at 1:1000, as described in the Materials and Methods. Cells were treated with an application of GLOX mounting fluid for dual-channel TIRF imaging. Movies were taken spanning 2000 frames, at a frame rate of 8fps and 100ms exposures. Movies were registered using AlignFFT, processed using SOFI, and dual-channel overlays aligned manually. This experiment was performed with Dr. Mark Willett on a TIRF microscope built by Dr. Mark Osborne, and is representative of more than 10 other imaged cells.
Panel A. FMRP at the lamellipodium shown averaged over 100 frames; a magnified image of the ROI drawn in Panel B applied to the FMRP channel; a post-SOFI processed image. **Panel B.** CYFIP1 at the lamellipodium shown averaged over 100 frames; a magnified image of the ROI; a post-SOFI processed image. **Panel C.** Overlaid post-SOFI images, showing FMRP in red, CYFIP1 in green. Colocalisation of CYFIP1 and FMRP is shown in yellow and highlighted with yellow arrows.

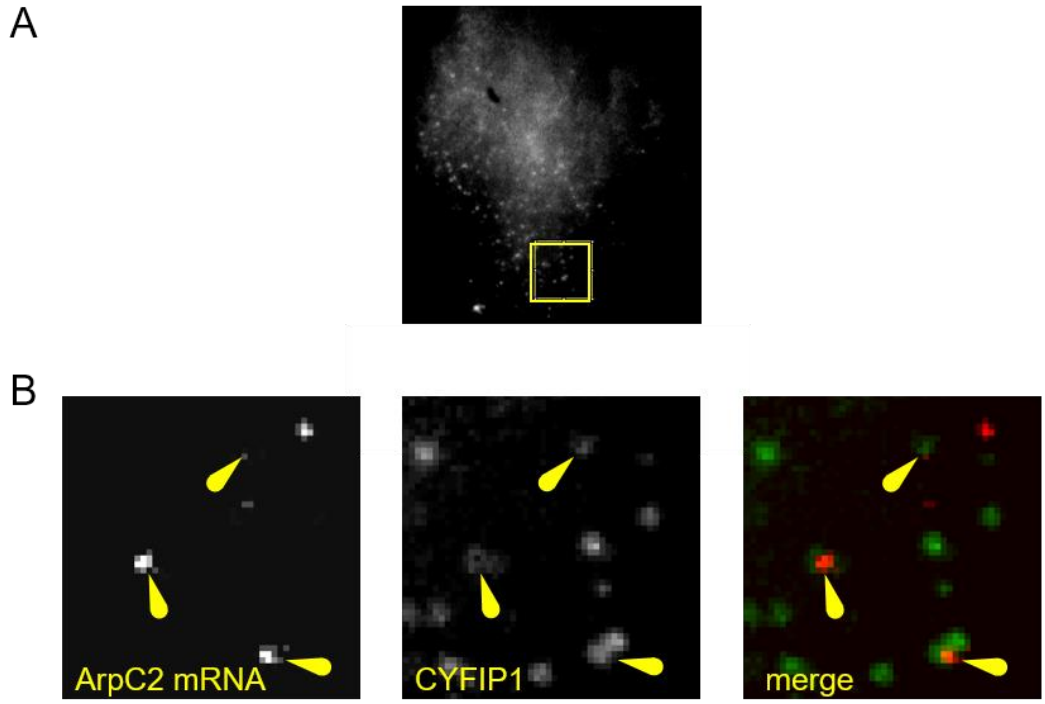

Figure 4.11 ArpC2 and CYFIP1 colocalise in spreading cells

MRC-5 SV2 cells were seeded onto methanol-cleaned, and ozonated coverslips coated with 8µg/cm2 rat tail collagen I, at a density of 15,000 cells/cm2 and incubated in MEM supplemented with 15% (v/v) FCS at 37ºC for 40 mins. Cells were fixed using 4% (v/v) PFA, and permeabilised using ethanol treatment for fluorescence in situ hybridisation of ARPC2 mRNA, as described in the Materials and Methods. After spreading, cells underwent processing for dual ICC with FISH as described in the Materials and Methods. Stellaris probes were used for the hybridisation of ArpC2 mRNA as well as with the dual-immuno-fluorescence staining for anti-CYFIP1 (Ab30) diluted at 1:1000. Stellaris Cal Fluor Orange mRNA probes with peak excitation at 538nm and emission at 559nm required a 532nm laser, a long-pass 547nm dichroic mirror and an emission filter of 593-40. CYFIP1 (diluted at 1:1000) was imaged using Alexa Fluor 488 secondary antibody conjugates, necessitating the use of a 473nm laser, a long-pass 493nm dichroic mirror and an emission filter of 529-24. Movies were taken with 100ms frame exposures and a frame interval of 20ms Cells were treated with an application of GLOX mounting fluid prior to dual-channel TIRF imaging. Movies were taken spanning 2000 frames, at a frame rate of 8fps and 100ms exposures. Movies were registered using AlignFFT, processed using SOFI, and dual-channel overlays aligned manually. **Panel A.** Movie-averaged, non-SOFI processed dual channel ArpC2 mRNA and CYFIP1 merged images of a lamellipodium, showing an ROI from which other images in this figure are derived. **Panel B.** Stellaris Arcp2 mRNA probe, and immuno-staining of CYFIP1 in AlignFFT, post-SOFI processed aligned images, where ArpC2 is pseudo-coloured red and CYFIP1 is shown in green. Yellow arrows highlight ArpC2 mRNA and CYFIP1 colocalised fluorescence.

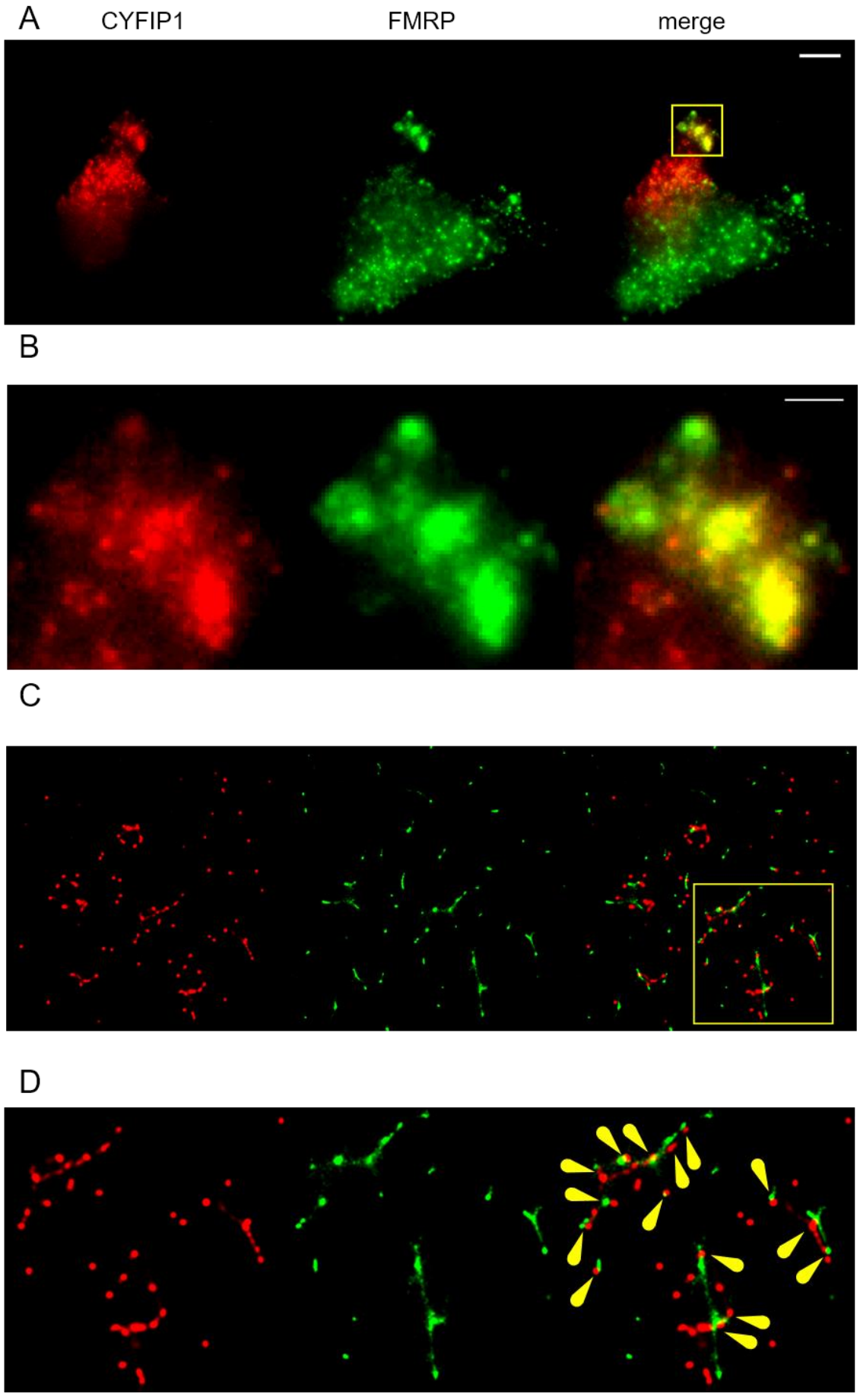
A
CYFIP1
FMRP
merge
B
C
D

Figure 4.12 Super-resolution imaging of FMRP and CYFIP1

MRC-5 SV2 cells were treated in the manner described in Figure 4.10 for dual-channel TIRF imaging of FMRP and CYFIP1. Movies were taken spanning 2000 frames, at a frame rate of 8 fps and 10 0ms exposures. Movies were registered using AlignFFT, and ROIs selected for further processing by Bayesian analysis of blinking and bleaching, or 3B microscopy (Cox & Jones 2013; Rosten et al. 2013).

Panel A. A 200 frame averaged composite image showing FMRP and CYFIP1 are co-located at the leading-edge of a spreading cell.
Panel B. A magnified view of the ROI shown in Panel A.
Panel C. 3B processing of the images shown in Panel B took 24 hours, and after manual alignment appears to show a high incidence of colocalised FMRP and CYFIP1.
Panel D. A magnified view of the ROI in Panel C shows the colocalisation of both species of fluorophore, with a subset of colocalised or near-colocalised species highlighted with yellow arrows.

A

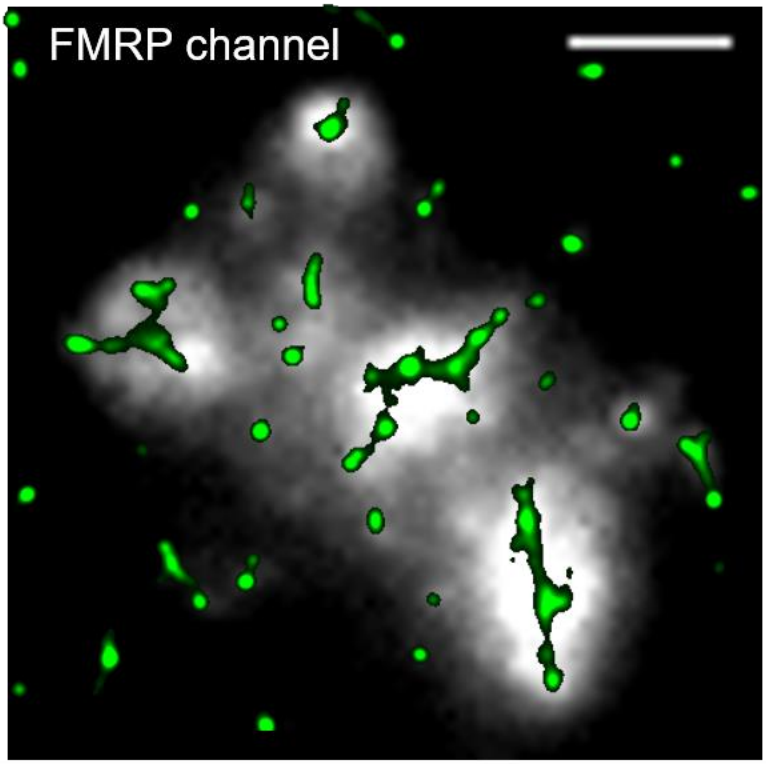

B

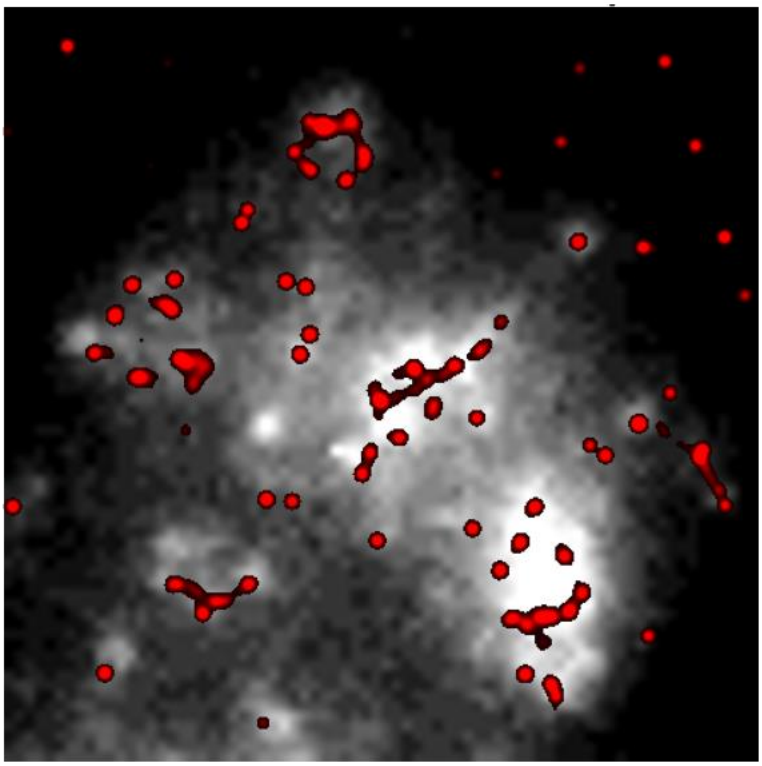

Key : FMRP CYFIP1

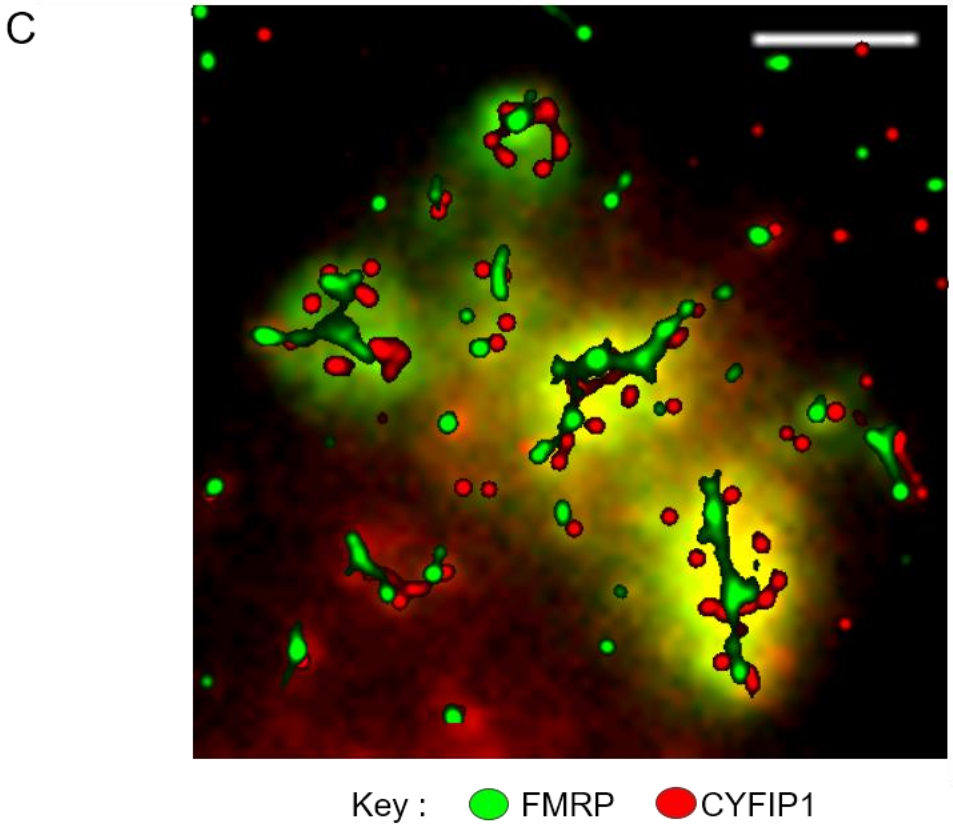

Figure 4.13 Super-resolution colocalisation of FMRP with CYFIP1

Super-resolution 3B-processed images from Figure 4.12 (with manual alignment onto diffraction-limited TIRF movie-averaged images), show the colocalisation of FMRP and CYFIP1. Scale bars indicate 1µm.

Panel A. FMRP to a resolution of 50nm **Panel B.** FMRP to a resolution of 50nm **Panel C.** Combining of CYFIP1 and FMRP super-resolution images onto the original TIRF movie-averaged image indicates probable areas of interaction between the two proteins.

4.13 Summary

m^7GTP–Sepharose chromatography and immunoprecipitation reveal that eIF4E, CYFIP1 and FMRP form part of a complex in spreading cells, either via direct binding to one another or through interactions with mRNA as part of RNPs. Confocal microscopy provides some evidence to show that CYFIP1 colocalises with the trans-Golgi network, and is also found at the leading edge of cells in limited quantity. Some evidence suggests that CYFIP1 colocalises with FMRP on the cytoskeleton, and actin fibres may facilitate transport for a sub-population of CYFIP1 to move to the periphery of the cell. FMRP appears to be found in abundance around certain cellular stress fibres, and in phosphorylated form appears to be manifestly present in large concentrations at the leading edge of the cell. These data suggest that actin may be a primary facilitator for the trafficking of FMRP. In stressed cells, eIF4E and phospo-FMRP have been seen to coalesce in stress granules and in punctate foci in mitotic cells which might be stress granules or, less probably, in processive P-bodies.

The use of TIRF microscopy to obtain low-noise diffraction limited images suggested that CYFIP1 and FMRP colocalise at the leading edge of spreading cells. Using super-resolution techniques such as 3B, colocalisation of CYFIP1 and FMRP proteins in the lamellipodia of spreading cells can be suggested to be possible, given the constraints of 50nm resolution, and of a TIRF microscopy system limited in its capability to reduce stage drift in the x, y and z axes. For these reasons, other methods of protein co-localisation were deemed worthy of investigation, including the use of Förster resonance energy transfer (FRET) and the *in situ* Proximity Ligation Asssay (PLA).

5 PLAY

Software for *in situ* Proximity Ligation Assay Analysis

5.1 The *in situ* Proximity Ligation Assay

The *in situ* Proximity Ligation Assay (PLA) (Söderberg et al. 2006) is a specific and sensitive immunofluorescence technique able to yield clear and intense fluorescent signals between closely located endogenous proteins, or between epitopes of the same protein. Creation of a genuine PLA fluorescence point source between two putative interacting proteins is an improbable event when the epitopes are further than 40nm apart, meaning that such a system offers the stringency of a super-resolution system able to colocalise proteins beyond the physical constraints of the optical diffraction barrier (Huang et al. 2010). As a result, this places PLA within the category of *in situ* super-resolution techniques such as Förster resonance energy transfer (FRET), FRET derivatives such as bioluminescence resonance energy transfer (BRET), and bimolecular fluorescence complementation (BiFC) (Zhou et al. 2016). All of these rely on observed fluorescent signals to confirm the presence of two closely located or interacting proteins. The combining of two stringent recognition events - antibody binding and even more stringent oligonucleotide binding, endows PLA with greater sensitivity than can be gained solely with standard immunocytochemistry/Immunofluorescence (ICC/IF) techniques.

In ICC, initial antibody-antigen binding occurs through processes dependent not only on the specificity of the antibody for target epitopes but also the antibody concentration and disassociation constant (K_d) compared to other competing molecules, be they cross-reacting antibodies or proteins added during the blocking stages. Such competitive binding environments inevitably lead to some amount of cross-reactivity and non-specific adsorption mitigated in part by reducing antibody concentrations and increasing the strength of blocking reagents. The corollary of taking such precautions may lead to an increase in the specificity of the correct binding of the appropriate antibodies; however, the number of correctly targeted antibodies and the strength of the resultant fluorescent signals will often diminish, compromising the signal to noise ratio. PLA excels in such conditions where antibody binding is quantitatively small

and highly specific. Under these circumstances the low stoichiometry of antibody to target creates an environment which makes the second selectivity step in the PLA process - oligonucleotide hybridization, act as a most stringent binary filter in reducing non-proximal antibodies to a non-participatory state, unable to contribute to any fluorescence in the final image.

5.2 An overview of PLA methodology

When working with adherent cells for the detection of two epitopes of a common protein or of the interaction of two proteins, the PLA method functions in the manner summarised in Figure 5.1A.

Cells are grown on coverslips or in glass-bottomed dishes, then fixed, permeabilised and blocked as per a standard ICC protocol described in the Materials and Methods. Primary antibodies, the same as would be used for a standard ICC protocol, are added in order to bind to the specific proteins or epitopes under investigation. PLA probes, secondary antibodies with covalently-linked single-stranded oligonucleotide proximity probes are added (Figure 5.1 Ai). Such PLA probes are currently available off-the-shelf from a company called Duolink, who have commercialised the product first developed by Ulf Landegren at Uppsala, Sweden. When the PLA probe pairs are in close enough vicinity to each other the addition of complementary connector oligonucleotides is enough to form a circular polynucleotide DNA bridge between them (Figure 5.1 Aii). The addition of ligase and free nucleotides allows for the ligation of a fully circular DNA bridge between the two proximity probes (Figure 5.1 Aiii). The closed-circle of DNA is now capable of being amplified by phi29 DNA polymerase, facilitating the creation of hundreds of copies of concatenated single-stranded DNA with complementary bases to the circular template, in a process called rolling circle amplification (RCA). The DNA circle and its concatemeric product remain covalently conjugated to a single antibody-antigen complex, with the other proximity probe cleaved early in the RCA process. Hybridisation of complementary fluorescently-labeled oligonucleotides to the single-stranded DNA concatemeric product of RCA, allows for the indirect visualisation of the proximal proteins using both confocal and standard epifluorescence microscope imaging (Figure 5.1).

When performing PLA alone and without the introduction of another fluorescent stain common to ICC, acquired images present the researcher with many of the same post-acquisition processing issues as would be encountered when imaging strongly fluorescent materials such as quantum dots (Figure 3.20). Images comprised of relatively sparse and intensely bright foci each express high signal to background (S/B) and signal to noise (S/N) ratios compared to levels typically encountered with ICC using organic fluorophores. Theoretically, such intense signals should allow for easy image interpretation and data-harvesting. However, many physical properties of the specimen most notably its z-plane depth, and inherent constraints due to the quality of the microscope hardware (most notably the quality of its objective lens), camera sensitivity and resolution can lead to it having a characteristic point spread function (PSF) which may hinder precise and fast evaluation of every spot. Such issues as these have to be properly managed when designing PLA analysis software and in the interpretation of PLA results data.

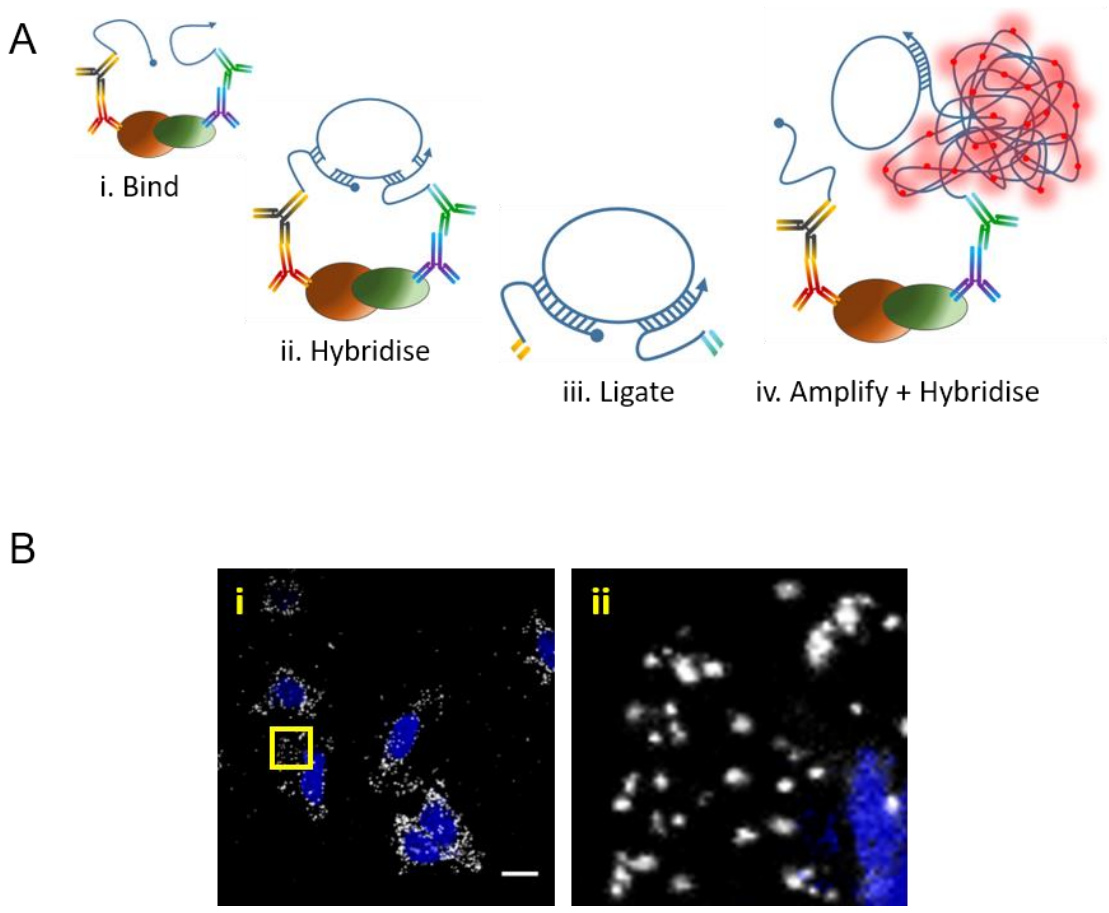

Figure 5.1 The *in situ* Proximity Ligation Assay (PLA)

The Proximity Ligation Assay (PLA) in fixed cells, provides an alternative technique to study putative binding of proteins *in situ.*

Panel A. i. Primary or secondary PLA antibodies bind to their cognate epitopes, allowing their covalently-linked oligonucleotide proximity probes to come into close vicinity to each other. **ii.** Complementary connectors hybridise to form an oligonucleotides bridge between the two proximity probes **iii.** Ligase forms a closed-circle single-stranded DNA polynucleotide bridge **iv.** Rolling Circle Amplification forces initial cleavage of one of the proximity probes, before massive amplification of concatenated single-stranded DNA with complementary bases to the circular template. Fluorescent probes are then hybridised onto the ssDNA bundle, allowing for visualisation of each proximal antibody pair as an intense fluorescent spot when imaged on an epifluorescent or confocal microscope. **Panel B. i.** MRC-5 SV2 cells expressing punctate fluorescent PLA foci, serving to show where DDX3X and eIF4E proteins are in close proximity *in vitro*. DAPI staining of the nucleus shown in blue. Scale bar indicates 20µm. **ii.** A magnified view of the ROI in inset i.

5.3 The Development of PLAY – generating novel software for PLA analysis.

As with all *in situ* visual detection techniques, interpretation of PLA-produced images presents a unique set of challenges, many of which can only properly be mitigated with a full and proper understanding of the assay characteristics and of the pros and cons of employing one of the many analysis tools now available.

5.3.1 Consideration of available tools

For most research applications there are proprietary and open-source software packages available to help the biologist garner specific information from images, helping to semi-automate processes. These also add a greater element of objectivity to the decision-making. The automation of repetitive tasks speeds up data collection and aids the production of reproducible quantitative results. There are many image analysis programs available, each of them offering particular algorithms specialised for niche tasks and to users whose programming experience may range from none to expert.

In order to meet the objectives of the experiment, the basic criteria in choosing any analysis tool were reduced to three – each considered as completely essential:

i. **Spot counting:**
   To correctly identify and count all cellular foci such that the automated spot counts per cell come close to a count performed by a trained image analyst. Although this criterion may make little sense intuitively since a computer algorithm has the potential to find real foci that would elude the human eye, it is important that at least for the first implementation of any algorithm, automated counting can be manually verified as being accurate.

ii. **Spot localisation:**
   Protein complexes located close to the periphery or leading edge of a cell are more likely to play a direct and active role in the morphological transformation of the cell membrane prior to or

during cell spreading (Willett et al. 2013; Willett et al. 2010). In contrast, nuclear proteins tend to have a less direct affect, often through an interplay with DNA or nascent mRNA complexes. The biological relevance of protein location is therefore of critical importance, arguably even more important in some assays than spot counting given that each spot signifies a putative protein-protein interaction.

iii. **Spot characteristics:**

Initial PLA assays showed that foci of DDX3X and eIF4E interactions differ both in their intensities, shape and their size (Figure 5.1B). All three parameters are influenced by the number of rolling circle amplicon product (RCP) steps which increase the length of target ssDNA product to which the fluorescent probes hybridise (Clausson et al. 2015).

After a trial PLA experiment, images such as that shown in Figure 5.1B were analysed by eye before a number of image analysis and programming environment packages were considered for the data interpretation stage. These included ImageJ and Fiji (Schindelin et al. 2012); CellProfiler (Lamprecht et al. 2007), MetaMorph (Eliceiri et al. 2012); Image-Pro Plus (Frantz et al. 2013) ; Matlab (Driscoll 1975) and the programming languages Python (Lutz 2007) and R (R Development Core Team 2011)

5.3.2 PLA analysis - Program Design Overview

In order to best interpret images produced by the Duolink Proximity Ligation Assay, an application design had to be specified to suit the needs of the particular project. It had to offer enough robustness to be applicable to an array of different experiment conditions using other cultured adherent cell types besides the MRC-5 SV2 cell line for which this program was to be initially used. As a secondary goal, it had to be capable of evolving into a tool which could be adopted and used by other researchers without the need for programming experience.

After identification of preferred software tools, a design specification was created for a tool which would be known as PLAY (Figure 5.2), referring to its objective of performing PLA analYsis. The specification of PLAY was put together such that it would utilise tried and tested Fiji plug-ins which allowed for dimensional analysis of cells, cellular adjacency measurements, and foci localisation. All other necessary customisation would be performed primarily through the development of a bespoke Fiji macro. In order to compile all Fiji gathered data into a data-structure for in-depth analysis, including experimental design information meta-data, Python (Fallis 2013) was decided upon as the programming environment of choice. This was in part because Python is well-known for having a relatively shallow learning curve, but still offers a number of libraries which could be utilised for data manipulation. These include the PANDAS library (McKinney 2010) and a comprehensive suite of scientific analysis packages such as Numpy and SciPy (Van Der Walt et al. 2011) for data manipulation and statistical methods; Matplotlib (Hunter 2007) a flexible graphics environment for data visualisation; and IPython (Rossant 2013). Jupyter Notebook (Perez, Fernando and Granger 2007) offers a user interface with the ability to provide a rich and interactive visual component to the user.

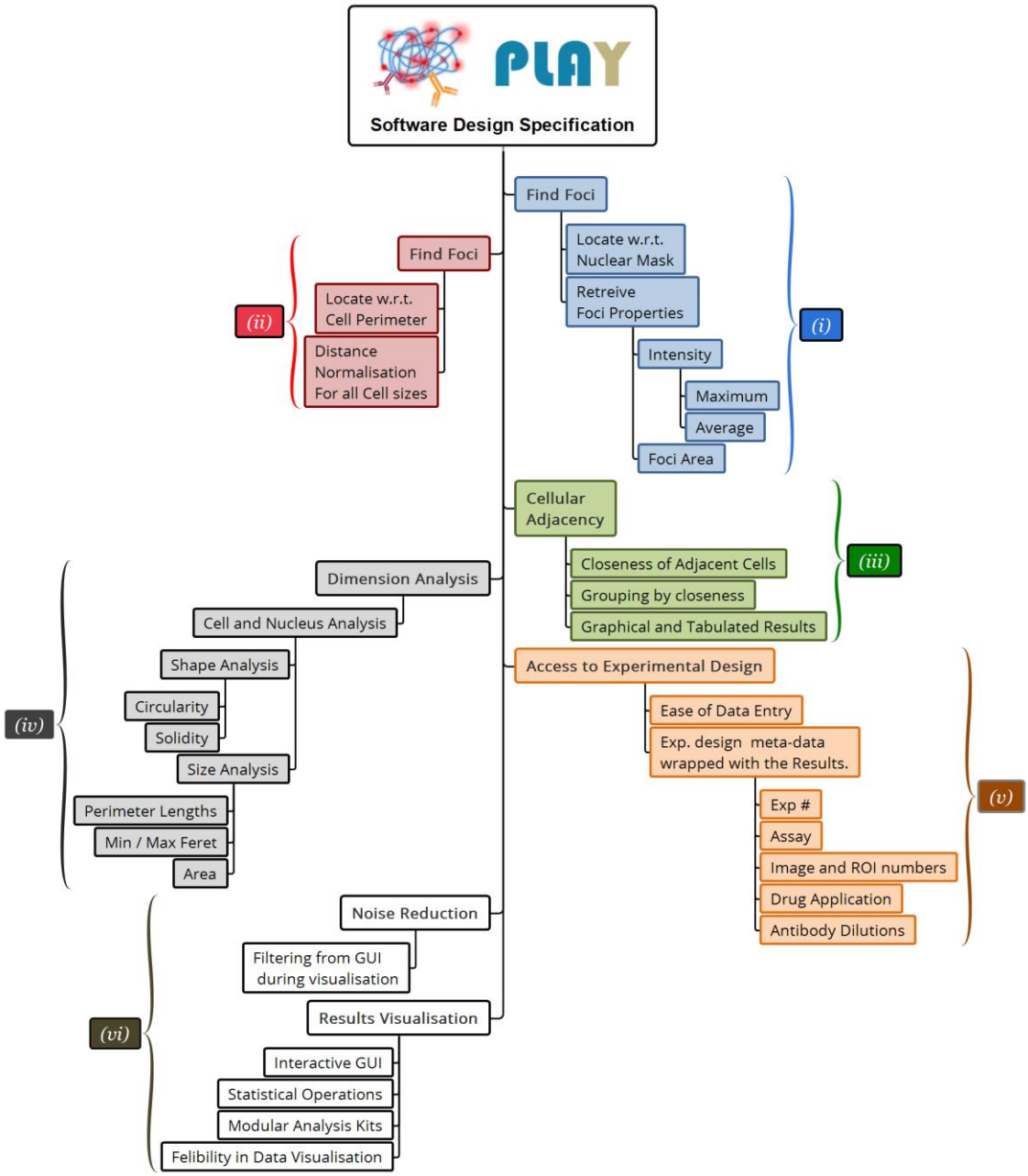

Figure 5.2 Proximity Ligation Assay analYsis "PLAY" Software design specification

Major branches of the software design of PLAY could be potentially implemented using self-built or already-available code within the two primary platforms of ImageJ or Python:

i. Available in Fiji "FindFoci" plug-in (Herbert et al. 2014)

ii. Catered for using dual and inverted masking techniques, within Fiji.

iii. Available in Fiji "Graph" plug-in.

iv. Fiji default measurement set (Fiji version 1.50)

v. User-friendly Data Entry using Microsoft Excel configuration "PLAY Sheet"

vi. Front-End User Application Based on Jupyter Notebook.

5.3.3 “4PLAY”

4PLAY was designed to utilise ImageJ/Fiji plugins already available to the imaging community (Figure 5.3). Their choice fulfilled the need to apply tried and tested analysis tools to mitigate issues with reliability as well as to ensure that any unexpected behaviour with the plug-ins could be addressed through widely used user forums. Plug-ins were chosen for their ability to meet the design specification (Figure 5.2) and batch execution was enabled through the use of a script written in ImageJ’s own macro language.

With the main Python analysis code called PLAY (PLA analYsis), it seemed appropriate to give the ImageJ program a fitting name. 4PLAY executes plug-ins to take the required measurements from an image, whilst concurrently giving the user the ability to provide manual interventions. It then formats all the results data into a form which is most accessible and efficient ‘for PLAY’ to analyse effectively.

Results from 4PLAY are tabulated and stored as comma separated files within a folder associated with each cell’s ROI. All results garnered from 4PLAY’s measurement algorithms and third party plug-ins can be accessed directly by the user if needed. However, the current version of PLAY software uses a reduced set of these gathered results for current analysis needs. The inclusion of all measured results for further processing by PLAY is entirely possible with minimal changes to the PLAY source code.

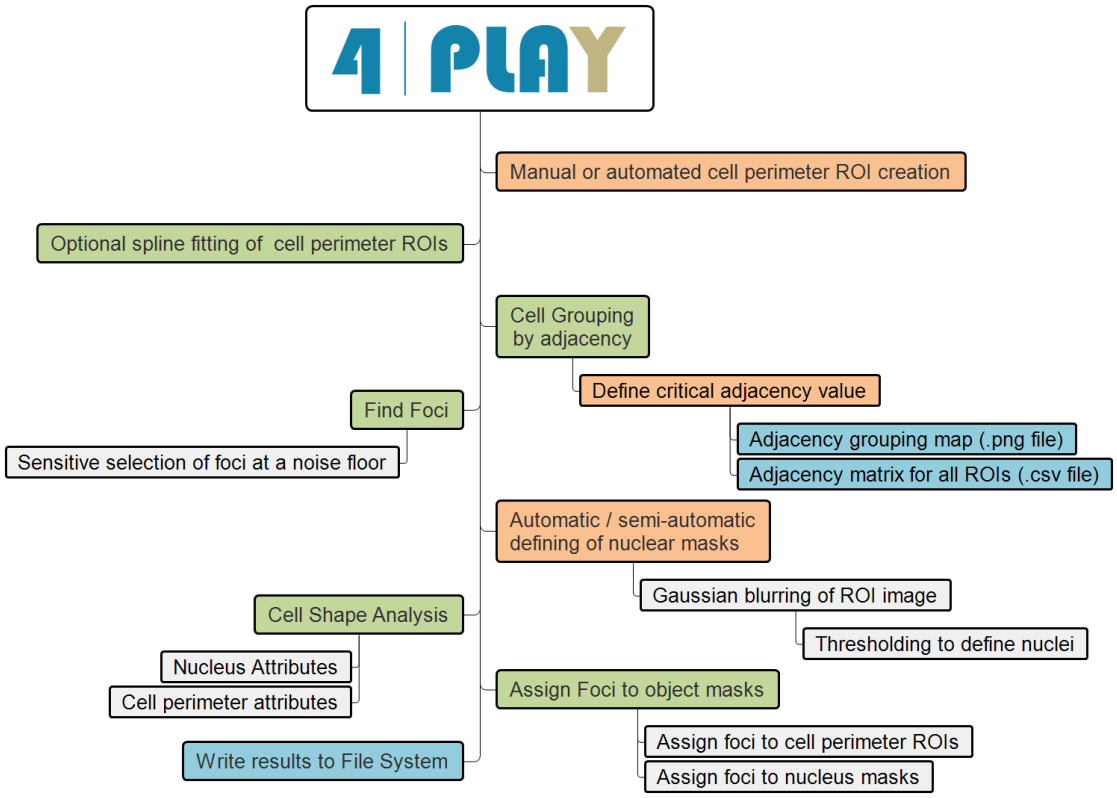

Figure 5.3 4PLAY design specification

4PLAY was designed to be a pure ImageJ data-gathering platform, analysing PLA images and creating all the preliminary results tables and images necessary for the core PLAY analysis and visualisation routines implemented in the Python-based Jupyter platform.

4PLAY prepares all datasets for Proximity Ligation Assay analYsis.

5.3.4 Spot Finding, Characterisation and Cellular Localisation

ImageJ and Fiji have a growing user-base and a growing number of mature plug-ins to aid in image analysis, including many plug-ins specifically for ‘blob analysis’ and spot localisation.

FindFoci (Herbert et al. 2014), an open-source plug-in for ImageJ, was chosen as the main PLA foci finding engine of 4PLAY (Figure 5.4A). It was originally developed to count distinct nuclear foci of an accumulated form of phosphorylated γH2AX, a biomarker for the genotoxic insult which aggregates in response to DNA damage. However, its technical specification also showed it to have many of the attributes needed to localise and discriminate other foci such as those created by the Duolink® PLA system.

FindFoci identifies all peaks above background noise levels for ROIs drawn within 8-bit or 16-bit greyscale images (Figure 5.4B). It is able to merge sub-peaks into their parent peak by applying optional merging criteria, then ranks the peaks according to their relative intensities and presents results both in tabular form as well as graphically. It does this firstly by labelling masked objects, and secondly by overlaying foci rank information and identifying sub-pixel intensity maxima on a copy of the original PLA image. FindFoci is a fast-running Java plug-in for ImageJ with the ability to work headless for command-line script execution, making it fully utilisable as a callable program executed from the 4PLAY ImageJ macro. FindFoci has at its core an algorithm able to perform peak-finding, it is also able to merge sub-peaks into parent peaks, and perform distance mapping of foci relative to any pre-defined image mask.

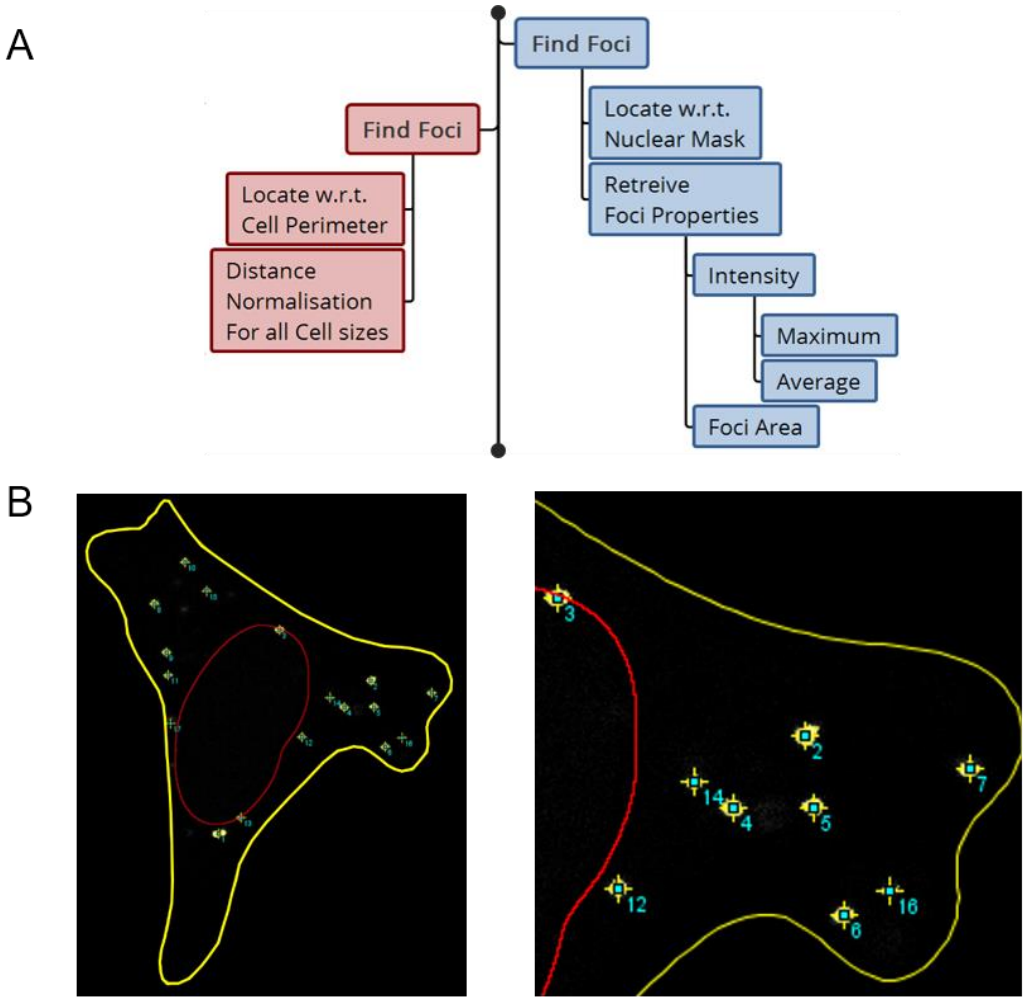

Figure 5.4 '4PLAY' and foci finding graphical results.

Panel A. 4PLAY's sub-specification for foci finding and characterisation. **Panel B.** Cells were seeded onto coverslips coated with 8µg/cm^2 collagen I, at a density of 15,000 cells/cm^2 and incubated in MEM with 15% (v/v) FCS at 37ºC for 40 mins. Cells were fixed using 4% paraformaldehyde (PFA), saponin permeabilised and dual immuno-fluorescence stained with anti-DDX3X (Ab62) diluted at 1:1000 and anti-eIF4E (Ab53) diluted at 1:200, according to the Proximity Ligation Method, as described in the Materials and Methods. Using a scanning confocal microscope images were obtained using a confocal pinhole set to 6.8 Airy Units (AU) for the PLA channel, and 1 AU for the DAPI channel. All PLA foci indicate putative interactions between DDX3X and eIF4E where the two proteins are within 40nm of each other. Scale bar indicates 20µm. All images were processed using PLAY, a novel PLA analysis software created especially for this project and discussed in this chapter. **Left Panel:** For each cell, and with some specifically requested user intervention, 4PLAY defines the nuclear and cellular peripheries with respect to which the Euclidian shortest distances are measured to each and every PLA spot. **Right Panel:** A zoomed-in image of the same cell shows how each PLA spot is allocated a specific identification number which identifies it and all its associated attributes even after importation into the PLAY dataframe.

5.3.4.1 Peak Finding:

FindFoci works by finding all points of maximum intensity and merging them into identifiable regions. The noise-floor is defined wherein any local intensity peaks are ignored, and local maxima are defined each being assigned to their own locale in a process called peak expansion. In this process regions exhibiting a consistent negative intensity slope from a peak become assigned to that peak.

5.3.4.2 Merging of Peaks:

FindFoci was originally designed to offer optional functionality to limit the effects of noise on the foci-locating algorithm. In particular scenarios, noise can introduce insignificant intensity peaks into any image. If, however, the noise modulates the slopes of another real intensity spot signal then it is possible that the intensity contribution from the real signal will be enough to pull this noise off the noise floor such that it becomes interpretable as a false positive - noise in the guise of an authentic sub-peak.

5.3.4.3 Distance Mapping:

FindFoci has the ability not only to count and quantify foci but also to log the coordinates of each spot and measure its Euclidean distance from any pre-defined mask. 4PLAY takes advantage of this distance mapping by separately applying two masks and recording foci distances for each. One mask is defined by the user to accurately represent the cell nucleus, and another to represent the perimeter of the cell. In this way, a spot distance from both the nucleus and the perimeter can be accurately defined, and a normalised distance measurement (percentage distance from the nucleus to the perimeter) computed which can be applied to cells of all sizes.

5.3.5 4PLAY Measurement Harvesting

All 4PLAY algorithm harvested measurements are shown below. Measurements of cellular dimensions (Figure 5.5A) including some fundamental shape descriptors performed using ImageJ's built-in measurement functions which are able to calculate numerous standard measurements to infer cell size, shape, and even object orientation. There are infinite ways to be non-circular, which makes concise shape description complex. 4PLAY uses a limited library of shape descriptors to allow simple comparison of some fundamental morphologies most prevalent in spreading and growing adherent cell lines.

FindFoci Results: Located in the "Perimeter FindFoci Results.csv" file: X, Y, Z, Size, Max, Total, Av.

Foci Distances: Located in the "Perimeter Foci Distances.csv" and "wrt-Nucleus Foci Distances.csv" files: x, y, Object, Distance.

Foci Results: Located in the "Perimeter Foci Results.csv" and "wrt-Nucleus Results" files:
Image, Object, cx, cy, Size, Valid, Count

Nucleus Foci Summary: Located in the "wrt-Nucleus Foci Summary.csv" file:
Image, nObjects, Valid, nFoci, In, Ignored, Out, Min, Max, Av, Med

Cell Measurements: Located in the "Cell Measurements.csv" file:
Area, Perim., Circ., Feret, Solidity.

Some of the measurement types included in the results files include:

Area: The maximum space enclosed by the outer boundary of the object, measured in the plane of the coverslip and calculated in square pixels or in calibrated metric units.

Perimeter: The length of the outer boundary of the object.

Convex Hull: The vector of smallest length which completely encompasses the entire area of the object. The complex hull may be most easily visualised by the hypothetical placement of an elastic band around the object, which would naturally take on the characteristic of a complex hull or complex envelope (Figure 5.5Bi).

Convex Hull Area: The area enclosed by the convex hull of the object (Figure 5.5Bi).

Feret: The longest distance between any two parallel tangents as they touch the object's outer perimeter, also known as Feret diameter and maximum caliper (Figure 5.5ii).

Minimum Feret: The shortest distance between any two parallel tangents as they touch the object's outer perimeter (Figure 5.5Bii).

Circularity: A measure of the compactness of the 2-dimensional object as compared to an isoperimetric circle (a circle with the same perimeter length). Where a circularity value of 1.0 indicates a perfect circle, and a tendency to 0.0 indicates an elongation of the object (Figure 5.5C).

Solidity: The solidity of an object is the measurement of the extent to which an object is concave or convex, based on the ratio of its area compared to its convex hull, where the solidity of a convex shape will be 1.0 (Figure 5.5C).

A

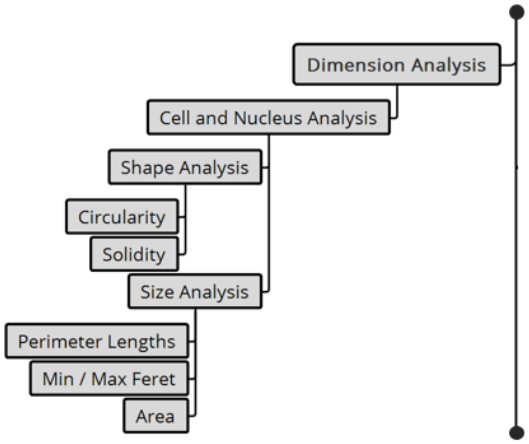

B

i. Convex hull & convex hull area

ii. Feret diameters

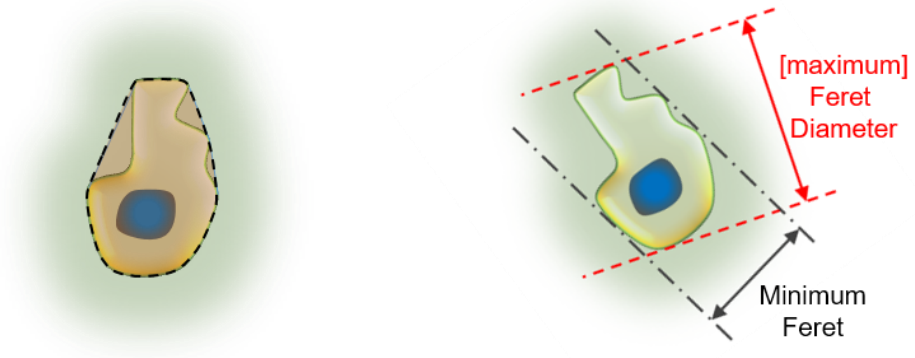

C

$$Circularity = 4\pi . Area . (Perimeter)^{-2}$$

$$Solidity = Area . (Convex\ Hull\ Area)^{-1}$$

Figure 5.5 The Architecture of 4PLAY – Dimension Analysis

Panel A. 4PLAY's sub-specification for Dimension Analysis.
Panel B. i. 'Convex hull': The vector of smallest length which completely encompasses the entire area of the object (dashed line). Convex hull area is the area enclosed by the convex hull (shaded brown) **ii.** 'Feret diameter': The longest distance obtainable between two infinitely long parallel tangents as they touch the object's outer perimeter, also known as Feret, maximum Feret diameter and maximum caliper. **iii.** 'Minimum Feret': The shortest distance obtainable between any two infinitely long parallel tangents as they touch the object's outer perimeter, also known as minimum caliper. *iii.* **Panel C.** Mathematical definitions of circularity and solidity.

5.3.5.1 Cellular adjacencies

Graph (https://ImageJ.nih.gov/ij/plugins/graph/index.html) is an ImageJ plug-in for the creation of adjacency lists in both tabular and graphical form (Figure 5.6). When provided with an image containing binary masked ROIs it can calculate the shortest distance between all masked objects in an image (Figure 5.6Bi). Separation distances may be calculated in a variety of ways. However, 4PLAY solely uses distances calculated between the closest edges of neighbouring cells. The resulting matrix file consists of sub-pixel accuracy distance measurements allowing for metric scaling in a later step if necessary. These tabular results comprehensively describe cellular separation for all cells on the image (Figure 5.6C). Visualisation of these data uses a user-defined distance discriminator to display the image as a number of sub-grouped cells, with each subgroup containing cells which are no further apart than the distance discriminator value (Figure 5.5Bii). Subgrouping of cells aids visual interpretation with subgroupings colour-coded and the cells' closest separation points annotated with connecting lines. One fundamental issue of adjacency measurement collection is that it is limited to considering distances between all cells on the image without consideration for those cells which may be out-of-frame but influencing in-frame cell behaviour via intercellular signalling, due to their relative closeness (Figure 5.6D).

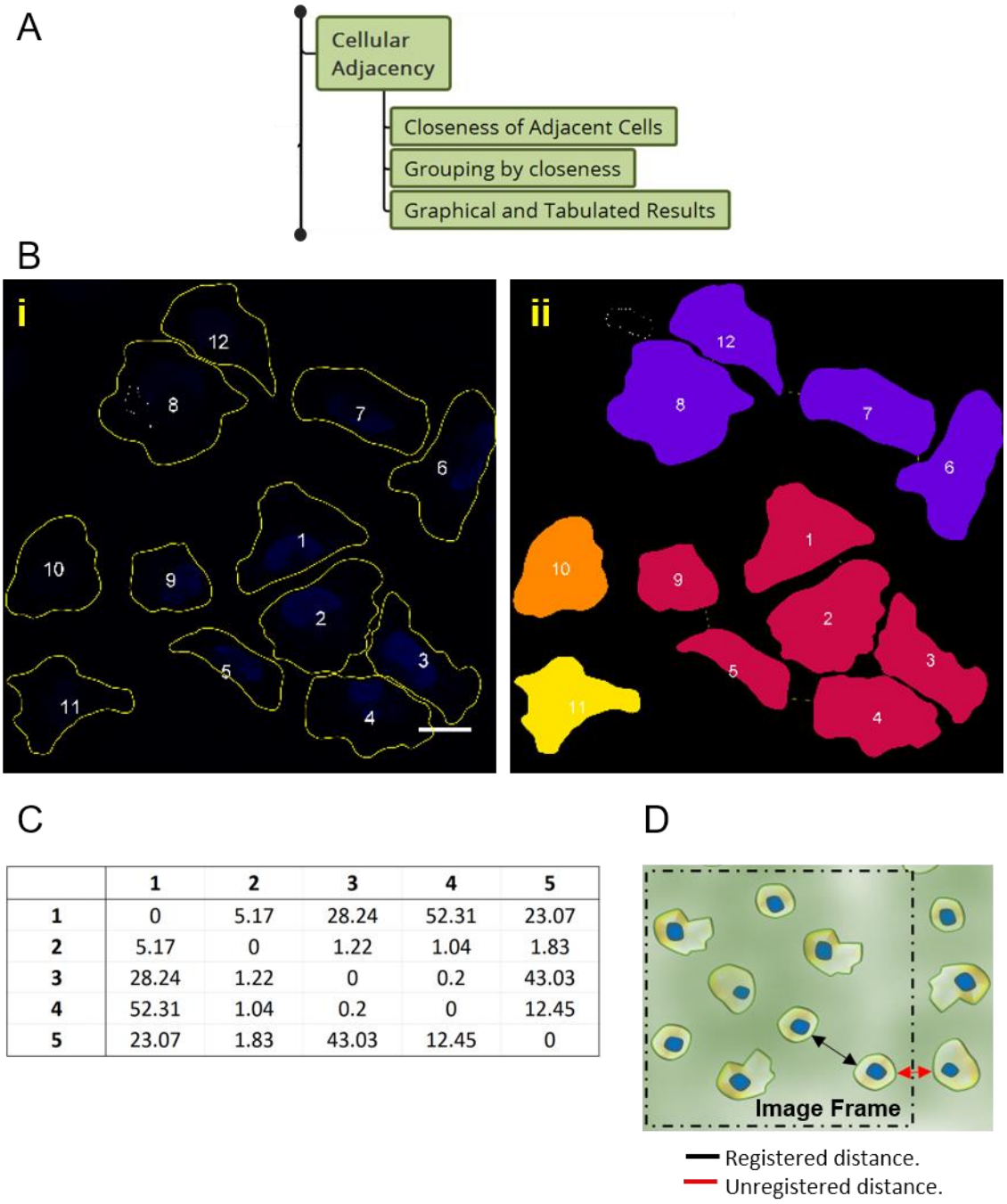

	1	2	3	4	5
1	0	5.17	28.24	52.31	23.07
2	5.17	0	1.22	1.04	1.83
3	28.24	1.22	0	0.2	43.03
4	52.31	1.04	0.2	0	12.45
5	23.07	1.83	43.03	12.45	0

Figure 5.6 The Architecture of 4PLAY – Cellular Adjacency

Panel A. 4PLAY's Sub-specification for Cellular Adjacency.

Panel B.*i.* 4PLAY's Cellular Adjacency graphical results. Numbered ROIs with a scale-bar of fixed width (20µm). ***ii.*** Cells/ROIs are grouped by colour according to the distance discriminator value and their distance to their closest neighbour **Panel C:** A partial results table for the image in panel B. Each numbered ROI/Cell has its Euclidian shortest distance (in pixels) to all other cells annotated on a comprehensive distance matrix. **Panel D:** Cellular adjacency, measures the distance between each cell and the closest perimeter of its nearest neighbor within the recorded image.

5.3.6 PLAYmate

PLAY architecture (Figure 5.7) was designed such that the main application front-end would be as user-friendly as possible, hiding much complexity from the users with no programming knowledge. Ultimately, it still provides more advanced users access with the ability to customise analysis routines and visual output using any of Python's broad array of libraries. IPython's Jupyter Notebook (Perez, Fernando and Granger 2007) was identified as a suitable interactive environment for this purpose, enabling less advanced users to perform basic statistical analysis and data visualisation utilising pre-programmed generic modular analysis kits. Furthermore, it allows more experienced programmers freedom to enjoy complete dataframe manipulation, statistical analysis and visualisation using the entire SciPy library. The Jupyter notebook is a recently developed programming environment based on a set of open standards for interactive computing, offering the user an ability to present their results in an interactive manner as well as publishing and sharing them with the scientific community in a manner that has been hitherto difficult. The latter mainly reflects the restraints of journal articles, papers or PhD theses where the reader has limited ability to directly view entire datasets or to fully reproduce data analysis routines in order to comprehensively validate results or algorithm implementation.

From PLAYmate, aggregation of all 4PLAY data is performed with a single command (Figure 5.8A) which prompts the PLAY dataframe building algorithm to access experiment design information from a configuration sheet, the 'PLAY sheet' (Figure 5.8B). The user is prompted to select the assay which they wish to be gathered into the dataframe, before the final dataframe is created and backups archived on the user's computer as a standard Python '.pickle' file as well as in Microsoft excel format. Once the dataframe is created the user may opt to continue using PLAYmate in one of two modes, Basic or Advanced:

In Basic mode, the user is provided with a set of pre-created analysis tools called ‘PLAYkits’ which may be used to show a broad set of analysis results both in tabular and visual form. PLAYkits include tools for:

- Post-acquisition noise reduction
- Correlation analysis
- Statistical Analysis
- Regression Plots
- Histograms
- Kernel Density Estimations
- Varied 1D and 2D plotting functions

In ‘Advanced mode’ users are given full access to the PANDAS-based dataframe and PLAYkits source code for full and unhindered customisation of the basic PLAYkits. Users also can create their own PLAYkits which in theory could be distributed to other researchers around the world using open-source sharing models such as that adopted by the ImageJ community. The latest versions of 4PLAY, PLAY and PLAYmate are held by the Morley laboratory.

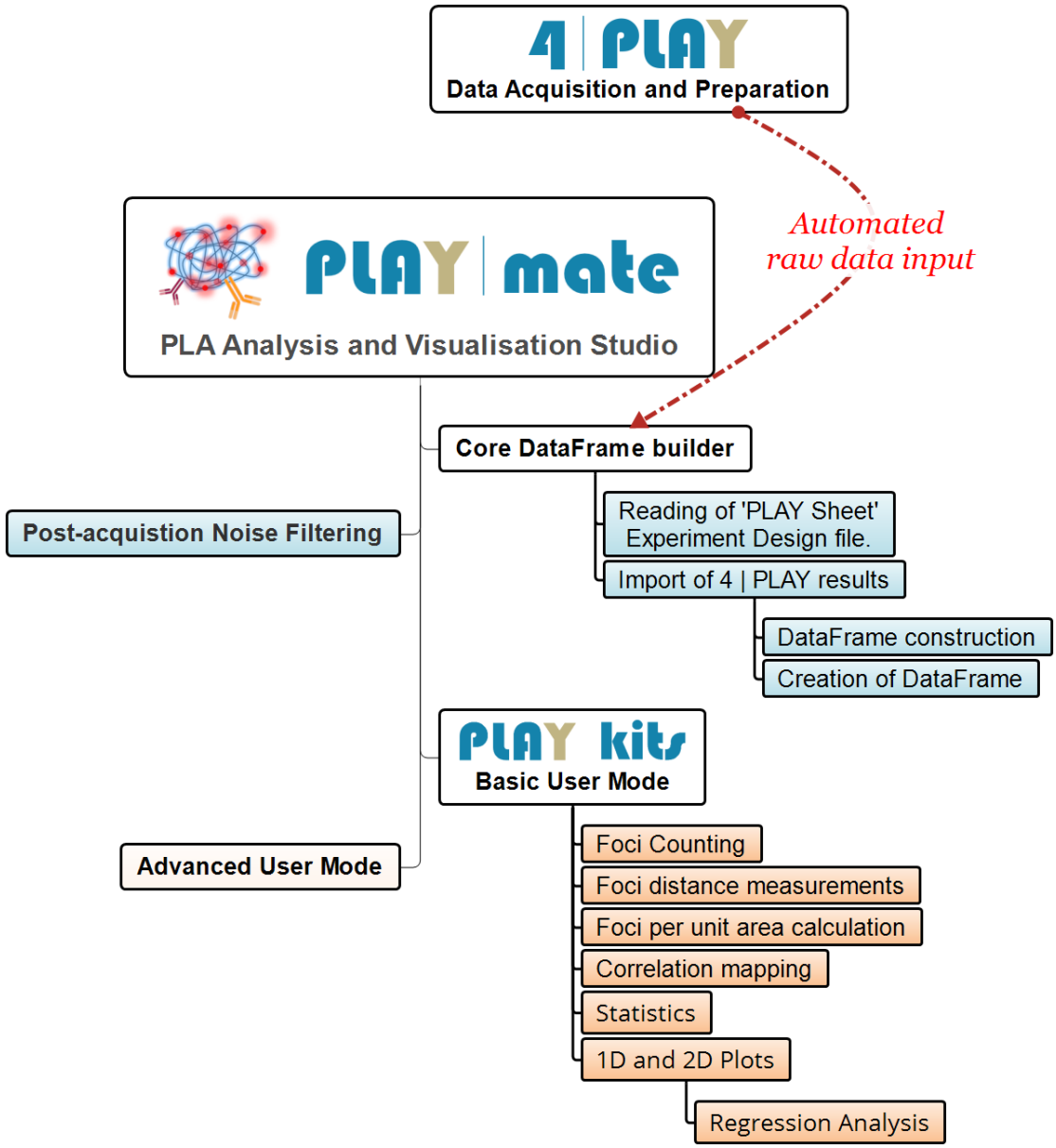

Figure 5.7 The Architecture of PLAY

The PLAYmate PLA analysis and visualisation studio runs on the JUPYTER Notebook, and provides a flexible tool for novice or more advanced users to query the experimental dataset. Initial data acquisition is performed by the PLAY Core Dataframe builder, which scans the users' file system for pre-formatted results tables and images previously created by 4PLAY. Noise-filtering is performed in all cases from PLAYmate's user interface (UI) prior to data analysis being performed using either pre-made analysis modules (PLAYkits) or for more advanced Python users through a combination of PLAYkits and user-created code.

A

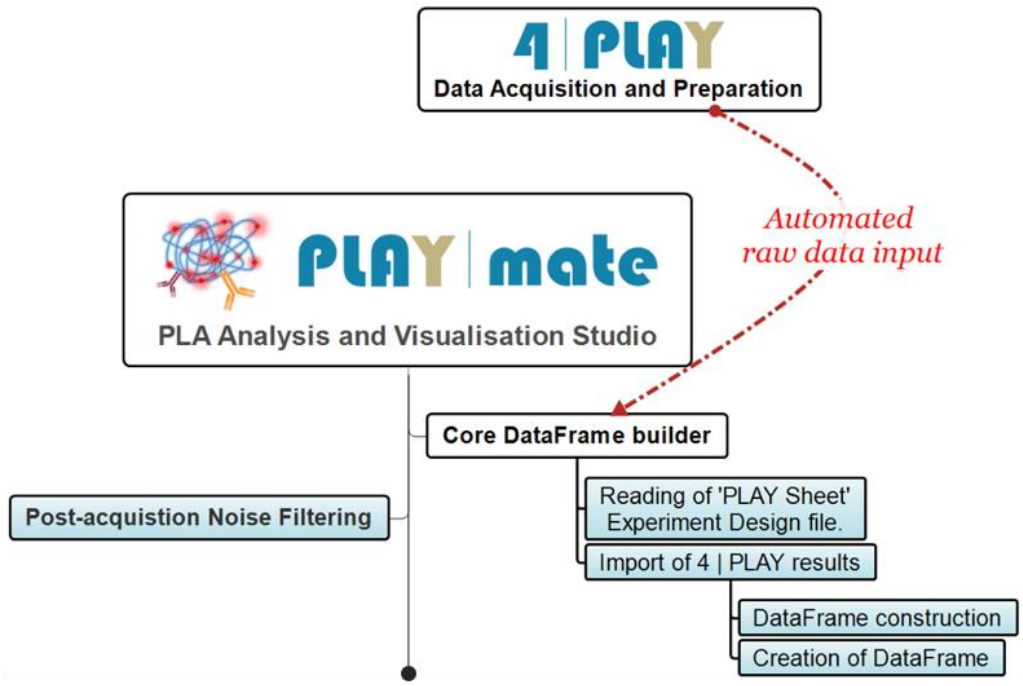

B

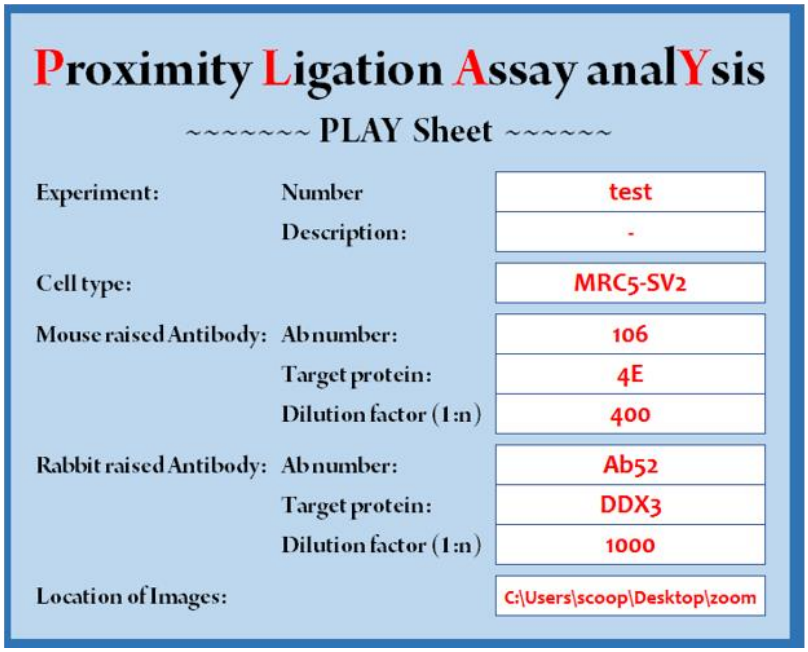

Figure 5.8 Importation of results files PLAY Core Dataframe builder

Panel A. Data transfer from the 4PLAY created files into the core dataframe building routine requires user intervention, specifying the absolute path to the 4PLAY results files, as well as user input of experimental metadata not usually stored with the original image files. Such user-intervention necessarily requires a friendly interface, for which PLAYsheet was devised. **Panel B.** PLAYsheet is an excel template which allows the user to enter optional and basic metadata for the experiment. The only wholly required user input is the specifying of the path on which the experimental images (and therefore the 4PLAY results) are to be found.

5.3.7 The PANDAS Dataframe

Dataframes are tabular data structures representing observations or measurements in a multi-dimensional array format. This allows for the storage, retrieval and manipulation of heterogeneous data types via direct coordinate indexing, or via powerful conditional querying instructions somewhat similar to those used in the programming languages R and SQL. Such potential for manipulation of data gives dataframes a significant advantage over less sophisticated querying such as that available with Microsoft excel and the Visual Basic language. Dataframes have been embraced by many statistics platforms, including for use as primary data management tools, and also have many advantages over other database packages such as SQL. With relative ease other Python libraries can be called to facilitate the creation of plots as well as statistical computation, making Python a superbly flexible language for adoption in a vast range of data science projects.

Python's PANDAS is a relatively new library addition to Python and fills a gap where otherwise large-scale data analysis would have to be performed outside of the Python environment. Upon import of the 4PLAY data sets, a single large PANDAS dataframe is created giving the advanced user access to all experimental observations and their attributes. The header columns from a dataframe created from PLA assay data shown in Table 5.1, are described in more detail below:

Experiment Setup data including assay and image names are accessed v columns 0 to 5 (Panel A): The first column is the PANDAS-generated index, which starts at 0 to signify the first experimental reading or observation. The 'Assay' column holds assay information- a short description differentiating one cell treatment from another. The 'Exp' (experiment), 'Image' and 'ROI' fields allow the exact cell to be located amongst all the images taken in each experiment. Antibody Information, including antibody reference numbers and concentrations used for each assay, are provided in columns 6 to 11 (Panel B): Experimental meta-data stores information regarding the exact primary antibodies used in each experiment and involved in each observation. Mouse and Rabbit-raised antibody types are recorded alongside information on their concentration when dissolved in a buffer prior to application. Cellular

measurements, including intercellular adjacency information and individual cellular shape descriptors, are given in columns 12 to 18 (Panel C): All cells measurements except for Inter-cellular adjacencies are stored with sub-pixel accuracy and using pixels as fundamental measurement units, conversion to metric units can be performed if necessary, via PLAYmate. Likewise, measurements of nuclear size and shape descriptor information are accessed through columns 19 to 24 (Panel D), again utilising pixels as the fundamental unit of measurement. Foci Measurements: counts, characteristics and spot location information are stored in dataframe columns 25 to 33 (Panel E): The spot count number remains constant within each ROI, however, all other measurements in these columns are associated with different individual foci. The area and intensity measurements are originally derived from the 4PLAY FindFoci routine, with the nuclear distance and perimeter distance calculations both somewhat dependent on the way the nuclear and perimeter masks are created prior to 4PLAY implementing an ‘Assign foci to objects’ subroutine of the FindFoci plugin. Additional data points for program robustness are available to the Advanced user, including x and y coordinates of each PLA spot as well as a column for the purposes of implementing Boolean masking for additional conditional sorting and matching of data (Panel F).

A

	Assay	Image	Roi	Exp	DrugTime	Dose
4167	-'ve Ctrl	Ex88 MRC5 Cnt No-Ab dish0.lif - Series002	1	88	0	0
4168	-'ve Ctrl	Ex88 MRC5 Cnt No-Ab dish0.lif - Series002	1	88	0	0
4169	-'ve Ctrl	Ex88 MRC5 Cnt No-Ab dish0.lif - Series002	2	88	0	0

B

	MAbTarget	RAbTarget	MAb	MAbDil	RAb	RAbDil
4167	4E	DDX3	106.0	400.0	52.0	1000.0
4168	4E	DDX3	106.0	400.0	52.0	1000.0
4169	4E	DDX3	106.0	400.0	52.0	1000.0

C

	Adjacency	Perimeter Size	Cell Area	Circularity	Solidity	Feret	Min Feret
4167	1.0	2082.7874	95811.0	0.2775	0.6508	881.6439	229.7545
4168	1.0	2082.7874	95811.0	0.2775	0.6508	881.6439	229.7545
4169	1.0	1183.8089	75838.0	0.6800	0.8765	390.0628	295.8264

D

	NucArea	NucPerim	NucCirularity	NucSolidity	NucFeret	NucMinFeret
4167	26777.0	664.7666	0.7614	0.9724	246.0183	142.6773
4168	26777.0	664.7666	0.7614	0.9724	246.0183	142.6773
4169	14837.0	485.0021	0.7926	0.9801	173.3667	111.8935

E

	Spot Count	Area	Max Intensity	Total Intensity	Av Intensity	nucDist	periDist	Foci per Cell Unit Area	%Dist
4167	2.0	223.0	255.0	9307.0	41.74	3.606	43.84	0.002087	7.600219
4168	2.0	53.0	213.0	3060.0	57.74	109.600	21.19	0.002087	83.798456
4169	2.0	78.0	255.0	15916.0	204.05	23.600	18.00	0.002637	56.730769

F

	X	Y	nucObj	periObj	void
4167	269.0	308.0	1.0	1.0	0.0
4168	194.0	383.0	1.0	2.0	0.0
4169	246.0	23.0	1.0	2.0	0.0

Table 5.1 The PLAY dataframe

A. Experiment Setup i.: Assay and Image Data
Dataframe columns 0 to 5, showing 3 example header rows:
“Assay” defines the assay type, drug treatment, controls or wild type name. “Image” refers directly to the original image name, of which there may be many. “Roi” is the region of interest, a defined boundary defining the perimeter of peach cell under study. “Exp” defines the experiment number or name defined by the researcher. “Drugtime” references the time duration for which cells were incubated with a drug treatment. “Dose” refers to the drug dosage applied in micromolar.
B. Experiment Setup ii.: Antibody Information
Dataframe columns 6 to 11, showing 3 example header rows:
“MAbTarget” and “RAbTarget” define the protein targets of the mouse/rabbit-raised antibodies. “MAb” and “RAb” reference the specific stock mouse/rabbit-raised antibodies used. “MAbDil” and “RAbDil” define the dilutions of mouse/rabbit antibodies used (1:n).

Table 5.1 (continued)

C. Cell Measurements i.: Adjacency and Shape Descriptors
Dataframe columns 12 to 18, showing 3 example header rows:
“Adjacency” minimum separation distance between a cell and nearest neighbour. Intercellular adjacency measurements are initially stored with sub-pixel accuracy and using pixels as measurement units with direct scaling to metric units performed via a small PLAYmate routine if and when necessary. “Perimeter Size” defines the length of the cell boundary. “Cell Area” defines the Area of the cell in square pixels. “Circularity” gives a measure of cell circularity between c.0.0 (elongated) and 1.0 (a perfect circle). “Solidity” defines the solidity of the cell. “Feret” is the Feret’s Diameter of the cell. “Min Feret” is the Minimum Feret’s Diameter of the cell (see Figure 5.5B).
D. Nucleus Measurements: Shape Descriptors
Dataframe columns19 to 24, showing 3 example header rows:
“NucArea” defines the Area of the nucleus in square pixels. “NucPerim” defines the length of the nucleus boundary. “NucCircularity” gives a measure of nucleus circularity between 0.0 (infinitely elongated) and 1.0 (a perfect circle). “NucSolidity” defines the solidity of the nucleus. “NucFeret” is the Feret’s Diameter of the nucleus.
E. Foci Measurements: Counts, Characteristics and Spot Location
Dataframe columns 25 to 33, showing 3 example header rows:
“Spot Count” defines the total number of foci in the current ROI (Cell). “Area” is an area measurement of the spot for all intensity values above the noise floor in square pixels. “Max Intensity” defines the peak fluorescent intensity of the spot (255 for an 8-bit image). “Total Intensity” is a cumulative sum of all spot intensity around a local peak, and above the noise floor. “Average Intensity” averages the Total Intensity by the spot Area. “nucDist” is the shortest Euclidian distance between the spot and the cell nucleus (as defined by a nuclear mask). “periDist” ” is the shortest Euclidian distance between the spot and the cell perimeter.
“Foci per Cell Unit Area” = [Spot Count].[Cell Area]$^{-1}$ “%Dist” is the normalised spot distance from the nucleus to cell perimeter, calculated as the percentage distance where 0% is at or in the nucleus, and 100% is at the cell perimeter.
F. House-keeping: Additional Data points for program robustness
Dataframe columns 34 to 38, showing 3 example header rows:
All DataFrame columns in this section provide additional programming flexibility. “X” and “Y” define the precise x and y co-ordinates of the spot in the ROI. “nucObj” and “periObj” define the number of masked objects nuclear object (usually only one) and perimeter objects used to calculate spot distances and derived from the FindFoci plug-in.
“void” is a column especially dedicated to adding calculation flexibility for the PLAY programmer.

5.3.8 PLAYkits

5.3.8.1 Standardised Graphical Outputs

PLAYmate provides access to PLAYkits for both textual results output, including statistical results, but it also excels at presenting results in an accessible graphical format through a number of standard plotting methods. Initially, PLAYmate was designed to rely on bar graphs for visualisation of means. However, bar graphs of data such as average values are more frequently perceptually misinterpreted by the reader than other plots such as violin plots, with the readers' natural inclination to judge values inside the bar as more probable than other equidistant values falling outside of the bar (Newman & Scholl 2012). For this reason, other plotting modes are made available in PLAYkits, including box plots and a more recent form of data visualisation – the paired and unpaired violin plot (Hintze 1988). For more complex visualisation, 2D plots such as histograms, rug-plots and kernel density estimations are also available for use.

Violin plots are effectively sideways transposed density plots. Although density plots and histograms display clear density measurements as the height component, violin plots usually omit this information and depend on the reader to visually compare relative values of the distribution envelope. Violin plots are a useful tool not only in allowing the researcher to easily estimate the modal range (as well as median and interquartile ranges, should such markers be superimposed), they also allow for the general data distribution to be characterised by eye - providing the researcher with a visual model of the sample distribution, its skewness and closeness to normality.

Scatter plots are another analytical tool made available to the operator via PLAYkits. The most basic versions allow for the simple assessment of covariance between any two populations under investigation. The addition of a statistical annotation in the form of either Pearson r, or R^2 correlation coefficient values provides an objective measurement of such relationships. Linear and polynomial regression lines are also available through the basic PLAYkits modules.

Another powerful analysis technique rarely available in analysis packages without a core dataframe manipulation library is that of correlation mapping. PLAYkits was designed to allow up to 21 individual cell and foci attributes to be cross-correlated in a single graphical matrix combining numerical correlation coefficients in an easy to visualise heat-map format.

5.3.8.2 Standardised Statistical calculations

Within PLAYkits, three statistical tests have been implemented for their applicability to PLA analysis, although more tests can be adopted in the advanced user mode if necessary, simply by importing the relevant scipy.stats Python packages:

Welch's t-test

To test the null hypothesis that two population have equal means, Welch's t-test (Welch 1947) is implemented in PLAY in preference to Student's t-test. This is because it performs better than Student's t-test for samples of unequal sample sizes and unequal variances, and similarly well to Student's t-test when sample sizes and variances are equal (Ruxton 2006). Implementing Welch's t-test also means that a prior test for equivalence of variance becomes unnecessary.

Although t-tests assume means of different samples to be normally distributed, they do not assume the population to be normally distributed. The central limit theorem (Hannan 1978) states that means of samples from a population with finite variance approach a normal distribution regardless of the distribution of the population as a whole. It is generally accepted that as long as sample sizes are over 30, then the sample means will effectively show normal distribution, and therefore t-tests will in these circumstances be effective statistical instruments. However, for smaller samples, the population distribution needs to be approaching normal for a t-test to remain valid. In such cases when a normal distribution of the population is unlikely, PLAY provides both a normality test and a robust Mann-Whitney-Wilcoxon test (MWW) if t-tests are not applicable for use. It should be noted that t-tests differ significantly in their statistical method, providing a test for mean values only, whereas the MWW

test is a non-parametric test comparing entire sample distributions with some sensitivity to a location shift (With 1945).

Testing for normality

PLAY has been designed to incorporate a normality test using scipy.stats.normaltest to test the hypothesis that the sample comes from a normal distribution. It combines tests by D'Agostino and Pearson to produce an omnibus test of normality (SciPy Community 2013).

Mann-Whitney-Wilcoxon (MWW) test

When the underlying assumptions made for performing t-tests are questionable (see above), then the testing of two independent data samples from distinct populations may be performed using the MWW test. This provides a comparison of the distribution of two datasets (With 1945; Jones et al. 2001).

By default, the 95% confidence interval is chosen as PLAYmate's default level for expressing the point mean of any population. Statistically, 95% of the confidence intervals will correctly include the population mean (μ), with only 5% likely to exclude it (Jones et al. 2001).

5.4 PLAY System Testing

In order to test the functionality and robustness of PLAY, three main system tests were performed: (i) Validation of the type of image characteristics acceptable as inputs; (ii) Discovery of the noise filtering requirements for rational image analysis using PLAY; (iii) A full system test of PLAY performed using an full PLA image set.

"Pray, Mr Babbage, if you put into the machine wrong figures, will the right answers come out?" (Babbage 1864).

The performance of any system is heavily reliant on the system input, a fact not lost on any computer scientist. PLAY system performance will always depend on the quality and character of the images to be processed. To establish what these conditions were, a number of tests were performed to assess the type of image that would be most efficiently handled by the program to help to ascertain system robustness given such varied datasets as an input.

5.4.1 Testing how best to Image a Specimen

Cells were seeded onto coverslips coated with 8µg/cm^2 collagen I, at a density of 15,000 cells/cm^2 and incubated in MEM with 15% (v/v) FCS at 37ºC for 40 minutes. Cells were fixed using 4% paraformaldehyde (PFA), saponin permeabilised, with experimental groups stained with mAb anti-DDX3 (Ab62) diluted 1:1000 and rAb anti-eIF4E (Ab53) diluted 1:200, and with control groups stained without the addition of the anti-DDX3X primary antibody, according to the Proximity Ligation Assay method, as described in the Materials and Methods.

Figure 5.9 shows that upon hybridisation with hundreds of fluorescently labelled detection oligonucleotides, each PLA RCP presents itself as a sub-micrometer sized, distinct and bright spot distinguishable from background noise (Kerppola 2009; Leuchowius et al. 2013; Weibrecht et al. 2010). In order to establish a common focal-plane between specimens, it was decided that a scanning confocal microscope would offer particular functionality above and beyond that offered by a standard or wide-field fluorescence

microscope. With the confocal microscope's pinhole set to a diameter of 1 Airy Unit (AU).

To allow both good visibility of the slim-bodied lamellipodia as well as the precise and consistent establishment of a near-basal focal point during all imaging, the PLA foci themselves were used as a strong homing-beacon. However, in control groups with little or no fluorescent PLA spots, DAPI images were used to provide an effective guide to finding the near-basal z-plane of lamellipodia through the expression of the limited amount of cytoplasmic fluorescence available from DAPI:RNA complexes (Tanious et al. 1992). This was used as an alternative to introducing cytoskeleton markers such as Alexa Fluor-conjugated Phalloidin. To accomplish a consistent focal plane with all control specimens, the reduced quantum yield of the DAPI:RNA complex (approximately 20% that of the DAPI:dsDNA complex), means that imaging required the DAPI excitation laser (405nm) and the detector gain to be raised above the usual levels used for normal immunofluorescence imaging as is noted in the system testing of PLAY (Figure 5.20). In practice, such a reliance on a weak fluorescent marker does introduce focal bias away from the coverslip. PLA work should be performed with phalloidin markers when possible, as they have been seen not to adversely affect the PLA reaction (Söderberg 2016, personal communication).

Using the confocal microscope with a 63x 1.40NA oil objective and 2.016 x 2.016-megapixel resolution together with the confocal scanning of just the two essential channels (DAPI and the far red PLA channel), images were gathered using a single slide created using the PLA protocol, as described in the Materials and Methods. Primary antibodies were applied at the same concentrations used for ICC, two images were taken (Figures 5.9A-C), each using a different microscope setting, and data were processed appropriately prior to PLAY:

Single z-Slice Setup (Figure 5.9C)

Imaging was performed using the protocol 'Imaging *in situ* Proximity Ligation Assays', as described in the Materials and Methods. The DAPI channel was configured with a 1AU diameter pinhole, and UV laser and associated

detector gain set appropriately high, prior to the location of the mid-z-section of the lamellipodia. To ensure that as many spots were captured within the image, the confocal pinhole for the red PLA channel was opened to its maximum of 6.28AU, allowing foci out of the field of focus to contribute more of their emission light to the final image. This also effectively allows the entire depth of the lamellipodia and a significant proportion of the cytoplasm to contribute a bigger portion of their PLA emission light. Without such a large pinhole on the red channel, a significant number of foci were not seen in the image. No further image processing was performed.

Multiple z-Slices Setup (Figures 5.9A and B)

Using the same DAPI channel setup as for the single z-slice image acquisition, the red PLA channel was also configured to have a 1AU pinhole prior to image acquisition. 47 z-sliced images were taken at 0.292µm intervals and post-processing conducted in ImageJ using the default z-projection algorithm to produce one single image of 'Maximum projection' (Figure 5.9A), with a second procedure implemented to produce a single 'Mean projection' (Figures 5.9B).

All three images were processed by PLAY using a single square ROI enclosing a particularly bright area of the cell. The spot finding results of PLAY were then compared between each image (Figure 5.9A-C insets iii). In the single-frame image, fourteen foci were located, in the maximum projection, thirty-seven foci, and in the average projection nineteen were noted.

Examination of background noise characteristics was carried out by selecting an ROI outside of the cell perimeter, in an area where no PLA fluorescence was perceived. A large ROI was selected in this 'dark space' and the pixel values characterised using the standard measurement tools built into ImageJ. The results in Figure 5.9D show that the averaged z-projection of 47 frames gave a considerably low background with mean, mode, minimum and maximum measured fluorescent pixel values consistently at zero, emphasising the power of noise reduction through simple frame averaging. For the single sliced image, mean, standard deviation and maximum values were as expected – lower in all cases with results collected from the maximum projection image

where all 47 frames are considered and the highest pixel values from all frames considered. From the perspective of noise reduction, averaging wins outright, but as seen in Panel E, the real signal is significantly reduced also. It is evident that using the maximum projection model for data preparation contributes to false positive foci counts due to the increased noise when compared to the other image acquisition and preparation models tested.

Clearly, the maximum projection rendering 2.64 times the number of identifiable foci than the single z-sliced image, gave the best resolution of the three images, with visually identifiable individual punctate foci detectable in the concentrated cluster of PLA fluorescence. However, a clear drawback of using such an image is the low s/n ratio of 31.9 using the mode as an estimate of the noise floor. With both other images, an s/n ratio was shown to be infinity, more conservatively estimated at >255 for the single slice and >61 for the average projection (Figure 5.9E). Theoretically, this leaves the maximum projection mode more vulnerable to giving false positive results in the foci count.

The average projection rendered 1.36 times more foci counts than the single z-sliced image, yet the s/n ratio was constrained in its size by the limitation of 8-bit imaging, essentially giving a theoretical s/n ratio of equal magnitude to the single sliced image. The maximum pixel value in the entire image was only 61, compared to both other techniques giving a value of 255 (Figure 5.9E). From the point of view of obtaining a good s/n ratio, averaging image information is a simple and effective method. However, this constrains the intensity landscape and flattens out peaks to discrete quanta within a more limited range of quantised levels. Therefore, to get the most out of an averaging technique, it is important that the image is not over-sampled in the z-plane.

The single z-sliced image gave the least foci counts of all three methods. With only 14 foci found in total. However, the modal value of the entire image was only 1.2, with the maximum pixel value for the entire image at 255 making the s/n ratio acceptable at more than 255 (Figure 5.9E).

To understand what was happening in a little more depth, a single PLA spot from the experiment described in Figure 5.9 was examined over a number of different z-slices (Figure 5.10A). In addition, as shown in Panels B and C, the intensity profile of this single PLA spot was measured over all 47 frames. These data show that for only 5 frames of the 47, the maximum

intensity ranged above 100 with a significantly narrower full-width half maximum (FWHM) value achieved in a single z-slice when compared to all other slices. This shows how obtaining the maximum z-projection will have widened the spot more than was entirely necessary with a sharper spot obtained if another algorithm had been employed. Other frames will have also contributed to the extended width of the maximum projection with Figure 5.10C showing the actual maximum projection profile (red), close to twice the width of the narrowest (green) profile in Figure 5.10B. Figure 5.10A (ii, iii and iv) show how the light from essentially a point source disperses over a greater area when the source is slightly out of focus. Such light, forming the Airy pattern around the spot centre will have contributed to all three acquired images in the test (Figure 5.9), and could only be discounted practically minimized by use of deconvolution. Figure 5.10C also shows how the average intensity profile is smooth and forms an almost Gaussian curve, where the peak marks the centre of the fluorescent spot, although greatly diminished in its amplitude compared to the maximum projected value.

From the perspective of foci counting, using a maximum projection technique pre-PLAY processing appears to give a superior performance over the other methods tested. However, from a pragmatic point of view imaging 47 slices, instead of a single slice using a larger confocal pinhole for a pseudo-wide-field mode, takes significantly more time. With a typical large assay taking 2-3 hours to image using a single frame imaging, taking ~47 slices increases acquisition time by at least twenty-fold. Even reducing the number of z-slices to 10 or more would make acquisition times impracticably long given the cost of time on the microscope and the fact that storage of the PLA samples appeared to cause loss of adherence of the cell to the collagen substrate over just two days of sample storage at -20^{o}C. Moreover, it needs to be considered that the issue of undercounting by the single slice method tends to happen in areas of dense concentrations of PLA foci, in which case PLAY's ability to measure the size of each spot could be utilized to great effect. It should be noted that future testing of pre-PLAY image manipulation is planned to include the technique known as focus stacking for extended depth of field.

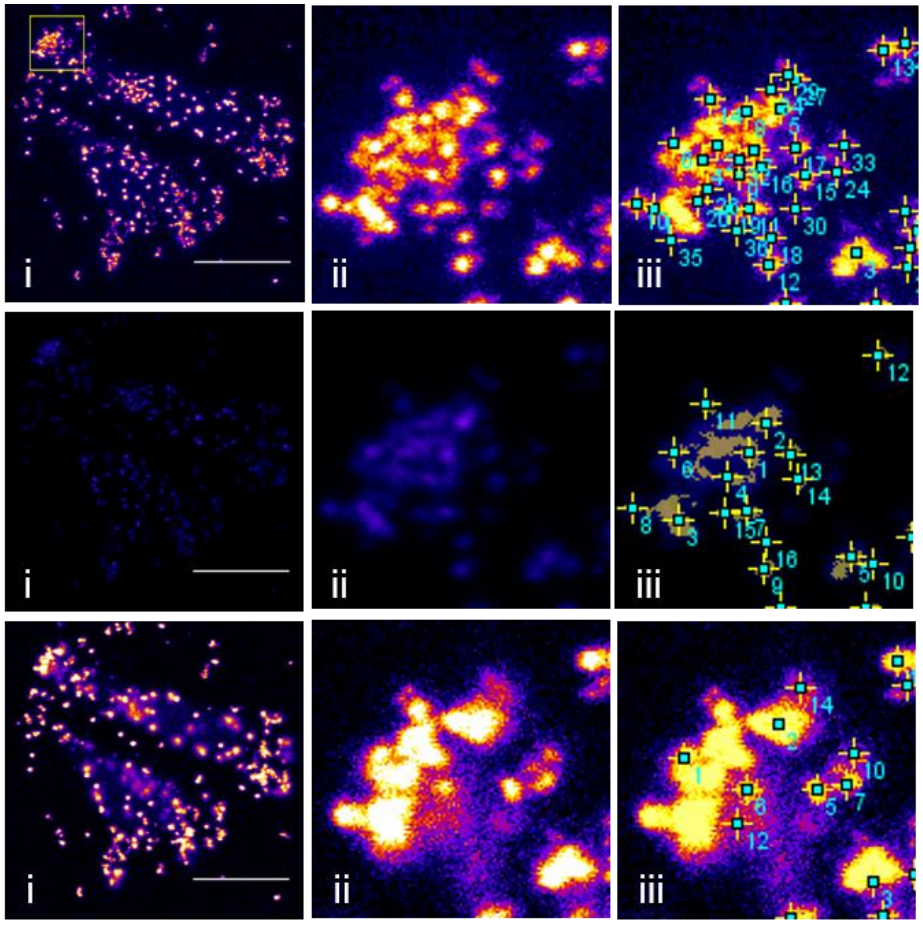

D

Source Image	Pixel Values				
	Mean	Std Dev	Mode	Minimum	Maximum
Single Image	1.2078	3.1774	0	0	16
Average Projection	0	0	0	0	0
Maximum Projection	3.6549	4.2018	0	0	24

E

Source Image	Pixel Values			
	Mode	Minimum	Maximum	s/n (using mode)
Single Image	0	0	255	infinity
Average Projection	0	0	61	infinity
Maximum Projection	8	0	255	31.9

Figure 5.9 Selecting the best Method for PLA Imaging

Cells were seeded onto coverslips coated with 8µg/cm^2 collagen I, at a density of 15,000 cells/cm^2 and incubated in MEM with 15% (v/v) FCS at 37ºC for 40 mins. Cells were fixed using 4% PFA, saponin permeabilised and dual immuno-fluorescence stained with anti-DDX3X (Ab52) diluted at 1:1000 and anti-eIF4E (Ab106) diluted at 1:400, according to the PLA method as described in the Materials and Methods. Using a scanning confocal microscope, images were obtained at 2.016 by 2.016 megapixel resolution and Z-projected images derived from 47 slices taken at 0.292µm intervals using a confocal pinhole set to 1 AU. All images showing the PLA channel only, with Fire LUT applied in ImageJ. **A**. Maximum z-projections, rendering a total foci count of 37. **B**. Averaged z-projections, rendering a total foci count of 19. **C**. A single one z-sliced image taken using a PLA confocal pinhole of 6.28AU, rendering a total foci count of 14. **Panel D.** Comparison of background noise between image types. **E.** Image statistics. **Sub-panels** indicate i. The source image. ii. The ROI from panel Ai. iii. 4PLAY results.

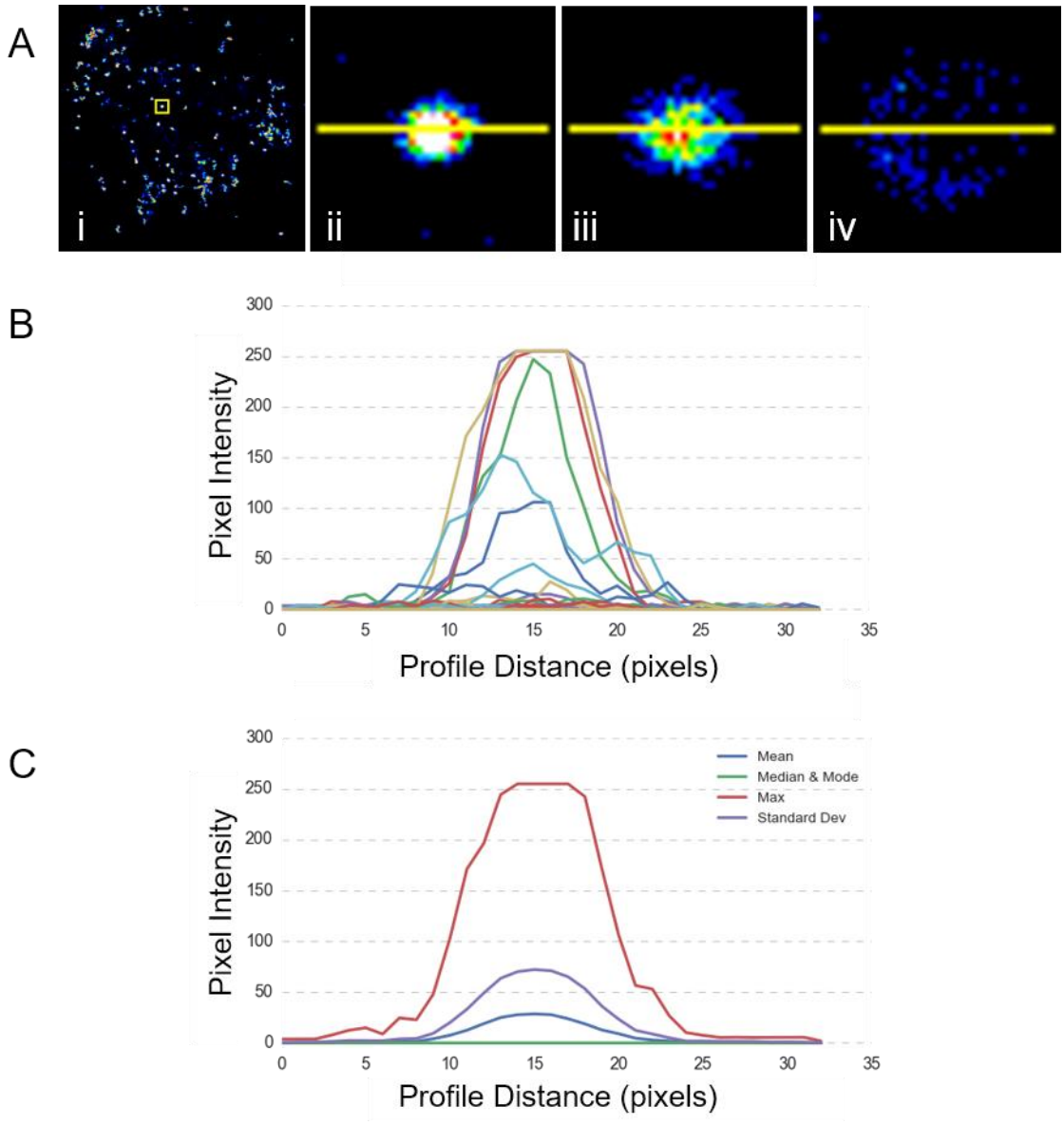

Figure 5.10 The Z-profile Characteristics of a Fluorescent PLA Spot

Images derived from the experiment described in Figure 5.8.

Panel A. ***Inset i.***, A single frame of a 47 frame z-stack showing two cells in the PLA channel, with 16 colour LUT applied in ImageJ. An ROI highlighted in yellow encloses a single PLA spot from which insets ii, iii and iv are derived. **Insets ii, iii and iv.** Frames 10, 12 and 14 respectively show how a 0.292µm step between slices can significantly change the apparent characteristic size and intensity of a spot by capturing out-of-focus light (interpolated images shown for ease of visualisation). **Panel B.** Taking an intensity profile along the straight line ROI bisecting the spot of interest over each of the 47 frames of the z-stack, it can be seen how each pixel varies in intensity as the PLA spot goes in and out of focus. For one frame only the intensity profile of the spot (green profile) has a significantly smaller full width half maximum (FWHM) than in any other z-slice. **Panel C.** Mean (blue), Median and mode (green), maxima (red), and standard deviations (purple), for all 47 frames of the z-stack.

5.4.2 The PLAY Interactive Noise Filter

Initial system calibration was necessary to facilitate the proper discrimination of real foci from that of noise. It was decided early in the PLAY design process that the fastest and most pragmatic implementation of the PLAY ecosystem required a one-time pass of the 4PLAY routine with reliance being placed on the end-user to utilise the graphics of PLAYmate to aid in the choosing of the best noise-filtering algorithm for each experimental dataframe.

Without the implementation of a noise filter, false positive results may be recorded from PLAY even in negative control assays which were used with only a single primary antibody. In essence, such assays should yield very few, if any PLA foci, yet 4PLAY implements an algorithm which scours the image for any intensity peaks. From one peak, however small, 4PLAY will go on to look for others at relatively similar intensities. Thus, in the low or zero signal environment of a negative control assay (Figure 5.11A), 4PLAY will tend to find many hundreds of peaks which were hitherto just peeking over the noise floor. In contrast, within a cell or ROI where there are one or more real PLA foci, other peaks have to be proportionally intense in value if they are to register as valid foci in the PLAY dataframe. Thus, PLA foci with intensities close to the noise-floor are ignored with only genuine PLA foci registered, even if there is only a single PLA fluorescent spot in the entire cell (Figure 5.11B).

Upon further examination of unfiltered images (Figure 5.12A), it can be clearly seen that the negative controls (use of only one single primary antibody) tend to have foci registering much further down in the intensity spectrum relative to cells stained with 2 primary antibodies producing real PLA rolling circle amplification (RCA) products. Looking into the intensity values closer to the noise floor, it can be seen that the total integrated intensity values of the negative control assay as a whole have a mass of foci shown with modal intensity around 500, and still with a significant proportion at less than 1500. Considering that the maximum spot intensity value from a genuine PLA source is 33,050 (a value 22 times more intense than this modal number (Figure 5.12C)), then adding a threshold filter at 1500 to remove such foci with low intensities would be a good first foray into defining the perfect filter set for a PLA experiment.

To further improve the noise filter, PLAY allows manipulation of further thresholding criteria linked to Maxima pixel intensity ‘Max’, Average overall pixel intensity of a spot ‘Av’, as well as being able to specify area criteria ‘Area’ (Figure 5.12D). By manipulating all these filter criteria in conjunction with the visual output of the PLAYmate bar-charts showing foci count information (Figure 5.12E) with relative ease the user can get a good insight into what are the best filtering criteria for each experiment. Real Foci are distinct in their general size, intensity, and individual pixel characteristics, meaning that when the user is close to establishing a perfect noise filter, further slight manipulation of thresholds has little effect on the foci numbers displayed in the bar-chart and in tabular format – another readily accessible PLAYkit tool (Figure 5.12C)

Once a reasonable filter has been established, and the intensity spectra of both negative controls and wild type assays take on a more highly spread form (Figure 5.12B) then the user can continue directly to use other analysis PLAYkits certain in the knowledge that noise will no longer play a significant role. However, it may be useful for the researcher to perform a direct check of some images to compare manually counted foci numbers with PLAY defined foci. Of course, the automated analysis will always differ to some extent compared to a human count. The ability for PLAY to detect out-of-focus PLA spots by allowing larger areas of foci pixels all at lower general intensities (Figure 5.10A) allows some degrees of freedom in how an automated count may be allowed to function. Of course, in many respects defining a perfect filter is not simply a Sisyphean task, but also a pointless one. If filter criteria are approximately right (however that is defined), consistent and objective filtering criteria ensure that every spot in every cell in every image is treated with the very same critical *in silico* eye, making analysis reproducible and fundamentally an exercise in comparison of the different species under test rather than simply a spot counting procedure.

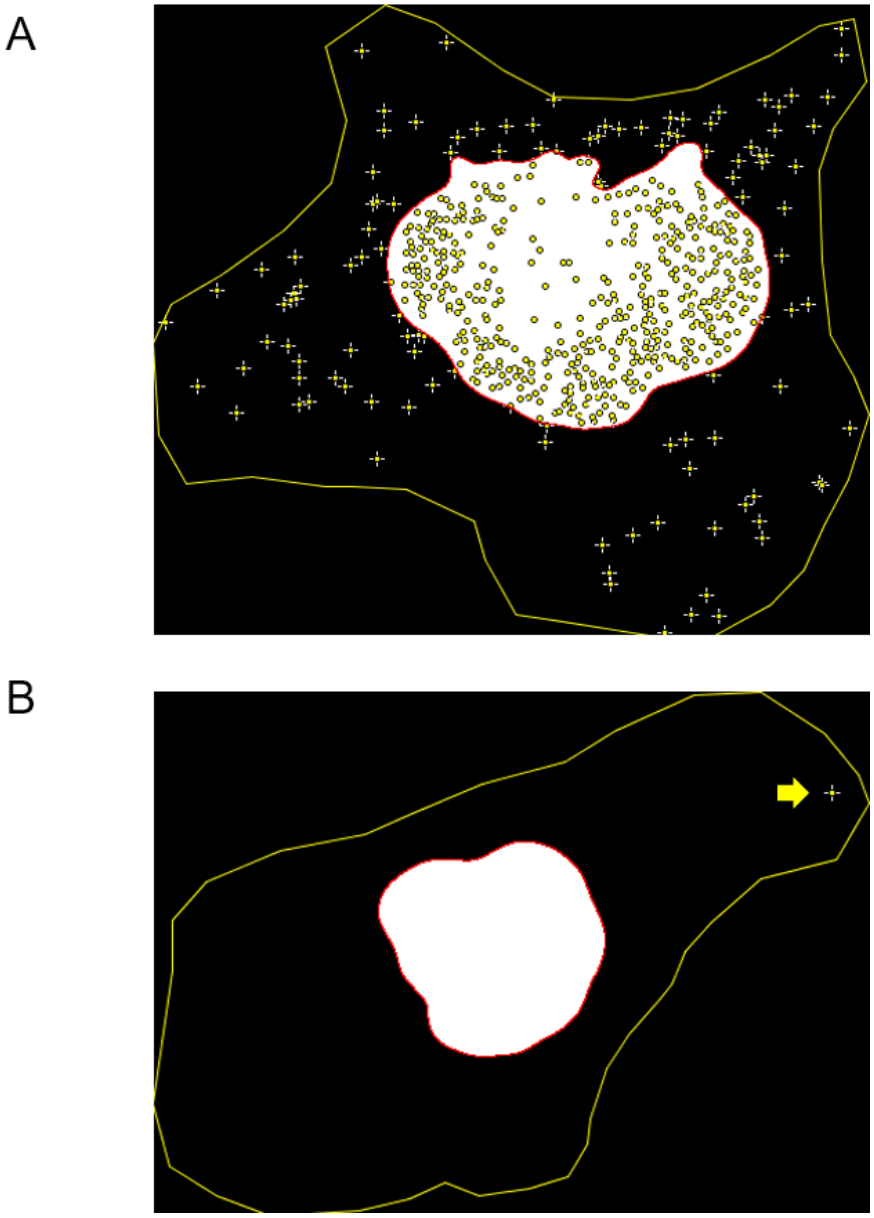

Figure 5.11 Without the presence of single genuine PLA foci, negative control assays register large numbers of false positive PLA foci

Cells were seeded onto coverslips coated with 8µg/cm^2 collagen I, at a density of 15,000 cells/cm^2 and incubated in MEM with 15% (v/v) FCS at 37ºC for 40 mins. Cells were fixed using 4% PFA, saponin permeabilised and dual immuno-fluorescence stained with only a single primary antibody, anti-DDX3X (Ab52) diluted at 1:1000 according to the PLA method as described in the Materials and Methods, to make a negative PLA control. **Panel A:** An ROI from the negative control assay post-4PLAY processing, showing the results of the FindFoci algorithm, identifying over 400 foci of low total intensities (cytoplasmic foci registration visualised with cross-hairs and nuclear foci visualised as circular). **Panel B:** An ROI from a negative control assay post 4PLAY processing, showing the results of the FindFoci algorithm which has identified a single genuine PLA spot of medium total intensity within the cytoplasmic region of a cell (shown by arrow).

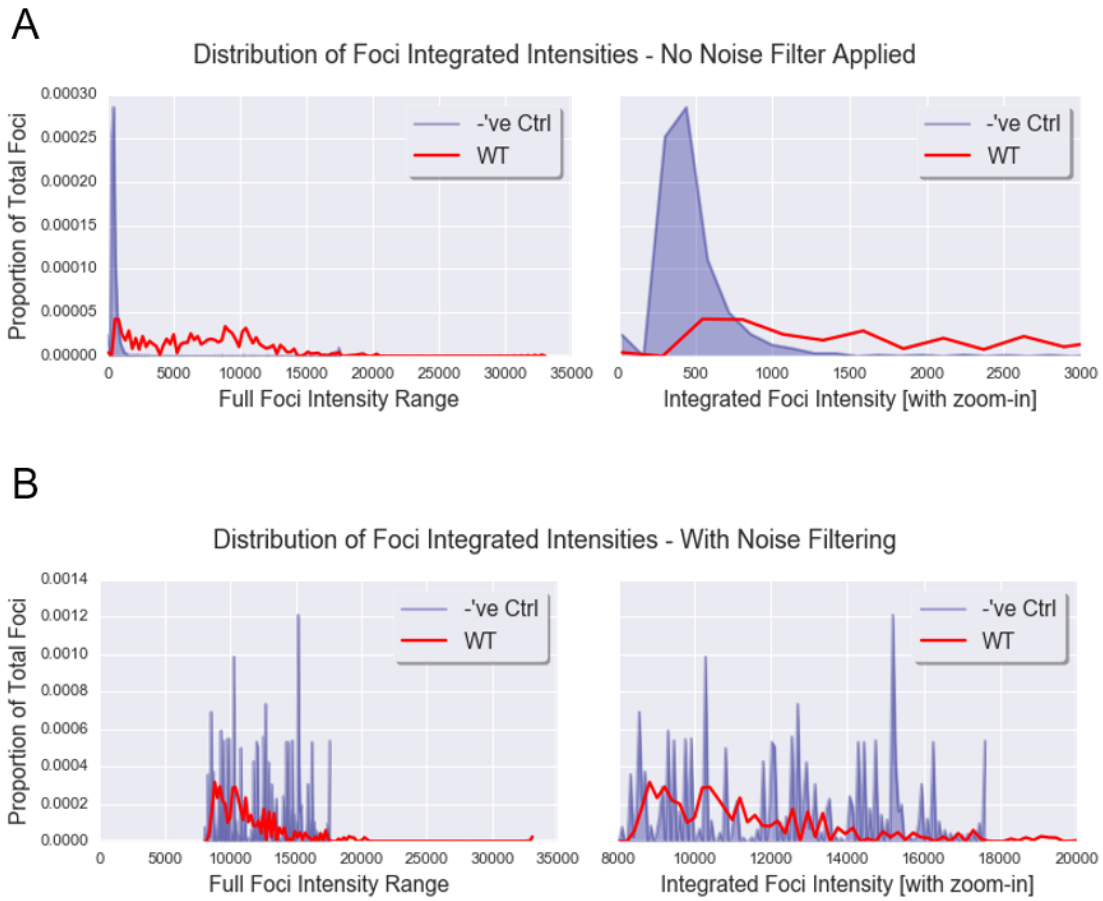

Figure 5.12
Foci Intensity Analysis and the effect of Noise Filters

Cells were seeded onto coverslips coated with 8µg/cm^2 collagen I, at a density of 15,000 cells/cm^2 and incubated in MEM with 15% (v/v) FCS at 37ºC for 40 mins. Cells were fixed using 4% PFA, saponin permeabilised and dual immuno-fluorescence stained with anti-DDX3X (Ab52) diluted at 1:1000 and anti-eIF4E (Ab106) diluted at 1:400, according to the PLA method as described in the Materials and Methods. Using a scanning confocal microscope images were obtained using a confocal pinhole set to 6.8AU for the PLA channel, and 1AU for the DAPI channel. Foci intensities were analysed using PLAYmate, part of PLAY - a novel PLA analysis software created especially for this project and discussed in this chapter. **Panel A.** Pre-noise filtering, a comparison of foci intensities from a typical MRC-5 (WT) cell shown in red, and that of a typical MRC-5 cell used as a negative control in the PLA assay. Virtually all foci found in the negative control have intensity values below 1500, compared to WT with genuine PLA spots ranging in intensity from around 2000 to over 30000 for the very brightest. **Panel B.** After the application of a noise filter to threshold foci values, integrated foci intensity spectra were re-examined. Plots show a comparison of WT to negative controls [left inset], with magnified views of the lower region of the intensity spectrum [right inset].

C

	Negative Control		Wild Type	
	Without filter	WITH Filter	Without filter	WITH Filter
Number of Foci:	29016	39	2565	287
Mean foci intensity:	146	12258	1844	11142
Maximum Integrated Spot Intensity:	17603	17603	33050	33050
Standard deviation in foci intensity:	502	2663	3782	2804

D

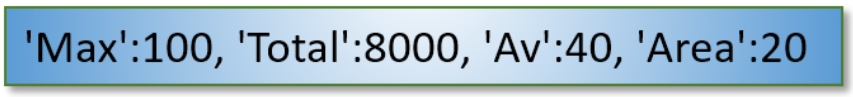

E*i*.

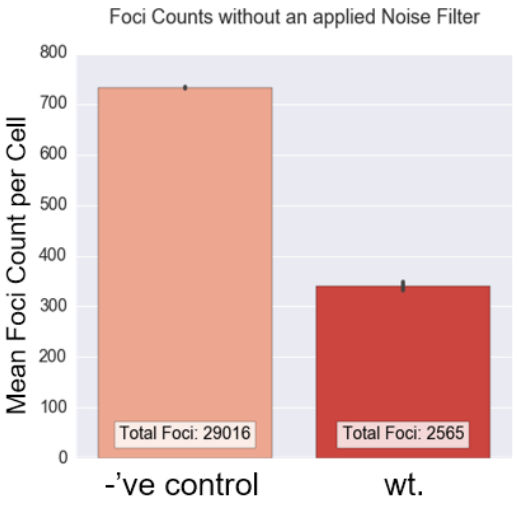

E*ii*.

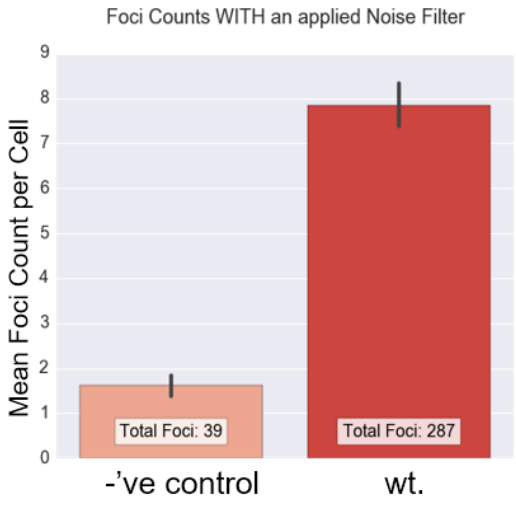

Figure 5.12 (continued)

Panel C. Applying a typical PLAYmate implemented noise filter to a noisy image can significantly reduce the foci count in negative control cells to a number more truly reflective of a manual counting result. In this case it gives a 744 times reduction in the foci count prior to filtering. Using the same filter on the wild type cells, foci numbers are reduced by a factor of 9, most principally due to the occasional cell which shows no 'real' PLA foci but non-PLA foci buried poking out of the noise floor. **Panel D.** A typical (but not generic) noise filter criteria for an 8-bit image. **Panel E.** Comparison of mean foci counts per cell show that without applying a noise filter, the 4PLAY program searches the noise floor to find putative foci peaks if no 'real' PLA foci exist in the negative control cells (inset i.). In wild type cells, a single PLA spot found in a cell causes the 4PLAY program to halt further searches for foci close to the noise floor. Thus the algorithm is much more likely to find only 'real' foci (real foci being those which would otherwise be identified as spots by manual spot counting). A filtering process can reduce foci counts in negative control images as well as those with anticipated PLA foci (inset ii).

5.5 PLAY System testing

As part of an investigation into the role of DDX3X in cellular translation processes (Chapter 6), the CRISPR/Cas9 targeted gene editing system was utilised with the aim of making a DDX3X genetic knockout of the MRC-5 SV2 hyper-diploid cell line. The result of the gene editing was a partial knockout of DDX3X protein expression (Chapter 6) in a new cell line named “KO:2a”. Having a cell line expressing approximately 30% of normal levels of DDX3X was seen as an opportunity to test the robustness of PLAY. Therefore, an assay was performed using both the knockdown cell line and parental wildtype (WT) MRC-5 SV2 cells; both were also utilised for the creation of negative controls, where only one of the pair of primary antibodies was added in the PLA process. Imaging was performed as described in the Materials and Methods. Post-acquisition processing was performed using PLAY, with a noise filter setting of ['Area': 20, 'Av': 0,'Max': 40, 'Total': 1400]; some basic PLAYkits were further utilised to test for PLAY program robustness.

5.5.1 Interrogating the dataset using Scatterplots.

To get a better understanding of basic PLA spot characteristics, scatterplots were utilised to visualise the relationship between the area of each DDX3X:eIF4E PLA spot and its overall integrated ‘total’ intensity (Figure 5.13).

Although the Pearson r value was only 0.33 for the entire dataset (Figure 5.13A), the scatterplot shows a visually compelling suggestion that a subset of outliers might be skewing the overall resulting correlation value, with a large swathe of foci of relatively low total intensity (<5000). They also displayed some of the largest overall foci sizes, implying that the average pixel intensity would be very low and certainly not characteristic of the typical small, bright PLA spot for which the assay is so well known.

Experimental controls are visualised together in Figure 5.13B, and comparison of this controls scatterplot is performed against the individual scatter plots of the DDX3X-knockdown assay (Figure 5.13C) and wild type MRC-5 SV2 cells (Figure 5.13D). It becomes evident here that the controls contribute significantly to depressing the overall assay correlation statistic. These data show an almost bimodal appearance to their scatterplots inferring

that many large foci of low integrated ‘Total’ intensity reside in the control samples. Having already followed the normal procedure to define the noise filter such that it worked sufficiently well when compared to a spot count by eye, it was realised that the issue flagged up here was directly related to the focus of the confocal microscope during image capture.

Mapping only the maximum spot intensity values (Figure 5.14), both DDX3X knockdown and parental (WT) cells show, coincidentally, 85% of their foci having maximum pixel values at the maximum achievable value of 255 (using 8-bit quantised original images). Both analyses show a relatively even distribution of other intensities down to values on or approaching the noise filter’s implicit intensity threshold of 40.

For controls carried out in both the DDX3X knockdown and parental cells, maximum pixel intensities are achieved in only 43% and 50% of foci, respectively. There is a relatively greater proportion of other pixels spread evenly throughout the entire remaining intensity range. As already indicated, automated analysis differs to some extent compared to a human count, as PLAY can pick up out-of-focus PLA spots from images. Out-of-focus spots with lower pixel intensities over a greater area are found in the negative control groups only. When imaging cells which harbour genuine PLA foci, these foci can often be seen throughout the cell body stretching to the limits of the cellular membrane at the leading edge of lamellipodia protuberances. During the image capture process, large concentrations of fluorescent light in both the DAPI and PLA channels provide a navigational guide in finding the required near-basal imaging plane, necessary to fully capture protein interactions in lamellipodia. PLAY can assign out-of-focus light to a single central putative source, thereby registering a spot observation even when light levels are distributed over several pixels. So, although the controls show potentially bimodal correlation between foci area and spot intensity, this will not affect the spot count other than to raise the observation numbers where PLA foci are present but not directly located in the focal plane.

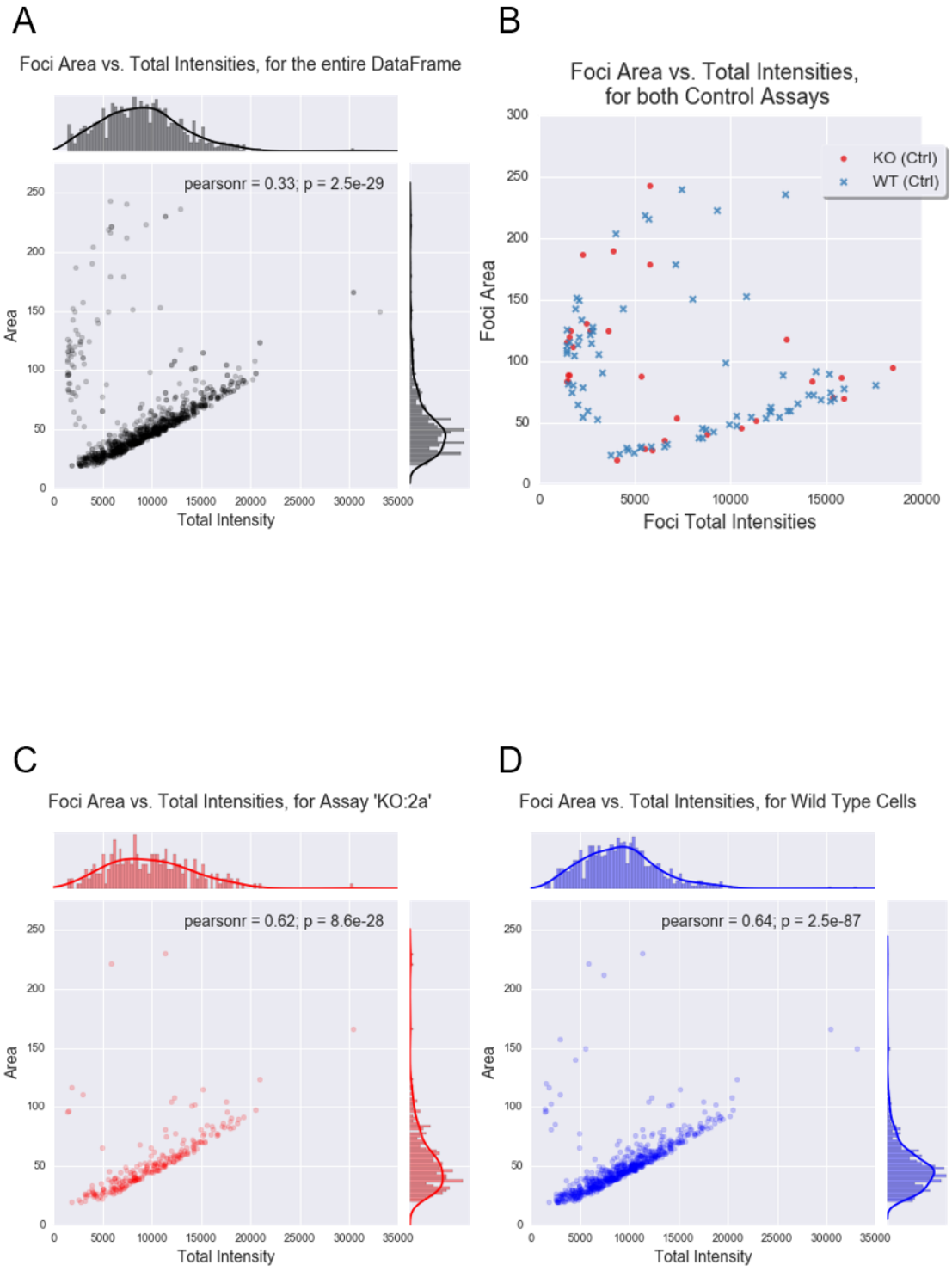
A
Foci Area vs. Total Intensities, for the entire DataFrame
pearsonr = 0.33; p = 2.5e-29
Area
Total Intensity
B
Foci Area vs. Total Intensities,
for both Control Assays
KO (Ctrl)
WT (Ctrl)
Foci Area
Foci Total Intensities
C
Foci Area vs. Total Intensities, for Assay 'KO:2a'
pearsonr = 0.62; p = 8.6e-28
Area
Total Intensity
D
Foci Area vs. Total Intensities, for Wild Type Cells
pearsonr = 0.64; p = 2.5e-87
Area
Total Intensity

Figure 5.13 Genuine PLA foci contribute towards a correlation of foci intensities and their size

In an assay of two different cell lines, putative CRISPR generated DDX3X knockout cells (KO:2a), and MRC-5 SV2 wild type cells were seeded on to coverslips coated with 8µg/cm^2 collagen I, at a density of 15,000 cells/cm^2 and incubated in MEM with 15% (v/v) FCS at 37ºC for 40 mins. Cells were fixed using 4% PFA, saponin permeabilised and dual immuno-fluorescence stained with anti-DDX3X (Ab52) diluted at 1:1000 and anti-eIF4E (Ab106) diluted at 1:400, according to the PLA method as described in the Materials and Methods. Negative controls were created for both cell lines by the exclusion of primary anti-DDX3X antibodies from the protocol. Using a scanning confocal microscope images were obtained using a confocal pinhole set to 6.8AU for the PLA channel, and 1AU for the DAPI channel. Cell and PLA foci attributes were analysed using PLAYmate, part of PLAY - a novel PLA analysis software created especially for this project and discussed in this chapter. PLAY noise filter attributes were set to: 'Area': 20, 'Av': 0,'Max': 40, 'Total': 1400.

Panel A: Scatterplot for the entire assay including putative knockout KO:2a, KO:2a negative control, wild type MRC-5 SV2 cells and associated negative control. The analysis shows little overall correlation between the total area of each spot when compared to its ‘total intensity’ (i.e. integrated intensity value), with the Pearson r value low (0.33) due to primarily the bimodality characteristic in the plot. **Panel B:** The scatterplot of just the negative controls show that most of the secondary mode of scattering in the entire assay (Panel A) is by a contribution from the negative control assays, most notably from the wild type control. **Panels C and D:** With the controls eliminated from the plots, both the putative knockout and WT assays show a much stronger correlation in their plots (with Pearson r values of 0.62 and 0.64, respectively), suggesting that both measurements may be seen to be reasonable proxies of one another.

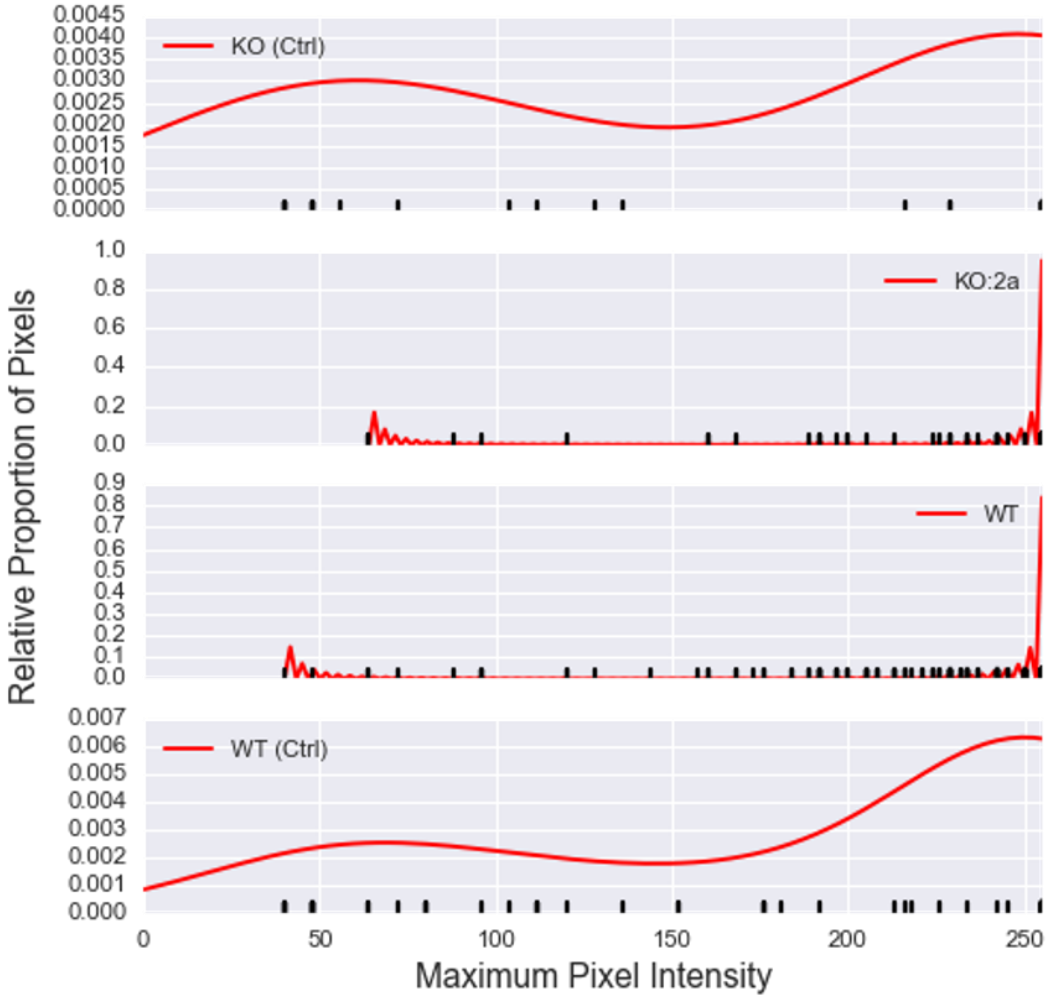

Figure 5.14 Pixel Intensity Analysis

In an assay of two different cell lines, putative CRISPR generated DDX3X knockout cells (KO:2a), and MRC-5 SV2 wild type cells were seeded on to coverslips coated with 8µg/cm^2 collagen I, before further treatment with DDX3X and eIF4E antibodies, according to the PLA protocol described in Figure 5.12. Analysis of resultant images was performed using PLAY software. Rug-plots and kernel density estimates (KDEs) with a bandwidth defined using Scott's equation (Scott, 1979) were plotted for all assay types, to show the relative proportion of pixels at specific intensities over an entire PLA assay. For the negative control knockout assay - KO (Ctrl), out of 30 foci, 13 (43 %) have the maximum obtainable intensity and for the experimental assay KO:2a , out of 246 foci, 210 (85 %) have the maximum obtainable intensity. For the experimental wild type (WT) assay, out of 748 foci, 638 (85 %) have the maximum obtainable intensity, and for the wild type control assay - WT (Ctrl), out of 75 foci, 38 (50 %) have the maximum obtainable intensity. Pixel intensity analysis shows a much smaller quantity of pixels reaching the maximum intensity value for both control groups as compared to the two other experimental assays.

5.5.2 Correlation Mapping

Perhaps one of the most useful PLAYkits to allow the researcher to visualise potential relationships between assay measurements is the correlation mapping tool (Figure 5.15). Performing correlations on an entire dataset may be interesting, but only when subsets of the assay are used do correlation maps come into their own. A correlation map for the Wild Type assay (Figure 5.15) provides Pearson r values for all 21 PLAY measured attributes, allowing a visual scan of all relationships to find potential areas of interest which may be worthy of further investigation. To visualise relative changes between assays, 'difference of correlation' mapping is also available in PLAYkits, and a detailed explanation of their use is covered in Chapter 7.

5.5.3 PLAYkit Distribution Charts

PLAYkit's 'Distribution Charting' consist of 3 subplots: A Violin plot, box plot and plot of means. Each provides the researcher with meaningful information about a DDX3X:eIF4E characteristic distribution in spreading cells (Figure 5.16A).

The default plotting mode creates Violin plots utilising Scipy's implementation of Scott's rule of thumb for bandwidth selection, to produce either a Kernel Density Estimate (Terrell & Scott 1992) or a smoothed histogram. This reveals the structure and gross distribution of the underlying data points. No kernel 'cut-off' is applied by default (which can be changed by the advanced user). If applied, the MWW defined p-value is provided here, to signify the likelihood of the populations being equal.

The box plot shows information about a sample's median, spread, asymmetry and of the outliers. In addition, a 95% confidence notch is applied by default to the median value. N statistics, such as the default Cell/ROI number are also applied at the bottom of each bar plot.

The "Plot of Means", provides a zoomed in y-axis, giving more visual definition to their confidence intervals. 95% confidence intervals are applied by default and are visualised as notches around the mean values, with statistical significance p-values calculated using Welch's t-test and indicated graphically with asterisks.

PLAYmate's statistical output for the 'Spot Max Intensity' assay characteristics consists of a list of assay median values, Welch's t-test t-statistics and p-values and a normality test and MWW test with U-statistics and associated p-values (Figure 5.16B). For all significance testing, be it a t-test or non-parametric test such as the MWW, by default one star signifies $p \leq 0.05$, two stars signify $p \leq 0.01$ and three stars signify $p \leq 0.001$.

5.5.3.1 Characteristic Distributions of the Test Assays

Spot Max Intensity Profile

By examining the Spot Max Intensity Graphical Distribution (Figure 5.16), as well as the statistics profile, several conclusions can be drawn. Bi-modality dominates the controls, with maximum spot intensity values concentrated at or close to the maximum possible (255) as well as at the lowest end of the of the range where KO(Ctrl) in particular has substantial concentrations (an entire 1st quartile) close to the noise filter threshold value of 40. The large confidence intervals of the KO(Ctrl) median and mean points indicate that foci numbers are lowest in this assay, and the median value (222.5) also suggests that levels of well-defined PLA foci were low. WT(Ctrl) has more real foci (reaching intensities of 255), but again the CIs are wide in comparison to the experimental groups, providing clear evidence of greater deviation in values. The entire upper 3 quartiles of the experimental groups clump to the 255 value, with very small Cis, indicating that PLA was functioning correctly.

The Central Limit Theorem (Hannan 1978) states that the sample mean $\overline{X}$ follows approximately the normal distribution with mean μ and standard deviation $\frac{\sigma}{\sqrt{n}}$, where μ and σ are the mean and standard deviation of the population from where the sample was selected. If the population is non-normal, to rely on a t-test such as Welch's, the sample size n has to be large (usually $n \geq 30$). If the population follows the normal distribution, then the sample size n can be smaller yet still rely on Welch's t-test for a good representation of the population mean (μ).

All assays fail D'Agostino and Pearson's Omnibus Test of Normality, but since sample sizes are above 30 for all assays, Welch's (two-sided) t-test

was chosen as a suitable test for the null hypothesis that two independent samples have identical mean values. It's noteworthy that the MWW test also results in the similar statistical p-values for the null hypothesis that two samples come from the same population.

Using Welch's t-test, the sample data supports the null hypothesis (H0) that the two populations KO:2a and WT have equal means, and there is sufficient evidence to warrant rejection of the claims (H0) that each group KO:2a and WT have equal means to their respective control groups. This is simple statistical evidence to show that the foci located in the control groups are different to those in the experimental groups, as expected from foci derived from other sources than PLA fluorescent reactions.

Intercellular Adjacency

Intercellular adjacency is known to have an influence on cellular growth, but how it affects cells or DDX3X and eIF4E association by PLA after seeding is unknown. Time constants influence both chemokine production and diffusion, so for a spreading assay finding correlations between adjacencies and cell shape or endogenous protein colocalisation would itself be of considerable interest. However, this assay was soon to raise some interesting technical limitations in the conduct of such tests (Figure 5.17A). The first limitation is found buried in the PLAY dataframe. In this assay, the 4PLAY routine for collecting adjacency measurements was seen to fail for a small proportion of cells. Upon investigation, it was seen that an initial 4PLAY spline fit of the cellular ROIs was the cause. The imageJ implementation of spline fitting enables jagged ROIs composed of multiple straight lines encompassing a cell periphery, to be converted to a single smooth continuous curve which passes through all the points that connected the original lines. Spline fitting introduces a more natural looking periphery curve to the ROI, but in so doing will also introduce other unwanted fitting anomalies which don't properly reflect the real periphery of the cell. Creating an option to not spline fit (implemented in a later version of the software) solved this issue. For close neighbouring cells, a manually drawn ROI around the cellular perimeter will have these two ROIs coming within just a few pixels of each other (Figure 5.6). A spline fit will

automatically introduce a convex form to some areas of these cellular envelopes, often pushing the envelopes to nearly touch, or in some cases cross each other entirely. When ROIs touch, the ImageJ 'Graph' plug-in assumes the two ROIs enclose one single large cell, and so any adjacency matrix formed of the ROIs in the image becomes adulterated and partially filled with NaN ('Not a number').

As with all measurements held on the dataframe, the 'pixel' is the default measurement unit with conversion to metric performed by PLAYmate if and when the user requires, this is simply to obtain dataframe consistency.

Calculated Median adjacency figures [KO (Ctrl)=49.04; KO:2a=9.22; WT=10.77; WT (Ctrl)=40.80] (Figure 5.17B) are significantly higher in magnitude within the control groups, showing an unusual inconsistency in cell seeding, which may have been procedural and an aspect due to the miscounting of cells prior to seeding. Welch's t-test completely fails due to NaNs in the adjacency data series. However, Scipy's implementation of MWW manages NaN values better and the algorithm results in p-values showing that the distribution of adjacency distances between KO:2a and WT are significantly different. By eye, neither the violin nor box plots (Panel A) indicate a significant difference in distribution other than for a number of outliers in the WT spanning up to 800 pixels in distance. Median values between the two groups are similar at 9.2 and 10.7pixels for the DDX3X knockdown (KO:2a) and WT cells, respectively, implying a consistent seeding density over the two assays.

Perhaps the most apparent deficiency with this measurement comes from the data collection protocol, where cells on the periphery of the image may or may not be in close vicinity to cells located just outside of the image under review (Figure 5.6). For adjacency results to be more robust, cells on the periphery of each image would have to be ignored to eliminate unknown adjacencies with cells outside the field of view. Alternatively, image collection would have to be performed so as to create a single large mosaic consisting of multiple images, prior to PLAY processing. Until these protocol techniques are fulfilled, adjacency measurements should be interpreted with the full understanding of the limitations introduced by the particular imaging technique used in their capture.

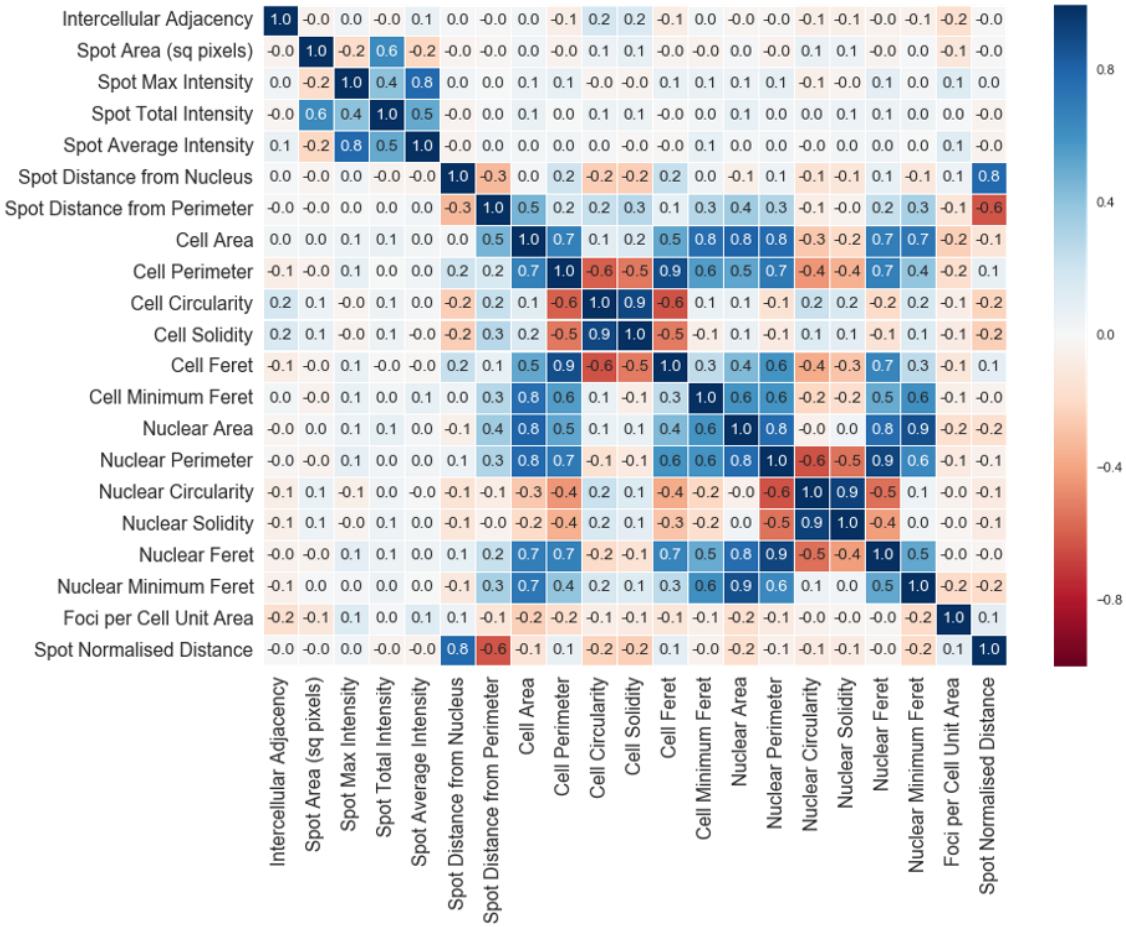

Figure 5.15 The Correlation Map PLAYkit

The correlation mapping PLAYkit is perhaps one of the most useful PLAYkits in that it allows the researcher to visualize potential relationships between a host of assay measurements in a single heat-mapped image.

MRC-5 SV2 wild type cells were seeded on to coverslips coated with 8µg/cm^2 collagen I, before further treatment with DDX3X and eIF4E antibodies, according to the PLA protocol described in Figure 5.12. Analysis of resultant images was performed using PLAY software.

A correlation map for the wild type MRC-5 SV2 cell assay provides Pearson r values for all 21 PLAY measured attributes, allowing the researcher to quickly perform a visual scan of all relationships to find potential areas of interest which may be worthy of further investigation. To visualise relative changes between assays, ‘difference of correlation’ mapping is also available in PLAYkits.

A

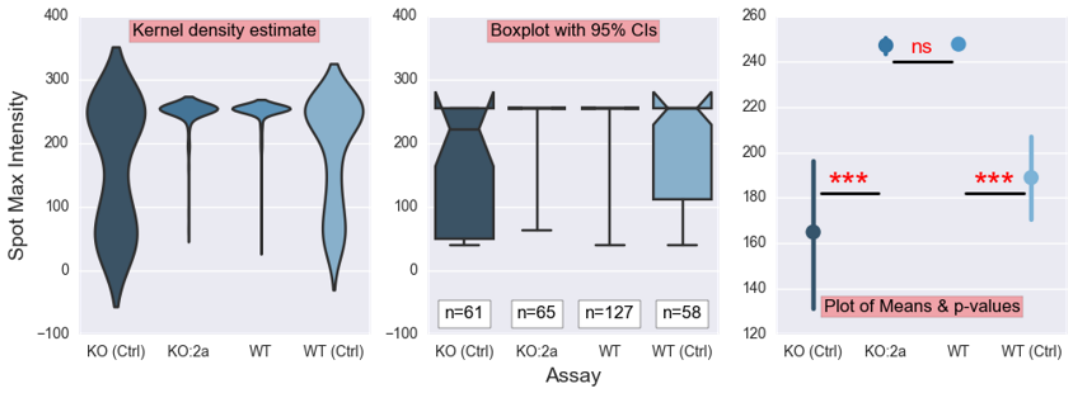

B

```
Spot Max Intensity Statistics Profile:

Noise filter settings:
Area:20, Maximum Intensity:40, Total Intensity:1400, Average Intensity:0

Calculated median values:
KO (Ctrl)=222.50; KO:2a=255.00; WT=255.00; WT (Ctrl)=255.00;

Welch's t-Test:
Between KO (Ctrl) & KO:2a:              t-stat:-4.70 p-value=5.59E-05 (***)
Between KO:2a & WT:                     t-stat:-0.27 p-value=7.87E-01 (ns)
Between WT & WT (Ctrl):                 t-stat:6.09 p-value=4.39E-08 (***)
Between KO (Ctrl) & WT (Ctrl):          t-stat:-1.21 p-value=2.33E-01 (ns)

D'Agostino and Pearson's Omnibus Test of Normality:
For assay KO (Ctrl):                    p-value=5.08E-11 [*]
For assay KO:2a:                        p-value=5.42E-58 [*]
For assay WT:                           p-value=3.62E-166 [*]
For assay WT (Ctrl):                    p-value=6.44E-06 [*]
*  Test failed. If sample size is >30 continue to use Welch's t-Test.
   If >20 but <30, consider use of the MWW test.

Mann-Whitney-Wilcoxon (MWW) test:
Between KO (Ctrl) & KO:2a:              U stat=0.00 p-value=3.64E-10 (***)
Between KO:2a & WT:                     U stat=1.00 p-value=9.96E-01 (ns)
Between WT & WT (Ctrl):                 U stat=0.00 p-value=3.60E-17 (***)
Between KO (Ctrl) & WT (Ctrl):          U stat=0.24 p-value=2.36E-01 (ns)
```

Figure 5.16 Distribution Charts for 'Spot Maximum Intensity'
Cells were processed and analysed as described in Figure 5.12.
Panel A: Bi-modality dominates the controls, with maximum spot intensity values concentrated at or close to the maximum possible (255) as well as at the lowest end of the of the range where KO(Ctrl) in particular has substantial concentrations (an entire 1st quartile) close to the noise filter threshold value of 40. The entire upper 3 quartiles of experimental groups (KO:2a and WT) clump to the 255 value, with very small CIs we can be confident that PLA was functioning correctly. **Panel B:** PLAYmate's statistical output for the 'Spot Max Intensity' assay characteristics, consisting of a list of assay median values, Welch's t-Test t-statistics and p-values, a normality test and MWW test with U-statistics and associated p-values.

A

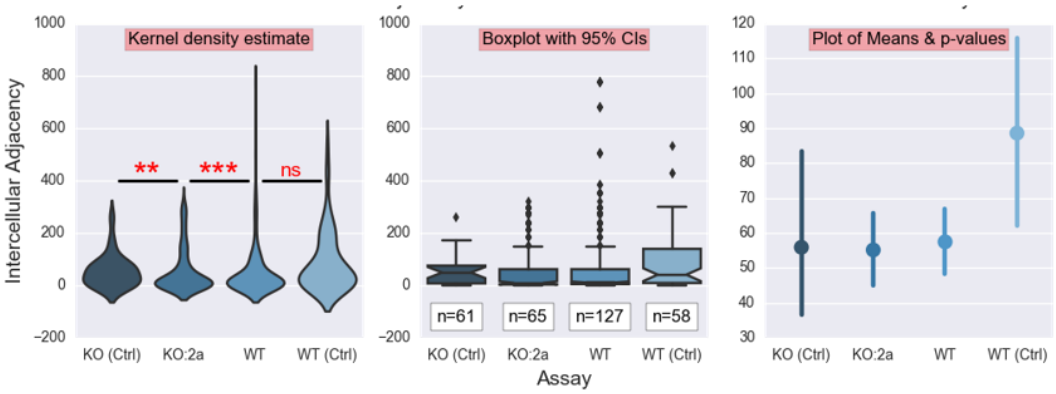

B

```
Intercellular Adjacency Statistics Profile:

Noise filter settings:
Area:20, Maximum Intensity:40, Total Intensity:1400, Average Intensity:0

Calculated median values:
KO (Ctrl)=49.04; KO:2a=9.22; WT=10.77; WT (Ctrl)=40.80;

Welch's t-test:
Between KO (Ctrl) & KO:2a:              t-stat:nan p-value=NAN ( ns )
Between KO:2a & WT:                     t-stat:nan p-value=NAN ( ns )
Between WT & WT (Ctrl):                 t-stat:nan p-value=NAN ( ns )
Between KO (Ctrl) & WT (Ctrl):          t-stat:nan p-value=NAN ( ns )

D'Agostino and Pearson's Omnibus Test of Normality:
For assay KO (Ctrl):                    p-value=NAN
For assay KO:2a:                        p-value=6.81E-18 [*]
For assay WT:                           p-value=NAN
For assay WT (Ctrl):                    p-value=NAN
*  Test failed. If sample size is >30 continue to use Welch's t-Test.
   If >20 but <30, consider use of the MWW test.

Mann-Whitney-Wilcoxon (MWW) test:
Between KO (Ctrl) & KO:2a:        U stat=0.00 p-value=3.26E-03 ( ** )
Between KO:2a & WT:               U stat=0.00 p-value=1.09E-14 ( *** )
Between WT & WT (Ctrl):           U stat=0.63 p-value=6.34E-01 ( ns )
Between KO (Ctrl) & WT (Ctrl):    U stat=0.95 p-value=9.49E-01 ( ns )
```

Figure 5.17 Plotting the distribution of intercellular adjacencies.
Cells were processed and analysed as described in Figure 5.12.

Panel A: Intercellular adjacency is known to have an influence on cellular growth, but how it effects the association of DDX3X with eIF4E has yet to be investigated. These data analyse correlations between adjacencies and cell shape or endogenous protein co-localisation. **Panel B:** The tabular PLAYkit output provided by PLAY fails normality testing due to 4PLAY's spline-fitting of some close-neighbouring ROIs.

5.5.3.2 Analysis of the Foci Area

Spot Area

The ‘Spot Area’ analysis (Figure 5.18A) shows statistically that the foci areas of genuine PLA spots differ dramatically from non-PLA foci seen in the control groups. Median values for KO:2a and WT are 49 and 46 pixels, respectively, which at less than 10% difference suggests that the technical protocol for finding a consistent plane of focus between images and individual cells was pragmatic and able to meet expectations of reasonable consistency. The KDE for both control groups was relatively broad throughout a larger range of values, implying a lack of strong point sources of fluorescence and no particular focal sweet-spot, which is to be expected.

Spot Total Intensity

Actual Spot Total Intensity Statistics data returned by PLAY (Figure 5.18A) showed that normalised (relative to WT) median values for the total intensities of Foci were: KO(Ctrl): 61%; KO:2a: 105%; WT: 100%; WT(Ctrl): 65%, with experimental groups expressing a large proportion of defined PLA foci. This data is shown graphically most effectively in the box-chart of Figure 5.18B. Other than having a protocol aimed at consistent focusing throughout all assays, achieving a general consistency in PLA foci mean intensity also implies that the focal plane is likely consistent between slides and assays. If most of the PLA foci are in the thin lamellipodia, then a consistent focus on those lamellipodia will render similar intensity foci. The overall closeness of both control means and non-control means also implies experimental consistency.

Spot Average Intensity

Examination of the Spot Average Intensity Statistics Profile (Figure 5.18C) indicated that there is a clear bimodality to the control groups which is non-existent in the experimental groups. Controls also exhibit an additional clumping of intensity values on or around the filter threshold (40) for Maximum [pixel] intensity. These data suggest a strong case for attempting an additional filter setting of approximately 100, particularly given that this value falls below all four quartiles of the box plot for non-control assays.

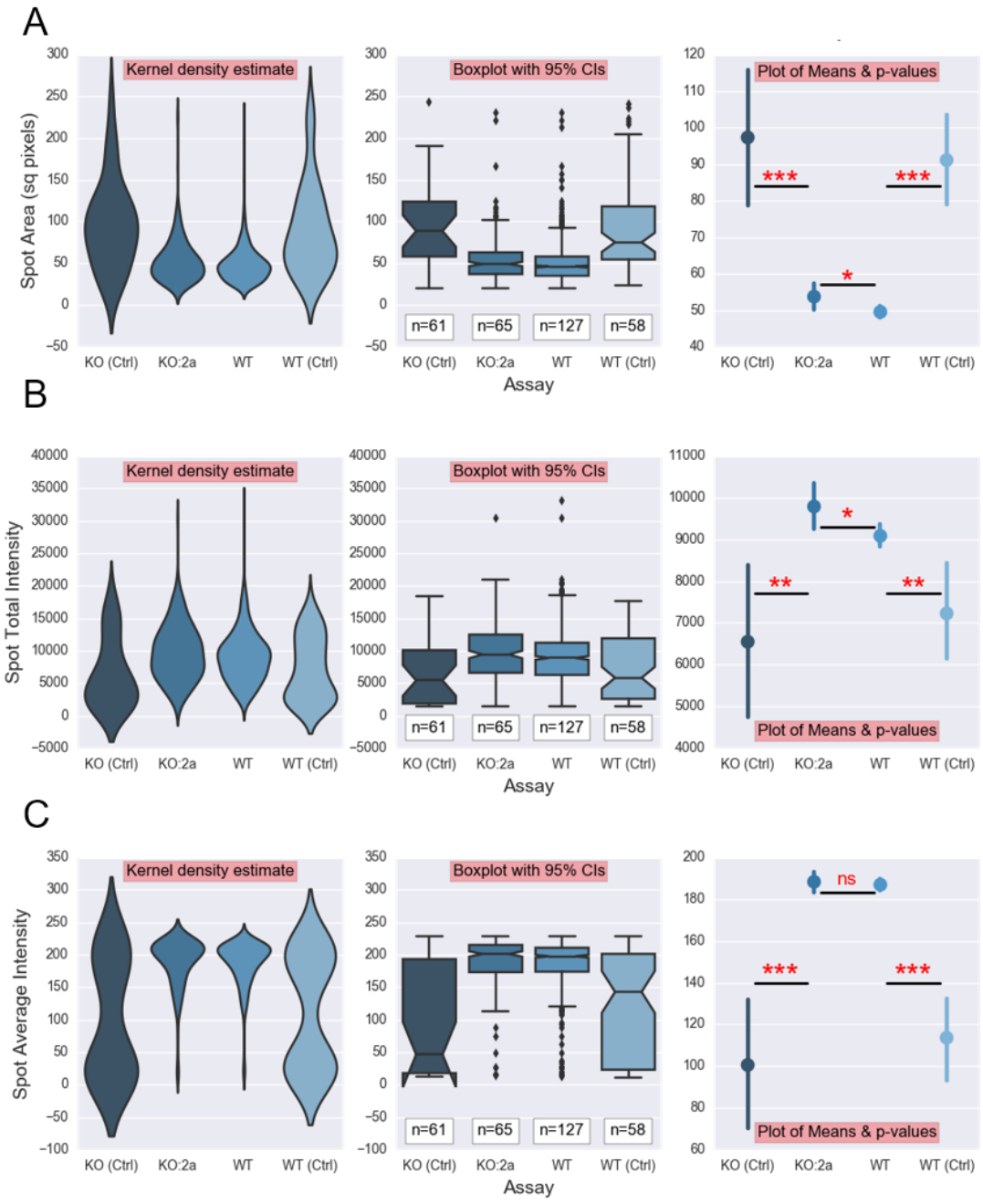

Figure 5.18 DDX3X:eIF4E PLA Spot Characterisation
Cells were processed and analysed as described in Figure 5.12.

Panel A. PLA spot sizes (area). KO:2a and WT cells have spot areas of 49 and 46 pixels respectively, which at < 10% difference suggests that the technical protocol for finding a consistent plane of focus between images and individual cells was pragmatic and able to functioned to meet expectations of reasonable consistency. **Panel B: Spot total (integrated) intensity.** The overall closeness of both control means and experimental means implies experimental consistency. **Panel C: Spot average pixel intensity.** There is a clear bimodality to the control groups is non-existent in the experimental groups, with a concentrations around the 200 mark for experimental groups, signifying sharp, bright and defined PLA spots.

5.5.3.3 Spot Distance from Nucleus Statistics Profile

PLAY may also be utilised to localise foci within the nuclear envelope (Figure 5.19A), or with higher precision distance-mapped within the cytoplasmic region (Figure 5.19B). Spot Distances from both the nucleus and cell perimeter are normalised in a single dataframe series ‘Spot Normalised Distance’ (Figure 5.19C). The data in Panels A and C shows that in DDX3X depleted cells, DDX3X:eIF4E foci remain closer to the nucleus upon spreading cells for 40 minutes, relative to control MRC5 cells.

Relying on Euclidian spot distance measurements from either the nucleus or periphery of the cell can give a misrepresentative account of reality in a population of mixed sizes cells. Using Figure 5.19D as an example, by comparing foci Xμm from the periphery of a well-spread cell (Inset i), with a less spread cell (Inset ii), provides little information about the possible function or effect of such an interaction of proteins. ‘Spot Normalised Distance’ measurements are cell-size ambivalent, providing a simple percentage distance measurement with the ability to place each foci precisely between the nuclear membrane and the closest part of the cell periphery, where a measurement of 0% places a spot in the nucleus or on its nuclear envelope, and 100% places the spot at the cell periphery. Such a normalised measurement does need to be considered with care in cells of low solidity where two foci at a similar distance to the cell periphery (Xμm) will be attributed with widely different normalised distance measurements given the variation in their distances from the nucleus (inset iii).

These data can also be used to analyse cell area, nuclear area, and cell perimeter profiles (Figure 5.20). These data when shown graphically, raise some striking visually differences between the assayed groups: The significant differences shown between control and experimental cell area (Panel A), nuclear areas (Panel B) and cell perimeter lengths (Panel C) may be as a consequence of variation in the focal plane (Panel D). With genuine PLA foci present in the experimental groups (Panel D, inset i), fluorescent light emitted from the PLA foci aid in the establishment of a focal plane (FP) in the near basal membrane locale. Without PLA foci in the lamellipodia of cells (Panel D, inset ii), it is easy to establish a focus in the plane with most fluorescence, be it from

non-specific PLA reactions on the membrane of the cells, or from other sources of fluorescence and auto-fluorescence. This focal plane will tend to be further from the coverslip, the corollary being that the focal plane intersection at the nucleus will produce a larger nuclear profile image than in the experimental groups. This is corroborated with the point plots for the DDX3X knockdown control, where a small mean cell area (Panel A) has an associated shorter mean perimeter length (Panel C) but also a bigger nuclear area than the other three groups.

Figure 5.20A, shows that when analysing DDX3X and eIF4E foci, the relative area means are statistically non-significant between wild type cells, but the KO(control) appears significantly smaller in area than both experimental groups. From the box plots in Panel A, it can be seen that a few large outliers will be skewing the calculated mean values, and extending the 95% confidence intervals shown graphically on the plot of means. Why should the experimental assays be showing such outliers of such large size? There are two possibilities. The first is that such area deviations could be a consequence of the volume of seeding media – with high volumes of media, cells held in suspension near the top of the liquid might take some minutes to drop to the collagen matrix covering the slide, whereas cells in suspension at the bottom of the growth media will start to adhere to the collagen almost immediately. These cells feasibly have minutes within which to start their spreading process before all the other cells have dropped out of suspension (experiments to measure this settle time are yet to be conducted). Such a time lag between the initial and last cells to adhere will undoubtedly introduce a size gradient to the entire assay (a theoretical phenomenon utilised for novel “pseudo-time-course assays” as discussed in Chapter 6). However, a smooth area gradient as one might expect from such a phenomenon would not easily account for outliers *per se*. When Cell Areas (Panel A) are analysed alongside the measurements for Nuclear Area (Panel B) a similar number of large-sized outliers possessing nuclear areas in the region of 2-3 times the size of the median can be seen.

Performing a dataframe query to select all cells in the assays with the following characteristics, it was possible to confirm that the four major outliers in both Size measurement tests for KO:2a and WT were the very same cells:

```
'Nuclear Area'>38000 & 'Cell Area'>200000
```

Indeed, the solo outlier shown for the experimental assays in the Cell Perimeter box-plot (Panel C) was also confirmed to be one of the very same cells.

Performing a correlation analysis between nuclear area and cell area (Figure 5.20E), with a Pearson r score of 0.78 we see that the measurement pairs are highly correlated, corroborating the current theory that cell size and nuclear size are linked in the natural world. This is consistent with the belief that during the cell cycle an increase in DNA content of a cell goes hand-in-hand with an increase in both nuclear and whole cell size (Good 2015; Neumann & Nurse 2007; Webster et al. 2009). In conclusion, because outlier cells were found to have cell and nuclear sizes just over double that of the median, this is strong evidence to suggest that they were in the midst of passing through the G2 phase of the cell cycle, where DNA content and cell mass is at its greatest (approximately double the normal mass) prior to mitosis. To overcome such size discrepancy issues, should they be issues for the experiments undertaken, it would be possible to synchronise the cells in their cell cycles prior to running such tests again.

The software developed here can also be used to investigate a number of cell morphology criteria. As shown in Figure 5.21, measurement can be made of cell solidity and cell circularity. A bivariate KDE plot shows the relationship is strong, with a Pearson r correlation coefficient of 0.9, as would be expected.

Another investigation possible is that of cell Feret (Figure 5.22) as discussed in Figure 5.5. The expectation here is that there should be consistency between measurements of the control and its experimental counterpart. However, that doesn’t clearly exist in any of the assays when considering the mean values determined here. There is an overlap of confidence intervals in the bar chart of the Cell Feret medians, which could be taken as a more conclusive sign that cells were from a heterogeneously sized population of cell morphologies, influenced in some part by the time-lag in cell:ECM adhesion due to the initial suspension volume. The fact the bivariate

KDE plot (Figure 5.22C) also shows that correlation between the two variables is low at 0.34, supports such a theory.

PLAY software can also be used to describe and inform on details of nuclear morphology, such as circularity and perimeter profiles (Figure 5.23), solidity (Figure 5.24), and Feret profiles (Figure 5.24B). Regarding circularity (Figure 5.23A), median values between assays show overlapping confidence intervals, implying homogeneity between assays. This is confirmed by the near-non-statistical differences between mean values. The violin plots show a generally reciprocated shape between tests, as would be expected from a morphology tending to become circular. The bivariate KDE plot (Figure 5.23C) shows the negative correlation with associated Pearson r value of -0.6, also to be expected as a cell tends to a circular shape with the lowest theoretical perimeter length for an enclosed area.

The nuclear solidity profile (Figure 5.24A) indicates that average values are consistent throughout the assay, with solidity ratio means and medians all falling into the top solidity decile. Gaussian blurring prior to masking the nucleus during 4PLAY will undoubtedly have pushed up the solidity values, and non-blurring of the image might be worth considering if such a measurement becomes crucially important in any future experiments. To explain this more fully, nuclear measurements are based on an ROI asserted either manually or semi-manually by the user, during the execution of 4PLAY. 4PLAY currently steps through its process by first asserting a look-up table onto the DAPI image, to make the changes in intensity levels visually more perceptible, the user is then asked if they would like to assign a Gaussian blur to the DAPI Channel – this can be particularly useful if there are small but high-intensity artifacts outside of the nucleus which need to be discounted as belonging to the nucleus. Gaussian blurring facilitates this by greatly reducing the pixel intensity of particularly small objects in the image space. Thus, 4PLAY's Gaussian blur operation allows the user to define a single area of high DAPI concentration which is the nucleus (Figure 23D*i*). Once blurred, the user is asked to participate in selecting the appropriate intensity threshold necessary to properly define the nuclear envelope for the creation of a nuclear ROI mask (Figure 23D*ii*), to be used later by 4PLAY in the nuclear measurements (Figure 5.20B), nuclear shape descriptors, and in the definition of foci distance

measurements such as ‘Spot Distance from Nucleus’ (Figure 5.19). As a result of this blurring operation, high fluorescence cytoplasmic artefacts are erased, leaving a nuclear object with a smoother outline and a reduced pixel intensity on its inner perimeter. As a consequence of increased blurring, nuclear circularity will tend to increase and without a systematic approach to thresholding, the nuclear size and perimeter lengths will tend to decrease due to the blur around the original nuclear boundary. This effect of blurring means that it should always be done with care, and most of all, with consistency throughout the experiment.

As with the nuclear area measurements (Figure 5.20B), the KO(Control) shows some larger nuclear measurements compared to other experimental variables, yet the mean stays relatively consistent with the other groups under test. The significant differences between control and experimental cell nuclei areas may be because of variation in the focal plane (Figure 5.20D). With genuine PLA foci present in the experimental groups fluorescent light emitted from the PLA foci aid in the establishment of a focal plane (FP) in the near basal membrane locale. Without PLA foci in the lamellipodia of cells it is easy to establish a focus in the plane with most fluorescence, be it from non-specific PLA reactions on the membrane of the cells, or from other sources of fluorescence and auto-fluorescence. This focal plane will tend to be further from the coverslip, the corollary being that the focal plane intersection at the nucleus will produce a larger nuclear profile image than in the experimental groups.

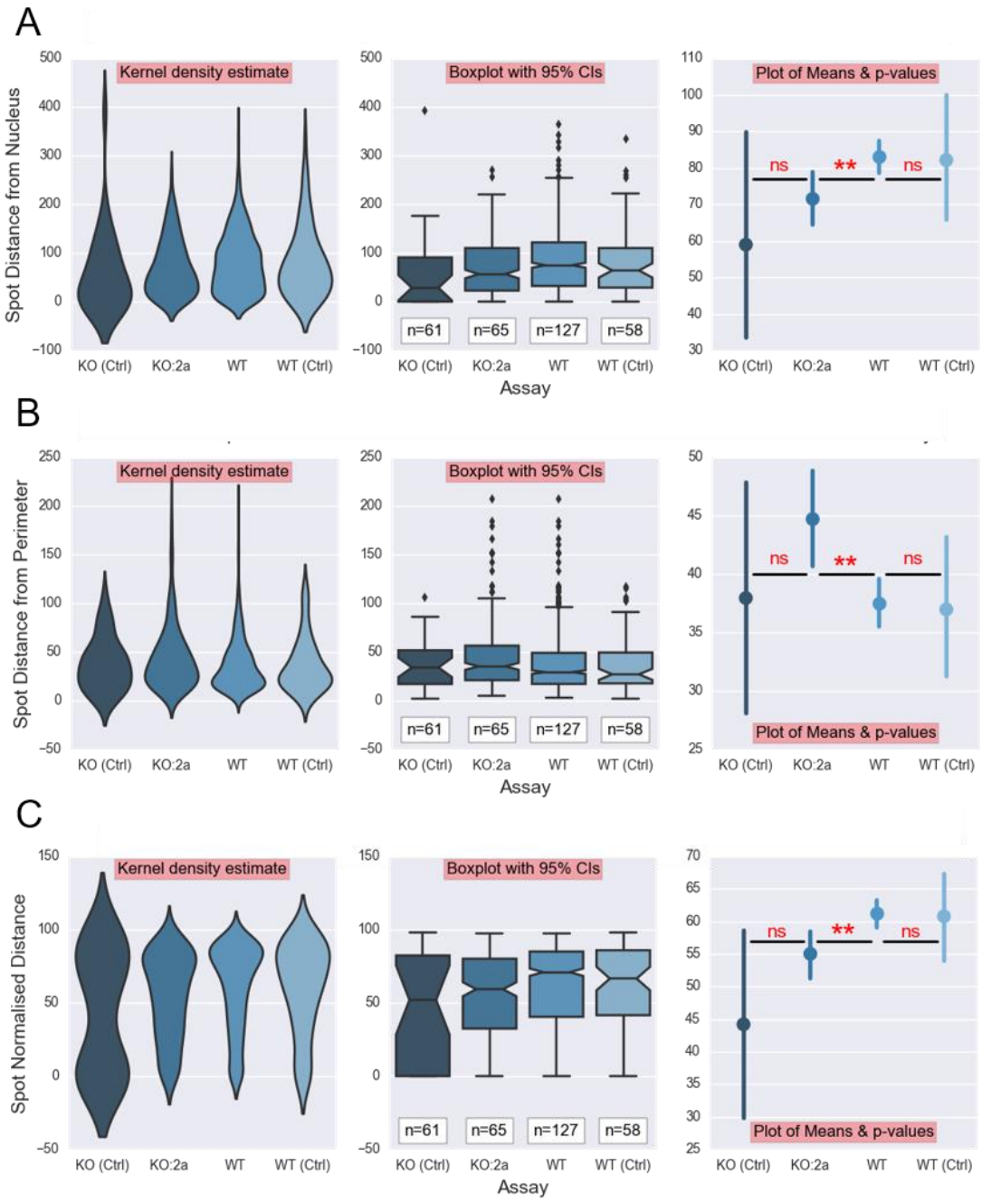
A
Spot Distance from Nucleus
Kernel density estimate
Boxplot with 95% CIs
Plot of Means & p-values
ns
**
ns
n=61
n=65
n=127
n=58
KO (Ctrl)
KO:2a
WT
WT (Ctrl)
Assay
B
Spot Distance from Perimeter
Kernel density estimate
Boxplot with 95% CIs
Plot of Means & p-values
ns
**
ns
n=61
n=65
n=127
n=58
KO (Ctrl)
KO:2a
WT
WT (Ctrl)
Assay
C
Spot Normalised Distance
Kernel density estimate
Boxplot with 95% CIs
Plot of Means & p-values
ns
**
ns
n=61
n=65
n=127
n=58
KO (Ctrl)
KO:2a
WT
WT (Ctrl)
Assay
D
i.
ii.
iii.
x
4x
y
y

Figure 5.19 PLA spot location profiling

Cells were processed and analysed as described in Figure 5.12.
One of the main functions of PLAY will be to localise as best possible, foci within the nuclear envelope or with higher precision distance-mapped within the cytoplasmic region.

Panel A. Spot distances from the nucleus indicate clearly distinguish nuclear-bound foci and foci on the nuclear envelope, from cytoplasmic foci.
Panel B. Spot distances from the cell perimeter make possible the measurement of putative protein interactions at the leading edge. In wild type cells, DDX3X : eIF4E interactions happen significantly nearer the cell periphery in wild type cells than in the DDX3X knockout cells. The more random foci seen in the controls, and generated by cellular auto-fluorescence and a small number of PLA foci show a much greater variance in their locale, as would be expected from foci generated by non-specific processes.
Panel C. The 'Normalised spot distance' measurement is cell-size ambivalent, based solely on the relative distance of a PLA spot between the nucleus and cell periphery. This is a particularly useful measurement for early spreading cells which generally have a solid and circular morphology. Here we see additional confirmation that in wild type cells, DDX3X : eIF4E interactions happen significantly nearer the cell periphery than in the knockout, with re-confirmation of a more random distribution of foci in the controls.
Panel D. Relying on Euclidian spot distance measurements from either the nucleus or periphery of the cell can give a misrepresentative account of reality in a population of mixed sizes cells. Comparing foci Xμm from the periphery of a well-spread cell (inset i), with a less spread cell (inset ii), provides little information about the possible function or effect of such an interaction of proteins. 'Spot Normalised Distance' measurements are cell-size ambivalent, providing a simple percentage distance measurement with the ability to place each foci precisely between the nuclear membrane and the closest part of the cell periphery. A measurement of 0% places a spot in the nucleus or on the nuclear envelope, and 100% places the spot at the cell periphery. Such a normalised measurement does need to be considered with care in cells of low solidity where two foci at a similar distance to the cell periphery (Xμm) will be attributed with widely different normalised distance measurements given the variation in their distances from the nucleus.

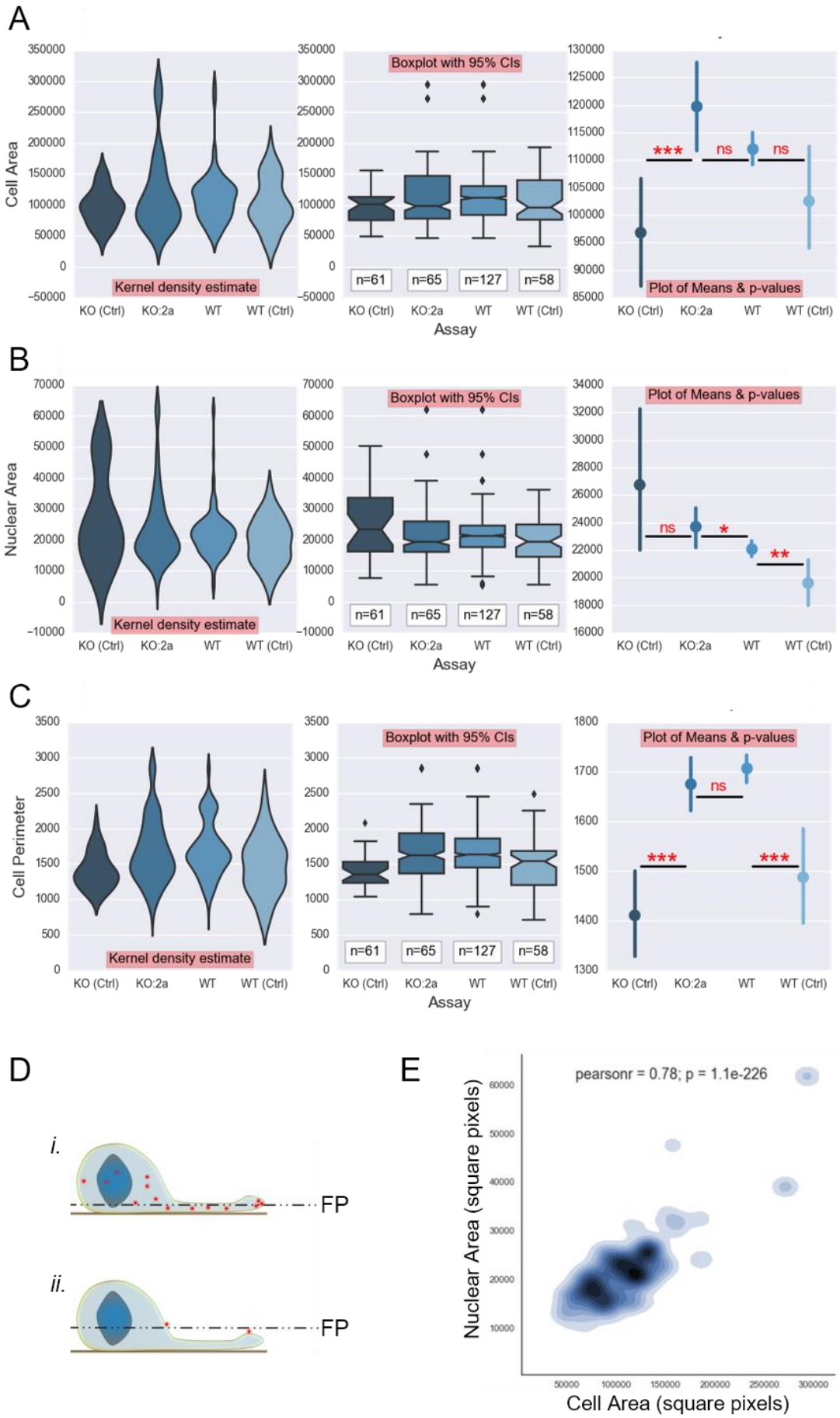
A
Cell Area
Kernel density estimate
Boxplot with 95% CIs
n=61
n=65
n=127
n=58
Plot of Means & p-values
***
ns
ns
KO (Ctrl)
KO:2a
WT
WT (Ctrl)
Assay
B
Nuclear Area
Kernel density estimate
Boxplot with 95% CIs
Plot of Means & p-values
ns
*
**
C
Cell Perimeter
Kernel density estimate
Boxplot with 95% CIs
Plot of Means & p-values
ns
***
***
D
i.
FP
ii.
FP
E
pearsonr = 0.78; p = 1.1e-226
Nuclear Area (square pixels)
Cell Area (square pixels)

Figure 5.20 Cell Area, Nuclear Area and Cell Perimeter Statistics Profile

Cells were processed and analysed as described in Figure 5.12.

Panels A, B, C. Such area deviations could be a consequence of the volume of seeding media leading to a differential time for initial cell adherence to the extra-cellular matrix (a phenomenon utilised for pseudo-time-course assays as discussed in Chapter 7). Alternatively, this could be as a consequence of these cells passing through stage G2 of the cell cycle and undergoing a near-doubling of their nuclear and cytoplasmic volume.

Panel D. The significant differences shown between control and experimental cell area (Panel A), nuclear areas (Panel B) and cell perimeter lengths (Panel C) may be as a consequence of variation in the focal plane (Panel D). With genuine PLA foci present in the experimental groups (Panel D, inset *i*), fluorescent light emitted from the PLA foci aids in the establishment of a focal plane (FP) in the near basal membrane locale. Without PLA foci in the lamellipodia of cells (Panel D, inset *ii*), it is easy to establish a focus in the plane with most fluorescence, be it from non-specific PLA reactions on the membrane of the cells, or from other sources of fluorescence and auto-fluorescence. This focal plane will tend to be further from the coverslip, the corollary being that the focal plane intersection at the nucleus will produce a larger nuclear profile image than in the experimental groups.

Panel E. When looking at the entire assay, there exists a strong correlation between nuclear area and cell area, corroborating the current theory that cell size and nucleus size are highly related and change together with positive correlation, through the cell cycle (Good 2015; Neumann & Nurse 2007; Webster et al. 2009).

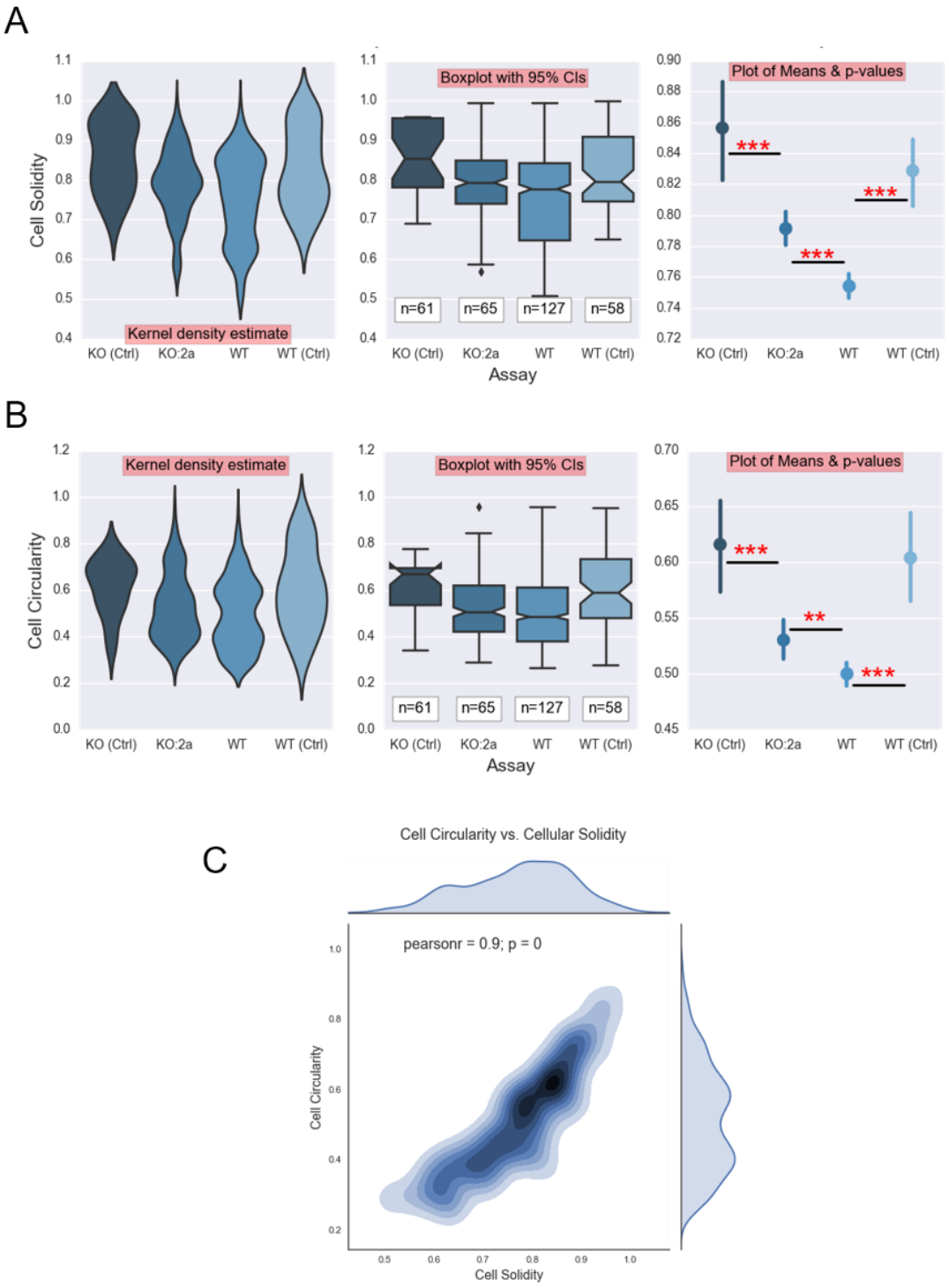

Figures 5.21 Cell Solidity and Cell Circularity Statistics Profiles
Cells were processed and analysed as described in Figure 5.12.
Panels A and B. Both the Cell Solidity and Cell Circularity profiles exhibit some similar features, with relative mean and median values reflected in both assays, suggesting some correlation between both measurement types. A bivariate KDE plot. **Panel C.** The relationship between cell circularity and solidity is strong for the whole assay, with a Pearson r correlation coefficient of 0.9, which is as expected for early stage spreading prior to large-scale cell polarisation.

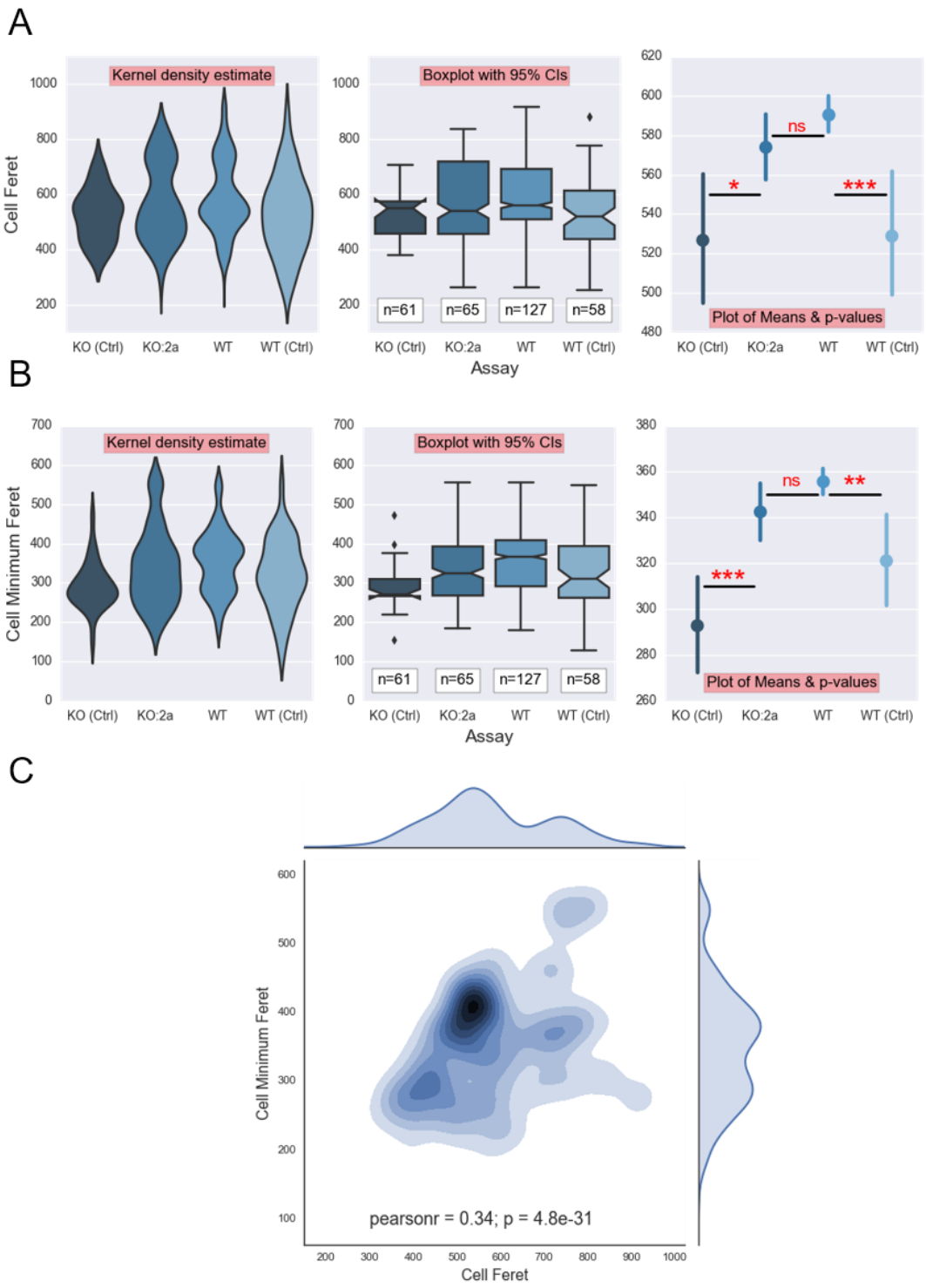

Figures 5.22 Cell Feret and Cell Minimum Feret Statistics Profiles Cells were processed and analysed as described in Figure 5.12. **Panels A & B** The statistical differences in mean values between experimental groups and their associated controls suggests that the focal plane established in the controls may have affected ferret measurements, discussed in Figure 5.19. **Panel C.** A bivariate KDE plot also shows that correlation between the two variables is low at 0.34, and likely to be significantly disbursed due to the variation in measurements highlighted by the extended confidence intervals of the control groups only.

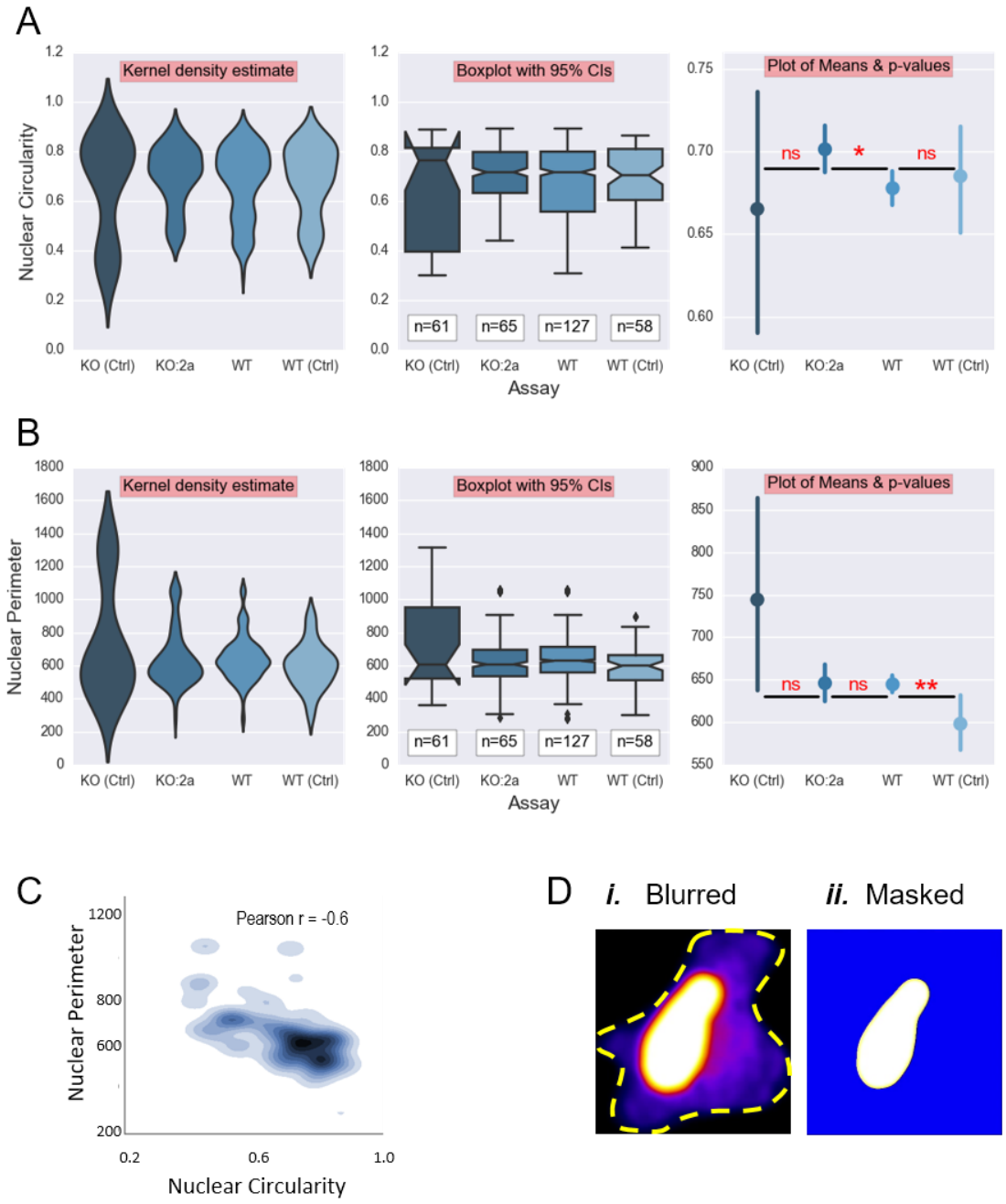

Figures 5.23 Nuclear Profiles
Cells were processed and analysed as described in Figure 5.12.

Panel A. Nuclear Circularity profiles are show high median and mean values. **Panel B.** Nuclear Perimeter Profiles. **Panel C.** KDE plot showing the relationship between nuclear perimeter and nuclear circularity. **Panel D.** During 4PLAY data harvesting the user is asked to ***i.*** apply a Gaussian blur on the DAPI channel (optional), and define the appropriate intensity threshold in order to ***ii.*** create a nuclear mask. The yellow dashed line of Panel D*i.* indicates the boundary of the cell where DAPI fluorescence intensity levels are close to negligible.

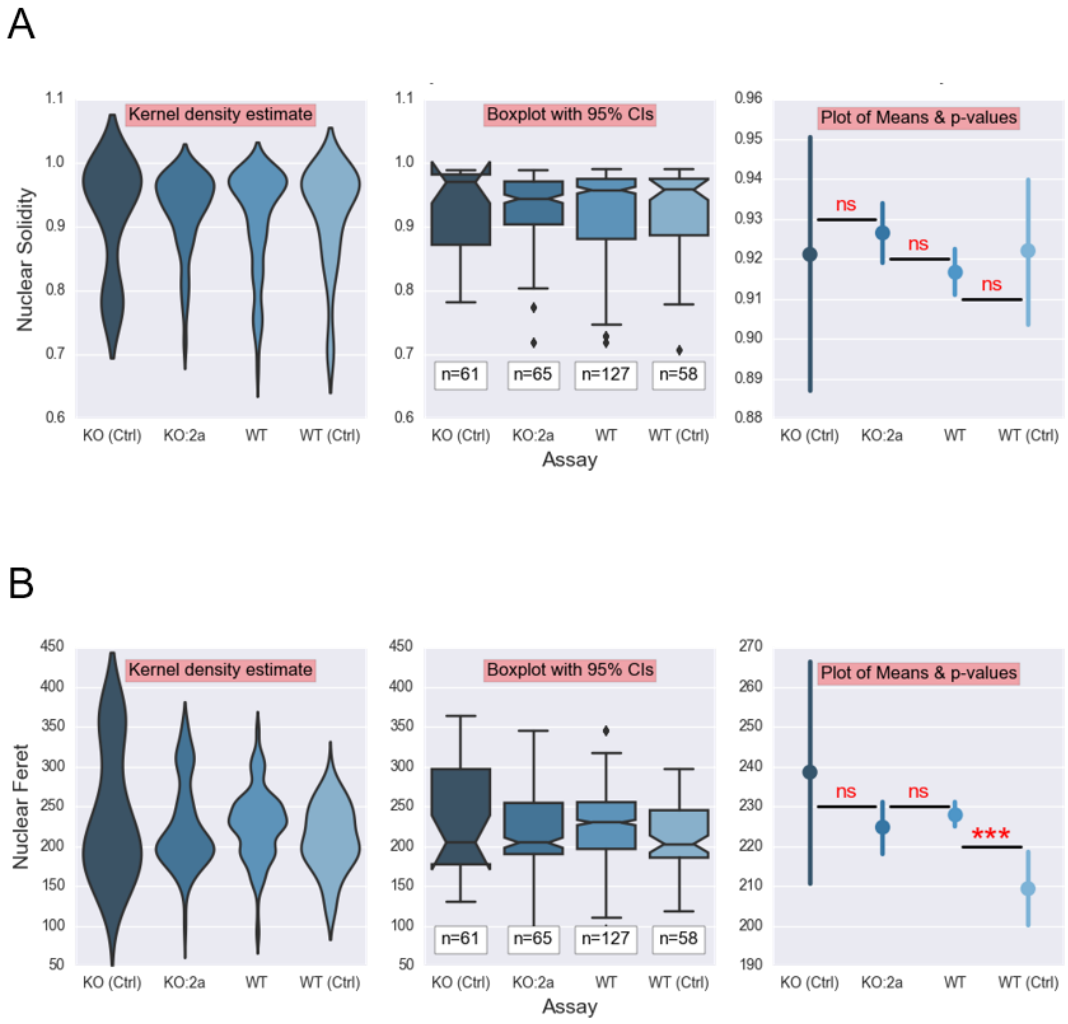

Figures 5.24 Nuclear Solidity and Feret Profiles
Cells were processed and analysed as described in Figure 5.12.

Panel A. Nuclear solidity statistics show average values are consistent throughout the assay, with solidity ratio means and medians all falling into the top solidity decile. Gaussian blurring prior to masking the nucleus during 4PLAY will undoubtedly have pushed-up the solidity values.
Panel B: Nuclear ferret profiles show that the KO(Control) has larger nucleus measurements compared to the rest of the assay, yet the mean stays relatively consistent with the other groups under test.

5.5.3.4 Spot Count and Foci per Cell Unit Area Statistics Profiles

The ‘Foci per Cell Unit Area’ measurement (Figure 5.25B) is a PLAY-derived measurement, created as a way to normalise spot counts and allow a useful quantitative comparison of putative protein interactions between cells of different sizes. Both spot count (Figure 5.25A) and foci per cell unit area count (Figure 5.25B) show clear relationships to each other, which is to be expected given the provenance of the latter, as derived in part from the former. The bivariate KDE plot shows this relationship well (Figure 5.26A), with a Pearson r value of 0.82.

Interestingly there is little correlation between Cell area and its derivative Foci Counts per Unit Area, where for the entire assay (Figure 5.26B) there is a Pearson r correlation coefficient of -0.19 and for the WT assay only, which has a significantly different distribution than all other assays. The correlation is almost the same at -0.24 (Figure 5.26C), implying a weak inverse correlation between cell area and the number of PLA foci.

A

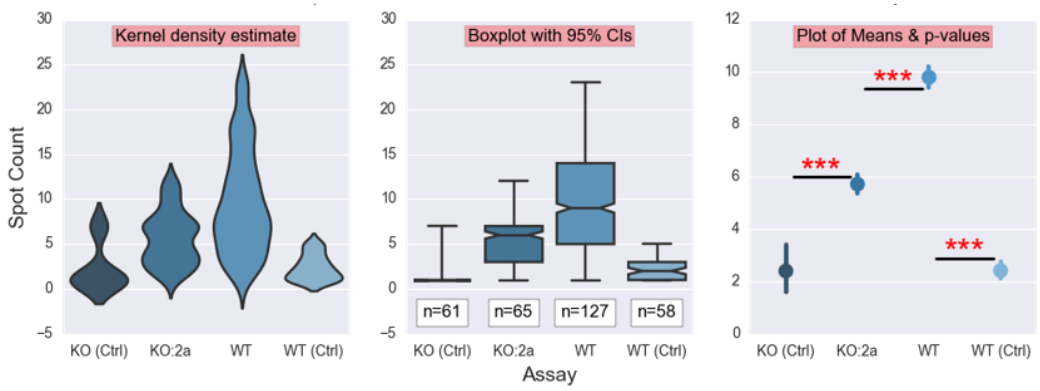

B

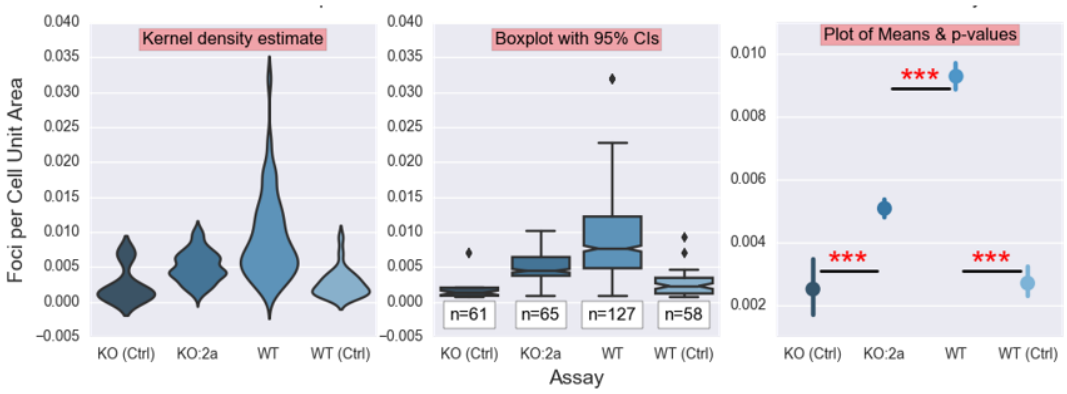

Figure 5.25 Spot Count and Foci per Cell Unit Area Statistics Profiles
Cells were processed and analysed as described in Figure 5.12.

Panels A and B. Both assay show clear relationships to each other, which is to be expected since both the 'spot count' and 'foci per cell unit area' counts are performed at the level of individual ROIs/cells, and 'foci per cell unit area' is a derivative measurement of 'spot count'.

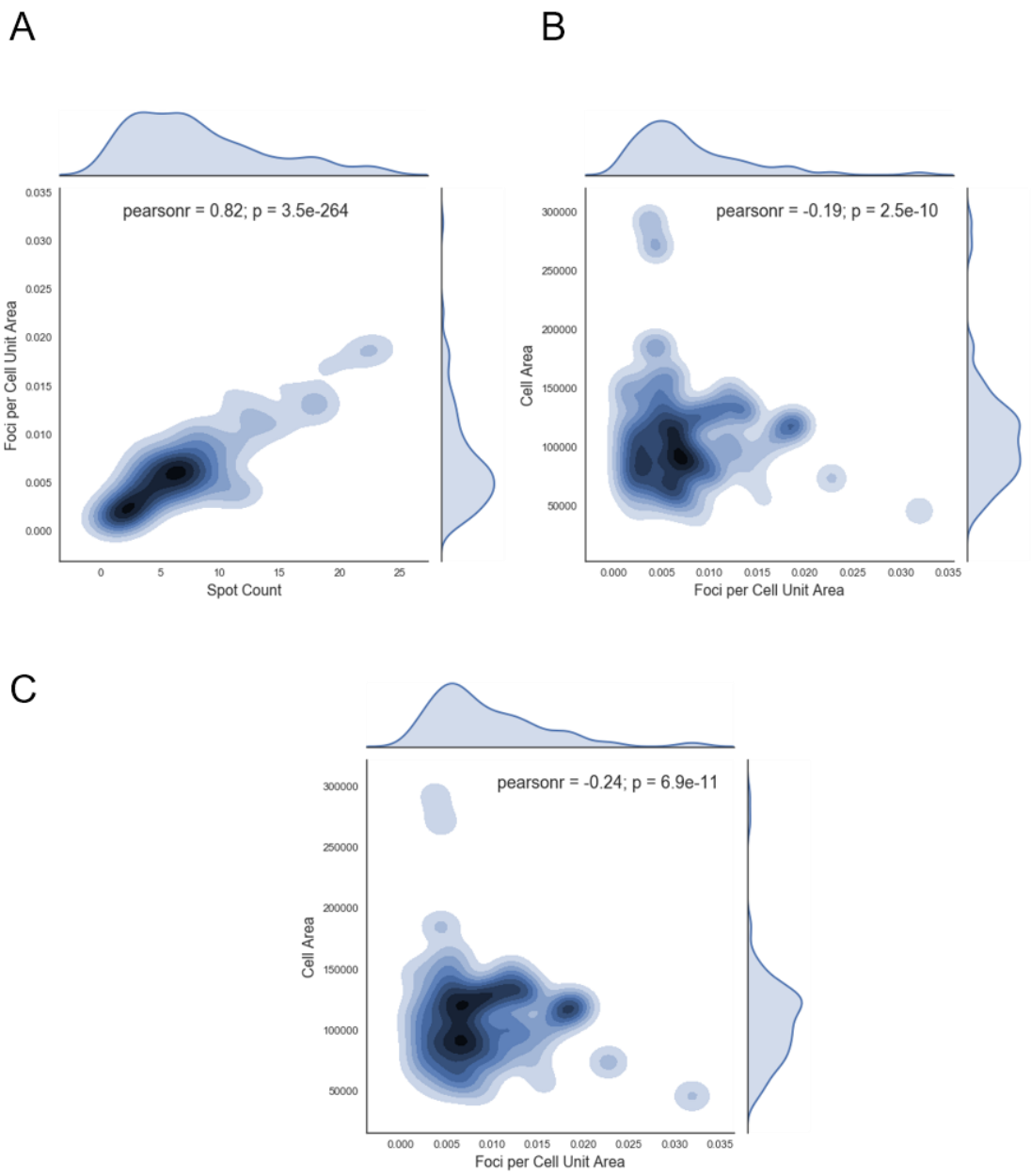

Figure 5.26 Characterisation of foci counts using bivariate KDE plots
Cells were processed and analysed as described in Figure 5.12.

Panel A. Bivariate KDE plots shows the strong linear and correlation between Foci per Unit Cell Area and actual Spot Counts, with a Pearson r value of 0.82. **Panel B & C.** There is little correlation between Cell area and its derivative Foci Counts per Unit Area, where for the entire assay we see a Pearson r correlation coefficient of -0.19 and for the WT assay only, which has a significantly different distribution than all other assays, the correlation is almost the same at -0.24. Implying that there is a weak inverse correlation between cell area and the number of PLA foci in this case.

5.6 Summary

A new type of Proximity Ligation Assay analysis software, called ‘PLAY’ (PLA analYsis) has been created. It is capable of semi-autonomously gathering a plethora of information regarding intracellular protein interactions as visualised by PLA foci, as well as quantifying gross cellular morphological changes which may be correlated or even caused by these same interactions.

Post-acquisition processing of images by PLAY is complemented by the PLAYsheet - a simple template allowing the researcher to add experimental conditions to the results in the form of metadata, providing for uncomplicated management and archiving of acquired data until it is required.

PLAY offers a huge spectrum of analysis tools – PLAYkits, for the immediate processing of single experiments, or for meta-analyses of multiple archived experiments. These PLAYkits are designed to be easy to use by people with minimum programming experience (rationalisation of the code into user-friendly modules is currently an on-going process). For more advanced or novel analysis approaches, researchers can customise PLAYkits for bespoke analyses, or make new analysis routines from scratch utilising any libraries which Scientific Python (SciPy) can offer.

PLAY is based on Python and PANDAS dataframes for results management. As such, it has the flexibility of a general programming language, but also provides the operator with the ability to create a compelling visual interpretation of data along with powerful statistical analysis routines which are commensurate with analytical power to the well-known scientific statistical language, R.

PLAY has been system tested by comparing its analyses of PLA images with those same images analysed by a researcher, and correct implementation of the PLAY noise-filter allows the sensitivity of the foci counting routine to match that of the human eye.

After several rigorous tests, PLAY may be considered as a powerful new tool in the analysis of the Proximity Ligation Assay. Latest revisions of the software are held by the Morley laboratory.

6 Elucidating the role of DDX3X in spreading cells

6.1 Introduction

DDX3X (aka DBX; HGNC: 2699; GenBank accession no.: NM_001356), is part of the DEAD (D-E-A-D: Asp-Glu-Ala-Asp)-box RNA helicase family, the largest group of RNA helicases within the SF2 superfamily of helicases. DDX3X has high amino acid sequence similarity >94% to its sole other human Y chromosome homologue, DDX3Y (aka. DBY; HGNC: 2699; GenBank accession no.: NM_004660) (Rauschendorf et al. 2014). Both are generally divergent in their roles, with DDX3X unable to rescue a loss-of-function of DDX3Y (Rosner & Rinkevich 2007), although a common helicase domain appears to make them functionally exchangeable for some specific cytoplasmic mRNA translation processes (Chuang et al. 1997). DDX3X is ubiquitous in all tissues, whereas the DDX3Y protein is expressed only in the germline in spermatogonia and is one of the essential genes involved in human spermatogenesis and male fertility (Rauschendorf et al. 2011; Lardone et al. 2007). DDX3X is an ATPase-dependent RNA helicase, found in many eukaryotes including humans and yeast (Jankowsky 2011). Human DDX3X encodes a transcript (5.3 Kb) that translates into a polypeptide 662 amino acids in length, which when crystallised has two distinguishable domains, an N-terminal DEAD-box domain in residues 211 to 403, and a C-terminal helicase domain consisting of residues 411 to 575 (Samal et al. 2015).

DDX3X participates in both nuclear functions and cytoplasmic functions, working as a chaperone taking RNA between these two cellular compartments. It is implicated in various roles with respect to RNA metabolism (Rosner & Rinkevich 2007), including RNA splicing, mRNA transport (Mahboobi et al. 2015), cell cycle regulation and apoptosis (Li et al. 2014). Most interestingly for this research, DDX3X has been suggested to have important roles in translational control with evidence for interactions with eukaryotic initiation factors eIF4A, eIF4E, eIF4G and PABP1 (Lai et al. 2008; Lai et al. 2010; Soto-Rifo et al. 2012). Numerous reports suggest that its dysregulation is implicated in both epithelial-mesenchymal transitions (EMT) and tumourigenesis (Botlagunta et al. 2008; Samal et al. 2015).

The Tip-associated protein (TAP)-dependent bulk mRNA export pathway is the main export pathway for the transport of mRNA from the nucleus to the cytoplasm. TAP forms a heterodimer with p15 and docks with the nucleoporins of the nuclear pore complex (NPC). In so doing, TAP places messenger ribonucleoproteins (mRNPs) directly at the nuclear pore for transit to the cytoplasm (Huang & Steitz 2005). Recent reports suggest that DDX3X associates with mRNAs and TAP in the nucleus, and accompanies mRNPs to the cytoplasm via the TAP-dependent bulk mRNA export pathway (Lai et al. 2008). DDX3X also participates in the CRM1-dependent nucleocytoplasmic shuttling of RNA (Figure 6.7 and 6.8), a pathway which has garnered much attention due to its role in the progression of human immunodeficiency virus (HIV).

DDX3X has been a focus of research for some years due to its involvement in the replication of viruses including HIV, Hepatitis B and C (HBV and HCV, respectively), with some therapeutic drugs having been developed with the aim of inhibiting the binding of DDX3X to the HIV RNA. Evidence suggests that in the early stages of HIV infection, fully spliced human HIV-1 transcripts encoding Rev (a virally encoded sequence-specific RNA binding protein), are exported to the cytoplasm in a manner reliant on the TAP-dependent mRNA export pathway. Once translated, the Rev protein is transported back into the nucleus aided by its nuclear localisation signal (NLS). Once in the nucleus, Rev binds to the Rev response element (RRE) located in the second intron of unspliced HIV-1 genomic RNA (gRNA) (Cullen 2000; Taniguchi et al. 2014), to facilitate the shuttling of this gRNA to the cytoplasm. This export of unspliced gRNA requires Rev protein in complex with chromosome region maintenance-1 (CRM1) and DDX3X (Yedavalli et al. 2004; Bushman et al. 2009). DDX3X binds CRM1 and localises to the nuclear pore; a suggested mechanism of action is that DDX3X facilitates the unwinding of the complex ternary gRNA structures or removes obstructive proteins from the gRNA to allow it passage to the cytoplasm, functioning in a similar manner to the yeast nuclear pore-associated DEAD-box protein, Dbp5p (Snay-Hodge et al. 1998). This thereby provides cytoplasmic access to unspliced transcripts, which then have the ability to be translated into many different viral protein factors, ultimately leading to the further propagation of the virus. Knocking down

of the DDX3X protein has been shown to dramatically downregulate such nucleocytoplasmic transport and in so doing greatly impair HIV-1 replication, making it a potential target for anti-HIV therapy (Sharma & Bhattacharya 2010; Lai et al. 2013).

There is now a huge amount of evidence to support the involvement of DDX3X in translation initiation, although the exact details of how it functions is a matter of some debate. The common theme is that DDX3X is implicated in both canonical translation and in the less common non-cap-dependent form utilising internal ribosome entry sites (IRES). DDX3X has been shown to suppress cap-dependent translation and up-regulate cap-independent translation (Shih et al. 2008). By utilising its consensus eIF4E-binding sequence, YIPPHLR, to interact with the dorsal surface of eIF4E in the same mode as a 4E-BP1, DDX3X can trap eIF4E in a translationally inactive complex, which is then unable to interact with the scaffold protein, eIF4G. However, when interacting with hepatitis C virus (HCV) RNA, DDX3X facilitates the activation of the IRES to allow translation to proceed (Shih et al. 2008).

DDX3X and its homologues have also been shown to be present in, and a critical component for the assembly of cytoplasmic stress granules (SGs) (Shih et al. 2012). Genomic studies suggest that mutations causing nucleotide substitutions in DDX3X are commonplace in many tumours. In medulloblastoma, all such mutations map to the helicase domain. Experimental evidence showed that with these mutations, although DDX3X binding of its RNA target remained unaffected, RNA unwinding decreased (Floor et al. 2016), and translation was impaired. Such translation impairment due to DDX3X point mutations has also been seen to correlate with SG hyper-assembly, and a downregulation of global translation (Valentin-Vega et al. 2016).

Investigations into DDX3X as a facilitator of viral replication has especially led to a better understanding of its helicase domain and the role it plays not only in viral replication but also in the canonical form of eukaryotic translation. Here it is believed to help unwind cellular mRNAs with highly structured 5’ UTRs. In the canonical form of eukaryotic translation, the initial step of ribosomal scanning of the mRNA is facilitated by the binding of the 40S ribosomal subunit (together with initiation factors and the met-tRNAi) to the 5’

cap of mRNA, prior to the subsequent 5' UTR scanning for the AUG start codon by the 43S PIC (see Chapter 1). Scanning is arrested and translation ultimately fails in the presence of unresolved complex 5' UTR secondary structures in the near vicinity of the 5' cap. Structures such as highly stable multiple stem-loops are enough to confound the already low processivity of the eIF4A helicase (Pause et al. 1994). Recruitment of additional helicases, such as the DEAH (D-E-A-H: Asp-Glu-Ala-His)-box RNA helicase DHX29, are required to remodel the 40S ribosomal subunit to enable it to better maneuver through such structures (Pickering & Willis 2005; Parsyan et al. 2009). DDX3X has been shown to associate at the 5' terminus of viral (Hilliker et al. 2011) and cellular mRNA. This can occur *via* direct binding as well as indirect binding with RNA *via* eIF4F, helped by interactions with eIF4G and PABP (Soto-Rifo et al. 2012). Once at the 5' terminus, DDX3X may facilitate the entry and binding of the 43S ribosomal unit to the mRNA by destabilising complex local mRNA structures. This then, facilitates gross unwinding of the structure by eIF4A, leaving the mRNA available for scanning and subsequent translation.

Concerning the influence of DDX3X on oncogenic pathways, the evidence is varied and somewhat contradictory; some evidence suggests it has tumour suppressor functions, but the overwhelming majority now points to DDX3X as oncogenic in nature. Evidence for DDX3X acting as a tumour suppressor comes from an investigation into its effect on p21/WAF1/Cip1. P21/WAF1/Cip1 is a cyclin-dependent kinase (cdk) inhibitor, influential in the progression of the eukaryotic cell cycle and able to modulate cdks to arrest the cell cycle and promote apoptotic pathways. As such, p21 is an important upstream component of the tumour protein p53 (p53) tumour suppressor pathway, a broad pathway in which p53 integrates myriad stress-induced signals and responds by initiating DNA repair proteins, or by arresting the cell cycle and initiating apoptosis (Zilfou & Lowe 2009). DDX3X up-regulates the promoter activity of cell cycle inhibitor, p21/WAF1/Cip1, by collaborating with the ubiquitous transcription factor, Sp1. This enhancement of the expression level of p21 is performed by DDX3X in an ATPase-dependent, but helicase-independent manner, and provides evidence of DDX3X acting as a tumour suppressor. Indeed, in surveys of hepatocellular carcinoma from HBV-positive

patients, between 58% and 73% show a reduced expression of DDX3X and an associated reduction in p21/WAF1/Cip1 (Chao et al. 2006).

Other evidence suggests that DDX3X is also involved in the promotion of oncogenic signalling by interfering with another critical pathway responsible for cell apoptosis. The death receptor, TNF-related apoptosis-inducing ligand receptor-2 (TRAIL-R2, *aka* DR5/Apo2/TRICK2/KILLER), part of the tumour necrosis factor (TNF) family of receptors, is capable of inducing cellular apoptosis upon receipt of the TNF-related apoptosis-inducing ligand (TRAIL/Apo2L). This is an extrinsic apoptotic signal able to specifically induce programmed death in cancer cells with no toxicity against normal tissues, thereby making it an attractive avenue for therapeutic research (Szliszka et al. 2009; Peter & Krammer 2003). Once TRAIL has bound to its trimeric membrane receptor (TRAIL-R1 or TRAIL-R2), death-inducing signalling complexes (DISCs) are formed in the cellular cytoplasm – a complex of the death receptor, adaptors, and cysteine aspartate protease (caspase) -8 (Fabian et al. 2010). At this point, caspase-8 is an enzymatically inactive pro-caspase. Only when the DISC undergoes conformational change due to extracellular ligand binding, does caspase-8 become fully activated by auto-catalytic cleavage. Release of active caspase-8 homodimers from the DISC, allows them to activate downstream substrates of the apoptotic pathway (including caspase-3 and -7) and to initiate a positive feedback loop of caspases activating other caspases until apoptosis is finally achieved (Shalini et al. 2014; Morley & Pain 2001; Lemke et al. 2014). Such routes to apoptosis form one of the body's main sources of defense against cancer (Labi & Erlacher 2015). However, certain proteins and protein complexes can be recruited to the DISC to arrest initiation of this fatal act, frustrating caspase-8 cleavage and/or encouraging pro-survival pathways. Such receptor conjugates include the TRAIL death receptor-capping complex, DDX3/cIAP-1/GSK-3.

Other evidence is growing to suggest that upregulation of DDX3X can result in deleterious, oncogenic effects by influencing other pathways. When over-expressed, DDX3X has been directly implicated in EMT of immortalised non-tumourigenic breast epithelial cells (MCF10A). DDX3X binding of the E-cadherin promoter has been seen to downregulate its expression, and in lung, breast and prostate cancer, this down-regulation

facilitates cellular proliferation and neoplastic transformation (Botlagunta et al. 2008; Samal et al. 2015). Evidence suggests that E-cadherin is also affected by DDX3X levels *via* the Snail pathway. Snail is a transcription factor, which regulates aspects of tumour development, driving EMT and enabling metastasis. Snail down-regulates E-cadherin expression facilitating EMT. In glioblastoma multiforme (GBM) tumours, DDX3X levels have been seen to be highly positively correlated with Snail abundance, suggestive of a link between DDX3X and the promotion of cancer progression (Sun et al. 2011).

6.2 DDX3X is enriched at the leading edge of cells undergoing early-stage spreading

Although DDX3X is known to have nuclear and cytoplasmic functions, it is unclear where DDX3X protein is localised under steady state conditions during cell spreading. To address this, MRC-5 SV2 cells were seeded onto coverslips coated with collagen and allowed to spread for 40 minutes. As described in the Materials and Methods, Immunofluorescence imaging and confocal microscopy were used to test where DDX3X was located in spreading cells. The results showed that DDX3X is often found in abundance at the edges of cells during the earliest stages of cell spreading (Figure 6.1A). Cells were imaged and a Gaussian blur applied prior to the examination of the cross-sectional profile using intensity plotting (Figure 6.1B). The intensity plot renders a profile suggestive of an increasing overall gradient in DDX3X concentration between the nucleus and the left-most periphery of the cell. These data provide some evidence to show that membrane-localised DDX3X may be implicated in the formation of lamellipodia during the early stages of cell spreading.

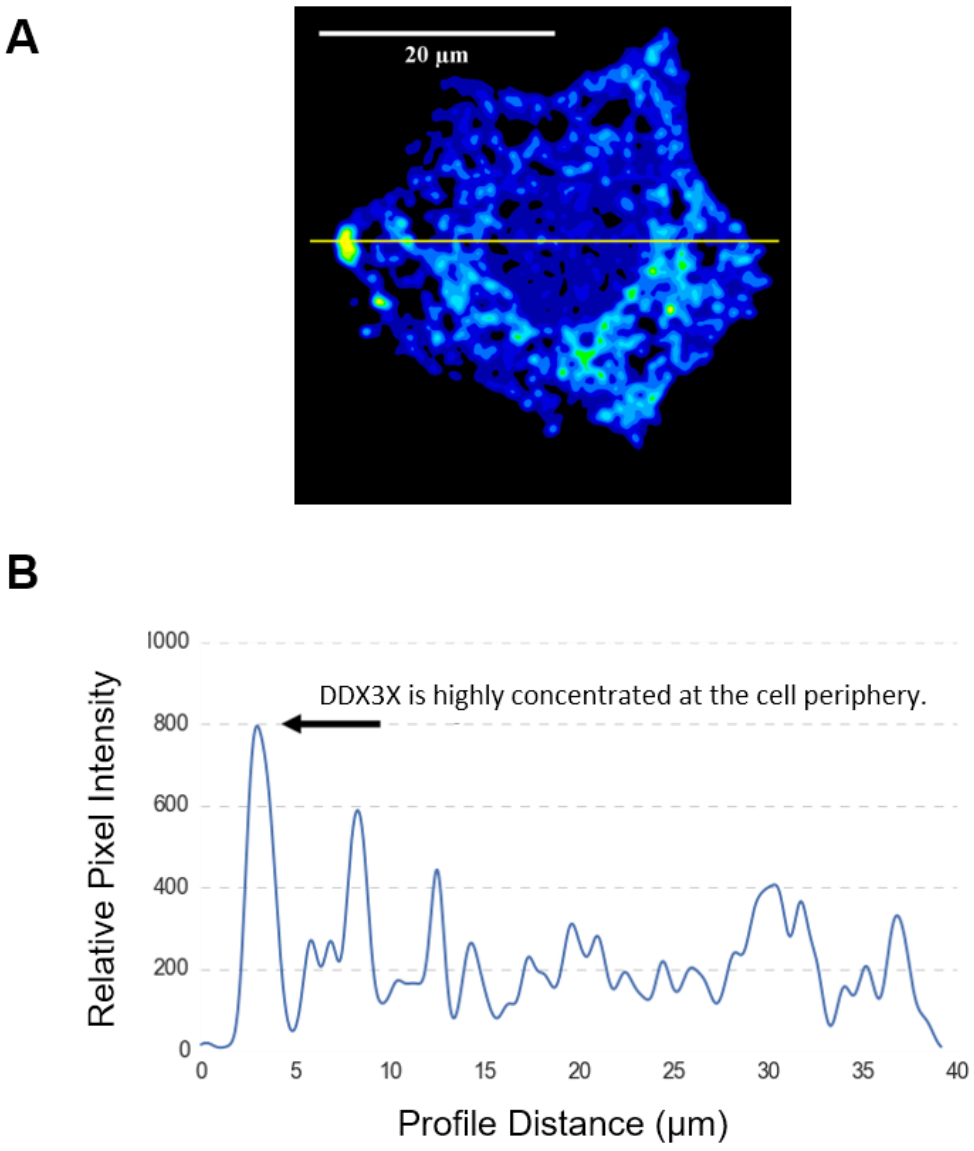

Figure 6.2 DDX3X co-localises with eIF4E at the leading edge of the cell

MRC-5 SV2 cells were seeded onto coverslips coated with 8µg/cm^2 collagen I, at a density of 15,000 cells/cm^2 and incubated at 37ºC for 40 mins. Cells were fixed using 4% (v/v) PFA, saponin permeabilised and dual immuno-fluorescence stained anti-DDX3X (Ab54) diluted at 1:600 and anti-eIF4E (Ab55) diluted at 1:400, as described in the Materials and Methods. Images were obtained using a Leica SP8 confocal microscope at 63x magnification. Scale bar indicates 20µm. **Panel A.** DDX3X (red) co-localises with eIF4E (green) at the leading edge of the cell. **Panel B.** With low antibody concentrations, eIF4E (green) and DDX3 (red) are visually punctate and are seen to co-localise at the leading edge of the cells. A close-up of the ROI in Panel A, showing DDX3X (red) co-localised with eIF4E (green) at the leading edge of the cell (shown as yellow, and highlighted with a yellow arrow).

These data are representative of those obtained from at least three separate experiments.

6.3 DDX3X colocalises with eIF4E at the cell periphery

The data shown above suggested that DDX3X can be localised to the cell periphery during cell spreading. Previously, it has been shown that DDX3X can suppress cap-dependent translation by binding to the dorsal surface of eIF4E in a similar manner to 4E-BP1 (Shih et al. 2008). However, overwhelming evidence suggests that the main role of DDX3X and it yeast DDX3X orthologue, Ded1, lies with the upregulation of translation of mRNAs harbouring complex secondary structures in their 5' UTRs (Rauschendorf et al. 2014; Sen et al. 2015). To determine whether eIF4E was colocalised with DDX3X is spreading cells, MRC-5 SV2 cells were seeded onto collagen-coated coverslips and allowed to spread for 40 minutes. Cells were fixed, permeabilised using saponin and dual-immunofluorescence stained with rabbit anti-DDX3X and mouse anti-eIF4E antibodies, as described in the Materials and Methods. With these low antibody concentrations, eIF4E and DDX3X were visually punctate and appeared colocalised at the leading edge of cells (Figure 6.2).

6.4 DDX3X forms striations in early-spreading cells

To look further into the localisation of DDX3X in fibroblasts, MRC-5 SV2 cells were seeded and allowed to spread as above. Cells were then fixed and confocal microscopy was used to visualise DDX3X described in Materials and Methods. Figure 6.3 demonstrates that DDX3X was seen to form striated patterns in cells, in general running laterally from a perinuclear position towards the lamella and occasionally into the lamellipodia. Such patterns appeared representative of the underlying actin cytoskeleton although no cytoskeleton markers were used in these experiments. Different DDX3X antibodies used at different titrations helped confirm that this did not reflect non-specific binding to actin stress fibres (data not shown), highlighting a possibility that such patterns may possibly implicate DDX3X in the utilisation of the actin cytoskeleton for intracellular transport.

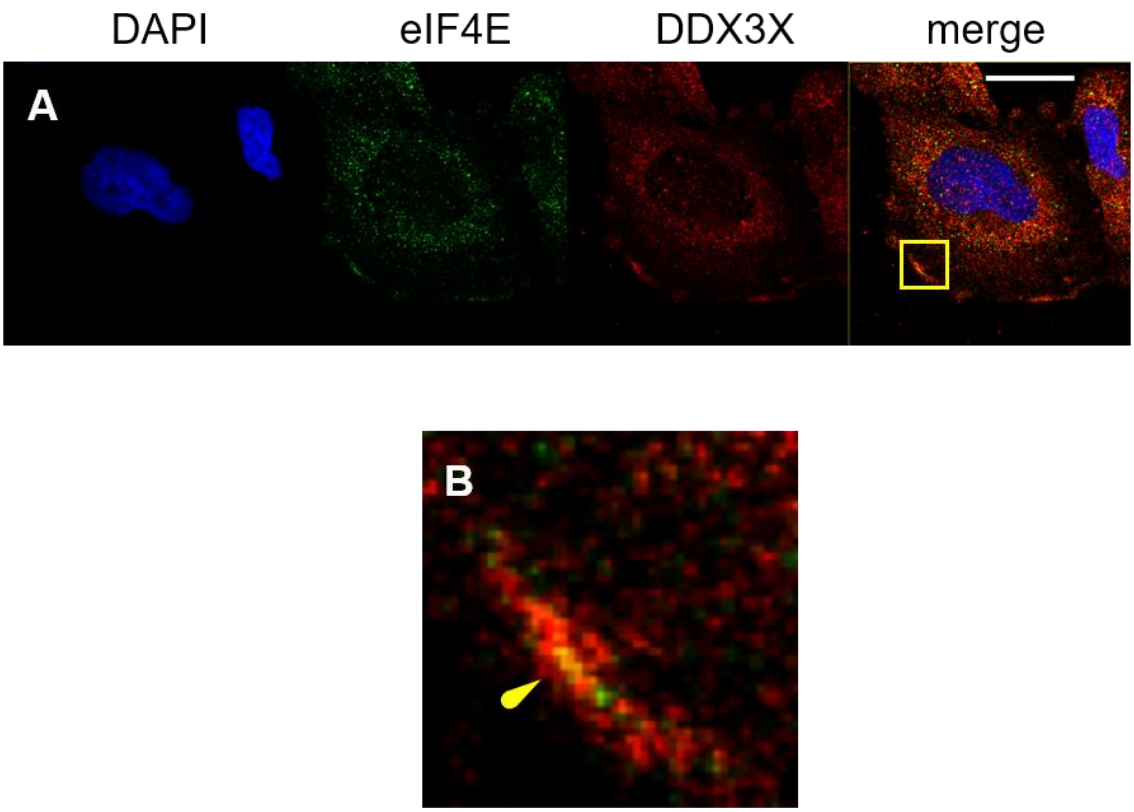

Figure 6.2 DDX3X co-localises with eIF4E at the leading edge of the cell

MRC-5 SV2 cells were seeded onto coverslips coated with 8µg/cm^2 collagen I, at a density of 15,000 cells/cm^2 and incubated at 37°C for 40 mins. Cells were fixed using 4% (v/v) PFA, saponin permeabilised and dual immuno-fluorescence stained anti-DDX3X (Ab54) diluted at 1:600 and anti-eIF4E (Ab55) diluted at 1:400, as described in the Materials and Methods. Images were obtained using a Leica SP8 confocal microscope at 63x magnification. Scale bar indicates 20µm. **Panel A.** DDX3X (red) co-localises with eIF4E (green) at the leading edge of the cell. **Panel B.** With low antibody concentrations, eIF4E (green) and DDX3 (red) are visually punctate and are seen to co-localise at the leading edge of the cells. A close-up of the ROI in Panel A, showing DDX3X (red) co-localised with eIF4E (green) at the leading edge of the cell (shown as yellow, and highlighted with a yellow arrow).

These data are representative of those obtained from at least three separate experiments.

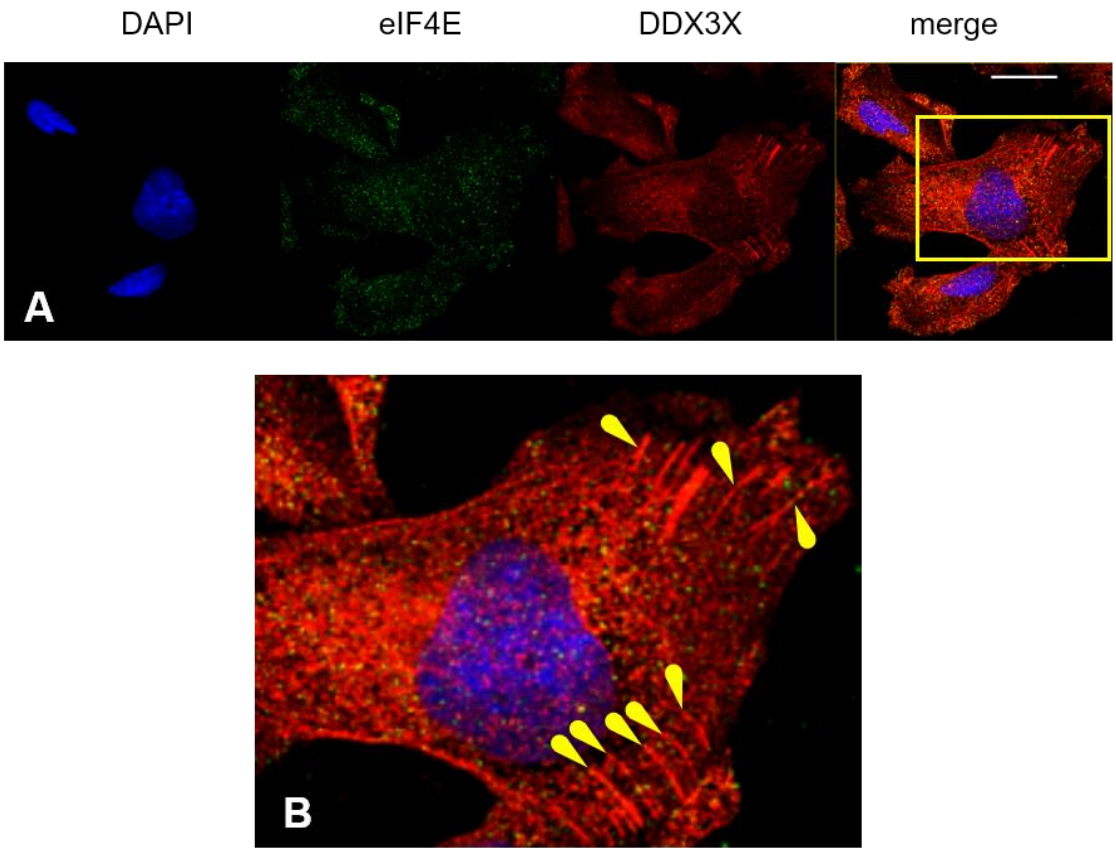

Figure 6.3 In early stage spreading cells, DDX3X is found in striated patterns suggesting possible interactions with the actin cytoskeleton

MRC-5 SV2 cells were seeded onto coverslips coated with 8µg/cm^2 collagen I, at a density of 15,000 cells/cm^2 and incubated at 37ºC for 40 mins. Cells were fixed using 4% (v/v) PFA, saponin permeabilised and dual immuno-fluorescent stained with anti-DDX3X (Ab62) and 1:500 and anti-eIF4E (Ab53) diluted at 1:100, as described in the Materials and Methods. Images were obtained using a Leica SP8 confocal microscope at 63x magnification. Scale bar indicates 20µm. These data are representative of those obtained from at least three separate experiments. **Panel A.** DDX3X appears in striated patterns within early-spreading cells. **Panel B.** A close-up of the ROI in Panel A, showing DDX3X striations (highlighted with yellow arrows), and DAPI staining of the nucleus.

These data are representative of those obtained from at least three separate experiments.

6.5 DDX3X is found at the leading edge and associates with the cytoskeleton

Further colocalisation experiments were performed using phalloidin-Alexa Fluor conjugates to visualise the cytoskeleton in conjunction with DDX3X. Figure 6.4A shows clear localisation of DDX3X (red) to growth cones in spreading cells and the possible association of DDX3X with the actin cytoskeleton (Panels B and C). Visually this may suggest the possibility that DDX3X colocalises to the actin cytoskeleton prior to adopting a function at the leading edge of cells.

6.6 Colocalisation analysis provides evidence for DDX3X association with the actin cytoskeleton

Colocalisation by visual means is a pragmatic first step in identifying interacting proteins by interpretation of microscopy images. The next step is to analyse colocalisation more objectively. Using the Manders' colocalisation coefficients (MCC) (Manders et al. 1993), together with Costes's method for the automatic thresholding and elimination of background 'noise' from an image (Costes et al. 2004), in an imageJ plug-in (http://sites.imagej.net/GDSC/), colocalisation between DDX3X and actin fluorescence channels was performed (Dunn et al. 2011; Bolte & Cordelieres 2006). This showed that 83% of pixels displaying DDX3X-associated fluorescence above thresholded levels were colocalised with actin-associated fluorescence (tM1=0.83), and 69% of all actin-associated fluorescence was colocalised with DDX3X-based fluorescence (tM2=0.69). Visualised graphically, red pixels show non-colocalised DDX3X, green pixels show non-colocalised actin, and shades of blue indicate a degree of colocalisation between the two channels or proteins, where light blue indicates weak colocalisation and dark blue indicates a strong colocalisation coefficient in both channels (Figure 6.5B). These data suggest the possibility that DDX3X is colocalised with the actin cytoskeleton in much of the cell, with the caveat that such colocalisation appears weakest at the leading edge, in a region of the highest concentration of DDX3X.

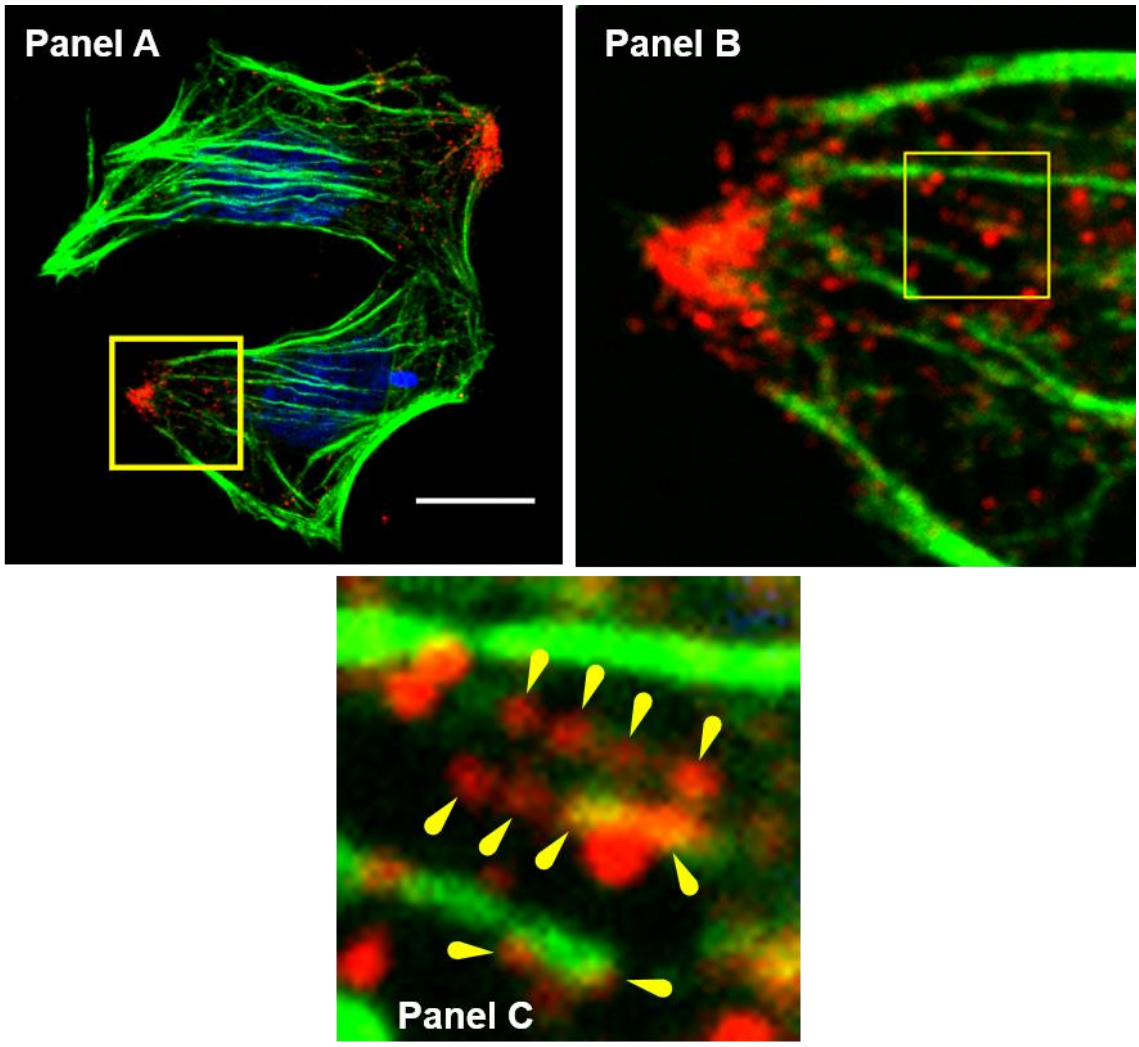

Figure 6.4 DDX3 is found at the leading edge in early stage spreading cells and associates with the cytoskeleton in spreading cells

MRC-5 SV2 cells were seeded onto coverslips coated with 8µg/cm^2 collagen I, at a density of 15,000 cells/cm^2 and incubated at 37ºC for 40 mins. Cells were immersed in ice cold saponin solution for 5 seconds prior to fixation using 4% (v/v) PFA, saponin permeabilised and dual immuno-fluorescence stained using anti-DDX3X (Ab62) diluted at 1:500, with the addition of Alexa Fluor conjugated phalloidin, as described in the Materials and Methods. Images were obtained using a Leica SP8 confocal microscope at 63x magnification. Scale bar indicates 20µm. **Panel A.** High concentrations of DDX3X (red) accumulate the edge of early stage spreading cells. **Panel B.** A close-up of the ROI in Panel A. **Panel C.** A close-up of the ROI in Panel B shows DDX3X decorating actin stress fibres (green), highlighted with yellow arrows.

These data are representative of those obtained from at least three separate experiments.

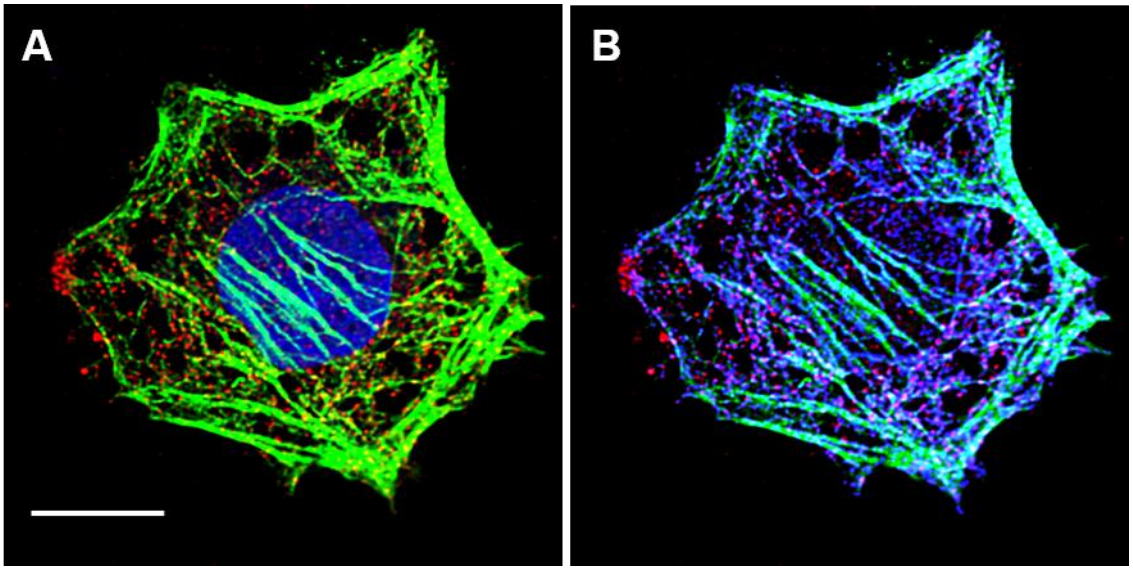

Figure 6.5 Co-localisation analysis provides evidence for DDX3X association with the Actin cytoskeleton

MRC-5 SV2 cells were seeded onto coverslips coated with 8µg/cm^2 collagen I, at a density of 15,000 cells/cm^2 and incubated at 37ºC for 40 mins. Cells were immersed in ice cold saponin solution for 5 seconds prior to fixation using 4% (v/v) PFA, saponin permeabilised and dual immuno-fluorescence stained using anti-DDX3X (Ab62) diluted at 1:500, with the addition of Alexa Fluor conjugated phalloidin, as described in the Materials and Methods. Images were obtained using a Leica SP8 confocal microscope at 63x magnification. Deconvolution was performed using Huygens Professional deconvolution software, using defaults, including a signal/noise ratio of 20dB. Scale bar indicates 10µm.

Panel A. Early-stage spreading wt. MRC-5 SV2 cell at 40 mins, showing DDX3X (red) and the actin cytoskeleton (green). **Panel B.** The result of co-localisation threshold analysis. This image shows only pixels above threshold levels with the original channels in red (DDX3X) and green (Actin); the blue channel shows co-localised pixels from both red and green channels.
These data are representative of those obtained from at least three separate experiments.

6.7 DDX3X and eIF4E localisation is differentially affected by Leptomycin-B

The antifungal antibiotic Leptomycin-B (LMB) was first isolated from Streptomyces in 1983 and has since been seen to be a potent tumour suppressor in mammalian fibroblast and fission yeast cells (Yoshida et al. 1990), specifically causing cell cycle arrest at both G1 and G2 phases. A study of *Schizosaccharomyces pombe* identified the cellular target of LMB as the exportin, CRM1 (Nishi et al. 1994; Mahboobi et al. 2015). CRM1 is a nuclear export receptor for proteins carrying the leucine-rich nuclear export signal (NES) (Fornerod et al. 1997) and for the export of RNA. LMB is a specific inhibitor of CRM1-mediated nuclear export introducing a covalent modification to CRM1 at Cys-539 (Kudo et al. 1999). CRM1 binds its cargo in the nucleus, before translocating it to the cytoplasm for release (Figure 6.6). CRM1 then returns to the nucleus to repeat the cycle in a RanGTPase-dependent manner (Mattaj & Englmeier 1998; Kau et al. 2004). Nuclear export of DDX3X has been reported to be at least in part facilitated by CRM1-mediated nuclear export, (Sekiguchi et al. 2004; Lai et al. 2008). In contrast, eIF4E localisation is unaffected by LMB in fibroblasts (Linda McKendrick et al. 2001; Lasko et al. 2005).

To investigate whether the steady state localisation of DDX3X affected the localisation of eIF4E in fibroblasts, MRC-5 SV2 cells were allowed to grow to 70% confluency before being trypinised and re-spread for 40 minutes on collagen-coated coverslips. DDX3X and eIF4E were visualised by confocal microscopy. As shown in Figures 6.7A and B, and in agreement with previous data (Figure 6.2), both eIF4E and DDX3X were perinuclear, with a large degree of colocalisation (as shown by the yellow pseudo-colour in the merged images). However, as expected a population of these proteins was also localised to the leading edge of the cells. LMB treatment (Panels C and D) potently inhibited the steady state localisation of DDX3X in the early-stages of fibroblast spreading (Figure 6.7D; quantified in Figure 6.8). However, localisation of eIF4E at the cell periphery appeared to be unaffected by LMB treatment. These data confirm that DDX3X shuttles between the nucleus and cytoplasm in a CRM-1 dependent manner, and suggest that the peripheral localisation of eIF4E is not dependent upon DDX3X.

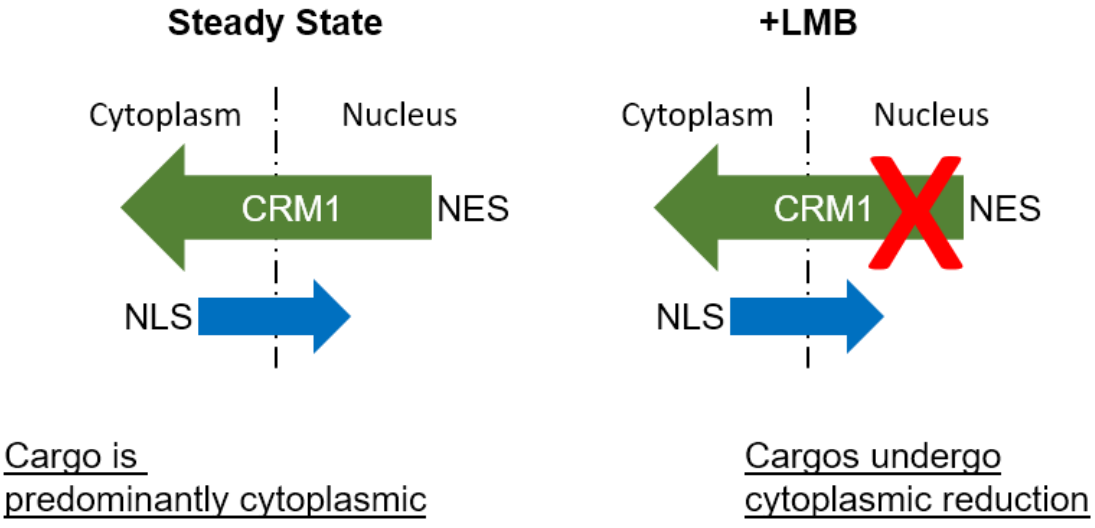

Figure 6.6 The effect of Leptomycin-B on CRM1, a nucleo-cytoplasmic shuttling protein.

CRM1 is a nuclear export receptor for proteins carrying the leucine-rich nuclear export signals (NES). CRM1 binds nuclear proteins expressing NES and translocate them through the nuclear pore complex (NPC) for release into the cytoplasm. Leptomycin-B (LMB) is a specific inhibitor of CRM1-mediated nuclear export, disrupting the normal function CRM1 by introducing a covalent modification at Cys-539. In the cytoplasm, importins bind to their cargo via a recognition sequence called the nuclear localisation signal (NLS). This importin : cargo complex then translocate through the NPC by interacting with nucleoporins. This mechanism of NLS facilitated transport remains unaffected by the action of LMB (Kau et al. 2004).

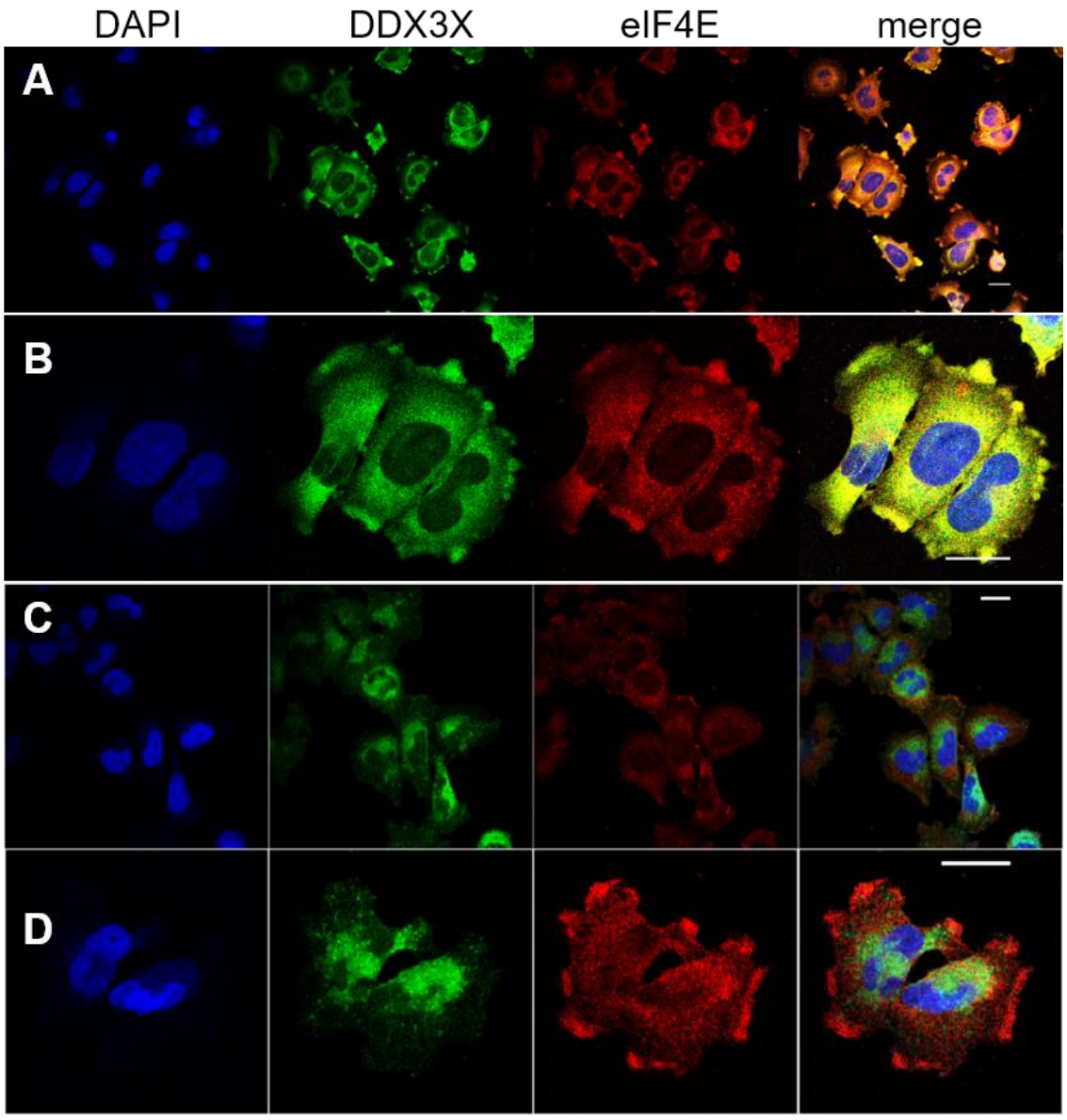

Figure 6.7 The effect of Leptomycin-B (LMB) on the association of eIF4E and DDX3X at the periphery of a fibroblast cell in the early stages of spreading

MRC-5 SV2 cells at 70% confluency were incubated for 2 hours in the absence (Panels A and B) or presence (Panels C and D) of 4ng/mL leptomycin-B (LMB). Cells were dissociated from the substrate using trypsin and re-seeded onto coverslips coated with 8µg/cm^2 collagen I, at a density of 15,000 cells/cm^2. Original media (+/- LMB) was reapplied to all cells, before incubation at 37ºC for 40 mins. Fixation was performed using 4% (v/v) PFA prior to saponin permeabilised and dual immuno-fluorescence stained with anti-DDX3X (Ab62) diluted at 1:500 and anti-eIF4E (Ab53) diluted at 1:100, as described in the Materials and Methods. Images were obtained using a Leica SP8 confocal microscope at 63x magnification. Scale bars indicates 20µm. These data are representative of those obtained from at least three separate experiments.
Panel A. In wild type, DDX3X and eIF4E is found throughout the cell, but most specifically at the leading edges of lamellipodia. **Panel B.** A close-up of wild type cells. **Panel C.** LMB causes a dramatic change in DDX3X localisation. **Panel D.** A close-up of cells grown in the presence of LMB.

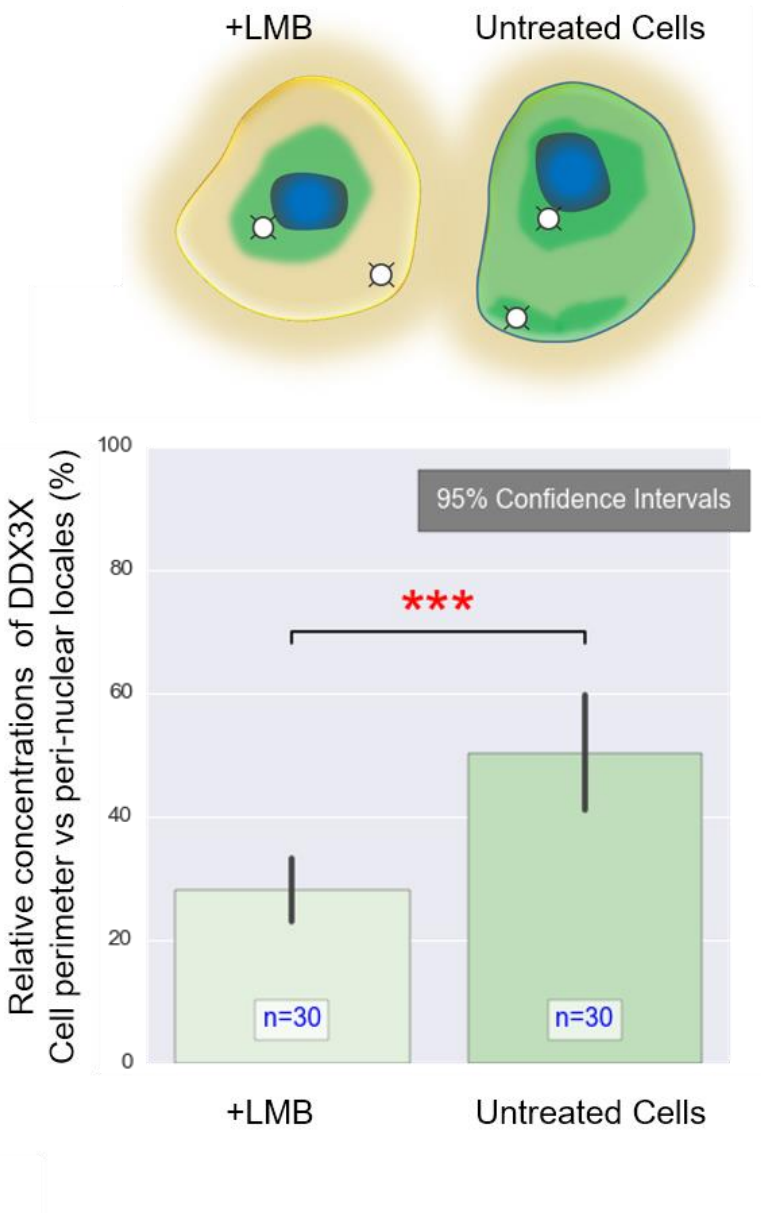

Figure 6.8 Application of Leptomycin-B at low concentrations has a greater affect on the steady-state localisation of DDX3X than on eIF4E

Cells were prepared and treated as described in Figure 6.2. In the presence of LMB, DDX3X concentrations reduce significantly at the periphery of the cells. However, there was no apparent visual change in the location or concentrations of eIF4E when comparing treated to untreated cells.

Statistics were obtained by examination of regions of interest (ROIs) close to the inner periphery of cells where there appeared to be the highest concentration of DDX3X fluorescence. ROI mean pixel intensities were recorded for the DDX3X channel only. This process was repeated for the same shape ROI, in an area of the cell close to the nucleus which appeared to be expressing the most DDX3X fluorescence (top inset). For each cell the intensity ratio between the distal ROI and the peri-nuclear ROI were recorded. Bar chart confidence intervals are 95%. Statistical analyses were performed using Welch's t-test (***, $p \leq 0.001$)

6.8 The *in situ* Proximity Ligation Assay

The *in situ* Proximity Ligation Assay (PLA) (Söderberg et al. 2006) is a specific and sensitive immunofluorescence technique able to yield clear and intense fluorescent signals between closely located endogenous proteins, or between epitopes of the same protein. Creation of a genuine PLA fluorescence between two putative interacting proteins is an improbable event when the epitopes are further than 40nm apart, meaning that such a system offers the stringency of a super-resolution system able to colocalise proteins beyond the physical constraints of the optical diffraction barrier (Huang et al. 2010). This places PLA within the category of *in situ* super-resolution techniques such as Förster resonance energy transfer (FRET), FRET derivatives such as bioluminescence resonance energy transfer (BRET), and bimolecular fluorescence complementation (BiFC) - all of which provide fluorescent signals to confirm the presence of two closely located or interacting proteins. The combining of two stringent recognition events - antibody binding and even more stringent oligonucleotide binding, endows PLA with greater sensitivity than can be gained solely with standard immunocytochemistry/Immunofluorescence (ICC/IF) techniques.

In ICC, initial antibody-antigen binding occurs through processes dependent not only on the specificity of the antibody for target epitopes, but also the antibody concentration and disassociation constant (K_d) compared to other competing molecules, be they cross-reacting antibodies or proteins added during the blocking stages. Such competitive binding environments inevitably lead to some amount of cross-reactivity and non-specific adsorption mitigated in part by reducing antibody concentrations and increasing the strength of blocking reagents. The corollary of taking such precautions may lead to an increase in the specificity of the correct binding of the appropriate antibodies; however, the number of correctly targeted antibodies and the strength of the resultant fluorescent signals will often diminish, compromising the signal to noise ratio. PLA excels in such conditions where antibody binding is quantitatively small and highly specific. Under these circumstances the low stoichiometry of antibody to target creates an environment which makes the second selectivity step in the PLA process - oligonucleotide hybridisation, act as a most stringent

binary filter in reducing non-proximal antibodies to a non-participatory state, unable to contribute to any fluorescence to the final image.

6.9 Proximity Ligation Assay – An overview of methodology

When working with adherent cells, for the detection of two epitopes of a common protein, or of the interaction of two proteins, the PLA method functions in the following manner: Cells are generally grown on coverslips or in glass-bottomed dishes, then fixed, permeabilised and blocked as per a standard ICC protocol. Primary antibodies, the same as would be used for a standard ICC protocol, are added to bind to the specific proteins or epitopes under investigation. PLA probes, secondary antibodies with covalently-linked oligonucleotide proximity probes are added (Figure 5.1 Ai). Such PLA probes are currently available off-the-shelf from Sigma-Aldrich, and sold under the brand-name Duolink®, a product originally commercialised by Olink Bioscience and first developed by Ulf Landegren at Rudbeck laboratory, Uppsala, Sweden. When the PLA probe pairs are in close enough vicinity to each other, the addition of complementary connector oligonucleotides is enough to form a circular polynucleotide DNA bridge between itself and the two proximity probes harbouring complementary single-stranded DNA sequences (Figure 5.1 Aii). The addition of ligase and free nucleotides allows for the ligation of a fully circular DNA bridge between the two proximity probes (Figure 5.1 Aiii). The closed-circle of DNA is now capable of being amplified by phi29 DNA polymerase, facilitating the creation of hundreds of copies of concatenated single-stranded DNA with complementary bases to the circular template, in a process called rolling circle amplification (RCA). The DNA circle and its concatemeric product remain covalently conjugated to a single antibody-antigen complex, with the other proximity probe cleaved early in the RCA process. Hybridisation of complementary fluorescently-labeled oligonucleotides to the single-stranded DNA concatemeric product of RCA, allows for the indirect visualisation of the proximal proteins using both confocal and standard epifluorescence microscope imaging (Figure 5.1 B).

When performing PLA alone and without the introduction of other fluorescent stains common to ICC, acquired images present the researcher with

many of the same post-acquisition processing issues as would be encountered when imaging strongly fluorescent materials such as quantum dots. Images comprised of relatively sparse and intensely bright foci each express high signal to background (S/B) and signal to noise (S/N) ratios compared to levels typically encountered with ICC. Theoretically, such intense signals should allow for easy image interpretation and data-harvesting. However, many physical properties of the specimen most notably its z-plane depth, and inherent constraints due to the quality of the microscope hardware (most notably the quality of its objective lens), camera sensitivity and resolution can lead to it having a characteristic point spread function (PSF) which may hinder precise and fast evaluation of every spot. Such issues as these should be properly managed when designing PLA analysis software, and in the interpretation of PLA results data.

As with all *in situ* visual detection techniques, interpretation of PLA-produced images presents a unique set of challenges. Many of these can only properly be mitigated with a full and proper understanding of the assay characteristics and of the pros and cons of employing one of the broad arrays of analysis tools now available. All images were processed using PLAY, Proximity Ligation Assay analysis software developed for the analysis of PLA produced images, their foci characteristics, their cellular location, as well as the characteristics of the cell within which the foci reside. PLAY performs statistical analyses and presents results both in tabular form and graphically using heat-maps, point plots, density plots, scatter plots, and more. The development and specifications of PLAY are discussed at length in Chapter 5.

6.10 Using the Proximity Ligation Assay to investigate the interactions of eIF4E and DDX3X

Initial studies were employed to investigate putative associations between DDX3X and eIF4E (Figure 6.9). As shown in Panels A and B, these representative cells showed an enrichment for colocalised DDX3X and eIF4E at the leading edge of the spreading cells. Further analysis (insets Ai, Aii and Bi) demonstrated that this association was particularly prevalent where nascent lamellipodia appeared to be forming. However, interactions in some other areas of the cytoplasm show that these associations are not solely confined to the cell

periphery (inset Bii). To confirm these results, suitable controls were also analysed using PLAY software (see Chapter 5).

6.11 Confirmation of a DDX3X knock-down cell line using PLAY

An important control for the PLA analysis is to determine what happens when one of the partner protein has reduced expression in the cell. To facilitate this, CRISPR/Cas9 was used in an attempt to deplete DDX3X from the MRC-5 SV2 cell line, as described in the Materials and Methods. Figure 6.10 shows two of the clonal cell lines that were obtained, DDX3_2A and _2C. Western blot analysis of cell extracts (Panel A) showed that DDX3X protein levels were reduced, but not ablated. Quantification of these data showed a 60% and 42% decrease in DDX3X levels, respectively (Figure 6.10B). When parental cells and DDX3X_2A cells were allowed to spread on collagen for 40 minutes, clear differences were seen in their morphology and spreading behaviour. The data shown in Figure 6.11 summarises results from the analysis of over 60 individual cells of each cell line and PLAY analysis confirms that levels of DDX3X:eIF4E interactions are significantly lower in all cellular compartments of the DDX3X knock-down (KD) cells when compared to wild type cell. Data presented in Figure 6.11 shows that the DDX3X KD cells showed on average 5.73 foci per cell as opposed to the wild type having 9.79, a reduction of putative DDX3X:eIF4E interactions of 41.5%. These findings are comparable to the reduction in DDX3X protein levels seen in the Western Blot analysis (Figure 6.10). In addition, analysis of the DDX3X : eIF4E foci in different cellular compartments show that, as expected, there was a significant difference in the number of foci between knock-down cells and wild type cells in both the nuclear and cytoplasmic compartments (Figure 6.11).

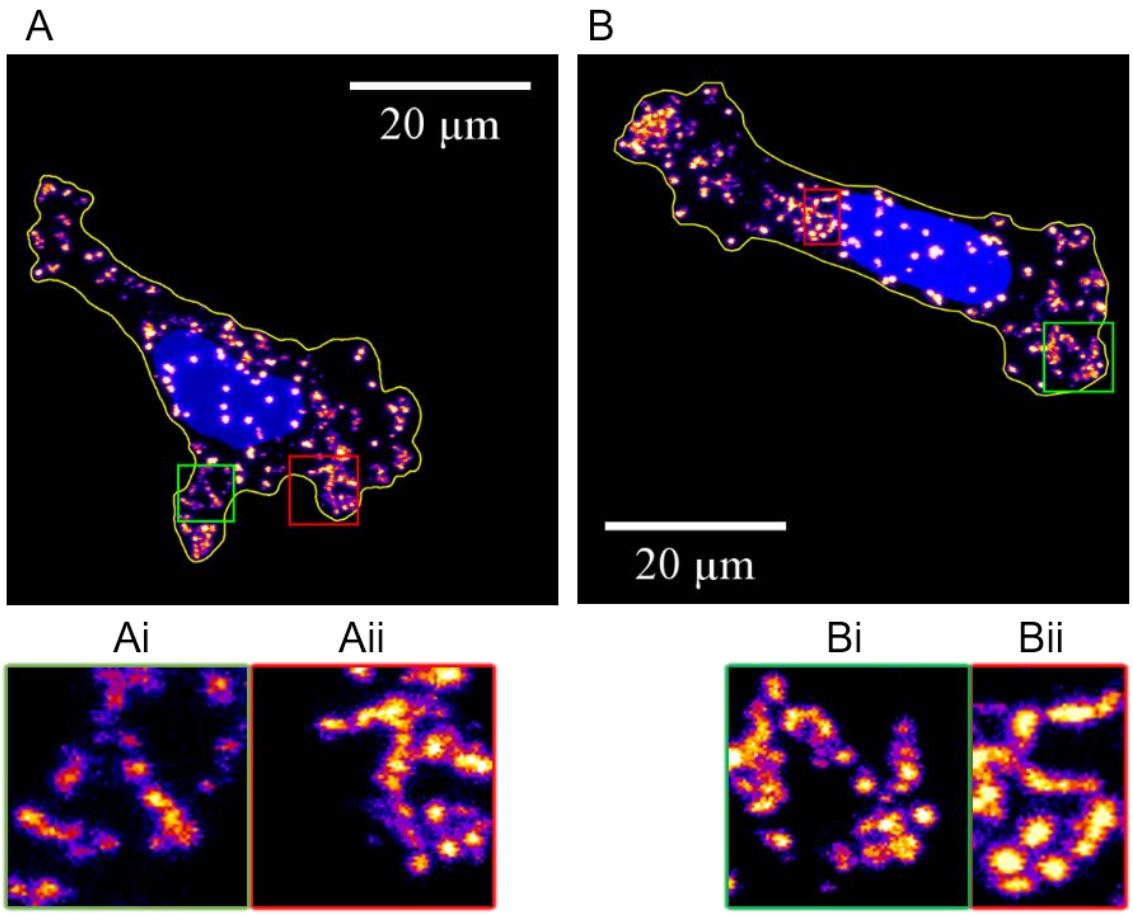

Figure 6.9 Proximity Ligation Assays show putative association between DDX3X and eIF4E

MRC-5 SV2 cells were seeded onto coverslips coated with 8µg/cm^2 collagen I, at a density of 15,000 cells/cm^2 and incubated at 37ºC for 40 mins. Cells were fixed using 4% (v/v) PFA, saponin permeabilised and dual immuno-fluorescence stained with anti-DDX3X (Ab52) diluted at 1:1000, anti-eIF4E (Ab106) diluted at 1:400, as described according to Materials and Methods. Using a scanning confocal microscope Images were obtained by a maximum intensity projection over 47 z-slices each taken with a z interval of 0.292µm. All images show the PLA channel with a Fire intensity gradient applied with ImageJ, and the DAPI channel shown in blue. **Panel A.** Proximity Ligation Assay, shows DDX3X and eIF4E in close proximity, with putative DDX3X-eIF4E complexes forming striated patination as would be expected if it was transported over the cytoskeleton. **Panel B.** Putative interactions between eIF4E and DDX3X are particularly vivid at the edge of cells, where nascent lamellipodia appear to be forming. **Insets (Ai, Aii, Bi,Bii).** Close-ups of ROIs featured in the main panels.

These data are representative of those obtained from at least three separate experiments.

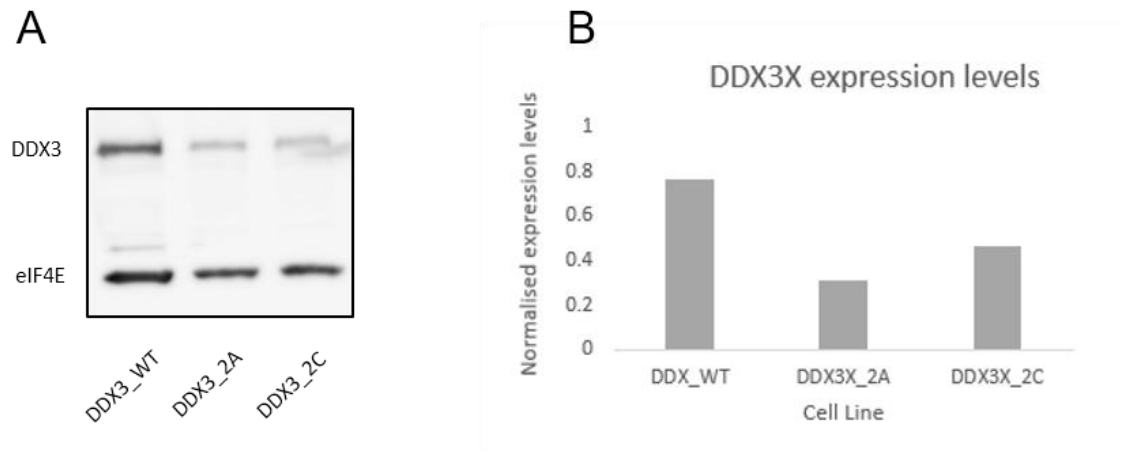

Figure 6.10 CRISPR knock-out of the DDX3X gene in MRC-5 SV2 cells results in a knock-down of protein expression

Panel A: A Western Blot showing DDX3X expression levels in MRC-5 SV2 cells. With eIF4E as a loading control, putative DDX3X gene knockouts using CRISPR show the new cell lines DDX3_2a and DDX3_2c with reduced levels of DDX3X expression. **Panel B:** Quantification of the levels of DDX3X in the Western blot (Panel A) shows the DDX3X_2A cell line expressing approximately 40% of the wild type DDX3X expression, and DDX3X_2C expressing approximately 58% of the levels seen in the wild type cells.

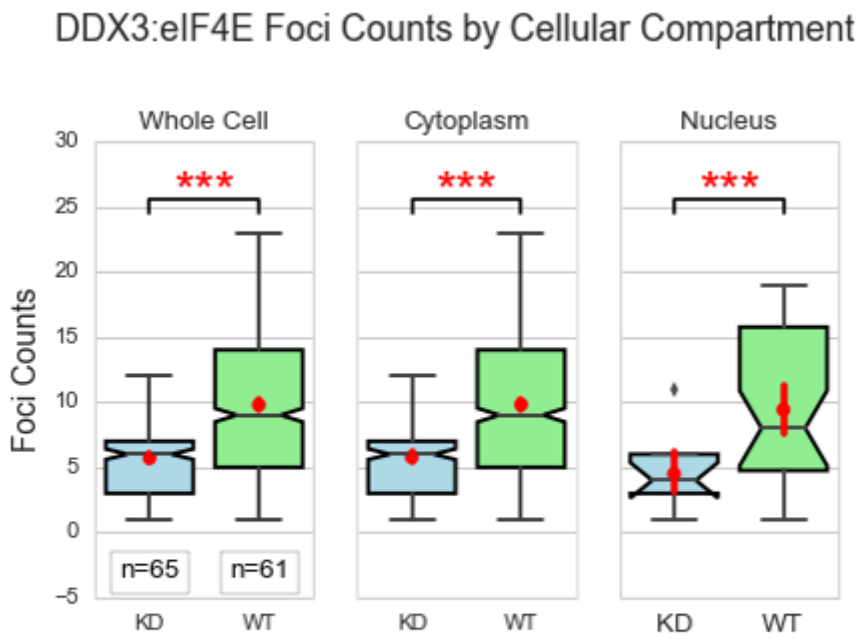

Figure 6.11 The Proximity Ligation Assay (PLA) confirms a greater than a 40% reduction in DDX3X expression levels in the CRISPR knock-down (KD) cell line compared to wild type

CRISPR knock-out cell line DDX3X_2A, confirmed to be a knock-down with DDX3X expression levels at just 40% of wild type, is now referred to as the knock-down (KD).

DDX3X CRISPR knock-down (KD) and wild type cells were seeded, fixed, stained and visualised using the Proximity Ligation Method as described in Figure 6.11. PLAY analysis confirms levels of putative DDX3X:eIF4E interactions are significantly lower in all cellular compartments, when compared to wild type.

The knock-down shows a 41.5% reduction in DDX3X : eIF4E interactions, suggesting a comparative reduction in DDX3X native protein levels. 95% confidence intervals are marked as notches around the median and as red bars around the mean point estimate. Welch's t-Test p-values are shown for all mean point estimates (***, $p \leq 0.001$) .

6.12 Correlation maps elude to significant differences between parental and DDX3X KD cell lines

Utilising the Pearson r correlation coefficient as a basis for comparison, PLAY software allowed for the creation of matrices made for the wild type (Figure 6.12) and DDX3X KD (Figure 6.13) cell lines. The software also allowed for the generation of a 21-attribute differential correlation map (Figure 6.14A) from these original data. These included foci count and intensity characteristics, cell shape and size, intercellular adjacent measurements, nuclear volume etc. as discussed in detail in Chapter 5. From the differential correlation map (Figure 6.14A), correlation values show particularly strong changes between cell lines as highlighted in red on the heat-map as well as in tabular form with more mathematical precision (Figure 6.14B). These are summarised below:

i. **'Foci per cell unit area' vs. 'intercellular adjacency'**
   'Foci per cell unit area' shows stronger positive correlation with 'intercellular adjacency' in DDX3X KD cells than in wild type cells. This is suggestive of intercellular communication having more of an effect on intracellular signalling pathways in the knock-down cell line than in wild type cells. As such it poses an interesting question as to if this is a real phenomenon, and if so could be worth pursuing with further research. However, intercellular adjacency distance profiling is an inaccurate measure at best, whilst using currently implemented image acquisition protocols. These protocols do not methodically ensure that cells slightly outside of the periphery of each captured image are incorporated part of a full dataset from which all intracellular distances are considered. The issues around the accuracy of adjacency measurement are discussed in more detail in Chapter 5.

ii. **'Spot Distance from Perimeter' vs. 'Cell Perimeter size'**
   In the DDX3X KD cell line, 'Spot Distance from Perimeter' shows moderate positive correlation with Cell Perimeter size ($r \approx 0.5$). This suggests that as the perimeter grows in KD cells, DDX3X interactions occur further away from the perimeter. Taking these

data on their own, one might hypothesise that during the earliest stages of spreading when the cell area and the cell perimeter are at their smallest, more DDX3X:eIF4E foci were found closer to the cell perimeter. These data suggest that these interactions could be a necessary component in the initial stages of active actin polymerisation helping to remodel the leading membrane edge.

iii. **'Spot Distance from Perimeter' vs. 'Cell feret'**

In the DDX3X KD cell line, 'Spot Distance from Perimeter' shows low positive correlation to cell feret size ($r \approx 0.3$) where negligible correlation exists in wild type cells between ($r \approx 0.2$ and $r \approx 0.1$, respectively). These data may be interpreted as DDX3X:eIF4E interactions taking place further away from the cell perimeter as the cell grows in their area as well as in their feret length.

iv. **'Cell perimeter length' vs. 'Cell solidity'**

In DDX3X KD cells, there is a significantly less negative correlation between cell perimeter lengths and cell solidity ($r \approx -0.2$) compared with wild type cells ($r \approx -0.5$). These data imply that as the cells spread and the perimeter becomes larger, DDX3X KD cells are staying more solid in shape (discussed in Chapter 5) than wild type cells. As wild type cells spread and develop in size, they tend to have a much less smooth outline and more podium outgrowths than the DDX3X KD cells.

v. **'Solidity' vs. 'Cell feret'**

In DDX3X KD cells, there is a significantly less negative correlation between cell solidity lengths and cell feret ($r \approx -0.2$) when compared with wild type cells ($r \approx -0.5$). These data imply that as parental cells grow in feret diameter (essentially, their length), they become substantially less solid (spikier) than their DDX3X KD counterparts do. As DDX3X KD cells lengthen they tend to stay relatively more solid. Taken with the findings above, this suggests that DDX3X KD cells tend to spread more evenly with fewer podial outgrowths than wild type (parental) cells.

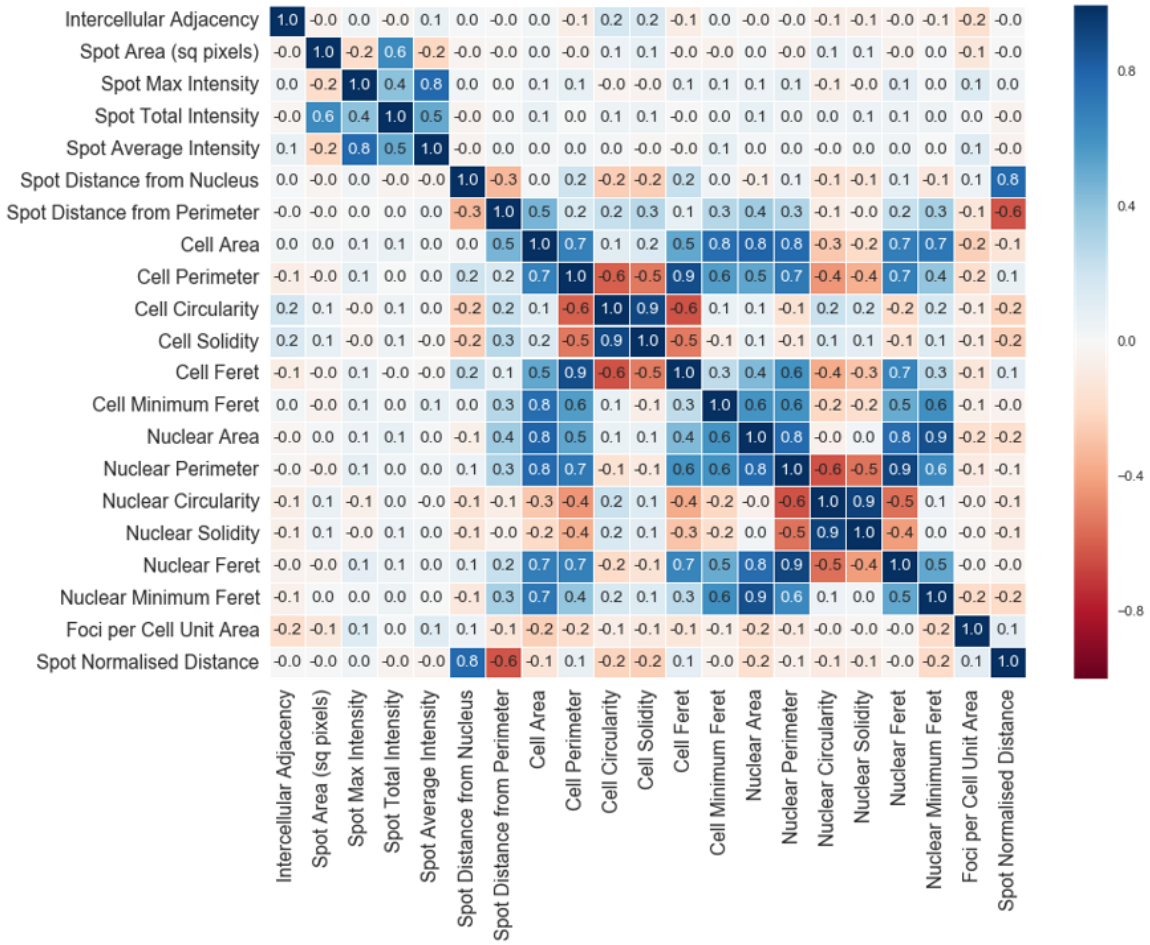

Figure 6.12 Correlation map, for attributes of wild type cells expressing DDX3X : eIF4E PLA foci

Using wild type MRC-5 SV2 cells and the PLA method described in Figure 6.11 to visualise putative DDX3X : eIF4E interactions, post-acquisition processing of PLA images was performed using PLAY, as described in Chapter 5.

This results matrix summarises the strength in correlation between 21 attributes, and displays them in heat-map form along with associated Pearson r correlation coefficients (to one decimal place).

This map is a copy of that found in Figure 5.15, reproduced here to enable analysis in the context of this experiment as opposed to using it as an example of PLAY's correlation mapping function.

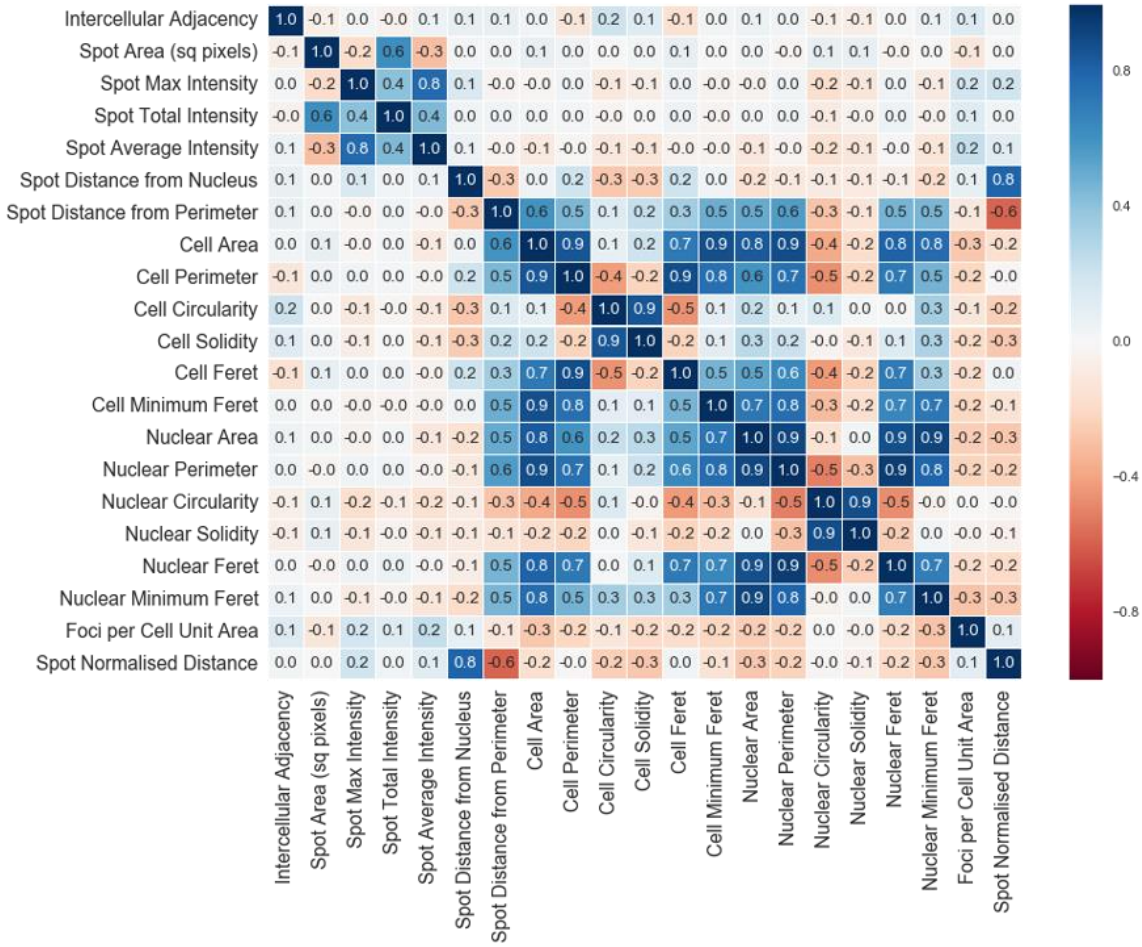

Figure 6.13 Correlation map, for attributes of CRISPR DDX3X Knock-down cells expressing DDX3X : eIF4E PLA foci

Using CRISPR DDX3X knock-down (KD) cells, and the PLA method described in figure 6.11 to visualise putative DDX3X : eIF4E interactions, post-acquisition processing of PLA images was performed using PLAY, as described in Chapter 5.

This results matrix summarises the strength in correlation between 21 attributes of the knock-down cells, and displays them in heat-map form along with associated Pearson r correlation coefficients (to one decimal place).

A

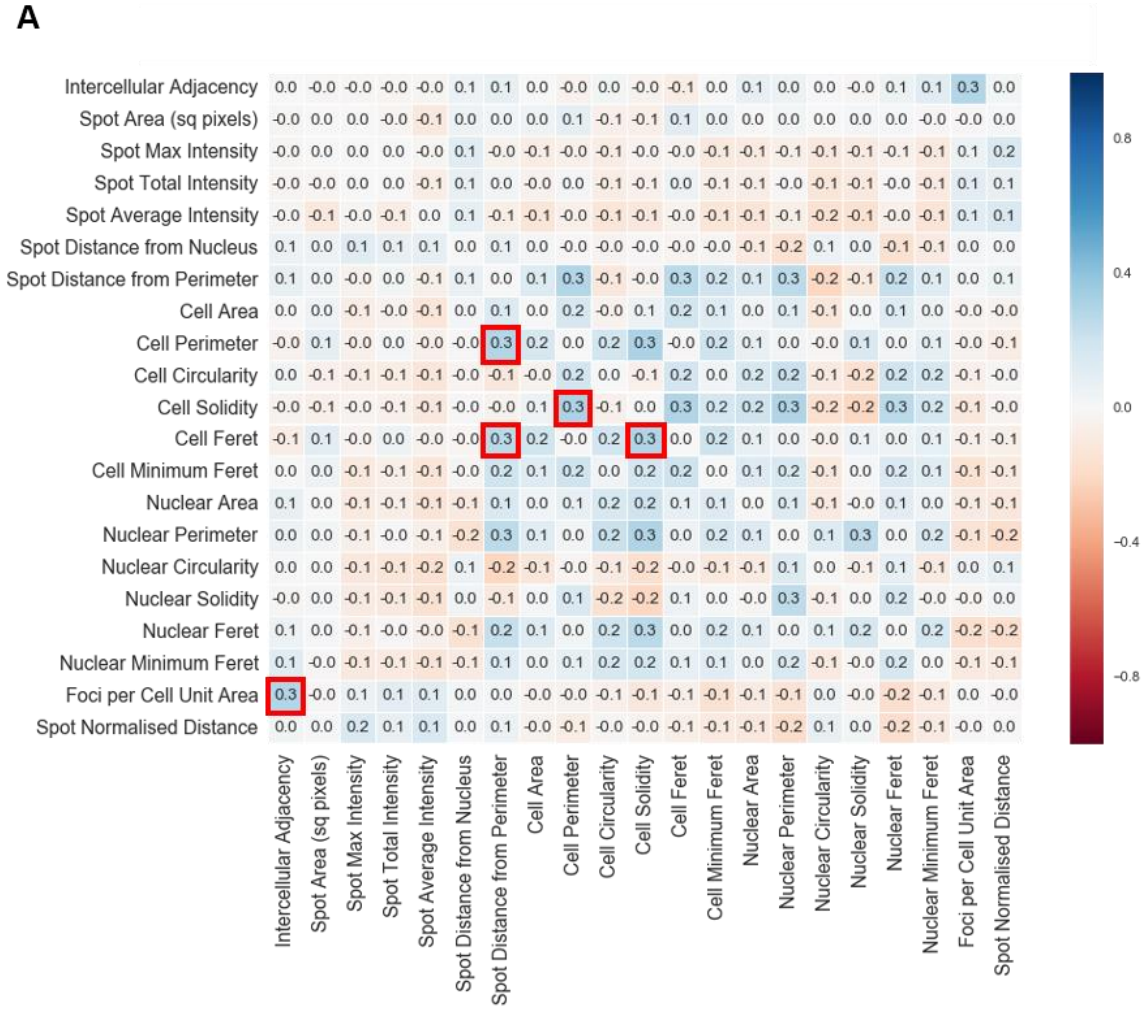

B

	Intercellular Adjacency	Spot Distance from Perimeter	Cell Perimeter	Cell Solidity
Cell Perimeter	-0.044	**0.29**		
Cell Solidity	-0.034	-0.033	**0.309**	
Cell Feret	-0.075	**0.266**	-0.002	**0.3**
Cell Minimum Feret	0.003	0.202	0.197	0.173
Foci per Cell Unit Area	**0.289**	0.021	-0.035	-0.107

Figure 6.14 Differential correlation mapping provides an insight into cellular processes influenced by DDX3X

Panel A. A difference of correlation maps, highlighting the differences between correlation maps for CRISPR KD and wild type cells (Figures 6.12 and 6.11, respectively): *Difference map = (KD map) - (WT map)* Any positive value in the difference map is attributed to a more positive Pearson r value in the knock-down cell line. **Panel B.** Further numerical precision is provided for the correlation coefficients of most interest, highlighted in Panel A (red). These data elude to amongst other things, a change in PLA foci locale between cell lines.

6.13 DDX3X KD cells have a significantly smaller surface area than parental cells

Figure 6.11 shows that, as expected, the number of interactions between DDX3X and eIF4E was lower in the DDX3X KD cells compared to parental cells. However, the distribution of cell sizes between groups may be skewing the interpretation of the number of putative interactions, given that the median cell areas differ so greatly (Figure 6.15A). Normalising the foci counts for cell size ambivalence enables the foci count to be indifferent to this variable metric and provides further evidence that foci counts significantly differ between the experimental groups (Figure 6.15B). This analysis backs up the evidence to show that the CRISPR/Cas9 editing process genuinely created a DDX3X KD cell line. This normalised form of spot counting cannot, however, normalise for the stage at which the cells are in the spreading process. The number of DDX3X:eIF4E foci in both cell lines negatively correlates with the area of the spreading cells (Figure 6.15C), suggesting higher levels of DDX3X:eIF4E interactions exist during the earliest stages of the cell spreading process. This may indicate that such interactions are necessary to initiate the spreading process, and are not present simply as a response to other spreading processes.

6.14 DDX3X:eIF4E interactions occur closest to the cell periphery in the acute stages of spreading

In early stage spreading cells, DDX3X:eIF4E interactions identified by PLA are highly concentrated at the periphery of the cell (Figure 6.9). Analysis of at least 60 cells using PLAY shows a significant difference between parental cells and DDX3X KD cells, with more foci, found closer to the cell perimeter in parental cells (Figure 6.16A). However, this measurement relied on Euclidian spot distance measurements from the periphery. As these are mixed cell populations, errors could be introduced here; an absolute distance could reflect one thing in a highly spread, large cell, or something entirely different in a small cell (Figure 6.16B, insets i and ii). For this reason, a ‘spot normalised distance’ measurement was employed (Figure 6.16C). This measurement is a simple percentage of the distance between the nuclear membrane and the closest part

of the periphery. Here, a spot normalised distance measurement of 0% places a spot in the nucleus or on its nuclear envelope, and a value of 100% places the spot at the cell periphery, although this normalized measurement will tend to fail as the cells become less round and less solid (Figure 6.16B, inset iii). Spot normalised distance measurements of foci (Figure 6.16C) confirms that foci are significantly closer to the perimeter of the parental cells when compared to the DDX3X KD cells. These data confirm the finding implied in Figure 6.16A.

Further analysis of these data sets showed that DDX3X:eIF4E interactions occurred closest to the cell periphery in the cells with the smallest areas of spread (Figure 6.16D) or in the context of a normalised spot distance (Figure 6.16E), albeit with a low correlation value. These data are consistent with DDX3X being necessary for interactions with eIF4E at the periphery of the cell during acute phases of cell spreading.

6.15 DDX3X knock-down cells are more solid and circular than wild type

Figure 6.17A shows that DDX3X KD cells are significantly more solid than their parental cells. This implies a shape which is less rough at the periphery, less ‘spikey’, with fewer protuberances by way of narrow podia structures such as lamellipodia. DDX3X KD cells also show a significant bias towards being more circular than wild type cells (Figure 6.17B), a characteristic which is in keeping with the phenotypical high solidity measure of the DDX3X KD cells (Figure 6.17A). When considering cells with small areas and those with larger areas, there was no correlation between cell size and circularity for either experimental group (Figure 6.17C). The Pearson r correlation coefficients for cell solidity relative to cell surface area was also very weak (not shown graphically: KD ($r = +0.20704$), parental ($r = +0.154393$)). The implication here is that DDX3X KD cells tend to remain without many podia protuberances for the entire time-course of spreading. These data suggest that DDX3X KD cells were less effective at spreading after initial attachment to the collagen extracellular matrix (ECM).

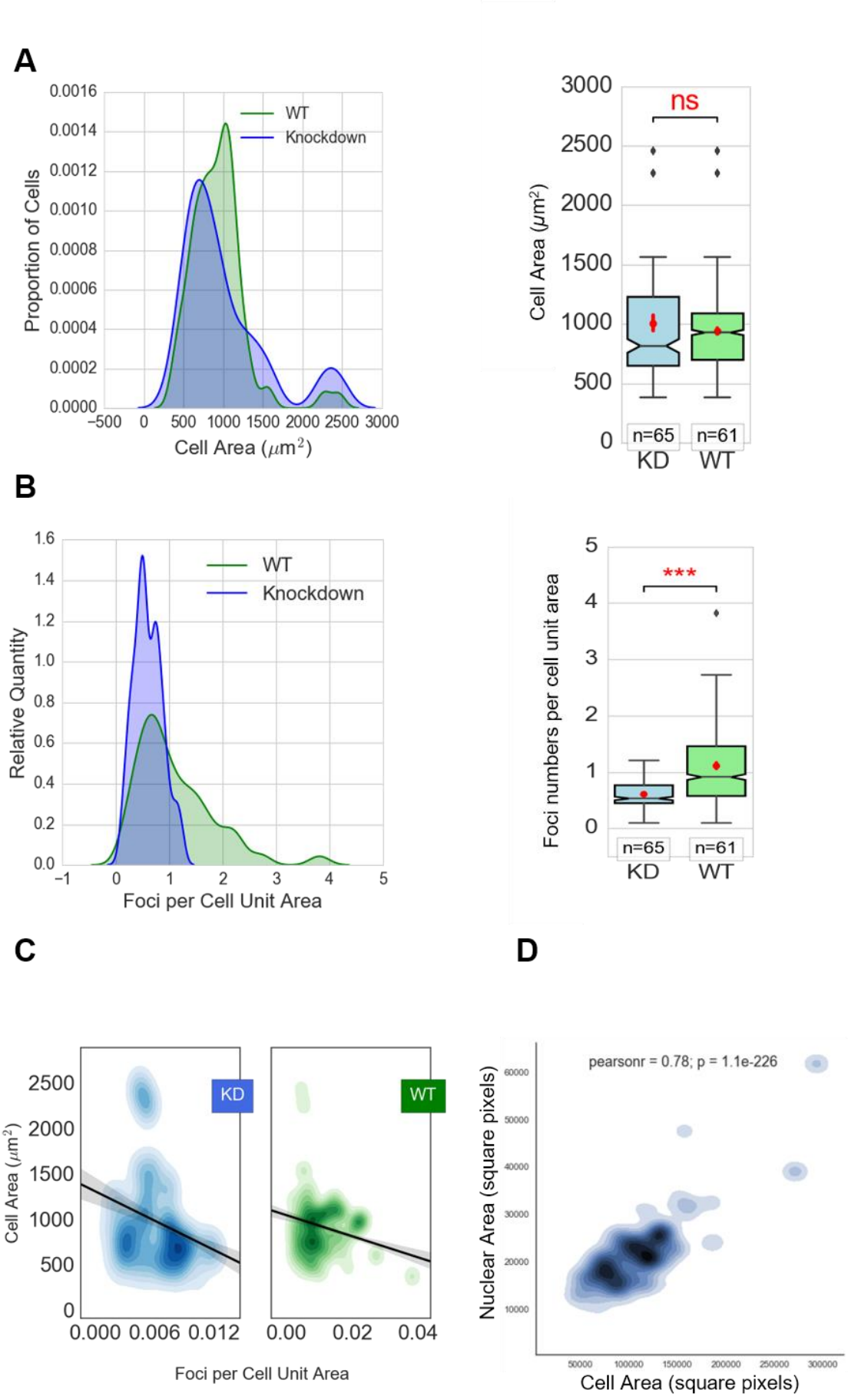
A
WT
Knockdown
Proportion of Cells
Cell Area (μm^2)
ns
Cell Area (μm^2)
n=65
n=61
KD
WT
B
WT
Knockdown
Relative Quantity
Foci per Cell Unit Area
***
Foci numbers per cell unit area
n=65
n=61
KD
WT
C
KD
WT
Cell Area (μm^2)
Foci per Cell Unit Area
D
pearsonr = 0.78; p = 1.1e-226
Nuclear Area (square pixels)
Cell Area (square pixels)

Figure 6.15 Wild type cells show more putative DDX3X:eIF4E interactions than the CRISPR knock-down. In both cell lines, interactions are most abundant in the very earliest stages of cell spreading

DDX3X knock-down cells and wild type cells were grown on collagen-covered coverslips for 40 mins prior to fixation with 4% (v/v) PFA and dual-immunofluorescent staining by using the Proximity Ligation Assay as described in Figure 6.11. Post-acquisition processing of PLA images was performed using PLAY, as described in Chapter 5, and graphs and statistics generated with the appropriate PLAYkits. Statistical analyses were performed using Welch's t-test. Point-estimated means are shown in red with 95% confidence intervals. Median values are embellished with notches signifying 95% confidence intervals. n-statistics signify the number of cells tested for each assay. Statistical analyses were performed using Welch's t-test (ns $P > 0.05$, * $P \leq 0.05$, ** $P \leq 0.01$, *** $P \leq 0.001$) unless stated otherwise. Kernel Density Estimates (KDEs) are visualised using an estimate based on Scott's rule of thumb for bandwidth selection (Terrell & Scott 1992; Hintze 1988). Regression lines show 95% confidence intervals as shaded areas.

Panel A. There is no significant difference in the mean cell areas of KD or wildtype cells, however a large difference in median values intimates that lack of cell-cycle synchronisation may be an issue.
Panel B. Wild type cells have significantly more putative DDX3X:eIF4E interactions per unit area of cell than the knock-down, in line with evidence shown in the Western blotting for the DDX3X protein.
Panel C. Both wild type and knock-down cell lines show a moderate inverse correlation between the number of putative DDX3X:eIF4E interactions per unit area, and the area of basal membrane attached to the coverslips.
Panel D. Using entire assay data, a strong correlation (Pearson's $r = 0.78$), lies between nuclear area and cell area measurements.

A

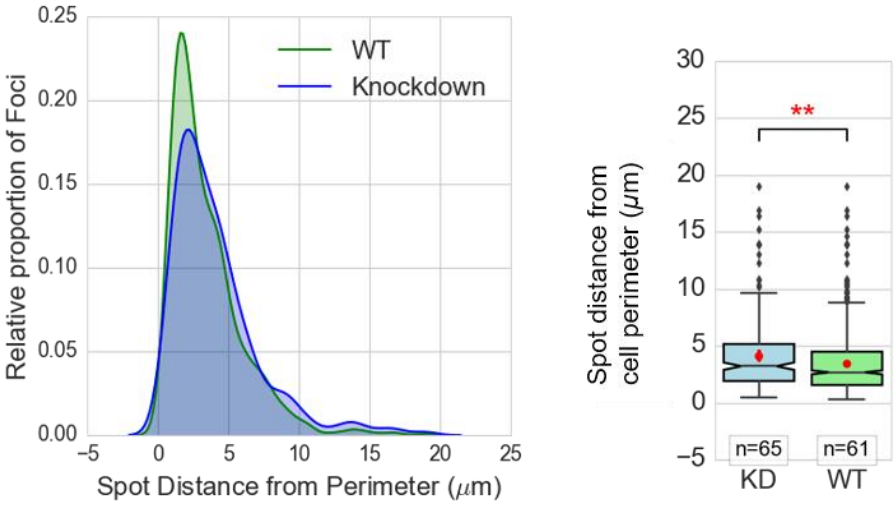
WT
Knockdown
Relative proportion of Foci
0.25
0.20
0.15
0.10
0.05
0.00
−5
0
5
10
15
20
25
Spot Distance from Perimeter (μm)
Spot distance from cell perimeter (μm)
30
25
20
15
10
5
0
−5
**
n=65
n=61
KD
WT

B

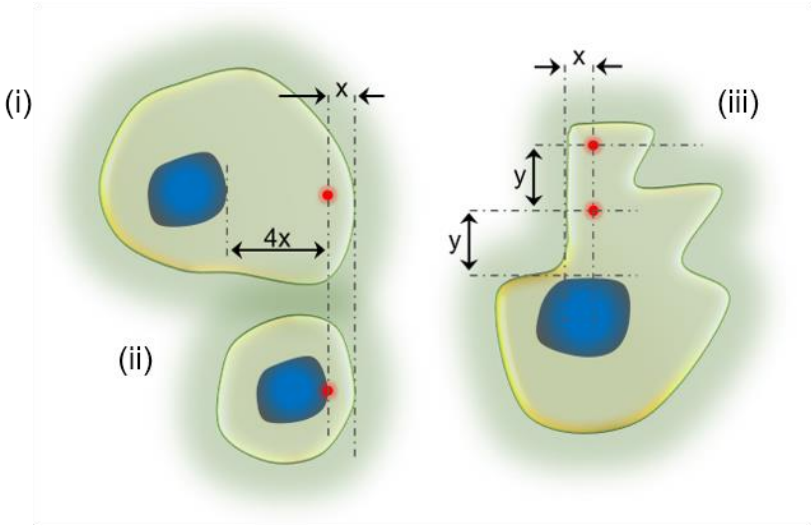
(i)
x
4x
(ii)
x
(iii)
y
y

C

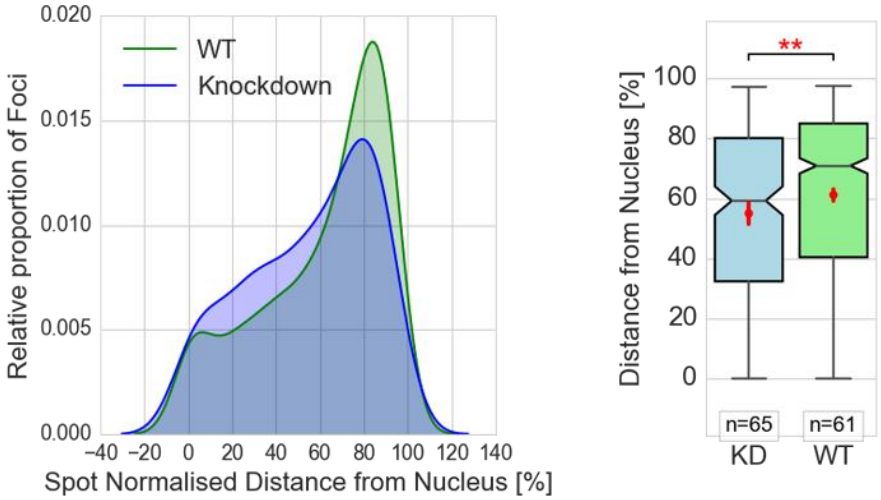
WT
Knockdown
Relative proportion of Foci
0.020
0.015
0.010
0.005
0.000
−40
−20
0
20
40
60
80
100
120
140
Spot Normalised Distance from Nucleus [%]
Distance from Nucleus [%]
100
80
60
40
20
0
**
n=65
n=61
KD
WT

D

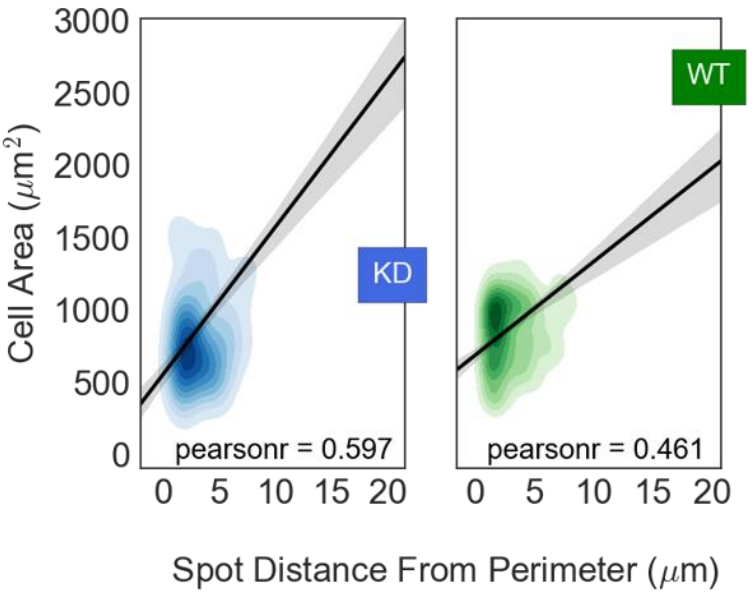
3000
2500
2000
1500
1000
500
0
Cell Area (μm^2)
KD
WT
pearsonr = 0.597
pearsonr = 0.461
0 5 10 15 20
0 5 10 15 20
Spot Distance From Perimeter (μm)

E

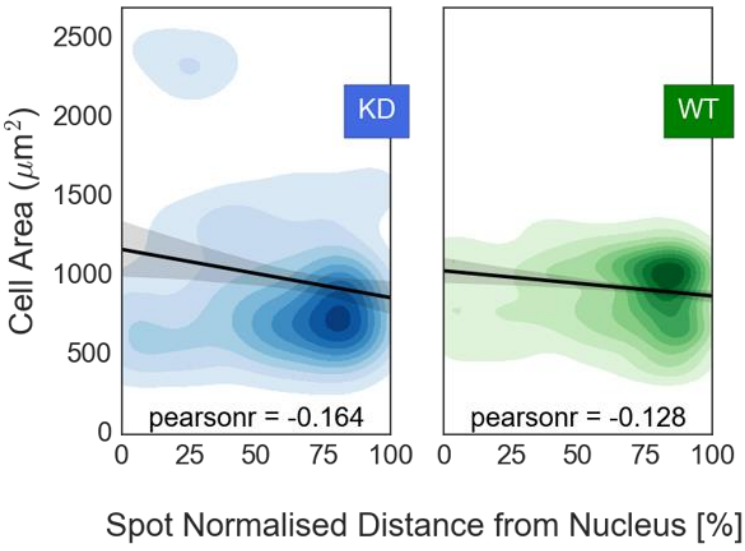
2500
2000
1500
1000
500
0
Cell Area (μm^2)
KD
WT
pearsonr = -0.164
pearsonr = -0.128
0 25 50 75 100
0 25 50 75 100
Spot Normalised Distance from Nucleus [%]

Figure 6.16 The smaller the basal spread of the cell, the closer putative DDX3X : eIF4E interaction are to the cell periphery, with wild type cells showing foci significantly closer to the periphery than the DDX3X knock-down

DDX3X knock-down cells (KD) and wild type cells were grown on collagen-covered coverslips for 40 mins prior to fixation with 4% (v/v) PFA and dual-immunofluorescent staining by using the Proximity Ligation Assay as described in Figure 6.11. Post-acquisition processing of PLA images was performed using PLAY, as described in Chapter 5, and graphs and statistics generated with the appropriate PLAYkits. Statistical analyses were performed using Welch's t-test. Point-estimated means are shown in red with 95% confidence intervals. Median values are embellished with notches signifying 95% confidence intervals. n-statistics signify the number of cells tested for each assay. Statistical analyses were performed using Welch's t-test (ns $P > 0.05$, * $P \leq 0.05$, ** $P \leq 0.01$, *** $P \leq 0.001$). Kernel Density Estimates (KDEs) are visualised using an estimate based on Scott's rule of thumb for bandwidth selection (Terrell & Scott 1992; Hintze 1988). Regression lines show 95% confidence intervals as shaded areas.

Panels A and B.
Both absolute foci distances from the periphery, and relative distance measurements confirm that in early stage spreading cells, putative DDX3X:eIF4E interactions are highly concentrated at the periphery of the cell, with wild type cells showing this effect to a significantly greater extent than the DDX3X knock-down cell line.

Panel C. Relying on Euclidian spot distance measurements from either the nucleus or periphery of the cell can give a misrepresentative account of reality in population of mixed sizes cells (insets I and ii). In more circular cells 'Spot Normalised Distance' measurements are cell-size ambivalent, but this measurement fails in cells of low solidity (inset iii).

Panels C and E.
Cells with a larger basal spread tend to have putative DDX3X:eIF4E interactions happening less close to the cell periphery. This suggests that cells may necessitate such periphery-localised interactions in order to facilitate nascent lamellipodial growth.

A

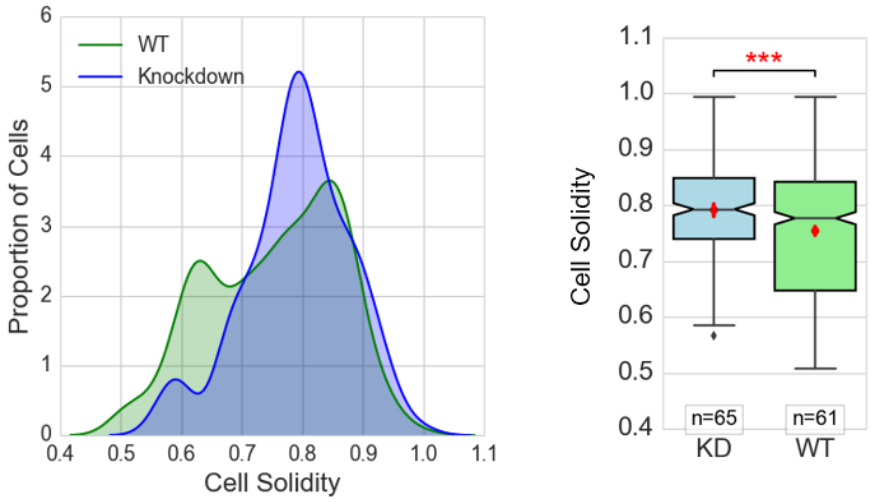
WT
Knockdown
Proportion of Cells
Cell Solidity
***
Cell Solidity
n=65
n=61
KD
WT

B

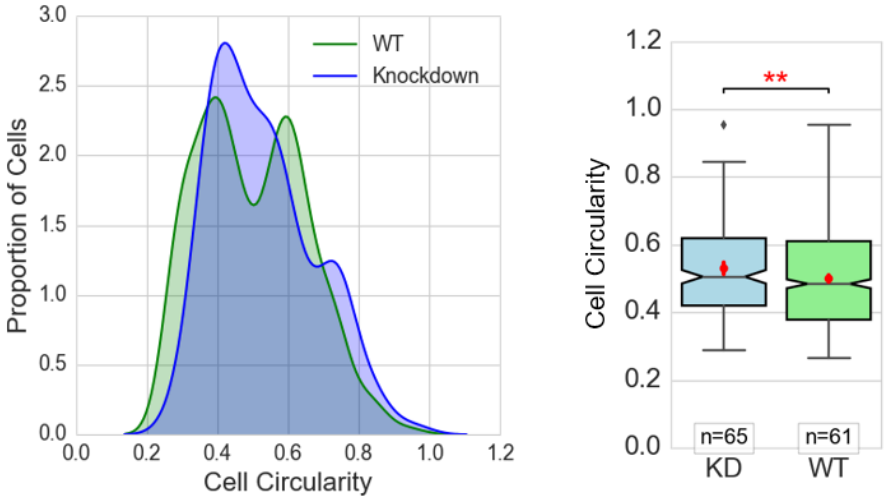
WT
Knockdown
Proportion of Cells
Cell Circularity
**
Cell Circularity
n=65
n=61
KD
WT

C

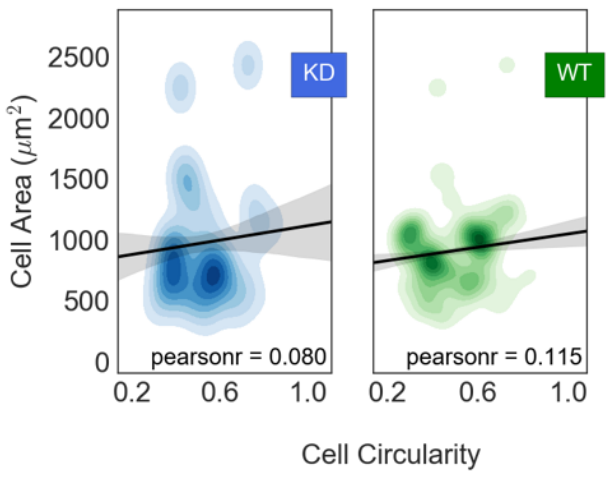
KD
WT
Cell Area (μm^2)
pearsonr = 0.080
pearsonr = 0.115
Cell Circularity

Figure 6.17 DDX3X knock-down cells are significantly more solid and significantly more circular in nature than wild type

DDX3X knock-down cells (KD) and wild type cells were grown on collagen-covered coverslips for 40 mins prior to fixation with 4% (v/v) PFA and dual-immunofluorescent staining by using the Proximity Ligation Assay as described in Figure 6.11. Post-acquisition processing of PLA images was performed using PLAY, as described in Chapter 5, and graphs and statistics generated with the appropriate PLAYkits. Statistical analyses were performed using Welch's t-test. Point-estimated means are shown in red with 95% confidence intervals. Median values are embellished with notches signifying 95% confidence intervals. n-statistics signify the number of cells tested for each assay. Statistical analyses were performed using Welch's t-test (ns $P > 0.05$, * $P \leq 0.05$, ** $P \leq 0.01$, *** $P \leq 0.001$). Kernel Density Estimates (KDEs) are visualised using an estimate based on Scott's rule of thumb for bandwidth selection. Regression lines show 95% confidence intervals as shaded areas.

Panel A. DDX3X knock-down cells are significantly more solid: less 'spikey', with less podial protuberances and with overall more gently curving peripheries than wild type cells.
Panel B. DDX3X knock-down cells are significantly more circular than wild type cells.
Panel C. Any correlation between cell circularity and cell surface area is weak for both experimental groups. The Pearson r correlation coefficients for cell solidity relative to cell surface area (not shown graphically) is also very weak KD ($r = +0.20704$), WT ($r = +0.154393$).

6.16 DDX3X knock-down cells show significant differences in their feret lengths and perimeter lengths compared to wild type cells

PLAY can interrogate cellular shape and lengths (Feret). Although differences in cell length are seen here, the mixed population of cell sizes tends to confound straightforward analysis of these particular parameters. However, no significant difference in these parameters was seen between parental and DDX3X KD cells (Figure 6.18, Panel A and B). Further data analysis of DDX3X KD cells (Panel C, insets i and ii) shows a higher positive correlation than in parental (wild type) cells when comparing perimeter lengths against cellular area (Pearson r correlation coefficient of 0.856). These data suggest that parental cells grow either in a more polarised and/or more protuberant fashion as they spread compared to DDX3X KD cells. Cell Feret (Panels D-F) is also slightly more highly correlated with cell area in DDX3X KD cells relative to parental cells (Figure 6.18E), suggestive of the parental cells creating podia outgrowths in many directions rather than asserting smooth and uniform growth during the early stage spreading process. In contrast, as DDX3X KD cells spread and their area enlarges, it enlarges in all directions, reminiscent of an enlarging circle.

6.17 PLAY analysis after the removal of cellular outliers

The box plot in Figure 6.15A shows that there was no significant difference in the mean cell areas between DDX3X KD and parental cells. However, the violin plot shows a large difference in cell size variation suggesting that outlying cells, with cell areas over 2000μm^2, may be skewing mean values. No steps were taken to synchronise the cell cycle prior to assaying. These cell area data show several outliers, all having approximately double the size (area) of the median in each experimental group. When cross-referenced with the correlation map in Figure 6.15D, not only is there a strong correlation between cell area and nuclear area, but the outlying cells with largest cellular areas specifically have the largest nuclei. This likely implicates these cells as being in the G2 phase of the cell cycle (Good 2015; Neumann & Nurse 2007; Webster et al. 2009). The consequence of modelling the morphological effects of a DDX3X KD is made more difficult with such variability

in cell size. Therefore, noting that practical cell-cycle synchronisation techniques often can be harsh on cells (Rieder & Cole 2002; Fox 2004; Davis et al. 2001), PLAY was queried in such a way as to ignore these specific outliers from its dataset.

After the purging of all unusually large (outlier) cells and repeating the PLAY statistical analyses (as described in Chapter 5), it became evident that parental cells were statistically longer and wider than the DDX3X KD cells (Figure 6.19, Panels A and B). In addition, cell perimeters were also significantly smaller in the DDX3X cells (Figure 6.19C). As shown in Figure 6.19D and E, the median cell area of the parental cells was significantly larger than in the DDX3X KD cells (significance implied by the non-overlapping 95% confidence interval notches visualised around the median lines of each box-plots). The modal cell area of the parental cells was approximately 1035μm^2; this was over 50% larger than that of the DDX3X KD cells with a modal area of approximately 675μm^2 (Panel E). The point mean estimates (Panel D, in red) show no significant difference between the mean areas of the two groups. However, using the Mann-Whitney-Wilcoxon (MWW) test for differences in distributions, the result shows that a highly significant difference exists between the area of cells when comparing parental (wild type) cells with the DDX3X knock-down cells (**, $P \leq 0.01$). These data imply an underlying slowing of the spreading process in the DDX3X KD cell line, with parental cells having a less solid shape than the DDX3X KD cells. These findings are summarised in Figure 6.20.

A

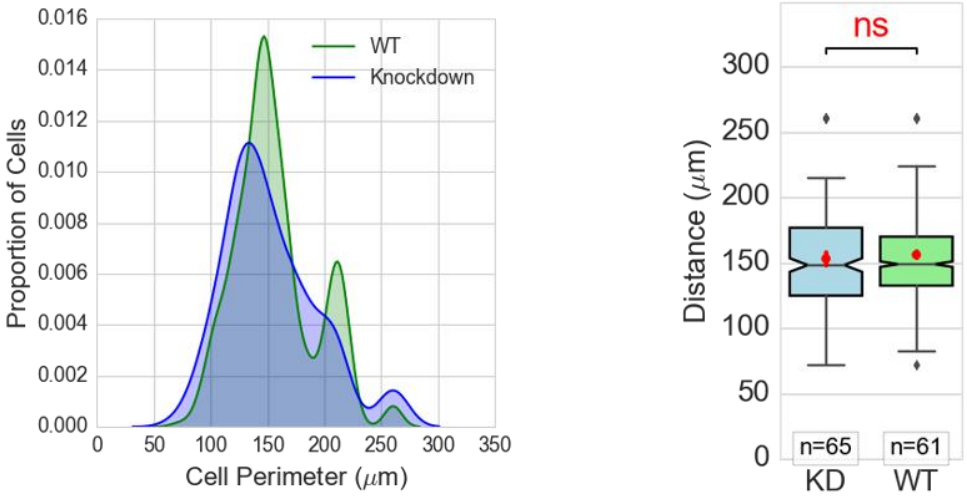

B

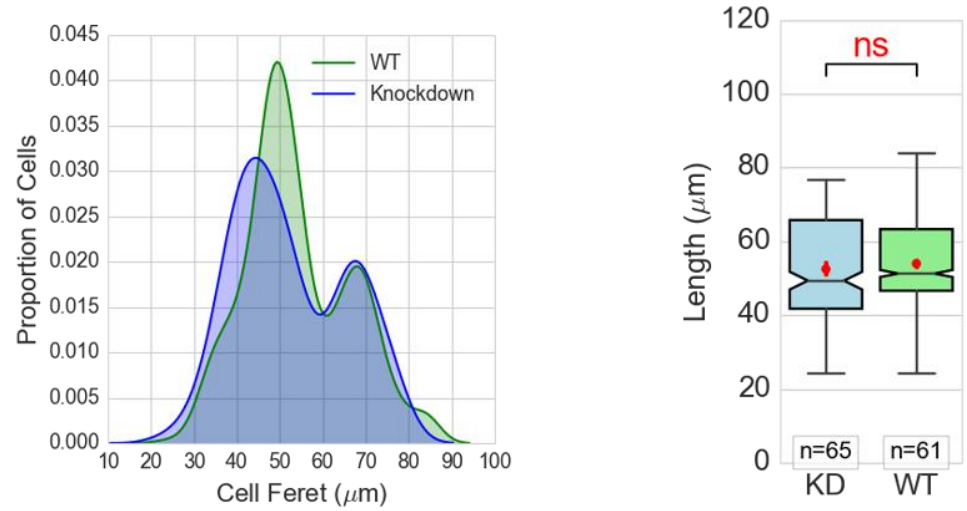

C *inset i* *inset ii*

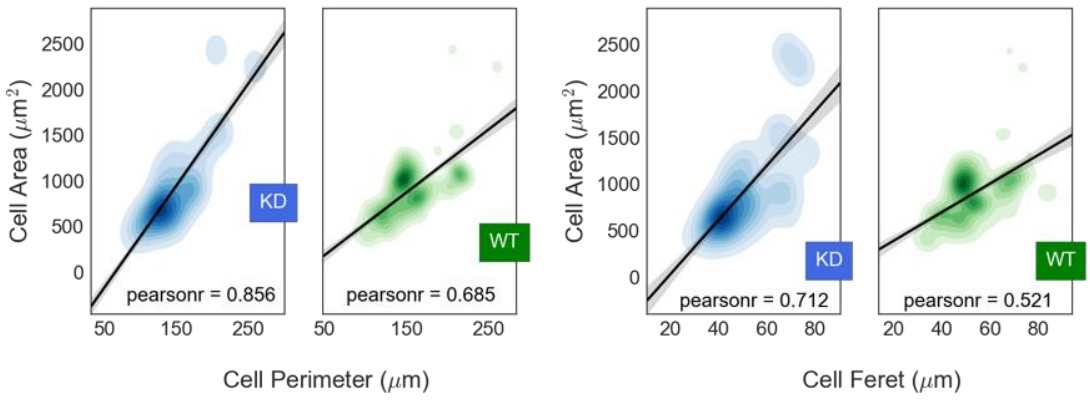

D

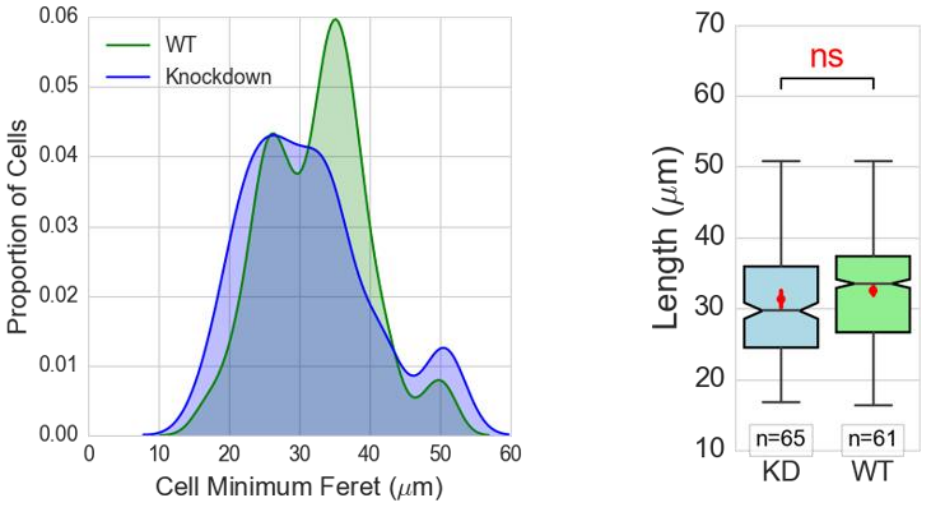
WT
Knockdown
Proportion of Cells
Cell Minimum Feret (μm)
ns
Length (μm)
n=65
n=61
KD
WT

E

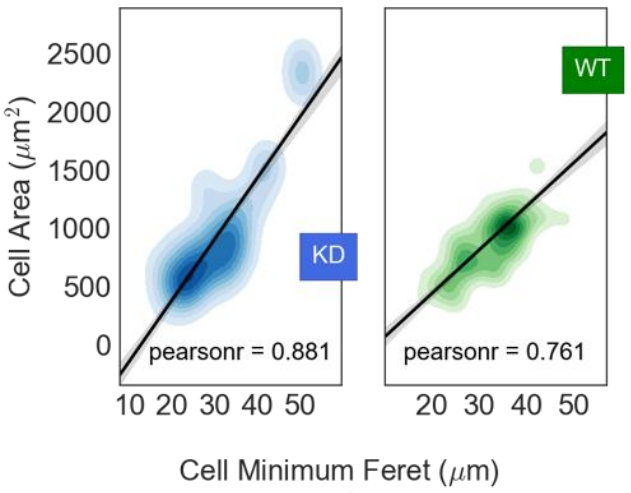
Cell Area (μm²)
KD
WT
pearsonr = 0.881
pearsonr = 0.761
Cell Minimum Feret (μm)

F

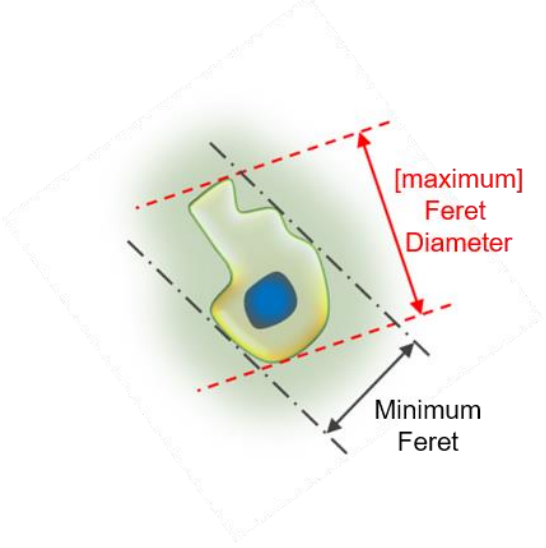
[maximum]
Feret
Diameter
Minimum
Feret

Figure 6.18 DDX3X knockout cells differentially increase Feret diameter and cell body perimeter lengths in early stages of spreading, compared to wild type cells

DDX3X knock-down cells (KD) and wild type cells were grown on collagen-covered coverslips for 40 mins prior to fixation with 4% (v/v) PFA and dual-immunofluorescent staining by using the Proximity Ligation Assay as described in Figure 6.11. Post-acquisition processing of PLA images was performed using PLAY, as described in Chapter 5, and graphs and statistics generated with the appropriate PLAYkits, using statistical analyses as described in Figure 6.16. When analysing the entire dataset, DDX3X knockout cells show themselves to have no statistical difference in their perimeter lengths or Feret Diameters compared to wild type. However, these results are biased by outlier cells, and are re-characterised in a more useful way in Figure 6.20.

Panel A. DDX3X wild type cells show no significant difference from KD cells in estimated point mean, or median values for cell perimeter lengths.
Panel B. DDX3X wild type cells show no significant difference from KD cells in estimated point mean, or median values for cell Feret lengths.
Panel C. With a Pearson r correlation coefficient of 0.856, there is a strong correlation between the cell perimeter length and enclosed cell area in KD cells, more-so than in wildtype (inset i). Cell Feret is slightly more strongly correlated with cell area in knock-down cells relative to wild type (inset ii), suggestive of the wild type cells creating podial outgrowths in many directions rather than asserting polarised growth at such an early stage in ECM adherence.
Panel D. DDX3X wild type cells show no significant difference from KD cells in estimated point mean values for minimum cell Feret, yet median values show a significant difference when comparing 95% confidence intervals - with KD cells less wide. If the outlier cells with areas greater than 2000μm^2 were purged from the dataset then there is a likelihood that median values would also show significant differences.
Panel E. Minimum cell Feret is highly correlated to cell area in both experimental groups, but more strongly in the KD group, implying a tendency for greater circularity in the KD group.
Panel F. Feret diameters, otherwise known as caliper diameters, are maximum and minimum lengths which are tangential between imaginary parallel lines which cover the entire object, in the manner of a caliper with extended lengthy jaws.

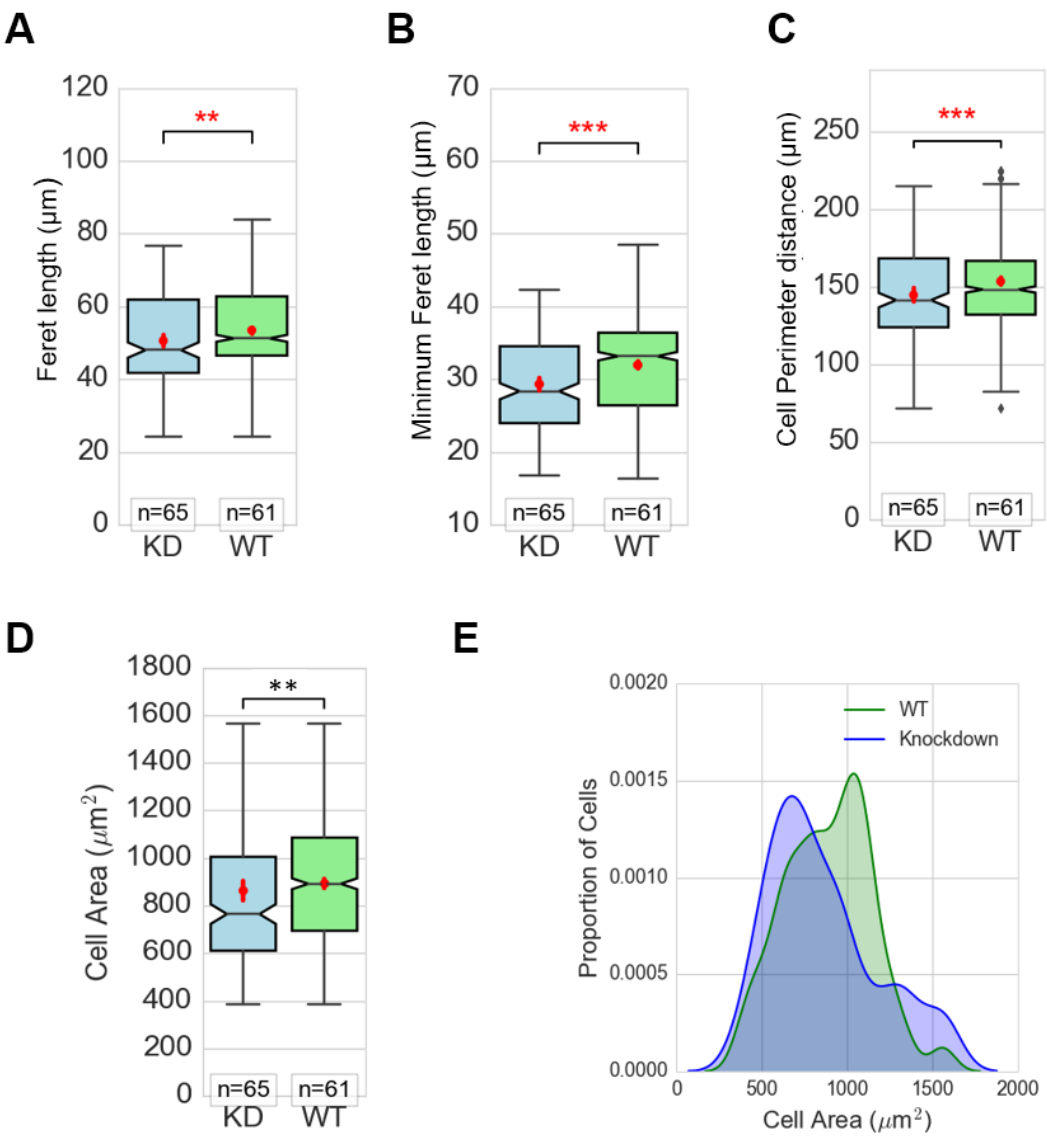

Figure 6.19 PLAY Analyses after purging outlier 'unusually large cells' from the dataset

Using statistical analyses as described in Figure 6.16.
Panels A and B. Wild type cells are statistically longer and wider than the DDX3X 2A knock-down cell group. **Panel C.** Wild type cell perimeters are significantly larger than the DDX3X knock-down (KD) group. Taken with cell area data (Panels D and E), this would suggest a less solid shape in the WT cells than the KD group. **Panel D.** Point mean estimates show no significant difference between the mean areas of the two groups. However, using Mann-Whitney-Wilcoxon (MWW) test for differences in distributions between the two groups, the result shows that a highly significant difference exists between the area of cells when comparing wild type cells with the DDX3X knock-down cells (**, $P \leq 0.01$). **Panel E.** The modal cell area of the wild type is ~1035µm^2, over 50% larger than that of the DDX3X knock-down cell line with a modal area of ~675µm^2.

	Difference of Means			Regression Fitting: Correlation with change in Cell Area		
	Descriptive details of observered changes		p-value	Correlation coefficients (Pearson's r)		KD's relative correlation cf. WT.
	KD	WT		KD	WT	
Cell Feret †	-	Longer than KD .	**	0.712	0.521	0.191
Minimum Feret †	-	Wider bodied than KD.	***	0.8811	0.7606	0.1205
Cell Perimeter †	-	Greater than KD.	***	0.8557	0.6854	0.1703
Spot distance from Perimeter	-	Closer to Periphery than KD.	**	0.5968	0.4613	0.1355
Spot Normallised Distance	-	Closer to Periphery than KD.	**	-0.1639	-0.1276	-0.0363
Cell Circularity	More circular than wt.	-	**	0.0796	0.1153	-0.0357
Cell Solidity	More Solid than wt.	-	***	0.20704	0.154393	0.052647
Cell Area		Larger than KD. ††	ns			
Foci per Cell Unit Area	Less variance than wt.	Large varience across wt cells.	***	-0.2663	-0.2356	-0.0307

Figure 6.20 Summary of cellular and foci attribute differences in DDX3X knock-down and wild type cells

† indicates no statistical significance in difference of means in the original dataset. However, there is significant difference (as annotated in the p-value column) when the dataset is purged of the largest outlying cells (cell areas > 2000 μm^2 , which are likely to be passing through the G2-phase of the cell cycle).
†† indicates a statistically significant difference in the median values of the attributes, based on 95% confidence intervals (as visualised on the box-plot median value notches).

6.18 During acute cell spreading, DDX3X:eIF4E interactions are highest near the cell periphery

Confocal images suggest that DDX3X levels rise at the leading edge of cells in the early stages of cell spreading (Figure 6.4). Empirical evidence suggested that DDX3X was most highly concentrated at the edge of cells prior to large-scale lamellipodial outgrowths. To test this observation, the PLAY dataframe was queried to separate wild type cells by size, and compare the number and location of DDX3X:eIF4E foci in the smallest cells against the largest cells. This generates split-violin plots that can also represent a pseudo-time-course of cell spreading (Figure 6.21). Comparing sub-populations of cells of different areas, it is shown that the smallest 20% of cells express the most DDX3X:eIF4E foci per unit area. This analysis was extended to examine DDX3X:eIF4E foci relative to the cell periphery. By examining the shape of the plots alongside the median and interquartile markers, Figure 6.22 indicates that DDX3X:eIF4E foci are closest to the cell periphery in the smallest 50% of cells. With PLA evidence to suggest that DDX3X:eIF4E foci are most prevalent early in the acute stages of cell spreading, and because during this spreading phase they tend to be located closest to the cell periphery, a possible hypothesis is that DDX3X:eIF4E interactions at the leading edge of spreading cells is necessary for the initiation of lamellipodial outgrowth. To test this hypothesis, PLAY was utilised to produce a split-violin plot to compare the number of foci in different solidities of the cells. In the least solid 20% of cells, there was an enrichment of DDX3X:eIF4E foci per cell unit area when compared to the most solid 20% of cells (Figure 6.23). These data confirm that DDX3X:eIF4E interactions are likely to be closest to the cell periphery in the acute (very earliest) stages of cell spreading

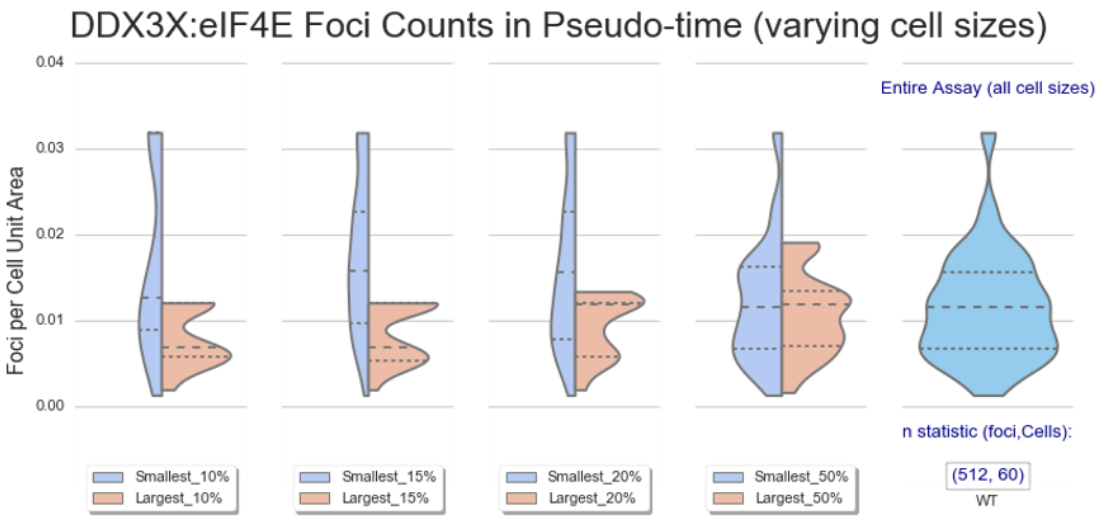

Figure 6.21 Putative DDX3X:eIF4E interactions are likely to be at their greatest number, at the very earliest stages of cell spreading

DDX3X wild type cells were grown on collagen-covered coverslips for 40 mins prior to fixation with 4% (v/v) PFA and dual-immunofluorescence stained using the *in situ* Proximity Ligation Assay method as described in Figure 6.11. Post-acquisition processing of PLA images was performed using PLAY, as described in Chapter 5, and graphs and statistics generated with the appropriate PLAYkits. Violin plots are visualised using a kernel density estimate based on Scott's rule of thumb for bandwidth selection (Terrell & Scott 1992; Hintze 1988). Split-violin plots show the difference in DDX3X : eIF4E foci concentrations throughout the cell, when comparing groups of the smallest cells against the largest. 1st quartile, 3rd quartile and median values are annotated, statistical significance values will be forthcoming in a later release of the PLAY.

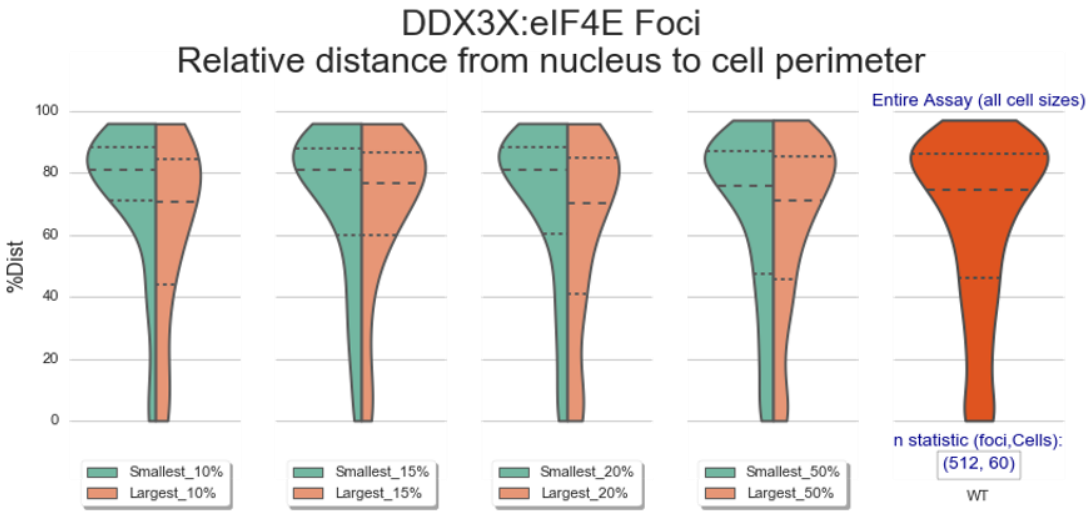

Figure 6.22 Putative DDX3X:eIF4E interactions are likely to be closest to the cell periphery at the very earliest stages of cell spreading

DDX3X wild type cells were grown on collagen-covered coverslips for 40 mins prior to fixation with 4% (v/v) PFA and dual-immunofluorescence stained using the *in situ* Proximity Ligation Assay method as described in Figure 6.11. Post-acquisition processing of PLA images was performed using PLAY, as described in Chapter 5, and graphs and statistics generated with the appropriate PLAYkits. Violin plots are visualised using a kernel density estimate based on Scott's rule of thumb for bandwidth selection (Terrell & Scott 1992; Hintze 1988). Split-violin plots show the difference in DDX3X : eIF4E foci concentrations throughout the cell, when comparing groups of the smallest cells against the largest. 1st quartile, 3rd quartile and median values are annotated, statistical significance values will be forthcoming in a later release of the PLAY.

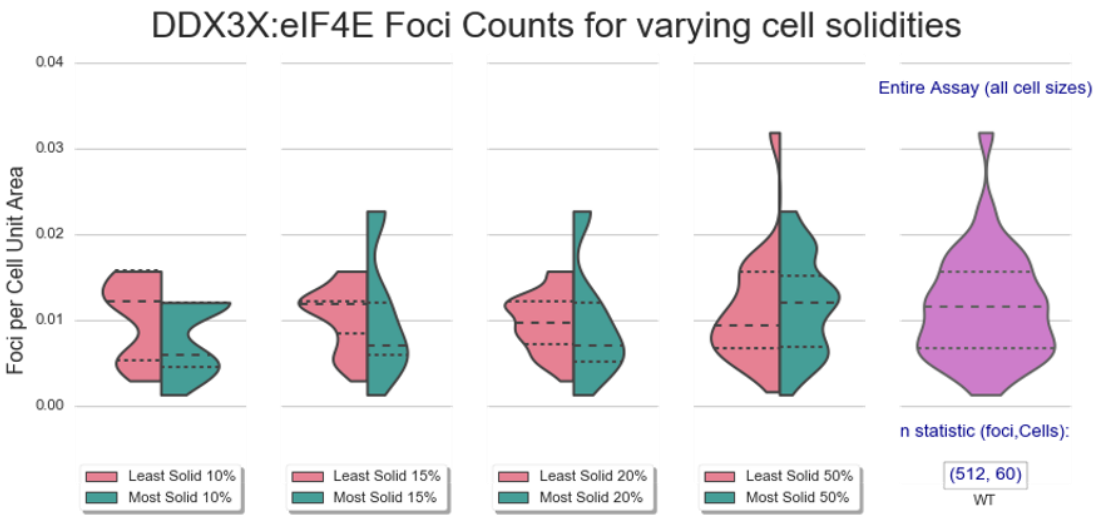

Figure 6.23 Putative DDX3X:eIF4E interactions are at their greatest number, relative to cell area, in the least solid decile of MRC-5 SV2 cells

DDX3X wild type cells were grown on collagen-covered coverslips for 40 mins prior to fixation with 4% (v/v) PFA and dual-immunofluorescence stained using the Proximity Ligation Assay as described in Figure 6.11. Post-acquisition processing of PLA images was performed using PLAY, as described in Chapter 5, and graphs and statistics generated with the appropriate PLAYkits. Violin plots are visualised using a kernel density estimate based on Scott's rule of thumb for bandwidth selection (Terrell & Scott 1992; Hintze 1988). Split-violin plots show the difference in DDX3X : eIF4E foci concentrations throughout the cell, when comparing groups of the smallest cells against the largest. 1st quartile, 3rd quartile and median values are annotated, statistical significance values will be forthcoming in a later release of the PLAY.

6.19 Summary

Confocal microscopy images suggest that DDX3X is found in high concentrations at locales spanning the periphery of the cells during the acute stages of cell spreading. DDX3X has been shown to utilise the CRM1 export pathway from the nucleus (Figures 6.7 and 6.8), and confocal imaging presented here suggests that DDX3X may traverse the actin cytoskeleton to reach the leading edge of the cell (Figures 6.3, 6.4 and 6.5). It is possible that DDX3X then colocalises with eIF4E associated with specific mRNAs at the cell periphery to allow for localised translation to prime lamellipodial outshoots. Knocking down levels of DDX3X protein appeared to retard cell spreading, leaving DDX3X knockdown cells smaller, more rounded more and solid than their parental (wild type) counterparts (Figure 6.20). These data highlight the possibility that DDX3X may have a role in facilitating cytoskeletal rearrangement for morphological changes required for the spreading process. These data also suggest that DDX3X:eIF4E interactions may be implicated in cellular polarisation and general podial growth, meaning that DDX3X may play a part in migratory processes including metastasis disease.

7 The effect of signalling inhibitors on the colocalisation of DDX3X, 4E-BP1 and eIF4E during cell spreading

7.1 Introduction

The work described in this chapter aims to determine the effect of inhibitors of the mTOR/AKT signalling pathway, on the interaction and localisation of binding proteins DDX3X and 4E-BP1 with translation factor eIF4E. Previous work has shown that the migration of eukaryotic cells *in vitro* involves complex regulatory pathways which integrate stimuli received from the engagement of the extracellular matrix (ECM) and from intercellular signalling from adjacent cells (Parsons et al 2010). Cell migration is an essential process in development, morphogenesis, angiogenesis and regeneration of tissues. The mechanism of cell migration towards external attractants comprises a cycle in which cells are stimulated to polarise by the actions of Rho GTPases (Parsons et al 2010) and extend protrusions formed of lamellipodia or filopodia, both of which are driven and formed of filamentous actin networks (reviewed in Ridley, 2001). These protrusions are then stabilised by focal adhesions which link the actin cytoskeleton to the ECM. Such lamellipodia are large flattened structures formed from large dense branched actin networks (Abercrombie et al, 1970), with their formation dependent on protein co-factors that mediate their local regulation, structural characteristics and dynamics (Ridley, 2001; Abercrombie et al, 1970; Pollard et al, 2003; Bugyi and Carlier, 2010). These include Rac1, which stimulates the recruitment of the WAVE complex and actin nucleation complex, Arp2/3 to the plasma membrane (Bugyi and Carlier, 2010). The WAVE complex, which is composed of five subunits (WAVE, Brk1, Abi, Nap, CYFIP), is required for lamellipodium formation and is activated downstream of Rac1 (Wang et al, 2012; Rotty et al, 2013).

Previous work in the Morley laboratory has shown that eIF4G, 4E-BP1 and ribosomal subunits colocalise with eIF4E in the lamellipodia of migrating fibroblastic cells, suggesting the regulation of localised translation in this cellular compartment (Willett et al 2010; Willett et al 2011). The data

presented in this thesis also suggests that DDX3X is localised to the leading edge of spreading cells (Chapter 6). However, little is known about the role of the mTORC1/Mnk1 signalling pathways in regulating this process. The work described in this chapter addresses this lack of knowledge.

7.2 mTOR signalling, rapamycin and rapalogs

Schreiber *et al*. (1994) first identified the mTOR protein as the target of the macrolytic fermentation product of the bacterium *Streptomyces hygroscopicus,* rapamycin. Rapamycin was found to possess immunosuppressive and anti-proliferative properties in mammalian cells, promoting interest in identifying its mode of action. Rapamycin forms a gain-of-function complex with the 12-kDa FK506-binding protein (FKBP12), and this complex binds and specifically acts as an allosteric inhibitor of mechanistic TOR (mTOR, also known as mammalian TOR) complex 1 (mTORC1; reviewed in Li et al, 2014).

mTOR belongs to the PI3K-related kinase family of proteins and is involved in the regulation of the phosphorylation of downstream targets such as $p70^{S6K}$, Grb10 and 4E-BP1 by mitogens; extracellular signalling molecules; glucose availability; hypoxia; and amino acid availability (Figure 7.1 and see Chapter 1). The mTOR pathway responds to these signals by regulating essential cellular functions, such as protein synthesis, lipid synthesis, autophagy, lysosome biogenesis, energy metabolism, cell survival and cytoskeletal reorganisation (reviewed in Laplante and Sabatini, 2012). Grb10 is involved in feedback regulation of insulin signalling and 4E-BP1 phosphorylation is required for cap-dependent translation (see below).

The mTOR protein is currently known to interact with numerous proteins to form two distinct complexes, mTOR complex 1 (mTORC1) and 2 (mTORC2). Although mTORC1 contains six proteins, and mTORC2 contains seven (reviewed in Laplante and Sabatini, 2012), both mTOR complexes share the mTOR protein, mammalian lethal with sec-13protein 8 (mLST8) (Kim et al, 2003; Jacinto et al, 2004), DEP domain containing mTOR-interacting protein (DEPTOR; Peterson et al, 2009) and the Tti1/Tel2 scaffold protein complex (Kaizuka et al, 2010). The two remaining proteins that participate in mTORC1

are the regulatory-associated protein of mammalian target of rapamycin (Raptor; Hara et al, 2002; Kim et al, 2002) which is responsible for the sensitivity of mTORC1 to rapamycin, and the proline-rich Akt substrate 40 kDa (PRAS40; Vander Haar et al, 2007). Instead of Raptor, mTORC2 contains the rapamycin-insensitive companion of mTOR (Rictor), the mammalian stress-activated map kinase-interacting protein 1 (mSin1) and the protein observed with Rictor 1 and 2 (Protor1/2; reviewed in Laplante and Sabatini, 2012).

A number of signalling pathways converge at the activation of the mTORC1 complex, it is therefore not surprising that the rapamycin-sensitive regulation of mTORC1 is important in relation to cap-dependent translation (see Chapter 1). Phosphatidylinositol-3-kinases (PI3Ks) are lipid kinases that have a role in growth factor-mediated regulation of mTOR signalling (Lemmon and Schlessinger, 2010). The activation of mTORC1 directly results in the phosphorylation of $p70^{S6K}$ at its Thr389 site and its release from eIF3. $p70^{S6K}$ is a serine-threonine kinase that, when active, phosphorylates multiple residues in the carboxyl-terminal region of the ribosomal S6 protein (Ser235, Ser236, Ser240, and Ser244), eIF4B (Ser422) and Pdcd4; the latter control the availability of eIF4A to participate in translation initiation which is activated under these conditions (reviewed in Holz et al, 2005; Ma and Blenis, 2009).

A key factor involved in promoting 4E-BP1 phosphorylation is the rapamycin-sensitive mTORC1 complex. The ability of rapamycin to inhibit 4E-BP1 phosphorylation is important for the pro-apoptotic effect of this drug. Phosphorylation of 4E-BP1 can also be prevented by a new generation of inhibitors which target the ATP-binding pockets of mTOR kinase, such as the dual mTORC1 and mTORC2 inhibitor, KU0063794 (Smalley et al 2014). In proliferating cells, 4E-BP1 is phosphorylated and remains dissociated from eIF4E (see Chapter 1). Hypo-phosphorylated 4E-BP1 binds efficiently to eIF4E, reducing the availability of eIF4E for the translation initiation process. In contrast, multisite phosphorylation of 4E-BP1 at Thr37/46, Ser65 and Thr70 inhibits this interaction, allowing initiation complex assembly (Gingras et al, 1999). The phosphorylation of Thr37/46 by mTORC1 is thought to prime 4E-BP1 for subsequent phosphorylation at Ser65 and Thr70 (Sonenberg and Hinnebusch 2009; Jackson et al, 2010; Laplante and Sabatini, 2012).

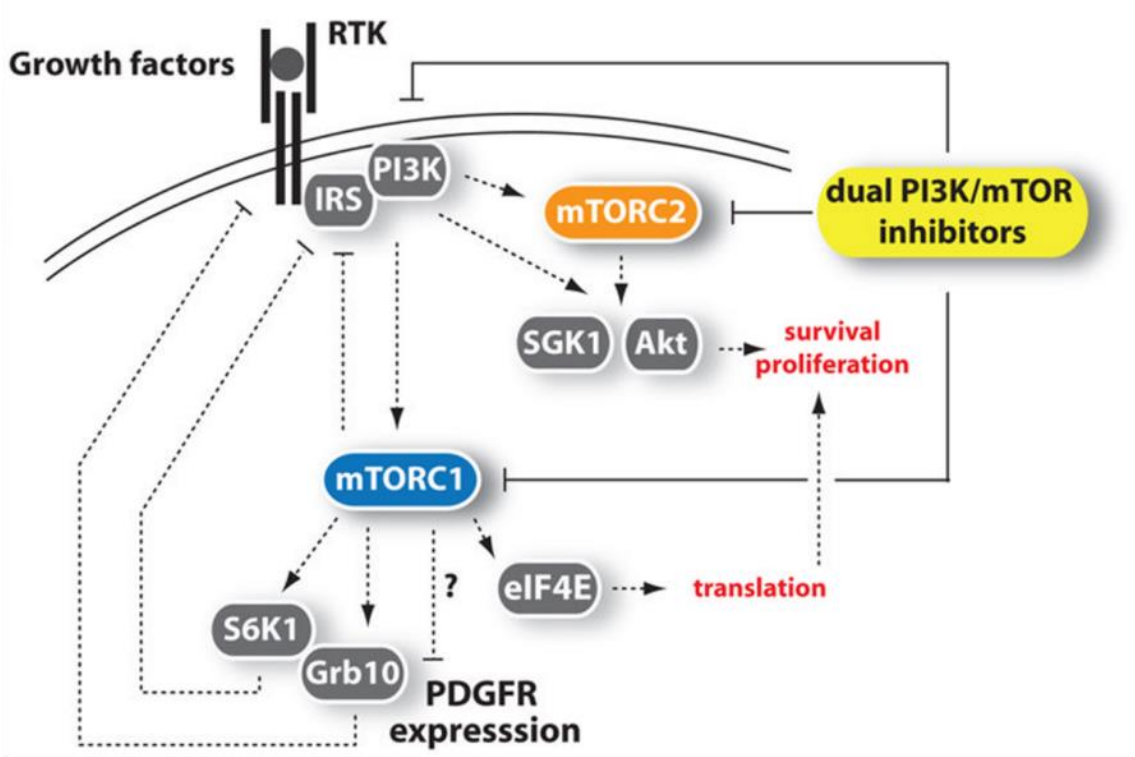

Figure 7.1 Schematic representation of the mTOR signalling pathway and associated proteins

The mTOR signalling pathway integrates signals from extracellular signalling molecules, hypoxia, and amino acid sensing.

Taken from Laplante and Sabatini, 2012.

7.3 ERK1/2, p38MAPK and Mnk1/2 signalling inhibitors

The extracellular signal-regulated kinase 1 and 2 (ERK1/ 2) signalling pathway can be activated by G-protein coupled receptors (GPCRs), integrin receptors and most commonly, receptor tyrosine kinases (see Chapter 1; reviewed in Pearson et al, 2001). The 44-kDa ERK1 and 42-kDa ERK2 proteins were the first MAPKs to be discovered to take part in a MAPK cascade (Wortzel & Seger 2011). In general, growth factor binding activates ERK1/2 in a *ras*-dependent manner following activation of the raf signalling cascade. The activated ERK1/2 targets the phosphorylation and activation of MAPK-interacting protein kinase (Mnk1; Fukunaga and Hunter 1997; Waskiewicz et al, 1997; Ueda et al 2004). However, the activation of the Mnk1/2 kinases is not restricted to the ERK1/2 cascade, as they are also activated by the p38MAPK cascade, mainly under stress conditions (Morley, 2001; Morley and Naegele, 2002). The p38 MAP kinases are a family of stress-activated MAP kinases that contribute to the regulation of cell proliferation and autophagy (Shi and Gaestel, M. (2002). The phosphorylation of eIF4E which drives cell proliferation (Topisirovic et al 2004) is mediated by Mnk1/2 which binds to the C-terminus of eIF4G (Pyronnet et al 1999) and phosphorylates eIF4E in *cis* (reviewed in Sonenberg and Hinnebusch 2009; Jackson et al, 2010). In addition to known inhibitors such as CGP57380 (Morley, 2001; Morley and Naegele, 2002), a new class of Mnk1/2 inhibitor (MnkI-19) has been described which prevents cell migration (Beggs et al, 2015).

7.4 DDX3X levels are unaffected when cells grow in the presence of inhibitors of the mTOR /AKT and/or Mnk signalling pathways.

To determine whether inhibition of either mTOR or Mnk1/2 signalling affected the interaction between DDX3X and eIF4E, cells were pre-incubated in the absence or presence of 10μM MnkI-19, KU-0063794, CGP57380 or combinations of inhibitors, and allowed to spread under the same inhibitor conditions. Western blot analysis of aliquots of extract containing equal amounts of protein (using β-actin as a loading control) shows that DDX3X protein levels remain constant after growing cells in the presence of inhibitors

(Figure 7.2A). Similar results were observed in cells incubated with CGP57380 alone (data not shown).

7.5 The effect of inhibitors on eIF4E's interactions with DDX3X

Figure 7.2B shows PLAY analysis of cells stained to visualise foci formed between DDX3X and eIF4E in the absence or presence of inhibitors, as described in Panel A. These data indicate that there was a specific interaction between DDX3X and eIF4E, with about 7 foci/cell (lane 2), compared to approximately one spot in cells lacking one of the primary antibodies (lane 1). The addition of all inhibitor combinations significantly changed the number of DDX3X:eIF4E interactions seen in the PLA assay (lanes 3-6 vs lane 2). Compared to untreated control cells (lane 2), DDX3X showed higher levels of interaction with eIF4E in the presence of the Mnk inhibitor, MnkI-19 (lane 3). However, all other drug combinations, including KU-0063794 alone (lane 4), or MnkI-19 in combination with either CGP-57380 (lane 5) or KU-0063794 (lane 6) led to a significant reduction in interaction between these proteins. These data suggest that phosphorylation of eIF4E might have a negative effect on its interaction with DDX3X. In addition, hypophosphorylation of 4E-BP1 in the presence of mTOR inhibitor might affect the binding of eIF4E with DDX3X by increasing the levels of eIF4E/4E-BP1 complexes in the cell. Using the 'Spot Normalised Distance' calculation for all foci in each cell, as discussed in Chapter 6, normalised foci distances from the cell perimeter were calculated for each drug assay (Figure 7.3). Except for cells spread in the absence of mTOR signalling (KU-0063794), all other cells had foci which were unaffected in their mean distance from the cell perimeter when compared to untreated cells. When cells were treated with KU-0063794 alone, interactions shifted further into the cell body, and away from the cell periphery. This might reflect a requirement for mTOR signalling to facilitate cell spreading.

A

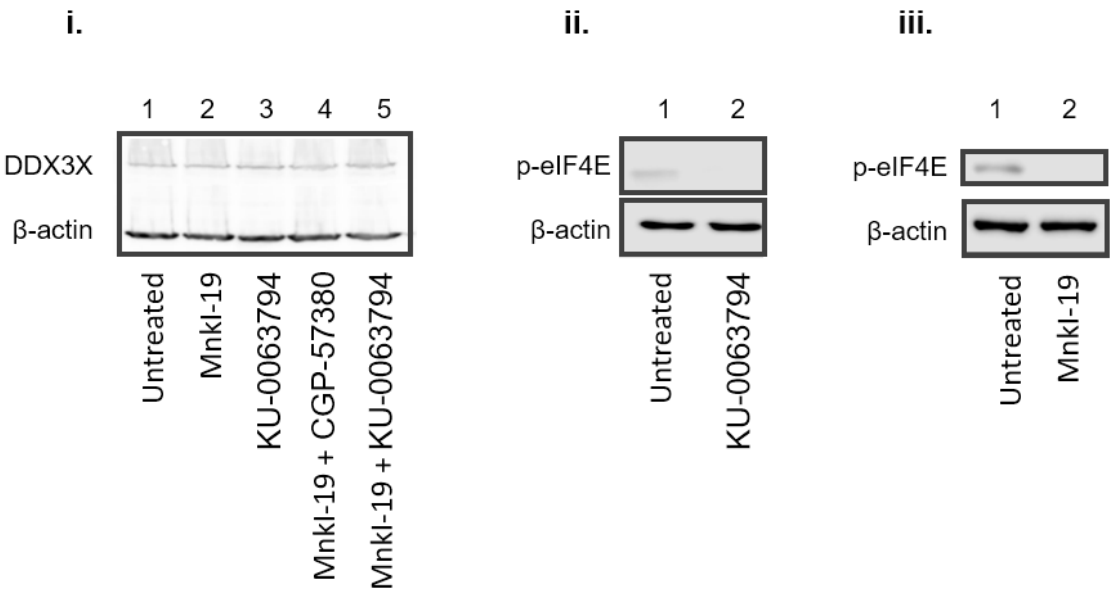
i.
ii.
iii.
1 2 3 4 5
DDX3X
β-actin
Untreated
Mnkl-19
KU-0063794
Mnkl-19 + CGP-57380
Mnkl-19 + KU-0063794
1 2
p-eIF4E
β-actin
Untreated
KU-0063794
1 2
p-eIF4E
β-actin
Untreated
Mnkl-19

B

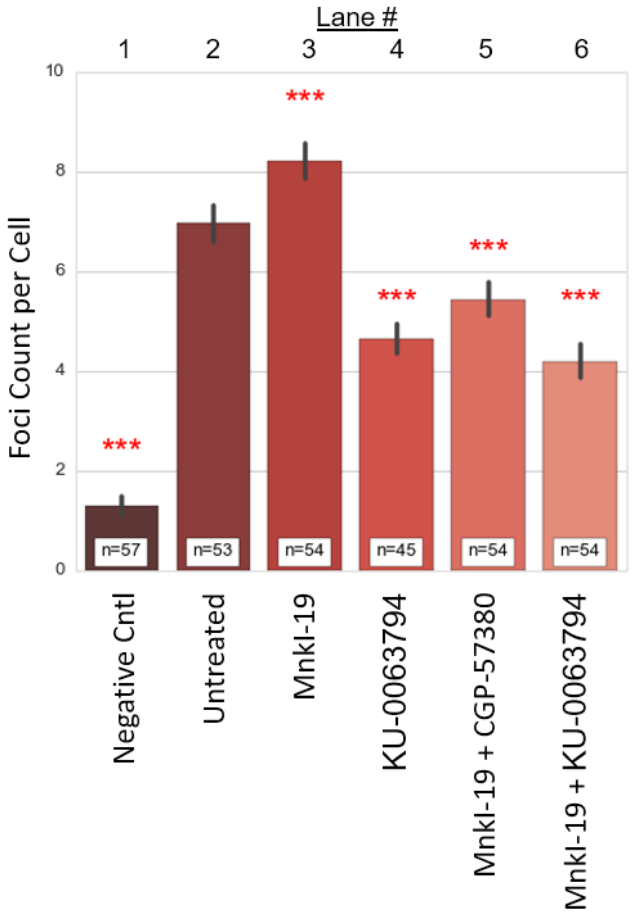
Lane #
1 2 3 4 5 6
Foci Count per Cell
0 2 4 6 8 10
***
n=57
n=53
n=54
n=45
n=54
n=54
Negative Cntl
Untreated
Mnkl-19
KU-0063794
Mnkl-19 + CGP-57380
Mnkl-19 + KU-0063794

Figure 7.2
Inhibitors affect the number of DDX3X : eIF4E interactions per cell.

Panel A. Cells were grown with and without the presence of inhibitors for two hours, trypsinised and re-seeded onto 15cm diameter petri dishes, at a density of 15,000 cells/cm^2 and incubated at 37ºC for an additional 40 mins in their original media prior to harvesting. Cells were harvested, lysed and immuno-blotted for the presence of DDX3X, phospho-eIF4E(ser209), and β-actin (loading control), as described in the Materials and Methods. **Inset i.** Lane 1: Untreated (10μM), Lane 2: MnkI-19 (10μM), Lane 3: KU-0063794 (10μM), Lane 4: MnkI-19 (10μM) + CGP-57380 (10μM), Lane 5: MnkI-19 (10μM)+ KU-0063794 (10μM). **ii.** Untreated, Lane 2: KU-0063794 (10μM). **iii.** Untreated (10μM), Lane 2: MnkI-19 (10μM). **Inset ii.** Lane 1: Untreated, Lane 2: KU-0063794 (10μM), **Inset iii.** Lane 1: Untreated (10μM), Lane 2: MnkI-19 (10μM).

Panel B. Cells were grown in T75-flasks to 70% confluency prior to drug application (10μM in each application of DMSO, MnkI-19, KU-0063794, and CGP-57380) as described in the Materials and Methods. After two hours, the cells were dissociated using trypsin and re-seeded onto coverslips coated with 8μg/cm^2 collagen I, at a density of 15,000 cells/cm^2 and incubated at 37ºC for 40 mins in their original media. Cells were fixed using 4% paraformaldehyde, saponin permeabilisation, application of primary antibodies anti-DDX3X (Ab52) diluted at 1:1000 and anti-eIF4E (Ab106) diluted at 1:400. Negative controls were made by addition of only the anti-DDX3X antibody. Further treatment was performed as per the proximity ligation assay (PLA) protocol, as described in the Materials and Methods. Using a scanning confocal microscope images were obtained using a pinhole set to 6.8AU for the PLA channel, and 1AU for the DAPI channel. Images were analysed and results graphically visualised using PLAY software (described in Chapter 5). Statistical analyses were performed using Welch's t-test (ns $P > 0.05$, * $P \leq 0.05$, ** $P \leq 0.01$, *** $P \leq 0.001$). Mean values are shown with 95% confidence intervals, and n-statistics signify the number of cells tested in each assay.

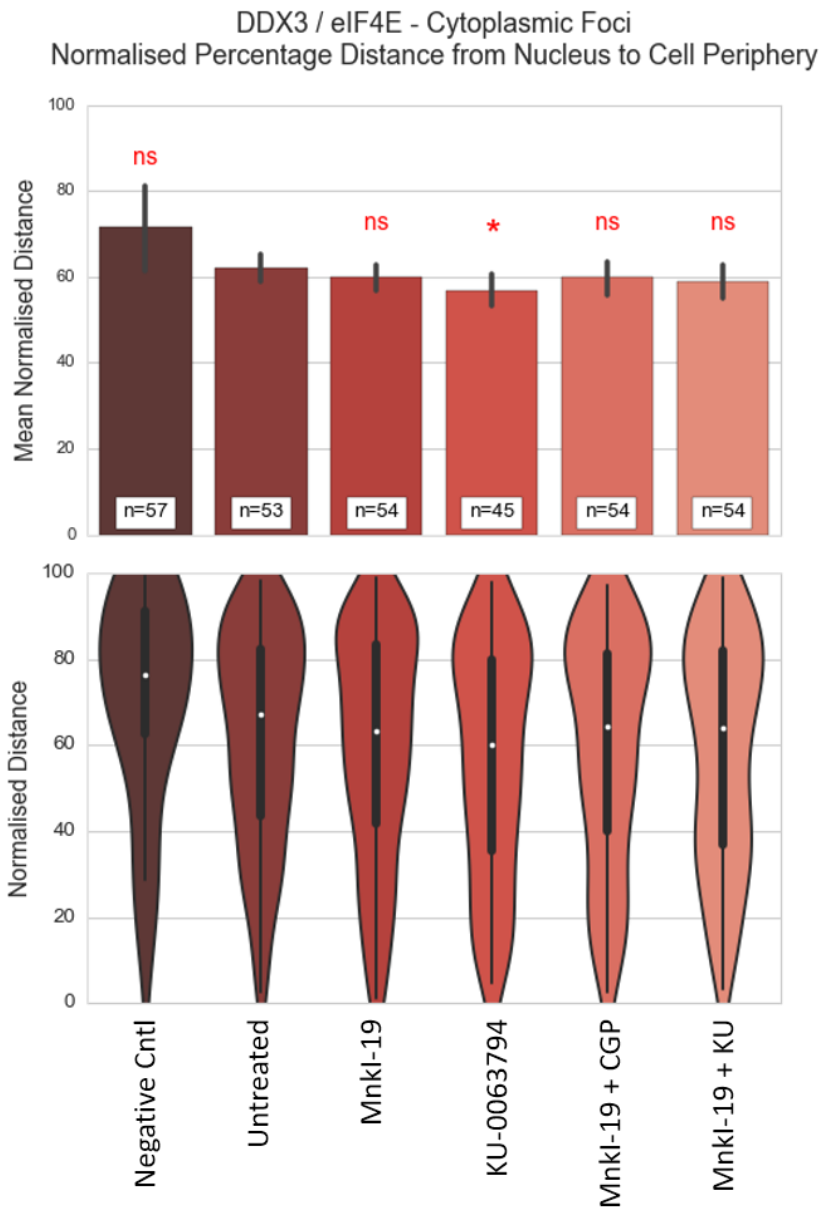

Figure 7.3 The affects of inhibitors on the location of DDX3X : eIF4E interactions in spreading cells.

Cells were grown, treated and imaged using the PLA protocol as described in Materials and Methods, and in the specific manner as described in Figure 7.2B. Images were analysed and results graphically visualised using PLAY software, described in Chapter 5.
Statistical analyses were performed using Welch's t-test (ns $P > 0.05$, * $P \leq 0.05$, ** $P \leq 0.01$, *** $P \leq 0.001$). Normalised distance measurements are based on the 'Spot Normalised Distance' measurement as discussed in Chapter 5. Mean normalised distances for foci were values are shown with 95% confidence intervals, and n-statistics signify the number of cells tested in each assay. Violin plots were visualised using a kernel density estimate based on Scott's rule of thumb for bandwidth selection (Terrell & Scott 1992; Hintze 1988), and combined with integrated box plots showing median values in white.

7.6 The affect of inhibitors on the interaction of 4E-BP1 with eIF4E

Given that these data from Section 7.5 suggest that phosphorylation of eIF4E has a negative effect on its interaction with DDX3X. An experiment was designed to test whether there was also a change in the interactions between eIF4E and eE-BP1 in the presence of inhibitors which may indicate the possibility of competition between BP1 and DDX3X for a common binding site on eIF4E. Cells were pre-incubated in the absence or presence of 10μM MnkI-19, KU-0063794, CGP57380 or combinations of inhibitors, and allowed to spread under the same inhibitor conditions, as described. In this case, PLA was seen between eIF4E and 4E-BP1 (Figure 7.4). Surprisingly, during cell spreading, the addition of the mTOR inhibitor did not increase the amount of interaction between 4E-BP1 and eIF4E (lane 4 vs lane 2), even though phosphorylation of 4E-BP1 was ablated here (Figure 7.4B, lane 3 vs lane 1; quantified in Panel C). In contrast, the addition of the Mnk inhibitor, MnkI-19, had no effect on the phosphorylation of 4E-BP1 (Panels B and C) but gave a small, but statistically significant increase in the binding of 4E-BP1 to eIF4E. This was slightly more robust with the simultaneous use of two different Mnk1/2 inhibitors (Figure 7.4B, lane 5 vs lane 2), but more evident with inhibition of both mTOR and Mnk1/2 signalling (lane 6 vs lane 2). Figure 7.5 shows that inhibition of mTOR or Mnk1/2 signalling alone or in combination did not result in any statistically significant change in the mean location of 4E-BP1:eIF4E foci with respect to the periphery of the cells. Together, these data suggest that mTOR can affect the position of eIF4E/DDX3X complexes but not that of eIF4E/4E-BP1 complexes in spreading cells.

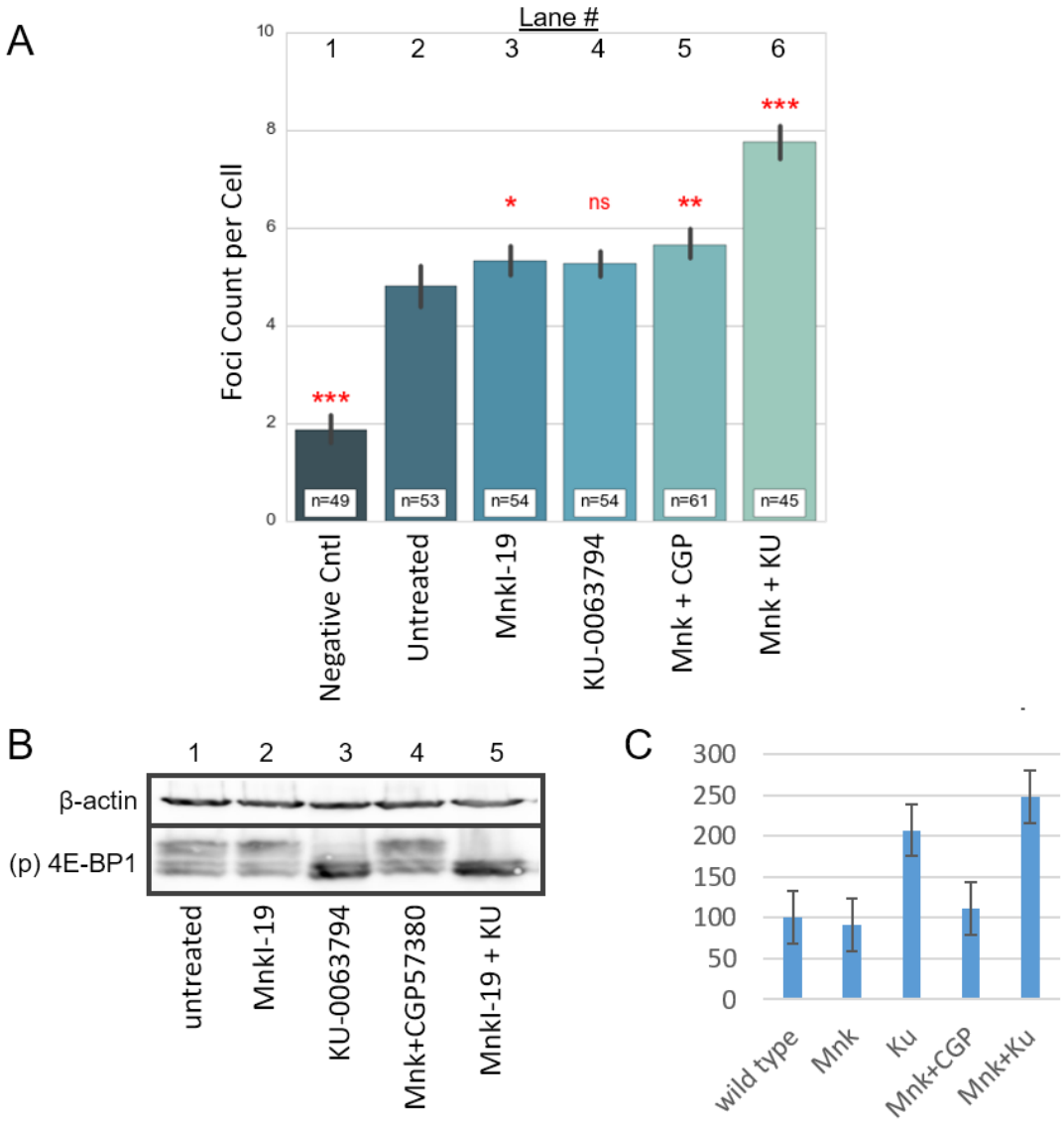

Figure 7.4 Inhibitors affect the number of 4E-BP1 : eIF4E interactions per cell.

Panel A. Cells were grown and treated according to the PLA protocol as described in Figure 7.2B., with the sole change being the type of primary antibodies applied. In this case primary antibodies were anti-4E-BP1 (Ab1) diluted at 1:800, and anti-eIF4E (Ab106) diluted at 1:400. Images were acquired in the same manner and analysis performed by PLAY software. Statistical analyses were performed using Welch's t-test (ns $P > 0.05$, * $P \leq 0.05$, ** $P \leq 0.01$, *** $P \leq 0.001$). Mean values are shown with 95% confidence intervals, and n-statistics signify the number of cells tested in each assay. **Panel B.** Cells were grown, harvested and lysed for western blotting (as described in Figure 7.2), for the presence of β-actin (loading control) and 4E-BP1 as described in the Materials and Methods. **Panel C.** Analysis of the intensity of the two fastest migrating bands - the α and β isoforms of 4E-BP1 of the western blot. Error bars show S.E.M., n=3.

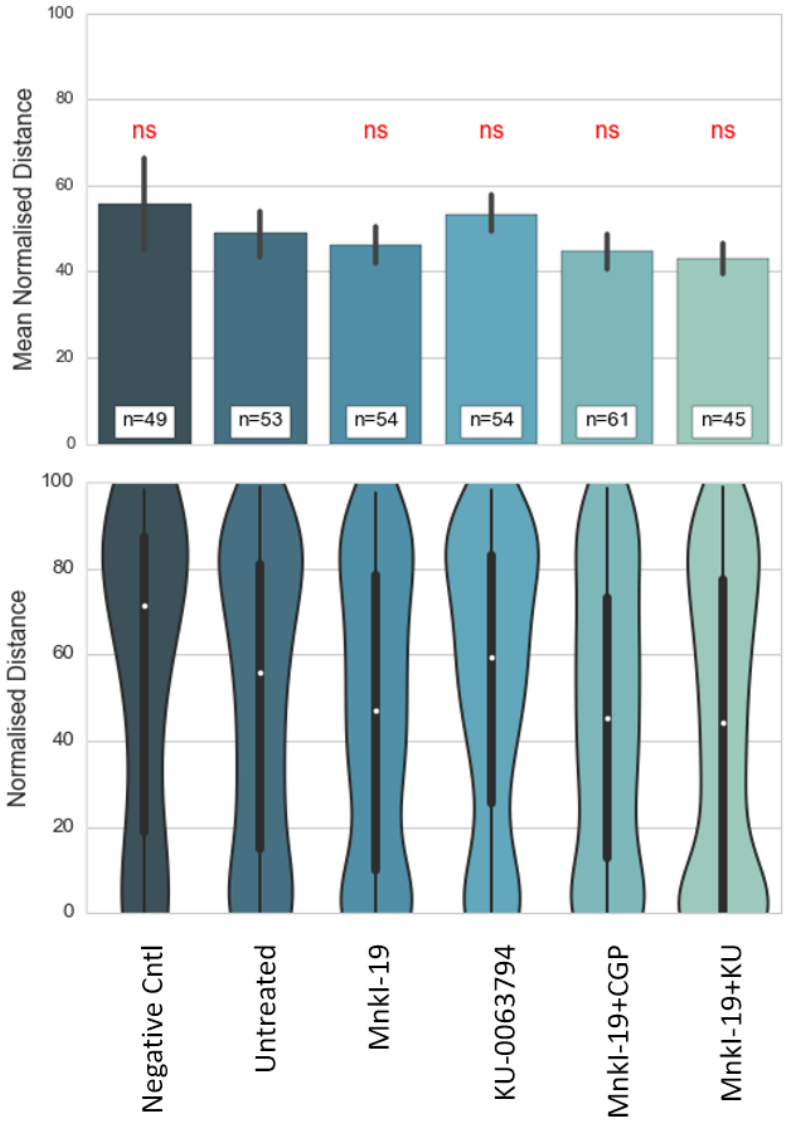

Figure 7.5 Inhibitors do not affect the location of 4E-BP1 : eIF4E interactions in spreading cells.

MRC-5 SV2 cells were grown, treated with inhibitors and processed as described in Figure 7.4. Images were analysed and results graphically visualised using PLAY software (as described in Chapter 5). Statistical analyses were performed using Welch's t-test (ns $P > 0.05$, * $P \leq 0.05$, ** $P \leq 0.01$, *** $P \leq 0.001$). N-statistics signify the number of cells tested for each assay. Normalised distance measurements are based on the 'Spot Normalised Distance' measurement as discussed in Chapter 5. Mean normalised distances for foci were values are shown with 95% confidence intervals, and n-statistics signify the number of cells tested in each assay. Violin plots were visualised using a kernel density estimate based on Scott's rule of thumb for bandwidth selection, and combined with integrated box plots showing median values in white.

7.7 The effect of mTOR and Mnk1/2 inhibitors on cell morphology

7.7.1 The cell spreading process for untreated cells

Utilising PLAY, software which was designed and written especially for this project (see Chapter 5), a meta-analysis was conducted over two prior experiments which had been carried out exactly under the same experimental conditions. Analysis of a total of 106 untreated MRC5-SV2 cells produced a cross-correlation heat-map of 12 cellular morphology attributes (Figure 7.6A-C) and their associated Pearson r correlation coefficients (Figure 7.6D).

For a cell spreading assay, characteristics of most importance are how the cell changes in morphology as the cell spreads. The cell area attribute is a direct measure of cell spread given its derivation from cell ROI overlays on the DAPI channels on original experimental images (see Chapter 5). Cell area is also an indirect proxy for spreading time, given that the mean cell areas tend to increase throughout the course of these spreading experiments. Correlations to cell area are therefore also expressive of what the average cell is doing over the course of time.

The correlation matrix provides a snapshot of the heterogeneity in cell morphology within the experimental group, but also provides an implicit indication of the spreading process of cells - from cells which have taken longer to fall out of suspension having less time to adhere to the ECM and start their spreading processes.

Considering selected elements of the correlation map (highlighted green; Figure 7.6D), a story of cell spreading can be built, based fundamentally on how well correlated processes are to the cell area attribute. This analysis shows that as cells spread and their imaged area increases, there is a corresponding increase in membrane adhesion to the ECM, bringing more of the cytoplasm into focus and extending the cell's inferior profile (cell area; cell perimeter; Figure 7.6C), as the superior portion is pulled lower (Panels B and C). The cell increases in its longitudinal axis (cell Feret; Panels A and B), but even more-so, there is a lengthening of the cell minimum Feret (Panel A) implying that the transverse axis also lengthens (Panel B). The mechanism by which this lengthening of Feret is carried out cannot be implied without looking

at other map coefficients - cell circularity and solidity - which together imply that the larger, more spread cells have, relative to their area, no more podial outgrowths or protrusions than the smallest set of cells. Larger cells are no more non-circular or rough around their edges than the smaller cells. This means that as the cells spread, there is a general enlargement without specifically strong growth in any one axis. Strong positive correlations between cell area and nuclear area (highlighted yellow) may be symptomatic of one or two processes at work. As the cells adhere and spread the nucleus tends to be pulled towards the ECM and to the focal plane of the microscope (Panel C). This brings a larger cross-sectional area of the nucleus into focus. So it can be seen that in a spreading cell, cell area nearly always exhibits a high correlation to the nuclear area (at least in the earliest stages of spreading). As this is a heterogeneous population of cells, many of which are in a different phase of the cell cycle, cell volumes (in the 2D analysis, the area proxy) tend to differ. Since nuclear volume has already been proven to have a positive correlation outside of a spreading environment (Good 2015; Neumann & Nurse 2007; Webster et al. 2009), then this correlation also enhances that particular correlation in spreading assays. In contrast, the circularity and solidity of both the cells and nuclei express negligible correlation to the cell area.

On the other hand, cell Feret has a moderate correlation with cell area, but less-so than cell minimum Feret. This implies that the minimum Feret increases more linearly with cell area than longitudinal extension. Cell minimum Feret does not correspond exactly to the minimum width of the cell but is influenced by a variety of possible lateral outgrowths in many possible directions (Panel A). Therefore, the likelihood of small cellular extension from any random part of the cell membrane is always more likely to contribute to raising the minimum Feret than to specifically contribute to an extension of the longitudinal axis alone - from which the cell Feret measurement is derived. In effect, the cells are not tending to elongate in any substantial manner during spreading. This is to be expected from cells which are in a spreading phase rather than the migratory stage. In the latter case, the cells generally become polarised and more directed on their protuberances and lamellipodial leading-edge growth.

A

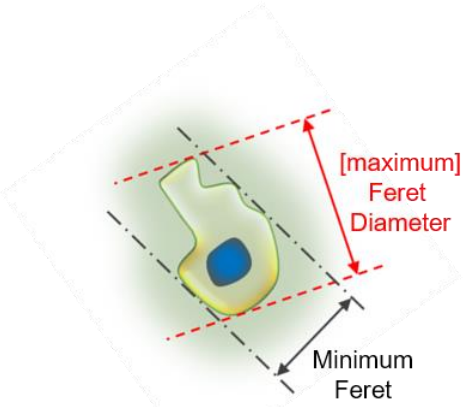
[maximum]
Feret
Diameter
Minimum
Feret

B

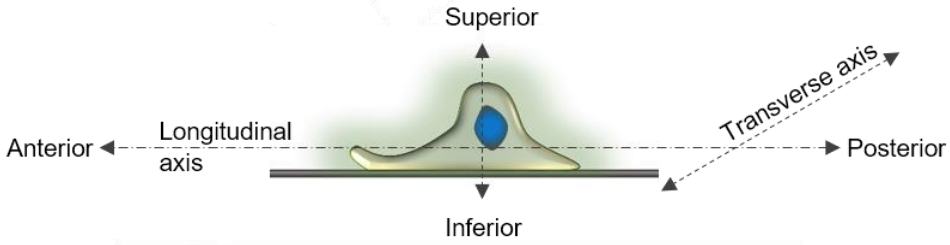
Superior
Anterior
Longitudinal
axis
Transverse axis
Posterior
Inferior

C

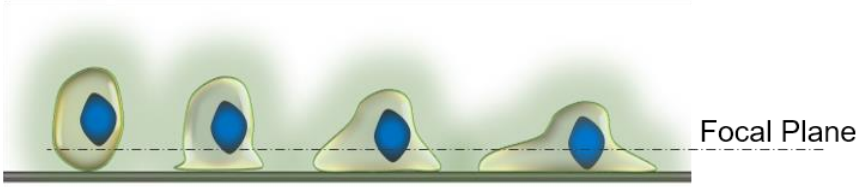
Focal Plane

D

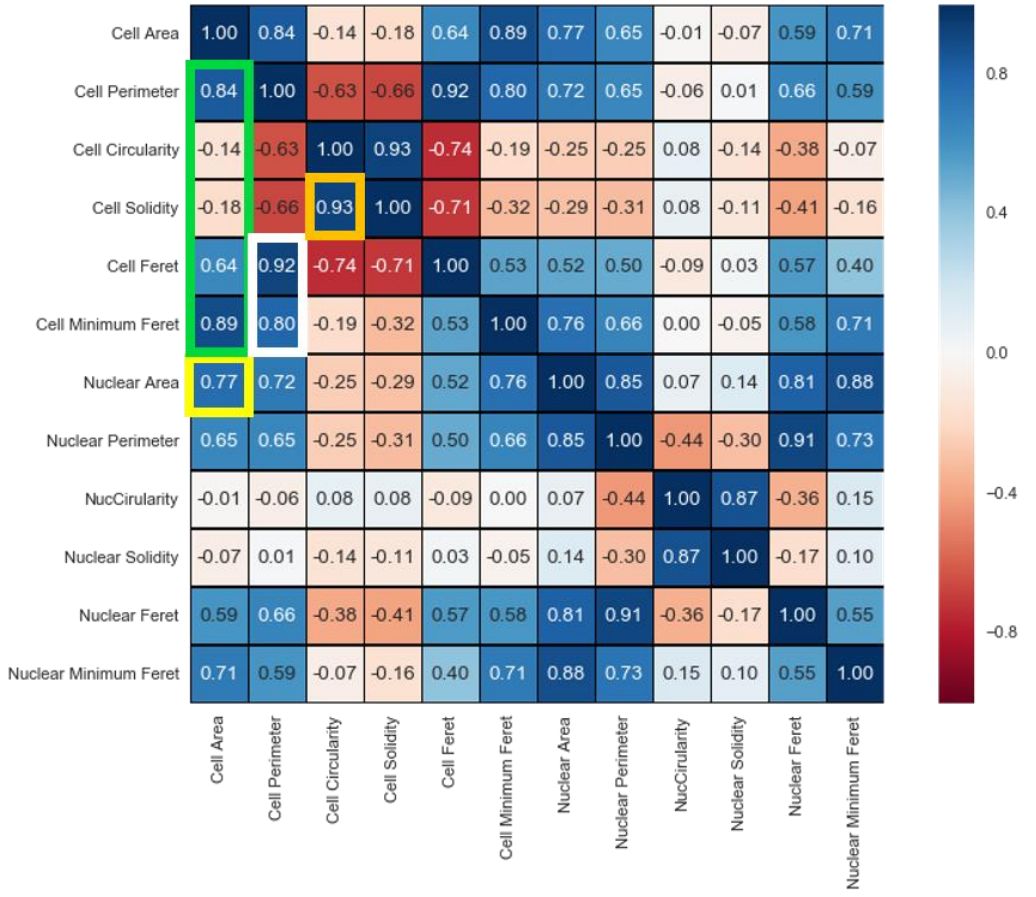
Cell Area 1.00 0.84 -0.14 -0.18 0.64 0.89 0.77 0.65 -0.01 -0.07 0.59 0.71
Cell Perimeter 0.84 1.00 -0.63 -0.66 0.92 0.80 0.72 0.65 -0.06 0.01 0.66 0.59
Cell Circularity -0.14 -0.63 1.00 0.93 -0.74 -0.19 -0.25 -0.25 0.08 -0.14 -0.38 -0.07
Cell Solidity -0.18 -0.66 0.93 1.00 -0.71 -0.32 -0.29 -0.31 0.08 -0.11 -0.41 -0.16
Cell Feret 0.64 0.92 -0.74 -0.71 1.00 0.53 0.52 0.50 -0.09 0.03 0.57 0.40
Cell Minimum Feret 0.89 0.80 -0.19 -0.32 0.53 1.00 0.76 0.66 0.00 -0.05 0.58 0.71
Nuclear Area 0.77 0.72 -0.25 -0.29 0.52 0.76 1.00 0.85 0.07 0.14 0.81 0.88
Nuclear Perimeter 0.65 0.65 -0.25 -0.31 0.50 0.66 0.85 1.00 -0.44 -0.30 0.91 0.73
NucCirularity -0.01 -0.06 0.08 0.08 -0.09 0.00 0.07 -0.44 1.00 0.87 -0.36 0.15
Nuclear Solidity -0.07 0.01 -0.14 -0.11 0.03 -0.05 0.14 -0.30 0.87 1.00 -0.17 0.10
Nuclear Feret 0.59 0.66 -0.38 -0.41 0.57 0.58 0.81 0.91 -0.36 -0.17 1.00 0.55
Nuclear Minimum Feret 0.71 0.59 -0.07 -0.16 0.40 0.71 0.88 0.73 0.15 0.10 0.55 1.00
Cell Area
Cell Perimeter
Cell Circularity
Cell Solidity
Cell Feret
Cell Minimum Feret
Nuclear Area
Nuclear Perimeter
NucCirularity
Nuclear Solidity
Nuclear Feret
Nuclear Minimum Feret
0.8
0.4
0.0
−0.4
−0.8

Figure 7.6 Correlation mapping for untreated cells spreading cells.

MRC-5 SV2 cells were grown without drug treatment, in two separate experiments for Proximity Ligation Assays described in Figures 7.2 and 7.4. Images were analysed and correlation results graphically visualised using PLAY software (described in Chapter 5).

Panel A. ***Feret diameter:*** The longest distance obtainable between two infinitely long parallel tangents as they touch the object's outer perimeter, also known as Feret, maximum Feret diameter and maximum caliper. ***Minimum Feret:*** The shortest distance obtainable between any two infinitely long parallel tangents as they touch the object's outer perimeter, also known as minimum caliper.
Panel B. Anatomical terms of location.
Panel C. During the earliest stages of the cell spreading process the imaged nucleus [nuclear area] is positively correlated with cell area.
Panel D. Using PLAY analysis software to perform meta-analyses, cell shape and size measurements were cross-correlated and displayed in heat-map form, along with a Pearson r correlation. For untreated cells, cell count (n)=106.

7.7.2 Cell spreading processes following the inhibition of Mnk1/2

Previous data (Figure 7.3) suggested that inhibition of Mnk1/2 did not alter the distance of DDX3X/eIF4E foci from the cell perimeter. PLAY analysis of 106 untreated MRC5-SV2 cells, produced a cross-correlated heat-map of 12 cellular morphology attributes and their associated Pearson correlation coefficients (Figure 7.6D). Performing a similar analysis on cells grown and then allowed to spread in the presence of 10μM MnkI-19 generated a correlation heat-map shown in Figure 7.7. Panel A compares the first column of both original correlation maps for each assay (+/- MnkI-19). From these two maps, a 'difference of correlation maps' can be derived, highlighting the difference of correlation coefficients for each assay. This highlights differences by simple interrogation of a single matrix (Figure 7.7B). The difference map is derived from the subtraction of the untreated cell Pearson values from those derived from the drug-treated cells. Taking the cross-correlation value for cell area vs. cell circularity as an example, as highlighted in red in Panels A and B, inhibition of Mnk1/2 results in a Pearson r correlation coefficient of 0.4. A value of this magnitude is classed as low but significant (Mukaka 2012), and as such is worthy of attention. To add some background as to how such a Pearson correlation coefficient is derived in each cell of the heat-map, Panel C shows the actual bivariate KDE plots of the data for this particular example. These data show regression lines (with 95% confidence intervals) to allow visualisation of the underlying linearity of distribution. Pearson r correlation coefficients, although not directly derived from the regression line are another standard calculation of such bivariate relationships. The Pearson r coefficient is not a regression calculation, it simply defines how two variables vary together and if both variables are derived from normal distributions. Confidence intervals of Pearson r can be derived if necessary. These data provide some suggestion that when Mnk1/2 is inhibited, asymmetric cell spreading may be retarded, in turn highlighting the plausibility of eIF4E phosphorylation or another target of Mnk1/2 having some possible influence over the process of protrusive growth in MRC5 cells. Recently, it has been shown that inhibition of Mnk1/2 inhibits migration in other human cells (Beggs et al, 2015). The reasons for this are unclear and were investigated further. From the difference of correlation maps

(Panel B), a number of relationships are highlighted (red and green) as being substantially different in the drug-treated group compared to untreated. In Mnk1/2 inhibited cells, cell circularity and solidity are significantly more correlated with a change in the cell area, meaning that relative to untreated cells they become rounder and smoother as the cells adhere and spread onto the ECM. Their minimum Feret also shows a low positive correlation to both circularity and solidity too, implying that as the cells become more circular they are in fact expanding this particular Feret dimension – suggestive of cells spreading in a circular manner.

In summary, from these few coefficients, it may be read that the cells with inhibited Mnk1/2 signalling are spreading in a more circular manner than untreated cells. This renders the question, are these cells more rounded because they are retarded in their spreading, or are they spreading normally and with smooth rounded form suggestive of a membrane re-structuring without polarisation and podial creation? The answer may lie in the lack of change in correlation between cell circularity and cell (maximum) Feret (highlighted yellow). This shows that there is a low correlation between an increasingly circular cell and its Feret, or longitudinal length, meaning the cells are tending to spread more in a transversal manner (Figure 7.6B). Real Feret measurements should be compared in order to answer this question fully.

7.7.3 Inhibition of Mnk1/2 promotes rounded forms of spreading, without many podial outshoots

Using a PLAYkit (described in Chapter 5), it was possible to create a visualisation of absolute values for cell areas, circularity and solidity, with associated Welch's t-tests for significance. Figures are shown for the cell areas measured for each assay; the statistical significance of the difference of the cell sizes was established, relative to the untreated group (Figures 7.8 to 7.10). In this analysis, when compared to untreated cells, the inhibition of Mnk1/2 signalling did not affect cellular areas (Figure 7.8), circularity (Figure 7.9A) or cell solidity (Figure 7.10A) even though eIF4E phosphorylation was prevented at these concentrations (data not shown). However, the addition of multiple Mnk1/2 inhibitors to the same cells did affect cell solidity and circularity, but this

may reflect off-target effects of CGP57380. Inhibition of mTOR signalling affected cell spreading in a statistically significant manner, whether used alone or in combination with the Mnk1/2 inhibitor (Figure 7.8; see below for further analysis). A small effect was observed on cell solidity (Figure 7.10A) when both mTOR and Mnk1/2 were inhibited (see below for further analysis).

This poses the question, why are certain correlation coefficients found in Mnk1/2 inhibited cells so different to those derived from experiments assays performed with untreated cells? The answer, in large part is elucidated by the implementation of split-violin plots, which show that during the spreading process the smaller cells rapidly become much more circular as they grow (Figures 7.9B) and from relatively unsolid small cells, grow very much more solid larger cells (Figures 7.10B). In summary, these data suggest that inhibition of Mnk1/2 signalling doesn't so much retard growth, but appears to mostly accommodate for rounded forms of spreading, without many podial outshoots.

7.7.4 Inhibition of mTOR signalling retards general spreading

For cells grown in the presence of Ku-0063794:

The PLAY-generated 'difference of correlation maps' map (Figure 7.11) shows only a single large difference in assay correlation coefficients. The cell area of KU-0063794 treated cells is significantly smaller than the untreated group (Figure 7.8), with significantly more cell circularity (Figure 7.9A), and no real change in solidity compared to untreated (Figure 7.10A). Looking at the split-violin plot for cell circularity, it can be seen that there is a bi-modality of distribution in the larger cells which is more explicit than the smaller set. However, on the whole, there is no real change to the median form throughout the spreading process for mTOR inhibited cells (Figure 7.9A). As they spread, there is a slight tendency for a lessening of cell solidity. mTOR signalling, therefore, appears to have a role in cell spreading. However, when spreading happens, there appears to be a similar shift away from solidity to podial growth whether mTOR signalling is active or not.

7.7.5 Use of multiple Mnk1/2 signalling inhibitors does not affect cell area during spreading

As part of this study, multiple Mnk1/2 inhibitors were added to the same cultures. This was in part to ensure that eIF4E phosphorylation was ablated. It was also due to the fact that MnkI-19 is poorly characterised at this time. The PLAY-generated 'difference of correlation maps' map (Figure 7.12) shows only two correlation attributes strong enough to be considered significant; nuclear Feret vs. cell solidity and cell circularity (highlighted red). Growth in any nuclear aspect generally is a consequence of the spreading process, bringing the nucleus into a more inferior position on the coverslip (Figure 7.6B and C).

The cell area box-plot (Figure 7.8) suggests that overall spreading is not retarded. In Mnk1/2 + KU-0063794 inhibited cells, cell circularity is significantly less overall (Figure 7.9A), a characteristic implied in both small and larger subsets of cells (Figure 7.9B). These cells are significantly less solid overall (Figure 7.10A), with a tendency to become slightly more solid with growth (Figure 7.10B). This suggests that the nucleus is indeed being pulled towards the inferior floor during spreading and that the correlation is not destroyed throughout spreading as there is no significant up-regulation of podial outbursts as the cells reach a larger size.

7.7.6 Inhibition of both mTOR and Mnk1/2 signalling retards spreading but promotes podial outgrowth at later times

Preliminary studies indicated that inhibition of both mTOR and Mnk1/2 signalling might retard general spreading (Figure 7.8; Mnk1/2 + KU-0063794). To investigate this further, the PLAY-generated 'difference of correlation maps' map was generated (Figure 7.13). This summary shows no correlations strong enough to be considered anything more than negligible ($0 < r < 0.3$). Cell area is significantly smaller than the untreated group, also when compared to all other groups (Figure 7.8). Cell circularity overall shows no significant difference to untreated cells. But when from initially being very small and circular cells, the circularity is quickly lost as the cells enlarge in size (Figure 7.9B). This is also reflected in the manner in which the small cells lose

their very solid aspect and become much less solid as they grow (Figure 7.10B). It seems that inhibition of mTOR signalling exhibits itself in a similar manner, whether on its own or in combination with inhibition of Mnk1/2 (Figure 7.9 and 7.10). Cell spreading is retarded, and there is a real shift away from solidity and circularity to podial growth as the cells mature in the spreading process.

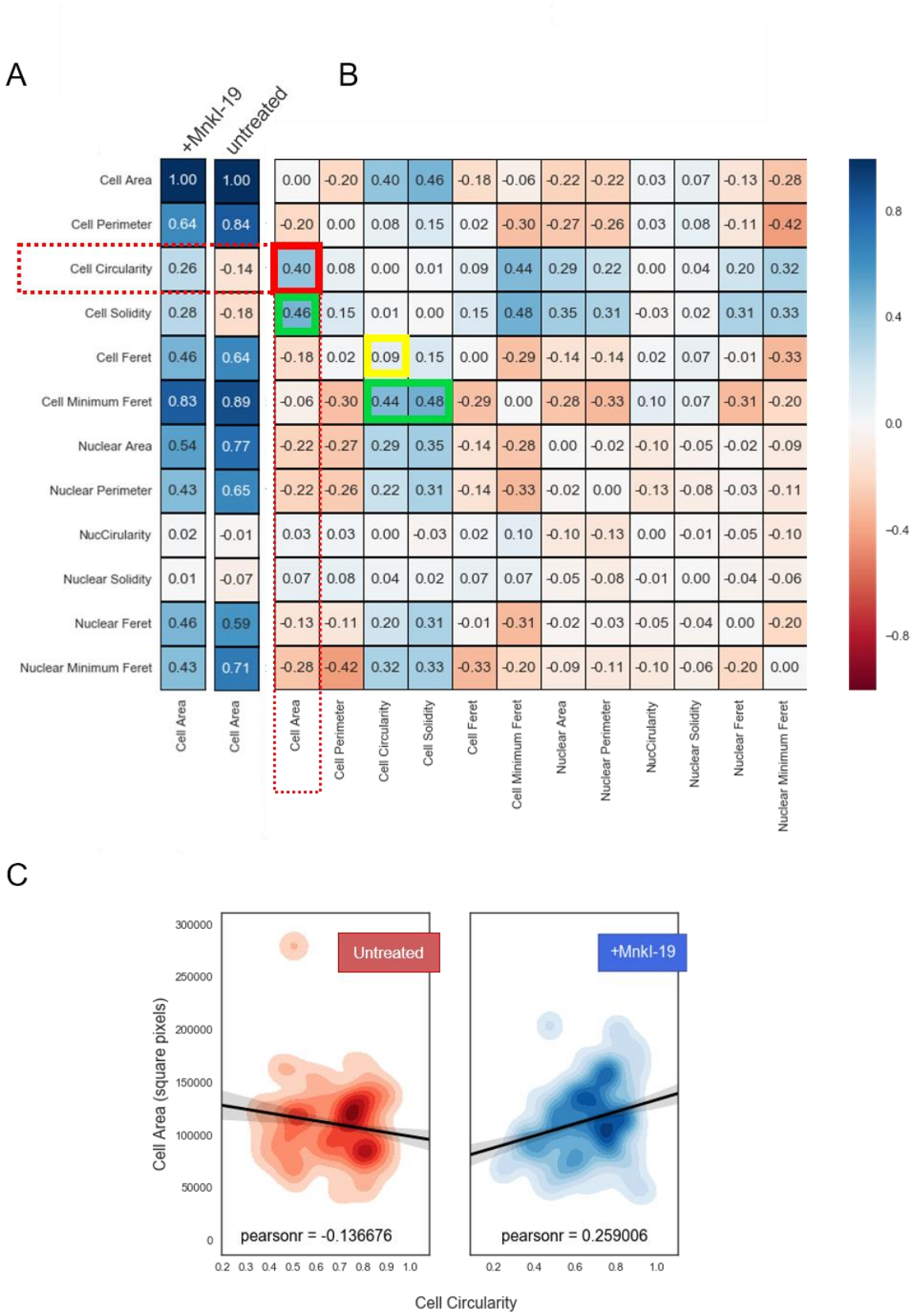
A
B
+MnkI-19
untreated
Cell Area 1.00 1.00 0.00 -0.20 0.40 0.46 -0.18 -0.06 -0.22 -0.22 0.03 0.07 -0.13 -0.28
Cell Perimeter 0.64 0.84 -0.20 0.00 0.08 0.15 0.02 -0.30 -0.27 -0.26 0.03 0.08 -0.11 -0.42
Cell Circularity 0.26 -0.14 0.40 0.08 0.00 0.01 0.09 0.44 0.29 0.22 0.00 0.04 0.20 0.32
Cell Solidity 0.28 -0.18 0.46 0.15 0.01 0.00 0.15 0.48 0.35 0.31 -0.03 0.02 0.31 0.33
Cell Feret 0.46 0.64 -0.18 0.02 0.09 0.15 0.00 -0.29 -0.14 -0.14 0.02 0.07 -0.01 -0.33
Cell Minimum Feret 0.83 0.89 -0.06 -0.30 0.44 0.48 -0.29 0.00 -0.28 -0.33 0.10 0.07 -0.31 -0.20
Nuclear Area 0.54 0.77 -0.22 -0.27 0.29 0.35 -0.14 -0.28 0.00 -0.02 -0.10 -0.05 -0.02 -0.09
Nuclear Perimeter 0.43 0.65 -0.22 -0.26 0.22 0.31 -0.14 -0.33 -0.02 0.00 -0.13 -0.08 -0.03 -0.11
NucCirularity 0.02 -0.01 0.03 0.03 0.00 -0.03 0.02 0.10 -0.10 -0.13 0.00 -0.01 -0.05 -0.10
Nuclear Solidity 0.01 -0.07 0.07 0.08 0.04 0.02 0.07 0.07 -0.05 -0.08 -0.01 0.00 -0.04 -0.06
Nuclear Feret 0.46 0.59 -0.13 -0.11 0.20 0.31 -0.01 -0.31 -0.02 -0.03 -0.05 -0.04 0.00 -0.20
Nuclear Minimum Feret 0.43 0.71 -0.28 -0.42 0.32 0.33 -0.33 -0.20 -0.09 -0.11 -0.10 -0.06 -0.20 0.00
Cell Area
Cell Area
Cell Area
Cell Perimeter
Cell Circularity
Cell Solidity
Cell Feret
Cell Minimum Feret
Nuclear Area
Nuclear Perimeter
NucCirularity
Nuclear Solidity
Nuclear Feret
Nuclear Minimum Feret
0.8
0.4
0.0
−0.4
−0.8
C
Untreated
+MnkI-19
Cell Area (square pixels)
300000
250000
200000
150000
100000
50000
0
pearsonr = -0.136676
pearsonr = 0.259006
0.2 0.3 0.4 0.5 0.6 0.7 0.8 0.9 1.0
0.2 0.4 0.6 0.8 1.0
Cell Circularity

Figure 7.7 Meta-Analysis: The influence of MnkI-19 on cell shape and size

MRC-5 SV2 cells were grown with and without the presence of 10μM MnkI-19 prior to undergoing two separate experiments, conducted at the same time and under the same conditions as for the Proximity Ligation Assays described in Figures 7.2 and 7.4. Using PLAY analysis software to perform meta-analyses (untreated cells cell count (n)=106, MnkI-19 cell count (n)=108), cell shape and size measurements were cross-correlated. From the resulting correlation map created from cells grown in the presence of the drug, the untreated cells correlation coefficient mapped values were deducted on an element by element basis, resulting in a heat-map 'difference of correlation maps' map. Each element shows the difference between cells grown with and without the presence of the drug. Positive Pearson r values imply a much stronger positive correlation in the assay with drug present.

Meta-analysis was performed by combining two PLA experiments for finding putative interactions between 4E-BP1/eIF4E (Figure 7.5) and DDX3/eIF4E (Figure 7.2) performed under the exact same conditions, in this way cell assay numbers were increased to n = 108 (Mnk inhibited cells) and n = 106 (untreated ells).

Panel A. The Cell Area column from correlation maps of both WT and Mnk1/2 inhibited cells. **Panel B.** 'Difference of correlation maps' for Mnk1/2 inhibited vs. WT, where the correlation figure in each cell corresponds to the Mnk inhibited mapped value minus the value in the WT correlation map. The highlighted cells show particularly large differences between untreated cells and drug-inhibited parameters. **Panel C.** Cell Circularity is more strongly positively correlated with cell area in Mnk1/2 inhibited cells than in untreated cells.

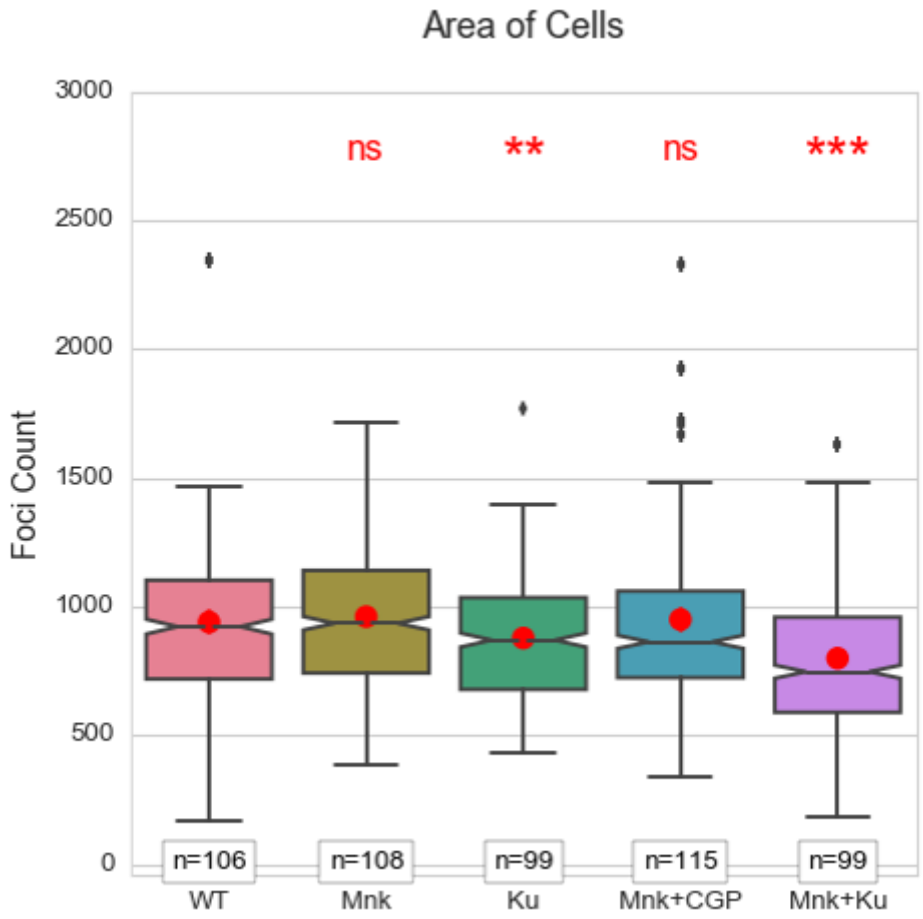

Figure 7.8 Cell spreading is affected by the presence of drugs.

MRC-5 SV2 cells were grown with or without the presence of the inhibitors shown prior to undergoing two separate experiments, conducted at the same time and under the same conditions as for the Proximity Ligation Assays described in Figures 7.2 and 7.4.

Using PLAY analysis software (designed especially for this project and discussed in Chapter 5) to perform meta-analyses, the following results were obtained. Statistical analyses were performed using Welch's t-test to show the difference relative to untreated cells (ns $P > 0.05$, * $P \leq 0.05$, ** $P \leq 0.01$, *** $P \leq 0.001$). N-statistics signify the number of cells tested for each assay. Point estimated mean values are shown in red with 95% confidence intervals visualised as vertical bars around the means. Median values are associated with 95% confidence intervals as visualised by notches around the median lines.

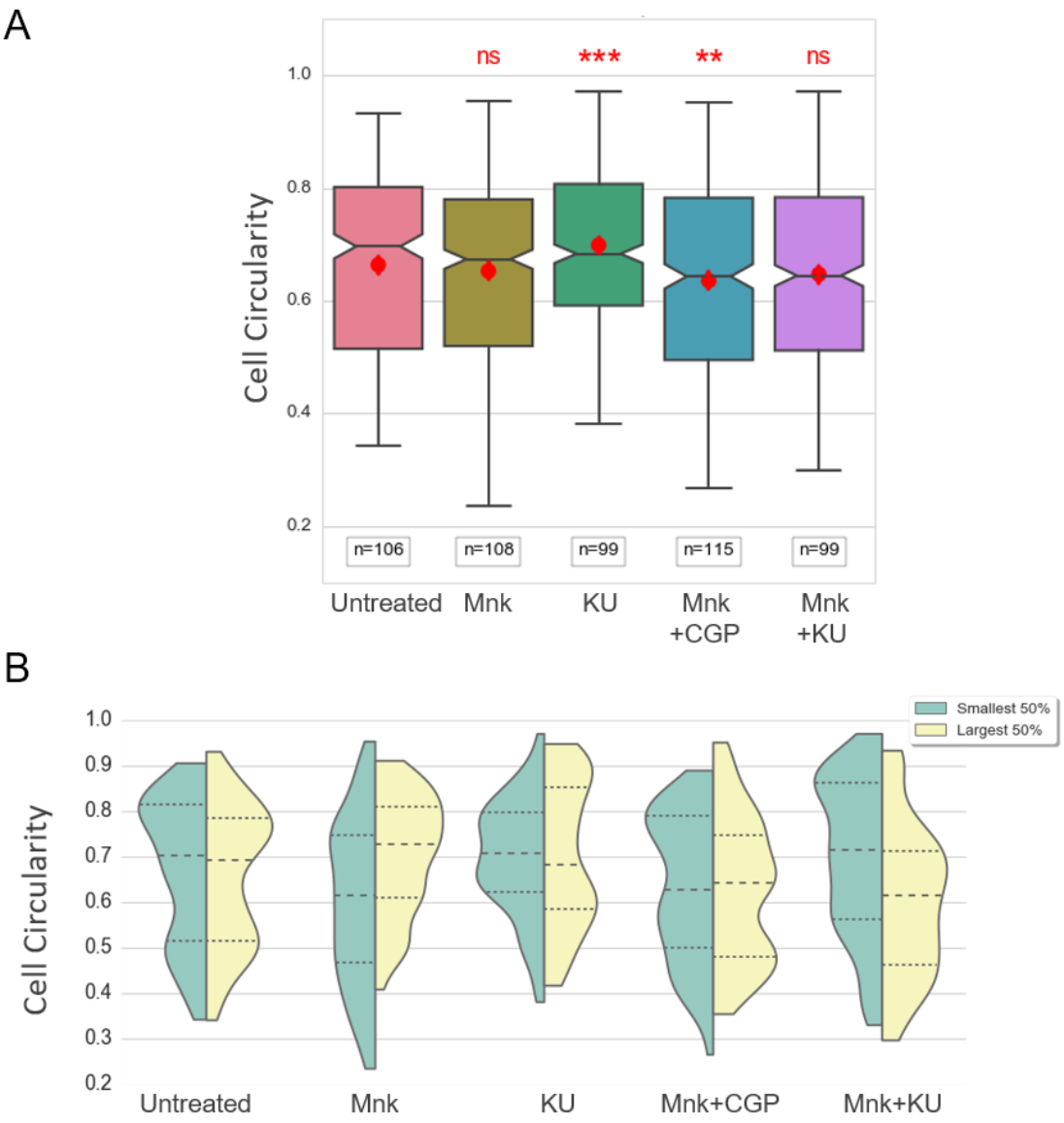

Figure 7.9 Cell Circularity is affected by the presence of inhibitors.

Using the same experimental protocols as discussed in Figure 7.8, meta-analysis was performed using PLAY software (discussed in Chapter 5), to obtain cell circularity values for all assayed cells. Box-plot statistical annotations are the same as those described in Figure 7.8, With Welch's t-test employed to show the statistical difference relative to untreated cells (ns $P > 0.05$, * $P \leq 0.05$, ** $P \leq 0.01$, *** $P \leq 0.001$).

Panel A. Cell circularity is significantly affected by the presence of certain inhibitors during cell spreading.
Panel B. Split-violin plots showing the difference in distribution of cellular areas, between the smallest 50% of cells as compared to the largest 50%. Median, 1st quartile and 3rd quartile boundaries are marked for each group under investigation.

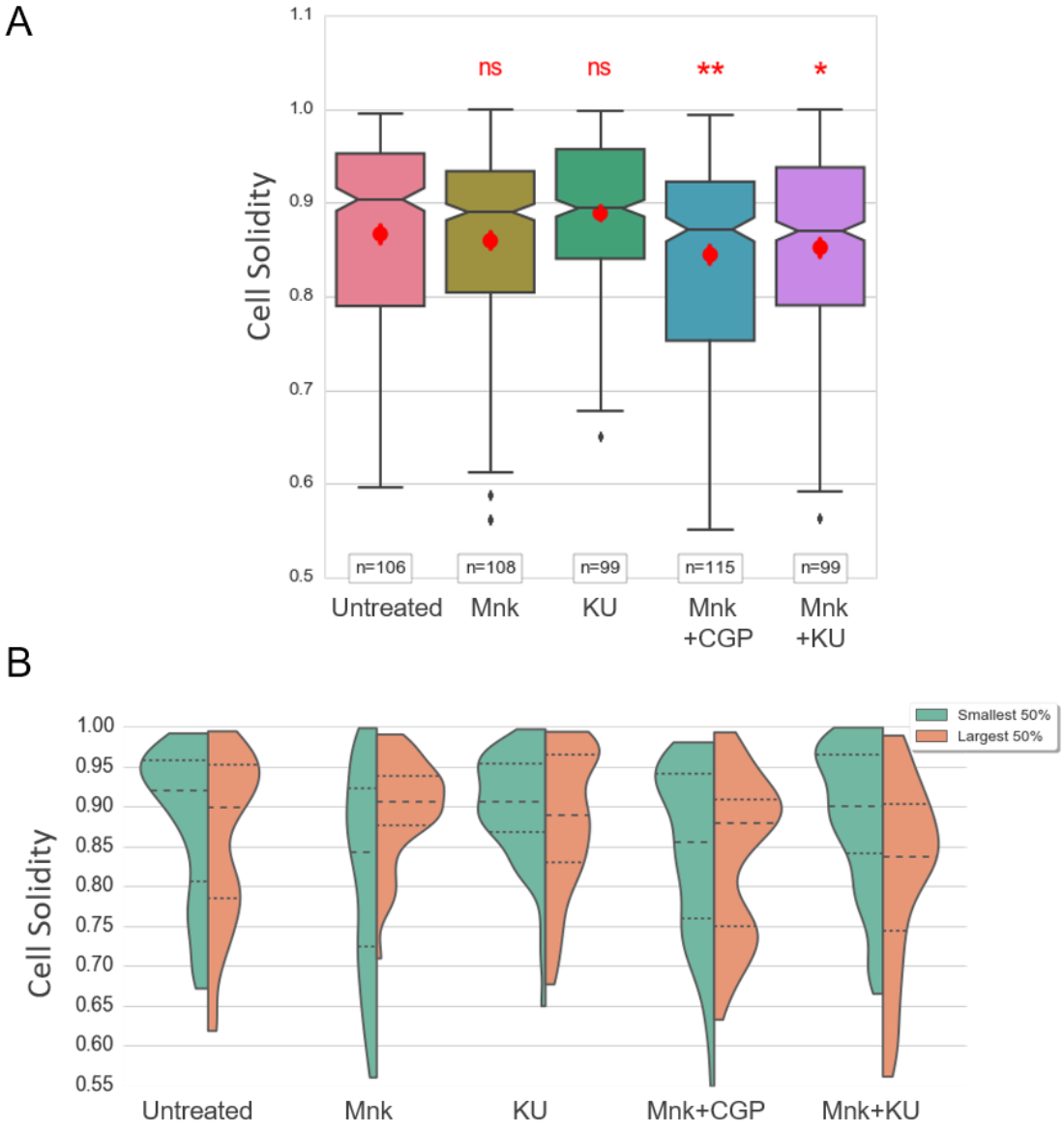

Figure 7.10 Cell Solidity is affected by the presence of inhibitors.

Using the same experimental protocols as discussed in Figure 7.8, meta-analysis was performed using PLAY software (discussed in Chapter 5), to obtain cell circularity values for all assayed cells. Box-plot statistical annotations are the same as those described in Figure 7.8, With Welch's t-test employed to show the statistical difference relative to untreated cells (ns $P > 0.05$, * $P \leq 0.05$, ** $P \leq 0.01$, *** $P \leq 0.001$).

Panel A. Cell solidity is significantly affected by the presence of certain inhibitors during cell spreading.
Panel B. Split-violin plots showing the difference in distribution of cellular solidity, between the smallest 50% of cells as compared to the largest 50%. Median, 1st quartile and 3rd quartile boundaries are marked for each group under investigation.

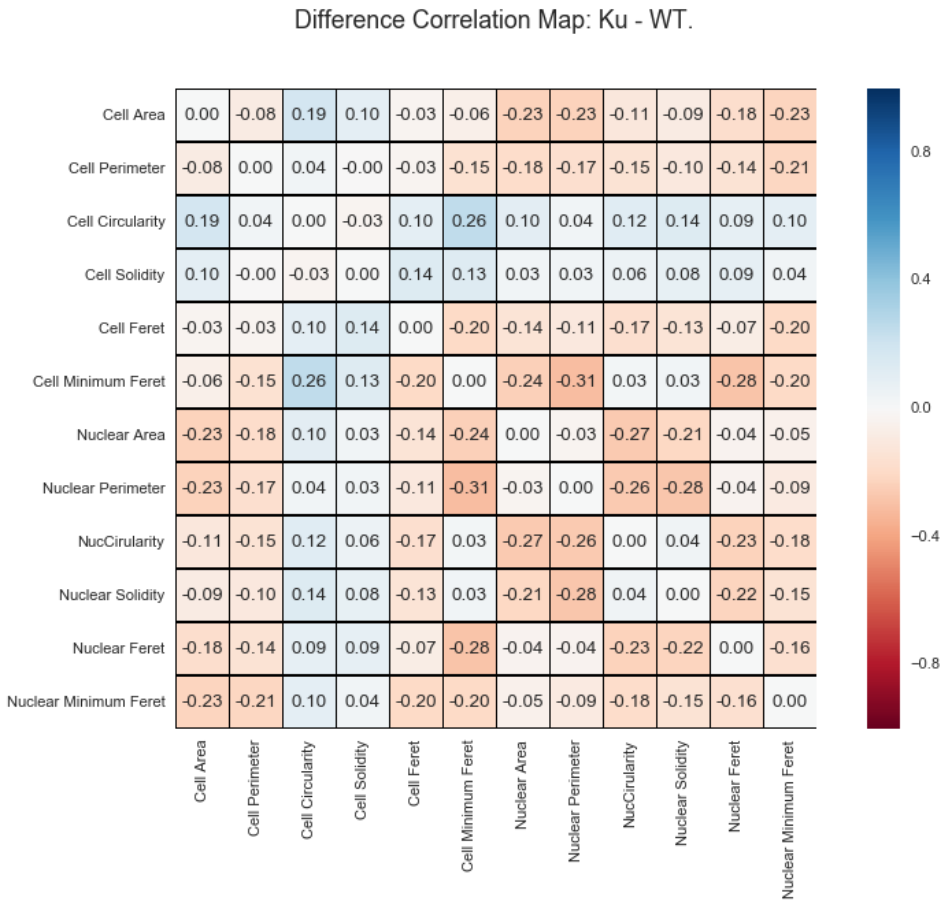

Figure 7.11 Difference of correlation maps following inhibition of mTORC1 signalling

MRC-5 SV2 cells were grown in the absence and presence of 10μM KU-0063794 prior to undergoing two separate experiments, conducted at the same time and under the same conditions as for the Proximity Ligation Assays described in Figures 7.2 and 7.4. Using PLAY analysis software (designed especially for this project and discussed in Chapter 5) to perform meta-analyses (untreated cells cell count (n)=106, KU-0063794 treated cell count (n)=99), cell shape and size measurements were cross-correlated. From the resulting correlation map created from cells grown in the presence of the drug, the untreated cells correlation coefficient mapped values were deducted on an element by element basis, resulting in a heat-map 'difference of correlation maps' map, with each element showing the difference between cells grown with and without the presence of the drug. Positive Pearson r values show a much stronger positive correlation in the assay with drug present.
Difference of correlation maps' for KU-0063794 inhibited vs. untreated, where the correlation figure in each cell corresponds to the KU-0063794 inhibited mapped value minus the value in the WT correlation map.

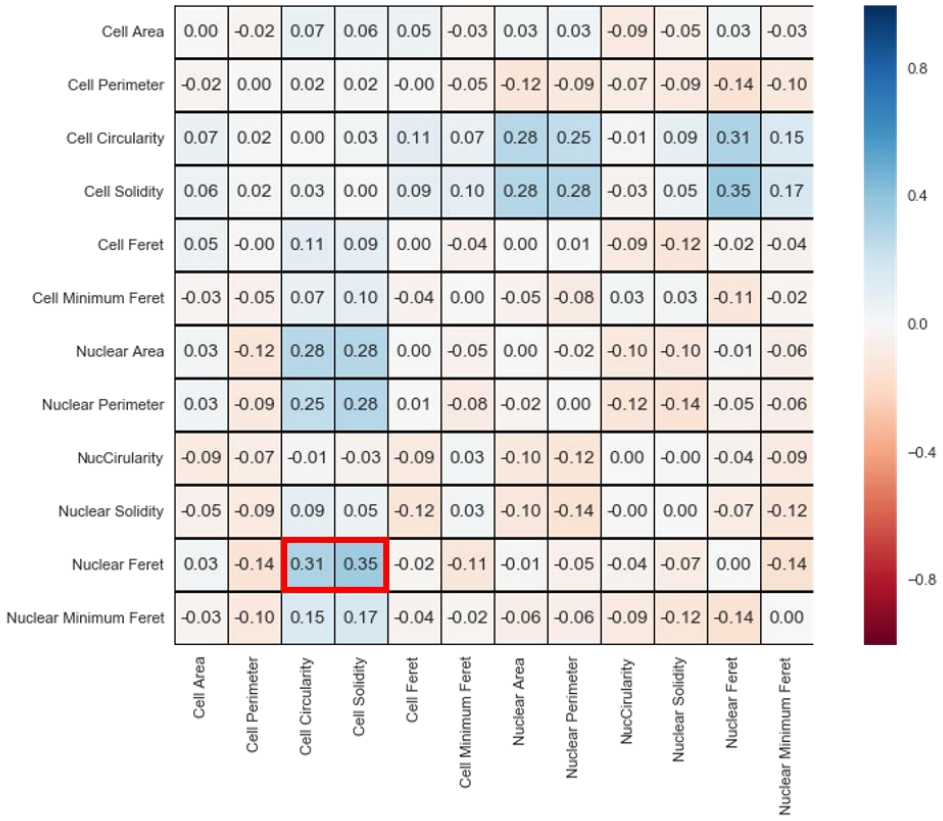

Figure 7.12 Difference of correlation maps following inhibition of Mnk1/2 signalling with MnkI-19 and CGP-57380

MRC-5 SV2 cells were grown in the absence and presence of 10μM MnkI-19 and CGP-57380 prior to undergoing two separate experiments, conducted at the same time and under the same conditions as for the Proximity Ligation Assays described in figures 7.1 and 7.4. Using PLAY analysis software (designed especially for this project and discussed in Chapter 5), to perform meta-analyses (untreated cells cell count (n)=106, MnkI-19 + CGP-57380 cell count (n)=115), cell shape and size measurements were cross-correlated. From the resulting correlation map created from cells grown in the presence of the drug, the untreated cells correlation coefficient mapped values (Figure 7.7) were deducted on an element by element basis, resulting in a heat-map 'difference of correlation maps' map, with each element showing the difference between cells grown with and without the presence of the drug.Positive Pearson r values imply a much stronger positive correlation in the assay with drug present.
Difference of correlation maps' for MnkI-19 + CGP-57380 inhibited vs. untreated, where the correlation figure in each cell corresponds to the MnkI-19 and CGP-57380 inhibited mapped value minus the value in the WT correlation map.

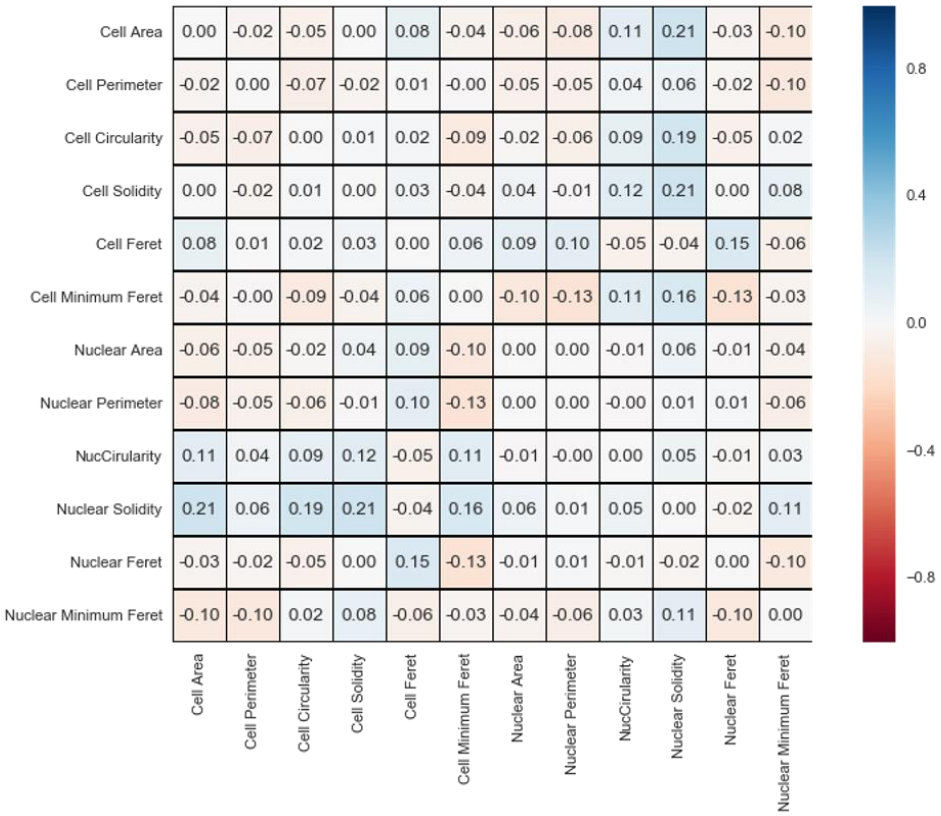

Figure 7.13 Difference of correlation maps following the inhibition of both Mnk1/2 and mTORC1 signalling

MRC-5 SV2 cells were grown in the absence and presence of 10μM MnkI-19 and KU-0063794 prior to undergoing two separate experiments, conducted at the same time and under the same conditions as for the Proximity Ligation Assays described in Figures 7.2 and 7.4. Using PLAY analysis software (designed especially for this project and discussed in Chapter 5) to perform meta-analyses (untreated cells cell count (n)=106, MnkI-19 + KU-0063794 cell count (n)=99), cell shape and size measurements were cross-correlated. From the resulting correlation map created from cells grown in the presence of the drug, the untreated cells correlation coefficient mapped values were deducted on an element by element basis, resulting in a heat-map 'difference of correlation maps' map, with each element showing the difference between cells grown with and without the presence of the drug.Positive Pearson r values imply a much stronger positive correlation in the assay with drug present.

Difference of correlation maps' for MnkI-19 and KU-0063794 inhibited vs. untreated, where the correlation figure in each cell corresponds to the MnkI-19 + KU-0063794 inhibited mapped value minus the value in the WT correlation map.

8 Discussion

8.1 Localised translation in spreading cells

There is extensive literature showing the compartmentalisation and trafficking of mRNA in cells (Donnelly et al. 2010; Medioni et al. 2012), with asymmetric distribution of mRNAs evident in fibroblasts. In response to migratory stimuli, a large number of mRNAs accumulate in the tips of cellular protrusions of NIH3T3 cells (Mili et al, 2008), facilitating localised protein synthesis. However, the regulatory interactions between the translational machinery, localised mRNAs, cellular structures and fibroblastic cell spreading/migration are relatively unexplored. The overall aim of this work was to identify the presence of novel proteins/mRNA complexes at the leading edge of spreading fibroblasts; to this end, focused was put on discovering more about the presence and role of the CYFIP1-FMRP-eIF4E complex.

The migration of eukaryotic cells *in vitro* involves complex regulatory pathways which integrate stimuli received from the engagement of the extracellular matrix (ECM) and from contact with adjacent cells (Parsons et al, 2010). Cell migration is an essential process in development, morphogenesis, angiogenesis and regeneration of tissues. The mechanism of cell migration towards external attractants comprises a cycle in which cells are stimulated to polarise by the actions of Rho GTPases (Parsons et al, 2010) and extend protrusions formed of lamellipodia or filopodia, both of which are driven and formed of filamentous actin networks (Ridley, 2001). These protrusions are then stabilised by focal adhesions which link the actin cytoskeleton to the ECM. Such lamellipodia are large flattened structures formed from the large dense branched actin networks (Abercrombie et al, 1970), with formation dependent on protein cofactors that mediate their local regulation, structural characteristics and dynamics (Ridley, 2001; Abercrombie et al 1970; Pollard and Borisy, 2003; Bugyi and Carlier, 2010). These include Rac1, which stimulates the recruitment of the WAVE complex and actin nucleation complex, Arp2/3 (including ArpC2) to the plasma membrane (Figure 4.11). The WAVE complex, which is composed of numerous subunits (including CYFIP1), is required for

lamellipodium formation and is activated downstream of Rac1 (Wang et al, 2012; Rotty et al, 2013), with WAVE complex binding to Rac1 *via* CYFIP1.

Previous work from the Morley laboratory has shown that eIF4G, 4E-BP1 and ribosomal subunits colocalise with eIF4E in the lamellipodia of migrating fibroblastic cells (Willett et al, 2010; Willett et al, 2011), suggesting the regulation of localised translation in this cellular compartment. In neuronal cells, another protein has been implicated in localised translation at the leading edge of cells (Brinegar and Cooper, 2016); this is FMRP (Bagni and Greenough, 2005), a known regulator of translation which binds to polysomes. FMRP binds its cargo mRNAs in the nucleus and in mammals is able to recognise a large number of mRNAs (Miyashiro et al, 2003; Darnell et al, 2011). In neurones, FMRP can co-sediment with the monomeric 80S ribosomes and polysomes, CYFIP1, and translation initiation factors (Lacoux et al, 2012; Ramos et al, 2003; Blackwell et al, 2010). In fibroblasts, FMRP-mediated repression of translation requires a sub-population of FMRP to interact with CYFIP1 which is recruited to active Rac1/GTP as part of the WAVE complex. Binding of FMRP to CYFIP1 increases the affinity of CYFIP1 for capped mRNAs (Napoli et al, 2008), stabilising CYFIP1 on specific mRNAs to repress translation at the leading edge of spreading cells. CYFIP1 binds directly to eIF4E (and hence mRNA) using a surface similar to that of 4E-BP1. In the brain, CYFIP1 forms a complex with specific FMRP-target mRNAs; either reduced levels of CYFIP1 or FMRP cause an increase in the synthesis of MAP1B, αCaMKII, and APP (Bagni and Greenough, 2005; Westmark and Malter, 2007), and promotes neurite migration. Loss of CYFIP1 in fibroblasts is associated with a tumourigenic phenotype (Napoli et al, 2008). When FMRP is phosphorylated by p70S6K on Ser499, FMRP represses the translation of specific mRNAs, such as MAP1B, αCaMKII, PSD-95, SAPAP3 in neurones (Narayanan et al 2008; Todd et al, 2003). Synaptic activity promotes the dephosphorylation of FMRP and the release of CYFIP1 and bound RNAs from eIF4E, resulting in the alleviation of translation repression (Westmark and Malter, 2007).

8.2 A population of FMRP and CYFIP1 are localised to the leading edge of cells in spreading fibroblasts

The aim of the work described here was to identify the presence of novel proteins/mRNA complexes at the leading edge of spreading fibroblasts with a specific emphasis on CYFIP1-FMRP-eIF4E complexes. To facilitate this, conditions were optimised to visualise proteins at the leading edge of spreading cells (Chapter 3). Confocal microscopy confirmed that CYFIP1 colocalised with the trans-Golgi network, and was also found at the leading edge of cells (Figure 4.4). Some evidence suggested that CYFIP1 colocalised with FMRP on the cytoskeleton and that actin fibres may facilitate the transport of a small population of CYFIP1 to the periphery of the cell (Figure 4.5). In spreading fibroblasts, FMRP was found in abundance around actin stress fibres, and the phosphorylated form of FMRP (Ser499) was concentrated at the leading edge of cells (Figures 4.4 - 4.7). These data indicated that actin may be a primary facilitator for the trafficking of FMRP to the edge of the cell.

Evidence suggests that unphosphorylated FMRP is associated with actively translating polyribosomes, whilst phosphorylated FMRP (Serine 499) is required for in translational repression (Ceman et al. 2003), probably in a suppressive complex with CYFIP1 and eIF4E. The phosphorylation status of FMRP (Ser499) is unaffected by mTORC1-S6K1 signalling (Bartley et al. 2014). Just as the question has been posited, does Mnk1/2 signalling affect the translational repression activity of CYFIP1? We can ask the same of FMRP. Yet still the question remains, why is there so much phosphorylated FMRP(Ser499) to be found at the leading edge of spreading cells? It seems unlikely that it is simply stalling translation processes, and it is tempting to consider it as an activator of some other metabolic processes.

The use of TIRF microscopy to obtain low-noise diffraction limited images suggested that CYFIP1 and FMRP colocalised at the leading edge of spreading cells (Figure 4.12). Through the use of super-resolution techniques such as 3B, colocalisation of these two proteins were confirmed to be within 50nm (Figure 4.13). However, the low level of expression of CYFIP1 and FMRP made the planned biochemical analysis of these complexes impossible at this time.

8.3 The development of software for *in situ* Proximity Ligation Assay Analysis

With the use of the *in situ* Proximity Ligation Assay and fluorescence microscopy, it was possible to visualise interactions between proteins as distinct and intense foci within an image. PLA analysis software (PLAY) and associated packages were developed. Not only does PLAY count foci in cells, it is also able to localise these foci with respect to the cell perimeter, whilst considering other properties of the cell such as cell shape (Chapter 5). With such information defined within a managed dataframe, correlations were derived from the number and location of protein interactions and to the cell shape and size within which the foci resided. The system was optimised by monitoring foci formed between DDX3X and eIF4E, and using a DDX3X knock-down cell line generated using CRISPR/Cas9 gene editing as an experimental control (Chapter 6).

8.4 Elucidating the role of DDX3X in spreading cells

In addition to CYFIP1 and FMRP, DDX3X has been suggested to have important roles in translational control. There is evidence for its interaction with eIF4A. eIF4E, eIF4G and PABP (Lai et al. 2008; Lai et al. 2010; Soto-Rifo et al. 2012). DDX3X is also implicated in both epithelial-mesenchymal transitions (EMT) and tumourigenesis (Botlagunta et al. 2008; Samal et al. 2015). However, the exact role of DDX3X in translation initiation is a matter of some debate. DDX3X has been shown to suppress cap-dependent translation and up-regulate cap-independent translation (Shih et al. 2008). Utilising its consensus eIF4E-binding sequence, DDX3X is able to interact with the dorsal surface of eIF4E in the same mode as a 4E-BP1. This traps eIF4E in a translationally inactive complex which is then unable to interact with the scaffold protein, eIF4G. In addition to eIF4E-CYFIP1-FMRP, it is possible that eIF4E-DDX3X complexes might also regulate translation at the leading edge of spreading cells.

Therefore, to complement the work above, the interactions of DDX3X with eIF4E were investigated within spreading cells. Confocal microscopy was used alongside PLAY analysis software, and in conjunction with a DDX3X

knockdown cell line made using CRISPR/Cas9 gene editing. Deconvolved confocal microscopy imaging showed that DDX3X was found in high concentrations at particular locales spanning the periphery of the cells during the acute stages of cell spreading (Chapter 7). These data also suggest that DDX3X colocalises to the actin cytoskeleton, possibly using it as a transport route to facilitate its movement to the leading edge, in complex with eIF4E.

Using the *in situ* proximity ligation assay (PLA) method together with software designed specifically for the interpretation of PLA images (PLAY), these results shed some light on how under-expression of DDX3X protein affects its interactions with eIF4E. These data show that a reduction in DDX3X protein expression may retard the mechanism of cell spreading, leaving cells significantly more rounded, and more solid, and smaller than their parental counterparts (Chapter 7). These data also suggest that DDX3X protein may have a role in facilitating cytoskeletal rearrangement for morphological changes required for the spreading process. It also suggests that DDX3X protein may facilitate cellular polarisation and general podial growth, meaning that DDX3X could be playing a part in migratory processes including metastasis disease.

8.5 The effect of signalling inhibitors on cell spreading

Results show that mTOR signalling appears to have a role in the acute phase of cell spreading but the exact mechanism remains unclear. In contrast, inhibition of Mnk1/2 signalling appeared to cause cells to spread in a more circular manner than untreated cells, a characteristic similar to that shown in the DDX3X knock-down cell line. This suggests that Mnk1/2 may be directly phosphorylating DDX3X causing it to leave the translationally repressive state at the leading edge of the cell. Without Mnk1/2 kinase activity, DDX3X is no-longer available at the leading edge to participate in the unwinding of mRNAs with more complex secondary structures such as WAVE1, ArpC2 and β-actin. Building on this theory, recently, it has been shown that inhibition of Mnk1/2 inhibits migration in other human cells (Beggs et al, 2015). In neurones, CYFIP1 complexes are known to have a function in synaptic protein synthesis and actin polymerisation and protein-phosphatase2A-mediated dephosphorylation of Ser499 on FMRP is required for localised protein synthesis (Narayanan,

Nalavadi, Nakamoto, Thomas, Ceman, Gary J. Bassell, et al. 2008). Activated Rac1/GTP reshapes the CYFIP1-eIF4E complex *via a* conformational change in CYFIP1, freeing CYFIP1 from the repressive complex, and allowing it to become a component in the upregulation of actin polymerisation *via* the WRC (DeRubeis et al. 2013). It remains a hypothesis then, that inhibition of Mnk1/2 signalling may be affecting the conformational change necessary in CYFIP1 to allow the release of eIF4E for eIF4F complex formation on target mRNAs at the leading edge of the cell.

8.6 A model of fibroblast spreading.

Based on the data presented in this thesis, Figure 8.1 shows a possible model for how localised translation may be modulated by DDX3X. The helicase binds to the dorsal surface of the eIF4E associated with the mRNA cap of some structurally complex RNAs whilst in the nucleus. This facilitates mRNA export to the cytoplasm *via* CRM1 (Snay-Hodge et al. 1998), whilst keeping eIF4E in a translationally repressed state (Shih et al. 2008). Once in the cytoplasm, the DDX3X:eIF4E complex traverses F-actin towards the cell membrane. At the leading edge of the cell, Mnk1/2 phosphorylates DDX3X causing it to be released, and allowing eIF4E to form the eIF4F complex (Lai et al. 2008; Lai et al. 2010; Soto-Rifo et al. 2012) to drive localised synthesis of actin, ArpC2 and WAVE1 proteins. The mRNAs encoding such proteins are delivered to the leading edge in a translationally repressed state within the CYFP1:FMRP:eIF4E complex. It is possible that in a co-ordinated way, Mnk1/2 also phosphorylates CYFIP1 to facilitate a change in conformation to allow WAVE complex formation and release the translation inhibition of target mRNAs. It is suggested that DDX3X facilitates the unwinding of the complex ternary RNA structures or removes obstructive proteins from the RNA to allow translation. Highly stable multiple stem-loops can confound the already low processivity of the eIF4A helicase (Pause et al. 1994) and additional helicases such as DDX3X are required to remodel the 40S ribosome/mRNA complex (Pickering & Willis 2005; Parsyan et al. 2009). DDX3X has been shown to associate with the 5’ terminus of mRNA (Hilliker et al. 2011). This can occur *via* direct binding as well as indirect binding with RNA *via* eIF4F, helped by

interactions with eIF4G and PABP (Soto-Rifo et al. 2012). Once at the 5' terminus, DDX3X may facilitate the entry and binding of the 43S ribosomal unit to the ArpC2 and WAVE1 mRNAs by destabilising complex local mRNA structures. This then, may facilitate gross unwinding of the structure by eIF4A, leaving the mRNA available for scanning and subsequent translation. Such a model would be consistent with the findings that decreased levels of DDX3X in DDX3X knockdown cell spreading assays, appear to leave cells smaller and more rounded and solid than their parental (wild type) counterparts (Chapter 6). These data suggest that DDX3X may have a role in facilitating cytoskeletal rearrangement required for the cellular spreading process. These data also suggest that DDX3X may facilitate cellular polarisation and general podial growth, meaning that DDX3X could be playing a part in migratory processes including metastasis disease.

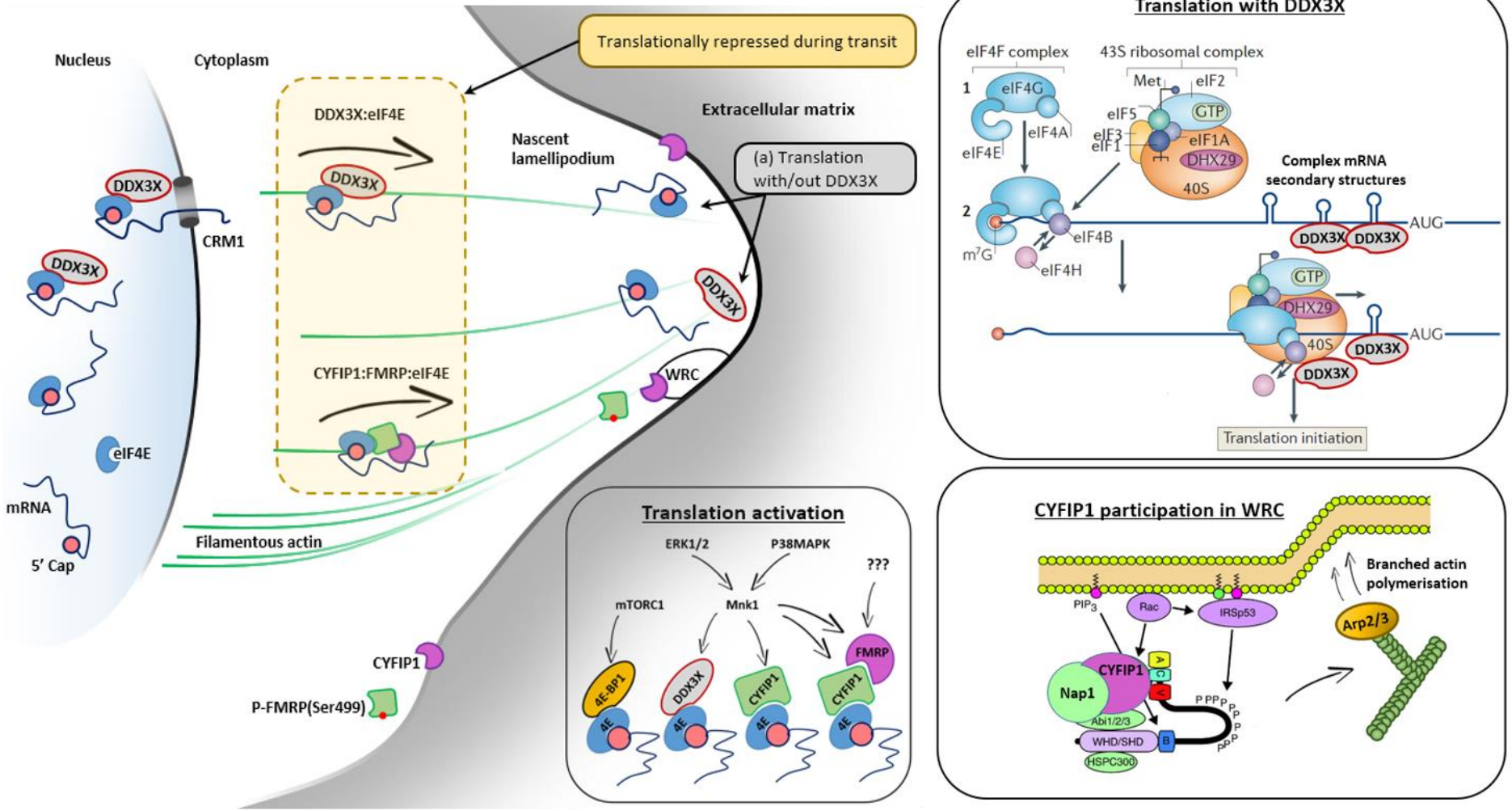
Nucleus
Cytoplasm
Translationally repressed during transit
Extracellular matrix
DDX3X:eIF4E
Nascent lamellipodium
(a) Translation with/out DDX3X
DDX3X
CRM1
eIF4E
mRNA
5' Cap
CYFIP1:FMRP:eIF4E
WRC
Filamentous actin
CYFIP1
P-FMRP(Ser499)
Translation with DDX3X
eIF4F complex
43S ribosomal complex
eIF4G
eIF4A
eIF4E
Met
eIF2
GTP
eIF5
eIF3
eIF1
eIF1A
DHX29
40S
Complex mRNA secondary structures
eIF4B
eIF4H
m7G
AUG
Translation initiation
Translation activation
ERK1/2
P38MAPK
???
mTORC1
Mnk1
FMRP
4E-BP1
CYFIP1
4E
CYFIP1 participation in WRC
Branched actin polymerisation
PIP3
Rac
IRSp53
Arp2/3
Nap1
Abi1/2/3
WHD/SHD
HSPC300

Figure 8.1 DDX3X, FMRP and CYFIP1 participate in the transport and translation of mRNA within nascent lamellipodia

Transport of mRNA to the leading edge of the cell
DDX3X localises to the nuclear pore upon binding CRM1. A suggested mechanism of action is that DDX3X facilitates the unwinding of the complex ternary RNA structures or removes obstructive proteins from the RNA to allow it passage to the cytoplasm (Snay-Hodge et al. 1998). Once in the cytoplasm DDX3X traps eIF4E in a translationally inactive complex as the RNP transits towards the leading edge of the cell.
The transport of β-actin, ArpC2 and WAVE1 mRNA to the leading edge of the cell is performed by the translationally repressive complex of the eIF4E:FMRP:CYFIP1 complex, serving to transport and simultaneously translationally repress mRNA with complex secondary structures, such as β-actin, ArpC2 and WAVE1, until the RNP arrives at the leading edge of the cell.

Promotion of translation at the leading edge of the cell.
At the leading edge of the cell, dephosphorylation of p-FMRP(Ser499) serves to promotes the release of mRNA making them available for translation. Upon arrival of the DDX3X:eIF4E RNP, DDX3X releases eIF4E allowing it to form the eIF4F complex (Lai et al. 2008; Lai et al. 2010; Soto-Rifo et al. 2012) and drive localised synthesis of β-actin, ArpC2 and WAVE1 proteins. Now free from an RNP, CYFIP1 becomes available for participation in, and activation of the WAVE regulatory complex. This facilitates the polymerisation of branched actin and the eventual protrusion of lamellipodia.

Diagrams on the right-hand side of this figure are adapted from [top] Parsyan et al., 2011 [bottom] Leszek Kotula, FEBS Letters, 586:17, August 2012.

9 References

Akhdar, O. et al., 2009. A new CLEAN algorithm for angle of arrival denoising. *IEEE Antennas and Wireless Propagation Letters*, 8, pp.478–481.

Altman, J.K. et al., 2013. Inhibition of Mnk kinase activity by cercosporamide and suppressive effects on acute myeloid leukemia precursors. *Blood*, 121(18), pp.3675–81. Available at: http://www.pubmedcentral.nih.gov/articlerender.fcgi?artid=3643766&tool=pmcentrez&rendertype=abstract [Accessed February 29, 2016].

Ambrose, E.J., 1956. A Surface Contact Microscope for the study of Cell Movements. *Nature*, 178(4543), pp.1194–1194.

Anitei, M. et al., 2010. Protein complexes containing CYFIP/Sra/PIR121 coordinate Arf1 and Rac1 signalling during clathrin-AP-1-coated carrier biogenesis at the TGN. *Nature cell biology*, 12(4), pp.330–340. Available at: http://dx.doi.org/10.1038/ncb2034.

Aravind, L. & Koonin, E. V, 2000. Eukaryote-specific domains in translation initiation factors: implications for translation regulation and evolution of the translation system. *Genome research*, 10(8), pp.1172–84. Available at: http://www.ncbi.nlm.nih.gov/pubmed/10958635 [Accessed September 28, 2016].

Axelrod, D., 1981. Cell-substrate contacts illuminated by total internal reflection fluorescence. *Journal of Cell Biology*, 89(1), pp.141–145.

Axelrod, D., 2008. Total Internal Reflection Fluorescence Microscopy. *Biophysical Tools for Biologists, Vol 2: In Vivo Techniques*, 89, pp.169–221.

Babbage, C., 1864. Passages from the Life of a Philosopher. *Search*, p.67. Available at: http://books.google.com/books?hl=en&lr=&id=Nr9UbN4JTxYC&oi=fnd&pg=PA1&dq=Passages+from+the+Life+of+a+Philosopher&ots=bAL3LwHBzS&sig=bzQVYMHMGRBwcqy3kDvnUnGtOSA.

Bagni, C. & Greenough, W.T., 2005. From mRNP trafficking to spine dysmorphogenesis: the roots of fragile X syndrome. *Nature reviews. Neuroscience*, 6(5), pp.376–387.

Bagni, C. & Oostra, B.A., 2013. Fragile X syndrome: From protein function to therapy. *American Journal of Medical Genetics, Part A*, 161(11), pp.2809–2821.

Bain, J. et al., 2007. The selectivity of protein kinase inhibitors: a further update. *Biochemical Journal*, 408(3), pp.297–315. Available at: http://biochemj.org/lookup/doi/10.1042/BJ20070797.

Bandi, H.R. et al., 1993. Identification of 40 S ribosomal protein S6 phosphorylation sites in Swiss mouse 3T3 fibroblasts stimulated with serum. *The Journal of biological chemistry*, 268(6), pp.4530–3. Available at: http://www.ncbi.nlm.nih.gov/pubmed/8440735 [Accessed September 25, 2016].

Bardoni, B., Schenck, a & Mandel, J.L., 2001. The Fragile X mental retardation protein. *Brain research bulletin*, 56(1), pp.375–82. Available at: http://www.ncbi.nlm.nih.gov/pubmed/12837692.

Bartley, C.M., O'Keefe, R. a. & Bordey, A., 2014. FMRP S499 is phosphorylated independent of mTORC1-S6K1 activity. *PLoS ONE*, 9(5).

Bates, M., Jones, S. a. & Zhuang, X., 2013. Stochastic optical reconstruction microscopy (STORM): A method for superresolution fluorescence imaging. *Cold Spring Harbor Protocols*, 8(6), pp.498–520.

Beggs, J.E. et al., 2015. The MAP kinase-interacting kinases regulate cell migration, vimentin expression and eIF4E/CYFIP1 binding. *The Biochemical journal*, (JANUARY). Available at: http://www.ncbi.nlm.nih.gov/pubmed/25588502.

Besse, F. & Ephrussi, A., 2008. Translational control of localized mRNAs: restricting protein synthesis in space and time. *Nature reviews. Molecular cell biology*, 9(12), pp.971–980.

Betzig, E. et al., 2006. Imaging intracellular fluorescent proteins at nanometer resolution. *Science (New York, N.Y.)*, 313(5793), pp.1642–1645.

Bolte, S. & Cordelieres, F.P., 2006. A guided tour into subcellular colocalisation analysis in light microscopy. *Journal of Microscopy*, 224(3), pp.13–232.

Borel, W. & Jansen, H., 2009. Microscopy Milestones: Stains and fluorescent

dyes. *Nature Cell Biology*, 11, pp.S6–S22. Available at: All Papers/B/Borel and Jansen 2009 - Stains and fluorescent dyes.pdf.

Botlagunta, M. et al., 2008. Oncogenic role of DDX3 in breast cancer biogenesis. *Oncogene*, 27(28), pp.3912–3922. Available at: http://www.nature.com/onc/journal/v27/n28/full/onc200833a.html%5Cnhttp://www.nature.com/onc/journal/v27/n28/pdf/onc200833a.pdf.

Bramham, C.R., Jensen, K.B. & Proud, C.G., 2016. Tuning Specific Translation in Cancer Metastasis and Synaptic Memory: Control at the MNK–eIF4E Axis. *Trends in Biochemical Sciences*, xx, pp.1–12. Available at: http://linkinghub.elsevier.com/retrieve/pii/S0968000416300950.

Brown, T. a. et al., 2011. Superresolution Fluorescence Imaging of Mitochondrial Nucleoids Reveals Their Spatial Range, Limits, and Membrane Interaction. *Molecular and Cellular Biology*, 31(24), pp.4994–5010.

Bryce, N.S. et al., 2005. Cortactin promotes cell motility by enhancing lamellipodial persistence. *Current biology : CB*, 15(14), pp.1276–85. Available at: http://www.ncbi.nlm.nih.gov/pubmed/16051170 [Accessed September 29, 2016].

Burkhard, S.J. & Traugh, J.A., 1983. Changes in ribosome function by cAMP-dependent and cAMP-independent phosphorylation of ribosomal protein S6. *The Journal of biological chemistry*, 258(22), pp.14003–8. Available at: http://www.ncbi.nlm.nih.gov/pubmed/6643464 [Accessed September 25, 2016].

Bushman, F.D. et al., 2009. Host cell factors in HIV replication: meta-analysis of genome-wide studies. *PLoS Pathogens*, 5(5), p.e1000437.

Cannell, M., McMorland, a & Soeller, C., 2006. Image enhancement by deconvolution. *Handbook of biological confocal …*, pp.488–500. Available at: http://link.springer.com/chapter/10.1007/978-0-387-45524-2_25.

Ceman, S. et al., 2003. Phosphorylation influences the translation state of FMRP-associated polyribosomes. *Human Molecular Genetics*, 12(24), pp.3295–3305.

Chaffer, C.L. & Weinberg, R.A., 2011. A perspective on cancer cell metastasis. *Science (New York, N.Y.)*, 331(6024), pp.1559–64. Available at: http://www.ncbi.nlm.nih.gov/pubmed/21436443 [Accessed September 29,

2016].

Chao, C.H. et al., 2006. DDX3, a DEAD box RNA helicase with tumor growth-suppressive property and transcriptional regulation activity of the p21waf1/cip1 promoter, is a candidate tumor suppressor. *Cancer Research*, 66(13), pp.6579–6588.

Chen, Z. et al., 2010. Structure and control of the actin regulatory WAVE complex. *Nature*, 468(7323), pp.533–538. Available at: http://dx.doi.org/10.1038/nature09623.

Choo, A.Y. et al., 2008. Rapamycin differentially inhibits S6Ks and 4E-BP1 to mediate cell-type-specific repression of mRNA translation. *Proceedings of the National Academy of Sciences of the United States of America*, 105(45), pp.17414–17419.

Chrestensen, C.A. et al., 2007. MNK1 and MNK2 regulation in HER2-overexpressing breast cancer lines. *Journal of Biological Chemistry*, 282(7), pp.4243–4252.

Chuang, R.-Y. et al., 1997. Requirement of the DEAD-Box protein ded1p for messenger RNA translation. *Science*, 275(5305), pp.1468–1471.

Clausson, C.-M. et al., 2015. Compaction of rolling circle amplification products increases signal integrity and signal-to-noise ratio. *Scientific reports*, 5(July), p.12317. Available at: http://www.nature.com/srep/2015/150723/srep12317/full/srep12317.html.

Clegg, R.M., 1995. Fluorescence resonance energy transfer. *Current Opinion in Biotechnology*, 6(1), pp.103–110.

Cook, K.B. et al., 2011. RBPDB: a database of RNA-binding specificities. *Nucleic acids research*, 39(Database issue), pp.D301-8. Available at: http://nar.oxfordjournals.org/content/early/2010/10/28/nar.gkq1069.abstract [Accessed February 10, 2016].

Coons, A.H., 1961. The beginnings of immunofluorescence. *Journal of immunology (Baltimore, Md. : 1950)*, 87(5), pp.499–503. Available at: http://www.jimmunol.org/content/87/5/499.abstract [Accessed February 10, 2016].

Cope, C.L. et al., 2014. Adaptation to mTOR kinase inhibitors by amplification of eIF4E to maintain cap-dependent translation. *Journal of cell science*, 127(Pt 4), pp.788–800. Available at:

http://www.ncbi.nlm.nih.gov/pubmed/24363449.

Cornwell, T.J., 2008. Multiscale CLEAN deconvolution of radio synthesis images. *IEEE Journal on Selected Topics in Signal Processing*, 2(5), pp.793–801.

Cory, G.O.C. et al., 2003. Phosphorylation of the WASP-VCA domain increases its affinity for the Arp2/3 complex and enhances actin polymerization by WASP. *Molecular Cell*, 11(5), pp.1229–1239.

Costes, S. V et al., 2004. Automatic and quantitative measurement of protein-protein colocalization in live cells. *Biophysical journal*, 86(6), pp.3993–4003.

Cox, S. et al., 2012. UKPMC Funders Group Bayesian localisation microscopy reveals nanoscale podosome dynamics. , 9(2), pp.195–200.

Cox, S. & Jones, G.E., 2013. Imaging cells at the nanoscale. *International Journal of Biochemistry and Cell Biology*, 45(8), pp.1669–1678. Available at: http://dx.doi.org/10.1016/j.biocel.2013.05.010.

Crick, F., 1970. Central Dogma of Molecular Biology. *Nature*, 227(5258), pp.561–563. Available at: http://www.nature.com/nature/journal/v227/n5258/abs/227561a0.html.

Cullen, B.R., 2000. Nuclear RNA export pathways. *Molecular and Cellular Biology*, 20(12), pp.4181–4187.

David, A. et al., 2012. Nuclear translation visualized by ribosome-bound nascent chain puromycylation. *Journal of Cell Biology*, 197(1), pp.45–57.

David, A. et al., 2011. RNA binding targets aminoacyl-tRNA synthetases to translating ribosomes. *Journal of Biological Chemistry*, 286(23), pp.20688–20700.

David, A., Bennink, J.R. & Yewdell, J.W., 2013. Emetine optimally facilitates nascent chain puromycylation and potentiates the ribopuromycylation method (RPM) applied to inert cells. *Histochemistry and Cell Biology*, 139(3), pp.501–504. Available at: http://www.pubmedcentral.nih.gov/articlerender.fcgi?artid=3574230&tool=pmcentrez&rendertype=abstract [Accessed April 23, 2015].

Davis, P.K., Ho, A. & Dowdy, S.F., 2001. Biological methods for cell-cycle synchronization of mammalian cells. *BioTechniques*, 30(6), pp.1322–1331.

DeMali, K. a., Wennerberg, K. & Burridge, K., 2003. Integrin signaling to the

actin cytoskeleton. *Current Opinion in Cell Biology*, 15(5), pp.572–582.

Dertinger, T. et al., 2009. Fast, background-free, 3D super-resolution optical fluctuation imaging (SOFI). *Proceedings of the National Academy of Sciences of the United States of America*, 106(52), pp.22287–22292.

Dertinger, T. & Heilemann, M., 2010. Superresolution optical fluctuation imaging with organic dyes. *Angewandte …*, 49(49), pp.9441–9443. Available at: http://onlinelibrary.wiley.com/doi/10.1002/ange.201004138/full.

DeRubeis, S. et al., 2013. CYFIP1 coordinates mRNA translation and cytoskeleton remodeling to ensure proper dendritic Spine formation. *Neuron*, 79(6), pp.1169–1182.

Deschout, H. et al., 2014. Precisely and accurately localizing single emitters in fluorescence microscopy. *Nature Methods*, 11(3), pp.253–266. Available at: http://www.nature.com/doifinder/10.1038/nmeth.2843 [Accessed September 26, 2016].

Diab, S. et al., 2014. MAP kinase-interacting kinases - Emerging targets against cancer. *Chemistry and Biology*, 21(4), pp.441–452. Available at: http://dx.doi.org/10.1016/j.chembiol.2014.01.011.

Donnelly, C.J., Fainzilber, M. & Twiss, J.L., 2010. Subcellular Communication Through RNA Transport and Localized Protein Synthesis. *Traffic*, 11(12), pp.1498–1505.

Driscoll, 1975. *Learning MATLAB*, Available at: http://epubs.siam.org/doi/abs/10.1137/1017068.

Dunn, K.W., Kamocka, M.M. & McDonald, J.H., 2011. A practical guide to evaluating colocalization in biological microscopy. *American journal of physiology. Cell physiology*, 300(4), pp.C723–C742.

Eden, S. et al., 2002. Mechanism of regulation of WAVE1-induced actin nucleation by Rac1 and Nck. *Nature*, 418(6899), pp.790–3. Available at: http://www.ncbi.nlm.nih.gov/pubmed/12181570 [Accessed September 29, 2016].

Eliceiri, K.W. et al., 2012. Biological imaging software tools. *Nature Methods*, 9(7), pp.697–710.

Ellinger, P. & Hirt, A., 1929. Mikroskopische Beobachtungen an lebenden Organen mit Demonstrationen (Intravitalmikroskopie). *Archiv für Experimentelle Pathologie und Pharmakologie*, 147(1–3), pp.63–63.

Available at: http://link.springer.com/10.1007/BF01946036 [Accessed February 10, 2016].

Erickson, F.L. & Hannig, E.M., 1996. Ligand interactions with eukaryotic translation initiation factor 2: role of the gamma-subunit. *The EMBO journal*, 15(22), pp.6311–6320.

Fabian, M.R., Sonenberg, N. & Filipowicz, W., 2010. Regulation of mRNA translation and stability by microRNAs. *Annual review of biochemistry*, 79, pp.351–379.

Fallis, A.., 2013. Python for data analysis. *Journal of Chemical Information and Modeling*, 53(9), pp.1689–1699. Available at: http://it-ebooks.info/book/1041/%5Cnpapers3://publication/uuid/4DB3AB3B-524B-49D1-A3AC-784734442303.

Feldman, M.E. et al., 2009. Active-site inhibitors of mTOR target rapamycin-resistant outputs of mTORC1 and mTORC2. *PLoS Biology*, 7(2), pp.0371–0383.

Floor, S.N. et al., 2016. Autoinhibitory interdomain interactions and subfamilyspecific extensions redefine the catalytic core of the human DEAD-box protein DDX3. *Journal of Biological Chemistry*, 291(5), pp.2412–2421.

Fornerod, M. et al., 1997. CRM1 is an export receptor for leucine-rich nuclear export signals. *Cell*, 90(6), pp.1051–1060.

Fox, M.H., 2004. Methods for synchronizing mammalian cells. *Methods in molecular biology (Clifton, N.J.)*, 241(6), pp.11–16.

Frantz, E.D.C. et al., 2013. Renin-Angiotensin System Blockers Protect Pancreatic Islets against Diet-Induced Obesity and Insulin Resistance in Mice. *PLoS ONE*, 8(7).

Fresnel, A., 1816. No Title. *Ann. Chem. Phys.*, 1, p.239.

Fresnel, A., 1826. No Title. *Mem. Acad.*, 5, p.339.

Furic, L. et al., 2010. eIF4E phosphorylation promotes tumorigenesis and is associated with prostate cancer progression. *Proceedings of the National Academy of Sciences of the United States of America*, 107(32), pp.14134–9. Available at: http://www.pubmedcentral.nih.gov/articlerender.fcgi?artid=2922605&tool=pmcentrez&rendertype=abstract.

Garcia-Garcia, C. et al., 2015. Factor-dependent processivity in human eIF4A DEAD-box helicase. *Science*, 348(6242), pp.1486–1488. Available at: http://www.sciencemag.org/cgi/doi/10.1126/science.aaa5089.

Ghosh, M. et al., 2004. Cofilin promotes actin polymerization and defines the direction of cell motility. *Science (New York, N.Y.)*, 304(5671), pp.743–6. Available at: http://www.ncbi.nlm.nih.gov/pubmed/15118165 [Accessed September 29, 2016].

Gingras, A.C. et al., 1999. Regulation of 4E-BP1 phosphorylation: A novel two step mechanism. *Genes and Development*, 13(11), pp.1422–1437.

Gingras, a. C., Raught, B. & Sonenberg, N., 2001. Regulation of translation initiation by FRAP/mTOR. *Genes and Development*, 15(7), pp.807–826.

Good, M.C., 2015. Turn Up the Volume: Uncovering Nucleus Size Control Mechanisms. *Developmental Cell*, 33(5), pp.496–497. Available at: http://www.sciencedirect.com/science/article/pii/S1534580715003512.

Goyer, C. et al., 1993. TIF4631 and TIF4632: two yeast genes encoding the high-molecular-weight subunits of the cap-binding protein complex (eukaryotic initiation factor 4F) contain an RNA recognition motif-like sequence and carry out an essential function. *Molecular and cellular biology*, 13(8), pp.4860–74. Available at: http://www.ncbi.nlm.nih.gov/pubmed/8336723 [Accessed September 28, 2016].

Grzmil, M. et al., 2011. MAP kinase-interacting kinase 1 regulates SMAD2-dependent TGF-?? signaling pathway in human glioblastoma. *Cancer Research*, 71(6), pp.2392–2402.

Haghighat, A. & Sonenberg, N., 1997. eIF4g dramatically enhances the binding of eIF4E to the mRNA 5'-cap structure. *Journal of Biological Chemistry*, 272(35), pp.21677–21680.

Hannan, E.J., 1978. A NOTE ON A CENTRAL LIMIT THEOREM. *Econometrica*, 46(2), pp.451–453. Available at: http://search.ebscohost.com/login.aspx?direct=true&db=bth&AN=6857704&site=ehost-live&scope=site.

Heimstädt, O., 1911. Das Fluoreszenzmikroskop. *Z. Wiss. Mikrosk.*, (28), pp.330–337.

Henriques, R. et al., 2011. PALM and STORM: Unlocking live-cell super-

resolution. *Biopolymers*, 95(5), pp.322–331.

Henriques, R. et al., 2010. QuickPALM: 3D real-time photoactivation nanoscopy image processing in ImageJ. *Nature methods*, 7(5), pp.339–340. Available at: http://dx.doi.org/10.1038/nmeth0510-339.

Herbert, A.D. et al., 2014. FindFoci: A focus detection algorithm with automated parameter training that closely matches human assignments, reduces human inconsistencies and increases speed of analysis. *PLoS ONE*, 9(12), pp.1–33.

Hilliker, A. et al., 2011. The DEAD-Box Protein Ded1 Modulates Translation by the Formation and Resolution of an eIF4F-mRNA Complex. *Molecular Cell*, 43(6), pp.962–972. Available at: http://dx.doi.org/10.1016/j.molcel.2011.08.008.

Hintze, J.L.N.R.D., 1988. Violin Plots: A Box Plot-Density Trace Synergism. , p.Vol. 52, No.2. 181-184.

Hooke, R., 1665. Micrographia: or, Some Physiological Descriptions of Minute Bodies Made by Magnifying Glasses with Observations and Inquiries Thereupon. *Royal Society*. Available at: http://selfdefinition.org/science/25-greatest-science-books-of-all-time/24. Robert Hooke - Micrographia (1665).pdf [Accessed January 27, 2016].

Hou, J. et al., 2012. Targeting Mnks for cancer therapy. *Oncotarget*, 3(2), pp.118–131. Available at: http://www.impactjournals.com/oncotarget/index.php?journal=oncotarget&page=article&op=view&path%5B%5D=453&path%5B%5D=766.

Hsieh, A.C. et al., 2012. The translational landscape of mTOR signalling steers cancer initiation and metastasis. *Nature*, 485(7396), pp.55–61. Available at: http://dx.doi.org/10.1038/nature10912.

Hu, Y.S. et al., 2013. Accelerating 3B single-molecule super-resolution microscopy with cloud computing. *Nature methods*, 10(2), pp.96–7. Available at: http://www.ncbi.nlm.nih.gov/pubmed/23361087.

Huang, B., Babcock, H. & Zhuang, X., 2010. Breaking the diffraction barrier: Super-resolution imaging of cells. *Cell*, 143(7), pp.1047–1058. Available at: http://dx.doi.org/10.1016/j.cell.2010.12.002.

Huang, C.-L. et al., 2006. MRP-1/CD9 gene transduction regulates the actin cytoskeleton through the downregulation of WAVE2. *Oncogene*, 25(49),

pp.6480–8. Available at: http://www.ncbi.nlm.nih.gov/pubmed/16682943 [Accessed September 29, 2016].

Huang, Y. & Steitz, J.A., 2005. SRprises along a Messenger's Journey. *Molecular Cell*, 17(5), pp.613–615. Available at: http://linkinghub.elsevier.com/retrieve/pii/S1097276505011196.

Hunter, J.D., 2007. Matplotlib: A 2D graphics environment. *Computing in Science and Engineering*, 9(3), pp.99–104.

Huschtscha, L.I. & Holliday, R., 1983. Limited and unlimited growth of SV40-transformed cells from human diploid MRC-5 fibroblasts. *Journal of cell science*, 63, pp.77–99. Available at: http://www.ncbi.nlm.nih.gov/pubmed/6313714 [Accessed January 14, 2016].

Huttenlocher, A. & Horwitz, A.R., 2011. Integrins in cell migration. *Cold Spring Harbor perspectives in biology*, 3(9), p.a005074. Available at: http://www.ncbi.nlm.nih.gov/pubmed/21885598 [Accessed September 29, 2016].

Huygens, C., 1690. *Trait´e de la Lumiere*, Leyden.

Imataka, H., Gradi, A. & Sonenberg, N., 1998. A newly identified N-terminal amino acid sequence of human eIF4G binds poly(A)-binding protein and functions in poly(A)-dependent translation. *The EMBO journal*, 17(24), pp.7480–9. Available at: http://www.ncbi.nlm.nih.gov/pubmed/9857202 [Accessed September 28, 2016].

Imataka, H. & Sonenberg, N., 1997. Human eukaryotic translation initiation factor 4G (eIF4G) possesses two separate and independent binding sites for eIF4A. *Molecular and cellular biology*, 17(12), pp.6940–7. Available at: http://www.pubmedcentral.nih.gov/articlerender.fcgi?artid=232551&tool=pmcentrez&rendertype=abstract.

Jackson, R.J., Hellen, C.U.T. & Pestova, T. V, 2010. The mechanism of eukaryotic translation initiation and principles of its regulation. *Nature reviews. Molecular cell biology*, 11(2), pp.113–127. Available at: http://dx.doi.org/10.1038/nrm2838.

Jankowsky, E., 2011. RNA helicases at work: Binding and rearranging. *Trends in Biochemical Sciences*, 36(1), pp.19–29.

Jiang, L. et al., 2015. Exome sequencing identifies somatic mutations of DDX3X

in natural killer/T-cell lymphoma. *Nature Genetics*, 47(9), pp.1061–1066. Available at: http://www.nature.com/doifinder/10.1038/ng.3358.

Jones, E. et al., 2001. SciPy.org. *SciPy: Open source scientific tools for Python2*. Available at: https://www.scipy.org/.

Joshi, B., Cameron, A. & Jagus, R., 2004. Characterization of mammalian eIF4E-family members. *European Journal of Biochemistry*, 271(11), pp.2189–2203.

Joshi, S., 2014. Mnk kinase pathway: Cellular functions and biological outcomes. *World Journal of Biological Chemistry*, 5(3), p.321. Available at: http://www.wjgnet.com/1949-8454/full/v5/i3/321.htm.

Jung, H., O'Hare, C.M. & Holt, C.E., 2011. Translational regulation in growth cones. *Current opinion in genetics & development*, 21(4), pp.458–64. Available at: http://www.pubmedcentral.nih.gov/articlerender.fcgi?artid=3683644&tool=pmcentrez&rendertype=abstract [Accessed February 19, 2016].

Keene, J.D. & Tenenbaum, S.A., 2002. Eukaryotic mRNPs may represent posttranscriptional operons. *Molecular Cell*, 9(6), pp.1161–1167.

Kerppola, T.K., 2009. Visualization of Molecular Interactions Using Analysis : Characteristics of Protein Fragment Complementation. *Chemical Society reviews*, 38(10), pp.2876–2886.

Khaleghpour, K. et al., 1999. Translational homeostasis: eukaryotic translation initiation factor 4E control of 4E-binding protein 1 and p70 S6 kinase activities. *Mol Cell Biol*, 19(6), pp.4302–4310. Available at: http://www.ncbi.nlm.nih.gov/cgi-bin/Entrez/referer?http://mcb.asm.org/cgi/content/full/19/6/4302.

Kimball, S.R., 1999. Eukaryotic initiation factor eIF2. *The International Journal of Biochemistry & Cell Biology*, 31(1), pp.25–29. Available at: http://www.sciencedirect.com/science/article/pii/S1357272598001289.

Klar, T. a, Engel, E. & Hell, S.W., 2001. Breaking Abbe's diffraction resolution limit in fluorescence microscopy with stimulated emission depletion beams of various shapes. *Physical review. E, Statistical, nonlinear, and soft matter physics*, 64(6 Pt 2), p.66613.

Konicek, B.W. et al., 2011. Therapeutic inhibition of MAP kinase interacting kinase blocks eukaryotic initiation factor 4E phosphorylation and

suppresses outgrowth of experimental lung metastases. *Cancer Research*, 71(5), pp.1849–1857.

Koos, B. & Söderberg, O., 2015. Closing in on life: proximity dependent methods for life sciences. *Oncotarget*, 6(20), pp.17867–8. Available at: http://www.pubmedcentral.nih.gov/articlerender.fcgi?artid=4627219&tool=pmcentrez&rendertype=abstract.

Krishnaswami, V. et al., 2014. Towards digital photon counting cameras for single-molecule optical nanoscopy. *Optical Nanoscopy*, 3(1), p.1. Available at: http://www.optnano.com/content/3/1/1/abstract.

Kudo, N. et al., 1999. Leptomycin B inactivates CRM1/exportin 1 by covalent modification at a cysteine residue in the central conserved region. *Proceedings of the National Academy of Sciences of the United States of America*, 96(16), pp.9112–7. Available at: http://www.pubmedcentral.nih.gov/articlerender.fcgi?artid=17741&tool=pmcentrez&rendertype=abstract.

Kurisu, S. & Takenawa, T., 2009. The WASP and WAVE family proteins. *Genome biology*, 10(6), p.226.

Kurisu, S. & Takenawa, T., 2010. WASP and WAVE family proteins: Friends or foes in cancer invasion? *Cancer Science*, 101(10), pp.2093–2104.

Labi, V. & Erlacher, M., 2015. How cell death shapes cancer. *Cell death & disease*, 6(3), p.e1675. Available at: http://www.ncbi.nlm.nih.gov/pubmed/25741600.

Lai, M.-C. et al., 2010. DDX3 regulates cell growth through translational control of cyclin E1. *Molecular and cellular biology*, 30(22), pp.5444–53. Available at: http://www.pubmedcentral.nih.gov/articlerender.fcgi?artid=2976371&tool=pmcentrez&rendertype=abstract.

Lai, M.-C., Lee, Y.-H.W. & Tarn, W.-Y., 2008. The DEAD-box RNA helicase DDX3 associates with export messenger ribonucleoproteins as well as tip-associated protein and participates in translational control. *Molecular biology of the cell*, 19(9), pp.3847–3858. Available at: http://eutils.ncbi.nlm.nih.gov/entrez/eutils/elink.fcgi?dbfrom=pubmed&id=18596238&retmode=ref&cmd=prlinks%5Cnpapers2://publication/doi/10.1091/mbc.E07-12-1264.

Lai, M.C. et al., 2013. Human DDX3 Interacts with the HIV-1 Tat Protein to Facilitate Viral mRNA Translation. *PLoS ONE*, 8(7), pp.1–14.

Lamouille, S., Xu, J. & Derynck, R., 2014. Molecular mechanisms of epithelial-mesenchymal transition. *Nature reviews. Molecular cell biology*, 15(3), pp.178–96. Available at: http://www.pubmedcentral.nih.gov/articlerender.fcgi?artid=4240281&tool=pmcentrez&rendertype=abstract.

Lamphear, B.J. et al., 1995. Mapping of functional domains in eukaryotic protein synthesis initiation factor 4G (eIF4G) with picornaviral proteases. Implications for Cap-dependent and Cap-independent translational initiation. *Journal of Biological Chemistry*, 270(37), pp.21975–21983.

Lamphear, J.B. & Panniers, R., 1989. Cap Binding Protein Complex That Restores Protein Synthesis in Heat-shocked Ehrlich Cell Lysates Contains Highly Phosphorylated eIF-4E. *The Journal of Biological Chemistry*, 265(10), pp.5333–5337.

Lamprecht, M.R., Sabatini, D.M. & Carpenter, A.E., 2007. CellProfiler: Free, versatile software for automated biological image analysis. *BioTechniques*, 42(1), pp.71–75.

Laplante, M. & Sabatini, D.M., 2013a. mTOR signaling in growth control and disease. *Cell*, 149(2), pp.274–293. Available at: http://dx.doi.org/10.1016/j.cell.2012.03.017.

Laplante, M. & Sabatini, D.M., 2012. MTOR signaling in growth control and disease. *Cell*, 149(2), pp.274–293. Available at: http://dx.doi.org/10.1016/j.cell.2012.03.017.

Laplante, M. & Sabatini, D.M., 2013b. Regulation of mTORC1 and its impact on gene expression at a glance. *Journal of cell science*, 126(Pt 8), pp.1713–1719. Available at: http://www.ncbi.nlm.nih.gov/pubmed/23641065.

Lardone, M.C. et al., 2007. Quantification of DDX3Y, RBMY1, DAZ and TSPY mRNAs in testes of patients with severe impairment of spermatogenesis. *Molecular Human Reproduction*, 13(10), pp.705–712.

Lasko, P. et al., 2005. Contrasting mechanisms of regulating translation of specific Drosophila germline mRNAs at the level of 5'-cap structure binding. *Biochemical Society transactions*, 33(Pt 6), pp.1544–6. Available at: http://www.ncbi.nlm.nih.gov/pubmed/16246166.

Lebensohn, A.M. & Kirschner, M.W., 2009. Activation of the WAVE complex by coincident signals controls actin assembly. *Molecular cell*, 36(3), pp.512–24. Available at: http://www.ncbi.nlm.nih.gov/pubmed/19917258 [Accessed September 29, 2016].

Lemke, J. et al., 2014. Getting TRAIL back on track for cancer therapy. *Cell death and differentiation*, 21(9), pp.1350–64. Available at: http://dx.doi.org/10.1038/cdd.2014.81.

Leuchowius, K.-J. et al., 2013. Parallel visualization of multiple protein complexes in individual cells in tumor tissue. *Molecular & cellular proteomics : MCP*, 12(6), pp.1563–71. Available at: http://www.pubmedcentral.nih.gov/articlerender.fcgi?artid=3675814&tool=pmcentrez&rendertype=abstract.

Li, Q. et al., 2014. DDX3X regulates cell survival and cell cycle during mouse early embryonic development. *Journal of biomedical research*, 28(4), pp.282–91. Available at: http://www.pubmedcentral.nih.gov/articlerender.fcgi?artid=4102842&tool=pmcentrez&rendertype=abstract.

Lorent, J.H., Quetin-Leclercq, J. & Mingeot-Leclercq, M.-P., 2014. The amphiphilic nature of saponins and their effects on artificial and biological membranes and potential consequences for red blood and cancer cells. *Org. Biomol. Chem.*, 12(44), pp.8803–8822. Available at: http://xlink.rsc.org/?DOI=C4OB01652A.

Lua, B.L. & Low, B.C., 2005. Cortactin phosphorylation as a switch for actin cytoskeletal network and cell dynamics control. *FEBS letters*, 579(3), pp.577–85. Available at: http://www.ncbi.nlm.nih.gov/pubmed/15670811 [Accessed September 29, 2016].

Lucá, R. et al., 2013. The Fragile X Protein binds mRNAs involved in cancer progression and modulates metastasis formation. *EMBO Molecular Medicine*, 5(10), pp.1523–1536.

Lüders, J. & Stearns, T., 2007. Microtubule-organizing centres: a re-evaluation. *Nature reviews. Molecular cell biology*, 8(2), pp.161–167.

Lukong, K.E. et al., 2008. RNA-binding proteins in human genetic disease. *Trends in genetics : TIG*, 24(8), pp.416–425.

Lutz, M., 2007. *Learning Python*, Available at:

http://books.google.com/books?hl=en%7B&%7Dlr=%7B&%7Did=ePyeNz2Eoy8C%7B&%7Doi=fnd%7B&%7Dpg=PR5%7B&%7Ddq=Learning+Python%7B&%7Dots=Mav78L2gAg%7B&%7Dsig=3N8twtfE36sZcke9Zj2MVzB-pkE$%5C$nhttp://linkinghub.elsevier.com/retrieve/pii/0019103589900778%5Cnhttp://books.google.com/books?hl=en&lr=&.

Maag, D. et al., 2005. A conformational change in the eukaryotic translation preinitiation complex and release of eIF1 signal recognition of the start codon. *Molecular Cell*, 17(2), pp.265–275.

Mader, S. et al., 1995. The translation initiation factor eIF-4E binds to a common motif shared by the translation factor eIF-4 gamma and the translational repressors 4E-binding proteins. *Molecular and cellular biology*, 15(9), pp.4990–7. Available at: http://www.pubmedcentral.nih.gov/articlerender.fcgi?artid=230746&tool=pmcentrez&rendertype=abstract.

Mahboobi, S.H., Javanpour, A.A. & Mofrad, M.R.K., 2015. The interaction of RNA helicase DDX3 with HIV-1 Rev-CRM1-RanGTP complex during the HIV replication cycle. *PLoS ONE*, 10(2).

Manders, E.M.M., Verbeek, F.J. & Ate, J.A., 1993. Measurement of co-localisation of objects in dual-colour confocal images. *Journal of microscopy*, 169(3), pp.375–382.

Marcotrigiano, J. et al., 1999. Cap-dependent translation initiation in eukaryotes is regulated by a molecular mimic of eIF4G. *Molecular Cell*, 3(6), pp.707–716.

Marcotrigiano, J. et al., 1997. Cocrystal Structure of the Messenger RNA 5' Cap-Binding Protein (eIF4E) Bound to 7-methyl-GDP. *Nucleic acids symposium series*, 89(36), pp.8–11.

Martinez-Quiles, N. et al., 2004. Erk/Src phosphorylation of cortactin acts as a switch on-switch off mechanism that controls its ability to activate N-WASP. *Molecular and cellular biology*, 24(12), pp.5269–80. Available at: http://www.pubmedcentral.nih.gov/articlerender.fcgi?artid=419870&tool=pmcentrez&rendertype=abstract.

Mathews, M.B., Sonenberg, N. & Hershey, J.W.B., 2007. 1 Origins and Principles of Translational Control. *Cold Spring Harbor Monograph Archive*, 48, pp.1–40. Available at:

https://cshmonographs.org/csh/index.php/monographs/article/view/3270.

Matsuo, H. et al., 1997. Structure of translation factor eIF4E bound to m7GDP and interaction with 4E-binding protein. *Nature structural biology*, 4(9), pp.717–24. Available at: http://www.ncbi.nlm.nih.gov/pubmed/9302999 [Accessed February 22, 2016].

Mattaj, I.W. & Englmeier, L., 1998. Nucleocytoplasmic transport: the soluble phase. *Annual review of biochemistry*, 67, pp.265–306.

McKendrick, L. et al., 2001. Phosphorylation of eukaryotic initiation factor 4E (eIF4E) at Ser209 is not required for protein synthesis in vitro and in vivo. *Eur J Biochem*, 268(20), p.5375–85. Available at: http://www.ncbi.nlm.nih.gov/htbin-post/Entrez/query?db=m&form=6&dopt=r&uid=11606200.

McKendrick, L. et al., 2001. Truncated initiation factor eIF4G lacking an eIF4E binding site can support capped mRNA translation. *EMBO Journal*, 20(15), pp.4233–4242.

McKinney, W., 2010. Data Structures for Statistical Computing in Python. *Proceedings of the 9th Python in Science Conference*, pp.51–56. Available at: http://conference.scipy.org/proceedings/scipy2010/mckinney.html.

Medioni, C., Mowry, K. & Besse, F., 2012. Principles and roles of mRNA localization in animal development. *Development*, 139(18), pp.3263–3276.

Microscopy, S.I., Depletion, S.E. & Microscopy, P.L., 2010. Sample Preparation Guidelines for Photo-activated Localization Microscopy (PALM) Imaging.

Mili, S., Moissoglu, K. & Macara, I.G., 2008. Genome-wide screen reveals APC-associated RNAs enriched in cell protrusions. *Nature*, 453(7191), pp.115–9. Available at: http://www.ncbi.nlm.nih.gov/pubmed/18451862 [Accessed September 29, 2016].

Millard, T.H., Sharp, S.J. & Machesky, L.M., 2004. Signalling to actin assembly via the WASP (Wiskott-Aldrich syndrome protein)-family proteins and the Arp2/3 complex. *The Biochemical journal*, 380(Pt 1), pp.1–17.

Minsky, M., 1988. Memoir on inventing the confocal scanning microscope. *Scanning*, 10(4), pp.128–138. Available at: http://doi.wiley.com/10.1002/sca.4950100403 [Accessed February 15, 2016].

Morley, S.J. & Pain, V.M., 2001. Proteasome inhibitors and immunosuppressive

drugs promote the cleavage of eIF4GI and eIF4GII by caspase-8-independent mechanisms in Jurkat T cell lines. *FEBS Letters*, 503(2–3), pp.206–212.

Mouneimne, G. et al., 2004. Phospholipase C and cofilin are required for carcinoma cell directionality in response to EGF stimulation. *The Journal of cell biology*, 166(5), pp.697–708. Available at: http://www.ncbi.nlm.nih.gov/pubmed/15337778 [Accessed September 29, 2016].

Mukaka, M.M., 2012. Statistics corner: A guide to appropriate use of correlation coefficient in medical research. *Malawi Medical Journal*, 24(3), pp.69–71.

Napoli, I. et al., 2008. The Fragile X Syndrome Protein Represses Activity-Dependent Translation through CYFIP1, a New 4E-BP. *Cell*, 134(6), pp.1042–1054.

Narayanan, U. et al., 2007. FMRP phosphorylation reveals an immediate-early signaling pathway triggered by group I mGluR and mediated by PP2A. *The Journal of neuroscience : the official journal of the Society for Neuroscience*, 27(52), pp.14349–14357.

Narayanan, U., Nalavadi, V., Nakamoto, M., Thomas, G., Ceman, S., Bassell, G.J., et al., 2008. S6K1 phosphorylates and regulates fragile X mental retardation protein (FMRP) with the neuronal protein synthesis-dependent mammalian target of rapamycin (mTOR) signaling cascade. *Journal of Biological Chemistry*, 283(27), pp.18478–18482.

Narayanan, U., Nalavadi, V., Nakamoto, M., Thomas, G., Ceman, S., Bassell, G.J., et al., 2008. S6K1 Phosphorylates and Regulates Fragile X Mental Retardation Protein (FMRP) with the Neuronal Protein Synthesis-dependent Mammalian Target of Rapamycin (mTOR) Signaling Cascade * □ S.

Narumiya, S., Tanji, M. & Ishizaki, T., 2009. Rho signaling, ROCK and mDia1, in transformation, metastasis and invasion. *Cancer metastasis reviews*, 28(1–2), pp.65–76. Available at: http://www.ncbi.nlm.nih.gov/pubmed/19160018 [Accessed September 29, 2016].

Nelson, W.J., 2009. Remodeling epithelial cell organization: transitions between front-rear and apical-basal polarity. *Cold Spring Harbor perspectives in*

biology, 1(1), p.a000513. Available at: http://www.ncbi.nlm.nih.gov/pubmed/20066074 [Accessed September 29, 2016].

Neumann, F.R. & Nurse, P., 2007. Nuclear size control in fission yeast. *Journal of Cell Biology*, 179(4), pp.593–600.

Newman, G.E. & Scholl, B.J., 2012. Bar graphs depicting averages are perceptually misinterpreted: The within-the-bar bias. *Psychonomic Bulletin & Review*, 19, pp.601–607. Available at: http://perception.research.yale.edu/preprints/Newman-Scholl-PBR.pdf.

Nishi, K. et al., 1994. Leptomycin B targets a regulatory cascade of crm1, a fission yeast nuclear protein, involved in control of higher order chromosome structure and gene expression. *Journal of Biological Chemistry*, 269(9), pp.6320–6324.

Nygård, O. & Nilsson, L., 1990. Translational dynamics. Interactions between the translational factors, tRNA and ribosomes during eukaryotic protein synthesis. *European journal of biochemistry / FEBS*, 191(1), pp.1–17. Available at: http://www.ncbi.nlm.nih.gov/pubmed/2199194 [Accessed September 25, 2016].

Ober, R.J., Ram, S. & Ward, E.S., 2004. Localization accuracy in single-molecule microscopy. *Biophysical journal*, 86(2), pp.1185–1200. Available at: http://dx.doi.org/10.1016/S0006-3495(04)74193-4.

Oikawa, T. et al., 2004. PtdIns(3,4,5)P3 binding is necessary for WAVE2-induced formation of lamellipodia. *Nature cell biology*, 6(5), pp.420–6. Available at: http://www.ncbi.nlm.nih.gov/pubmed/15107862 [Accessed September 29, 2016].

Parsyan, A. et al., 2011. mRNA helicases: the tacticians of translational control. *Nature reviews. Molecular cell biology*, 12(4), pp.235–45. Available at: http://www.ncbi.nlm.nih.gov/pubmed/21427765.

Parsyan, A. et al., 2009. The helicase protein DHX29 promotes translation initiation, cell proliferation, and tumorigenesis. *Proceedings of the National Academy of Sciences of the United States of America*, 106(52), pp.22217–22222.

Pause, A. et al., 1994. Insulin-dependent stimulation of protein synthesis by phosphorylation of a regulator of 5'-cap function. *Nature*, 371(6500),

pp.762–7. Available at: http://www.nature.com/nature/journal/v371/n6500/pdf/371762a0.pdf [Accessed February 11, 2016].

Pavitt, G.D., 2005. eIF2B , a mediator of general and gene-specific translational control. , pp.1487–1492.

Pengguang, Wu., Brand, L., 1994. Resonance Energy Transfer: Methods and Applications. , pp.218, 1–13.

Perez, Fernando and Granger, B.E. rpos., 2007. {IP}ython: a System for Interactive Scientific Computing. *Computing in Science and Engineering*, 9, pp.21–29.

Pestka, S., 1971. INIDBITORS OF RIBOSOME FUNCTIONS.

Pestova, T. V et al., 2001. Molecular mechanisms of translation initiation in eukaryotes. *Proceedings of the National Academy of Sciences of the United States of America*, 98(13), pp.7029–36. Available at: http://www.pubmedcentral.nih.gov/articlerender.fcgi?artid=34618&tool=pmcentrez&rendertype=abstract.

Peter, M.E. & Krammer, P.H., 2003. The CD95(APO-1/Fas) DISC and beyond. *Cell Death & Differentiation*, 10(1), pp.26–35. Available at: http://www.nature.com.gate1.inist.fr/cdd/journal/v10/n1/abs/4401186a.html%5Cnhttp://www.nature.com.gate1.inist.fr/cdd/journal/v10/n1/pdf/4401186a.pdf.

Pickering, B.M. & Willis, A.E., 2005. The implications of structured 5’ untranslated regions on translation and disease. *Seminars in Cell and Developmental Biology*, 16(1), pp.39–47.

Pisareva, V.P. et al., 2008. Translation Initiation on Mammalian mRNAs with Structured 5???UTRs Requires DExH-Box Protein DHX29. *Cell*, 135(7), pp.1237–1250. Available at: http://dx.doi.org/10.1016/j.cell.2008.10.037.

Pyronnet, S. et al., 1999. Human eukaryotic translation initiation factor 4G (eIF4G) recruits Mnk1 to phosphorylate eIF4E. *EMBO Journal*, 18(1), pp.270–279.

R Development Core Team, R., 2011. *R: A Language and Environment for Statistical Computing*, Available at: http://www.r-project.org.

Ramalingam, S. et al., 2014. First MNKs degrading agents block phosphorylation of eIF4E, induce apoptosis, inhibit cell growth, migration

and invasion in triple negative and Her2-overexpressing breast cancer cell lines. *Oncotarget*, 5(2), pp.530–43. Available at: http://www.pubmedcentral.nih.gov/articlerender.fcgi?artid=3964227&tool=pmcentrez&rendertype=abstract.

Rathinam, R. & Alahari, S.K., 2010. Important role of integrins in the cancer biology. *Cancer and Metastasis Reviews*, 29(1), pp.223–237.

Rauschendorf, M.A. et al., 2011. Complex transcriptional control of the AZFa gene DDX3Y in human testis. *International Journal of Andrology*, 34(1), pp.84–96.

Rauschendorf, M.A. et al., 2014. DDX3X, the X homologue of AZFa gene DDX3Y, expresses a complex pattern of transcript variants only in the male germ line. *Molecular Human Reproduction*, 20(12), pp.1208–1222.

Rees, E.J. et al., 2012. Blind assessment of localisation microscope image resolution. *Optical Nanoscopy*, 1(1), p.1. Available at: http://dx.doi.org/10.1186/2192-2853-1-12.

Rich, J.W. et al., 2008. Multi-scale clean: a comparison of its performance against classical clean on galaxies using THINGS. , pp.2897–2920. Available at: http://hdl.handle.net/2299/2708.

Ridley, A.J. et al., 2003. Cell migration: integrating signals from front to back. *Science (New York, N.Y.)*, 302(5651), pp.1704–1709.

Rieder, C.L. & Cole, R.W., 2002. Cold-Shock and the Mammalian Cell Cycle. *Cell Cycle*, 1(3), pp.169–175. Available at: http://www.tandfonline.com/doi/abs/10.4161/cc.1.3.119.

Rogers, G.W. et al., 2001. Modulation of the Helicase Activity of eIF4A by eIF4B, eIF4H, and eIF4F. *Journal of Biological Chemistry*, 276(33), pp.30914–30922.

Rosner, a & Rinkevich, B., 2007. The DDX3 subfamily of the DEAD box helicases: divergent roles as unveiled by studying different organisms and in vitro assays. *Current medicinal chemistry*, 14(23), pp.2517–2525.

Rossant, C., 2013. *Learning IPython for Interactive Computing and Data Visualization*,

Rosten, E., Jones, G.E. & Cox, S., 2013. ImageJ plug-in for Bayesian analysis of blinking and bleaching. *Nature methods*, 10(2), pp.97–8. Available at: http://www.ncbi.nlm.nih.gov/pubmed/23361088.

Roux, P.P. et al., 2007. RAS/ERK signaling promotes site-specific ribosomal protein S6 phosphorylation via RSK and stimulates cap-dependent translation. *Journal of Biological Chemistry*, 282(19), pp.14056–14064.

Royer, C. & Lu, X., 2011. Epithelial cell polarity: a major gatekeeper against cancer? *Cell death and differentiation*, 18(9), pp.1470–7. Available at: http://www.ncbi.nlm.nih.gov/pubmed/21617693 [Accessed September 29, 2016].

Rozovsky, N., Butterworth, A.C. & Moore, M.J., 2008. Interactions between eIF4AI and its accessory factors eIF4B and eIF4H. *RNA (New York, N.Y.)*, 14(10), pp.2136–48. Available at: http://www.pubmedcentral.nih.gov/articlerender.fcgi?artid=2553726&tool=pmcentrez&rendertype=abstract.

Rust, M.J., Bates, M. & Zhuang, X., 2006. Sub-diffraction-limit imaging by stochastic optical reconstruction microscopy (STORM). *Nature methods*, 3(10), pp.793–795.

Ruxton, G.D., 2006. The unequal variance t-test is an underused alternative to Student's t-test and the Mann-Whitney U test. *Behavioral Ecology*, 17(4), pp.688–690.

Samal, S.K. et al., 2015. Ketorolac salt is a newly discovered DDX3 inhibitor to treat oral cancer. *Scientific reports*, 5, p.9982. Available at: http://www.nature.com/srep/2015/150424/srep09982/full/srep09982.html.

Sapsford, K.E. et al., 2006. Biosensing with Luminescent Semiconductor Quantum Dots. *Sensors*, 6(8), pp.925–953.

Savage, R.S. & Oliver, S., 2005. Bayesian methods of astronomical source extraction. , pp.1339–1346. Available at: http://arxiv.org/abs/astro-ph/0512597.

Schalm, S.S. & Blenis, J., 2002. Identification of a conserved motif required for mTOR signaling. *Current Biology*, 12(8), pp.632–639.

Scheffler, J.M., Schiefermeier, N. & Huber, L. a., 2014. *Mild fixation and permeabilization protocol for preserving structures of endosomes, focal adhesions, and actin filaments during immunofluorescence analysis* 1st ed., Elsevier Inc. Available at: http://dx.doi.org/10.1016/B978-0-12-397925-4.00006-7.

Schenck, A. et al., 2003. CYFIP/Sra-1 controls neuronal connectivity in

Drosophila and links the Rac1 GTPase pathway to the fragile X protein. *Neuron*, 38(6), pp.887–898.

Scheper, G.C. et al., 2002. Phosphorylation of eukaryotic initiation factor 4E markedly reduces its affinity for capped mRNA. *Journal of Biological Chemistry*, 277(5), pp.3303–3309.

Schermelleh, L., Heintzmann, R. & Leonhardt, H., 2010. A guide to super-resolution fluorescence microscopy. *Journal of Cell Biology*, 190(2), pp.165–175.

Schindelin, J. et al., 2012. Fiji: an open-source platform for biological-image analysis. *Nature methods*, 9(7), pp.676–82. Available at: http://www.pubmedcentral.nih.gov/articlerender.fcgi?artid=3855844&tool=pmcentrez&rendertype=abstract [Accessed July 9, 2014].

SciPy Community, 2013. SciPy Reference Guide 0.13.0. , p.1229.

Sekar, R.B. & Periasamy, A., 2003. Fluorescence resonance energy transfer (FRET) microscopy imaging of live cell protein localizations. *Journal of Cell Biology*, 160(5), pp.629–633.

Sekiguchi, T. et al., 2004. Human DDX3Y, the Y-encoded isoform of RNA helicase DDX3, rescues a hamster temperature-sensitive ET24 mutant cell line with a DDX3X mutation. *Experimental Cell Research*, 300(1), pp.213–222.

Sen, N.D. et al., 2015. Genome-wide analysis of translational efficiency reveals distinct but overlapping functions of yeast DEAD-box RNA helicases Ded1 and eIF4A. *Genome research*, 25, pp.1196–1205.

Shahbabian, K. & Chartrand, P., 2012. Control of cytoplasmic mRNA localization. *Cellular and Molecular Life Sciences*, 69(4), pp.535–552.

Shalini, S. et al., 2014. Old, new and emerging functions of caspases. *Cell death and differentiation*, 22(4), pp.526–539. Available at: http://dx.doi.org/10.1038/cdd.2014.216.

Sharma, D. & Bhattacharya, J., 2010. Evolutionary constraints acting on ddx3x protein potentially interferes with rev-mediated nuclear export of hiv-1 rna. *PLoS ONE*, 5(3).

Shestakova, E.A., Singer, R.H. & Condeelis, J., 2001. The physiological significance of beta -actin mRNA localization in determining cell polarity and directional motility. *Proceedings of the National Academy of Sciences*

of the United States of America, 98(13), pp.7045–50. Available at: http://www.pnas.org/content/98/13/7045.abstract.

Shih, J.-W. et al., 2008. Candidate tumor suppressor DDX3 RNA helicase specifically represses cap-dependent translation by acting as an eIF4E inhibitory protein. *Oncogene*, 27(5), pp.700–14. Available at: http://www.ncbi.nlm.nih.gov/pubmed/17667941.

Shih, J.-W. et al., 2012. Critical roles of RNA helicase DDX3 and its interactions with eIF4E/PABP1 in stress granule assembly and stress response. *The Biochemical journal*, 441(1), pp.119–29. Available at: http://www.ncbi.nlm.nih.gov/pubmed/21883093.

Sibarita, J.B., 2005. Deconvolution microscopy. *Advances in Biochemical Engineering/Biotechnology*, 95, pp.201–243.

Sleeman, J.P. & Thiery, J.P., 2011. SnapShot: The Epithelial-Mesenchymal Transition. *Cell*, 145(1), p.162–162.e1. Available at: http://linkinghub.elsevier.com/retrieve/pii/S0092867411003060.

Slentz-Kesler, K. et al., 2000. Identification of the human Mnk2 gene (MKNK2) through protein interaction with estrogen receptor beta. *Genomics*, 69(1), pp.63–71. Available at: http://www.ncbi.nlm.nih.gov/pubmed/11013076 [Accessed September 28, 2016].

Smith, A., 2012. SUSSEXtractor in HIPE. , (April), pp.1–14.

Snay-Hodge, C.A. et al., 1998. Dbp5p/Rat8p is a yeast nuclear pore-associated DEAD-box protein essential for RNA export. *EMBO Journal*, 17(9), pp.2663–2676.

Söderberg, O. et al., 2006. Direct observation of individual endogenous protein complexes in situ by proximity ligation. *Nature methods*, 3(12), pp.995–1000. Available at: http://www.ncbi.nlm.nih.gov/pubmed/17072308 [Accessed April 3, 2015].

Sonenberg, N. & Hinnebusch, A.G., 2009. Regulation of Translation Initiation in Eukaryotes: Mechanisms and Biological Targets. *Cell*, 136(4), pp.731–745. Available at: http://dx.doi.org/10.1016/j.cell.2009.01.042.

Song, X. et al., 2006. Initiation of cofilin activity in response to EGF is uncoupled from cofilin phosphorylation and dephosphorylation in carcinoma cells. *Journal of cell science*, 119(Pt 14), pp.2871–2881.

Sossey-Alaoui, K., Li, X., et al., 2005. WAVE3-mediated cell migration and

lamellipodia formation are regulated downstream of phosphatidylinositol 3-kinase. *The Journal of biological chemistry*, 280(23), pp.21748–55. Available at: http://www.ncbi.nlm.nih.gov/pubmed/15826941 [Accessed September 29, 2016].

Sossey-Alaoui, K., Ranalli, T.A., et al., 2005. WAVE3 promotes cell motility and invasion through the regulation of MMP-1, MMP-3, and MMP-9 expression. *Experimental cell research*, 308(1), pp.135–45. Available at: http://www.ncbi.nlm.nih.gov/pubmed/15907837 [Accessed September 29, 2016].

Soto-Rifo, R. et al., 2012. DEAD-box protein DDX3 associates with eIF4F to promote translation of selected mRNAs. *The EMBO journal*, 31(18), pp.3745–56. Available at: http://www.pubmedcentral.nih.gov/articlerender.fcgi?artid=3442272&tool=pmcentrez&rendertype=abstract.

Stead, R.L. & Proud, C.G., 2013. Rapamycin enhances eIF4E phosphorylation by activating MAP kinase-interacting kinase 2a (Mnk2a). *FEBS Letters*, 587(16), pp.2623–2628. Available at: http://dx.doi.org/10.1016/j.febslet.2013.06.045.

Stokes, G.G., 1853. On the Change of Refrangibility of Light. No. II. *Philosophical Transactions of the Royal Society of London*, 143(0), pp.385–396.

Stryer, L., 1978. FLUORESCENCE ENERGY TRANSFER AS A SPECTROSCOPIC RULER. *Annual Review of Biochemisiry*, 47(5), p.819.

Sun, M. et al., 2011. The role of DDX3 in regulating Snail. *Biochimica et Biophysica Acta (BBA) - Molecular Cell Research*, 1813(3), pp.438–447. Available at: http://linkinghub.elsevier.com/retrieve/pii/S016748891100005X.

Szliszka, E. et al., 2009. TRAIL-induced apoptosis and expression of death receptor TRAIL-R1 and TRAIL-R2 in bladder cancer cells. *Folia Histochemica et Cytobiologica*, 47(4), pp.579–585.

Takada, Y., Ye, X.J. & Simon, S., 2007. The integrins. *Genome Biology*, 8(5).

Takizawa, P. a et al., 1997. Actin-dependent localization of an RNA encoding a cell-fate determinant in yeast. *Nature*, 389(6646), pp.90–93.

Taniguchi, I., Mabuchi, N. & Ohno, M., 2014. HIV-1 Rev protein specifies the

viral RNA export pathway by suppressing TAP/NXF1 recruitment. *Nucleic Acids Research*, 42(10), pp.6645–6658.

Tanious, F. a et al., 1992. DAPI (4',6-diamidino-2-phenylindole) binds differently to DNA and RNA: minor-groove binding at AT sites and intercalation at AU sites. *Biochemistry*, 31(12), pp.3103–3112.

Tarun, S.Z. & Sachs, A.B., 1996. Association of the yeast poly(A) tail binding protein with translation initiation factor eIF-4G. *The EMBO journal*, 15(24), pp.7168–77. Available at: http://www.pubmedcentral.nih.gov/articlerender.fcgi?artid=452544&tool=pmcentrez&rendertype=abstract.

Taylor, A.M. et al., 1975. Ataxia telangiectasia: a human mutation with abnormal radiation sensitivity. *Nature*, 258(5534), pp.427–9. Available at: http://www.ncbi.nlm.nih.gov/pubmed/1196376 [Accessed November 27, 2015].

Teo, T., Yang, Y., et al., 2015. An integrated approach for discovery of highly potent and selective Mnk inhibitors: Screening, synthesis and SAR analysis. *European Journal of Medicinal Chemistry*, 103, pp.539–550. Available at: http://dx.doi.org/10.1016/j.ejmech.2015.09.008.

Teo, T., Lam, F., et al., 2015. Pharmacologic Inhibition of MNKs in Acute Myeloid Leukemia. *Molecular pharmacology*, 88(2), pp.380–9. Available at: http://www.ncbi.nlm.nih.gov/pubmed/26044548.

Terrell, G.R. & Scott, D.W., 1992. Variable Kernel Density Estimation. *The Annals of Statistics*, 20(3), pp.1236–1265. Available at: http://projecteuclid.org/euclid.aos/1176348768.

Thomas, G., Siegmann, M. & Gordon, J., 1979. Multiple phosphorylation of ribosomal protein S6 during transition of quiescent 3T3 cells into early G1, and cellular compartmentalization of the phosphate donor. *Proceedings of the National Academy of Sciences of the United States of America*, 76(8), pp.3952–6. Available at: http://www.ncbi.nlm.nih.gov/pubmed/291054 [Accessed September 25, 2016].

Thompson, S.P., 2005. *Treatise on Light, by Christiaan Huygens, Translated by Silvanus P. Thompson*, www.gutenberg.net.

Tomoo, K. et al., 2005. Structural basis for mRNA Cap-Binding regulation of eukaryotic initiation factor 4E by 4E-binding protein, studied by

spectroscopic, X-ray crystal structural, and molecular dynamics simulation methods. *Biochimica et Biophysica Acta - Proteins and Proteomics*, 1753(2), pp.191–208.

Trachsel, H. & Staehelin, T., 1978. Binding and release of eukaryotic initiation factor eIF-2 and GTP during protein synthesis initiation. *Proceedings of the National Academy of Sciences of the United States of America*, 75(1), pp.204–208.

Ueda, T. et al., 2010. Combined deficiency for MAP kinase-interacting kinase 1 and 2 (Mnk1 and Mnk2) delays tumor development. *Proceedings of the National Academy of Sciences of the United States of America*, 107(32), pp.13984–90. Available at: http://www.pnas.org/content/107/32/13984.long.

Uruno, T. et al., 2001. Activation of Arp2/3 complex-mediated actin polymerization by cortactin. *Nature cell biology*, 3(3), pp.259–266.

Valentin-Vega, Y.A. et al., 2016. Cancer-associated DDX3X mutations drive stress granule assembly and impair global translation. *Scientific Reports*, 6(April), p.25996. Available at: http://www.nature.com/articles/srep25996.

Villa, N. et al., 2013. Human eukaryotic initiation factor 4G (eIF4G) protein binds to eIF3c, -d, and -e to promote mRNA recruitment to the ribosome. *Journal of Biological Chemistry*, 288(46), pp.32932–32940.

Van Der Walt, S., Colbert, S.C. & Varoquaux, G., 2011. The NumPy array: A structure for efficient numerical computation. *Computing in Science and Engineering*, 13(2), pp.22–30.

Wang, W. et al., 2006. The activity status of cofilin is directly related to invasion, intravasation, and metastasis of mammary tumors. *Journal of Cell Biology*, 173(3), pp.395–404.

Waskiewicz, A.J. et al., 1997. Mitogen-activated protein kinases activate the serine/threonine kinases Mnk1 and Mnk2. *The EMBO journal*, 16(8), pp.1909–20. Available at: http://www.pubmedcentral.nih.gov/articlerender.fcgi?artid=1169794&tool=pmcentrez&rendertype=abstract [Accessed February 29, 2016].

Waskiewicz, A.J. et al., 1999. Phosphorylation of the cap-binding protein eukaryotic translation initiation factor 4E by protein kinase Mnk1 in vivo. *Molecular and cellular biology*, 19(3), pp.1871–1880.

Wassler, M. et al., 1987. Differential permeabilization of membranes by saponin

treatment of isolated rat hepatocytes. Release of secretory proteins. *The Biochemical journal*, 247(2), pp.407–415.

Weaver, A.M. et al., 2001. Cortactin promotes and stabilizes Arp2/3-induced actin filament network formation. *Current Biology*, 11(5), pp.370–374.

Webb, N.R. et al., 1984. Purification of the messenger RNA cap-binding protein using a new affinity medium. *Biochemistry*, 23(2), pp.177–81. Available at: http://www.ncbi.nlm.nih.gov/pubmed/6696877.

Webster, M., Witkin, K.L. & Cohen-Fix, O., 2009. Sizing up the nucleus: nuclear shape, size and nuclear-envelope assembly. *Journal of Cell Science*, 122(10), pp.1477–1486. Available at: http://jcs.biologists.org/content/122/10/1477.full.

Weibrecht, I. et al., 2010. Proximity ligation assays: a recent addition to the proteomics toolbox. *Expert review of proteomics*, 7(3), pp.401–409.

Welch, A.B.L., 1947. The Generalization of “Student”s’ Problem when Several Different Population Variances are Involved. *Biometrika*, 34(1), pp.28–35.

Willett, M. et al., 2010. Localization of ribosomes and translation initiation factors to talin/beta3-integrin-enriched adhesion complexes in spreading and migrating mammalian cells. *Biology of the cell / under the auspices of the European Cell Biology Organization*, 102(5), pp.265–276.

Willett, M. et al., 2013. mRNA encoding WAVE-Arp2/3-associated proteins is co-localized with foci of active protein synthesis at the leading edge of MRC5 fibroblasts during cell migration. *The Biochemical journal*, 452(1), pp.45–55. Available at: http://www.ncbi.nlm.nih.gov/pubmed/23452202.

Willett, M. et al., 2011. Translation initiation factors and active sites of protein synthesis co-localize at the leading edge of migrating fibroblasts. *The Biochemical journal*, 438(1), pp.217–227.

With, S., 1945. Wilcoxon – Mann – Whitney. *Statistics surveys*, 4, pp.1–3. Available at: http://www.ncbi.nlm.nih.gov/pubmed/20826766.

Wortzel, I. & Seger, R., 2011. The ERK Cascade: Distinct Functions within Various Subcellular Organelles. *Genes & cancer*, 2(3), pp.195–209.

Yamaguchi, H. & Condeelis, J., 2007. Regulation of the actin cytoskeleton in cancer cell migration and invasion. *Biochimica et biophysica acta*, 1773(5), pp.642–52. Available at: http://www.ncbi.nlm.nih.gov/pubmed/16926057 [Accessed September 29, 2016].

Yedavalli, V.S.R.K. et al., 2004. Requirement of DDX3 DEAD box RNA helicase for HIV-1 Rev-RRE export function. *Cell*, 119(3), pp.381–392.

Yilmaz, M. & Christofori, G., 2009. EMT, the cytoskeleton, and cancer cell invasion. *Cancer metastasis reviews*, 28(1–2), pp.15–33. Available at: http://www.ncbi.nlm.nih.gov/pubmed/19169796 [Accessed September 29, 2016].

Yoshida, M. et al., 1990. Effects of Leptomycin B on the Cell Cycle of Fibroblasts and Fission Yeast Cells. *EXPERIMENTAL CELL RESEARCH*, 187, pp.0–156.

Zamir, E. & Geiger, B., 2001. Molecular complexity and dynamics of cell-matrix adhesions. *Journal of cell science*, 114(Pt 20), pp.3583–3590.

Zhang, S. et al., 2015. LK6/Mnk2a is a new kinase of alpha synuclein phosphorylation mediating neurodegeneration. *Scientific reports*, 5, p.12564. Available at: http://www.ncbi.nlm.nih.gov/pubmed/26220523%5Cnhttp://www.pubmedcentral.nih.gov/articlerender.fcgi?artid=PMC4518213.

Zhang, Y., Li, Y. & Yang, D.-Q., 2008. Phosphorylation of eIF-4E positively regulates formation of the eIF-4F translation initiation complex following DNA damage. *Biochemical and biophysical research communications*, 367(1), pp.54–9. Available at: http://www.ncbi.nlm.nih.gov/pubmed/18164262 [Accessed September 28, 2016].

Zhou, M., Li, Q. & Wang, R., 2016. Current Experimental Methods for Characterizing Protein-Protein Interactions. *ChemMedChem*, 11(8), pp.738–756.

Zigmond, S., 2004. Formin' adherens junctions. *Nature Cell Biology*, 6(1), pp.12–14.

Zilfou, J.T. & Lowe, S.W., 2009. Tumor suppressive functions of p53. *Cold Spring Harbor perspectives in biology*, 1(5), pp.1–12.

Zoncu, R., Efeyan, A. & Sabatini, D.M., 2011. mTOR: from growth signal integration to cancer, diabetes and ageing. *Nature reviews. Molecular cell biology*, 12(1), pp.21–35. Available at: http://dx.doi.org/10.1038/nrm3025.

10 Appendix

10.1 Computer Code

Latest releases of all code, including 4PLAY, PLAY and PLAYmate reside with the Morley Laboratory.

10.1.1 Image Drift calculator

An ImageJ Macro

```
// "Image Drift calculator version1" by Simon Cooper
//  (Utilising simple moving averages)

Dialog.create("Sliding 'averaging window' size");
Dialog.addNumber("Average each", 5, 0, 3, "frames");
Dialog.addNumber("Skip ahead", 10, 0, 3, "frames in the movie to take
each measurement");
Dialog.addMessage("(no averaging takes place for a window size of 1)")
Dialog.addCheckbox("Add bicubic Interpolation (and 10x scaling to
coordinates)",false);
Dialog.show();
winSize=Dialog.getNumber();
HiRes=Dialog.getCheckbox();
skipSize=Dialog.getNumber();

if (HiRes) {
run("Scale...", "x=10 y=10 z=1.0 interpolation=Bicubic average process
create");
run("Set... ", "zoom=200");
}

duplicateStackID = getImageID();
run("Enhance Contrast", "saturated=0.35");

n = nSlices();
for (i=1; i<=n; i+=skipSize) {
      selectImage(duplicateStackID);
      setSlice(i);
      j=i+winSize;
      run("Z Project...", "start=i stop=j projection=[Average
Intensity]");
      averagedFrames = getImageID();
      ans = getMinMax();
      close();
```

```
            xmin=ans[0];
            ymin=ans[1];
            pxlmin=ans[2];
            xmax=ans[3];
            ymax=ans[4];
            pxlmax=ans[5];

      print("slice ,"+i+", ,x,"+xmin+", ,y,"+ymin+", ,Minimum pixel
Value,"+pxlmin+", ,, ,x,"+xmax+", ,y,"+ymax+", ,Max pixel
Value,"+pxlmax);
}

function getMinMax() {
// Find Max and Min pixel values in each slice of a stack.

width = getWidth();
height = getHeight();
minVal = 9999999999999;
maxVal = 0;

      for (x=0; x<width; x++) {
            for (y=0; y<height; y++) {
                  val = getPixel(x,y);

                  if (val < minVal) {
                        minVal = val;
                        minValx = x;
                        minValy = y;
                        }
                  if (val > maxVal) {
                        maxVal = val;
                        maxValx = x;
                        maxValy = y;
                        }
                  }
            }

            pxlValues = newArray(6);
            pxlValues[0] = minValx;
            pxlValues[1] = minValy;
            pxlValues[2] = minVal;
            pxlValues[3] = maxValx;
            pxlValues[4] = maxValy;
            pxlValues[5] = maxVal;
            return pxlValues;
      }
```